Semi-active Control of Earthquake Induced Vibrations in Structures using MR Dampers: Algorithm Development, Experimental Verification and Benchmark Applications

A THESIS

SUBMITTED FOR THE DEGREE OF

Doctor of Philosophy

IN THE FACULTY OF ENGINEERING

by

Shaikh Faruque Ali

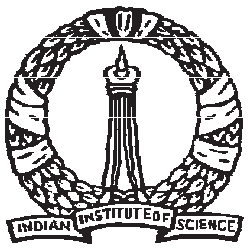

Department of Civil Engineering

Indian Institute of Science

BANGALORE – 560 012

July 2008

To

My Parents
and
my wife

Acknowledgements

I have been fortunate to have had the opportunity to collaborate with a broad range of faculty, students, and visitors during my graduate days at IISc. Its time to say thanks to all.

It has been a great opportunity and honour to work under the guidance of Prof. Ananth Ramaswamy. I am deeply indebted to him for providing me with the unique opportunity to work in the research area of structural control technology and also for enlightening me in his unique way of approaching the research problem. His valuable guidance, passion towards experiments, unlimited enthusiasm and optimistic attitude has always been a source of inspiration to me. The freedom I enjoyed and the productive years I spent in his association are always a pleasure to remember. I want to express my gratitude to him for his constant support, trust, advice, and patience he has shown, especially during the write-up of this thesis. His passion for research is to be commended and worth emulating. I am indebted to him for cajoling me into doing experiments and thus opening a whole new world of excitement for me.

The experiments would not have been completed without the MR dampers, which were provided by Prof. Anil K. Agrawal of City College of New York, NY. I would also like to appreciate the detailed discussions we shared during his presence in the institute as a visiting faculty in 2006 and thereafter in his visits to the institute.

I would like to present my special thanks to Mr. Shanta Kumar, Mr. S. Venkatesha and Mr. Vikash Khatri, who have helped me to finish my experimental work. A special thanks to all laboratory workers who have helped me directly/indirectly to carry on my experimental works.

The support, encouragement and insight to problems associated with experimental setups, offered at various stages of my experiment by Dr. K. S. Nanjunda Rao are gratefully

acknowledged.

I thank all the instructors who have trained me and set the necessary platform for my research work, especially Prof. C. S. Manohar, Prof. D. Roy, Prof. J. M. Chandrakisen, Prof. P. C. Pandey of Department of Civil Engineering. Special acknowledgement to Dr. Radhakant Padhi of Department of Aerospace Engineering for shaping my knowledge in control engineering and making himself generously available for various technical discussions.

I wish to express my gratitude to the present Chairman Prof. P. P. Mujumdar and previous Chairman Prof. B. K. Raghuprasad, Department of Civil Engineering, for providing the facilities for my work. I thank the staffs of the Civil Engineering Department, JRD Tata Memorial Library, Super-Computer Education and Research Centre (SERC) and also the authorities of Indian Institute of Science, Bangalore, for their timely help.

I have been lucky to have a very enthusiastic, entertaining and helping bunch of friends during my entire stay in IISc. I would like to thank all of them, by name, Dr. A. Shaw, Dr. V. B. Maji, Dr. N. Saha, Dr. T. Sain, Dr. R. Khandelwal, Dr. S. Ghosh, Dr. S. Halder, Biswanath, Neelesh, Vishwas, Manas, Srikant, *etc.*, for their support and the unforgettable hours that I have spent with them in Mini Computer Lab, Gymkhana, Tea board, Coffee board, Faculty club, Cauvery theatre and outskirts of Bangalore.

Words can not help me in expressing my deep sense of gratitude to my parents, who have given me roots and wings, the two important things in life, through their constant encouragement and moral support without which this work would not have materialized. Finally, I owe a special debt to my wife for her understanding and unwavering support throughout the course of this study. I appreciate Sanjukta's patience and the sacrifices that she made all this while.

Abstract

As Civil Engineering structures, *e.g.*, tall buildings, long span bridges, deep water offshore platforms, nuclear power plants, *etc.*, have become more costly, complex and serve more critical functions, the consequences of their failure are catastrophic. Therefore, the protection of these structures against damage induced by large environmental loads, *e.g.*, earthquakes, strong wind gusts and waves, *etc.*, is without doubt, a worldwide priority. However, structures cannot be designed to withstand all possible external loads and some extraordinary loading episodes do occur, leading to damage or even failure of the structure.

Protection of a structure against hazards can be achieved by various means such as modifying structural rigidities, increasing structural damping, and by attaching external devices, known as control devices. Control devices can be deployed either to isolate the structure from external excitation or to absorb input seismic energy to the structure (absorber) so as to mitigate vibration in the primary structure. Seismic base isolation is one such mechanism which isolates a structure from harmful ground excitations.

Seismic base isolation is a widely accepted and implemented structural control mechanism due to its robustness and ease in deployment. Following the Northridge earthquake (1994), and Kobe earthquake (1995), the interest of structural engineers in understanding near-source ground motions has enhanced. Documents published after these earthquakes emphasized the issue of large base displacements because of the use of none or little isolation damping (of viscous type only) prior to these events. More recent studies have investigated analytically and experimentally, the efficiency of various dissipative mechanisms to protect seismic isolated structures from recorded near-source long period, pulse-type, high velocity ground motions. Consequently, hybrid isolation systems, seismic base isolation supplemented with damping mechanisms, have become the focus of current research trend in structural vibration control.

Hybrid base isolation system incorporating passive supplemental damping devices like, viscous fluid dampers, *etc.*, performs satisfactorily in minimizing isolator displacement but at the same time increases superstructure acceleration response. Furthermore, the passive system can be tuned to a particular frequency range and its performance decreases for frequencies of excitation outside the tunning bandwidth. In such a scenario, active control devices in addition to base isolation mechanism provide better performance in reducing base displacement and superstructure acceleration for a broad range of excitation frequencies. Tremendous power requirement and the possibility of power failure during seismic hazards restrict the usage of active systems as a supplemental device.

Semi-active devices provide the robustness of passive devices and adaptive nature of active devices. These characteristics make them better suited for structural control applications. The recent focus is on the development of magnetorheological (MR) dampers as semi-active device for structural vibration control applications. MR dampers provide hysteretic damping and can operate with battery power. The thrust of this thesis is on developing a hybrid base isolation mechanism using MR dampers as a supplemental damping device.

The use of MR damper as a semi-active device involves two steps;

- development of a model to describe the MR damper hysteretic behaviour;
- development of a proper nonlinear control algorithm to monitor MR damper current / voltage supply.

Existing parametric models of MR damper hysteretic behaviour, *e.g.*, Bouc-Wen model, fail to consider the effect of amplitude and frequency of excitation on the device. Recently reported literature has demonstrated the necessity of incorporating amplitude and frequency dependence of MR damper models.

The current/voltage supply as the input variable to the MR damper restricts the direct use of any control algorithms developed for active control of structures. The force predicted by the available control algorithms should be mapped to equivalent current/voltage and then to be fed into the damper. Available semi-active algorithms in the literature used 'on-off' or 'bang-bang' strategy for MR applications due to nonlinear current/voltage-force relation of MR damper. The 'on-off' nature of these algorithms neither provides smooth change in MR damper current/voltage input nor considers all possible current/ voltage values within its

minimum to maximum range. Secondly, these algorithms fail to consider the effect of the MR damper applied and commanded current/voltage dynamics.

The thrust of this dissertation is to develop semi-active control algorithms to monitor MR damper supply current/voltage. The study develops a Bouc-Wen based model to characterize the MR damper hysteretic phenomenon. Experimental results and modeling details have been documented. A fuzzy based intelligent control and two model-based nonlinear control algorithms based on optimal dynamic inversion and integral backstepping have been developed. Performance of the fuzzy logic based intelligent control has been explored using experimental investigation on a three storey base isolated building. Further the application of the proposed controllers on a benchmark building; a benchmark highway bridge and a stay cable vibration reduction have been discussed.

Experimental study has revealed that the performance of optimal FLC is better than manually designed FLC in terms of reducing base displacement and storey accelerations. The performance of both the FLCs (simple FLC and genetic algorithm based optimal FLC) is better than 'passive-off' (zero ampere current supply) and 'passive-on' (one ampere current supply) condition of MR damper applications. The 'passive-off' results have shown higher base displacements with lower storey accelerations, whereas, the 'passive-on' results have reduced base displacement to the least but at the same time increased the storey acceleration too much. The FLC monitored MR damper show a compromise between the two passive conditions. Analytical results confirm these observations. Numerical simulations of the base isolated building with the two model based MR damper control algorithms developed have shown a better performance over FLC and widely used clipped optimal algorithms.

The applications of the proposed semi-active control algorithms (FLC, dynamic inversion and integral backstepping) have shown better performance in comparison to that of control algorithms provided with the benchmark studies.

Contents

List of Tables

List of Figures

Notation and Abbreviations

ALPHABETS

A	Area of cross section of a cable
$A,\ c_0,\ k_0$	Parameters of Bouc-Wen hysteretic model for MR damper
$A,\ B,\ E$ $C,\ D,\ F$	System state matrices
B_c	Control force influence matrix
c_b	Damping of the base isolator
c_i	Damping of i^{th} floor of the superstructure
$C,\ C_a$	Damping matrix of the superstructure
C_d	Damping coefficient of viscous fluid damper
e	Error variable
EA	Axial rigidity of a cable
f_c	Vector of control force
f_y	MR fluid yield force
$gBest$	Best particle position in a group of a PSO particles
i_{mr}, i_a	Supplied current to MR damper
i_c	MR damper commanded current
J_w	Cost function associated to natural frequencies
J_ϕ	Cost function associated to mode shapes
J_ζ	Cost function associated to damping coefficients
k_b	Stiffness of the base isolator
k_i	Stiffness of i^{th} floor of the superstructure
$K,\ K_a$	Stiffness matrix of the superstructure
K_g	LQR/LQG state feedback gain matrix
L	Span length of a cable

m	Mass per unit length of cable
m_b	Mass of the base isolator
m_i	Mass of i^{th} floor of the superstructure
$M,\ M_a$	Mass matrix of the superstructure
n	Total number of DOF in a structural model
N	Number of storey in the superstructure
$pBest$	Best position of a PSO particle in its history
Q	Weights for measured states in a LQR/LQG design
R	Earthquake influence co-efficient matrix
tol	Tolerance for state variables
T_c	Kinetic energy
$u,\ v,\ w$	Displacement of cable along X, Y, and Z directions, respectively
$u(t)$	MR damper control force input to the system
U_x	Vector of floor responses along X direction, $U_x = [x_1,\ \cdots,\ x_N]^T$
U_y	Vector of floor responses along Y direction
U_θ	Vector of floor rotations about mass center
U	Vector of floor responses, $U = [U_x,\ U_y,\ U_\theta]^T$
U_c	Potential energy
v_a	Supplied voltage to MR damper
v_c	MR damper commanded voltage
W_i	Weights associated to cost functions
x_a	Amplitude of a sinusoid
x_b	Isolator displacement relative to ground
$x_d,\ x_{mr}$	Relative displacement at the damper location
x_g	Seismic displacement at the ground
$\ddot{x}_g,\ \ddot{y}_g$	Seismic acceleration along X and Y direction of the structure respectively
x_i	i^{th} floor displacement relative to ground/base isolator
X	Vector of state variables
Y_z	Vector of output variables
Y_m	Vector of measured variables
z_{mr}	MR damper evolutionary hysteretic variable
z_w	Wen's hysteretic variable for sliding friction

GREEK LETTERS

$\alpha, \beta, \gamma, \eta$	Simple Bouc-Wen model parameters
β_w, γ_w	Wen's hysteretic model parameters
$\delta_1$to δ_9	Optimization variables in a PSO optimization
ϵ	Axial strain in a cable
$\phi_1,\ \phi_2$	Acceleration constant in a PSO
Φ	Multi-objective cost function
ω	Frequency in Hz
ζ	Damping ratio

ACRONYMS

CO	**C**lipped **O**ptimal
DI	**D**ynamic **I**nversion
DOF(s)	**D**egree(s) **O**f **F**reedom
FLC	**F**uzzy **L**ogic **C**ontrol
FRF	**F**requency **R**esponse **F**unction
GA	**G**enetic **A**lgorithm
GAFLC	**G**enetic **A**lgorithm optimized **F**uzzy **L**ogic **C**ontrol
IB	**I**ntegrator **B**ackstepping
IRF	**I**mpulse **R**esponse **F**unction
IHT	**I**mpulse **H**ammer **T**est
LVDT	**L**inear **V**ariable **D**isplacement **T**ransformer
MAC	**M**odal **A**ssurance **C**riteria
MDOF	**M**ulti **D**egree **O**f **F**reedom
MR	**M**agneto-rheological
MSF	**M**odal **S**cale **F**actor
PSO	**P**article **S**warm **O**ptimization
SDOF	**S**ingle **D**egree **O**f **F**reedom
SFLC	**S**imple **F**uzzy **L**ogic **C**ontrol

Publications based on this Thesis

(I) Book Chapter

1. Sk. F. Ali and A. Ramaswamy, (2007) "Developments in Structural Optimization and Applications to Intelligent Structural Vibration Control", In *Intelligent Computational Para digms in Earthquake Engineering*, Editors: N.D. Lagros and Y. Tsompanakis, published by Idea Group Inc., Ch–6 : 101 – 121.

(II) Journal Publications

Accepted (in press)

1. Sk. F. Ali and A. Ramaswamy, 2008, "GA optimized FLC driven semi-active control for Phase-II smart nonlinear base isolated benchmark building", *Structural Control & Health Monitoring*, vol-15, 797 – 820 (online).

2. Sk. F. Ali and A. Ramaswamy, 2008, "Optimal Fuzzy Logic Control for MDOF Structural Systems Using Evolutionary Algorithm", *Engineering Applications of Artificial Intelligence*, IFAC (online).

3. Sk. F. Ali and A. Ramaswamy, "Optimal Dynamic Inversion based Semi-active Control of Benchmark Bridge using MR Dampers", *Structural Control & Health Monitoring* (accepted).

4. Sk. F. Ali and A. Ramaswamy, "Testing and Modeling of MR Damper and its Application to SDOF Systems using Integral Backstepping Technique", *J. of Dynamical Systems Measurements and Control*, ASME, (accepted).

Manuscripts under review

1. Sk. F. Ali, S. Venkatesha and A. Ramaswamy, "Optimal Fuzzy Logic based Hybrid Isolation Systems for Buildings: an Experimental and Numerical Study", *Journal of Structural engineering, ASCE*.

2. Sk. F. Ali and A. Ramaswamy, "Hybrid Structural control using Magnetorheological Dampers for Base Isolated Structures", *Smart Materials & Structures*.

3. Sk. F. Ali and A. Ramaswamy, "Semi-active Vibration control of Stay Cables using MR Dampers", *Journal of Applied Mechanics, ASME*.

(III) Refereed Conference Papers

International

1. Sk. Faruque Ali and A. Ramaswamy, (2007),"GA Optimized Semi-Active Adaptive Fuzzy Logic Control for Stay Cable Vibration", *Structural Engineering World Congress (SEWC-2007)*, Bangalore, India, November $3-7$, In CD-ROM.

2. Sk. Faruque Ali, A. Ramaswamy, and A. K. Agrawal, (2007), "Semi-active Base isolation System for Buildings using MR Dampers", *World forum on Smart Materials & Smart Structures Technology (SMSST-07)*, Chongqing & Nanjing, China, May $3-7$, In CD-ROM.

3. Sk. Faruque Ali and A. Ramaswamy, (2007), "FLC-MR Damper Control of Stay Cable Nonlinear Vibration", *Civil Engineering in the New Millennium: Opportunities and Challenges (CENeM)*, Bengal Engineering and Science University, Kolkata, India, January $11-14$, In CD-ROM.

4. Sk. Faruque Ali and A. Ramaswamy, (2006) "FLC Based Semi-Active Control of Buildings using Magnetorheological Dampers", 2^{nd} *International Congress on Computational Mechanics and Simulation, (ICCMS-07)*, Indian Institute of Technology , Guwahati, India, December $10-12$, In CD-ROM.

5. Sk. Faruque Ali and A. Ramaswamy, (2006), "Benchmark Control Problem for Highway Bridge based on FLC", *Proceedings of* 2006 *Structures Congress, ASCE and SEI*, St. Louis MO, USA, May, In CD-ROM.

6. Sk. Faruque Ali and A. Ramaswamy, (2005), "Non-linear Modeling and Control of Cable-stay system under Tower flexibility using Passive and Semi-active Control", *Proceedings of the Structural Engineering Convention (SEC-2005)*, IISc Bangalore, India, December $8-10$, In CD-ROM.

National

1. Sk. Faruque Ali and A. Ramaswamy, (2006), "Optimal Preview Active Control of Structures During Earthquakes Using Feed-Back and Feed-Forward data", *National Conference on Recent Advancement on Structural Engineering, (NCRASE-2006)*, JNTU-Kakinada, AP, India, Febraury, In proceedings.

2. Sk. Faruque Ali and A. Ramaswamy, (2005), "Review and Development of Vibration Control Strategies for Cable Supported Bridges", *National Symposium on Structural Dynamics, Random Vibration and Earthquake Engineering (NSDD-2005)*, IISc Bangalore, July $22-23$, In proceedings.

Chapter 1

Introduction

1.1 Background

Progress in material science and manufacturing technology have resulted in the emergence of new construction materials characterized by light weight, higher strength and better performance, *e.g.*, high performance concrete, high strength structural steel and composites. These new construction material integrated with better quality control norms in the manufacturing process and during construction have led to the emergence of complex and slender structures such as high-rise buildings, long span bridges, deep water offshore platforms, *etc*. The design of such complex structures has been benefited with developments of computationally efficient and accurate methods of structural analysis, *e.g.*, finite element method (Weaver and Johnston (1987) [369]). The evolution of mathematical tools to handle uncertainties in external disturbances, *e.g.*, probability theory (Ang and Tang (1984) [29]; Dai and Wang (1982) [83]; Madsen et al. (1986) [218]), and their incorporation into the design stage has to some extent increased the performance of these structures.

As structures have become more complex with increased construction cost and serve more critical functions, their failure has catastrophic consequences. The safety of these structures during a hazardous earthquake or wind induced excitation applies not only to the structure but also to the life safety of their occupants and the equipments housed inside. Therefore, the protection of a building structure, the equipment housed within and safety of human occupants, against damage induced by large environmental loads, *e.g.*, earthquake, strong wind gusts *etc.*, is without doubt, a worldwide priority for the Structural Engineers community.

Significant research efforts have been made recently on protecting Civil infrastructures from strong earthquakes and wind loads. The objectives of these research studies range from developing protective schemes for occupant comfort and reliable operation of the structures to human safety and structural survivability. Traditional design strategies provide increased structural strengths to resist dynamic loadings and rely on the inelastic deformation of structural components to dissipate input (seismic/wind) energy. The idea is to develop plastic hinges within the structure during hazardous environmental loads without resulting in a complete collapse of the structure, thus protecting the occupants within the structure. Inelastic deformation (yielding) is permitted as means of dissipating a portion of the energy transfered to the structure by these environmental loads. However, plastic deformation due to the yielding results in permanent damage. Thus conventional structural design is often based on providing sufficient strength and stiffness to the structure such as to limit the inelastic deformation to an acceptable limit.

However, structures cannot be designed to withstand all possible external loads. Some extraordinary loading episodes do occur, leading to damage or even failure of the structure. Higher flexibility and low damping characteristic of slender high rise structure have given rise to higher material distress during large environmental loads resulting in the unacceptable levels of vibration and/or failure of the structure.

One way to mitigate the effects of these hazardous environmental loads and meet the stringent performance requirements is through the application of structural control technology. The control of structural vibrations can be accomplished through various means, such as, providing counter forces (active control), isolating and dissipating the energy of the excitation (base isolation), absorbing and dissipating the energy of the structural vibration (passive and semi-active control) (Soong (1990) [322]). Recent interest in the area of structural control, seismic isolation and supplemental damping is to combine these means to come up with a hybrid mechanism for structural protection. Full-scale implementation of these systems has been made and is being increasingly pursued around the world (Spencer and Nagarajaiah (2003) [326]). Effectiveness, reliability and other characteristics of these systems are being evaluated through large-scale testing and practical implementations on certain test structures.

Over the past three decades tremendous progress has been made to make control a viable technology for enhancing structural functionality and safety against natural hazards such as

strong earthquakes and wind gusts (Housner et al. (1997) [146]). The passive, active control and hybrid systems have been used in real applications to reduce the earthquake and wind induced lateral vibrations of buildings and bridges (Soong (1990) [322]; Housner et al. (1994) [145]; Soong and Dargush (1997) [324]; Spencer and Nagarajaiah (2003) [326]; Agrawal et al. (2003) [12]).

Passive control strategies, such as base isolation systems, passive energy dissipation systems, and tuned mass dampers, *etc.*, have been widely accepted by the engineering community for mitigating structural responses (Housner et al. (1997) [146]; Spencer and Nagarajaiah (2003) [326]). Passive control systems do not require any external energy supply. These systems either use potential energy generated by the response of the structure (fluid column dampers) to supply the control force or dissipate the energy of the excitation through friction or viscoelastic deformation (friction dampers and viscoelastic dampers). However, passive devices cannot be tuned to adjust themselves to a varied range of frequency content that may be present in the external loading. Hence, the efficiency of these systems cannot be assured if the actual excitations (amplitude and frequency content) are different from the one considered in tuning and design of these devices.

Active control systems operate using an external energy supply to apply control forces on structures. Active control systems use sensors to measure the response of the system and/or excitation, compute the control command from the sensor output using a control algorithm (coded in a hardware) and apply the control command to the structure by means of actuators. Active mass dampers, active mass drivers, active tendon system, *etc.*, are some of the active control devices developed and tested for actual structural applications during the last two decades (Soong (1990) [322]; Spencer and Sain (1997) [331]; Spencer and Nagarajaiah (2003) [326]). Active control systems are dependent on external power supply and for Civil Engineering structures the power requirement is quite high. This makes such systems vulnerable to power failure during extreme events. Moreover, due to high power requirement, it is difficult to provide an active control system with its own dedicated power supply.

On the other hand, semi-active systems have a significant practical implementation potential because they have inherent reliability of passive systems and the versatility and adaptability of active systems, using moderate power sources, that can be supplied by batteries (Symans and Constantinou (1999) [349]; Spencer and Nagarajaiah (2003) [326]).

Hybrid control systems use passive control components with active control counterpart to supplement and improve the performance of the passive control systems. This also decreases the energy requirement of a stand alone active control systems. In case of power failure or failure of active systems, the passive component of the hybrid control system still offers some degree of protection, making the system fail safe, an essential design requirement for the protection of life-line structures like, highway bridges, hospitals and official buildings and nuclear power plants. Because of the reliability of both semi-active and hybrid control systems, considerable attention has been paid recently to the research and implementation of these systems (Soong and Spencer (2002) [325]).

Hybrid Base Isolation

The most successful means of protecting structures and also the most practically implemented mechanism to mitigate the risk to life and property damage against severe seismic events is the base isolation technique (Kelly (1986) [181]; Skinner et al. (1993) [319]; Naeim and Kelly (1999) [243]). Base isolation systems incorporating rubber bearings can not provide any damping to the structure and therefore undergo large displacements at the base under pulse type near field seismic motions. Nonlinear isolation devices such as lead-rubber bearings, friction pendulum bearings, sliding bearing or high damping rubber bearings are often used to provide certain range of damping to the structure beside shifting the structural time period away from the excitation frequencies. The benefit of these types of bearings is that the restoring force and adequate damping capacity can be obtained in one device. However, because the dynamic characteristics of these devices are strongly nonlinear, the vibration reduction is not optimal for a wide range of seismic excitations. For example, the features of an isolation system designed for an El-Centro earthquake typically will not be optimal for a Kobe earthquake and vice versa. Studies reported in various literature aftermath Kobe (1995) and Northridge (1994) earthquake have questioned the effectiveness of many passive base isolation systems (Hall et al. (1995) [136]; Heaton et al. (1995) [141]).

The addition of damping to reduce base displacements may increase both inter-storey deformations and absolute accelerations of the superstructure, defeating many of the gains for which base isolation is intended (Naeim and Kelly (1999) [243]; Kelly (1999) [182]; Makris and Chang (2000) [224]; Politopoulos (2008) [277]). For example, the performance of highly

sensitive equipments and computer facilities in hospitals, communication centers, *etc.*, can be easily disrupted by moderate acceleration levels and can even get permanently damaged at high acceleration levels (Inaudi and Kelly (1993) [152]). Therefore the research trend has turned towards the use of supplemental active or semi-active devices along with seismic isolators, seeking to develop hybrid isolation systems that can be effective for a wide range of ground excitations (Inaudi and Kelly (1993) [152]; Nagarajaiah (1994) [244]; Symans and Kelly (1999) [351]; Agrawal et al. (2005) [7]; Nagarajaiah and Narasimhan (2006) [248]).

In general, protection of contents of a structure is achieved through reduction of structural accelerations. The advantages of hybrid base isolation systems lie in their high performance in reducing superstructure deformations, accelerations and the ability to adapt to different loading conditions. Active control devices, typically, require a large external power supply during extreme seismic events. Moreover, active systems have the additional risk of instability. The recent focus is on incorporating semi-active magnetorheological (MR) dampers as supplemental devices for hybrid base isolation systems. Various analytical studies, scaled experimental studies and simulation studies on benchmark base isolated structures with MR devices are on rise.

1.2 Motivation for the Present Study

Discussions in the preceding section demonstrate that hybrid base isolation systems incorporating MR dampers as supplemental damping devices form the focus of current research trend in structural control technology to mitigate damages induce in a structure under near-source, high-velocity, long period pulse seismic motions. Magnetorheological dampers are semi-active devices and need controllable current or voltage inputs to change their damping characteristics in real-time.

Development of semi-active control strategy using MR dampers involves two steps:

- Development of a model that can describe the MR damper hysteretic character properly. One can develop both parametric (design includes optimization of various parameters needed for the mathematical description of the damper hysteretic character) and non-parametric (damper hysteretic character is modeled based on intelligent methods like, neural networks).

- The damping force provided by the MR device is a nonlinear function of magnetic flux across the coil in the device. Therefore predicting the amount current/voltage required to be supplied to the device to obtain a desired damping force is a challenging task. This process involves the development of nonlinear control algorithms to monitor current/voltage supply to the MR damper to obtain a desired damping force.

Both parametric and non-parametric modeling of MR damper hysteretic character has been reported in the literature. Most widely accepted is the Bouc-Wen hysteretic model proposed by Spencer et al. (1997) [329]. Recent studies on large scale MR damper (maximum capacity is 20 tonnes) (Yang et al. (2002, 2004) [389, 390]) and on RD-1005-3 (Dominguez et al. (2004, 2006) [90, 91]) have reported the dependence of the Bouc-wen hysteretic parameters on amplitude and frequency of the input excitation. Bouc-Wen model is a simple model and does not incorporate the amplitude and frequency dependence of its parameters. Therefore, investigation of amplitude and frequency dependence in the Bouc-Wen parameters used to describe the MR damper hysteretic character forms one of the goals in this study. This can be further explored to provide a modified Bouc-Wen model that can alleviate some of the drawbacks described above.

Literature pertaining to the MR damper current/voltage monitoring mainly involves on-off type bang-bang control strategy (switching between zero and maximum current/voltage) designed based on the force feedback from the MR damper. Switching between zero and maximum current/voltage does not allow any intermediate current/voltage supply to the MR damper if needed. Therefore, these algorithms provide sub-optimal control of the structural vibration. This limitation in control algorithms can be alleviated using an intelligent control systems, *e.g.*, fuzzy logic control systems. This motivates the development of a fuzzy based intelligent semi-active control algorithm to monitor current/voltage input to the MR damper.

Fuzzy logic can handle nonlinearities, uncertainties, and heuristic knowledge present in a model effectively and easily but, the selection of optimal fuzzy parameters (membership function, rule base, scaling factors) needs heuristic optimization approaches. The optimization is computationally intensive and is mainly carried out off-line. Thereafter, the optimal FLC is used in on-line control of structural vibration. Development of strategies that will require few variables to obtain an optimal FLC (which is computationally efficient for real time deployment) is an open area of research and has been explored in the present study.

Furthermore, there is a time lag between the current/voltage supplied to the MR damper (supply current/voltage) and the current/voltage that actually produces the magnetic flux (commanded current/voltage). This lag is taken care of using a first order filter in the analytical modeling of the MR damper hysteretic phenomenon. This dynamics between supplied current/voltage and the commanded current/voltage can be neglected when the damper acts as a passive device (*i.e.*, supplying a constant current/voltage to the damper), but it becomes a major cause of concern when the damper current/voltage is varied continuously (for example under seismic excitations). Algorithms available in the literature never consider the effect of MR damper current/voltage dynamics. This forms the motivation for the development of model based control algorithms that can make use of the current/voltage dynamics.

1.3 Objectives of the Present Study

As discussed in the previous section the objective of the present study is to develop intelligent and model based control algorithms that can alleviate short comings of control algorithms reported in the literature for deployment with MR dampers. An intelligent controller can be designed without specifying a very precise and an accurate model of the structural dynamics. Whereas model based control algorithms require a mathematical model of the system and their performance depends on the accuracy of this mathematical model. To develop intelligent control, fuzzy logic based reasoning has been used. Nonlinear control algorithms like, integral backstepping (Krstic et al. (1995) [193]) and dynamic inversion (Marquez (2003) [227]) have been used to develop control algorithms based on the mathematical model of the structural system. The objectives of the present dissertation work can be summarized as the following.

1. Experimental investigation of RD-1005-3 MR damper (LORD® Corp. [214]) under various sinusoidal excitations with varying supply currents/voltages has been carried out. The dependence of the damper hysteretic phenomenon on frequencies and amplitudes of the excitations has been explored. Finally, development of a modified Bouc-Wen model to incorporate the amplitude dependency of the damper characteristic formed a part of the experimental study.

2. Development of an intelligent controller based on fuzzy logic for current/voltage monitoring of MR damper and developing optimization procedures to determine parameters

of the fuzzy logic control (FLC) are other goals of the study. The approach requires fewer variables making the procedure computationally less intensive, which is a benefit of the approach.

3. Experimental verification of the performance of the proposed optimal FLC algorithm for hybrid base isolation (sliding bearing and MR damper) of a three storey building structure has been undertaken.

4. Development of model based control algorithms, such that the dynamics of current/voltage supply to the MR damper can be incorporated, has then been explored.

5. Investigation of the performance of the proposed control algorithms in various international benchmark exercises provided by ASCE control task committee has then been studied. These studies have been performed on a benchmark building with nonlinear base isolation, a benchmark highway bridge and a stay cable problem under support excitations. Development of the cable equations of motion under support excitation forms a part of the study.

1.4 Scope and Limitations

The objectives of the present study are to develop semi-active control algorithms to monitor MR damper current/voltage for vibration mitigation of structures and experimental verification of one of the algorithm. The laboratory scaled building model for the experimental study has been idealized as a linear multi-storey shear building, regardless of all nonlinearities in the connections (at floor level and at the base). Floors are assumed to be rigid and supported on mass less inextensible columns. Effects of vertical components of the seismic excitations are not considered. Seismic records have been considered from a set of earthquake excitations and that they represent their respective soil conditions and a separate analysis is not performed to consider soil-structure interactions.

Though the results presented for the experimental study in this thesis are based on the assumptions mentioned above, the application of the proposed approaches is not limited to the building example in the experimental study. The proposed approach for optimal design of an intelligent controller can handle more complex and generalized structural models, provided

adequate computational resources are available.

The implementations of the proposed approach for optimal design of intelligent control system in international benchmark structures extend the applications of the proposed scheme. Although, the experimental study has been performed on a base isolated structures, the proposed algorithm can be used for structural control with/without isolation system. In this regard a three storey fixed base building and the stay cable problem have been considered.

For the model based control algorithms developed as a part of the study, both multi-inputs single output and multi-inputs multi-outputs cases have been considered. These are verified using numerical simulation on the analytical model of the experimental building with single actuator designed for the study and benchmark problem with multiple actuators.

1.5 Outline of the Dissertation

The focus of this dissertation is to develop a semi-active control algorithm and experimentally verifying intelligent control developed for the study. The organization of the chapters is as follows.

- Chapter 2 presents a critical appraisal of the current state-of-the-art in the field of structural vibration control, intelligent control systems and hybrid base isolation systems. A comprehensive review of the literature encompassing relevant issues related to structural vibration control, for *e.g.*, structural modeling related issues, control algorithms and devices, semi-active control algorithms to monitor MR dampers including intelligent control algorithms and model based algorithms are presented. Various mathematical models of buildings and characteristics of near source and far source seismic excitation are also discussed.

- Chapter 3 covers the details of MR damper experiments and analytical modeling. A comprehensive review of parametric and non-parametric models developed in the literature to predict MR damper damping behaviour are given. Based on test results, an amplitude dependent modified Bouc-Wen model is developed to provide an improved MR damper force-velocity relationship. This modified Bouc-Wen model has then been used to developed semi-active control algorithm in later chapters.

- The fuzzy logic based intelligent controller to monitor MR damper current/voltage input is detailed in Chapter 4. Architecture of the fuzzy logic control system and implementation related issues are discussed in the context of the present study. A geometric approach is developed to determine optimal rule base for the fuzzy control, which uses fewer number of variables for optimization. Details of the formulation of multi-objective optimization and a solution procedure using micro-genetic algorithm (micro-GA) and particle swarm optimization (PSO) are then presented. Performance of the proposed optimal FLC (using micro-GA and PSO) taking examples of a single-DOF system and a multi-DOF system is shown. A comparison of performance of non-optimal rule base and optimal rule base has been reported. The FLC with optimal rule base is then used for experimental verification of intelligent controller for a base isolated building developed in Chapter 5.

- Chapter 5 provides the details of the experimental verification of the optimal fuzzy logic control algorithm for MR damper voltage monitoring, on a base isolated three storey shear building model. Details of experimental set-up, sensor locations, MR damper position, *etc.*, are discussed. A particle swarm algorithm based system identification of the building parameters (mass, stiffness, and damping) has been described. Experimental results with analytical verification are presented. Finally, comparison of various test results obtained from fixed base, base isolated, and four cases of hybrid semi-active control ('passive-off', 'passive-on', MR damper with simple FLC and MR damper with optimal FLC) are reported.

- Model based semi-active control algorithms are formulated in Chapter 6. First a two stage control algorithm is developed, where the primary controller or the first stage controller can be any optimal control strategy, like, LQR, LQG *etc.* (as in case of a clipped optimal control). In the second stage current/voltage required by the MR damper to provide the control force prescribed by the primary controller is tracked using dynamic inversion technique. For systems with multiple MR dampers, a Lagrange multiplier based approach is formulated to determine optimal amount of current/voltage required by each of the MR dampers to provide the force prescribed by the primary controller. Chapter 6 also reports the development of an integral backstepping based semi-active

control algorithm, which alleviates the use of intermediate primary controller. Stability of the proposed controllers are shown in a Lyapunov sense. The dynamics of the MR damper input current/voltage is considered in both algorithms.

- Chapter 7 investigates the performance of the proposed controllers on different benchmark problems under seismic excitations. The chapter has been divided into three sections. First a benchmark building with nonlinear base isolation supplemented with MR dampers is considered. Optimal FLC control strategy developed in Chapter 4 is used to mitigate the building responses under various near and far source seismic ground motions. Secondly, the performance of the optimal dynamic inversion strategy developed in Chapter 6 for multi-input multi-output system has been explored on the benchmark highway bridge exercise. In the third section, an example of a stay cable with sag is considered for the application of optimal FLC based MR damper control. In all the above examples, the development of structural model and their performance objectives are discussed. A complete derivation of nonlinear coupled equations of motion of a stay cable vibration (with sag) has been presented under support motion. For the benchmark studies simulation results are compared with results reported in the literature.

- Chapter 8 summarizes the salient contributions that have emerged from the present study. Conclusion, recommendations and further direction of research in the field have been made based on the present study.

Finally the thesis concludes with a list of references used while carrying out this dissertation work and three appendices. Details of the instruments used for the experimental study reported in Chapter 3 and Chapter 5 are provided in Appendix A. All the test results of the experimental work presented in Chapter 3 and Chapter 5 are given in Appendix B and Appendix C, respectively.

Chapter 2

Literature Review

2.1 Overview

Recent earthquakes like Northridge (1994), Kobe (1995), Bhuj earthquake in Gujrat (January 2001) and most recently Great Sichuan earthquake in China (May 2008) have demonstrated the devastating effects of natural forces on Civil Engineering structures. These earthquakes around the world have underscored the tremendous importance of understanding the way in which Civil Engineering structures respond during such dynamic events. Today, one of the main challenges in earthquake engineering and structural control is to develop innovative design concepts to better protect Civil structures, including their material contents and human occupants, from these natural hazards.

Earthquakes and strong wind gusts induce severe vibration in flexible building structures causing discomfort to the occupants and sometimes even lead to total collapse of the structure. The level of vibration in a building depends on the characteristics of the dynamics of the structure such as natural frequencies, damping ratio, *etc.*, and the characteristics of the excitation such as frequency and amplitude. Thus, the description of the structural system (mass, damping and stiffness) and the input excitation play a crucial role in the vibration analysis. Dynamic responses of a structural system can be classified in terms of the displacement, velocity and acceleration responses in vertical, lateral and rotational directions. The occupant can perceive the acceleration response of the structure. Therefore, occupants comfort level is defined either in terms of the absolute acceleration or in the form of some other measure of the

acceleration response. As the stress level in the structural members depends on the displacement response (deformations or strains) of these components, safety of the structure mainly, depends on the displacement response.

The protection of structures and/or its occupants and instruments under natural hazards can be achieved by various means such as modifying the structural design, structural rigidity, structural damping, and/or by attaching external devices, known as control devices, either to isolate and/or dissipate vibrational energy of the structure or to impart a restoring force to the structure so as to reduce the structural vibration. The history of structural control can be traced back more than 100 years, when Milne (1886) [237] built a small house and placed it on ball bearings, to demonstrate that a structure can be isolated from earthquake excitations. But the structural engineering community first embraced the notion of structural control in the 1960's (Zuk, (1980) [425]). Since then a number of new techniques and devices have emerged and have been installed in a number of different structures (Soong (1990) [322]; Housner et al (1997) [146]).

This chapter, after giving a flavor of the mathematical models of building structures available in the existing literature, presents a critical appraisal of the developments and current state-of-the-art in structural vibration control technology. Finally based on an assessment of the literature on issues related to earthquake engineering and structural control, gaps in the state-of-the-art that have been identified are enumerated and form the motivation of this dissertation.

2.2 Mathematical Modeling of a Building

Design of control systems for buildings require mathematical models of the dynamics of the structure. All the real structures are spatially distributed parameter systems. Dynamics of distributed parameter system should be modeled using partial differential equations of motion (Meirovitch (1990) [235]; Clough and Penzian (1993) [76]; Lasiecka (1995) [201]). Closed form solutions for partial differential equations describing the distributed parameter structures are not possible or feasible in most of the cases. Lumping, generalized displacements and finite element discretization are some of the measures employed to discretize the structure in space. A number of numerical tools are available for solving the discretized structural model, *e.g.*,

Rayleigh Ritz method, Galerkin method, Newmark's β methods, *etc.*, (Weaver and Johnston 1987 [369]; Meirovitch 1990 [235]; Clough and Penzian (1993) [76]). The Lumped parameter discretization is the simplest one but this is suitable for structural systems that have a large proportion of the mass concentrated at few discrete locations. The masses of the structural elements supporting the concentrated masses can be included in the lumps (concentrated masses), treating the supporting elements as weight less (Clough and Penzien (1993) [76]). A major portion of the mass of the buildings is concentrated at the floor levels and the frames supporting the floors are relatively light. Hence, the dynamics of building structures can be modeled with sufficient accuracy using a simple lumped mass model.

A number of different models have been used to describe the structural dynamics, these includes shear beam, cantilever, plane frame and lateral-torsional coupled 3-D equivalent idealized lumped parameter models. In the present study, some of these methods have been employed for modeling the structural dynamics to include different level of complexities in the structural behaviour.

2.2.1 Framed building model

Availability of efficient finite element structural design softwares, *viz.* SAP, ABAQUS, NISA *etc.*, have made the modeling of building structures with complex geometry possible. Mostly, these models are based on the 3-D or 2-D frame model (plane frame model) of the building. In framed analysis of a building one considers the following assumptions,

- Nodes are located at beam column joints
- Choice of the number of degrees-of-freedom (DOF) at the node is based on the complexity of the structure and computational cost. One can choose full 6-D freedom at the nodes (3-D analysis) or 1D freedom considering only lateral motion of the building (2-D analysis, as in shear building model), as well as any judicial choice of DOF, such as permitting in plane rotations at the beam column joints
- Mass is lumped uniformly at the nodes
- Generally ground accelerations (in case of seismically excited building) are considered to be the same at all the points at the ground level unless the consideration of spatial variability of seismic excitations is important.

The mass and stiffness matrices obtained from the finite element software are then further used for control design. The damping matrix is generally obtained as a function of mass and stiffness matrix (Rayleigh damping) (Chopra (2005) [67]). Figure 2.1(a) shows a finite element model of a building provided for benchmark exercise by Narasimhan et al. (2006) [261].

2.2.2 Cantilever beam model

Cantilever beam model is applicable for buildings that are tall and symmetric, *i.e.*, there is no eccentricity in the axis of the mass centers and the axis of resistance, the response of the building is dominant in one direction and negligible in other orthogonal directions, *i.e.*, building is rectangular and responses in the direction of the length are negligible in comparison to the responses in the direction of the width, responses are same at all the points of a floor and the ground acceleration is same at all the points of foundation. In this model the portions between two adjacent floors are considered as a beam of uniform thickness. Thus, there are two degree of freedom at each floor, one translational and one rotational. The model is simple but because of two degrees of freedom at each floor level the size of the matrices will be $2N \times 2N$ for an N storey building. Figure 2.1(b) shows the cantilever beam model for a N storey building. At each node the DOFs are floor lateral displacement (x_i) and floor rotation (θ_i).

2.2.3 Shear Beam Model

Shear beam model is the simplest of building models available and is widely used for numerical simulations. Following assumptions are made for the idealized shear beam model of a building.

- Rigid floor decks are supported on the mass less flexible columns
- Columns are axially inextensible
- Building is symmetric, *i.e.*, there is no eccentricity in the axis of mass centers and the axis of resistance centers
- Response of the building is dominant in one direction and negligible in the other orthogonal direction, *i.e.*, the building is rectangular and the responses in the direction of the length are negligible in comparison to the responses in the direction of width

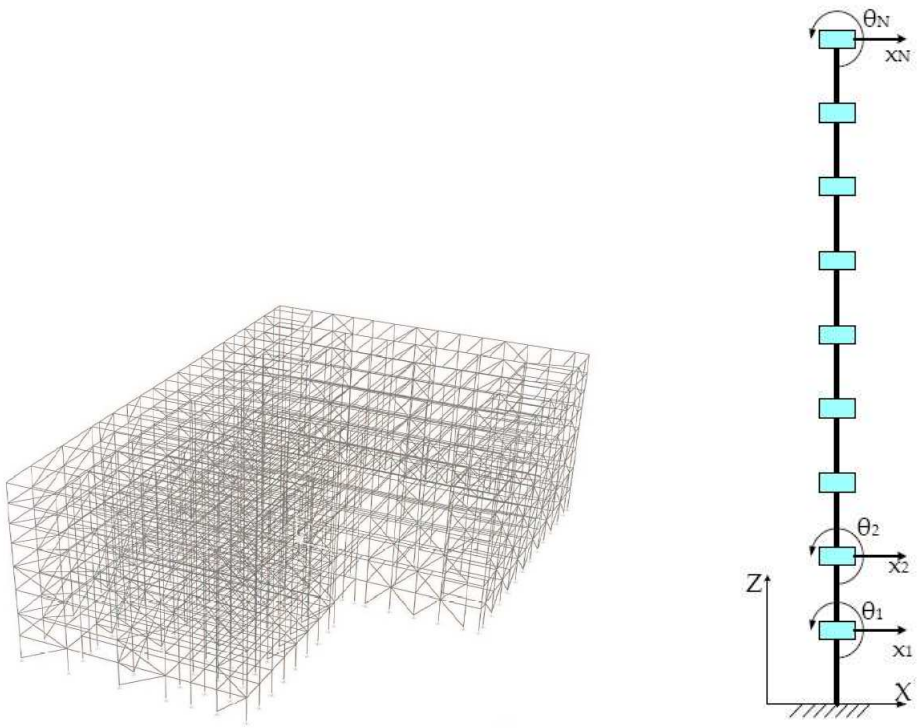

(a) Finite Element Model (Narasimhan et al. (2006) [261]) (b) Cantilever Beam Model

Figure 2.1: Finite elements and Cantilever beam model for buildings

- Ground acceleration is the same at all points of the foundation

Thus, there is only one degree of freedom, namely the lateral displacement at each floor of the building. An idealized three-storey shear beam building is shown in Fig. 2.2. The floor mass, damping and stiffness are represented by m_i, c_i, k_i. The floor displacements (x_i) are relative to the building reference frame. The ground excitation is represented by x_g.

2.2.4 Torsionally coupled model

Most of the actual building structures have intended or accidental eccentricities between their center of mass and center of resistance. Such asymmetric buildings have coupled lateral and torsional response under seismic and wind excitation. Symmetric buildings, *i.e.*, buildings that do not have any eccentricity between mass center and center of resistance, have coupled lateral and torsional responses under seismic and wind excitations. To analyze the lateral-torsional coupled responses, the building model can be idealized to have three degrees of

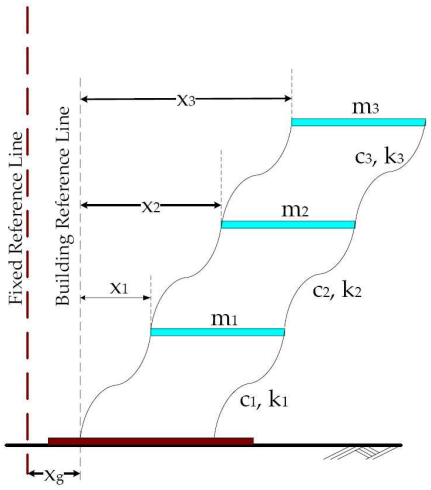

Figure 2.2: Shear beam building model

freedom at each floor, *i.e.*, two orthogonal lateral displacements with respect to the ground and a rotation with respect to the vertical axis (see Fig. 2.3).

Assuming the building to be consisting of rigid floor diaphragms supported on flexible, massless and axially inextensible columns, an idealized model of a general torsionally coupled N storey building is formulated. The reference axes are assumed to pass through the center of mass of the building, which result in a diagonal mass matrix and coupled stiffness and damping matrices. The coupling of stiffness and damping matrices depend on the position of the center of resistance of the structure.

$$M_{n\times n}\,\ddot{U}_{n\times 1} + C_{n\times n}\,\dot{U}_{n\times 1} + K_{n\times n}U_{n\times 1} + B_{c\;n\times m}\,f_{c\;m\times 1} = -M_{n\times n}R_{n\times 3}\ddot{U}_{g\;3\times 1} \tag{2.1}$$

where, $n = 3 \times N$, is the total DOF of the structure. The matrix B_c and R are the control force influence matrix and matrix of earthquake influence co-efficients respectively. $U = [U_x,\, U_y,\, U_\theta]^T$ is the vector of structural responses with $U_x = [x_1,\, \cdots,\, x_N]^T$ containing the structural displacements (x_i) in X direction. Similarly, U_y and U_θ represent the vector containing floor displacement (y_i) in Y and floor rotations (θ_i) respectively. The seismic excitation vector U_g contains the excitations along X direction (x_g), along y direction (y_g) and any rotational component if present (θ_g). The control force is given in the vector f_c with m being the number of control actions.

For a shear beam building model considering only the X direction motion and neglecting the Y direction responses and torsional responses, the mass, damping and the stiffness matrices are given as

$$M_a = \begin{bmatrix} m_1 & 0 & \cdots & 0 & 0 \\ 0 & m_2 & \cdots & 0 & 0 \\ \vdots & \vdots & \ddots & \vdots & \vdots \\ 0 & 0 & \cdots & m_{N-1} & 0 \\ 0 & 0 & \cdots & 0 & m_N \end{bmatrix}; \quad C_a = \begin{bmatrix} c_1 + c_2 & -c_2 & 0 & \cdots & 0 \\ -c_2 & c_2 + c_3 & -c_3 & \cdots & 0 \\ \vdots & \vdots & \ddots & \vdots & \vdots \\ 0 & \cdots & -c_N & c_N + c_{N-1} & -c_N \\ 0 & 0 & \cdots & -c_N & c_N \end{bmatrix}$$

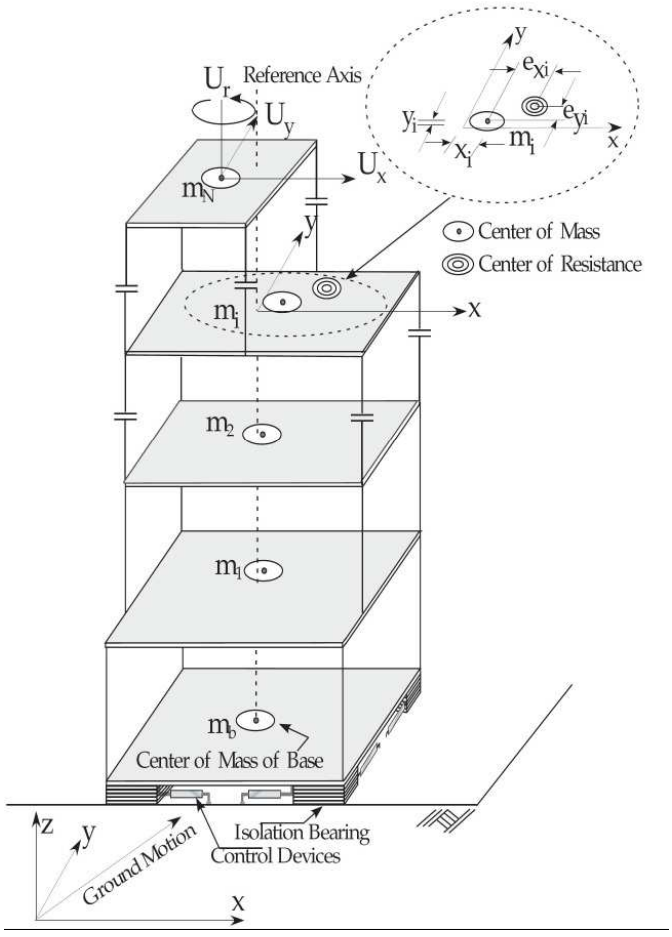

Figure 2.3: Torsional Building Model (Narasimhan et al. (2005) [261])

$$K_a = \begin{bmatrix} k_1 + k_2 & -k_2 & 0 & \cdots & 0 \\ -k_2 & k_2 + k_3 & -k_3 & \cdots & 0 \\ \vdots & \vdots & \ddots & \vdots & \vdots \\ 0 & \cdots & -k_N & k_N + k_{N-1} & -k_N \\ 0 & 0 & \cdots & -k_N & k_N \end{bmatrix} \tag{2.2}$$

The floor mass, damping and stiffness are represented by m_i, c_i and k_i ($i \in [1,\ N]$) respectively. Equation 2.1 remains same but for the following changes, $M = M_a$, $C = C_a$, $K = K_a$, $n = N$, $U = U_x$, $U_g = x_g$ and $R_{n\times 3} \rightarrow R_{n\times 1}$. For the experimental study the above mentioned shear beam model is used with $N = 3$.

2.2.5 State space representation

The equation of motion described in previous section can be representated in state-space form to facilitate a numerical solution of the model. State space form of the equations of motion (Eq. 2.1) is given by Eq. 2.3.

$$\dot{X} = AX + Bf_c + E\ddot{U}_g \tag{2.3}$$

The output (Y_z) and the measurement (Y_m) equations are given by,

$$Y_z = C_z X + D_z f_c + F_z \ddot{U}_g \tag{2.4}$$

$$Y_m = C_m X + D_m f_c + F_m \ddot{U}_g + \nu \tag{2.5}$$

In the above equations, $X = \left\{U^T,\ \dot{U}^T\right\}^T$ is the state vector consisisting of $2n \times 1$ elements. A, B and E are the system state matrices, $\ddot{U}_g$ is the ground acceleration vector in three directions. The regulated output (Y_z) and the measurement output (Y_m) equations are given in Eqs. 2.4 and 2.5 respectively, where the matrices C, D and F are mapping matrices of appropriate dimensions and ν is the noise associated with the sensor measurements.

2.3 Structural Model Reducing Methods

Structural models that are based on finite element discretization technique provide large number of degrees of freedom. For example the benchmark highway bridge exercise considered in Chapter 7 has 430 degrees of freedom (DOF) in its full order model (FOM) (Agrawal et al. (2005) [7]). Control design based on full order model requires enormous computational time and hence the corresponding implementation costs increase drastically. Moreover, earthquake excitations and wind loads excite only few frequencies of high rise and flexible building structures. Therefore, to reduce computational costs, reduced order models (ROM) are developed from the full order model of the system for controller design (for example the benchmark highway bridge exercise considered in Chapter 7 has 28 degrees of freedom in its ROM). Here a flavour of the literature pertaining to the reduced order modeling methods has been presented with special emphasis on the Guyan reduction technique, which has been implemented to obtain reduced order model for the benchmark highway bridge study (Agrawal et al. (2005) [7]).

In condensation techniques, the total DOFs of the full model is divided into the master DOFs or simply masters, which will be kept in the reduced model, and the slave DOFs or simply slaves, which will be deleted from the full model. A static or dynamic condensation matrix is then defined to relate the deformations or eigenvectors between the masters and slaves. Using the condensation matrix, the system matrices of a full size model can be condensed to a reduced size model represented only by the masters.

One of the oldest and most popular reduction methods is static or Guyan reduction introduced by Robert J. Guyan (Guyan (1965) [133]). Here, in the case of the reduced stiffness matrix, if the applied loads are static, none of the structural complexity applied is lost since all elements of the original stiffness contribute. However, to reduce the mass matrix, the purely static transformation between the eliminated co-ordinates and those retained co-ordinates is employed. Therefore, in this process the inertia terms associated with the discarded DOFs are neglected. Hence, the result is that the eigenvalue, eigenvector problem is closely but not exactly preserved. Therefore, the scheme provides exact results for a static model, but when applied to a dynamic model (where inertial effect of discarded DOFs is present) the reduced model generated is not exact and often lacks the required accuracy. Hence, many schemes have been proposed to improve the accuracy of the reduced order systems. O'Callaghan

(1989) [266] proposed a modified method which he called the Improved Reduced System (IRS) method. In this approach an extra term is added to the static reduction transformation to make some allowance for the inertia forces. This extra term allows the modal vectors of interest in the full model to be approximated more accurately but relies on the statically reduced model.

Among others, the iterative schemes are very popular. In these methods the condensation matrix is updated repeatedly until the desired convergent values are obtained. The Guyan condensation matrix is usually defined as an initial approximation for the iterative schemes. Because the dynamic condensation matrix is updated repeatedly until a desired convergence value is achieved, the selection of master and slave DOFs does not have much effect on the accuracy. In 1992, an iterative dynamic condensation scheme was proposed for eigenvalue-problems by Suarez and Singh (1992) [340]. In the scheme, a general eigenvalue-problem is transformed into a standard form with symmetry preserved. If the mass matrix is diagonal, the transformation becomes very simple. For consistent mass matrices, however, the preliminary procedure turns out to be a significant burden in eigenvalue-problems. The IRS method was extended to produce an iterative algorithm by Friswell et al. (1995, 1998) [119, 120]. Friswell et al. (1995) [119] developed an iterative scheme, to obtain the corrective term in the IRS technique, using the current best estimate of the reduced model. Convergence proof of the proposed scheme reported later in Friswell et al. (1998) [120] showed that the natural frequencies of the reduced model would converge to those of the full model.

Most recent works include iterative approaches for model reduction of non-classically damped systems (Rivera et al. (1999) [293]; Qu et al. (2003a, b) [281, 282]). The dynamic characteristics of the reduced model resulted from the iterative methods are usually very close to those of the full model in a given frequency range.

Guyan reduction technique

Guyan reduction method is also known as static condensation technique, since the damping and inertia forces on all degrees of freedom of the full model are ignored (Qu et al. (2003a) [281]). One advantage of these condensation methods is that the explicit forms of the reduced stiffness, mass, and damping matrices can be directly obtained from the reduced model. Hence, the accuracy fully depends on how many and which DOFs of the full order system are included in the master DOF set.

For the development of reduced order form of Eq. 2.1, a simplified form of Eq. 2.1 without damping, control forcing and excitation term but with an external forcing term (F) has been considered (see Eq. 2.6).

$$M_{n\times n}\,\ddot{U}_{n\times 1} + K_{n\times n}U_{n\times 1} = F \tag{2.6}$$

The full order system has n as the total number of DOF out of which p DOF will be considered in the ROM. The selection of the p states that will be accommodated in the ROM is a difficult task in static reduction techniques. Therefore, the master DOF contains p modes and the slave DOF contains $n-p$ modes. One can rearrange the stiffness matrix in the following partitioned form separating the master and slave DOFs.

$$K_{n\times n} = \begin{bmatrix} K_{11} & \vdots & K_{12} \\ \cdots & \vdots & \cdots \\ K_{21} & \vdots & K_{22} \end{bmatrix} \begin{Bmatrix} U_m \\ \cdots \\ U_s \end{Bmatrix} = \begin{Bmatrix} F_m \\ \cdots \\ F_s \end{Bmatrix} \tag{2.7}$$

where U_m, U_c are the master and the slave DOFs respectively. As the forces act only on the master DOFs, $F_s = 0$ and hence

$$\begin{aligned} K_{11}U_m + K_{12}U_s &= F_m \\ K_{21}U_m + K_{22}U_s &= 0 \end{aligned} \tag{2.8}$$

Therefore the displacement transformation in the Guyan reduction is given by

$$U_s = -K_{22}^{-1}K_{21}U_m \tag{2.9}$$

Substituting Eq. 2.9 into Eq. 2.8 leads to

$$\left(K_{11} - K_{12}K_{22}^{-1}K_{21}\right)U_m = F_m \tag{2.10}$$

Eq. 2.10 can be written as

$$K_m U_m = F_m \tag{2.11}$$

Therefore, the reduced Guyan Stiffness matrix (Guyan (1965) [133]) is given by

$$K_m = K_{11} - K_{12}K_{22}^{-1}K_{21} \tag{2.12}$$

Similarly the reduced mass matrix can found to be (see Guyan (1965) [133] for details)

$$M_m = M_{11} + M_{12}\left[K_{22}^{-1}K_{21}\right] + \left[K_{22}^{-1}K_{21}\right]^T M_{21} + \left[K_{22}^{-1}K_{21}\right]^T M_{22}\left[K_{22}^{-1}K_{21}\right] \tag{2.13}$$

As shown in the above derivation the full order system with n DOFs can be reduced to p DOF system. Proper choice of p DOFs is indeed needed for better accuracy of the ROM. The use of ROM for the controller design reduces the computation time for determining the feedback gains required by the actuators and therefore improves the overall performance of the combined structure-controller system. Apart from control applications of ROM, it has been successfully applied to the test-analysis model correlation, finite element model updating, parameter identification, dynamic modeling, *etc.*, (Qu et al. (2003a, b) [281, 282]).

2.4 Input Seismic Excitations

Strong ground motion (earthquakes) is generated by a sudden release of energy in the Earth's crust caused by various natural phenomena, such as a tectonic process, volcanic eruption and human activities, *e.g.*, explosion, *etc.*, (Bullen and Bolt (1985) [47]). The seismic waves generated at the source (hypocenter) propagate through different layers of the rock and soil before reaching the earth's surface. On their way to the surface, the seismic waves not only get reflected and refracted but also get filtered and amplified/attenuated. Thus, ground motions generated from earthquakes differ from one another in magnitude, source mechanism, direction from the rupture location, distance from the epicenter and local soil conditions. Broadly from structural engineering point of view, the seismic ground motion is classified into far-fault and near-fault seismic motions.

Near-fault ground motions are measured in the vicinity of an earthquake fault and they are responsible for causing extensive damages to structures. Near-fault ground motions are strongly influenced by the earthquake faulting mechanism exhibiting distinct long period pulses with amplitudes depending on the orientation of the site with respect to the rupture

direction. Near fault seismic motions are characterized by high ratio of peak ground velocities to peak ground acceleration (PGV/PGA). In near field seismic motions the fault-normal component can be several times stronger than its fault-parallel counterpart (Bertero et al. (1978) [41]; Singh (1985) [317]; Erdik and Durukal (2001) [106]).

Either a response spectrum or a time history analysis can be undertaken to obtain the dynamic response of a structure. As the response spectrum analysis of the structure does not provide temporal information of the structural response, a linear or nonlinear time history analysis is performed for important and critical structures like bridges, nuclear power plants, administrative buildings, *etc*. The excitation time history can be generated using recorded data from past events, *e.g.*, available earthquake records for a region or else can be generated artificially using mathematical models. A number of mathematical models have been developed to generate artificial data for earthquakes (Clough and Penzien (1993) [76]). Due to the complex nature of the seismic waves and their travel path before reaching a structure, stochastic approaches have been widely used in the development of the model for an earthquake record. Stationary white noise random process based models are the earliest earthquake simulation methods (Housner and Jennings (1964) [147]). The most favored model is a stationary filtered white noise based Kanai-Tajimi model (Liu and Jhaveri (1969) [213]; Clough and Penzien (1993) [76]).

The Kanai-Tajimi spectral density function may be interpreted as a simulation of an ideal white noise excitation at the bedrock filtered through the overlaying soil deposit at the site. However, earthquake is not a stationary process as it has been treated in the Kanai-Tajimi model. To overcome this shortcoming of the Kanai-Tajimi model, a number of non-stationary stochastic earthquake models have been developed (Shinozuka and Sato (1967) [314]; Claugh and Penzien (1993) [76]; Iyengar and Iyengar (1969) [158]; Ahmadi and Fan (1990) [18]; Rofooei et al. (2001) [295]).

Several analytical models have been proposed for the study of near-fault ground motions. Makris and Chang (2000) [224] classified velocity pulses in near-field ground motions into types A , B and C_n pulses to investigate the performance of various damping systems systematically. These pulses are represented by a unique set of closed-form functions. Type A is a half-cycle forward ground motion pulse; type B approximates a full-cycle forward-and-backward motion and a type C_n approximates a ground motion pulse having n main pulses in

its displacement time history. The velocity histories of all type-A, type-B and type-C_n pulses are differentiated to obtain signals that result in acceleration values. The proposed cycloidal pulses capture the kinematics of the displacement and velocity time histories of recorded near-fault ground motions. The simulated acceleration time history shows poor predictions of the recorded histories, which has been attributed to the high-frequency fluctuations in the near-source ground motions (Makris and Chang (2000) [224]). Alavi and Krawinkler (2004) [25] have proposed three piecewise-linear equivalent velocity pulses and have investigated their suitability in lieu of recorded ground motions. The study (Alavi and Krawinkler (2004) [25]) reported quantitative knowledge on important response characteristics of elastic and inelastic frame structures subjected to near-fault ground motions. The results demonstrate that structures with a period longer than the pulse period respond very differently from structures with a shorter period. For the former, early yielding occurs in higher stories but the high ductility demands migrate to the bottom stories as the ground motion becomes more severe. For the latter, the maximum demand always occurs in the bottom stories.

Mavroeidis and Papageorgiou (2003) [231] have proposed an analytical model of ground motion pulses modeled by Gabor wavelet, which is essentially an amplitude modulated sinusoid. Recently, He (2005) [139] proposed an analytical model of ground motion velocity pulses to incorporate the dominant parameters of ground motions in the design of seismic protective systems. The model is continuous in nature and can be varied to generate various waveforms to represent different excitations. Characteristic parameters of a near-field ground motion can be obtained through curve-fitting analysis on the velocity time history. Then, the displacement and acceleration could either be obtained through integrating or deriving the model velocity history, or be generated directly through the corresponding mathematical expressions with the gained parameters. Validity of the pulse model has been demonstrated through comparison with numerous recorded ground motions, corresponding response spectra and performance of passive energy dissipation systems (He and Agrawal (2005, 2007) [139, 140]).

Pulse models discussed above have been used in the seismic analysis of structures in lieu of recorded ground motions (Makris and Chang (2000) [224]; Alavi and Krawinkler (2004) [25]). However, inclusion of ground motion characteristics in the design of protective systems, *e.g.*, passive, semi-active and active systems, has also been investigated (Agrawal et al. (2006) [8];

Xu (2006) [383]). Results have shown that active and semi-active systems designed for base-isolated buildings by considering ground motion characteristics perform significantly better than those designed without considering ground motion characteristics.

2.5 Structural Control Systems and their Applications

The desired performance of the structure in terms of the safety of the structure as well as the comfort level of the occupants during hazardous environmental loads, *e.g.* earthquake and wind gusts, can be achieved through the applications of structural control technology. As the magnitude of the forces and excitation involved in Civil Engineering structures are quite large and uncertainties involved with both the structural properties (material) and input excitation, the control technology developed for any other engineering applications viz. Aerospace, Chemical and Electrical Engineering problems are not directly applicable to Civil Engineering applications (Leipholz and Abdel-Rohman (1986) [203]).

The basic idea of structural control is to either isolate and/or absorb or reflecting a portion of the input energy that would otherwise be transmitted to the structure itself. The following energy conservation relationship (Uang and Bertero (1988) [360]) shows an illustration of this approach.

$$\mathbf{E} = \mathbf{E}_k + \mathbf{E}_s + \mathbf{E}_h + \mathbf{E}_d \tag{2.14}$$

Where $\mathbf{E}$ = total input energy from environmental forces; $\mathbf{E}_k$ = absolute kinetic energy; $\mathbf{E}_s$ = recoverable elastic strain energy; $\mathbf{E}_h$ = irrecoverable energy dissipated by the structural system through inelastic or other inherent forms of damping; and $\mathbf{E}_d$ = energy dissipated by structural protective systems. From Eq. 2.14, it is evident that, with certain input energy, the demand on energy dissipation through inelastic deformation can be reduced by using structural protective systems. As a result of this approach, many new and innovative concepts for structural protection have been advanced and are at various stages of development (Soong (1990) [322]; Housner et al (1997) [146]; Soong and Dargush (1997) [324]; Symans and Constantinou (1999) [349]; Soong and Spencer (2002) [325]; Spencer and Nagarajaiah (2003) [326]). These control systems are usually classified into four groups, *i.e.*, passive systems, active systems, semi-active systems and a combination thereof known as hybrid systems, depending on

control devices used, control strategies adopted and the requirement on external power supply for actuation of control devices. Full-scale applications of various control systems have been accomplished in many countries, worldwide for both the retrofit of existing structures and in new constructions (Spencer and Nagarajaiah (2003) [326]). Apart from this various benchmark studies have been developed to measure relative performance of various control devices and strategies.

Different control devices used along with the various deployment strategies have been discussed in the next section, with focus being given to base isolated and hybrid base isolation mechanism as they form the basis of the present study.

2.5.1 Passive Control System

Passive control systems are based on the concept of isolating (base isolation) the primary structure from excitation and/or absorbing a part of the vibrational energy as a secondary systems (tuned mass dampers and hydraulic dampers), thereby reducing possible structural damage (Housner et al. (1997), [146]). Passive control devices utilize the motion of the structure to develop control forces and do not require external power supplies during their operation. Therefore, they do not impart external force to the system.

However, passive control systems are of limited capacity in that they can not deal with the change in the external loading conditions. Passive control systems are non-adaptive and are designed optimal for a particular excitation frequency range. Therefore, they do not guarantee safety for all excitation frequencies (for *e.g.*, base isolation optimally designed for Elcentro-1940 earthquake may not have satisfactory performance under Northridge-1994 earthquake).

Various passive control devices designed, developed and deployed on structures are base isolation systems, metallic yield dampers, friction dampers, fluid dampers, tuned mass dampers, tuned liquid dampers, *etc*.

Base Isolation Systems

Most reliable and widely used passive control systems is the base isolation (often referred as seismic isolation) technique. A seismic isolation system, as shown in Fig. 2.4, is typically placed at the foundation of a structure. The isolation system introduces flexibility and energy absorption capabilities, thereby reduces the magnitude of energy transmitted to the structure.

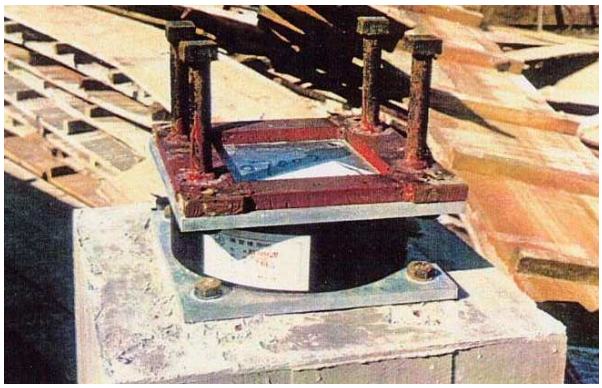

Figure 2.4: Seismic base isolation during deployment [105]

The most important requirement for an isolation system is its flexibility to lengthen the natural period and produce an isolation effect to the structure. It should be sufficiently rigid under service loads, against ambient vibrations and in vertical direction. It should also have energy dissipation capability (Buckle and Mayes (1990) [46]).

Seismic isolation is modeled mathematically as a system that decouples the building or the primary structure from the components of the (ground) excitations by interposing structural elements with low horizontal stiffness, high vertical stiffness and low damping between the structure and the foundation. Figure 2.5 shows a three storey fixed base shear building and a base isolated shear building. The equation of motion for the fixed base building is given in Eq. 2.1. The equation of motion for the base isolated building is given as

$$M_{n\times n}\,\ddot{U}_{n\times 1} + C_{n\times n}\,\dot{U}_{n\times 1} + K_{n\times n}\,U_{n\times 1} = -M_{n\times n}\,R_{n\times 3}\left(\ddot{U}_g + \ddot{U}_b\right)_{3\times 1} \tag{2.15}$$

$$\begin{aligned} R^T_{3\times n}\,M_{n\times n}\,\left[\ddot{U}_{n\times 1} + \,R_{n\times 3}\left(\ddot{U}_g + \ddot{U}_b\right)_{3\times 1}\right]_{n\times 1} + \,M_{b_{3\times 3}}\,\left(\ddot{U}_g + \ddot{U}_b\right)_{3\times 1} \\ +C_{b_{3\times 3}}\,\dot{U}_{b_{3\times 1}} + K_{b_{3\times 3}}\,U_{b_{3\times 1}} + f_{b_{3\times 1}} + f_{c_{3\times 1}} = 0 \end{aligned} \tag{2.16}$$

Equation 2.15 describes the dynamics of the super structure *w.r.t.* to the building reference frame (see Fig. 2.5(b)).

Similar to Eq. 2.1, $U = [U_x,\, U_y,\, U_\theta]^T$ is the vector of structural responses with $U_x = [x_1,\, \cdots,\, x_N]^T$ containing the structural displacements (x_i) in X direction. The seismic excitation vector U_g contains the excitations along X direction (x_g), along y direction (y_g) and any rotational component if present (θ_g). $U_b = [x_b,\, y_b,\, \theta_b]^T$, where, the base isolator displacement

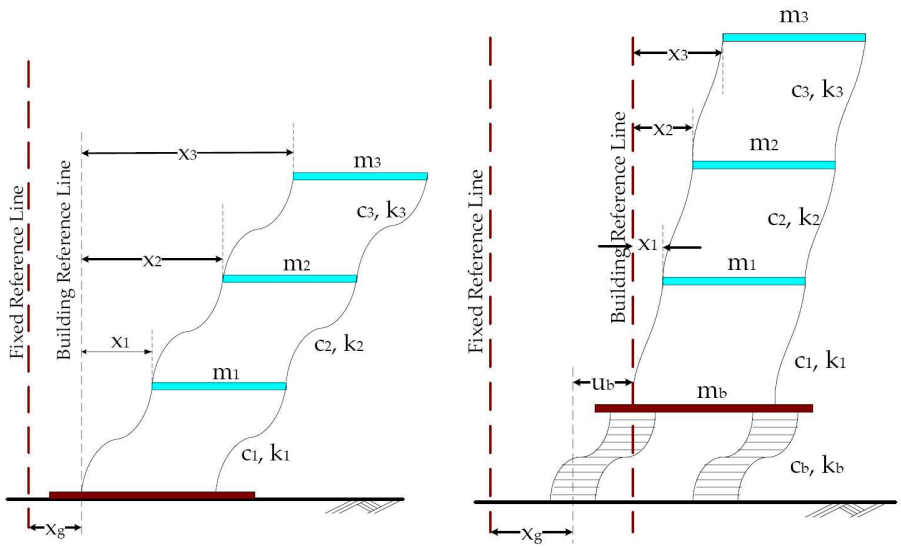

(a) Fixed base building (b) Base isolated building

Figure 2.5: Philosophy of seismic base isolation

along X and Y directions have been represented by x_b and y_b respectively. The rotation at the mass center of the base has been represented by θ_b. Similarly, $\ddot{U}_b = [\ddot{x}_b,\ \ddot{y}_b,\ \ddot{\theta}_b]^T$. R is earthquake influence co-efficients matrix. Equation 2.16 shows the dynamics of the base isolator, in which M_b is the diagonal mass matrix of the rigid base, C_b is the resultant damping matrix of the isolation elements, K_b is the resultant stiffness matrix of elastic isolation elements, f_b is the vector containing the nonlinear bearing forces which may arise due to nonlinear force displacement or nonlinear force-velocity behaviour of the isolators (Narasimhan et al. (2006) [261]) and f_c contains the control device forces. If a linear bearing is assumed without any hysteretic damping the term f_b can be assumed to be zero.

Equations 2.15 and 2.16 can be written in a state space form as shown in Eq. 2.17.

$$\dot{X}(t) = AX(t) + B_b F_b(t) + B_c F_c(t) + E\ddot{U}_g \tag{2.17}$$

with

$$A = \begin{bmatrix} 0 & I \\ -\bar{M}^{-1}\bar{K} & -\bar{M}^{-1}\bar{C} \end{bmatrix};\quad B_b = B_c = \begin{bmatrix} 0 \\ -\bar{M}^{-1}\begin{Bmatrix} 0 \\ I \end{Bmatrix} \end{bmatrix};$$

$$E = \begin{bmatrix} 0 \\ -\bar{M}^{-1} \begin{Bmatrix} MR \\ R^T MR + M_b \end{Bmatrix} \end{bmatrix}; \quad F_b = \begin{bmatrix} 0 \\ f_b \end{bmatrix}; \quad F_c = \begin{bmatrix} 0 \\ f_c \end{bmatrix} \tag{2.18}$$

$$\bar{M} = \begin{bmatrix} M & MR \\ R^T M & R^T MR + M_b \end{bmatrix}; \quad \bar{C} = \begin{bmatrix} C & 0 \\ 0 & C_b \end{bmatrix}; \quad \bar{K} = \begin{bmatrix} K & 0 \\ 0 & K_b \end{bmatrix}$$

where, the state $X = \left\{U^T,\, U_b^T,\, \dot{U}^T,\, \dot{U}_b^T\right\}^T$ is a vector of dimension $2(n+3) \times 1$. In the above equations, A, B_b, B_c and E are condensed system matrices of appropriate dimensions. 0 represents a square matrix of dimension $(n+3) \times (n+3)$ containing zeros in all elements and I represents an identity matrix of dimension $(n+3) \times (n+3)$. As shown in Eq. 2.16 the controller force is assumed to be acting only at the base of the structure, for controller acting other than at base the state space should contain another term as shown in Eq. 2.3.

Since the base of a base isolated structure has less stiffness, the first dynamic mode of the isolated structure involves deformation only in the isolation system, the structure above behaves as a rigid mass (see Fig. 2.5). Therefore seismic isolation systems are effective in reducing inter-storey drift and storey acceleration at the cost of large base displacement. The large base displacement makes the connection of the infrastructural utilities such as water and power supply, communication lines, *etc.*, difficult and various innovation means are used to protect them from failure during large earthquakes (Hussain and Satary (2007) [150]). The excessive flexibility at the base of the building also becomes a cause of concern during excessive wind (Hussain and Satary (2007) [150]). Therefore, a certain level of damping is desirable to suppress wind induced displacement at the base as well as a possible resonance condition at the isolation frequency. *Lead rubber bearings*, *high damping rubber bearings*, *sliding friction pendulum bearings*, or *elastomeric bearing* with supplemental viscous dampers are used to provide additional damping to the isolated structure (Soong and Constantinou (1994) [323]; Naeim and Kelly (1999) [243]).

Numerous seismically isolated structures have been built in many countries during the last twenty years. In fact, of a total of about 5000 isolated structures existing in the world at the end of year 2006, of which over 3000 are in Japan, 600 in the Russian Federation and others

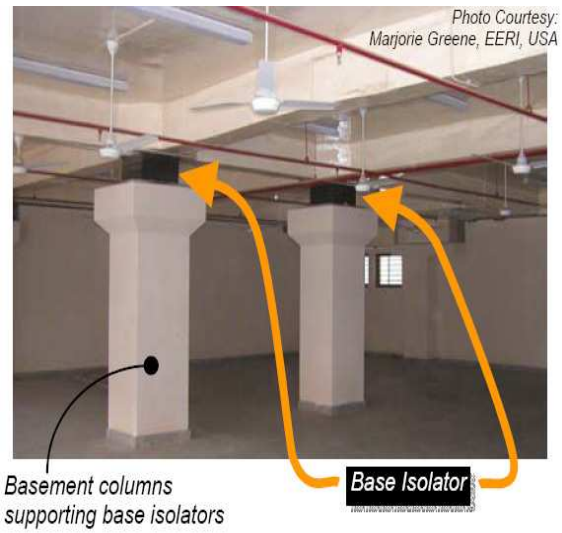

Figure 2.6: Base isolation in Bhuj Hospital Building, Gujrat, India (EERI (1999) [103])

in Italy, Turkey, Peoples Republic of China, United States, *etc.*, (Medeot (2007) [234]). Important buildings and public utility service buildings (like, hospitals, Government offices), have been constructed with base isolation system. In the United States, several implementations of seismic isolation systems have been reported; examples include the Salt Lake City Building (Mayes et al. (1988) [232]; Walters et al. (1986) [363]), the USC University Hospital (Asher et al. (1990) [34]), the Los Angeles City Hall (Youssef et al. (1995) [411]), and the San Bernardino County Medical Center (Asher et al. (1994) [33]), *etc.*, to name a few.

In India, base isolation technique has been first demonstrated after the 1993 Killari (Maharashtra) Earthquake (EERI (1999) [103]). Two single storey buildings (one school building and another shopping complex building) in relocated Killari town have been constructed with rubber base isolators resting on hard ground. Both are brick masonry buildings with concrete roof. After the 2001 Bhuj (Gujarat) earthquake, a four-storey Bhuj Hospital building has been built with base isolation technique (Fig. 2.6). Currently a army hospital building is being constructed with base isolation in Shimla (Himachal Pradesh, India) (Rai et al. (2007) [284]).

Base isolated structures undergo large base displacement in near field earthquakes as has been seen in recent earthquakes like, Northridge-1994, Kobe-1995, Turkey-1999 and Chi-Chi-1999. Therefore, the performance of seismic isolation under near field earthquake has been questioned (Celebi (1996) [56]; Hall et al. (1995) [136]; Heaton et al. (1995) [141]; Yoshioka et al. (2002) [410]).

Passive Energy Dissipation Devices

Another example of a passive control system is the passive supplemental damping devices. These devices protect a structure by increasing its energy dissipation capacity. A supplemental damping system absorbs a portion of the input seismic energy, thereby reducing energy dissipation demands and preventing damage to the primary structure. The method utilizes devices that operate on principles such as frictional sliding, yielding of metals and deformation of viscoelastic solids or fluids (Housner et al. (1997) [146]; Soong and Dargush (1997) [324]; Soong and Spencer (2002) [325]).

Metallic yield dampers: Inelastic deformation of metals is one of the effective mechanisms for dissipation of energy. Many of these devices use mild steel plates with triangular or X-shapes so that yielding is spread almost uniformly throughout the material. A typical X-shaped plate damper or ADAS (added damping and stiffness) device is shown in Fig. 2.7. Other configurations of steel yielding devices, used mostly in Japan, include bending type of honeycomb and slit dampers and shear panels. Materials, such as lead and shape-memory alloys, have also been evaluated (Aiken and Kelly (1992) [20]). Important features of these devices are their stable hysteretic behaviour, low-cycle fatigue property, long term reliability, and relative insensitivity to environmental temperature. Hence, numerous analytical and experimental investigations have been conducted to determine these characteristics of individual devices.

Metallic devices has been implemented in full-scale structures in New Zealand and Japan for the first time. A number of these interesting applications are reported in Soong and Spencer (2002) [325]. Examples of metallic yield dampers can be found in (Clark et al. (1999) [75]; Dargush and Soong (1995) [84]; Scholl (1993) [307]; Tsai et al. (1993) [358]; Wada et al. (1999) [362]; Whittaker et al. (1993) [373]; Xia and Hanson (1992) [380]), *etc.*

Friction dampers: Solid friction that develops between two solid bodies sliding relative to one another provides the desired energy dissipation in friction dampers. Several types of friction dampers have been developed depending upon mechanical complexity and sliding materials. The sliding surfaces generally consist of steel on steel, brass on steel and graphite bronze on stainless steel. An example of such a device is shown in Fig. 2.8. During cyclic loading, the mechanism enables slippage in both tensile and compressive directions. Generally, friction

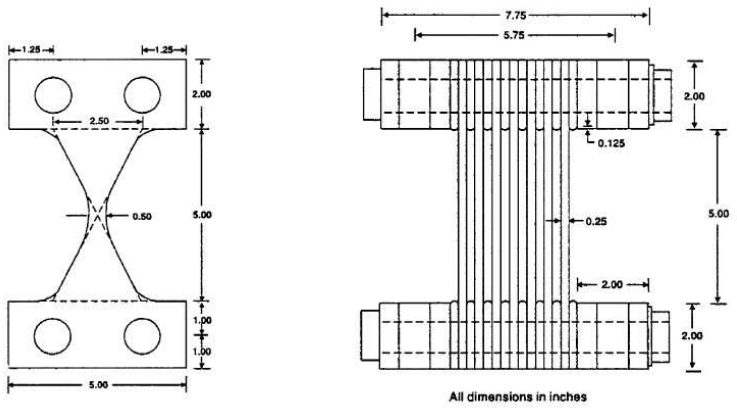

Figure 2.7: Metallic Yeild Dampers (ADAS) (Aiken and Kelly (1992) [20])

devices generate rectangular hysteretic loops similar to the characteristics of Coulomb friction.

Pall device (Pall and Marsh (1982) [270]), Sumitomo friction damper (Aiken and Kelly (1990) [19]), energy dissipating restraints (Nims et al. (1993) [265]) and slotted bolted connection energy dissipater (FitzGerald et al. (1989) [118]; Grigorian et al. (1993) [132]) are some of the commonly used friction dampers. Various other types of friction dampers have been reported in Colajanni and Papia (1997) [77]; Filiatrault and Cherry (1990) [116]; Filiatrault et al. (2000) [117]; Levy et al. (2000) [206]; Li and Reinhorn (1995) [208]; Scholl (1993) [307].

In recent years, there have been a number of structural applications of friction dampers aimed at providing enhanced seismic protection of new and retrofitted structures. Mualla and Belev (2002) [241] have proposed a friction damping device and its effectiveness has been investigated for an earthquake excited single storey steel frame building model.

Viscoelastic dampers: Viscoelastic materials like co-polymer or glassy substances are used between steel plates, which dissipates energy through shear deformation of Viscoelastic layer (see Fig. 2.9), *i.e.*, when there is a relative motion between outer and central steel plates (Housner et al. (1997) [146]; Soong et al. (2002) [325]). Other than glassy substances, solid thermoplastic rubber sheets are reported to be effective in reducing seismic responses (Fujita (1991) [125]). The damper contributes to increased viscous damping as well as lateral stiffness. Therefore, these devices are effective for both wind and seismic protection.

Viscoelastic material behaviour, under dynamic load, changes with vibrational frequency, strain and ambient temperature (Zhang et al. (1989) [417]; Tsai and Lee (1993) [356]; Housner

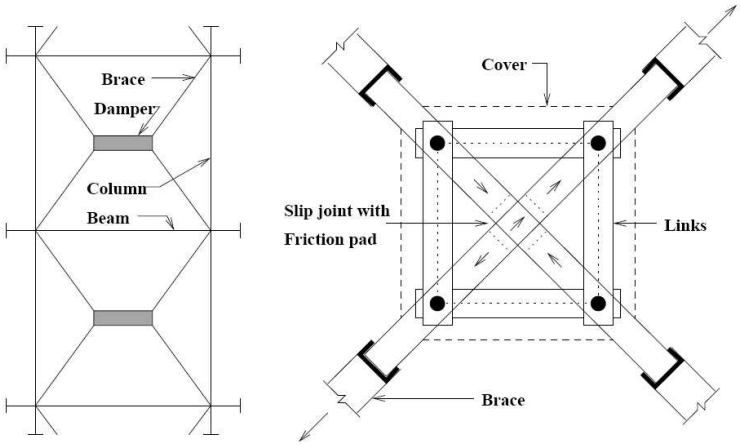

Figure 2.8: X-Braced Friction Damper (Pall and Marsh (1982) [270])

et al. 1997 [146]). One of the key issues before installing these devices is to verify the temperature sensitivity of the devices. Temperature effect on the behaviour of viscoelastic dampers has been investigated (Chang et al. (1992) [60]; Shen and Soong (1995) [313]) and it has been reported that the natural period of the visco-elastically damped system varies moderately at low temperatures. Therefore, they remain linear over a wide range of strain provided the temperature remains constant. At large strain or large amount of energy dissipation, self-heating of dampers result in nonlinear systems due to change in material properties (Nielsen et al. (1994) [263]). Various analytical models are available in literature to characterize the force deformation relation of these devices (Zhang et al. (1989) [417]; Zhang and Soong (1992) [416]; Shen and Soong (1995) [313]; Housner et al. (1997) [146]). Some of them are validated using experimental results (Chang et al. (1995) [61]). Other examples of viscoelastic dampers have been reported in Ferry (1980) [113]; Crosby et al. (1994) [82]; Makris and Dargush (1994) [225]; Shen and Soong (1995) [313]; Aprile et al. (1997) [30]; Higgins and Kasai (1998) [143]; .

The metallic yield and friction dampers are primarily intended for seismic applications because these devices are effective for large displacement levels. The displacement response of the building structure is, in general, low under wind excitation and low intensity earthquakes. Viscoelastic solid materials can be used to dissipate energy against wind gusts and earthquakes also. In fact experimental and analytical studies have demonstrated the effectiveness of the viscoelastic dampers for steel and reinforced concrete structures under a wide range of earthquake excitations (Chang et al. (1994, 1995) [59, 61]; Shen et al. (1995) [313]). A

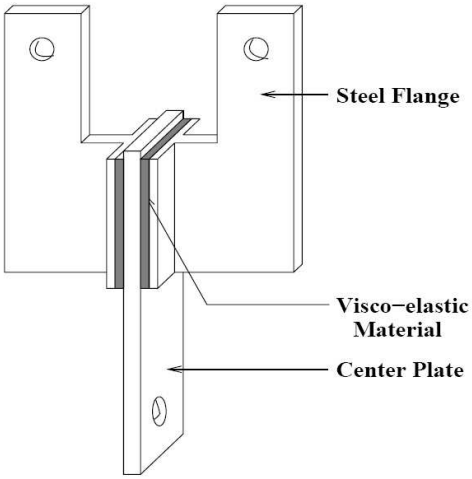

Figure 2.9: Viscoelastic Damper (Shen and Soong (1995) [313])

combination of the friction damping device for control of structural damage due to severe excitation and viscoelastic damping device for low energy excitations has also been investigated (Pong et al. (1994a, b) [278, 279]; Tsiatas and Dely (1994) [359]).

Viscous fluid dampers: Civil Engineering community adopted viscous fluid dampers from the military and aerospace industry, where it has been used for many years. The viscous fluid devices developed for Civil Engineering applications include viscous walls and viscous fluid dampers. The movement of steel plate (*viscous wall dampers*) or cylindrical piston (*viscous fluid dampers*) in a viscoelastic fluid causes the system to dissipate energy (Constantinou et al. (1993) [78]; Constantinou and Symans (1992,1993) [80, 81]; Makris (1991) [221]). The liquid used in a viscous fluid dampers is a compound of silicone or similar type of oil and the chamber may contain a number of orifices, so that the passage of fluid is allowed across the piston, thereby, dissipating energy.

Viscous fluid dampers have been incorporated into a large number of Civil Engineering structures due to linear viscous response achieved over a broad frequency range, insensitivity to temperature and compactness. A typical viscous fluid damper is shown in Fig. 2.10.

The general damping force-velocity relationship of a viscous damper is given by

$$f_c = C_d \left|\dot{x}_d\right|^n \text{sign}(\dot{x}_d) \tag{2.19}$$

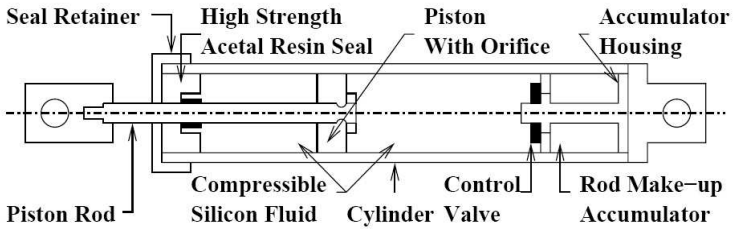

Figure 2.10: Viscous Fluid Damper (Constantinou et al. (1993) [78])

where f_c is the damping force across the viscous damper, C_d is the damping coefficient, which is determined experimentally and is a function of temperature of the fluid inside the damper. $\dot{x}_d$ is the relative velocity at the damper location. Factor n is a real positive exponent to be determined experimentally, its typical value ranges between $0.35 - 1$ (Agrawal et al. (2003) [12]) for seismic applications. For low damping force rates, *i.e.*, for small vibrating frequency, the value of factor n is considered to be 1, which represents a linear viscous damper.

Viscous fluid damper finds several applications, when they have been used in combination with seismic isolation systems to reduce the base displacement (Hussain and Satary (2007) [150]), for example, in 1995, dampers have been supplemented with base isolation systems for five buildings in the San Bernardino County Medical Center, located close to two major fault lines. It has also been used to reduce cable vibrations in cable supported bridges, where they are connected between the cable and the deck (Agrawal et al. (2003) [12]). In Italy, a 1 km bridge weighing $25,000$ ton is protected using 500mm stroke, 2m long viscous-silicon gel damper weighing 2 ton at each tower (Housner et al. (1997) [146]). Various application and details of viscous fluid dampers have been reported in Constantinou et al. (1993) [78]; Constantinou and Symans (1992,1993) [80, 81]; Makris (1991) [221]; Reinhorn et al. (1995) [290]; Taylor and Constantinou (1996) [355], and for viscous wall damping (Arima (1988) [31]; Miyazaki and Mitsusaka (1992) [238]; Reinhorn and Li (1995) [291]).

Tuned Dampers

The family of tuned dampers consists of tuned mass damper (TMD), tuned liquid dampers (TLD) and tuned liquid column dampers (TLCD). They are mostly efficient in reducing wind induced vibration of structures. They are tuned to the fundamental frequency of the primary

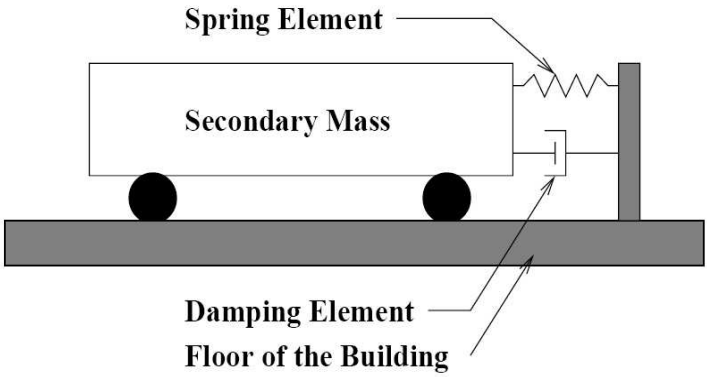

Figure 2.11: Tuned Mass Damper

structure such that the fundamental frequency of the overall system shift from the predominant frequency range of the excitation (Housner et al. (1997) [146]; Soong and Spencer (2002) [325]).

Tuned mass dampers (TMD): It consists of a secondary mass with properly tuned spring and damping elements, providing a frequency dependent hysteresis that increases damping in the primary structure. TMD can successfully mitigate the wind-excited responses of structures within its frequency band limits. This device is particularly effective for stationary narrow band excitations, but is less effective for broadband excitation such as earthquake. Early applications of tuned mass dampers (TMDs) have been directed towards mitigation of wind-induced excitations. Recently, numerical and experimental studies have been carried out to examine the effectiveness of TMDs in reducing seismic response of structures by integrating it with other seismic control devices (Ahlawat and Ramaswamy (2003, 2004) [16, 17]). It is noted that a passive TMD can only be tuned to a single structural frequency. While the first-mode response of a MDOF structure with TMD can be substantially reduced, the higher mode response may in fact increase as the number of stories increases. To overcome this multiple TMD (MTMD)are installed and tuned to different frequencies of the structure (Clark (1988) [74], Yamaguchi and Harnpornchai (1993) [386]; Setareh (1994) [312]; Jangid and Dutta (1997) [163]; Jangid (1999) [164]). Jangid and Dutta (1997) [163]; Jangid (1999) [164] analyzed the effectiveness of the MTMD for two DOF torsional system. Lin et al. (2000) [211] has studied the optimal orientation of one and two TMD for a multi-storey torsional building system.

Details of TMDs have been discussed in Den Hartog (1947) [85]; Clark (1988) [74]; Tsai and Lin (1993) [357]; Abe and Fujino (1994) [3]; Sadek et al. (1997) [299]; Jangid (1999) [164]; Li (2000) [207]; Ahlawat and Ramaswamy (2003, 2004) [16, 17].

Tuned liquid dampers (TLD) and Tuned liquid column dampers (TLCD): The basic concept of TLD, TLCD and TMD is same, *i.e.*, seismic energy dissipation through absorption. The only difference is that TLD absorbs structural energy by means of viscous action of fluid and wave breaking and TLCD diverts energy by the passage of liquid through orifices with inherent head loss characteristics.

However, in the case of TLD and TLCD, the damper response is highly nonlinear due to liquid sloshing and the presence of orifices. TLDs have also been used for suppressing wind-induced vibrations in tall structures. In comparison to TMDs, the advantages associated with TLDs include their low initial cost. They are virtually free of maintenance and are easy to tune to frequency range.

The TLD applications have taken place primarily in Japan for controlling wind-induced vibration. Examples of TLD-controlled structures include airport towers and tall buildings. Other applications of TLDs have been reported in Fujino et al. (1992) [123]; Xu et al. (1992) [382]; Balendra et al. (1995) [37]; Sun et al. (1995) [346]; Reed et al. (1998) [287]; Sadek et al. (1998) [298]; Yu et al. (1999) [412]; Banerji et al. (2000) [38].

A comprehensive review of the literature on passive supplemental damping devices for Civil Engineering structures can be found in Soong and Dargush (1997) [324] and Soong and Spencer (2002) [325].

Passive supplemental damping devices for structural applications have been researched and developed for the past thirty years. Recently, efforts to develop these concepts into a workable technology have increased significantly, and a number of these devices have now been installed in structures throughout the world. For example, metallic yield dampers have been used to retrofit a two-storey concrete building in San Francisco (Perry et al. (1993) [275]), and three reinforced concrete buildings in Mexico City (Martinez-Romero (1993) [228]). Pall friction dampers have been installed in thirteen buildings in Canada including six retrofits and seven new facilities. Viscoelastic dampers have been installed in the former World Trade Center in New York City to reduce wind-induced vibrations (Mahmoodi et al. (1987) [220]).

Taylor viscous fluid dampers have been installed in the newly-constructed San Bernardino County Medical Center in California as components in the rubber bearing seismic isolation system (Soong and Dargush (1997) [324]). TMDs have been installed in the Citicorp Center in New York City, the John Hancock Tower in Boston, the main towers of the Akashi-Kaikyo Bridge in Japan (Koshimura et al. (1994) [191]), and the Sydney Tower in Australia (Kwok and Denoon (2000) [198]) whereas tuned liquid dampers have been installed in the Nagasaki Airport Tower, the Yokohama Marine Tower, and the Shin-Yokohama Prince Hotel (Soong and Dargush (1997) [324]).

Although passive devices provide stable and robust performance during designed earthquakes, they are incapable of adjusting themselves in the cases of variable excitations. As a result, a passive system that works very well for one earthquake may be may not perform equally well during another earthquake. To design an optimal controller for multiple earthquake excitations, such that the system responds optimally to the change in frequency content of excitation, one has to adopt active and/or semi-active systems.

2.5.2 Active Control Systems

In active control system, an actuator driven by an external power source applies a control force to the structure in a prescribed manner to control the vibration. The ability to adapt to different loading conditions and to control different vibration modes of the structure make an active control systems attractive but tremendous power requirement for its deployment on Civil structures restricts its applications (Housner et al. (1997) [146]). The schematic diagram of an active control system (with feedforward-feedback loop) is shown in Fig. 2.12. In this system, the signals sent to control actuators are a function of responses of the system measured with the sensors (Soong (1990) [322]; Housner et al. (1997) [146]). Hence, the control force depends on the dynamics of the sensor and actuator, control law, and the measured response. For a given actuator, sensor and control law, the control force (f_c) is a function of the measured response (y_m) and given as

$$f_c = F(y_m) \tag{2.20}$$

The basic task for an active control system designer is to determine a control strategy (algorithm) that uses the measured structural responses (y_m) to calculate appropriate control

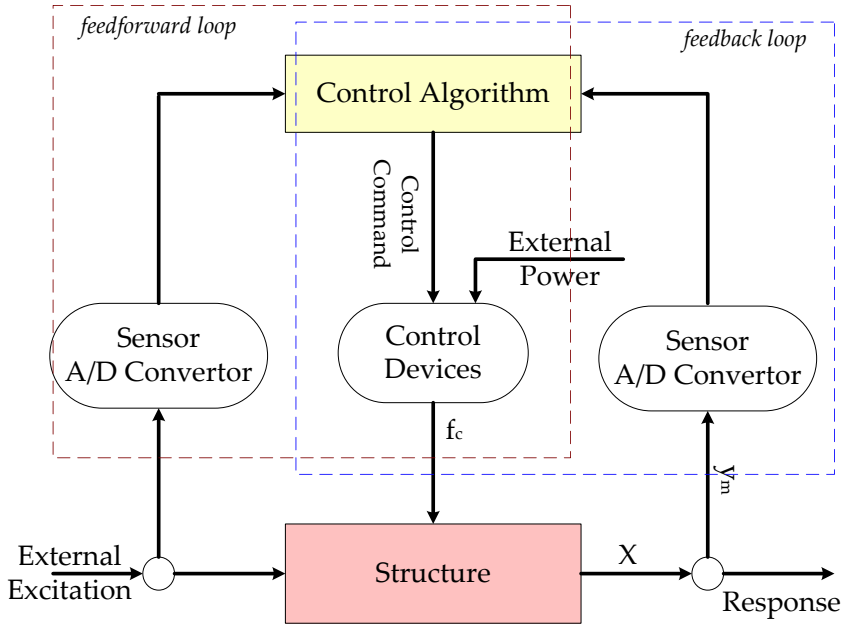

Figure 2.12: Feedforward-feedback active control system

signals to be sent to actuators.

Figure 2.12 shows feedforward and feedback loop together. In an open Loop (feed-forward) control system external excitation is measured alone to determine the control force (see Fig. 2.12). In a closed loop system (feedback loop) the external excitation is not measured instead some system responses were measured and control decision is taken based on the measured variables (y_m). For a proportional control law, displacement, velocity, and acceleration feedback modify the effective stiffness, damping and mass of the structure, respectively (Eqs. 2.1 and 2.20). Thus, using an active control system, the dynamics of the structure can be altered in a desired way.

Majority of the active control systems used for the structural vibration control are feedback control systems because of their better robustness in comparison to the feed-forward control system (Soong (1990) [322]). As the external energy source is used to apply the control force, the active control system provides better performance in terms of the reduction in the structural responses. However, unlike a passive control system, the active control systems are not inherently stable because of several factors related to the practical implementation of

an active control system, *e.g.*, computational time delay (due to dynamics of the sensors and actuators, *etc.* the control action computation from the measured response is not available instantaneously), huge power requirement. Thus there is a time lag between measurement of the response and application of the control force or in other words the applied control force is not in phase with the measured response. For a small time delay (less than the time periods of highest frequency of structure under consideration), a negative velocity feedback results in two components of the control force increasing the damping and stiffness of the structure. Similarly an acceleration feedback leads to increased mass and damping. Displacement feedback with a small time delay increases stiffness and decreases the damping in the dynamics of the structure. This decreased damping may result in an unstable system. Thus, the stability of an active control system depends on the dynamics of the sensors and actuators and the time delay in addition to the control law and must be considered in the design of the active control system (Goh and Caughey (1985) [131]).

Active control devices developed and investigated for vibration control of buildings include an active tendon system, an active mass damper system and an active mass driver system. All these active control devices employ a hydraulic, pneumatic, electromagnetic or an electric motor driven actuator.

Active tendon system

The active tendon system generally consists of a set of pre-stressed tendons connected to a structure and the tension in these tendons is controlled using actuators. A typical arrangement of the active tendon control system for building is shown in Fig. 2.13. Control force applied at the floor level of the building is given by

$$\begin{aligned} f_c &= -4k_t\, cos(\alpha_t) d_a \\ d_a &= F(u_c) \end{aligned} \tag{2.21}$$

Where k_t is the stiffness of the tendon, α_t is the angle of inclination of the tendon (see Fig. 2.13) with the floor and d_a is the actuator displacement that is a function of the control command u_c. The negative sign is because the direction of the control force f_c is opposite to the actuator displacement and the factor 4 accounts for the two pairs of tendons participating in the process. The effect of control force in the dynamics of the controlled structure mainly depends on

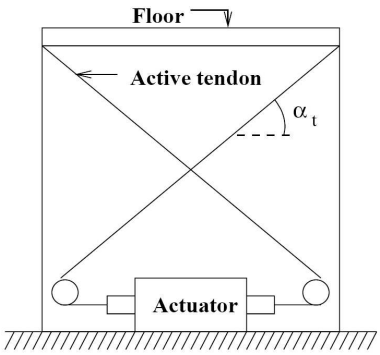

Figure 2.13: Active tendon system

the control law and the responses selected for the feedback.

The main advantage of the active tendon system is the utilization of already existing tendons in the structures. From Fig. 2.13 and Eq. 2.21 it is seen that the required actuator force to produce a displacement d_a is $4k_t d_a$. The force utilized for the control action is a fraction ($cos(\alpha_t)$) of the total actuator force because of the angle α_t of the tendon with the floor. Thus, the active tendon system can utilize only part of the force produces by the actuator.

Application of the active tendon system in vibration control of slender structures have been investigated by Roorda (1975) [296]; Yang and Giannopulos (1978) [396]. Juang et al. (1980) [172]; Yang and Samali (1983) [400]; Abdel-Rohman and Leipholz (1983) [2]; Samali et al. (1985) [305]; Abdel-Rohman (1987) [1] have investigated the effectiveness of the active tendon system for wind excited tall buildings. Yang and Giannopulos (1979a, b) [397, 398] have investigated the active tendon control system for cable stayed bridges. An experimental and analytical study on the active tendon system has been carried out at Structural Dynamics and Control/Earthquake Engineering Laboratory (SDC/EEL), Notre-Dame and presented as the first generation benchmark problem (Spencer et al. (1998a) [327]). The effectiveness of the various control strategies for this benchmark problem has been investigated by a number of researchers. Johnson et al. (1998) [171] has investigated the multi-objective H_2 norm performance with H_∞ and L_1 norm as constraint. Bani-Hani and Ghabousi (1998) [39] and Wu et al. (1998) [379] have investigated the performance of a neural network controller and fixed order mixed norm (H_2, μ) controller have been reported by Agrawal et al. (1998) [13] and Whorton et al. (1998) [374] respectively.

Active Mass Damper/Driver System

Tuned mass dampers are in general tuned to the first fundamental frequency of the structure and thus effectively control the structure only when the first mode of vibration is dominant. Effectiveness of the TMD over a narrow band of the excitation frequency, render these devices ineffective in the event of an excitation having vibrational energy spread over a wider frequency band leading significant contribution from the higher modes. This limitation of the TMD can be alleviated using an active controlled actuator with a TMD to supplement the passive control force. The effectiveness of TMD can be improved either using an actuator in parallel to the stiffness and the damping elements or by replacing the damping element or both the stiffness and damping element by an actuator. If an actuator is connected in parallel to the stiffness and damping elements of the TMD, the device is called active tuned mass damper (ATMD). If the damping element of the TMD is replaced by an actuator, the system is known as active mass damper and if both the damping and the stiffness elements are replaced by actuator the system is known as active mass driver (AMD).

The equation of motion of an active mass damper/active mass driver system is given by

$$\begin{aligned} m_a\ddot{d}_a + c_a\dot{d}_a + k_a d_a &= -m_a\ddot{x}_N + k_a u_c \\ f_c &= c_a\dot{d}_a + k_a d_a \end{aligned} \tag{2.22}$$

Where, m_a, c_a and k_a are the total mass, total damping and total stiffness of the AMD, respectively, including auxiliary mass and stiffness (in case of an active mass damper) of the AMD and mass, damping and stiffness of the actuator. d_a is the relative displacement of the auxiliary mass with respect to the floor on which the device is installed and $\ddot{x}_N$ is the floor acceleration. u_c is the control command. As the control command is computed from the measured response, the dynamics of the control device may be altered in a desired way to improve the effectiveness of the passive TMD system over a wider frequency range.

Feasibility and effectiveness of the AMD has been investigated experimentally and analytically (Abdel Rohman (1987) [1], Soong (1990) [322], Masri et al. (1982) [229]). The first generation benchmark problem (Spencer et al. (1998a) [328]) has also been developed using an AMD system. Effectiveness of the AMD in reducing the vibration of the structures is limited by two factors, (i) available power to drive the actuator and (ii) the dynamics of the

actuator. The control force and power requirement for the active control of Civil Engineering structure is quite large and forms the major constraint on the achievable performance of the AMD system.

The active control system was first implemented in a building by the Kajima Corporation in 1989. Two active mass drivers (AMDs) were installed in the Kyobashi-Seiwa building to reduce both transverse and torsional vibrations. Most of the real structures employ hybrid mechanism, where in active system have been supplemented with various passive damping devices. Detailed lists are provided by Soong and Spencer (Soong and Spencer 2002 [325]) and Spencer and Soong (Spencer and Soong 1999 [336]). However, in contrast to passive control systems, active control systems need large external power sources to control actuators which apply forces to the structure in a prescribed manner. These forces can be used to both add and dissipate energy in the structure, and have the possibility to destabilize the overall system. Therefore, a number of serious challenges need to be solved before active control technology can gain general acceptance by the engineering and construction professions at large. These challenges include: (i) reducing capital cost and maintenance; (ii) eliminating reliance on external power; (iii) increasing system reliability and robustness; and (iv) gaining acceptance of nontraditional technology (Spencer and Sain (1997) [331]).

As discussed earlier, active systems require large power and are not stable and robust like passive systems. Power failure during earthquakes makes an active system unreliable. Therefore, the focus if structural vibration has been on semi-active devices, which has both the properties passive and active systems.

2.5.3 Semi-Active Control Systems

A semi-active system has stability and robustness as a passive system and has adaptive properties of an active system *i.e.*, a semi-active control device can be looked upon as a passive device with real time controllable properties. Therefore they are frequently referred to as controllable passive dampers. The power required for the semi-active devices is far less than that of active systems and many of the semi-active devices can work on battery power. Semi-active devices do not impart force to the primary structure and therefore they are stable systems in a bounded input bounded output sense (Housner et al. (1997) [146]; Symans and Constantinou (1997, 1999) [348, 349]; Soong and Spencer 2002 [325]).

Semi-active control systems have attracted a great deal of attention of structural engineers as they can operate on battery power, proving advantageous during seismic events when the main power source to the structure may fail. Recent work by several researchers has indicated that semi-active control systems, when appropriately implemented, achieve significantly better results than passive control systems. They may even outperform fully active control systems, demonstrating significant potential for controlling structural responses over a wide range of dynamic loading conditions (Dyke et al. (1997, 1996a, b, 1998) [97, 99, 100, 101]; Jansen and Dyke (2000) [166]; Johnson et al. (2003, 2007) [169, 168]; Ramallo et al. (2001) [286]; Spencer et al. (2000)[330]; Yi and Dyke (2000)[404]; Yoshioka et al. (2002) [410]).

The family of semi-active devices include adjustable tuned liquid dampers, variable orifice dampers, variable friction dampers, controllable fluid dampers and variable stiffness system. Semi-active devices are inherently nonlinear and their implementation on a structure make the overall system nonlinear. Therefore, nonlinear control algorithms are necessary for monitoring these devices.

Variable orifice dampers

Variable orifice dampers can alter the damping of a hydraulic device by changing the hydraulic fluid flow resistance using an electromechanical variable orifice. The concept of applying this type of variable-damping device to control the motion of bridges experiencing seismic motion has been first introduced by Feng and Shinozuka (1990) [111] and Kawashima et al. (1992) [180]. After this various modified form of the device but on the same principle has been reported. Symans et al. (1994) [350] modified a passive fluid damper to develop a semi-active fluid damper by adding an external bypass loop which contains a controllable valve. The behaviour of semi-active fluid dampers is essentially the same as exhibited by passive fluid dampers, except that semi-active fluid dampers have an adjustable damping property, enabling them to deliver a wide range of damping levels. This damper needs can operate on battery power (Symans and Constantinou (1997) [348]).

Kobori et al. (1993) [189] presented a semi-active variable-stiffness system using variable orifice dampers. The system has been implemented on a building at the Kobori Research Complex to investigate the semi-active structural vibration control. More recently, full-scale semi-active hydraulic dampers were installed in a five-storey steel structure in the Kajima

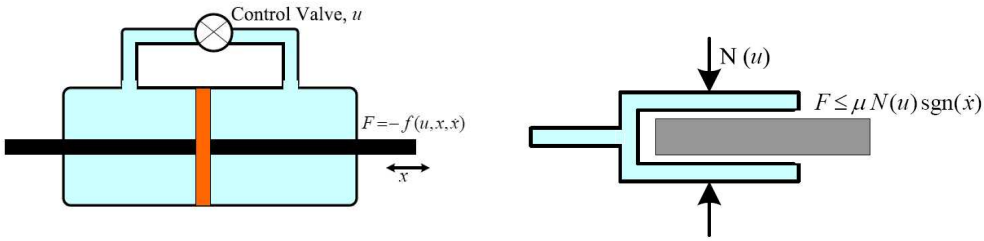

(a) Variable orifice damper (b) Variable friction damper

Figure 2.14: Semi-active dampers: (a) Variable orifice damper, (b) Variable friction damper

Shizuoka Building in Shizuoka, Japan (Kurata et al. (1999, 2000) [197, 196]). Each damper can produce a maximum damping force of 1000 kN. Patten (1998, 1999) [272, 273] has also designed a semi-active vibration damper which is comprised of a hydraulic actuator controlled by a motor operated valve, which has been installed on the Walnut Creek Bridge on Interstate Highway $I-35$ in Oklahoma to reduce vehicle-induced vibrations.

Figure 2.14(a) shows a schematic diagram of a typical semi-active variable orifice damper. Because of its time-varying damping coefficient, which makes it difficult to apply standard control methods, bang-bang control and instantaneous optimal control methods were developed for this system (Feng and Shinozuka (1990) [111]).

Variable friction dampers

Variable friction dampers (VFD) dissipate vibration energy in a structural system by utilizing force generated through surface friction. These devices typically consists of a preloaded friction shaft rigidly connected to the structural bracing (as shown in Fig. 2.14(b)). First study on VFD has been reported by Akbay and Aktan (1990, 1991, 1995), [21, 22, 23]. In these studies the operation of the brace has been controlled by the preload on the friction interface, which in turn hs been actively regulated through commands generated by the controller during earthquakes or severe wind excitations. A similar device has been studied by Dodwell and Cherry (1994) [89] who developed a clamp and release "On-Off" algorithm. In this algorithm, the slip load is maintained at a constant value until the inter-storey drift velocity approaches zero. At

zero velocity the slip force is momentarily reduced to zero (Off), allowing the brace to reposition itself, and then is returned to its original (On) value. Dodwell and Cherry (1994 [89]) developed another algorithm based on the linear quadratic regulator to control the normal force on the friction surface. The analytical and experimental results indicate that both the methods can reduce the inter-storey drift significantly. The "On-Off" control scheme seems to be most suitable for single-degree-of-freedom (SDOF) structures, while the active control approach is effective in both SDOF and multi-degree-of-freedom (MDOF) structures.

A semi-active friction controllable fluid bearing has been reported by Feng et al. (1993) [112] for a hybrid seismic isolation system. In this system, the pressure in the fluid can be varied to control the amount of friction at the isolation surface, providing the system with the ability to adapt to various excitations. Inaudi (1997) [151] modeled the semi-active friction damper as a modulated homogeneous friction (MHF) system. A control algorithm is proposed in which only the deformation of the damper is used as feedback signal for the controller. The MHF system yields a rate independent force-deformation relation when dissipating the same amount of energy in a sinusoidal deformation cycle for any frequencies.

Continuous variable stiffness/damping device

A variable stiffness device, whose stiffness varies between some particular values in steps, has been introduced by Kobori et al. (1993) [189], using on-off model to investigate semi-active control of Kajima Research Institute building. Application of sliding mode control technique with variable stiffness systems to seismic-excited buildings has been presented by Yang et al. (1996, 1997) [403, 401].

Nagarajaiah (Spencer and Nagarajaiah (2003) [326]) has developed another continuously varying stiffness device SAIVS (semi-active continuously and independently variable stiffness device). Its efficiency as a continuously varying stiffness device has been studied by Nagarajaiah and Mate (1998) [246]; Nagarajaiah and Varadarajan (1999) [257]. Effectiveness of SAIVS device in reducing seismic response of sliding base isolated buildings has also been shown analytically and experimentally (Nagarajaiah and Sahasrabudhe (2006) [254]; Nagarajaiah et al. (2006) [245]; Sahasrabudhe and Nagarajaiah (2005b, c) [300, 301]).

A new semi-active independently variable damper (SAIVD) has been developed by Nagarajaiah and Narasimhan (2007) [249] and shown to be effective in achieving response reductions in smart base isolated buildings under near fault earthquakes. The semi-active device consisted of four linear viscoelastic elements arranged in a rhombus configuration. The magnitude of force in the semi-active device can be adjusted smoothly in real-time by varying the angle of the viscoelastic elements of the device or the aspect ratio of the rhombus configuration. The smooth semi-active force variation eliminates the disadvantages associated with rapid switching devices. Experimental results have been presented to verify the proposed analytical model of the device. A H_∞ control algorithm has been implemented in order to reduce the response of base isolated buildings with variable damping semi-active control systems in near fault earthquakes.

A new semi-active mass damper consisting of semi-active variable stiffness system and tuned mass dampers has been reported by Nagarajaiah and Sonmez (2007) [256]. The device is popularly known as semi-active tuned mass dampers. The STMD has the distinct advantage of continuously retuning its frequency in real time, thus making it robust to changes in primary system stiffness and damping. The STMD device has been studied by developing on-line tuning using empirical mode decomposition-Hilbert transform (Nadathur and Nagarajaiah (2004) [242]) and short time Fourier transform (STFT) algorithms (Nagarajaiah and Nadathur (2005) [247]; Narasimhan and Nagarajaiah (2005) [258]), which tune the frequency of STMD and reduce the primary structural response. It has been shown that STMD is effective in reducing wind induced response of buildings and is robust against changes in building stiffness (Nagarajaiah and Sonmez (2007) [256]).

Resetting semi-active stiffness damper

Another type of hydraulic semi-active stiffness damper (SASD) has been proposed to be used as the energy dissipation device to suppress the structural response under seismic excitations (Yang et al. (2000) [399]; Yang and Agrawal (2002) [392]). The hydraulic damper consists of a cylinder piston system with a valve in the by-pass pipe connecting two sides of the cylinder. When the valve is closed, the damper serves as a stiffness element in which the stiffness is provided by the bulk modulus of the fluid in the cylinder. When the valve is open, the piston is free to move and the hydraulic damper provides only a small damping without stiffness.

Such a stiffness damper can be operated either in the resetting mode or in the switching mode.

During operation in the resetting mode, the valve is always closed, and hence the energy is stored in the hydraulic damper in the form of potential energy. At appropriate time instant, the valve is pulsed to open and close quickly. At the moment, the piston position is referred to as the resetting position, and the energy stored in the hydraulic damper is released and converted into the heat energy. Right after resetting, the pressure difference between two sides of the piston in the cylinder is reduced to zero. Hence, by pulsing the valve at appropriate time instants, energies can be drawn from the vibrating system to reduce the structural response.

For applications to base-isolated buildings, the SASD can be installed between the base and foundation of the building. The piston can be connected to the base of the building, whereas the cylinder is supported by the bracing that is connected to the foundation. The entire system consisting of the hydraulic damper and the bracing is referred to as the resetting semi-active stiffness damper (RSASD) when operating in the resetting mode.

The switching operational mode is to open the valve in a certain time interval and to close the valve in another time interval, referred to as the switching semi-active stiffness damper (SSASD). Such an onoff SSASD is identical to the variable stiffness system proposed by Kobori et al. (1993) [189]. It has been shown by Yang et al. (2000) [399]; Yang and Agrawal (2002) [392] that the performance of the RSASD is superior to that of the SSASD. Full scale experimental verification of RSASD has been performed by Yang et al. (2007) [395].

Adjustable tuned liquid dampers

Another type of semi-active control device utilizes the motion of a sloshing fluid or a column of fluid to reduce responses of a structure (see Fig. 2.15(a)). These adjustable tuned liquid dampers are based on passive tuned sloshing dampers (TSD) and tuned liquid column dampers (TLCD). Several semi-active adjustable tuned liquid dampers have been recently proposed, as they have the potential to improve upon the performance of passive tuned liquid dampers in reducing structural responses. Haroun et al. (1994) [137] introduced a hybrid liquid column damper (HLCD); this damper works by maintaining an optimal damping condition using a variable orifice in the TLCD. Another device has been proposed by Lou et al. (1994) [215], based on the passive TSD, where the length of the sloshing tank could be altered to change the natural frequency of the liquid damper. Yalla and Kareem (2003) [385] utilized

an electro-pneumatic actuator driving a ball valve to change the cross-section of a TLCD, thus adjusting the properties of the damper. Simulation results have shown that this semi-active system can achieve an additional $15 - 30\%$ response reduction over a passive system.

Controllable fluid dampers

Controllable fluid dampers form another class of semi-active devices, consisting of controllable fluids (electrorheological (ER) or magnetorheological (MR) fluids) in a fixed orifice chamber. Unlike the semi-active control devices mentioned previously, which employ electrically controlled valves or mechanisms, controllable-fluid dampers contain no moving parts other than a damper piston. The piston moves in a cylindrical chamber containing either electrorheological (ER) fluids or magnetorheological (MR) fluids. This feature makes them inherently more reliable and maintainable. Controllable fluids have a unique ability to reversibly change from free-flowing, linear viscous fluids to semi-solids with a controllable yield strength in only a few milliseconds when exposed to an electric (ER fluids) or magnetic field (MR fluids). These fluids can be modeled as Newtonian fluids in the absence of a magnetic field. When a field is applied, the visco-plasticity model (Philips (1969) [276]) may be used to describe the fluid behaviour. Although the discovery of ER and MR fluids dates back to the $1940s$, they have only recently been applied to Civil Engineering applications. To date, a number applications using ER fluid dampers have been investigated (Burton et al. (1996) [48]; Gavin et al. (1996a, b) [128, 129]; Kamath et al. (1996) [175]; Kamath and Wereley (1996) [176]; Makris et al. (1996) [223]) for structural vibration control. Gavin et al. (1996a, b) [128, 129] designed and tested an ER damper that consisted of a rectangular container and a moving plunger comprised of nine rigidly-connected flat plates. Makris et al. (1996) [223] developed an ER damper consisting of an outer cylinder and a double ended piston rod that pushes the ER fluids through an annular duct (see Fig. 2.15(b)).

Despite these advances in the development of ER fluid dampers, the development of commercially feasible damping devices using ER fluids is limited by several factors. First, the fluids have a very limited yield stress; even the best ER fluids currently available may only achieve stresses of 3.0 to 3.5 kPa. Also, common impurities that might be introduced during manufacturing significantly reduce the capacity of the fluids. Additionally, safety, availability

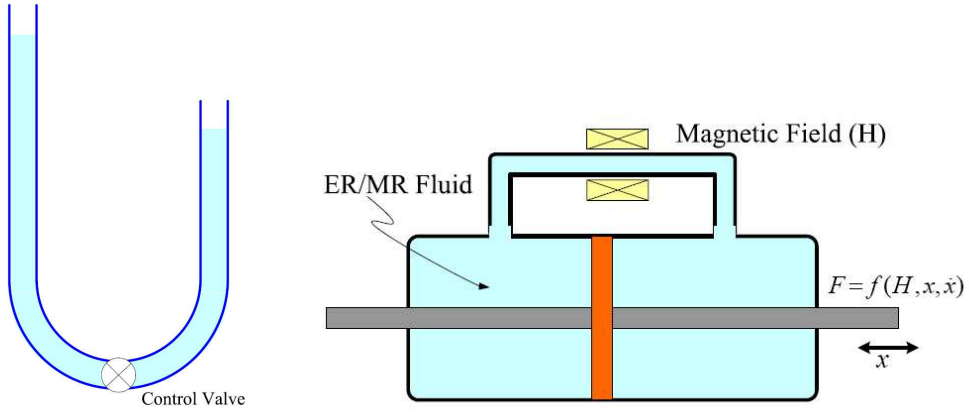

(a) Adjustable tuned liquid damper

(b) Controllable fluid damper

Figure 2.15: Semi-active dampers: (a) Adjustable tuned liquid damper, (b) Controllable fluid damper

and the cost of high-voltage (*e.g.*, 4000 volts) power supplies required to control the ER fluids are further considerations. MR fluids dampers, on the other hand, have a 50 to 100 kPa maximum yield stress, are not affected by most impurities, and are not sensitive to temperature. Moreover, MR fluids can be controlled with a low-voltage (*e.g.*, $0-5$ V), current-driven power supply with $1-2$ A output. Therefore, MR fluids are particularly promising for natural hazard mitigation and cost sensitive applications. Structural vibration control application of controllable fluid damper has two steps: first the damper model has to fixed and the hysteretic property of the damper has to be established. Once the mathematical model of damper hysteresis has been established the second step is to choose a proper control algorithm to monitor input current/voltage to the damper, such that its property changes on-line. Different techniques have been developed to model the behaviour of the controllable fluid dampers, which can be broadly classified into: non-parametric and parametric models. For the sake of completeness a flavour of these approaches has been presented here, details of these models has been discussed in Chapter 3.

Nonparametric approaches are based on the input-output data of the device. These input-output data are mapped using either neural networks or any other kind of training methods. Ehrgott and Masri (1992) [104] presented a nonparametric approach to model a small ER

damper that operates under shear mode by assuming that the damper force could be written in terms of Chebychev polynomials. Gavin et al. (1996a, b) [128, 129] extended this approach to model the ER damper. Chang and Roschke (1998) [57] developed a neural network model to emulate the dynamic behaviour of MR dampers. However, the non-parametric damper models are quite complicated and need huge amount of experimental data for training and testing.

Parametric models are based simple models consisting of springs and dash-pot, such that the combination of these simple models characterize the hysteretic property of the damper. Stanway et al. (1987) [338] proposed a simple mechanical model, the Bingham model, in which a Coulomb friction element is placed in parallel with a dash-pot. Gamoto and Filisko (1991) [127] extended the Bingham model and developed a viscoelastic-plastic model. The model consists of a Bingham model in series with a standard model of a linear solid model. Kamath and Wereley (1996) [175], Makris et al. (1996) [223], and Wereley et al. (1998) [372] developed parametric models to characterize ER and MR dampers. Dyke et al. (1996a, b) [99, 100], Spencer et al. (1997) [329] presented the Bouc-Wen model whose versatility has been utilized to describe a wide variety of hysteretic behaviour. This method has been modified for a MR damper with a capacity of providing 200kN force by Yang et al. (2001, 2001, 2002) [391, 388, 389].

A number of experimental studies have been conducted to evaluate the usefulness of MR dampers for structural vibration reduction under earthquakes and wind induced excitation. Dyke et al. (1997, 1996a, b, 1998) [97, 99, 100, 101], Jansen and Dyke (2000) [166], Spencer et al. (1996) [334], and Yi and Dyke (2000) [404] have implemented MR dampers to reduce the seismic vibration of building structures. Spencer et al. (2000) [330], Yoshioka et al. (2002) [410] have studied MR damper as an supplemental damping device with a base isolation system such that the isolation system would be effective under both strong and moderate earthquakes. Johnson et al. (2003, 2007) [169, 168] employed the MR damper to reduce wind-induced stay cable vibration. Reviews and details involving structural applications of MR fluid dampers have been presented by Carlson and Spencer (1996a, b) [50, 51]; Spencer and Sain (1997) [331]; Yang et al. (2002) [389].

Semi-active control systems combine the best features of both passive and active control systems, and they appear to offer the greatest likelihood for near-term acceptance of control

technology as a viable means of protecting Civil Engineering structures against earthquake and wind loadings. However, semi-active control systems are typically nonlinear due to the intrinsic nonlinearities of the devices. Therefore developing control strategies of a semi-active control system, based on the feedback of structural motions, is a challenging task. The development of efficient control strategies to monitor the MR damper current/voltage input is still an open research topic.

2.5.4 Hybrid Structural Control

The hybrid control system uses combination of a passive system supplemented with an active control component or a semi-active device to improve the performance of the passive control system and to decrease the energy requirement of the active control system. Therefore, hybrid systems are more reliable and fail-safe under severe earthquake, when there is chance of power failure. In case of power failure or failure of the active system, the passive component of the hybrid control system still offers some degree of protection, making the system fail safe, an essential design requirement for life-line structures like, highway bridges, hospitals, official buildings, and nuclear power plants, *etc*. Because of reliability of both semi-active and hybrid control systems, considerable attention has been paid recently to the research and implementation of these systems. Research in hybrid system has mostly been centered to hybrid mass damper system and hybrid base isolation system.

Hybrid mass dampers

Another commonly used control device in Civil Engineering structures is hybrid mass dampers (HMD). It is a combination of a passive TMD and an active mass damper or an active mass driver (as shown in Fig. 2.16). The active control component (AMD) improves the effectiveness and robustness of the passive TMD system, which on the other hand reduces the energy requirement (Housner et al. (1997) [146]). The energy requirements for HMD are much less than that of AMD for equivalent control.

Various linear and nonlinear algorithms have been reported to control the forces in passive TMD. Suhardjo et al. (1992b) [344], Spencer et al. (1994) [333] considered linear optimal control algorithm, whereas Adhikari et al. (1998) [5]; considered sliding mode algorithm. Ahlawat and Ramaswamy (2004) [17] studied a multi-objective genetic fuzzy control of seismically

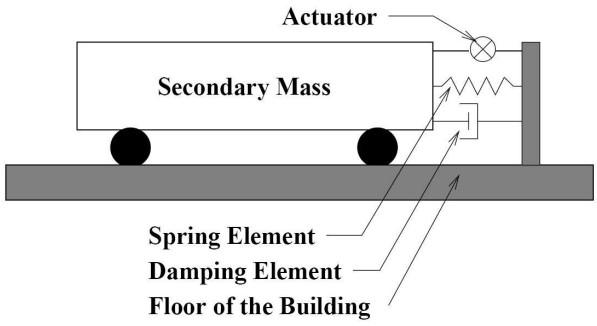

Figure 2.16: Active tuned mass damper (ATMD)

excited nonlinear buildings.

HMD's are compact, efficient, practically implementable and are available on various shapes and designs. Here mention may be made of V-shaped HMD (Koike et al. (1994) [190]), which has easily adjustable fundamental period combining a pendulum passive mass damper with an active system. The 52-storey Shinjuku Park Tower utilizes this system to reduce structural vibration under moderate earthquakes and strong wind. Duox HMD (Ohrui et al. (1994) [267]) has high control efficiency with lowest actuator force. This system has been installed in both the Ando Nishikicho Building and the Dowa Kansai Phoenix Tower in Japan (Soong and Spencer (2002) [325]).

Hybrid base isolation

The most successful means of protecting structures and most practically implemented mechanism to mitigate the risk to life and property damage against severe seismic events is base isolation technique (Skinner et al. (1993) [319]; Naeim and Kelly (1999) [243]). Base isolation system incorporating rubber bearings can not provide any damping to the structure and therefore undergoes a large displacement at the base under pulse type near field seismic motions. The large displacement at the base may prove fatal for nearby structures, utility services (water and electric connections, *etc*). Studies reported in various literature with many near-source, high-velocity, long period pulse seismic motions (*e.g.*, Kobe-1995, Northridge-1994, *etc.*) have questioned the effectiveness of many passive base isolation systems (Hall et al. (1995) [136]; Heaton et al. (1995) [141]).

Hybrid base isolation system is a combination of a seismic isolator supplemented with an

active or passive or semi-active devices (as damping devices) that can be effective for a wide range of ground excitations (Inaudi and Kelly (1993) [152]; Nagarajaiah (1994) [244]; Yang et al. (1996) [393]; Symans and Kelly (1999) [351]; Agrawal et al. (2005) [7]; Nagarajaiah and Narasimhan (2006) [248]). In general, protection of the contents of a structure is achieved through minimization of structural accelerations. The advantages of hybrid base isolation systems are high performance in reducing vibration, the ability to adapt to different loading conditions and control of multiple vibration modes of the structure.

Recent applications of hybrid seismic isolation systems have utilized either elastomeric or sliding bearings combined with passive fluid dampers (Constantinou et al. (1998) [79]; Asher et al. (1996) [35]; Makris and Chang (2000) [224]; Hussian and Satari (2007) [150]). There are limitations, however, to the performance of hybrid isolation systems incorporating passive dampers. For example, it has been recognized that inappropriate levels of supplemental damping in a base-isolation system can increase the response of the superstructure (*e.g.*, see, Makris (1997) [222], Kelly (1999) [182], Politopoulos (2008) [277]). In addition, such systems may not perform well for structures that are prone to disparate earthquake ground motions. An isolation system beneficial for stiff structures subjected to low-period, far-field ground motions, may experience an amplified response when subjected to long-period, near-field ground motions (Kelly (1986) [181]; Makris (1997) [222], Chang et al. (2002) [62]). Thus, the most appropriate seismic isolation system design may be different for each type of ground motion. One approach to address the limitations of hybrid isolation systems incorporating passive dampers is to replace the supplemental dampers with adaptive dampers (active or semi-active). There are a variety of adaptive control elements available for application within hybrid seismic isolation systems (*e.g.*, see Symans and Constantinou (1999) [349]).

A number of researchers have studied adaptive base-isolation systems for seismic protection of buildings (Kelly et al. (1987) [183]; Yoshida et al. (1994) [407]). However, a majority of the adaptive isolation systems that have been proposed employ active control devices at the isolation level to control the structural response. As an alternative, semi-active control devices which require a relatively small amount of power for operation could be used (Symans and Constantinou (1999) [349]). The number of studies on adaptive isolation systems that employ semi-active control devices is relatively small with most of the work being analytical and/or numerical (*e.g.*, Fujita et al. (1994) [126]; Nagarajaiah (1994) [244]; Yang et al. (1995) [402];

Makris (1997) [222]; Sadek and Mohraz (1998) [297]; Johnson et al. (1998) [170]; Symans and Kelly (1999) [351]; Agrawal and Yang (2000) [11]; Nagarajaiah et al. (1999) [257]; Ramallo et al. (2000) [285]; Sahasrabudhe et al. (2000) [303]; Symans et al. (2000) [352]; and Madden et al. (2002, 2003) [216, 217]). Very few experimental studies have also been performed which employed semi-active friction dampers (Fujita et al. (1994) [126]), semi-active viscous dampers (Symans et al. (2000) [352]), and MR dampers (Nagarajaiah et al. (2000) [255]; Sahasrabudhe et al. (2000) [303], Kim et al. (2006) [187], Shook et al. (2007) [316]).

Of the studies mentioned above, numerical simulations have been performed which employed semi-active viscous dampers (Nagarajaiah (1994) [244]; Yang et al. (1995) [402]; Symans and Kelly (1999) [351]; and Madden et al. (2002) [216]), MR dampers (Ramallo et al. (2000, 2002) [285, 286] and Yoshioka et al. (2002) [410], Lee et al. (2005) [202]), and studies with semi-active stiffness dampers have been done by Agrawal and Yang (2000) [11]. Lee et al. (2005) [202] applied a neural network controller for the optimal management of MR dampers that were installed with a number of rubber bearings. Their results indicate a substantial decrease in the acceleration response with only a modest increase in the displacement response. Jung et al. (2005) [173] evaluated the performance of several semi-active control algorithms, including a modified clipped-optimal controller, maximum energy dissipation control, modulated homogeneous friction control and fuzzy logic-based control (FLC). Each controller is evaluated according to how it performs in the management of an array of MR dampers. The results indicate that a modified clipped-optimal control algorithm is ideal for reducing displacements without increasing accelerations. Reigles and Symans (2006) [288] presented a supervisory fuzzy control algorithm for the management of semi-active viscous dampers. They generated two fuzzy logic controllers based on expert knowledge. A supervisory algorithm blends the two command signals into a single control signal. Results demonstrate that, in many cases, the fuzzy logic-based controller outperforms passive operation of the damper.

Kim and Roschke (2006a) [185] conducted numerical investigations of a single degree of freedom system, in which four FPS (friction pendulum system) devices were augmented with a 300kN MR damper for simultaneous suppression of displacement and acceleration responses of the superstructure. A multi-objective genetic algorithm (GA) with a local improvement mechanism is adopted to generate FLCs for optimal management of MR damper

resistance by changing the level of current applied to the damper coil. Results show that optimal FLC control outperforms a skyhook controller with reference to both displacement and acceleration responses. Kim and Roschke (2006b) [186] further examined GA-optimized FLCs with four concurrent structural response optimization objectives. The FLCs has been found to be more effective than prior efforts that involved only two optimization objectives.

Reinhorn and Riley (1994) [292] performed analytical and experimental studies of a small-scale bridge, where control actuator has been employed between the sliding surface and the ground to support the system. Another experimental and numerical study on a laboratory scaled sliding base-isolated bridge model has been reported by Sahasrabudhe and Nagarajaiah (2005a) [302], where MR damper has been used as a supplemental damping device monitored using Lyapunov based on-off control algorithm .

Laboratory work by Ramallo et al. (2002) [286] yielded favorable results on the protective capabilities of a small-scale rubber bearing system that is augmented with an MR damper. By optimizing an H_2/LQG clipped-optimal controller, they demonstrated robustness of control at low and high levels of peak ground acceleration (PGA). Wongprasert and Symans (2005) [377] used an H_∞ controller with a fuzzy gain-scheduling procedure for optimal control of a semi-active variable orifice damper. This procedure, along with a set of rubber bearings, effectively controlled a small-scale structure. Feedback from accelerometers has been exploited. Results indicate favorable reduction of the superstructure response to both near-field and far-field excitations when the control law is applied. Soda et al. (2003) [321] carried out large-scale experimental efforts to understand the effectiveness of a 40kN MR damper that is installed in parallel with several laminar rubber bearings. Results show promising reductions in superstructure response. Other large-scale endeavors include those by Kim et al. (2006) [187] who adopted a FPS (friction pendulum system) that is installed in conjunction MR dampers to mitigate unidirectional seismic loadings on a structure with a single degree of freedom system. MR damper resistance was managed by a fuzzy logic controller that is based on expert knowledge. The fuzzy controller reduced acceleration response while maintaining safe displacements. An excellent comparative study of experimental investigation using various control algorithm has been reported by Shook et al. (2007) [316].

In a nutshell, present focus of research in structural vibration control has been to develop isolation systems supplemented with sufficient levels of damping provided by MR dampers.

This hybrid mechanism controls the isolation level displacements while simultaneously limiting the transfer of force into the superstructure. Various analytical studies and experimental studies indicated above clearly demonstrate the need for further analytical and experimental study. In the next section, a survey of several control algorithms, with relative merit and demerits has been outlined.

2.6 Structural Control Algorithms

Actions of the active, semi-active and hybrid control systems are based on the measured excitation and/or response of the structure. Computation of the appropriate control action from the measured signal is based on the control algorithm that maps the input (measured signals) to the output (control command). When this map is linear the controller is linear and when the map is nonlinear, we refer it as nonlinear control algorithm. Thus, control algorithm plays a crucial role in the performance of the control system. Based on the measured signal used for the computation of the control command, the control algorithm may be classified as an open loop, closed loop and open-closed loop control algorithm. If any excitation measurements are used to derive the control action it is known as an open loop feedforward control. Closed loop or feedback control is a system that uses measured response of the system to compute and apply the control action. A feedforward-feedback control algorithm is one where both the excitation and the system response are used to decide the control action.

A control algorithm can be implemented digitally or in an analog mode. Analog implementation is limited to simple linear gain control algorithm applications. All the modern control systems are implemented digitally because of its several advantages. The main advantage associated with digital implementation are the easy and error free transmission of the signals and availability of tremendous computational power in the form of compact digital signal processing board and digital computers resulting in less computational time delay even for complex control algorithms.

Regardless of the control algorithm implementation, the design has to satisfy certain criteria, *e.g.*, stability, robustness, *etc*. In control engineering a number of strategies have been developed for the design of a control system comprising a simple classical (*e.g.* Root-Locus,

Nyquist plot, Bode plot, *etc*) for a single input single output system, pole placement methods for multimode systems and modern optimal and robust control strategies (Housner et al. (1997) [146]). Soong (1990) [322] and Housner et al. (1997) [146] have discussed a number of control algorithms for structural control applications. As the scope of the thesis is the hybrid base isolated control with MR damper as a supplemental energy dissipating device, we will focus our survey more on control algorithms that have been applied in connection to the MR dampers. A short description of the control algorithms that are used in general with active devices are discussed next. After that a detailed discussion on the MR damper current/voltage monitoring semi-active control algorithms has been provided.

2.6.1 Control Strategies

Literature pertaining to the control algorithms used in general for structural control using active devices or other semi-active devices can be found in Soong (1990) [322]; Housner et al. (1997) [146]. The broad range of control algorithm used for structural vibration control can be classified as optimal control, stochastic control, sliding mode control, robust control, intelligent control and adaptive control.

Optimal Control Algorithm

The optimal control algorithm provides the best design for a predefined performance criteria, *e.g.*, root mean square (rms) of output and control command. However, optimal control is good only if the cost function being minimized is truly meaningful for the system. In general, the output of the system and the control strategy are the two meaningful performance criteria. One way to formulate an optimization problem is to minimize one criteria subject to the constraint on the other. Using output of the system and the control energy as the performance criteria, two possible optimal control problems may be (i) input constraint control (ICC) and (ii) output constraint control (OCC). An ICC problem is defined as to minimize the L_2 norm of the output y $\left(\int_0^\infty y^T Q y dt\right)$ with a constraint on control energy $\left(\int_0^\infty f_c^T R f_c dt\right)$. Whereas an OCC problem has the control energy as an objective functions to be minimized subject to a constraint on the outputs. Here, Q, R are weight matrix.

If the weighted sum of both the criteria *i.e.*, system outputs and control energy is used as an objective for minimization, the approach is known as linear quadratic (LQ) control design

problem.

The statement of an optimal control problem is not complete if information of the characteristic of the input disturbance is not included. Disturbance model can be deterministic or stochastic. For deterministic excitation if a quadratic performance function as shown in Eq. 2.23 is used then the control design is known as linear quadratic regulator (LQR). By varying the weighting matrices in the performance function Q and R, a trade-off between response minimization and control energy minimization may be obtained.

$$\text{minimize} \quad J = \int_0^\infty \left(y^T Q y + f_c^T R f_c \right) dt \tag{2.23}$$

For stochastic input disturbance, the counterpart of LQR design is the linear quadratic Gaussian (LQG) control. The LQG combines the LQR and an optimal filtering by a Kalman-Bucy filter (Kuo (1995) [195]). LQG is the most commonly used control algorithm for vibration control of structures. An earthquake excitation is assumed to be zero mean filtered white noise for a LQG design of the controller (Spencer et al. (1998a, b) [328, 327]).

Another alternative is to use finite time control design *i.e.*, $\int_{t_1}^{t_2}$ instead of $\int_0^\infty$. Such controller will have time varying gain known as model predictive control (MPC) (Wang and Liu (1994) [367]). Another optimal control algorithm applied to structural control is H_∞ control (Zhu and Skelton (1994) [423]; Skelton et al. (1996) [318]; Helton and Merino (1998) [142]). H_∞ control algorithm design is based on a worst possible amplification of the input ensuring better robustness of the control system.

Stochastic control

Randomness and uncertainty are inherent to an environmental load. Uncertainties are also present in the structures due to material nonlinearity, measurement of damping and stiffness, *etc*. In addition to this, the structures are not completely observable from the sensors located at few locations and also the measurement contains noise. The stochastic control mainly deals with the problem of limited observability and sensor noise in the structural control system. Stochastic control application to Civil Engineering structures, its stability and robustness have been investigated by Spencer et al. (1992) [332]; Field et al. (1995, 1996) [114, 115]. A stochastic optimal control formulation using system reliability as a cost function has been proposed by

Spencer et al. (1996) [335] and a nonlinear stochastic optimal control approach for partially observable linear system has been reported by Zhu and Ying (2002) [424].

Robust control

Robust control theory is mainly based on a worst-case paradigm. As uncertainty is present in the structural system as well as in the excitation, performance and the stability of the control system can be ensured, designing it for the worst possible case. One way to design a controller for the worst is by minimizing the H_∞ norm of the closed loop transfer function of the system, *i.e.*, minimizing the upper limit on the ratio of the rms of the outputs including the control inputs to the rms of the input excitation Helton and Merino (1998) [142]. The earliest application of H_∞ control for wind excited buildings has been reported in Suhardjo (1990) [342]; Suhardjo et al. (1992a, b) [343, 344]. Breneman and Smith (1998) [44] have investigated a H_∞ feedback controller for the first generation AMD benchmark problem (Spencer et al. (1998) [337]). In a H_∞ control strategy, uncertainties are considered in a more systematic way than in a LQG control system and this results in an improved robustness and stability. The main limitation of this frequency domain control design approach is that the constraints for various time domain parameters cannot be incorporated easily. Further applications of robust control to structures has been reported in Dyke et al. (1995) [98]; Jabbari et al. (1995) [159]; Magana and Rodellar (1998) [219]; Spencer et al. (1994) [333]; Yoshida et al. (1998) [408].

Intelligent control

The control performance of the traditional control algorithms fully depends on the accuracy of the model of the system dynamics considered. Complex structural systems have nonlinearities and uncertainties, therefore it is difficult to derive and identify an accurate model of the structural dynamics for the traditional controller design. The stochastic control, robust control designs can treat uncertainties involved in the structural dynamics, input excitations and measurement but to a certain extent depending on the algorithm used.

In a broad perspective, intelligent systems underlie what is called "soft computing" techniques. Intelligent control considers the integration of the computational process, reasoning and decision making along with the level of precision or uncertainty in the available information as the design parameters. Therefore, an intelligent control system is more realistic and

often has multiple solutions. Eventually, this demands that the designer make a selection from a suit of non-dominated solutions. Unlike active control intelligent system does not need to handle the tedious mathematical models of the controlled structure. It needs only to set a simple controlling method based on engineering experience. Therefore, it is particularly useful in complicated structural control systems.

The concept of intelligent control has been proposed by Fu in 1971 (as discussed in Housner et al. (1997) [146]) to enhance and extend the applicability of the automatic control system. The increase in complexity due to design of more and more flexible Civil Engineering structures have led to the development of controllers that unlike conventional control system do not require complex models for its functioning, rather they rely on a knowledge base together with a rule base so as to decide and replicate human thought and decision making process. The principal tools in such a consortium are fuzzy logic, neural network computing, genetic algorithms and probabilistic reasoning. Furthermore, these methodologies, in most part, are complementary rather than competitive (Ali and Mo (2001) [28]). Increasingly, these approaches are also utilized in combination, referred to as "hybrid". Presently, the most well known systems of this type are neuro-fuzzy (Jang et al. (2005) [162]) and genetic-fuzzy systems (Ali and Mo (2001) [28]; Ahlawat (2002) [14]).

The main advantages of adopting fuzzy logic control (FLC) system can be summarized as follows

- The uncertainties in the model of the structure and measurement are treated in a much easier way in fuzzy control theory than the classical control theory. Fuzzy logic, which is the basis of the fuzzy logic controller, intrinsically accounts for uncertainties. Fuzzy logic controllers make use of an expert knowledge in the form of a linguistic rule base, resulting in an inherent robustness
- Fuzzy logic control easily maps nonlinear input-output relations
- The whole fuzzy controller can be implemented on a fuzzy logic chip or in a dSPACE hardware chip, which guarantees faster processing, resulting in less computational time delay.

The problem that a control engineer faces during FLC design is in selecting parameters for the fuzzy system to have an optimal performance. In this regard various methods have

been developed to optimize the FLC parameters using evolutionary optimization techniques (Ahlawat (2002) [14]). Previous studies on optimal FLC strategies focused on adaptively changing the fuzzy membership function (MF) parameters using evolutionary algorithms, while predefining the rule base and retaining it unaltered (Ahlawat and Ramaswamy (2001, 2003, 2004) [15, 16, 17]; Dounis et al. (2007) [92]). All these mentioned optimal FLCs have been optimized off-line for seismic applications. Real time implementation of an optimal FLC has not been studied much for structural control applications (Kim and Roschke (2006a) [185]). Therefore, on-line optimization of FLC with optimal design of fuzzy rule base remains a major research interest in field of adaptive fuzzy control.

Another concern of the control designers in implementing the FLC system, is the stability of the closed loop system because there is no proven mathematical model to check the stability of the fuzzy control system. A few mathematical methods developed to determine stability of the fuzzy controllers are limited to some simple membership functions and fuzzy rules. In fuzzy control literature the stability analysis of FLC systems has been considered in the view point of classical nonlinear dynamic system theory. In this view point the overall system is considered non-fuzzy and FLC is considered as a particular class of nonlinear controller (Driankov et al. (1992) [93]). There are a number of stability analysis criteria proposed in the literature, *e.g.*, phase plane trajectory method to reflect the dynamic properties of a control system in phase plane. Casciati (1997) [52] has proposed an approach based on the ability of the stable control system to reduce the response and drive the system to the rest condition after the initial transient phase excited by extreme initial conditions.

Applications of intelligent control that includes FLC has been reported in Battaini et al. (1998) [40]; Casciati et al. (1996) [54]; Faravelli and Yao (1996) [109]; Hung and Lai (2001) [149]; Subramaniam et al. (1996) [341]; Symans and Kelly (1999) [351]. Neural networks based control applications are reported in Bani-Hani and Ghaboussi (1998) [39]; De Stefano et al. (1999) [86]; Ghaboussi and Joghataie (1995) [130]; Hung et al. (2000) [148]; Hung and Lai (2001) [149]; Liu et al. (1999) [212]; Venini and Wen (1994) [361].

Adaptive control

Intelligent controllers are capable of handling the nonlinearities and uncertainties involved in the structural system especially during large environmental loads. However, an optimal

intelligent controller does not remain optimal if the parameters of the structural system and the excitation for which it was optimized, changes.

This problem of a fixed design type controller can be handled by incorporating a supervisory controller that can adjust the parameters of the fixed control system such that the controller remains optimal for the current structural dynamics of the system. An adaptive system can be active, semi-active, or a hybrid control system with real time tuning of the control parameters. Adaptive control systems can be classified into direct and indirect adaptive systems (Sastry and Bodson (1989) [306]; Tao (2003) [354]). In direct adaptive control system, controller parameters are adjusted directly based on the error between the measured and the desired response. In the indirect adaptive control system, parameters of the dynamics of the plant are estimated on-line and the controller parameters are computed as the underlying controller design problem based on the estimated parameters of the plant.

Rodellar et al. (1994) [294] have presented a direct adaptive control method for a base isolated structure with an active controller at the base, whose parameters are adjusted adaptively. Most of the reported research on adaptive control of Civil structures is limited to the direct adaptive control systems. Fuzzy logic control optimized using genetic algorithm has been proposed by Ahlawat and Ramaswamy (2001) [15]; Ahlawat and Ramaswamy (2003) [16]; Ahlawat and Ramaswamy (2004) [17].

Nonlinear control applications has also been studied by Agrawal and Yang (1996, 1997) [9, 10]; Spencer et al. (1996) [334]; Yang et al. (1996) [393].

2.6.2 MR Damper Current/Voltage Monitoring Strategies

MR damper is an intrinsically nonlinear device, which makes the design of a suitable control algorithm that can take advantages of the unique characteristics of the device, an interesting and challenging task. Numerous control algorithms that have been proposed and reported in the literature for the control of the MR systems, can be categorized as model-based control, *i.e.*, algorithms that require an accurate mathematical model of the system; and intelligent control, algorithms which provide control output based on the inputs to the algorithms only (Jung et al. (2004) [174]). The performance of some of the model based control algorithms has been compared through simulations in Dyke and Spencer (1997) [97] and Jansen and Dyke

(2000) [166], for single MR damper use, and in Jansen and Dyke (1999) [165], for implementation of multiple MR dampers.

Model based control

In one of its first examinations Karnopp et al. (1974) [178] proposed a "skyhook" damper control algorithm for a vehicle suspension system and demonstrated that this system offers improved performance over a passive system when applied to a SDOF system. Feng and Shinozuka (1990) [111] developed a bang–bang controller for a hybrid controller on a bridge.

Clipped-optimal control algorithm has been proposed by Dyke et al. (1995,1996a, b) [98, 100, 99] to monitor MR dampers. It is currently the most widely used algorithm for MR damper control (Jung et al. 2004 [174]). This strategy consists of a bang-bang (on-off) type of controller that causes the damper to generate a desirable control force which is determined by an "ideal" active controller (in state feedback form). As shown in the schematic diagram in Fig. 2.17(a), a force feedback loop is used to produce the desired control force (f_d), which is determined by a linear optimal controller ($\mathbf{K}_k(s)$), based on the measured structural responses (y) and the measured damper force (f_c) at current instant of time.

The damper force is then calculated by Eq. 2.24

$$f_d = L^{-1}\left\{-\mathbf{K}_k(s)L\left(\frac{y}{f_c}\right)\right\} \tag{2.24}$$

where $L(.)$ is the Laplace transform operator. The linear controller is usually obtained using H_2 or LQG strategies. As only the applied voltage, v_a, to the MR damper can be commanded and not the damper force, the following strategy has been used to obtain the desirable control force

when the actual force being generated by the MR damper, f_c, equals the desirable force, f_d, the voltage applied remains the same. When the magnitude of force f_c is smaller than the magnitude of f_d and both forces have the same sign, then the voltage applied is set to its maximum level, to increase the damper force. Otherwise, voltage is set to zero.

This algorithm for selecting the voltage signal is graphically represented in Fig. 2.17(b) and described by Eq. 2.25

$$v_a = v_{max}\, H(f_d - f_c) f_c \tag{2.25}$$

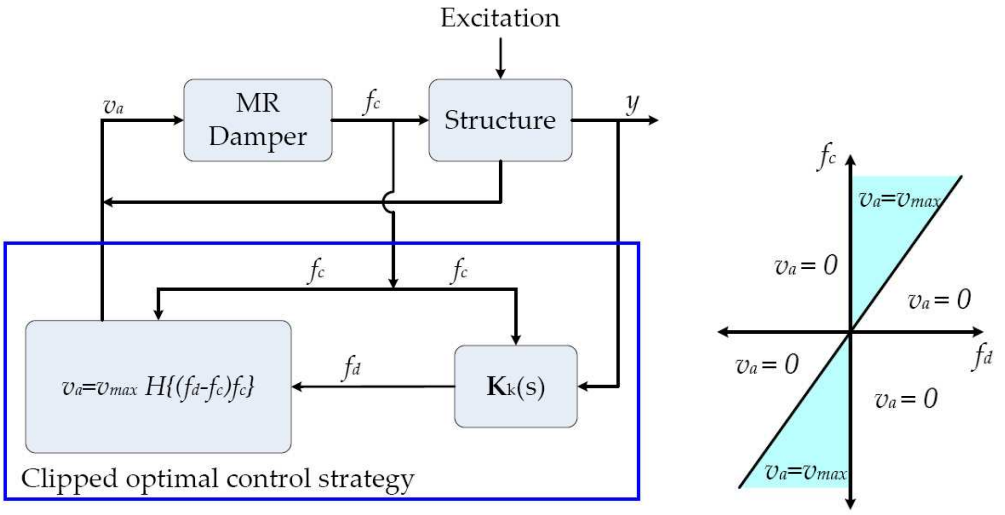

(a) Block diagram of Clipped optimal algorithm (b) Graphical representation

Figure 2.17: Clipped optimal algorithm (Dyke et al. (1996b) [100])

where v_{max} is the voltage level associated with the saturation of the magnetic field in the MR damper, and $H(.)$ is the Heaviside step function operator.

The performance of the clipped optimal control algorithm has been evaluated through numerical simulations (Dyke et al. (1996a) [99]) and experimental observations (Dyke et al. (1996b) [100]) on a three-storey model building. Results have been compared with two passive mode conditions. In the first case, referred to as 'passive-off', no voltage has been applied to the damper. In the second case, or 'passive-on', the voltage level has been held constant at its maximum value. It has been observed that the 'passive on' system performed better than the 'passive-off' configuration, in reducing floor displacements. However, it increased the peak absolute accelerations and the upper floors inter-storey drifts. The clipped-optimal algorithm produced better reductions in upper floors peak displacements and inter-storey drifts than the passive-on controller, while using smaller magnitude forces. However, higher peak accelerations have been observed than those obtained with 'passive-off' control in both the first and second floors. Comparison of the simulated results with that of the linear active controller (designed to have same peak control force as in semi-active controller) has shown better results in clipped-optimal in reducing the maximum third floor displacement and the maximum of the peak inter-storey drifts (Dyke et al. (1996a) [99]).

The effectiveness of the clipped-optimal algorithm has also been demonstrated for multiple MR damper (Dyke and Spencer (1997) [97]; Jansen and Dyke (1999) [165]; Dyke (1998) [95]) and comparison with other algorithms has also been presented (Jansen and Dyke (2000) [166]). Experimental verification for multiple dampers has been reported in Yi et al. (1998, 2001) [406, 405]. A six-storey test structure equipped with four MR dampers has been subjected to sinusoidal excitation having frequencies near to the first two modes of the structure (Yi et al. (1998) [406]) and to scaled versions of the El-Centro earthquake (Yi et al. (2001) [405]). In both cases the clipped-optimal controller has been found to satisfactorily reduce structural responses and outperform passive control strategies.

Other application of clipped optimal strategy includes a twenty-storey building (Dyke (1998) [95]), equipped with thirty-six sensors and thirty large scale MR dampers, vibrations mitigation in stay cables subjected to wind load (Johnson et al. (2003, 2007) [169, 168]), structural responses in coupled buildings (Christenson and Spencer (1999) [68], Christenson et al. (1999, 2000) [69, 72]), and control of torsional-lateral responses in irregular buildings (Yoshida et al. (2002) [409]).

Numerical simulations on stay cable have shown that the control algorithm is efficient in reducing cable vibrations (Johnson et al. (2003, 2007) [169, 168]). Experiments conducted by Christenson et al. (2001, 2002) [70, 71] have confirmed the effectiveness of MR dampers and this control algorithm in cable-stayed bridge applications.

Zhang and Roschke (1999) [415], Chang and Zhou (2002) [58] and Zhou et al. (2002) [421] studied optimal control strategies to monitor MR damper input voltage. Zhang and Roschke (1999) [415] used a linear quadratic Gaussian with loop transfer recovery (LQG/LTR) control strategy in conjunction with an MR damper to reduce structural vibrations due to strong winds. The structure controlled was a four-storey flexible laboratory model equipped with a small-size MR damper placed between the ground and the first floor of the structure. It has been reported that a reductions obtained ranged from 35% to 60% for the peak floor acceleration. The algorithm proposed by Chang and Zhou (2002) [58] and Zhou et al. (2002) [421] consists of a linear quadratic regulator to determine the optimal control force and an inverse neural network model of the damper to calculate the required voltage for the production of such force. The neural network model used a few previous time steps of displacement, damper force, voltage signal, and desirable control force to determine the required voltage setting for

achieving the optimal control force. Simulation results on a three storey building model with a single MR damper has been provided to demonstrate the efficacy of the algorithm. Results showed that both floor inter-storey drifts and accelerations have been reduced.

Approaches based on Lyapunov direct method have also been tried as a control algorithm to monitor the rheological damper. In this technique, the first step has been to select a Lyapunov function which must be a positive function of the systems states. Control inputs have then been chosen to make the derivative of the function negative and large in magnitude. This is because, according to the Lyapunov stability theory, if the rate of change of this function is negative semidefinite, the origin is stable in the sense of Lyapunov. Leitmann (1994) [204] proposed a control strategy, wherein the Lyapunov function has been taken as the second norm of the states of the system. The goal of these algorithms is to reduce the responses by minimizing the rate of change of a Lyapunov function. The method needed full system states to be measured for better performance.

McClamroch and Gavin (1995) [233] used a similar approach to develop a decentralized bang-bang controller. This control algorithm acts to minimize the total energy (kinetic and potential) in the structure (as a Lyapunov function). The purpose of the control strategy has been to reduce the rate at which the energy is transmitted to the structure. A modified form of homogeneous friction algorithm used for a variable friction device, has been also reported (Inaudi (1997) [151]). A comparative study of different schemes based on Lyapunov method and clipped optimal strategy has been reported in Dyke and Spencer (1997) [97]; Jansen and Dyke (1999, 2000) [165, 166]. A 'on-off' strategy based on Lyapunov method has been studied numerically and experimentally by Sahasrabudhe and Nagarajaiah for a base isolated building (Sahasrabudhe and Nagarajaiah (2005b) [301]) and a base isolated bridge (Sahasrabudhe and Nagarajaiah (2005a) [302]). The analytical and the experimental study reported that the semi-active controlled case reduces the bearing displacements further than the 'passive-off' and 'passive-on' cases, while reducing isolation level forces when compared to the 'passive-on' case. The developed control algorithm has been found to be effective under fault-parallel components of the earthquakes considered in this study.

The main disadvantage of the above mentioned methods is that it tries to change the voltage of the MR damper from zero to its maximum value. Therefore neither of them provides the optimal force required by the system. Moreover, some times this swift change in voltage

and therefore sudden rise in external control force increases system responses, which may lead to inelastic response of the structure. Therefore there is, indeed, a need for better control algorithms that can change the MR damper current/voltage slowly and smoothly, such that all voltages between maximum and zero voltage can be covered based on the feedback from the structure. In addition, these algorithms should consider the dynamics between the applied current/voltage and the commanded current/voltage (more on this will be discussed in subsequent chapters). Intelligent control algorithms have been used to solve the first of the above mentioned constraints. Recently, the application of intelligent controllers (*e.g.*, fuzzy logic controller (FLC), neural network Controller, ANFIS, *etc.*,) to structural control problem have been studied extensively. Some of which are discussed next.

Intelligent Control

As discussed earlier in this section the three main categories of intelligent control algorithms have been: neural network-based control, neuro-fuzzy based control, and fuzzy logic-based control.

Shiraishi et al. (2002) [315] proposed an adaptive neural network for control of a three storey structural model equipped with a prototype damper. The damper has been placed between the ground floor and the first floor. The control strategy consisted of two neural networks: one for structural identification and another for control decision. The identification network has been used to identify the first floor displacement and the controller network has been used to determine the control current, based on the past five values of the ground and of the first floor displacements.

Ni et al. (2002) [264] proposed two neural network based controllers for vibration control of sagged stay cables using MR dampers. The first algorithm has been designed for full-order model and the second one has been trained to consider reduced order models. Off-line training has been performed for the controller to emulate the force that would be obtained with an LQG controller with full state observation and with reduced state observation for first and second algorithms respectively. Clipping of the output was performed to ensure zero control force when the direction of the required damper force has been opposite to the damper velocity and to guarantee that the control force did not exceed the damper capacity. Analytical results showed that the performance of both the neuro-controllers developed have

comparable performance to that of LQG controllers with full state observation.

Xu et al. (2003) [384] proposed a neural network model that consisted of a four layer feed-forward neural network trained on-line with the Levenberg-Marquardt algorithm to solve the time delay problem. Simulation results on a scale model of a three-storey reinforced concrete structure showed that this control method is more effective than the traditional elastoplastic time-history analysis.

Unlike neural networks, fuzzy based control strategies do not require training of the algorithm, and therefore avoid the need to acquire large amounts of data. Resulting controllers are therefore simple and robust. FLC has been applied to structural vibration control mainly with active devices as discussed earlier in this section. Studies on semi-active control of structural vibration using FLC are few and mention may be made of (Nagarajaiah 1994 [244]; Sun and Goto (1994) [345]; Symans and Kelly (1999) [351]); Kim et al. (2006) [187]. In FLC based MR damper monitoring, the algorithm determine the current/voltage required to be applied to the MR damper based on the system feedback. A fuzzy logic controller (FLC) is used to modulate the MR damper because the FLC has an inherent robustness and ability to handle nonlinearities present in the current/voltage-force map of a MR damper.

A genetic algorithm based adaptive FLC has been developed for MR damper voltage monitoring to control a base isolated structure by (Kim and Roschke (2006a, b) [185, 186]). The isolator consists of a set of four friction pendulum system (FPS) bearings subjected to various intensities of near-fault and far-fault earthquakes. The main purpose of employing a GA is to determine appropriate fuzzy control rules as well to adjust parameters of the membership functions. Neuro-fuzzy models have been used to represent dynamic behaviour of the MR damper and FPS. It has been shown that the method can find optimal fuzzy rules and the GA-optimized FLC outperforms not only a passive control strategy but also a human-designed FLC and Sky-hook algorithm.

Kim et al. (2006) [187] also developed a full-scale experimental analysis of a single degree of freedom mass equipped with a hybrid base isolation system. The proposed fuzzy controller uses feedbacks from displacement or acceleration transducers attached to the structure to modulate resistance of the semi-active damper to motion. The study has shown that a combination of FPS bearings and an adjustable MR damper provide robust control of vibration for

a large full-scale structure undergoing a wide variety of seismic loads. Low power consumption, real-time feedback control, and fail-safe operation have been established from the study. Similar to Kim and Roschke (2006a, b) [185, 186], a neuro-fuzzy model is used to represent behaviour of the damper for various displacement, velocity, and voltage combinations that are obtained from a series of laboratory evaluation tests.

2.7 Identification of Open Problems

A review of literature on the issues related to the vibration problems in Civil Engineering structures and different control strategies have been presented in the preceding sections. As noted from various discussions reported in the earlier sections, a number of issues need to be addressed to make control strategies an efficient and effective means for disaster mitigation. In this section, these issues are outlined and form the motivation for the present study.

It is evident from the literature survey presented in earlier sections that following the Northridge earthquake (1994), and Kobe earthquake (1995), the interest of structural engineers to near-source ground motions has been revived. Documents published after these earthquakes accentuated the issue of large base displacements partly because they used none or little isolation damping of viscous type only, or because response quantities have been computed using artificially generated ground motions. More recent experiments and numerical studies have shown the efficiency of various dissipative mechanisms to protect seismic isolated structures (hybrid isolation system) from recorded near-source ground motions. The ground motions contained coherent long-duration pulses in their velocity-time histories. As a result, MR dampers with hysteretic damping at very little power supply became an important device to be used as a supplemental damping device along with seismic isolators.
The use of MR damper as a semi-active device involves two steps,

- Development of a model that can describe the MR damper hysteretic behaviour properly
- Development of a proper nonlinear control algorithm to monitor current/voltage supply to the MR damper, such that the device can provide a desired damping force

Discussion made in the earlier sections while documenting the literature required to develop the work in the subsequent chapters, clearly demonstrated the need for further investigation on these two points.

Existing parametric models of MR damper hysteretic behaviour (*e.g.*, Bouc-Wen model) fail to consider the effect of amplitude and frequency of excitations on the device and non-parametric approaches are damper specific. Recently reported literature, (for *e.g.*, Yang et al. (2004) [390]; Dominguez et al. (2006) [91]) have demonstrated the necessity of incorporating amplitude and frequency dependence of MR damper models. Therefore, existing MR damper models need further development.

The current/voltage supply as an input variable to the MR damper restricts the direct usage of the control algorithms developed for active control of structures. The force predicted by the available control algorithms should be mapped to equivalent current/voltage and then fed to the damper. Nonlinear current/voltage-force relationship of MR damper limits this map to 'on-off' or 'bang-bang' algorithms. The literature study highlights that all previous studies on semi-active algorithm development used 'on-off' or 'bang-bang' strategy for MR applications. The semi-active control algorithm demands further development such that the following two important characteristics can be incorporated into it.

- Smooth change in MR damper current/voltage input considering all possible current/voltage values within its minimum to maximum range

- Considering the effect of the MR damper applied and commanded current/voltage dynamics in the control algorithm

Discussions in the previous section reveal that intelligent algorithms are suitable for semi-active applications but more analytical and experimental studies are needed before they are made available for full scale implementations. Considering FLC based algorithms, design of optimal fuzzy rule-base, on-line optimization and experimental verification need further verification.

Based on the above discussion and current state-of-the-art literature survey, following issues that need further investigation are enumerated and form the motivation for the present study.

1. Development of a fail safe hybrid control strategy incorporating seismic isolators supplemented with MR dampers. Analytical and experimental verification of the performance of the hybrid scheme under a set of near-fault and far-fault seismic records

2. Experimental investigation of a MR damper to study its various parameter dependence and finally developing a amplitude dependent model to predict the hysteretic bahaviour of the damper

3. Development of an intelligent controller based on fuzzy logic for current/voltage monitoring of MR damper and developing procedures for on-line optimization of FLC parameters

4. Experimental verification of the proposed optimal FLC for hybrid base isolation of a three storey building structure

5. Development of model based control algorithms that consider the dynamics of applied and commanded current/voltage to the MR damper and modify the MR damper input current/voltage smoothly.

2.8 Summary

The goal of the present chapter has been to document a thorough study on various issues related to the structural dynamics and vibration control. The chapter deals with the developments made in modeling of building structures and various schemes available for making reduced order models out of full scale finite-element models. The chapter discussed various issues related to near and far fault seismic ground motions and attentions are drawn to the seismic vulnerability of near-fault earthquakes, which form the recent focus of the structural engineers world wide. To bring forth the essence and focus of current research trend in structural vibration control community, a detailed study of various structural control devices along with their applications have been documented. Control algorithms form a broad field of research and development and those related to structural control applications have only been discussed. Finally based on an assessment of the literature on issues related to earthquake engineering and structural control, gaps in the state-of-the-art are identified that form the motivations of this dissertation.

Discussion in the previous section revealed that the main motivation of the present study is to develop semi-active control algorithms and verify experimentally the intelligent control

technique. For this, one has to characterize the MR damper to be used in the experimental study. Therefore, the next chapter documents the experiments performed to model MR damper hysteretic behaviour and thereafter the model developed to characterize the damper behaviour. This model is later used in the subsequent chapters for the experimental and numerical studies.

Chapter 3

Magnetorheological Damper Testing and Modeling

3.1 Overview

The preceding chapter dealt with the review of literature encompassing issues related to structural dynamics, like, building models, reduced order modeling and variability in input seismic excitations, and structural control consisting of developments in various control devices and control strategies. These studies revealed that magneto-rheological (MR) dampers provide added robustness and stability to base isolated structures when deployed as supplemental damping devices.

In this chapter, after giving a short introduction to MR fluid dampers and their commercial usage, a comprehensive review of MR damper parametric and nonparametric models is documented. Then, details of MR damper RD-1005-3 (MR Dampers (2006) [240]) experimental set-up is outlined. MR damper response to sinusoidal excitations consisting of a set of amplitudes and frequencies for different input currents are reported. A set of experimental results for the variable input current tests, amplitude-dependent tests, frequency-dependent tests and constant peak velocity tests have been presented. Based on the test results an analytical model for the MR damper is developed. This model is used in the subsequent chapters for application to a three storey hybrid base isolated building developed for the experimental study.

Magneto-rheological dampers consist of a hydraulic cylinder containing a fluid that, in

the presence of a magnetic field, can reversibly change from a free-flowing, linear viscous fluid to a semi-solid with controllable yield strength. MR fluid is composed of micron-sized magnetically polarizable particles dispersed in a carrier medium such as water, mineral or synthetic oil. Typically, it contains 20 to 40% by volume of relatively pure carbonyl iron having diameter of 3 to 5 microns in size (Yang 2001 [387]). Figure 3.1 gives a description of the phenomenon of MR fluid under magnetic field. When no magneic field is created through the fluid, MR fluid behaves as a free flowing viscous fluid, but as the magentic field is created, the particles, inside, start forming chains and increase the fluid viscosity. At strong magnetic field the MR fluid becomes a semi-solid. Additives are commonly added to discourage settling, improve lubricity, modify viscosity, and reduce wear (Yang 2001 [387]).

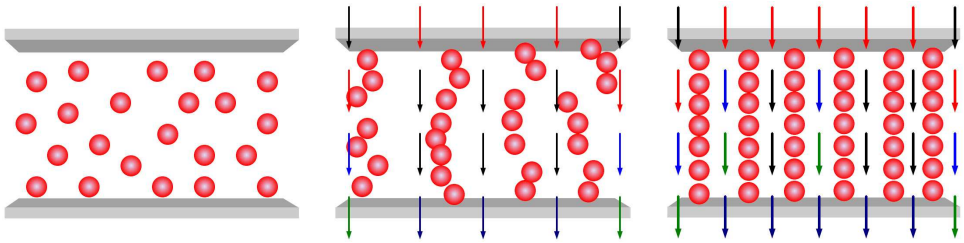

(a) No magnetic field (b) Medium magnetic field (c) Strong magnetic field

Figure 3.1: Effect of magnetic field on MR fluid

3.2 Commercial MR Dampers

Magneto-rheological devices for commercial applications ranging from automobile engineering to medical technology are manufactured by LORD Corporation (2008) [214]. Applications of MR devices in automobile industry include shock absorbers for racing cars, heavy duty truck seating, *etc*. They are also found to be more effective than air suspended seats, since they are able to adapt to both the drivers weight and the road vibrations. To increase automobile occupant safety, MR devices have also been used as components of airbag systems, seatbelt retractors, bumpers and vehicle seating, *etc*. These systems have the advantage of continuously and automatically account for forces exerted on the vehicle, and occupants physical attributes.

Other application of MR fluid devices includes the controllable friction damper manufactured to decrease noise and vibration in washing machines. MR fluid brakes have also been developed to provide controllable rotary resistance to aerobic exercise equipment. Another interesting and useful application is the use of these dampers in prosthetic knee to facilitate motion of above-the-knee amputees, especially up and down inclines or stairs (LORD Corporation (2008) [214]).

In the area of structural vibration control, MR dampers have several advantages over other commonly used seismic control devices. They are cost effective to manufacture and maintain. The response time to change from fluid to semi-solid on application of magnetic flux is in milliseconds. Mechanical simplicity and low operating power requirement are added advantages that make MR dampers more effective than passive and active devices (Dyke et al. (1997, 1996a, b, 1998) [97, 99, 100, 101]). MR dampers have also been found to be better candidates for seismic applications than electro-rheological (ER) dampers. This is because MR fluids are able to achieve yield stresses an order of magnitude greater than their ER counterparts. They also have a large operational temperature range that can span from -40°C to 150°C, compared to ER dampers that are effective between 10°C to 90°C. MR dampers are environmentally robust, that is, not sensitive to impurities encountered during manufacturing and usage. In contrast performances of ER fluids are greatly affected by the presence of contaminants, especially water or moisture. A wide number of additives can therefore be used with MR fluids to enhance stability against particle/carrier separation and bearing life (Carlson and Spencer (1996a) [50], Spencer and Sain (1997) [331]). Finally, MR dampers require much lower voltage source than ER dampers.

For real time applications on large structures a 180kN capacity MR damper has been developed by LORD corporation. It is a large-scale MR fluid damper unsurpassed in its combination of controllability, responsiveness and energy density. Real-time damping is controlled by the increase in yield stress of the MR fluid in response to magnetic field strength. The response time of the fluid damping is on average 60 milliseconds as the magnetic field is changed. Study on large scale MR damper with a capacity of 20 tonne has been reported by Yang (2001) [387].

For laboratory experiments or for small scale applications the most widely used MR damper has been RD-1005 series (MR Dampers (2006) [240]). A schematic diagram of RD-1005 series

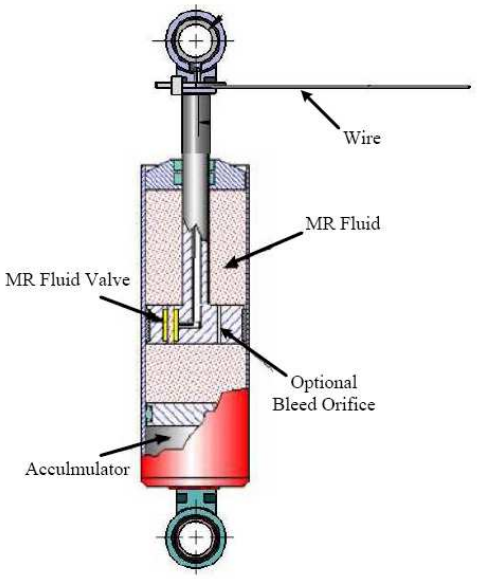

Figure 3.2: LORD Corporation MR damper^{TM}RD-1005 [240]

is shown in Fig. 3.2. Magneto-rheological damper ^{TM}RD-1005-series is a trademark of LORD Corporation (LORD Corporation (2008) [214]). For the three storey building control experiment reported later in this study, a RD-1005-3 MR damper is used. When a magnetic field is applied to the MR fluid inside the monotube housing, the damping characteristics of the RD-1005-3 changes in less than 25-millisecond. Experimental study and modeling of nonlinear hysteretic behaviour of RD-1005-3 MR damper are reported after presenting detailed survey on models developed in the literature to capture MR dampers hysteretic behaviour.

3.3 MR Damper Models

Several models have been developed to describe the hysteretic behaviour of MR dampers. Although these models are capable of describing the MR damper force-displacement behaviour reasonably well, they are not sufficient to describe the nonlinear damper force-velocity behaviour (Yang (2001) [387]). These models are therefore considered inadequate for structural vibration control simulations. A more accurate dynamic model of MR dampers is necessary to describe damper behaviour for structural vibration control applications. In this section, a review of several models for controllable fluid dampers reported in the literature is proposed.

Magneto-rheological damper models can be divided in two broad categories; namely, non-parametric and parametric models. Description of a few of these models has been reported in Spencer et al. (1997) [329]; Yang (2001) [387]; Jung et al. (2004) [174]. Salient features of these models are summarized here.

3.3.1 Non-parametric model

Non-parametric models are developed from the input-output data of the damper. They have device specific performance and usually require a large amount of experimental data for training and testing (Jung et al. (2004) [174]). Proposed models reported in the literature are based on Chebychev polynomials (Ehrgott and Masri (1992) [104]; Gavin et al. (1996a, b) [128, 129]); neural-networks (Chang and Roschke (1998) [57]; Zhang and Roschke (1998) [414]; Wang and Liao (2001) [364]); neuro-fuzzy systems (Schurter and Roschke (2000, 2001a, b) [308, 309, 310]), *etc*.

Ehrgott and Masri (1992) [104] used Chebyshev polynomials for modeling the hysteretic behaviour of electro-rheological dampers. Two approaches have been reported to emulate the force generated by the damper. In the first case, the force has been assumed to be a function of displacement and velocity and described by two-dimensional orthogonal Chebyshev polynomials. In the second case, the force has been assumed to be a function of velocity and acceleration. For this purpose two-dimensional orthogonal Chebyshev polynomials have been exploited. This method has been extended by McClamroch and Gavin (1995) [233] and Gavin et al. (1996a, b) [128, 129], who assumed the force to be a function of displacement, velocity, and the electric field.

Among training based intelligent methods, neural networks have been used to reproduce the nonlinear MR fluid behaviour widely and it has been shown that they perform very well to predict the damper force-velocity relationship. Typically a multi-layer perception (MLP) network with three layers has been reported for the modeling of the MR dampers. It is shown to accurately reproduce the nonlinear behaviour of MR damper hysteresis (Chang and Roschke (1998) [57]). As mentioned previously, these models require off-line training. Most of the reported neural network models (Chang and Roschke (1998) [57]) employed sets of input-output data describing the MR damper behaviour that are generated using a parametric model proposed by Spencer et al. (1997) [329]. Most of the neural network based models differ in the

training algorithm usage. The Gauss-Newton based Levenberg-Marquardt training algorithm is mostly used for training due to its rapid convergence and robustness. Chang and Roschke (1998) [57] employed the optimal brain surgeon (OBS) strategy, after the network has been trained, to remove superfluous weights and to optimize the network. This step, however, required retraining of the system and its intermediate parts, each time a weight is eliminated.

Zhang and Roschke (1998) [414] proposed two neural-network models for MR dampers. A forward model, capable of predicting the damper force when voltage is known, has been proposed. The other proposed model is designed to predict the voltage, when the damper force is known. It is referred to as the inverse model. The Gauss-Newton based Levenberg-Marquardt training algorithm and the OBS strategy are employed for the development of both the models.

Wang and Liao (2001) [364] proposed a neural-network based model for direct identification of MR dampers hysteresis. Their model consists of a recurrent neural-network in which the output is delayed and feedback to the input layer. The selected training method has been the Levenberg- Marquardt algorithm and the training data was obtained with the use of the phenomenological model developed by Spencer et al. (1997) [329]. Results show that the predicted damping force approximates the target data reasonably well. This work also includes an inverse model of the damper, where the output is the command voltage.

Neuro-fuzzy models are yet another example of non-parametric models proposed for emulating MR damper behaviour. In these models a nonlinear surface is developed based on fuzzy reasoning. The parameters of the fuzzy logic system have been selected based on neural network training using input-output data. This nonlinear surface is then used to model MR damper hysteretic behaviour. The neuro-fuzzy model proposed by Schurter and Roschke (2000) [308] for a small-scale MR damper, used neural-networks to train membership functions for simulating the relationship between the inputs (damper displacement, velocity, voltage signal) and the output (damper force). Adaptive Neuro-Fuzzy Inference System (ANFIS) from the MATLAB fuzzy logic toolbox has been used in their study to determine the parameters required for modeling the damper. This toolbox uses a learning algorithm that combines back-propagation, gradient descent and least squares methods. Training and validating data are generated using the phenomenological model proposed by Spencer et al. (1997) [329]. The model has accurately described the MR damper behaviour. Furthermore, a fully-trained

model has been found to be faster than the mathematical model, while keeping the error relatively small.

NARX (nonlinear autoregressive exogenous) based model has been proposed by Leva and Piroddi (2002) [205]. A NARX model can be built based on a nonlinear regressor by estimating in each iteration the next output value given the past input and the output measurements. In addition, the model contains an error or residual term which relates to the fact that knowledge of the other terms will not enable the present value of the model to be predicted exactly. This model consists of the nonlinear generalization of the ARX model, which has been commonly used in linear black-box model identification. A very interesting characteristic and advantage of this method has been to perform simultaneously the structure selection and parameter identification, addressed in a single optimization procedure. The optimal model is chosen by the identification method based on the input/output behaviour of the system. Magnetorheological damper models obtained with this method have shown to be accurate, simple, robust, invertible, and suitable for model-based control.

Although the non-parametric models effectively reproduce MR damper hysteretic behaviour, their application is often hindered by their complexity and the extensive amount of experimental data required for training and/or model validation. Parametric models have therefore been more commonly employed in simulations and in the development of control algorithms.

3.3.2 Parametric Model

Parametric models consist of arrangements of mechanical elements, such as springs and dashpots to emulate the damper behaviour. The parameters of these elements are determined by curve-fitting analysis on the experimental results. One of the first parametric models developed and reported has been the Bingham model, which consisted of a frictional element in parallel with a dash-pot. It was proposed by Stanway et al. (1985, 1987) [339, 338] for ER fluids and adapted by Spencer et al. (1997) [329] for a small-scale MR fluid damper. A schematic of such a model is presented in Fig. 3.3 and consists of a Coulomb friction element in parallel with a viscous damper. Equation 3.1 describes the force (f_c) generated by the device

$$f_c = f_y \; sgn(\dot{x}_{mr}) + c_0 \dot{x}_{mr} \tag{3.1}$$

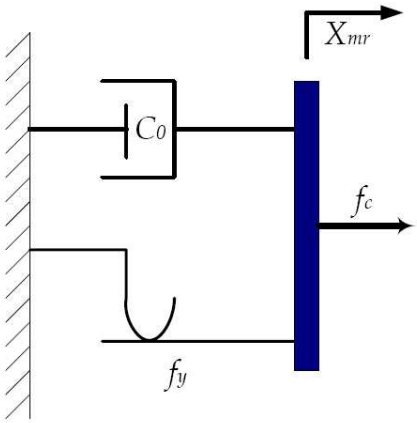

Figure 3.3: Schematic diagram of Bingham model (Stanway et al. (1987) [338])

where f_y is the yield force, c_0 is the damping coefficient and $\dot{x}_{mr}$ is the piston velocity. It is important to note that both f_y and c_0 depend on the applied voltage. Although this model accurately describes the fluid behaviour beyond the yield point, it does not capture its behaviour in the pre-yield region properly (Spencer et al. (1997) [329]; Jung et al. (2004) [174]).

Gamota and Filisko (1991) [127] proposed an extended version of the Bingham model. It consisted of the standard Bingham model and in additions a standard linear solid model connected in series with the original Bingham model, as shown in Fig. 3.4. The force in the system can be described by

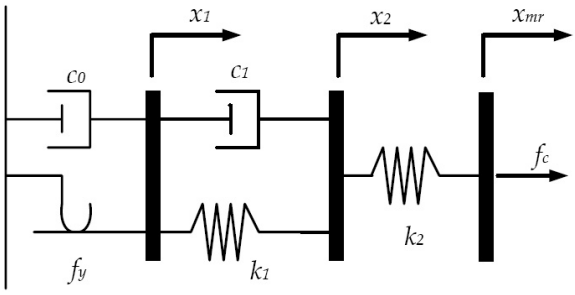

Figure 3.4: Extended Bingham model (Gamota and Filisko (1991) [127])

$$f_c = \left\{ \begin{array}{l} k_1(x_2 - x_1) + c_1(\dot{x}_2 - \dot{x}_1) \\ c_0\dot{x}_1 + f_y sgn(\dot{x}_1) \\ k_2(x_{mr} - x_2) \end{array} \right\} \quad |f_c| > f_y$$
$$f_c = \left\{ \begin{array}{l} k_1(x_2 - x_1) + c_1(\dot{x}_2 - \dot{x}_1) \\ k_2(x_{mr} - x_2) \end{array} \right\} \quad |f_c| \leq f_y \tag{3.2}$$

where k_1, k_2, and c_1 are the parameters associated with the linear solid model, c_0 is the damping coefficient for the Bingham model, and f_y is the yield force. Force velocity behaviour of this model has been found to more closely resemble experimental results. The fluid behaviour at the vicinity of zero velocity has not been accurately reproduced. It has also been observed by Spencer et al. (1997) [329] that these equations are computationally very expensive.

The Herschel-Bulkley visco-plasticity model has also been reported to describe MR fluid behaviour. However, both Wang and Gordaninejad (2000) [366] and Yang (2001) [387] reported that the model provides only a slight improvement on the Bingham model. Therefore, Herschel-Bulkley visco-plasticity model is not able to capture the details of the force-velocity hysteresis loops. Nonlinear hysteretic bi-linear viscous model proposed by Kamath and Wereley (1997) [177] and its extended form (Wereley et al. (1998) [372]) are also proposed. Figure 3.5 shows a schematic of the extended model which more closely reproduces the experimental response in the pre-yield region than the originally proposed model. Equation 3.3 describes the force generated.

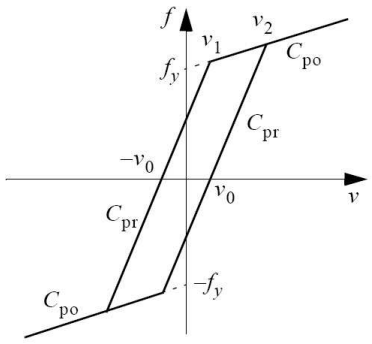

Figure 3.5: Nonlinear hysteretic bi-linear viscous model (Wereley et al. (1998) [372])

$$f_c = \left\{ \begin{array}{lll} C_{p0}\dot{x}_{mr} - f_y & \dot{x}_{mr} \leq = v_1 & \ddot{x}_{mr} > 0 \\ C_{pr}(\dot{x}_{mr} - v_0) & -v_1 \geq \dot{x}_{mr} \leq v_2 & \ddot{x}_{mr} > 0 \\ C_{p0}\dot{x}_{mr} + f_y & v_2 \leq = \dot{x}_{mr} & \ddot{x}_{mr} > 0 \\ C_{p0}\dot{x}_{mr} + f_y & v_1 \leq = \dot{x}_{mr} & \ddot{x}_{mr} < 0 \\ C_{pr}(\dot{x}_{mr} + v_0) & -v_2 \geq \dot{x}_{mr} \leq v_1 & \ddot{x}_{mr} < 0 \\ C_{p0}\dot{x}_{mr} - f_y & \dot{x}_{mr} \leq = -v_2 & \ddot{x}_{mr} < 0 \end{array} \right\} \tag{3.3}$$

Where v_1 and v_2 are the decelerating (given by Eq. 3.4) and accelerating (given by Eq. 3.5) yield velocities, respectively. C_{p0} and C_{pr} are coefficient of the velocities at different regions of the model (see Fig. 3.5).

$$v_1 = \frac{f_y - C_{pr}v_0}{C_{pr} - C_{p0}} \tag{3.4}$$

$$v_2 = \frac{f_y + C_{pr}v_0}{C_{pr} - C_{p0}} \tag{3.5}$$

Similar to the Bingham model described previously, this model is capable of reproducing the force-displacement behaviour very well, but does not replicate the force velocity behaviour accurately, especially in the region where velocity is low.

The nonlinear (bilinear) hysteretic viscous model has further been extended by Li et al. (2000) [210]. In the study, the behaviour of the MR damper under sinusoidal excitation has been addressed. The viscoelastic-plastic model developed is presented in Fig. 3.6. The governing equations of the bi-viscous model are given by,

$$\begin{array}{ll} f_c = f_{ve} + F_s & |f_c| \leq F_c \\ f_c = C_v\dot{x}_{mr} + R\ddot{x}_{mr} + F_c sgn(\dot{x}_{mr}) & |f_c| > F_c \end{array} \tag{3.6}$$

where F_s represents the stiction force, that is, the resistance to start motion, C_v is the viscous damping coefficient, R is the equivalent inertial mass, which depends on the displacement amplitude and the oscillatory frequency, F_c is the damper yield force, and f_{ve} is the viscoelastic force determined by Eq. 3.7 (Weiss et al. (1994) [370]).

$$\dot{f}_{ve} + \left\{ \frac{K_1 + K_2}{C_1} \right\} f_{ve} = \left\{ \frac{K_1 + K_2}{C_1} \right\} x_{mr} + K_2\dot{x}_{mr} \tag{3.7}$$

This model predicts the force-velocity behaviour of MR damper experimental results very

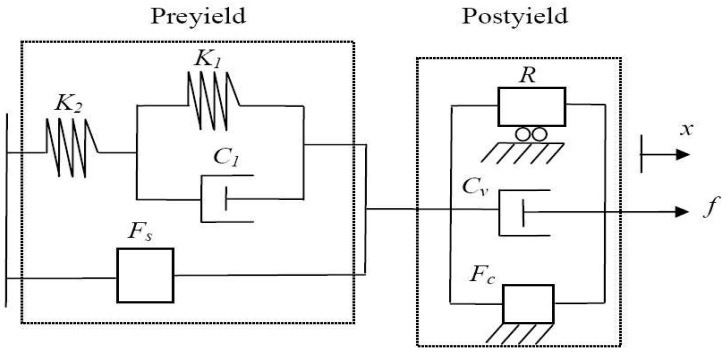

Figure 3.6: Visco-elastic plastic model (Li et al. (2000) [210])

well. However, only sinusoidal inputs are considered in the study with small-scale dampers. More extensive validation tests considering experimental responses of large-scale MR dampers under random excitation would still be required for practical applications (Jung et al. (2004) [174]).

A polynomial damper model has been proposed by Choi et al. (2001) [66], where the hysteresis loop has been divided into two regions. One consisted of positive acceleration and the other of negative acceleration. Sixth order polynomials have been fitted to these regions. The damping force is determined by the following equation.

$$f_c = \sum_{i=0}^{n} \left(b_i + c_i i_{mr}\right) \dot{x}_{mr}^{i} \tag{3.8}$$

Where i_{mr} is the input current to the damper. Coefficients b_i and c_i have been determined from curve fitting of the experimental data and have been kept independent of the input current.

The most widely used model for hysteretic system has been the Bouc-Wen model developed by Wen (1976) [371] based on Bouc hsyteretic model (Bouc (1967) [42]). It has also been reported to model hysteretic behaviour of MR damper by Spencer et al. (1997) [329]. Figure 3.7(a) shows a schematic diagram of Bouc-Wen model and Eqs. 3.9 and 3.10 describe the force generated by the device. The model contains in series, a spring, a dash-pot and the Bouc-Wen hysteretic element.

$$f_c = c_0 \dot{x}_{mr} + k_0 (x_{mr} - x_0) + \alpha z_{mr} \tag{3.9}$$

Where c_0 is the damping coefficient, k_0 is the linear spring parameter, x_0 is the initial displacement of spring, α is the coefficient of the Bouc-Wen parameter associated with evolutionary variable z_{mr}. The evolutionary variable accounts for the history dependence of the response and satisfies the following equation.

$$\dot{z}_{mr} = -\gamma \left|\dot{x}_{mr}\right| \; z_{mr} \; \left|z_{mr}\right|^{n-1} - \beta \dot{x}_{mr} \left|z_{mr}\right|^{n} + A\dot{x}_{mr} \tag{3.10}$$

The adjustment of hysteresis parameters γ, β, and A, determines the linearity in the unloading region as well as the transition smoothness from the pre-yield to the post-yield regions. The functional dependence of these parameters on the command voltage v_c (and therefore commanded current (i_c)) is expressed as (Spencer et al. (1997) [329], Tan and Agrawal (2005) [353]).

$$\begin{aligned} \alpha(v_c) &= \alpha_a + \alpha_b \, v_c; \\ c_0(v_c) &= c_{0a} + c_{0b} \, v_c; \end{aligned} \tag{3.11}$$

In addition to the dependence of the parameters on commanded voltage, the resistance and inductance present in the circuit introduce dynamics into this system. This dynamics has been accounted for by the first order filter on the voltage input given by

$$\dot{v}_c = -\eta(v_c - v_a) \tag{3.12}$$

where η is the time constant associated with the first order filter and v_a is the voltage applied to the MR damper. Bouc-Wen model has been found to describe the force-displacement behaviour of MR damper satisfactorily, however, the force-velocity behaviour has not been reproduced very well (Spencer et al. (1997) [329], Yang (2001) [387]). To improve the reproduction of the force-velocity behaviour of the MR damper, a modified Bouc-Wen model (also known as phenomenological model), has been proposed by Spencer et al. (1997) [329]. The schematic diagram of the model is shown in Fig. 3.7(b) and consists of a spring in parallel and a dash-pot in series with the simple Bouc-Wen model (Fig. 3.7(a)). The force produced by the damper can be described by

$$f_c \left\{ \begin{array}{l} = c_0(\dot{x}_{mr} - \dot{y}_{mr}) + k_0(x_{mr} - y_{mr}) + k_1(x_{mr} - x_0) + \alpha z_{mr} \\ = c_1 \dot{y}_{mr} + k_1(x_{mr} - x_0) \end{array} \right\} \tag{3.13}$$

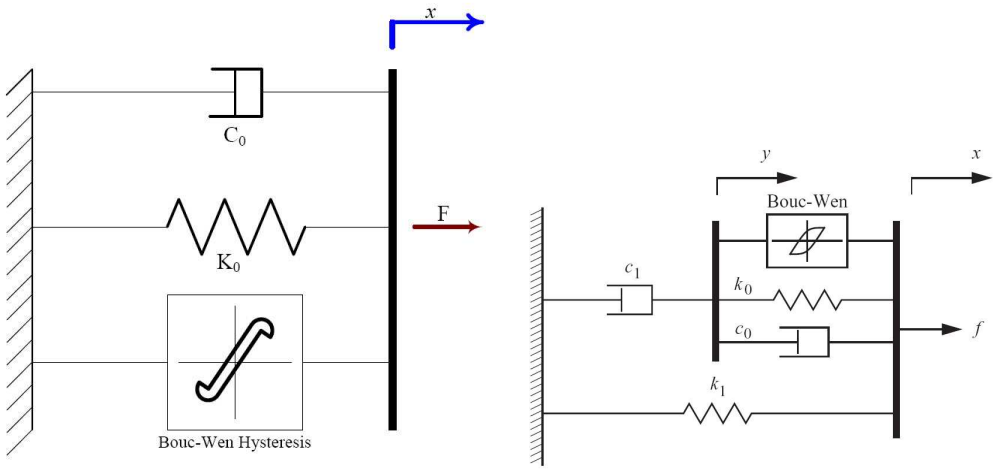

(a) Bouc-Wen model (b) Modified Bouc-Wen model

Figure 3.7: Bouc-Wen hysteretic model (Spencer et al. (1997) [329])

where x_{mr} is the damper displacement, y_{mr} is an internal displacement of the damper, α is the Bouc-Wen parameter describing the MR fluid yield stress, c_0 represents the viscous damping at large velocities, k_0 the stiffness at large velocities, k_1 is introduced to model the damper force due to the accumulator, and c_1 to reproduce the roll-off occurring in the experimental data when velocities are close to zero. Evolutionary variable z_{mr} and variable y_{mr} satisfy the following equations.

$$\dot{z}_{mr} = -\gamma \left|\dot{x}_{mr} - \dot{y}_{mr}\right| \; z_{mr} \; |z_{mr}|^{n-1} - \beta(\dot{x}_m r - \dot{y}_{mr}) \, |z_{mr}|^n + A(\dot{x}_{mr} - \dot{y}_{mr}) \tag{3.14}$$

$$\dot{y}_{mr} = \frac{1}{c_0 + c_1} \{\alpha z_{mr} + c_0 \dot{x}_{mr} + k_0(x_{mr} - y_{mr})\} \tag{3.15}$$

It is important to notice that variables α, c_0, and c_1 are functions of the input voltage (current) to the damper and have been represented by an equation similar to Eq. 3.11. This model can very well reproduce the force-velocity responses obtained experimentally. Similiar to Eq. 3.12 the dynamics involved in the MR fluid reaching rheological equilibrium has been accommodated using a first order filter. Although this model captures the MR fluid behaviour very well, it has been found to be computationally expensive (Jung et al. (2004) [174]).

Recent experiments to develop a large scale MR damper (20 ton) for application to huge

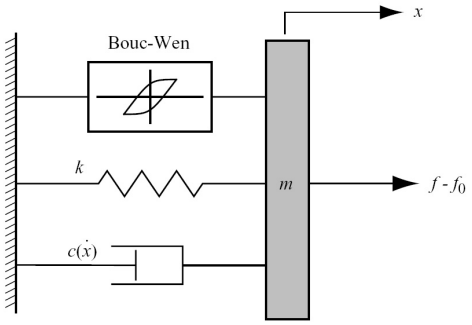

Figure 3.8: Modified Bouc-Wen hysteretic model with mass element (Yang (2001) [387])

structures have bought into light many new phenomena in modeling MR damper behaviour, for *e.g.*, amplitude and frequency dependence of MR damper parameters. A model that accurately predicts the behaviour of the 20-ton MR fluid damper includes a modified version of the phenomenological model and has been described by Yang (2001) [387] and Yang et al. (2002, 2004) [389, 390]. A mass element is added to the original Bouc-Wen model (as shown in Fig. 3.8) to consider the effect of MR fluid stiction or resistance to start motion. The force generated is described by Eq. 3.16.

$$f_c = c(\dot{x}_{mr})\dot{x}_{mr} + k(x_{mr}) + \alpha z_{mr} + m\ddot{x}_{mr} + f_0 \tag{3.16}$$

Where α is the Bouc-Wen parameter, k is the accumulator stiffness, mass m has been introduced to represent the fluid inertial effect, f_0 represents the damper friction force due to seals and measurement bias, and c is the post-yield plastic damping coefficient described by Eq. 3.17. Equation 3.16 shows that the damping coefficient is dependent on the magnitude of excitation and this dependence has been bought into the model using Eq. 3.17.

$$c(\dot{x}_{mr}) = a_1 e^{-(a_2|\dot{x}_{mr}|)^P} \tag{3.17}$$

Where a_1, a_2, and p are positive constants. In addition, the evolutionary variable z_{mr} is governed by the Eq. 3.10.

Dominguez et al. (2004) [90] have pointed out through various experiments on RD-1003-3 MR damper (MR Damper (2006) [240]) that considerable differences exist between the simulation and experimental results if Bouc-Wen model is used. The characteristic parameters in

the BoucWen model are not functions of the frequency and amplitude of excitations. Therefore, the estimated parameters can characterize the behaviour of the tested MR damper under specific excitation condition and must be re-evaluated if a different combination of excitation parameters is desired. This can be extremely cumbersome and computationally expensive. In Dominguez et al. (2006) [91], a new hysteresis model based on the BoucWen model has been developed to consider the effects of frequency and amplitude of excitations. This enables the model to predict efficiently and accurately the hysteresis force for changing excitation conditions. The proposed modified BoucWen model is validated using the experimental results and a better correlation has been found (Dominguez et al. (2006) [91]).

In the next section, details of the experiments carried out with MR damper RD-1005-3 are presented.

3.4 MR Damper RD-1005-3 Testing

3.4.1 Configuration of RD-1005-3

Magneto-rheological damper RD-1005-3 (MR Damper (2006) [240]) is employed for the experimental study and its specifications are given in Table 3.1. The device has a capacity to provide a peak to peak force of 2224 N at a velocity of 51 mm/s and at a continuous supply of 1 A current. The input current can be varied to a maximum (represented as Max. in Table 3.1) of 1 ampere (continuous supply) and 2 amperes (intermittent supply). The response time in Table 3.1 represents the time taken by the MR damper to reach 90% of its maximum level during a 0A to 1A step at 51mm/s. Further details about the damper are available with LORD Corporation (MR Dampers (2006) [240] and are also given in Appendix A.

3.4.2 Experimental Setup

To investigate the fundamental behaviour of the MR damper RD-1005-3, manufactured by Lord Corporation, a series of experiments are conducted. The MR damper is tested using a computer-controlled servo hydraulic MTS Universal Testing Machine. The schematic diagram of the experimental set up is shown in Fig. 3.9.

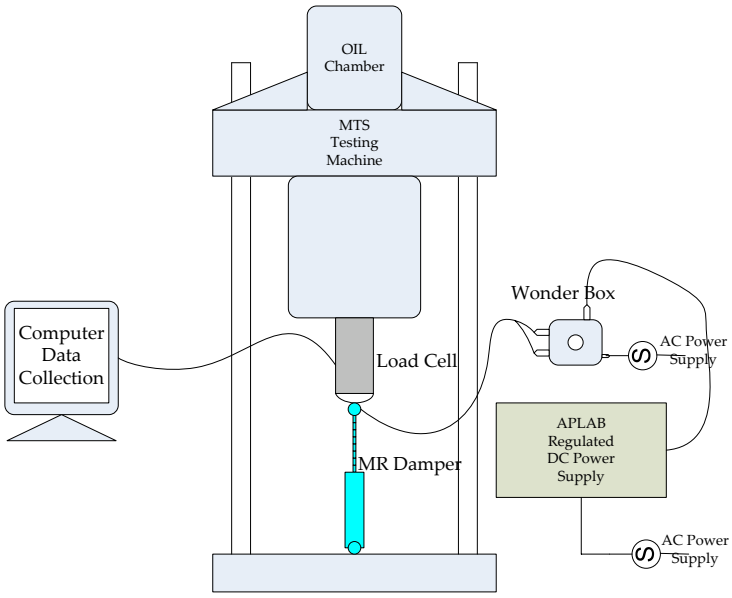

Figure 3.9: Schematic diagram of MR damper test set-up

A constant DC voltage supply is provided to the MR damper using an APLAB manufactured Regulated DC voltage power supplier (details of the instrument are given in Appendix A) through Wonder Box®. The Wonder Box® converts the DC voltage input to current supply. LORD Wonder Box® device controller kit is a companion product for the MR fluid devices. The Wonder Box device controller kit provides closed loop current control to compensate for changes in electrical loads up to the limits of the power supply. The exact voltage to current relationship of the Wonder Box® is given in Appendix A.

Table 3.1: Properties of MR Damper RD-1005-3

Parameter	**Value**	**Parameter**	**Value**
Extended length	208 mm	Compressed length	155 mm
Device stroke	± 25 mm	Response time	$<$ 10 ms
Max. tensile force	4448 N	Max. current supply	2 A
Max. temperature	71° C		

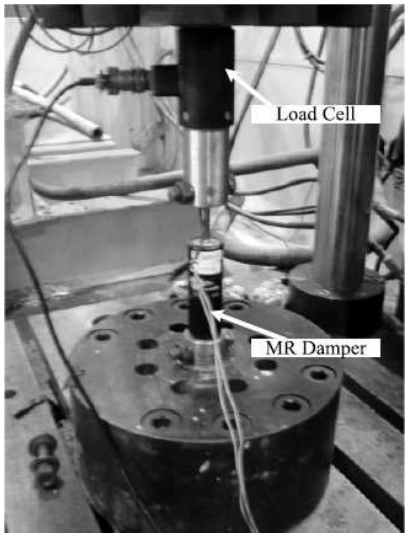

Figure 3.10: Magneto-rheological damper connection to MTS

The lower head of the MR damper is fixed to the base of the MTS machine. The upper head is attached to the hydraulic actuator that can move up and down and also incorporates a load cell of 5 kN, allowing the operator to measure the force applied across the damper. The displacement of the hydraulic actuator and the corresponding force across the load cell are automatically collected using MTS Multipurpose Testware® (Model 793.10) in a desktop PC. Velocities across the actuator are calculated using finite difference technique. Tests are carried out at room temperatures of 26°C–32°C. Figure 3.10 shows a snap shot of the experiment.

3.4.3 Sinusoidal Displacement Excitation

Series of tests are conducted to measure the responses of the damper under various combinations of frequencies, amplitudes of damper stroke and current supplies. In each test, the hydraulic actuator is driven with a sinusoidal signal having a fixed frequency and amplitude of excitation. A constant current (selected from a set) is supplied to the damper for each test. The data is sampled at 128 Hz. The input current is suppled using the Wonder Box®, which converts a voltage to a current supply. Therefore one can monitor either voltage or current to modify the characteristic of the damper. It is to be noted here that either voltage or current supply has to be monitored to obtain a desirable force as an output from the MR damper. Therefore, either 'voltage' or 'current' or in combination 'current/voltage' term will be used

in the subsequent chapters.

The MTS machine is activated by a hydraulic cylinder, thus it is difficult to carry out high frequency tests except for small displacement amplitudes. Therefore, a set of frequencies (0.1, 0.25, 0.50, 1.0, 1.5, 2.0, 2.5, 3.0 Hz), amplitudes (2.5, 5.0, 10.0, 15.0, 20.0 mm) and current supplies (0.0, 0.25, 0.50, 0.75, 1.0 A) formed the test program. Figure 3.10 shows the connection of MR damper with the MTS machine. All the experiments are conducted in displacement control mode using the MTS machine, *i.e.*, the actuator of the MTS machine provided a predefined displacement to the MR damper shaft. In this section typical experimental results of the MR damper tests are given, while the complete set of test results are reported in Appendix B. These tests include: variable input current tests, frequency dependent tests, amplitude-dependent tests, and constant peak velocity tests.

Variable input current tests

Variable input current tests include MR damper response under different input currents for a particular amplitude and frequency of sinusoidal excitation. As discussed previously the set of input currents considered is (0.0, 0.25, 0.50, 0.75, 1.0 A). To reduce the temperature effect on the MR fluid, the tests are conducted at room temperatures of 26°C–32°C as well as a gap of 10-15 minutes is given between the tests. Each test is carried out for a duration of 60 seconds.

Typical test results are shown in Fig. 3.11, and the complete set of experimental results are given in Appendix B. Figure 3.11 shows force-displacement behaviour (Fig. 3.11(a)), force-velocity behaviour (Fig. 3.11(b)) and the damper force time history (Fig. 3.11(c)) under sinusoidal excitation of amplitude 10mm and frequency 0.5Hz and at various input current levels. The inner curve represents the response at zero ampere and the outer curve represents response at 1 ampere. The effect of change in input current is readily observed. At an input current of 0A, the MR damper primarily exhibits less hysteretic damping than that observed at 1A (*i.e.*, the force-displacement relationship covers less area). As the input current increases, the force required to yield the MR fluid in the damper also increases, and a plastic-like behaviour is observed in the hysteresis loops.

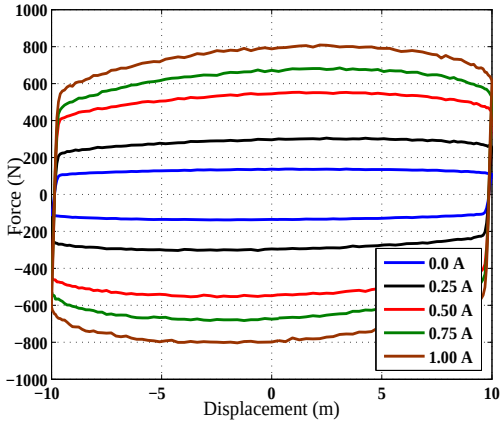

(a) Force-Displacement

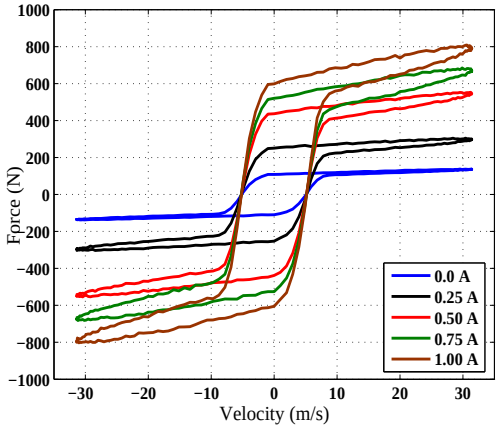

(b) Force-Velocity

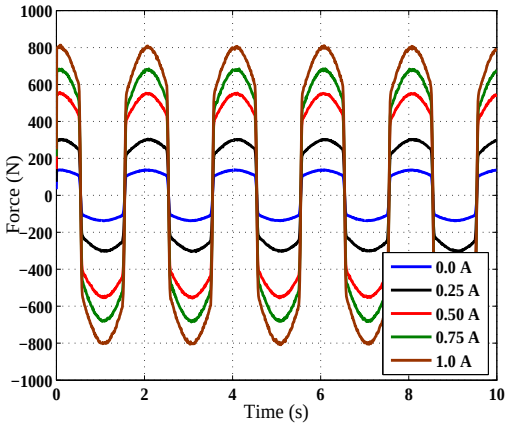

(c) Force Time History

Figure 3.11: Variable input current experimental curves ($x_{mr} = 10$mm, $\omega = 0.5$Hz)

Amplitude dependent tests

Tests are also conducted to investigate the effect of excitation amplitude on MR damper hysteretic behaviour. Here the frequency of excitation and input current supply are kept constant at various values from the set, while the amplitude of sinusoidal motion is varied from one test to another. In these experiments, sinusoidal displacement excitations with amplitudes of (2.5, 5.0, 10.0, 15.0, 20.0 mm) are considered.

Figure 3.12 shows the damper force-displacement, force-velocity behaviour and force time history for a sinusoidal excitation of 0.5Hz with a constant 0 ampere current supply.

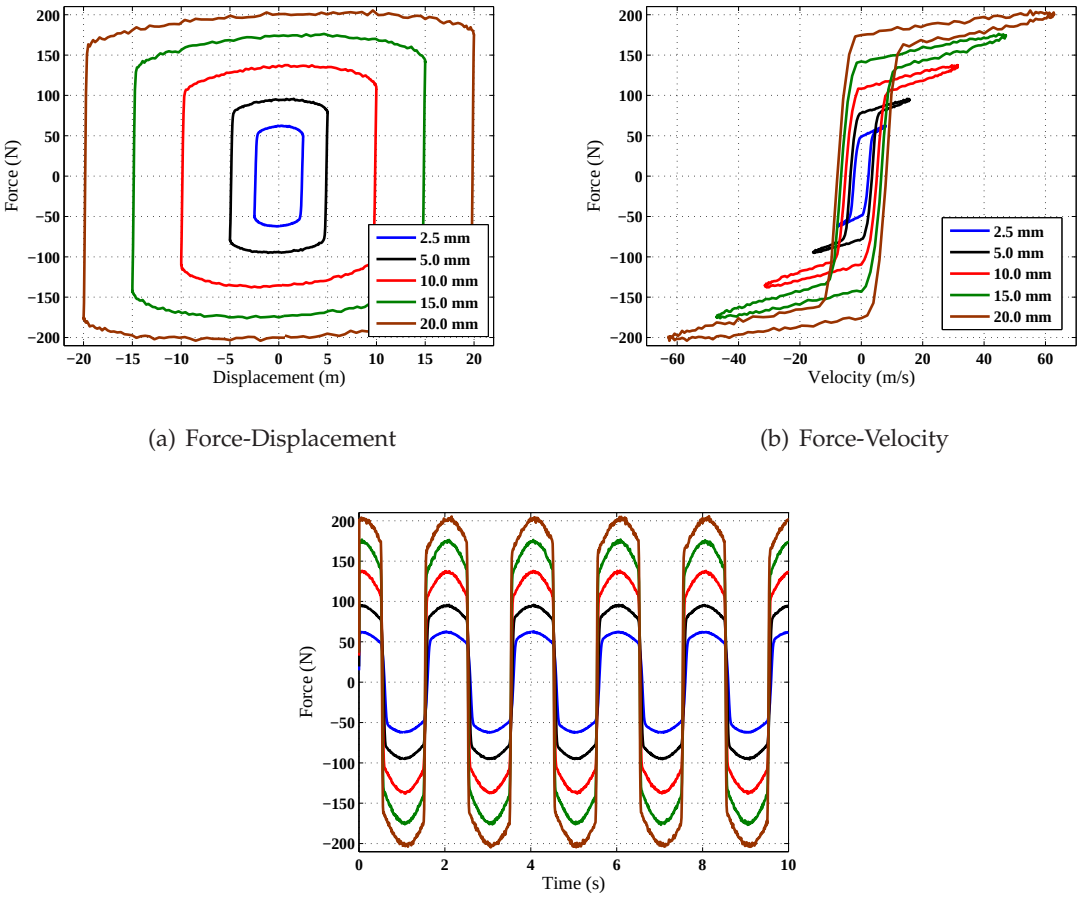

(a) Force-Displacement

(b) Force-Velocity

(c) Force Time History

Figure 3.12: Variable excitation amplitude test curves ($i_{mr} = 0$A, $\omega = 0.5$Hz)

It is observed that the resisting force in the damper increased with increase in excitation amplitude. The inner curve corresponds to response at 2.5mm amplitude and the outer curve corresponds to 20mm amplitude of excitation.

As shown in Fig. 3.12(b), when the displacement of excitation is small, such as the displacement amplitude of 2.5mm, the MR damper just crosses the pre-yield region (tails in velocity curve are less). As the amplitude increases, the velocity increases accordingly. Thus more MR fluids begin to yield, and a larger post-yield shear flow is seen to develop. Consequently, the plastic viscous force becomes significant, especially at large displacement amplitudes (*e.g.*, displacement amplitudes of 10mm and above).

Figure 3.13 shows another set of results for variable amplitude tests with frequency of

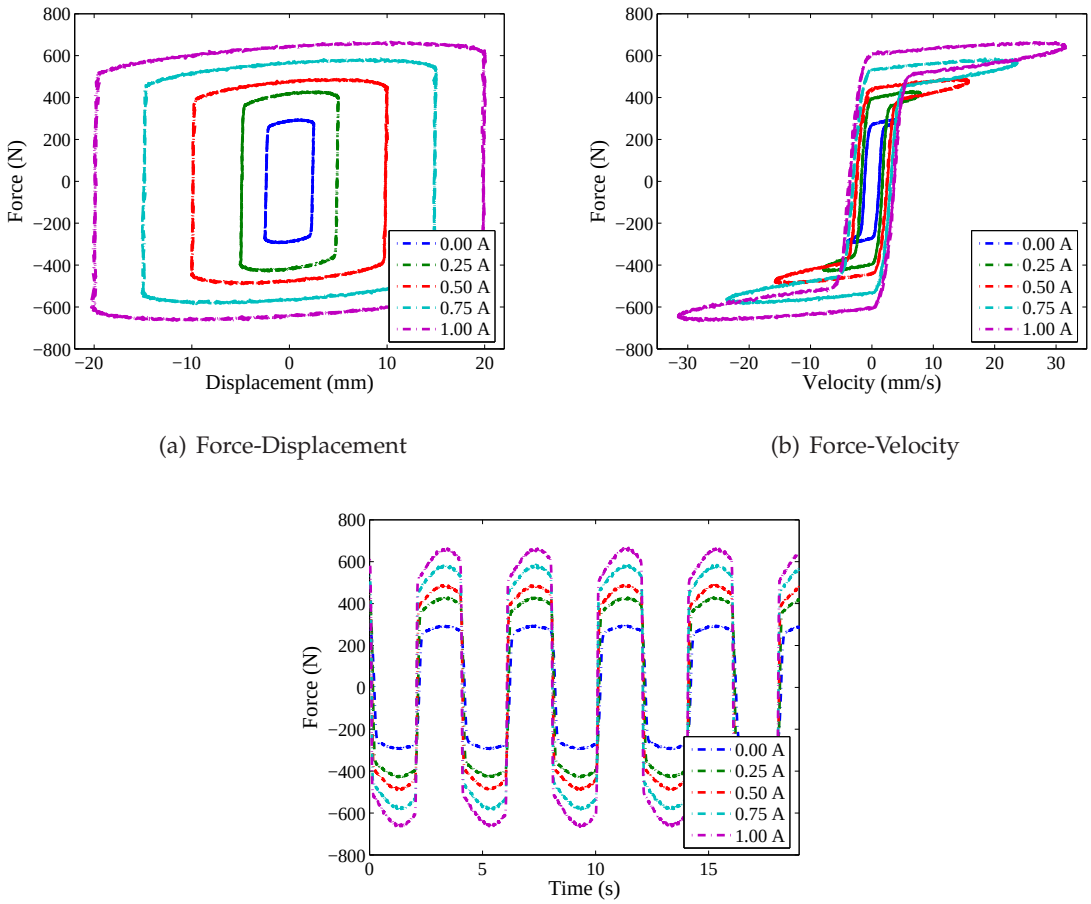

(a) Force-Displacement

(b) Force-Velocity

(c) Force Time History

Figure 3.13: Variable excitation amplitude test curves ($i_{mr} = 0.5$ A, $\omega = 0.25$ Hz)

excitation ($\omega = 0.25$Hz) and at an input current of ($i_{mr} = 0.5$A). It is observed that with increase in amplitude of excitation the damper force saturates as the force-displacement and the force-velocity curves get saturated near high amplitude excitations. Similar to Fig. 3.12, for the small displacement excitation, the MR damper just crosses the pre-yield region having less tail area in velocity curve. As the amplitude increases, the velocity increases accordingly.

Frequency dependent tests

The behaviour of the MR damper under different frequencies of sinusoidal excitations with fixed amplitude and at fixed input current are reported. The sinusoidal excitations consisted of a set of frequencies (0.1, 0.25, 0.50, 1.0, 1.5, 2.0, 2.5, 3.0 Hz).

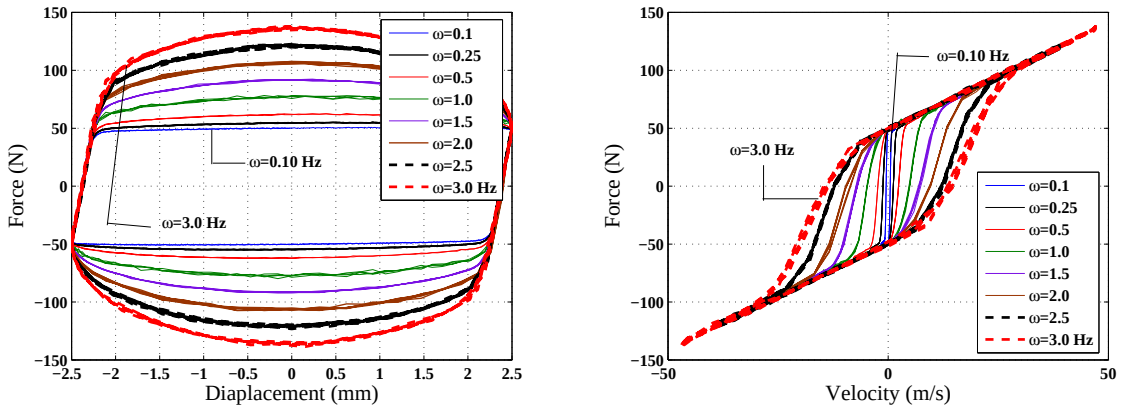

(a) Force-Displacement

(b) Force-Velocity

Figure 3.14: Constant frequency test curves ($i_{mr} = 0.25$ A, $x_{mr} = 2.5$ mm)

Figure 3.14 shows the MR damper force-displacement and force-velocity relation under a 2.5mm sinusoidal displacement excitation at an input current of 0.25A. The inner curve and the outer curve show responses due to 0.1Hz and 3.0Hz sinusoidal excitation frequency. One can see that the maximum damping force increases when the frequency of excitation increases due to the larger plastic viscous force at higher velocity (increase in frequency at fixed amplitude increases velocity).

Constant peak velocity tests

The frequency-dependent tests are conducted with variable frequencies at a particular amplitude of excitation and at a particular input current supply. Similarly, the amplitude dependent tests are conducted with fixed frequency of excitation and constant current input but with variable amplitude. Therefore, the peak velocities in those tests are different. No separate tests are conducted to obtain the MR damper response to constant peak velocity. Constant peak velocity response of MR damper are determined based on the response obtained for various combination of amplitudes and frequencies of excitation from the set of test amplitudes and frequencies already discussed.

Figure 3.15 provides the damper force-displacement and force-velocity relationships under a sinusoidal displacement excitation having a peak velocity of 31.40mm/s and input current of 0.75A. The various combination of frequencies and amplitudes that provide a peak

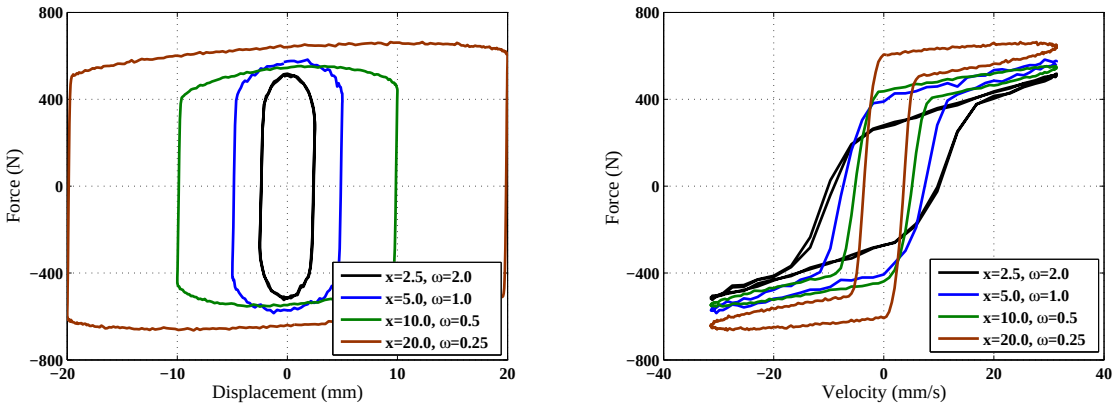

(a) Force-Displacement (b) Force-Velocity

Figure 3.15: Constant peak velocity test curves ($i_{mr} = 0.75$A, $\dot{x}_{mr} = 31.40$mm s^{-1})

velocity of 31.40mm/s are labeled in the Fig. 3.15.

It can be seen that the peak resisting forces are almost identical if the damper has the same peak velocity and input current, even though the amplitude and frequency vary. The experimental results are very promising, which implies that the damping force largely depend on the damper velocity and the input current (or MR fluid yield stress).

3.4.4 MR damper modeling using Bouc-Wen hysteresis

To analyze and model the RD-1005-3 MR damper, the simple Bouc-Wen model (Eqs. 3.9-3.10) is considered. The simple Bouc-Wen model requires optimization of seven parameters model in comparison to modified Bouc-Wen model that requires optimization of ten parameters. This makes the simple Bouc-Wen model computationally less intensive and is therefore considered for modeling RD-1005-3 MR damper.

The six parameters (c_0, k_0, α, γ, β, A) are estimated for every single frequency of excitation at a particular amplitude and input current on the basis of minimizing the error between the model-predicted force (f_c) and the force (Fe) obtained in the experiment. The parameter n is taken to be 2 and other parameters are optimized. The error in the model is represented by the objective function J given by

$$J = \frac{\sum_{i=1}^{N} (f_{ci} - Fe_i)^2}{\sum_{i=1}^{N} Fe_i^2} \tag{3.18}$$

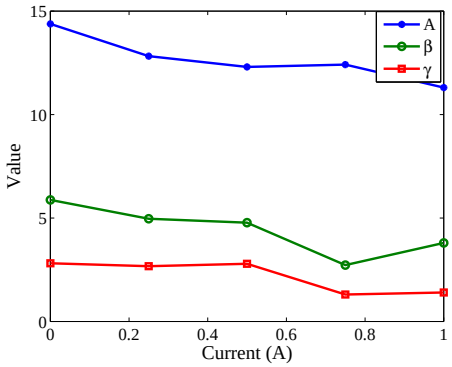

(a) Input current dependence (10 mm, 0.25 Hz)

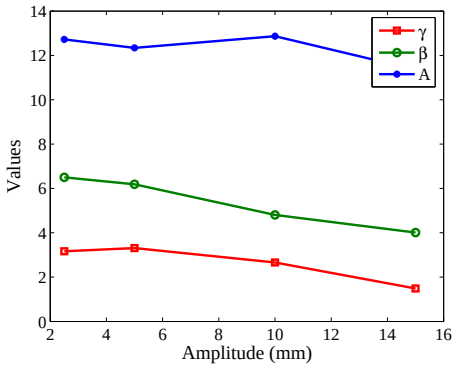

(b) Amplitude dependence (0 A, 0.25 Hz)

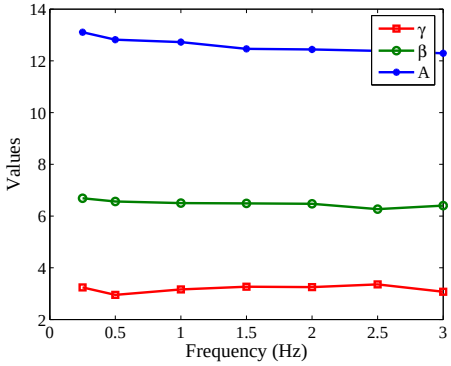

(c) Frequency dependence (0.5 A, 2.5 mm)

Figure 3.16: Dependence of γ, β, A on input current, amplitude and frequency of excitation

where N is the number of points in the experimental data. Optimum values for the six parameters are obtained using 'lsqcurvefit' (least square curve fitting) algorithm available in MATLAB® optimization toolbox (MATLAB (2004) [230]) for nonlinear curve fitting. This study employs a current driver to power the MR damper.

A preliminary set of analysis is performed to observe the variability of the parameters with independent variables, namely, frequency (ω), amplitude of sinusoid (x_a), applied current (i_a) for $n = 2$. It is observed that the parameters (γ, β, A) for the hysteretic behaviour of the MR damper show slow change with frequency, amplitude and input current. Figure 3.16 shows the change of the parameters (γ, β, A) *w.r.t.* (with respect to) the amplitude and frequency of excitation and input current.

As shown in Fig. 3.16, the parameters γ, β, A do not show much change with the change

in either input current (Fig. 3.16(a)), or amplitude of excitation (Fig. 3.16(b)) or frequency of excitation (Fig. 3.16(c)). Therefore, these three parameters are considered constant at their average to carry on with further analyses. This phenomenon is also reported in Dominguez et al. (2004, 2006) [90, 91]. Thereafter, the rest of the variables (c_0, k_0, α) and their dependence on frequency, amplitude and input current are evaluated to obtain the optimal values. For the present analysis (keeping in mind the application to seismic structural control) the effect of amplitude of excitation, and input current on the variables are studied (frequency is omitted as earthquake excitation frequencies are not certain). Therefore the current dependence of the parameters of MR damper is considered to be,

$$\begin{aligned} \alpha(x_a, i_c) &= \alpha_a(x_a) + \alpha_b(x_a)\, i_c; \\ c_0(x_a, i_c) &= c_{0a}(x_a) + c_{0b}(x_a)\, i_c; \\ k_0(x_a, i_c) &= k_{0a}(x_a) + k_{0b}(x_a)\, i_c \end{aligned} \tag{3.19}$$

where i_c is the commanded input current to the MR damper. x_a is the amplitude of sinusoidal excitation. In addition to the dependence of the parameters on amplitude and current, the resistance and inductance present in the circuit introduce dynamics into this system. This dynamics is accounted for by the first order filter (similar to Eq. 3.12) on the control input given by

$$\dot{i}_c = -\eta(i_c - i_a) \tag{3.20}$$

where η is the time constant associated with the first order filter and i_a is the current applied to the current driver.

3.5 Proposed Bouc-Wen Hysteretic Model

The dependence of the parameters c_0, k_0 and α on the amplitude and frequency of excitation and at the input current has been studied recently by Dominguez et al. (2004, 2006) [90, 91]; Yang et al. (2004) [390]. In these studies, the parameters c_0 and k_0 are observed to decrease with amplitude of excitation but increase with increase in input current. The experiments carried out in this dissertation also show similar behaviour of these parameters (see Figs. 3.17(a), (b)). On the other hand α increases with increase in both x_a and i_c (see Fig. 3.17(c)).

Bouc-Wen model is modified for velocity dependence of the c_0 parameter by Yang et al.

(2004) [390] using an exponential function. Dominguez et al. (2004, 2006) [90, 91] multiplied the right hand side of Eq. 3.9 with an exponential function to consider the effect of amplitude of stroke in the harmonic analysis of MR dampers. In the present analysis, the effect of amplitude of stroke separately for c_0, k_0, and α is considered. A quadratic function of amplitude of stroke (x_a) and linear function of input current (i_c) are considered for amplitude of excitation and input current dependence. This is shown in Eq. 3.21. Other polynomial forms of x_a and i_c can be accommodated in the model, but we have restricted the study to Eq. 3.21.

$$\begin{aligned} c_0 &= (c_1 + c_2\, x_a + c_3\, x_a^2) + (c_4 + c_5\, x_a + c_6\, x_a^2)\, i_c\,; \\ k_0 &= (k_1 + k_2\, x_a + k_3\, x_a^2) + (k_4 + k_5\, x_a + k_6\, x_a^2)\, i_c\,; \\ \alpha &= (\alpha_1 + \alpha_2\, x_a + \alpha_3\, x_a^2) + (\alpha_4 + \alpha_5\, x_a + \alpha_6\, x_a^2)\, i_c\,; \end{aligned} \tag{3.21}$$

The optimal values of the constants (c_1 to c_6, k_1 to k_6, α_1 to α_6) with the following constraints $c_0(x_a, 0) \geq 0$, $k_0(x_a, 0) \geq 0$, $\alpha_0(x_a, 0) \geq 0$ are obtained using nonlinear optimization. MATLAB function '*fmincon*' is used to minimize the following cost function.

$$J_{param} = \sqrt{\sum (y - \bar{y})^2 / \sum \bar{y}^2} \tag{3.22}$$

Where y represents the value of the parameters obtained for a particular choice of input current and amplitude of vibration and $\bar{y}$ represents corresponding value obtained through experimental data. The optimization is run for each of the parameters c_0, k_0 and α. '*fmincon*' is a constrained optimization function in MATLAB and uses a sequential quadratic programming method for optimization. The optimal parameters are tabulated in Table 3.2.

Figure 3.17 shows the match between the experimental and analytical surfaces. A surface plot is generated as the parameters are functions of both input current and amplitude of excitation. The parameter values are plotted in z axis. As shown in the Fig. 3.17 a satisfactory match between the experimental and analytical model is achieved. In addition to the graphical evidence of the superiority of the proposed model, a quantitative study of the error between the predicted model and the experimental data is conducted. The error between the predicted force and the measured force is calculated as a function of time. The following expression is

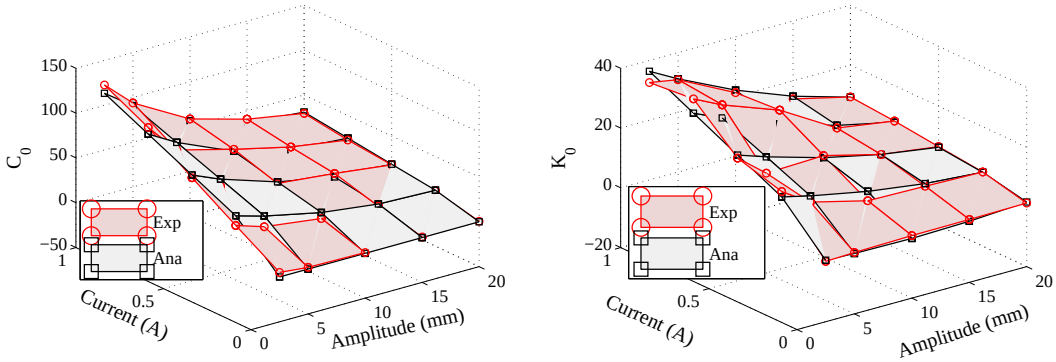

(a) Variability of parameter c_0

(b) Variability of parameter k_0

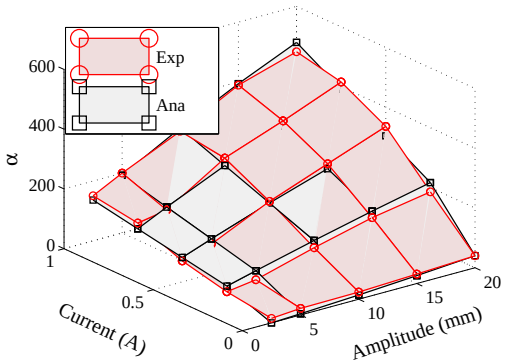

(c) Variability of parameter α

Figure 3.17: Comparison experimental and analytical model for parameters c_0, k_0 and α on input current and amplitude of excitation (Exp: experimental, Ana: analytical)

used to represent the error (Spencer et al. (1997) [329]; Yang (2001) [387]).

$$E_t = \sqrt{\frac{\int_0^T (Fe - f_c)}{\int_0^T (Fe - \mu_e)}} \tag{3.23}$$

Where, Fe is the experimentally obtained force, f_c is the model predicted force and μ_e is the mean value of the measured force. E_t is calculated for each data set. The maximum and minimum values of E_t obtained are 0.0479 and 0.0076 respectively. To compare the errors with other hysteretic models one has to carry out optimization of parameters involved in other models. This exercise is not carried out in the present study and hence the errors are

Table 3.2: Optimal Bouc-Wen Parameters

Parameter	Value	Parameter	Value	Parameter	Value
c_1	2.4346	c_2	-0.2804	c_3	0.0101
c_4	12.2252	c_5	-0.4560	c_6	0.0026
k_1	1.7194	k_2	-0.1244	k_3	0.0038
k_4	7.6337	k_5	-0.2127	k_6	0.0002
α_1	4.2188	α_2	10.0291	α_3	-0.0244
α_4	362.4943	α_5	1.0843	α_6	0.0229
γ	2.85	β	5.420	A	12.26

compared with the values provided in the literature (Spencer et al. (1997) [329]; Yang (2001) [387]). The minimum error norm calculated for the proposed model is smaller than those given in Spencer et al. (1997) [329] and Yang (2001) [387] for other models. The maximum error obtained with proposed model is however more than that given in the literature. The performance of the proposed model can improve if higher order terms in the polynomial are considered. This is kept outside the scope of the present study.

Figures 3.18 and 3.19 show the match between experimental and analytical model. Figure 3.18 shows the variable current plot at 10mm amplitude, whereas, Figure 3.19 shows the variable amplitude plot of the simulated and experimental results at $i_c = 1$ A. Both the results are simulated at a frequency (w) of 1Hz. A very good match between the experimental and the analytical results is observed.

The proposed model for the MR damper considers the magnitude of maximum displacement as a parameter to determine MR damper force. Therefore for applications like, seismic vibration mitigation, one has to consider the maximum stroke of the damper as the maximum displacement of the MR damper to determine the MR damper force. Considering RD-1005-3 MR damper (MR Damper (2006 [240]) (that is used for the present study) the damper parameters for the maximum stroke of the damper are tabulated in Table 3.3. These parameters are used in the subsequent chapters for simulation and experimental studies.

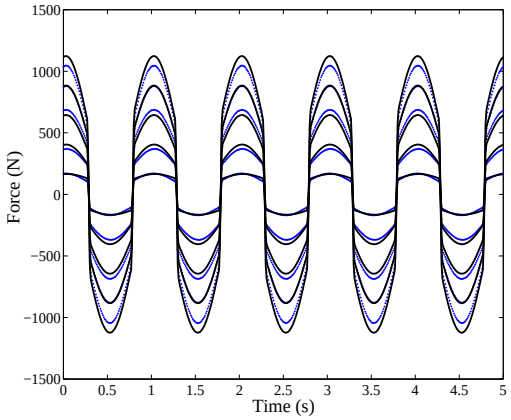

(a) Force Time History

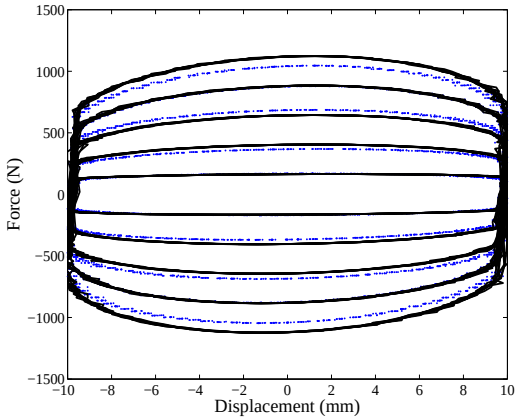

(b) Force-Displacement

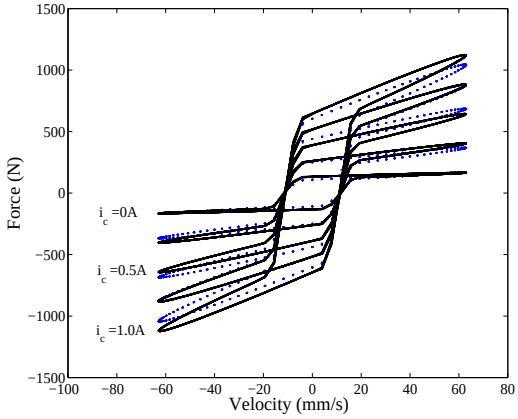

(c) Force-Velocity

Figure 3.18: Comparison of experimental (...) and analytical (–) model: Variable current ($x_a = 10$mm, $\omega = 1.0$Hz)

3.6 Summary

In this chapter, experimental details of a MR damper RD-1005-3 (manufactured by LORD Corporation) under sinusoidal excitations is reported. Experiments are carried out for force-displacement tests, amplitude dependent tests, frequency-dependent tests, constant peak velocity tests. The overall performance of the MR damper is found to be very promising.

A brief yet complete survey of MR damper parametric and non-parametric models is provided at the begining of the chapter. Simple Bouc-Wen hysteretic model is considered for

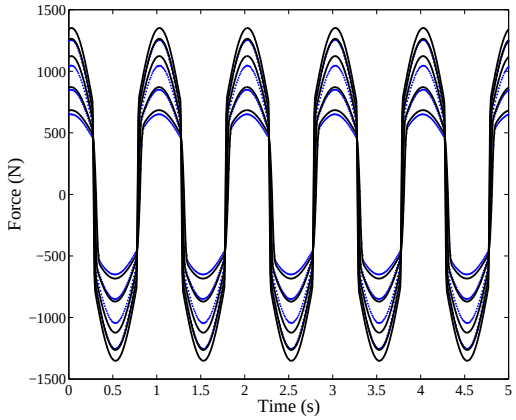

(a) Force Time History

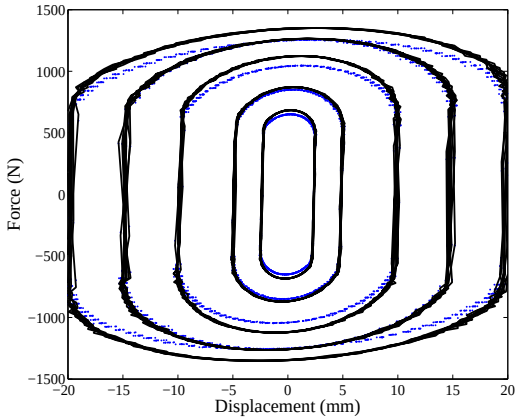

(b) Force-Displacement

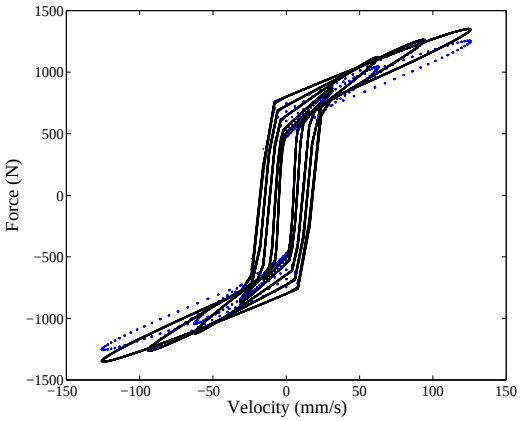

(c) Force-Velocity

Figure 3.19: Comparison of experimental (...) and analytical (–) model: Variable amplitude ($i_c = 1.0$A, $\omega = 1.0$Hz)

MR damper RD-1005-3, due to its simplicity and very few variables involved. It is observed from the optimization of the Bouc-Wen model to match the experimental results that some of the Bouc-Wen parameters (γ, β, A) remain unchanged with the change in amplitude and frequency of excitations and also with change in damper input current. Other parameters (c_0, k_0, α) are found to vary with the input current and excitation amplitude. Based on values obtained for the optimization variables of Bouc-Wen model to fit the experimental behaviour of the MR damper, a modified Bouc-Wen model is proposed, whose co-efficients are kept dependent on amplitude of input excitation and the commanded input current.

Table 3.3: MR Damper Parameter Values for Seismic Application

Parameter	**Value**	**Parameter**	**Value**
α_a	1.9504×10^5 N m^{-1}	α_b	1.57336×10^5 N m^{-1} V^{-1}
c_{0a}	8.666×10^2 N sec m^{-1}	c_{0b}	1.6580×10^3 N sec m^{-1} V^{-1}
k_{0a}	7.5140×10^2 N sec m^{-1}	k_{0b}	1.384×10^3 N sec m^{-1} V^{-1}
n	2	γ	2.85 m^{-1}
A	12.26	β	5.42 m^{-1}
η	190 s^{-1}	V_{max}	5 V

The model developed is based on sinusoidal tests, where the amplitude of excitation is known a priori. Therefore, the model does not consider the effects of random excitation on the MR damper. This forms a limitation of the present study. However, the proposed model is applied to seismic vibration mitigation of structures, using the maximum stroke (20mm) as the amplitude of excitation.

It is to be observed that the simple Bouc-Wen model shows a nonlinear force-command current relation. One can determine the force required to suppress the building vibration using feedback technique, but it is very hard to determine the amount of input current required by the damper to provide that particular force requirement. Therefore, there is a need for developing nonlinear control schemes which can directly monitor the current to be set to the damper based on the system feedback. The next chapter develops an optimal fuzzy logic controller to monitor the MR damper voltage directly based on the system responses. The proposed MR damper model is applied with control strategies developed and demonstrated to perform satisfactorily in subsequent chapters.

Chapter 4

Nonlinear Control: Optimal Fuzzy Logic Controller

4.1 Overview

The development of literature review in Chapter 2 has clearly pointed out the necessity of hybrid base isolation techniques in the present structural engineering scenario. It has also been observed that the magnetorheological (MR) damper is the most suitable semi-active device for structural protection and its deployment as a supplemental damping device is the current focus of the structural vibration control research. The deployment of MR damper for structural control applications involves two major steps, (a) to establish the nonlinear force-current/voltage relationship of the damper; (b) to develop a nonlinear control strategy that can monitor the supply current/voltage to the MR damper.

Chapter 3 dealt with the first step discussed above, where the nonlinear force-current relationship is developed using a set of experiments with a RD-1005-3 MR damper. It is observed in the preceding chapter (Chapter 3) that the input current to MR damper output force relation is a nonlinear map. This nonlinear map makes the prediction of input current to the MR damper for developing a particular force needed to control a structure, a difficult and a challenging task. Literature survey presented in Chapter 2 demonstrated that both model based and intelligent methods based control strategies are developed to monitor MR damper input current/voltage. It has been shown, that the model based control strategies (clipped optimal, skyhook control, Lypapunov based methods) provide a bang-bang or 'on-off' kind

of technique to monitor the MR damper current/voltage and therefore fail to make use of full damper input current/voltage range. In this respect the intelligent technique based approaches (neural network control, fuzzy logic based control, *etc.*), make full use of MR damper input current/voltage range, since they can map the nonlinear input-output relation of MR dampers easily. Neural networks based control strategy has been developed widely in comparison to fuzzy based approaches for MR damper current/voltage monitoring.

In this chapter an optimal fuzzy logic based MR damper current monitoring is proposed. The fuzzy logic controller (FLC) parameters are optimized using evolutionary algorithms (EAs) to suite the problem better. After giving comprehensive details of the FLC based control technique, formulation of an optimization scheme to optimize the FLC parameters with few variables is presented. Optimization of the proposed technique is carried out using evolutionary based algorithms. Thereafter, salient features of micro-genetic algorithms (μ-GA) and particle swarm optimization algorithms (PSO) are reported for use with FLC. Finally the efficacy of the proposed optimal FLC is shown taking examples from single degree of freedom (SDOF) and multi degree of freedom (MDOF) structures.

4.2 Fuzzy Logic Controller

Zadeh (1965) [413] introduced fuzzy set theory to treat imprecision and uncertainty that is often present in implementation of problems in real world. Mamdani (1974) [226], by applying Zadeh's theories of linguistic approach and fuzzy inference, successfully used the if-then rule on the automatic operating control of steam generator. Since then fuzzy control theory has been applied to a number of linear and nonlinear systems.

Fuzzy logic control is a simulation of logical reasoning of human brain; it maps an input space to a corresponding output space based on fuzzy rules specified in if-then format known as knowledge base. Fuzzy logic-based control includes a fuzzification interface, an inference engine and a defuzzification interface as shown in Fig. 4.1. Definitions of a few terms are provided here to facilitate the ensuing discussions.

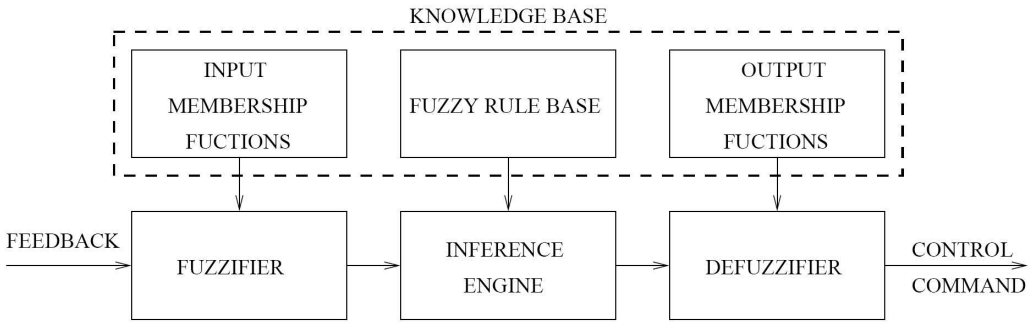

Figure 4.1: General structure for fuzzy logic controller design

Domain of discourse

The range over which input and output variable spaces are defined is known as the domain of discourse or universe of discourse (UOD). If the domain is not known properly, -1 to $+1$ are taken as the domain of discourse and pre-scaling and post-scaling are applied to the input and output variables. Examples given in the chapter take acceleration and pseudo-velocity as inputs and MR damper input current is given as the output. The inputs are scaled down to ± 1 using pre-scaling gains depending upon sensor range and sensitivity. Control current is scaled up based on MR damper current capacity.

Membership function

Unlike crisp set, fuzzy variable can take a value or a measure of the membership between 0 and 1. A measure of the degree to which a variable belongs to a particular set is determined using membership function (MF). There are various kinds of membership functions available and their shape depends upon the definition and the work they are to perform. The most frequently used membership functions are triangular, trapezoidal, generalized bell shaped and gaussian MFs.

A generalized bell shaped function can approximate other membership functions with appropriate choice of its parameters. Figure 4.2 shows the shape of a generalized bell shaped function describing parameters a, b, and c, which, as an example are taken as 0.2, 2.5, and 0 respectively. The membership grade μ_x for an input x in a generalized bell shaped MF is

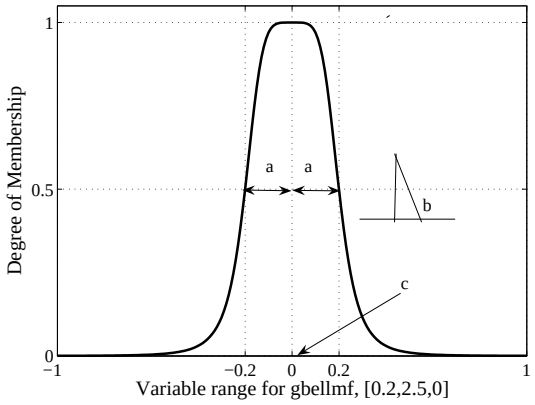

Figure 4.2: Generalized bell shaped membership function

given by (MATLAB® (2004) [230]).

$$\mu_x = \frac{1}{1 + \left(\frac{x-c}{a}\right)^{2b}} \tag{4.1}$$

The following steps provide a simple design for fuzzy logic controller.

Defining input/output variables

Decision on what responses of the system are subject to observation and measurement, leading to choice as input variables is the first step. Choice of control functions needed, results in the choice of output variables. In the simulation and experiments carried for the thesis work, relative velocity and absolute acceleration data are considered to be input variables and MR damper input current as an output variable. The choice of velocity and acceleration component for feedback can be explained in the context of the state of the system in the fundamental mode of vibration. These feedback components help in generating the initial inference rule base (*e.g.*, if velocity is zero and acceleration is high, the structure is at its extreme position and control action is not needed because it is going to return to its neutral position due to the restoring force). On the other hand, if the acceleration is zero and the velocity is high, then the structure is in its neutral position and control action should be applied so that it remains close to its neutral position in order to reduce the maximum displacement. At the intermediate states (*i.e.*, between the extreme and neutral position), if velocity and acceleration are of

the same signs, the structure is returning to its neutral position due to its restoring force, and, if the acceleration and velocity are of opposite signs, then the structure is moving towards its extreme position and accordingly the control action should be applied. Thus, both a velocity feedback and an acceleration feedback are necessary for an improved decision on control action.

Fuzzification of input variables

The fuzzification interface maps the measurable input variables in the form of a crisp set to a fuzzy linguistic values based on their membership grades in the domain of discourse (Casciati et al. (1996) [54]). Usually, within a domain of discourse the number of partitions for linguistic variables should be odd in number to keep the symmetry of the domain intact. This number will decide the status of a partition of the space. The more the linguistic variables, the more sophisticated is the partition of spaces but this increases the computational cost. In the present FLC control, 5 MFs are taken to cover the input domains, whereas 7 MFs are considered for the output. For the input variables the internal 3 MFs (out of 5) are considered generalized bell shaped and the two extreme MFs are kept unbounded in the respective positive (s-shaped) and negative (z-shaped) UOD (Jang et al. (2005) [162]). This is done to consider any variable values outside the UOD as of membership grade unity. All seven MFs for the output variable are considered to be generalized bell shaped. The initial input/output MFs considered for the optimization are shown in Fig. 4.3. The five input MFs are (NL=Negative Large, NS=Negative Small, ZE=Zero, PS=Positive Small, PL=Positive Large). The output space is mapped with two more MFs (NE=Negative and PO=Positive).

Inference engine

The inference engine has a dual role in fuzzy control theory. It maps the input fuzzified variables to the output variables based on user-defined rules known as knowledge base. It also provides a decision based on the results obtained from implementation of these rules. The most commonly used inference methods and the operators used for inference of these strategies are (Faravelli and Yao (1997) [110]),

- Mamdani's Strategy: This fuzzy inference method is based on fuzzy MAX-MIN operator.

- Larsen's Strategy: It is based on a fuzzy PRODUCT operator.
- Takagi and Sugeno's Strategy: Takagi and Sugeno's inference method characterizes the fuzzy outputs as the functions of fuzzy input set.

Mamdani's MAX-MIN operator is the most commonly used inference scheme (Casciati et al. (1996) [54]) for control applications and is adopted for the present study.

Usually, the rule base of the fuzzy controller is formed from operator's experience and expert knowledge (Casciati et al. (1995) [53]). The more the control rules, the more the efficiency of the control system. Control rules are usually in the form of if-then rules to link input to the output variables. Fuzzy 'if' is called antecedent and 'then' is called consequence.
For example rule R_i : if *relative velocity* is *positive large*; and *acceleration* is *positive large*; then the *control current* is *positive large*; $i = 1, \ldots, n$; where n represents the total number of control rules. The initial FLC rule base adopted in this study (which is modified based on evolutionary optimization) is shown in the Table 4.1. This rule base pattern is based on first mode of vibration of structures (Ahlawat and Ramaswamy (2003, 2004) [16, 17]).

Defuzzification interface

Defuzzification describes the mapping from the space of fuzzy outputs to a crisp set output. Defuzzification operation takes most of the processing time in a fuzzy control algorithm. A

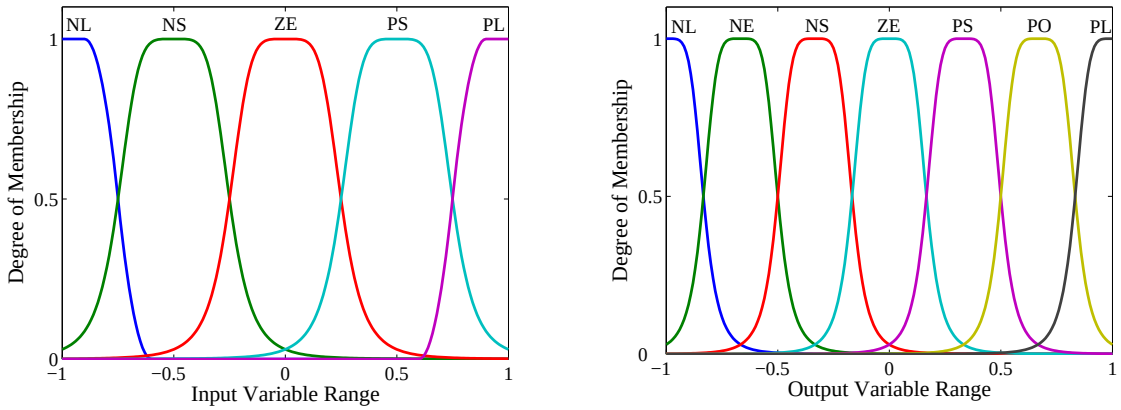

(a) Input membership functions

(b) Output membership functions

Figure 4.3: Initial input output membership functions

Table 4.1: Rule Base for FLC–FRB

	Acceleration				
Velocity	**NL**	**NS**	**ZE**	**PS**	**PL**
NL	NL	NE	NS	NS	ZE
NS	NE	NS	ZE	ZE	ZE
ZE	NS	ZE	ZE	ZE	PS
PS	ZE	ZE	ZE	PS	PO
PL	ZE	PS	PS	PO	PL

large number of defuzzification methods are available but only few are practically amenable for fuzzy control systems. They are center of area (COA); center of gravity (COG); center of largest area (COLA); height defuzzification (HD); mean of the maximum (MOM), *etc.*, (King (1999) [188]). In the present analysis COA defuzzification algorithm (MATLAB® [230]) is used.

Although fuzzy logic allows for the creation of simple control algorithms, the tuning of these fuzzy controllers is a more difficult and sophisticated procedure than that of conventional ones. This is due to the large number of parameters used to define membership functions and inference mechanisms (Zheng (1992) [420]; Li and Gatland (1996) [209]) as well as to decide the input/output scaling gains. Several methods have been developed for tuning fuzzy controllers. These involve adjusting membership functions (Arslan and Kaya (2001) [32]) and/or scaling factors (Woo et. al. (2000) [378]; Zhao and Collins (2003a,b) [418, 419]), dynamically changing the defuzzification procedure (Braae and Rutherford (1979) [43], Zheng (1992) [420]). Because scaling factors are responsible for mapping the inputs and outputs to the universes of discourse, they have a large effect on the controller's performances. Adjustment of these parameters is therefore the most commonly used method for tuning fuzzy controllers (Li and Gatland (1996) [209]). Methodologies proposed for tuning scaling factors are numerous and include, among others, hit-and-trial approaches (Driankov et al. (2001) [93]; Battaini et al. (1998) [40], Li and Gatland (1996) [209]), neuro-like approaches (Faravelli and Yao (1996) [109]; Chao and Teng (1997) [63]), genetic algorithms (Arslan and Kaya (2001) [32]; Zhao

and Collins (2003b) [419]), gain scheduling (Wilson (2005)[375]) and self–tuning (Guzelkaya et al. (2003) [134]; Zhao and Collins (2003a,b) [418, 419]).

4.3 Optimization of the FLC

As discussed in the preceding section that selection of fuzzy parameters, especially the rule base structure has been based on trial and error approach. A number of optimization schemes have been studied and reported in the literature (Driankov et al. (1992) [93]) to select optimal rule base structure, like, the Michigan technique, the iterative rule techniques, the Pittsburgh approach, *etc*. In this study, a geometric interpretation to the rule-base structure is given and based on that a relatively simple optimization scheme is adopted, which requires very few optimization variables. Optimization of the FLC is attempted with a priori information in relation to the number of rules and the number of MFs that give meaning to those rules. Fuzzy input scaling gains, membership function parameters (a and b) and the fuzzy rule base are optimized. The method proposed in this study considers only ten variables to obtain an optimal FLC structure. The optimization variables and their encoding are discussed next.

Encoding input/output scaling gains

The scaling gains of the relative velocity and acceleration inputs to the fuzzy system are encoded to determine optimal gains over the time of analysis.

4.3.1 Adaptive Membership Function Design

The present FLC has two inputs (premises), relative velocity and acceleration at the point of the action of the damper and one output (consequent), MR damper current, $i_c(t) \in [0,\ 1]$. The input variables are normalized over the UOD of $[-1,\ 1]$. It is to be noted that the output contains negative values, this is done to keep symmetry about the zero in UOD. Therefore to get output current as positive values between $[0,\ 1]$, the MATLAB® *abs* function is used.

Encoding membership function

To reduce the computational cost associated with the optimization scheme, two variables are selected for optimization, namely, the MF central width (a) and the MF slope at 0.5 membership grade (b). A maximum of 10% shift of its position as shown in Fig. 4.3 of the respective MFs is encoded. The MF width is changed with a constraint that the overall span of the MFs should range the UOD and each MF should maintain a 50% overlap with the neighbouring MFs. Membership function slope at 0.5 membership grade is changed by multiplying the slope at 0.5 membership grade of uniformly distributed MFs to a value between 0.5 to 2, *i.e.*, a change of 50% to 200% of its form at uniform distribution is encoded.

4.3.2 Adaptive Rule Base design

A geometric approach is adopted to optimize the rule base, such that it takes fewer variables for rule base optimization. In this approach we keep the symmetry in the rule base as shown in Table 4.1 about the premise $[0;\ 0]$ intact. Following assumptions are made while designing the rule base which are consistent with structural control design.

- To design an optimal rule base for the structural system we take advantage of the fact that control force input to the structure should increase when the structural responses increase, *i.e.*, the extreme input value (premise) results in an extreme output values (consequent), mid-range input values result in mid-range output values and small/zero input values result in small/zero output values (Ahlawat and Ramaswamy (2001, 2002) [15, 17]). This rule base pattern is true for both the negative and positive portion of UOD.

- Larger control force is provided by the MR damper with large input current. Therefore input current to the MR damper is consistent with the structural responses.

However, a situation may arise where the displacement of the structure keeps increasing at small rate or constant displacement which results in negligible/zero velocity and acceleration. In such a situation the FLC will provide a zero current output as intended and the structural displacements will be taken care by the force provided by the MR damper acting at zero ampere current.

To describe the optimization approach we define a 'premise coordinate system' which is as shown in Fig. 4.4, a coordinate system formed by the MFs of the two inputs, relative velocity

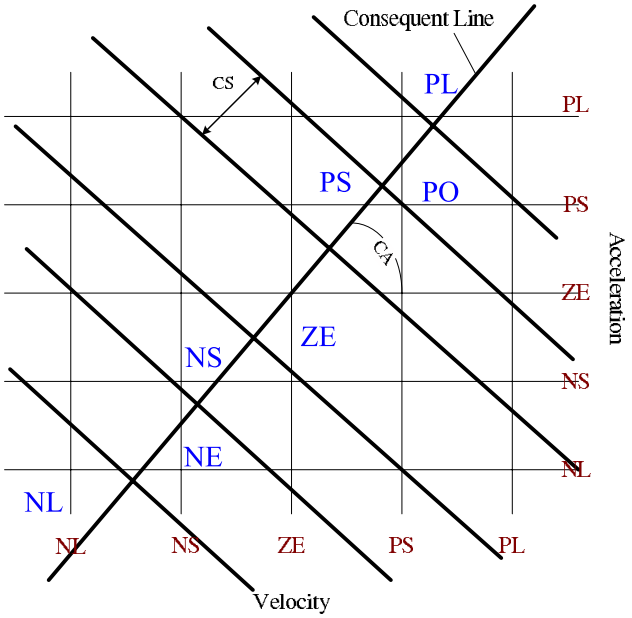

Figure 4.4: Optimal rule base design strategy

and acceleration. The consequent MFs are to be placed at the nodal locations formed by the connection of two MFs of each input variables.

Encoding rule base

In this geometric approach the consequent space is overlayed upon the 'premise coordinate system' and is in effect partitioned into seven small non-overlapping regions, where each region represents a consequent fuzzy set (see Fig. 4.4). To design an optimal rule base we define a consequent line as shown in Fig. 4.4. The line is made pivotal on premise zero-zero position (*i.e.*, both inputs being zero) and it is free to rotate over the consequent space and therefore the rule base adapts according to the optimization scheme. It is to be noted that the rule base remains symmetrical what ever be the position of the consequent line.

The rule base is extracted by determining the consequent region in which each premise combination point lies. The geometric approach is made possible using only two parameters (CA and CS).

- Slope of the consequent line angle (CA): It has been used to create different output space partitions. The angle has been encoded to cover angles between $0 - 180°$. As the consequent space is symmetric and the output $u(t)$ ranges between $[0,\ 1]$, $0-180°$ is equivalent

Table 4.2: Optimal rule base design (CA=$\pi/4$, CS=1)

	Acceleration				
Velocity	**NL**	**NS**	**ZE**	**PS**	**PL**
NL	NL	NL	NE	NS	ZE
NS	NL	NE	NS	ZE	PS
ZE	NE	NS	ZE	PS	PO
PS	NS	ZE	PS	PO	PL
PL	ZE	PS	PO	PL	PL

to $0 - 360°$.

- Consequent-region spacing (CS): As seen from Fig. 4.4 a proportion of the fixed-distance between the premises (NL, NS, ZE, PS, PL) on the coordinate system and is used to define the distance between consequent points along the consequent line.

Thus only two variables are needed to be encoded for optimization of the rule base. Making consequent line angle to be $45°$ and consequent region spacing to be 1, we get a rule base as shown in Table 4.2 analogous to the rule base that can be derived from the first mode vibration of the structure.

4.4 Formulation of the Optimization Problem

In the simulation studies a multi-objective optimal design approach, for the FLC driven semi-active control system is employed. The multi-objective cost function is deviced based on the weighted sum of several objective functions. These objective functions are formulated to increase the performance of the system over successive generations of optimization. The performance indices considered for the study in this chapter are discussed next.

4.4.1 Performance Indices

Performance of the control system is to be evaluated from the ratio of norms of the controlled responses of the structure to that of the uncontrolled responses. A set of performance indices

(see Eq. 4.2) are defined to determine the efficiency of the control techniques used for study.

$$J_1 = \frac{\max_t |x_c(t)|}{\max_t |x_{unc}(t)|} \quad J_2 = \frac{\max_t |\dot{x}_c(t)|}{\max_t |\dot{x}_{unc}(t)|} \quad J_3 = \frac{\max_t |\ddot{x}_c(t)|}{\max_t |\ddot{x}_{unc}(t)|}$$
$$J_4 = \frac{\|x_c(t)\|}{\|x_{unc}(t)\|} \qquad J_5 = \frac{\|\dot{x}_c(t)\|}{\|\dot{x}_{unc}(t)\|} \qquad J_6 = \frac{\|\ddot{x}_c(t)\|}{\|\ddot{x}_{unc}(t)\|} \tag{4.2}$$

where the subscript "c" denotes controlled responses and the subscript "unc" represents uncontrolled motion. "$\max_t$" represents maximum over time (t). The displacement response of the structure is represented by x and a single over-dot ($\dot{\cdot}$) denotes a single derivative with respective to time. The first three performance indices (*i.e.*, $J_{1,2,3}$) are based on the absolute value of the responses *i.e.*, $|x|$ denotes absolute value of x. These indices show how much the peak responses of the structure is reduced using the controller. The peak responses are responsible for yielding of the structure. The next three performance indices (*i.e.*, $J_{4,5,6}$) measure the performance of the controller over time and are based on L_2 norm of the responses ($\|.\|$ is L_2 norm operator). These performance indices are to be evaluated for each floor of the structure.

4.4.2 Multi-objective Optimization Cost Function

The fitness function is the main criterion that is used to evaluate each chromosome. It provides an important connection between the EA and the physical system that is being modeled. A controller should reduce structural displacements without increasing accelerations. Large displacement is catastrophic to the structure where as acceleration is concerned with the occupant comfort and contents inside. On the other hand MR damper depends on the structural velocity and therefore minimization of structural velocity is also taken into consideration in fitness function.

There are several methods that can combine multiple objective functions to make a single fitness function in a multi-objective optimization problem. One of these methods, a weighted sum approach, is employed in this study as shown in Eq. 4.3. The L_2 norm of displacement, velocity and acceleration are normalized with respect to their corresponding uncontrolled L_2 norm values (represented with subscript unc). Therefore the objective function for the design

of FLC using EA is taken as

$$\Phi = \sum_{floors} W_1 J_4 + W_2 J_5 + W_3 J_6 \tag{4.3}$$

where $W_{1,2,3}$ are the weights associated with the respective single objective cost functions. Their corresponding values will be discussed in the numerical simulation section.

4.5 Optimization Procedure

The design of an optimal FLC can be viewed as a search in a multi-dimensional space, or hypersurface, where combinations of different component properties of the fuzzy system (rule base, input–output membership functions, their properties and scaling gains) correspond to a point in that space. Fuzzy search surfaces are large, since the choice in the number and properties of fuzzy sets for each variable is unlimited, non-differentiable as changes in fuzzy set numbers and rules are discrete and therefore create points of discontinuity on the surface and multi-modal, since different rule bases and MFs may have comparable performance (Ali and Mo (2001) [28]). One way to design a fuzzy controller is on hit-and-trial basis or from previous experiences (Casciati et al. (1995) [53]). On the other hand optimization techniques can be used to choose optimal FLC parameters.

The optimization of the proposed strategy is made possible using evolutionary algorithms. A micro genetic algorithm with elitist strategy (μ GA) and a particle swarm optimization techniques (PSO) (flow diagram of μ-GA and PSO are shown in Figs. 4.5 and 4.6, respectively) are used to design the optimal FLC. The advantages of these optimization techniques relate to the use of a wide range of fitness functions. The fitness function can include variables that are not the state variables of the controlled system. In contrast, modern control theory that is based on the state space system can incorporate only state variables into the performance index. Details of μ GA and PSO are given next.

4.5.1 Micro-Genetic Algorithm

Micro-GA (μ-GA) has been proposed by Krishnakumar (1989) [192] to improve the performance of the GA at lower population sizes. The micro-GA operates on a family, or population, of designs similar to the simple genetic algorithm (SGA) but with lower population size. The basic idea is to use a smaller population GA and allow it to converge rapidly and invoke random population and start the search again (*i.e.*, restart the GA) keeping the elitist chromosome unchanged. Micro-GA performs better in multi-modal optimization problems and is therefore suitable for the FLC optimization. To restart the GA search the current population is aggressively mutated. In addition, Krishnakumar (1989) [192] reported that μ-GAs reach the optimum in fewer function evaluations compared to an SGA. This makes the application of micro GA suitable for large scale problems and parallel processing (Pulido and Coello (2003) [280]). The flow chart of μ-GA is shown in Fig. 4.5.

In this study, the micro genetic algorithm with following specifications is used.

1. Initial population search space is sub-divided into two complimentary subspaces. Half of the initial population is selected randomly and other half is obtained by taking compliment of the initial half. In this manner any localization of initial population is reduced. It is reported in Krishnakumar (1989) [192] that even as few as a 5 member population can provide a global convergence. Here, we use an initial population size of 7 members. Restart is initiated at every twentieth generation

2. Gray encoding and decoding is used (Houpt and Houpt (2004) [138]).
   Ordinary binary value representation in GA may sometimes be trapped in inefficient crossover (Houpt and Houpt (2004) [138]), *i.e.* offsprings result in lesser fitness value than parents. Gray code avoids this problem by redefining the binary numbers such that the consecutive numbers have a Hamming distance of 1. Gray code is obtained by passing every consecutive binary numbers through a *XOR* operation

3. A weighted multi-objective fitness function is adopted for the optimization of the FLC. The fitness function consist of individual fitness functions which are framed to minimize each of the states in L_2 norm sense and is described in Eq. 4.3

4. Proportional fitness with stochastic universal sampling (SUS) is used (Baker (1987) [36];

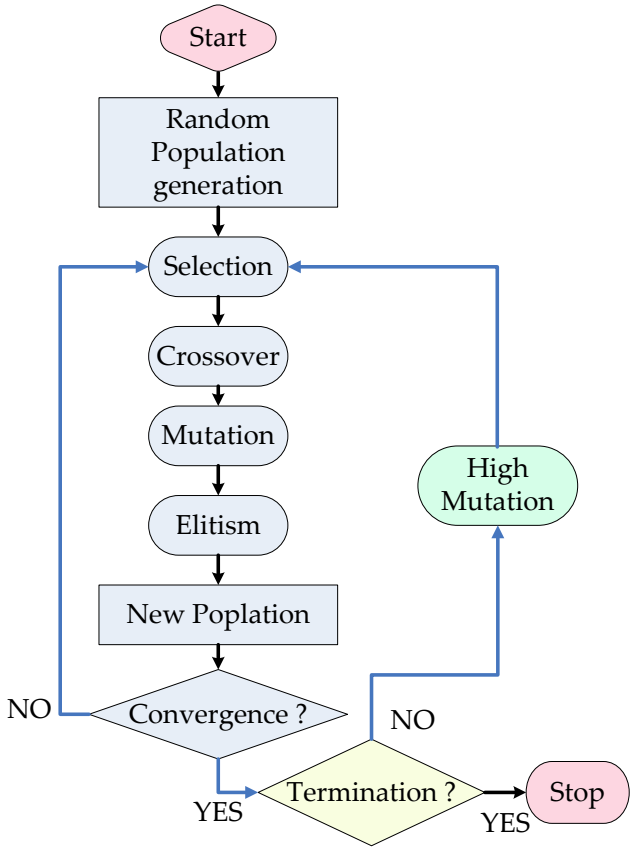

Figure 4.5: Flow diagram of micro genetic algorithm

Chipperfield et al. (2006) [65]; Houpt and Houpt (2004) [138]).

SUS is markedly different from Roulette Wheel selection technique. It is best described as a multi-pointer Roulette Wheel selection technique. In this method n (number of individuals in intermediate group) points are selected in the fitness line with the first one chosen randomly and others made equidistant from the previous one. Fitness values (a fitness function is a numeric value returned by the cost function) of individuals within this points are selected. Individuals having higher fitness are given higher share of fitness line (as in Roulette Wheel) and are therefore have greater chance of selection. Since, SUS selects individuals in a single turn it is faster and efficient than Roulette Wheel selection

5. Two point cross-over with probability of 0.4 is considered

6. Mutation probability of 0.01 is taken for all iterations, and at the restart generation 0.5 probability of mutation is considered

7. The best member in each population in each generation is always carried to the next generation as done in elitist approach

4.5.2 Particle Swarm Optimization

Particle swarm optimization (PSO) is a population based stochastic optimization technique developed by Kennedy and Eberhart (1995) [184], inspired by social behavior of bird flocking or fish schooling. It uses a number of particles that constitute a swarm. Each particle traverses the search space looking for the global minimum (or maximum). In a PSO system, particles fly around in a multidimensional search space. During flight, each particle adjusts its position according to its own experience, and the experience of neighbouring particles, making use of the best position encountered by itself and its neighbours. The swarm direction of a particle is defined by the set of particles neighbouring the particle and its past experience. PSO shares many similarities with other evolutionary computation techniques such as GA. The system is initialized with a population of random solutions and searches for optima by updating generations. The flow chart of PSO is shown in Fig. 4.6. As shown in Fig. 4.6, unlike GA, PSO has no evolution operators such as crossover and mutation. Compared to GA, the advantages of PSO are that PSO is easy to implement and there are few parameters to adjust. PSO is successfully applied in many areas, such as function optimization, artificial neural network training, fuzzy system control, and other areas where GA can be applied. The working strategy of PSO is given next.

Let x_p and v_p denote particle coordinates (position) and its corresponding flight speed (velocity) in a search space, respectively. The best previous position of a particle is recorded and represented as pBest . The index of the best particle among all the particles in the group is represented as gBest. To ensure convergence of PSO, use of a constriction function may be necessary (Eberhart and Shi (2000) [102]). At last, the modified velocity and position of each particle can be calculated as shown in the following equations.

$$\begin{aligned} v_{p_{g+1}} &= C\left[w \times v_{p_g} + \phi_1 c_1 \times \left(pBest - x_{p_g}\right) + \phi_2 c_2 \times \left(gBest - x_{p_g}\right)\right] \\ x_{p_{g+1}} &= x_{p_g} + v_{p_{g+1}} \end{aligned} \tag{4.4}$$

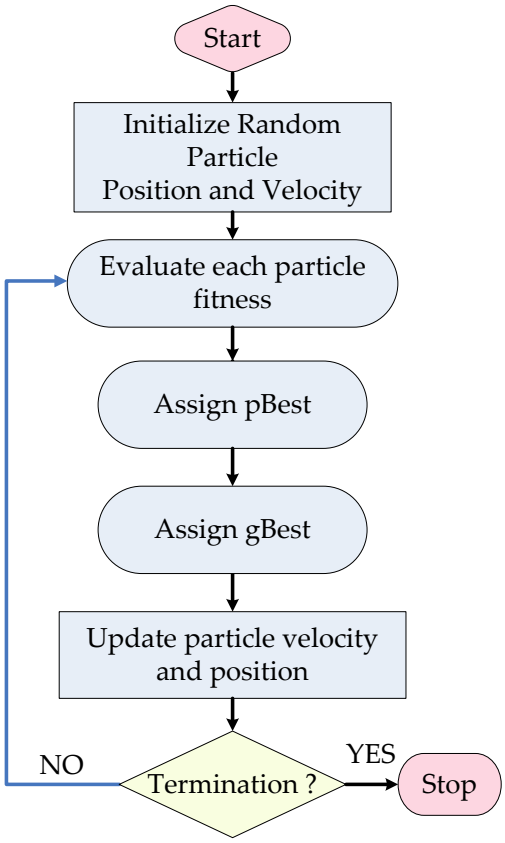

Figure 4.6: Flow diagram of Particle swarm optimization

Where g is the generation number, x_{p_g} is current position of particle at generation g and v_{p_g} is the corresponding velocity of particle. $w = 1$ is inertia weight factor, $\phi_1 = 2.05$ and $\phi_2 = 2.05$ are acceleration constant, c_1 and c_2 are uniform random value in the range $[0,\ 1]$, C is constriction factor which is a function of ϕ_1 and ϕ_2 as given in Eq. 4.5.

$$\begin{aligned} C &= \frac{2}{\left|2-\phi-\sqrt{\phi^2-4\phi}\right|} \\ \phi &= \phi_1 + \phi_2; \quad \phi > 4 \end{aligned} \tag{4.5}$$

A constant inertia weight of $w = 1$ is considered for all generations. PSO is run to optimize the same cost functions and for same number of generations as μ GA. Each school consists of 20 members.

4.6 Simulation of Building with Optimal FLC

Simulations are carried out for two different cases. In all cases a single MR damper is considered. The MR damper parameters considered for simulations studies are given in Table 3.3 of Chapter 3. First a SDOF system is taken and its vibration is reduced using FLC driven MR damper system. Then a three storey building is considered for the analysis under seismic ground acceleration. For each case under consideration four different strategies are employed for comparison, namely (i) FRB-PSO: fixed rule base FLC optimized using PSO, (ii) FRB-μGA: fixed rule base FLC optimized using micro-GA, (iii) ORB-PSO: optimal rule base FLC optimized using PSO, (ii) ORB-μGA: optimal rule base FLC optimized using micro-GA.

The different form of FLCs considered in the study that are optimized using EA are

- FLC-FRB: GA optimizes the scaling gains, MFs shape and parameters keeping the rule base fixed. The rule base is kept not optimized and is considered as shown in Table 4.1
- FLC-ORB: GA optimizes the scaling gains, MFs shape and parameters, as well as the rule base

Coding with micro GA

The input scaling gains for relative velocity and acceleration are coded with 5 binary bits each. The MF width is coded with 3 bits, which gives a precision of 0.0286 for a $\pm 10\%$ change in MF width. MF Slope at 0.5 membership grade is coded with 4 bits in the binary string for μ GA optimization. This gives a precision of 0.1 in the real value for the multiplication factor of MF slope, *i.e.*, any value among $[0.5, 0.6, ..., 2]$ can be used by the μ GA.

The micro GA optimizes 8 variables (scaling gains for each of the inputs, MF width and MF slope for each of the inputs and one output) for FLC-FRB. This makes the binary to be coded with a chromosome of length 31 [$2 \times 5(for\ scaling\ gains) + 3 \times 3(for\ MF\ width) + 3 \times 4(for\ MF\ slope)$]. The optimization of FLC-ORB is carried out using a total of 40 bits in a single chromosome (as it contains the 5 bits representing the CA and 4 bits representing CS).

Figures 4.7(a) and 4.7(b) show the convergence of μ GA and PSO for both FRB and ORB FLCs. The fitness value and the computational time required are tabulated in Table 4.3. It is to be observed that both the optimization schemes converge to the nearly same fitness value but PSO converges faster in terms of number of generations (see Figs. 4.7(a) and 4.7(b)).

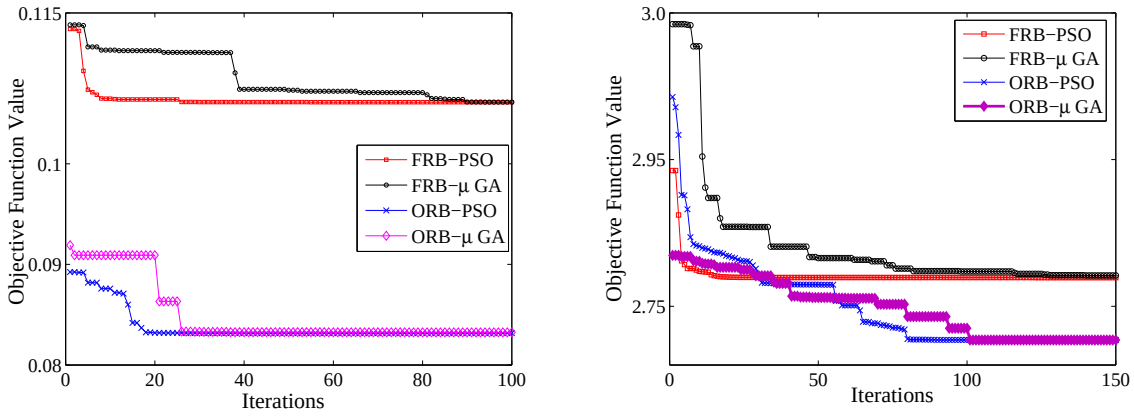

(a) SDOF case

(b) MDOF case

Figure 4.7: Convergence of FLC optimization: (a) SDOF Case; (b) MDOF Case

The computational time required by the PSO is much more than μ GA, as PSO evaluates fitness function 20×150 number of times, whereas μ GA evaluates it for only 7×150. Therefore where computational time is a constraint or each function evaluation takes large amount of time (as in case of large structures) μ GA should be preferred otherwise one has to use PSO with less number of generations (where a risk remains that PSO may converge to a non-global optima). Another interesting observation is that the ORB-FLC has lesser fitness function value than corresponding FRB-FLC although both used the same fitness function. This represents a better control of the structure using optimal rule base strategy.

4.6.1 Simulation Results of a SDOF System

A SDOF model is considered for the *impulse response analysis* of the proposed fuzzy logic systems. The equation of motion of the SDOF system is given as

$$\begin{aligned} m\ddot{x} + c\dot{x} + kx &= f_c(t) \\ x(0) = 0; \dot{x} &= \tfrac{1}{m} \end{aligned} \tag{4.6}$$

where $m = 56.52\ kg$, $c = 11.30\ Ns/m$, $k = 2.375 \times 10^3\ N/m$ are system mass, damping and stiffness parameters, respectively. The is represented by $f_c(t)$. $(\cdot)$ represents derivative with respect to time (t). The system is driven by giving an initial velocity of $\dot{x}(0) = 1/m$ to simulate the system response to an impulsive force. The objective is to bring the system responses to

zero. The FLC is trained using μ GA and PSO to minimize L_2 norm of displacement, velocity and acceleration responses of the system as given in Eq. 4.3. Equal weights ($w_i = 1,\ i = 1, 2, 3$) are taken for all the objective functions. The simulation is run for 5s as the controlled responses achieve the goal well before 5s.

Performance measure

Figure 4.8 shows the time history of the uncontrolled system responses for 5 seconds. The system responses continues even after $5s$ of vibration as the damping is very low. The controlled responses are shown in Fig. 4.9. The controlled system responses for SFLC and FRB-FLC are shown for $1s$ and for ORB-FLC, the responses are shown for $0.2s$ for clarity in the figure. The controlled responses are seen to die down well before the limits shown in the Fig. 4.9. Figure 4.9 contains results obtained from FLC manually configured (SFLC), FLC with optimal MF and scaling gains (FRB) and FLC with optimal MF, scaling gains and rule base (ORB). The results obtained through μ GA optimization (dashed line) and PSO (solid line) are shown together for better comparison. It is evident from the Fig. 4.9 FLC-FRB performs better than SFLC but FLC-ORB performs far better than FLC-FRB and SFLC. It is to be noted that the

Table 4.3: Computational Time Required

Case	No. of Function Evaluation	Computational Time (s)	Optimal Value
	SDOF Optimization		
FRB-μ GA	7×100	9.9893×10^3	0.10613
ORB-μ GA	7×150	28.527×10^3	0.08320
FRB-PSO	20×100	28.800×10^3	0.10612
ORB-PSO	20×150	113.99×10^3	0.08328
	MDOF Optimization		
FRB-μ GA	7×150	56.508×10^3	2.55261
ORB-μ GA	7×150	66.362×10^3	2.44510
FRB-PSO	20×150	163.059×10^3	2.54908
ORB-PSO	20×150	209.197×10^3	2.44246

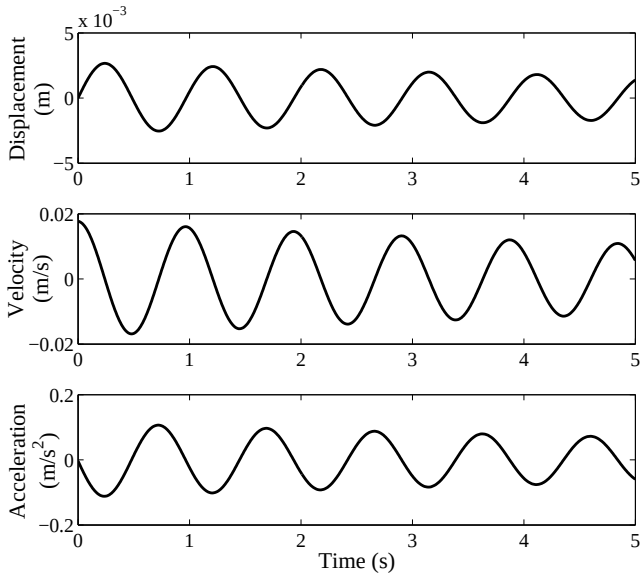

Figure 4.8: Uncontrolled responses of SDOF system

damping provided by MR damper in FLC-ORB case seems to be mostly like over damping.

4.6.2 Simulation Results of a MDOF System

A three storey shear building model is considered for the numerical simulation. The MR damper is assumed to be connected between the ground and the first floor of the structure. This is done with an idea of dissipating the seismic energy input to the structure. The equations of motion of shear building model for $'n'$ DOF are given in Eq. 2.1 in Chapter 2. Same equations are considered here for a 3 DOF system and are given in Eq. 4.7. Figure 4.10 shows the shear building model for the three storey building with the MR damper attached between the ground and the first floor.

$$M\ddot{X} + C\dot{X} + KX + B_c f_c(t) = -MR\ddot{x}_g \tag{4.7}$$

Where $X = \{x_1, x_2, x_3\}^T$ is the vector of floor displacements relative to the ground, subscript denotes storey number. $\ddot{x}_g$ is the seismic ground acceleration. M, and K are mass and stiffness matrices respectively (given in Eq. 4.8). The parametric values represent a laboratory scaled building model designed for the experimental validation of the optimal FLC proposed in the

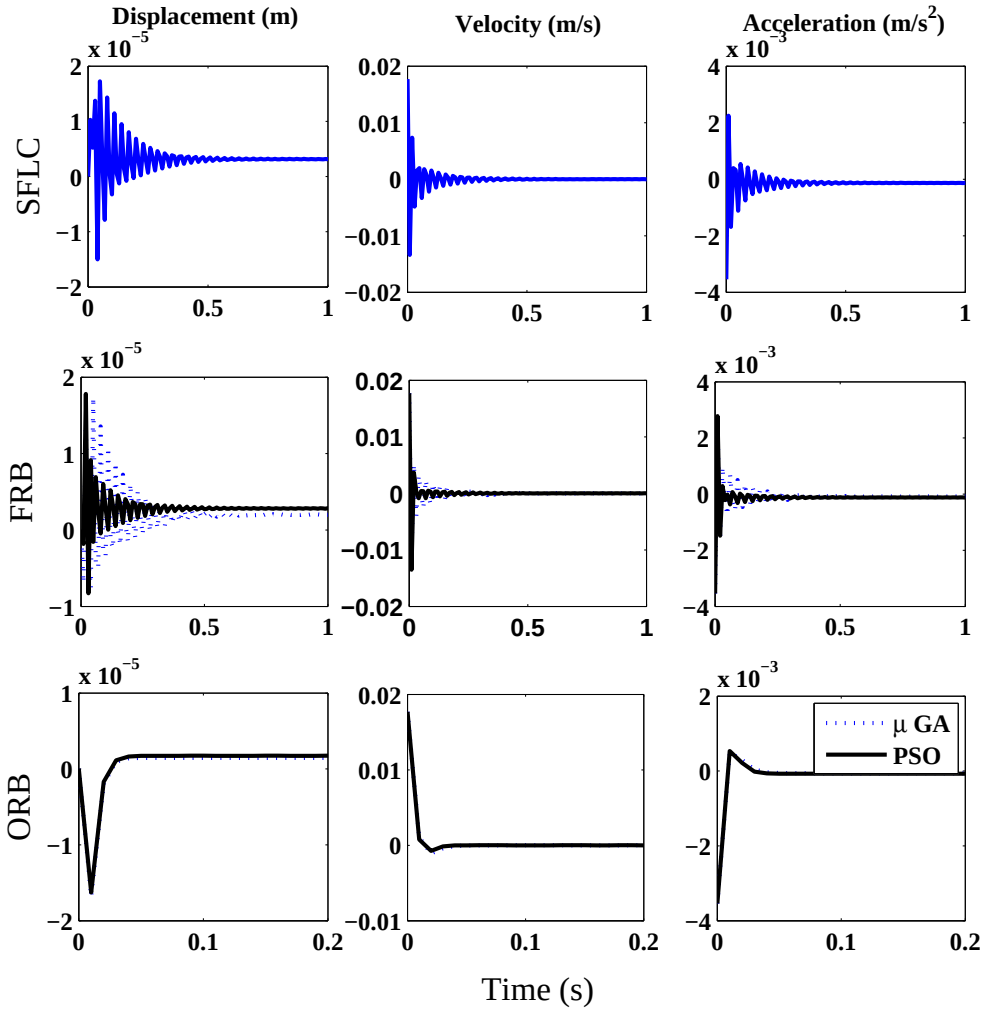

Figure 4.9: Controlled SDOF system (displacement, velocity, acceleration)

present chapter (details given in Chapter 5).

$$M = \begin{bmatrix} 56.52 & 0 & 0 \\ 0 & 56.52 & 0 \\ 0 & 0 & 56.52 \end{bmatrix} kg; \quad K = \begin{bmatrix} 4.75 & -2.375 & 0 \\ -2.375 & 4.75 & -2.375 \\ 0 & -2.375 & 2.375 \end{bmatrix} \times 10^5 \frac{N}{m} \tag{4.8}$$

C is the Rayleigh damping matrix and is constructed using 0.5% modal damping at all modes. The Rayleigh parameter ($\alpha_d,\ \beta_d$) are determined based on the first and third eigen frequencies

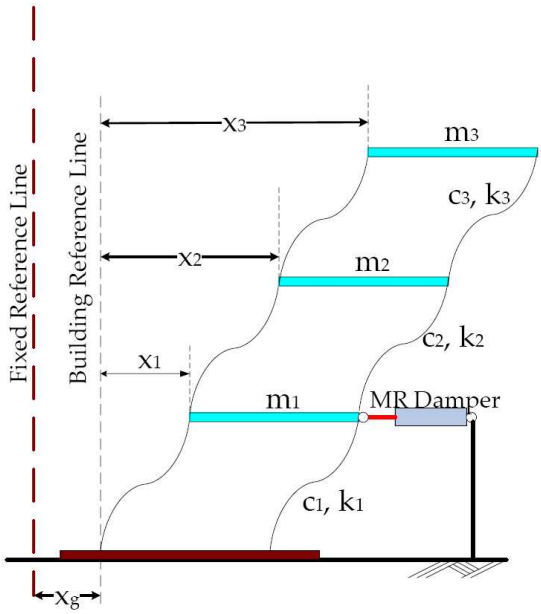

Figure 4.10: Schematic of fixed base building with MR damper at first floor

($\omega_1,\ \omega_3$) of the system [67]. Equation 4.9 shows the construction of the damping matrix.

$$\begin{aligned} C &= \alpha_d M + \beta_d K \\ \alpha_d &= 2\frac{\zeta\omega_1\omega_3}{\omega_1+\omega_3}; \qquad \beta_d = 2\frac{\zeta}{\omega_1+\omega_3} \end{aligned} \tag{4.9}$$

$B_c = [1,\ 0,\ 0]^T$ is the co–efficient vector determining the position of the damper (in this case damper is located at the first floor of the building). $R = [1,\ 1,\ 1]^T$ is the seismic influence vector.

The FLC is optimized for an initial displacement of 0.1m at the base and then the motion is allowed to decay under free vibration condition. The idea is to optimize the FLC to minimize the structural motion quickly when excited by a sudden base displacement which has the character of near source seismic motions. Optimization is performed using both μ GA and PSO and the objective function used is similar to that of the SDOF case, the only difference is that the normalized response L_2 norms are summed over all the floors (as shown in Eq. 4.3).

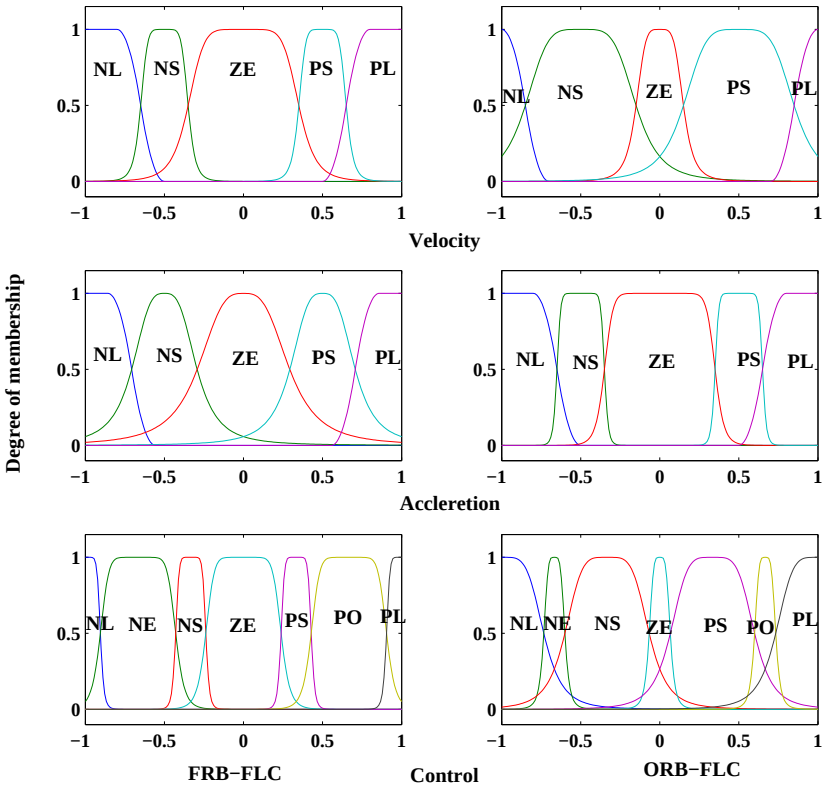

Figure 4.11: μ GA Optimized Input/Output MFs (MDOF system)

Performance measure

The convergence curves of the optimization schemes are shown in Fig. 4.7. It is evident from Fig. 4.7 that optimal rule base FLC performs better than fixed rule base FLC. Micro GA and PSO provide same optimal cost (see also Table 4.3). Figure 4.11 shows all the input-output MFs for both FLC-FRB and FLC-ORB cases obtained using μ GA. It is to be noted that the MFs have 50% overlap with each other and they range the domain of UOD *i.e.,* $[-1,\ 1]$, which are taken as constraints while generating MFs genetically. The μ GA optimized and PSO optimized input-output relation surface plots for FLC-ORB are shown in Figs. 4.12(a) and 4.12(b) respectively. Both the optimization schemes provide similar nature of rule surface. MDOF structural displacement and acceleration responses for first and third floor of the building in uncontrolled case are shown in Fig. 4.13. Figures 4.14 and 4.15 show the corresponding controlled structure responses. For clarity in figure the responses are shown for a duration of $1s$.

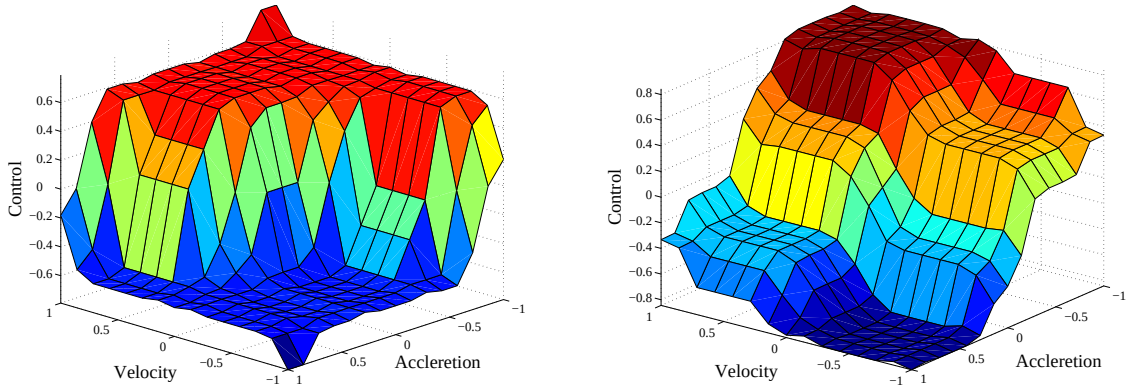

(a) Micro genetic algorithm (b) Particle swarm optimization

Figure 4.12: Optimized fuzzy rule base (MDOF system): (a) μ-GA; (b) PSO

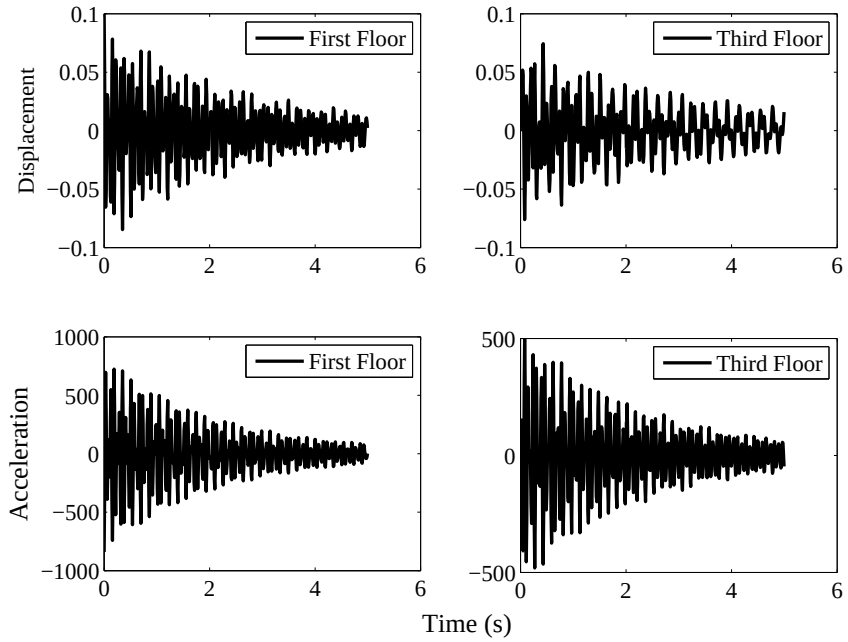

Figure 4.13: Displacement and acceleration time histories for 1^{st} and 3^{rd} floor (Impulse response)

Figures 4.14 and 4.15 contain responses obtained using PSO and μ GA optimization for both FLC-FRB and FLC-ORB. The responses are normalized with respect to their corresponding uncontrolled cases. It is to be noted that the results obtained through PSO and μ GA match

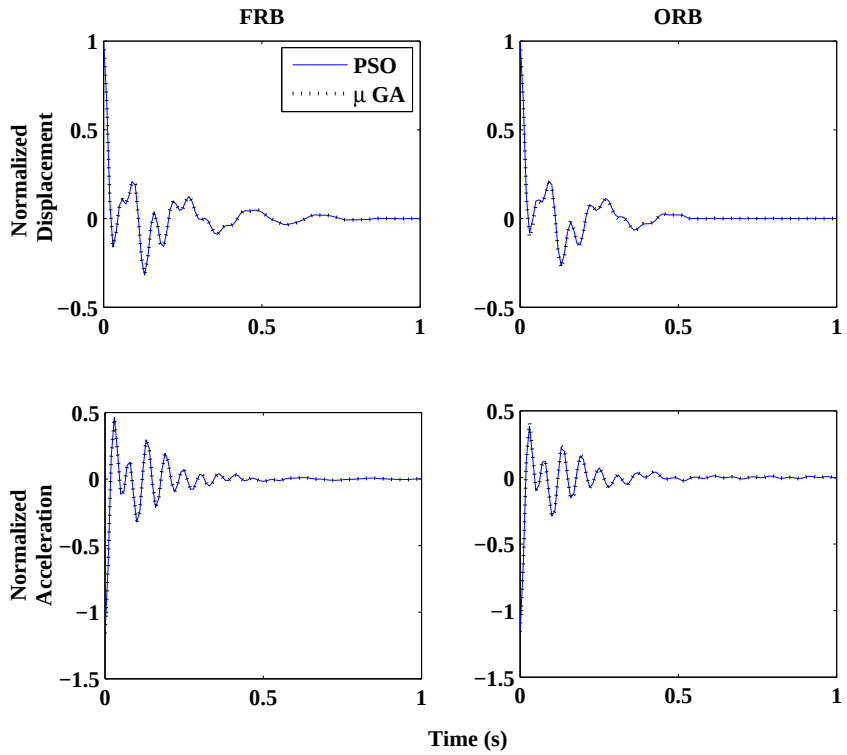

Figure 4.14: Displacement and acceleration time history for 1^{st} floor (Impulse response)

each other closely.

4.6.3 Seismic Vibration Mitigation

A set of seismic records consisting of Chichi, El-Centro-1940 and Northridge earthquake data are considered for the performance analysis of the three storey building using optimal FLC. As shown in the preceding example that the results of FLC-FRB and FLC-ORB optimized using μ GA match with the corresponding results obtained using PSO, therefore the optimal FLCs obtained using μ GA are considered for the seismic vibration mitigation of the building. In the present analysis the FLC is trained based on system response to sudden excitation using GA as discussed earlier. This off-line trained FLC is then used to control building structure. Nevertheless, this proposed scheme can also be used to control building structures on-line. This is demonstrated on a benchmark building exercise and is reported in Chapter 7.

Performance measure

The set of performance indices, defined in Eq. 4.2 is used to determine the efficiency of the control techniques used for the study. The performances of the system for all three seismic records are tabulated in Table 4.4 for both FLC-FRB and FLC-ORB. Comparing the results in table (Table 4.4) one can see that FLC-ORB is better than FLC-FRB in controlling all responses of the structure. Normed first floor velocity is the only case where FLC-FRB has shown better performance than that of FLC-ORB, the reason is that FLC-ORB adds more force to the system to mitigate its vibration which increases the velocity response at the damper location.

Figure 4.17 shows the uncontrolled and controlled floor displacements of the building under Chichi, El-Centro and Northridge earthquake ground motions. It is seen that the FRB-ORB does not only reduce the peak floor responses but also reduces the floor drifts. Figure 4.18

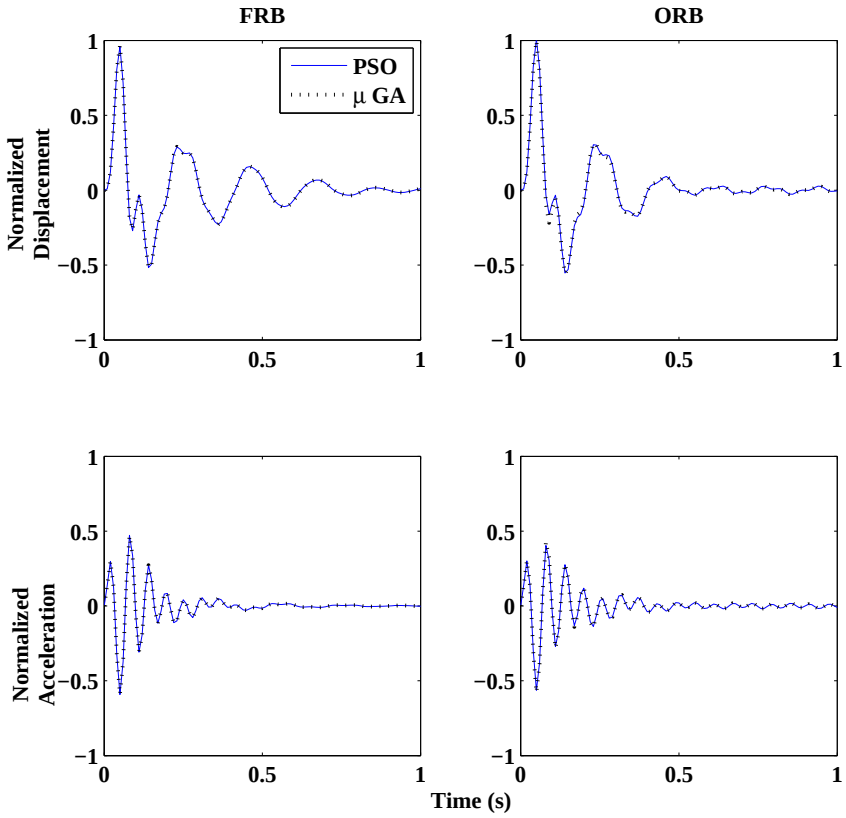

Figure 4.15: Displacement and acceleration time history for 3^{rd} floor (Impulse response example)

Table 4.4: Performance Indices of Control Strategies (FF=First Floor, SF=Second Floor, TF=Third Floor)

		Chichi		Elcentro		Northridge	
PI	**Floor**	ORB	FRB	ORB	FRB	ORB	FRB
J_1	FF	0.2372	0.264	0.1311	0.187	0.235	0.2869
	SF	0.3351	0.4304	0.2372	0.3451	0.3268	0.3753
	TF	0.3885	0.5086	0.2777	0.4005	0.3621	0.4149
J_2	FF	0.219	0.2093	0.1284	0.2065	0.2184	0.2516
	SF	0.4682	0.5193	0.3005	0.3972	0.3108	0.3139
	TF	0.5338	0.6031	0.3443	0.5022	0.358	0.3723
J_3	FF	1.4536	2.0051	1.3987	2.2985	1.3014	1.4814
	SF	0.4676	0.6238	0.4658	0.6239	0.5229	0.609
	TF	0.7517	0.8508	0.467	0.7125	0.4594	0.5693
J_4	FF	0.1671	0.1916	0.0863	0.1183	0.2211	0.2481
	SF	0.2581	0.3173	0.2176	0.2902	0.3284	0.3681
	TF	0.2941	0.3829	0.2633	0.3609	0.3744	0.4337
J_5	FF	0.0927	0.06	0.0682	0.0439	0.1493	0.1205
	SF	0.2477	0.3803	0.2676	0.3765	0.353	0.4286
	TF	0.3011	0.4808	0.3293	0.4762	0.4215	0.5294
J_6	FF	1.3821	2.2322	1.4469	2.2368	1.4216	1.9704
	SF	0.4507	0.5881	0.4065	0.5476	0.5517	0.6589
	TF	0.4656	0.682	0.4595	0.6606	0.5753	0.7214

shows the control force and the voltage required for FLC-FRB and FLC-ORB for Chichi earthquake. One should observe from Fig. 4.18 that the voltage supplied to the MR damper takes any voltage value within its range and seldom reaches its maximum voltage value (5V).

4.7 Summary

In this chapter the necessary background for the fuzzy logic control and its optimization using evolutionary algorithms has been outlined. The details of the development of an optimal FLC system to monitor MR damper current supply are presented. The parameters that are

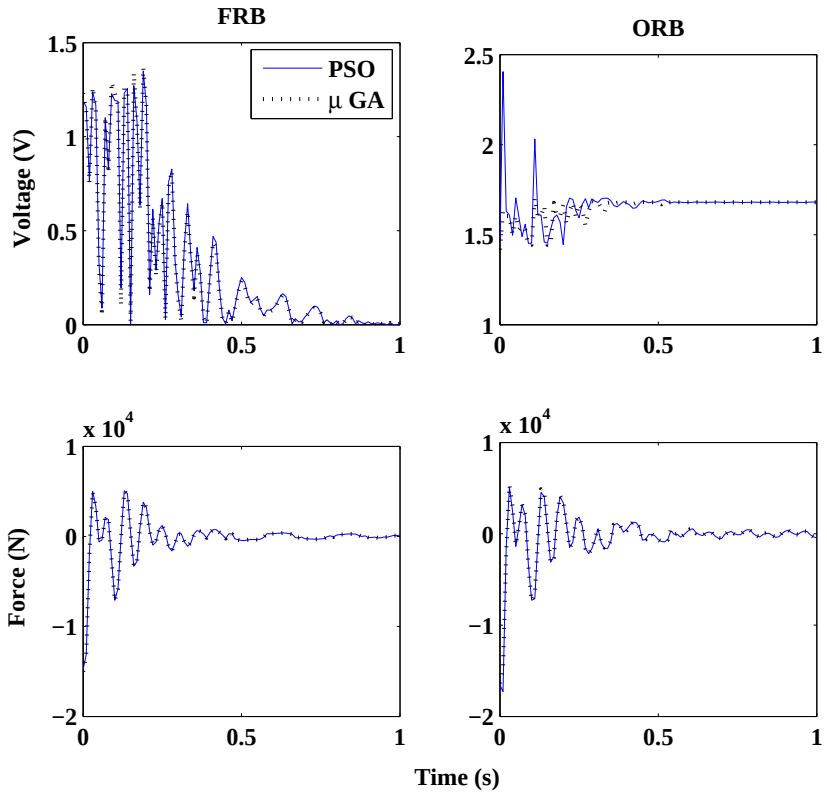

Figure 4.16: Input voltage and control force (MDOF system)

subjected to optimization are the fuzzy rule base, input-output scaling gains, membership function parameters (MF width and center slope). The study develops an easy and computationally less intensive technique to modify the rule base, which uses a few optimization variables. Optimization is carried out using micro-GA and particle swarm optimization. Both micro-GA and PSO provided optimal FLCs similar in performance to one another. To evaluate the efficiency of the optimal rule base FLC, a comparison with fixed rule base FLC with other parameters optimized is shown.

For the comparative analysis a SDOF system and a three storey building are considered, where MR damper has been connected to the first floor. It is shown that the FLC with optimal rule base modified using the proposed technique performs better than conventional FLC with predefined rule base. The optimization of FLC is carried out using μ GA with elitist mechanism and PSO with a constriction function. Results show that PSO converges faster in terms of number of generations than μ GA but takes larger time and more function evaluations than μ

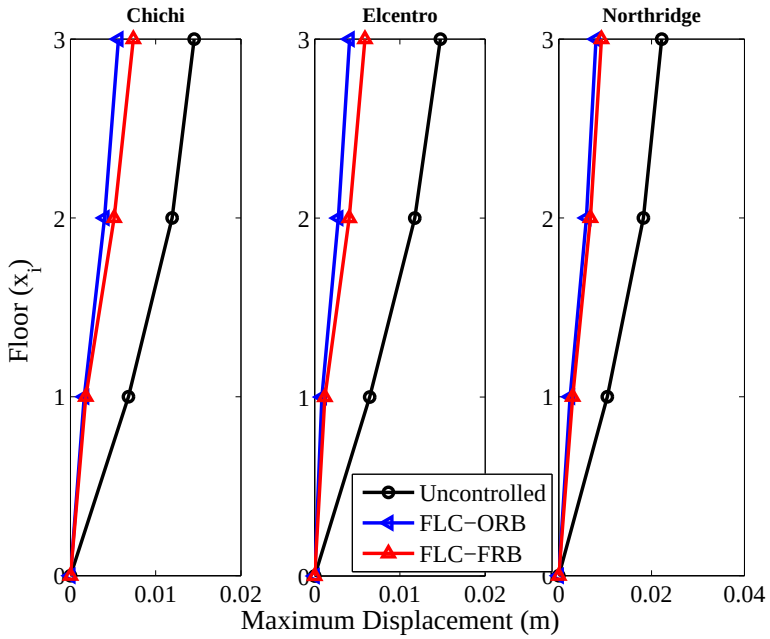

Figure 4.17: Peak floor response of 3 storey building (Chichi, El-Centro, Northridge)

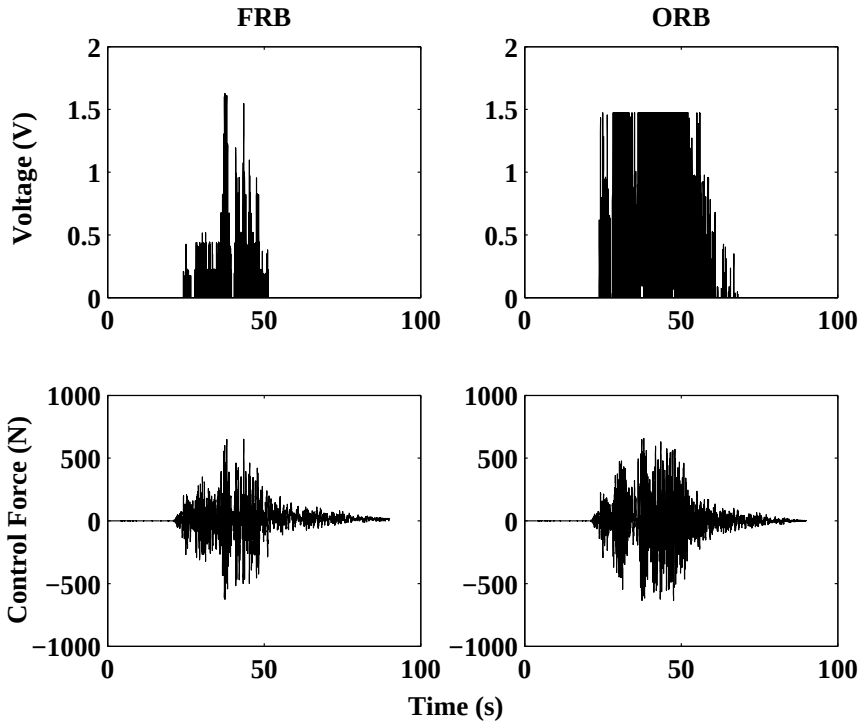

Figure 4.18: Input voltage and control force time history (Chichi Earthquake)

GA. Relative merits and demerits of the optimization schemes are outlined. It is seen from the examples under various conditions that the FLC monitored MR damper voltage effectively reduces structural vibration. Furthermore FLC driven MR damper voltage monitoring provides a gradual and smooth change of voltage and thereby increases the system stability.

As presented at the beginning of this chapter that monitoring the MR damper current/voltage provides a challenge in itself given the nonlinear relations of the force-current/voltage of the damper. Present chapter has outlined the development of an optimal intelligent controller for the above. The main motive behind the employment of a fuzzy based intelligent technique is to develop a control strategy that can make full utilization of the damper input current/voltage range. Another motive has been to provide a smooth update of MR damper current/voltage avoiding the 'on-off' strategy, a common approach reported in the literature.

Stability of fuzzy based intelligent technique can not be established mathematically unless some special cases are considered. This restricts the use of FLC to real life structural problem. In this chapter stability of the proposed optimal FLC is shown through numerical example of a SDOF and and MDOF system under impulsive load and sudden displacement respectively. The same optimal FLC and simple FLC algorithms are employed for the experimental study of a three storey hybrid base isolated building control (with MR dampers as supplemental energy dissipating devices). In the next chapter details of the experimental set up, model system identification and necessary experimental and analytical results to support the claims of this chapter are provided.

Chapter 5

Hybrid Base Isolated Building Control: Experiments and Analytical Results

5.1 Overview

Based on the review of literature (presented in Chapter 2) the need for a hybrid control mechanism combining a base isolation strategy and an MR damper has been identified and it has also been highlighted that there is a need for various experimental studies to develop this mechanism of hybrid isolation. In Chapter 4 development of an optimal fuzzy logic based MR damper current/voltage monitoring has been presented. In this chapter, the performance of the optimal fuzzy logic controller developed in Chapter 4 is studied on a laboratory scale three-storey base-isolated building model.

The thrust of the presentation of this chapter is a validation of the optimal fuzzy logic based controller for base isolated structures under a set of near fault and far fault seismic excitations. MR damper is supplemented with base isolation to provide an additional damping to the system, such that it reduces the large displacements demands in the base isolator. Results of the building with fixed base, base isolated building and hybrid base isolation, *i.e.*, base isolation with MR damper are reported.

As noted in Chapter 2, a few experimental studies have been reported in literature which employed MR dampers as a supplemental damping (Nagarajaiah et al. (2000) [255]; Ramallo et al. (2002) [286]; Sahasrabudhe et al. (2000) [303], Kim et al. (2006) [187], Shook et al. (2007)

[316]). All the experiments yielded favorable results on the protective capabilities of a small-scale rubber bearing system that is augmented with an MR damper and most of the studies have been to mitigate the effects of unidirectional seismic loadings.

Among large-scale experimental efforts mention may be made of Soda et al. (2003) [321]; Kim et al. (2006) [187]. Soda et al. (2003) [321] carried out large-scale experimental efforts to understand the effectiveness of a $40\ kN$ MR damper that has been installed in parallel with several laminar rubber bearings. Kim et al. (2006) [187] adopted a RPS (rolling pendulum system) that has been installed in conjunction with $7\ kN$ and $20\ kN$ MR dampers to mitigate unidirectional seismic loadings on a structure with a single degree of freedom having a mass of $13,620$kg. MR damper force has been managed by a fuzzy logic controller. The fuzzy controller reduces acceleration response while maintaining safe displacements. An H_∞ controller with a fuzzy gain-scheduling procedure for optimal control of a semi-active variable orifice damper has been reported by Wongprasert and Symans (2005) [377]. These studies indicated favorable reduction of the superstructure response to both near-field and far-field excitations.

A comparative study that includes a neural network control, LQR/clipped optimal control with variable gains and fuzzy logic control has been reported by Shook et al. (2007) [316]. Results of the numerical and large-scale experimental efforts have revealed that the response of the isolated structure is effectively alleviated by all of the considered control methods, although they do not perform equally well. The LQR/clipped optimal controller with variable gains has been found to be superior to the other controllers in half of the investigated cases, while neural network control has been found to be effective in minimizing the acceleration of the superstructure that is subject to moderate excitation. The fuzzy logic controller performs well for earthquakes with large accelerations (Shook et al. (2007) [316]). Thus, the study demonstrated the efficiency of fuzzy based control and also paved the platform for further experimental investigations on fuzzy based intelligent control of hybrid isolation systems.

In this chapter a fuzzy logic controller (FLC) with parameters optimized by a genetic algorithm (GA), termed GA-FLC control, is selected as a candidate for implementation with a semi-active isolation system. Numerical and experimental efforts are employed to evaluate the performance of the method along with 'passive-on' ($1A$ supply current), 'passive-off' ($0A$ supply current), and FLC with manually designed rule base (SFLC). The chapter is organized

as follows. Details of the experimental set-up are provided first. This is followed by the identification of the building model and the isolator characteristics. Thereafter, results obtained from various experimental sets are compared and discussed. Next, the experimental and analytical results are provided together for better comparison. The performances for various control mechanisms are tabulated. The chapter concludes by highlighting the suitability of the control strategy developed and its validation in laboratory scale studies.

5.2 Experimental Setup

This section provides the details of the experimental set-up of the base isolated three storey building for hybrid control using MR damper. The isolation is achieved using four sliding bearings at the four column bases of the building. A base plate is incorporated between sliding bearings and the building model as shown in the schematic diagram of the experimental set-up in Fig. 5.1. As shown in Fig. 5.1 the base plate moves along with the sliding bearings, that slides on two cylindrical shafts. The columns of the building are connected to the base plate. The stiffness of the bearing at the base is achieved connecting four linear springs coaxially with four sliding bearings. Figure 5.1 shows the position of accelerometers and displacement transducers. Three accelerometers and three capacitance type LVDT (linear variable differential transformer) are used to measure floor accelerations and floor relative displacements, respectively. Another pair of accelerometers are connected to the base plate and the shake table. Similarly a pair of spring LVDTs are mounted to the base plate and the shake table to measure relative displacement at the base and at the shake table. The measured acceleration from the base plate is fed as an input to the dSPACE hardware, where a decision about the voltage input to the MR damper is taken and feedback to the MR damper is given. The connection of the MR damper with the base plate and the shake table is shown in Fig. 5.2.

Set-up details of the building are given considering separately the characteristics of the fixed base building, base isolator and MR damper.

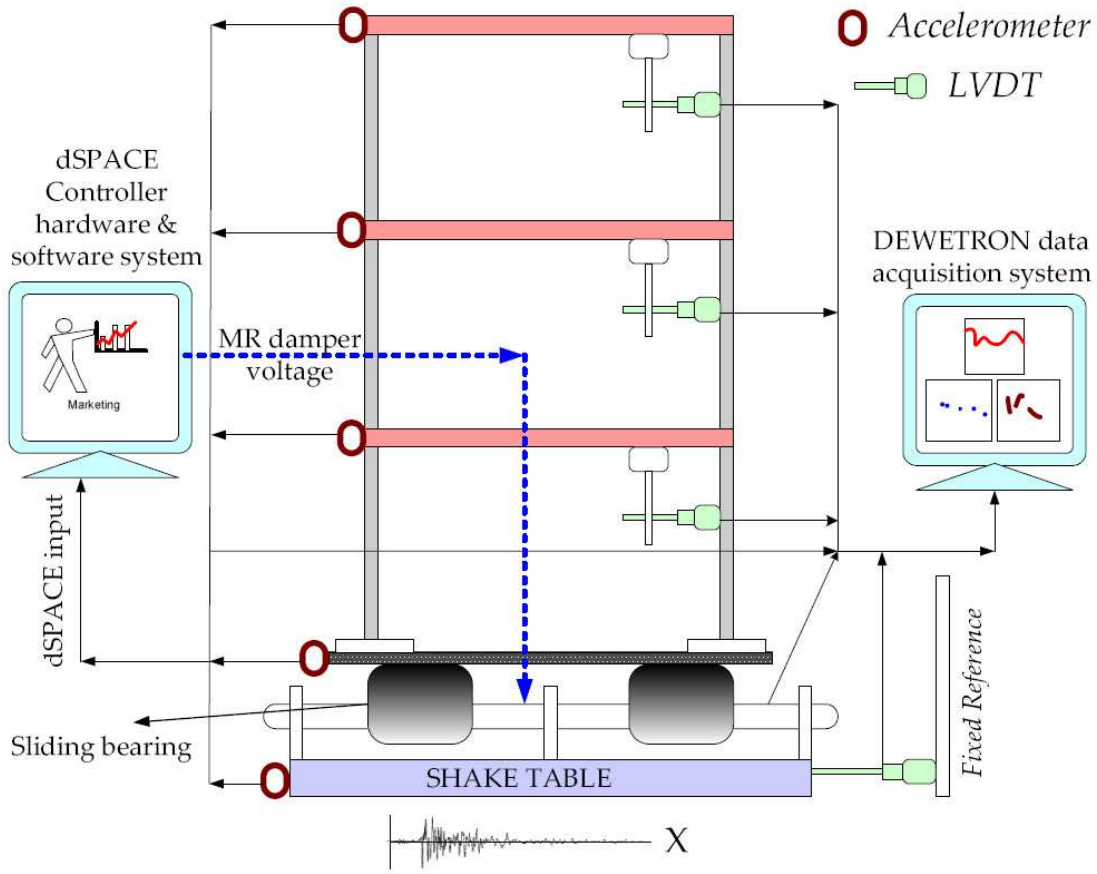

Figure 5.1: Schematic digram of the experimental set-up (elevation)

Fixed base building

The experimental building model is a single bay three storey steel frame building (base + three storey) with the columns at the corner having equal stiffness (see Fig. 5.2). Floor to floor height is taken to be $0.60\ m$ with the average column cross-section measurement found to be $0.02\ m$ by $0.016\ m$. The dimensions of the rigid floors are found to be $0.60\ m$ in length $0.40\ m$ in width and $0.03\ m$ in thickness. The experimental set-up is shown in Fig. 5.3.

The dimensions of the experimental building is designed based on an assumption that the maximum damping force provided by the MR device is 20% of the total inertial force of the structure system at $5g$ earthquake (Agrawal (2006) [6]) and the maximum pay-load of the shake table considering its performance limits is 3000-3500N. The stiffness of the building is decided to keep the fundamental frequency of the structure near 5Hz. Assuming a three

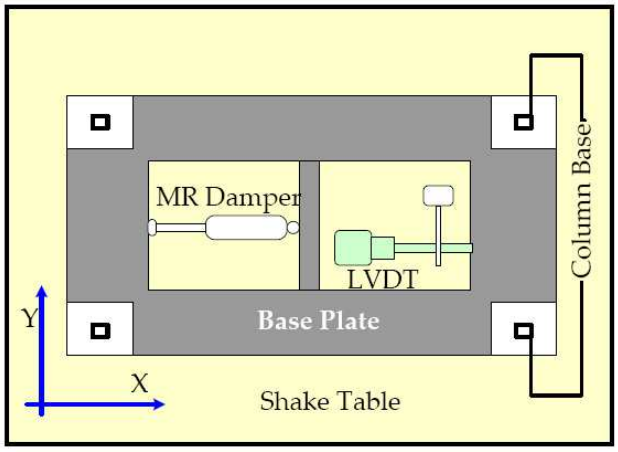

Figure 5.2: Plan at the base isolator level (LVDT and MR damper are connected between shake table and base plate)

storey shear building model (see Chapter 2 for details) to satisfy the above mentioned criteria, the structural dimensions, the building mass (M_s) and stiffness matrices (K_s) are obtained as the following.

$$M_s = \begin{bmatrix} 56.52 & 0 & 0 \\ 0 & 56.52 & 0 \\ 0 & 0 & 56.52 \end{bmatrix} kg; \quad K_s = \begin{bmatrix} 4.75 & -2.37 & 0 \\ -2.37 & 4.75 & -2.37 \\ 0 & -2.37 & 2.37 \end{bmatrix} \times 10^5 \frac{N}{m} \tag{5.1}$$

The three natural frequencies obtained (assuming a 2-D shear building modes) with the above mass and stiffness matrices are 4.5915, 12.8650, 18.5905Hz. A damping of 1% along with the above mass and stiffness matrices formed the initial parameters for the modal updation (discussed in the next section).

Figure 5.3(a) shows the accelerometer locations on the floors of the building (they are attached at the center of each floor along one edge). A total of 5 MEMs type accelerometers are installed to measure the floor accelerations. The accelerometer on the third floor is a tri-axial type to measure response along all the axes of the floor. All other accelerometers are of uni-axial type. Figure 5.3(b) shows the view of the building from another side with LVDT locations at the floors. Three capacitance type LVDTs are used to measure the inter-storey floor drifts and two spring type LVDTs are used to measure relative displacement at the base plate

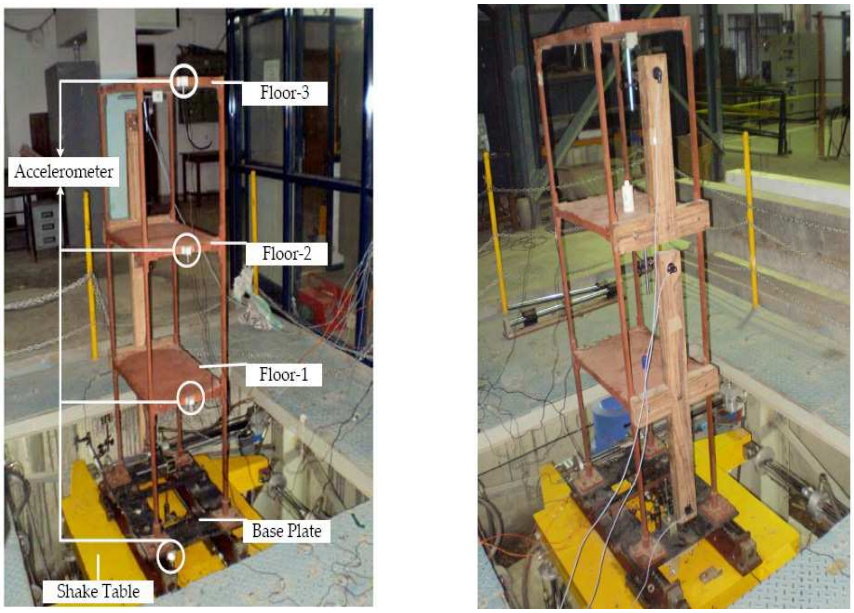

(a) Accelerometer locations (b) LVDT locations

Figure 5.3: Photographs of three storey building for experimental investigation

and absolute displacement at the shake table. Details of the connection of capacitance type LVDTs to measure floor drift are shown in Fig. 5.4(a). Figure 5.4(b) shows the connection of spring type LVDT to measure relative displacement of the base plate.

Base isolator

The isolation of the three storey building is considered using four linear sliding bearings, which are allowed to slide on two steel shaft specifically made to serve the purpose. The linear sliding bearings do not provide any resistance to the motion of the structure (except a little frictional force), therefore four linear compression springs are attached coaxially to the bearings to provide base stiffness to the system. The system is designed such that at any instant of time only two linear springs will resist the motion. The springs are designed such that the isolated structure has a fundamental frequency near $1\ Hz$. The mass (m_b) of the base plate is measured to be 38kg. The stiffness (k_b) and damping (c_b) of the isolator are determined experimentally and these details are provided in a later section. Figure 5.5(a) shows one of the four linear sliding bearing and spring connection. The experimental fixed base condition is obtained by providing four stoppers to the isolator motion, *i.e.*, fixing the sliding of the

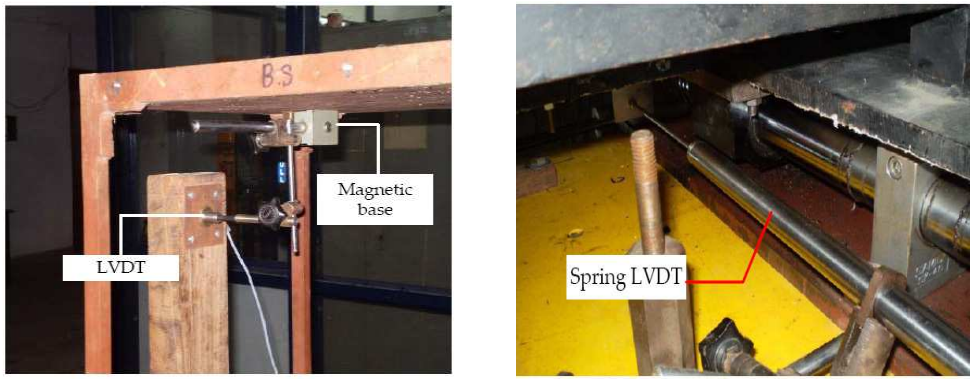

(a) LVDT connection: Capacitance type (b) LVDT connection: Spring type

Figure 5.4: Photographs of LVDT connections details

isolator. One such stopper to fix the sliding motion of the isolator is shown in Fig. 5.5(b).

MR damper

To experimentally verify the hybrid control mechanism of a base isolated structure an MR damper is connected between the base isolator and the shake table, such that it dampens the relative motion of the isolator. The schematic diagram is shown in Fig. 5.2 and a photograph from the experiment is shown in Fig. 5.6. Details of the RD-1005-3 MR damper (LORD (2008) [214]) are provided in Chapter 3. As shown in Fig. 5.6, a force transducer (details in Appendix A) is attached in series with the MR damper to measure the force across the device.

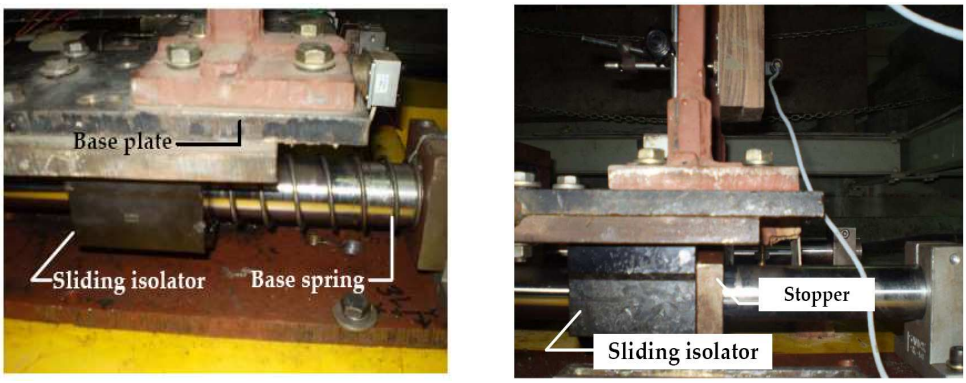

(a) Isolator connection (b) Fixed base connection

Figure 5.5: Photographs of connection details at base

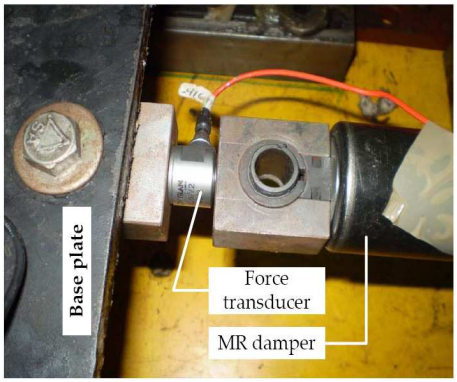

Figure 5.6: Photograph of MR damper connection

5.3 System Identification

In this section the details of the parameter identifications of the fixed base building and the base isolator are presented. Impulse hammer test is conducted to determine the fixed base building parameters, while sinusoidal base excitation is used to determine the damping character of the sliding base. The stiffness parameter of the base (linear spring stiffness) is determined experimentally using MTS testing machine.

5.3.1 Fixed base building system identification

Impulse hammer tests (IHT) are performed to determine the parameters of the fixed base building. The frequency response function (FRF) characteristic of the building is obtained from the IHT in IOtech DaqBoard/2000 device (IOtech (2006) [153]). Impulsive force is given at the top floor (third storey in fixed base case) and the acceleration responses are measured at all the floors along the direction of impulse. The FRF characteristics, *i.e.*, natural frequencies, damping coefficients and the mass normalized mode shapes are obtained using 'MEscope' software (MEscope (2003) [236]). Finally the building model is updated to match experimentally obtained results using particle swarm optimization (PSO).

Model updating aims at introducing correction to an initial model so that it predicts accurate and reliable dynamic behavior of the structure. The process of updating is performed by adjusting parameters of the initial model in such a way that the difference between analytical results and experimental data is minimized. In this study, the updating problem is considered

as an optimization problem and PSO algorithm is employed for optimization.

Optimization scheme

The optimization algorithm is used to find the vector of unknowns $\delta_k;\ k = [1, \cdots, 9]$, where δ_k is the multiplication factor on the coefficients of the mass, damping and stiffness matrices, so as to get the updated model (see Eq. 5.2). The first three $\delta_1, \delta_2, \delta_3$ must be multiplied with the initial floor masses to get the updated floor masses. Similarly the next six are multiplication factor for damping and stiffness matrices, respectively. The updated modal matrices have the following form,

$$M_a = \begin{bmatrix} \delta_1 m_1 & 0 & 0 \\ 0 & \delta_2 m_2 & 0 \\ 0 & 0 & \delta_3 m_3 \end{bmatrix}; \qquad C_a = \begin{bmatrix} \delta_4 c_1 + \delta_5 c_2 & -\delta_5 c_2 & 0 \\ -\delta_5 c_2 & \delta_5 c_2 + \delta_6 c_3 & -\delta_6 c_3 \\ 0 & -\delta_6 c_3 & \delta_6 c_3 \end{bmatrix}$$

$$K_a = \begin{bmatrix} \delta_7 k_1 + \delta_8 k_2 & -\delta_8 k_2 & 0 \\ -\delta_8 k_2 & \delta_8 k_2 + \delta_9 k_3 & -\delta_9 k_3 \\ 0 & -\delta_9 k_3 & \delta_9 k_3 \end{bmatrix} \tag{5.2}$$

where $m_i,\ c_i,\ k_i,\ (i = [1,\ 2,\ 3])$ represent mass, damping and stiffness of i^{th} floor of the building, respectively. The building parameters M_a, C_a and K_a are then used to determine the modal parameters ω_k^a, ζ_k^a and ϕ_k^a. These modal parameters are used by PSO algorithm to minimize the cost function defined in Eq. 5.3. Each school of swarm defines a new building parameter and each one of them is evaluated for the optimal building parameters. Final solution of the PSO provides the M_a, C_a and K_a matrix that have eigenvalues and damping coefficients closest to the values obtained from the experiment.

Setting up of an objective function and selecting updating parameters are essential steps in model updating. The objective function can be defined in the modal or frequency domain. In this work objective function in modal domain is selected for model updating. Several objective functions, relating to the modal domain, have been proposed and discussed in Mottershead and Friswell (1993) [239]; Friswell and Mottershead (1995) [121]; Ewins (2000) [108] and Kwon and Lin (2005a, b) [200, 199].

In the present analysis, apart from the mode shapes (J_ϕ) and modal frequency (J_ω) cost functions, a third cost function considering the experimental and analytical coefficient of damping (J_ζ, see Eq. 5.4) is added. Therefore the new cost function has been given as,

$$\Psi = W_\omega J_\omega + W_\zeta J_\zeta + W_\phi J_\phi \tag{5.3}$$

where J_ω, J_ζ and J_ω are the cost function components related to the natural frequency data, damping coefficients and the mode shape data, respectively, and W_ω, W_ζ and W_ϕ are the weight factors. The cost functions J_ω and J_ζ are given as,

$$J_\omega = \sum_{k=1}^{3} \left(\frac{\omega_k^m - \omega_k^a}{\omega_k^m} \right)^2; \qquad J_\zeta = \sum_{k=1}^{3} \left(\frac{\zeta_k^m - \zeta_k^a}{\zeta_k^m} \right)^2 \tag{5.4}$$

whereas the cost function related to mode shapes (J_ϕ) of the building is given by,

$$J_\phi = \sum_{k=1}^{3} \left\{ (MSF\phi_k^m - \phi_k^a)^T (MSF\phi_k^m - \phi_k^a) \right\} \tag{5.5}$$

where ω_k, ζ_k and ϕ_k are the k^{th} natural frequency, coefficient of damping and mode shape vector, respectively, and superscripts m, a represent experimental measured and analytical data (T is the transpose of a vector). MSF is modal scale factor which is used to keep the experimental and analytical mode shapes at equal scale while optimizing (see Eq. 5.7).

Itis known that proper weightings W_ω, W_ζ and W_ϕ of objective function in Eq. 5.3 can improve results significantly (Friswell et al. (1998) [122]; Xia (2001) [381]). Therefore, relative weights of natural frequencies and mode shapes should be chosen carefully. In most cases, the weighting values of W_ω on natural frequencies are recommended to be larger than that of mode shapes W_ϕ because measured data of natural frequencies are more accurate than that of mode shapes (Friswell et al. (1998) [122]; Xia (2001) [381]). However, it should be noted that too much weighting on natural frequencies may result in loss of information from mode shapes which are spatially informative. Systematic methods for determining the weighting factors have not been reported in the literature. Since, there are no fixed guidelines for selecting the values of the weight factors, equal weight factors for J_ω, J_ζ and J_ϕ, *i.e.*, $W_\omega = \frac{1}{3}$, $W_\zeta = \frac{1}{3}$ and $W_\phi = \frac{1}{3}$ are assumed.

Updated model

The updated mass (M_a), damping (C_a) and stiffness (K_a) matrices are given in Eq. 5.6. The experimental and analytical natural frequencies and damping coefficients are tabulated in Table 5.1. It is evident from the Table 5.1 that the natural frequencies of experimental and analytical models match well, whereas the analytical damping coefficient for the 1^{st} mode of the structure does not match with the experimental one.

$$M_a = \begin{bmatrix} 62.76 & 0 & 0 \\ 0 & 64.20 & 0 \\ 0 & 0 & 59.40 \end{bmatrix} kg; \quad C_a = \begin{bmatrix} 522.75 & -222.75 & 0 \\ -222.75 & 232.75 & -10.00 \\ 0 & -10.00 & 10.00 \end{bmatrix} \frac{Ns}{m}$$

$$K_a = \begin{bmatrix} 1.0394 & -0.7338 & 0 \\ -0.7338 & 1.4931 & -0.7593 \\ 0 & -0.7593 & 0.7593 \end{bmatrix} \times 10^6 \frac{N}{m} \tag{5.6}$$

Figures 5.7-5.9 show the comparison of amplitude and phase angles between experimental and analytical model measured at various floors but driven at third floor. Both initial and updated analytical FRFs show the convergence of updated model using PSO algorithm. There is a small peak at 27.1Hz in the experimental curve, which may be attributed to some transverse vibration present in the structure due to the imperfections attributed to fabrication. Transverse and lateral motion coupling may be present in the structure due to inherent eccentricity

Table 5.1: Modal Parameters: Experimental and Analytical Results

Mode	**Natural Frequency** (Hz)		**Damping Coefficient**	
	Experimental	**Analytical**	**Experimental**	**Analytical**
1^{st}	5.7302	5.7230	0.0482	0.0149
2^{nd}	19.2600	19.2478	0.0176	0.0179
3^{rd}	30.0966	30.0966	0.0169	0.0172

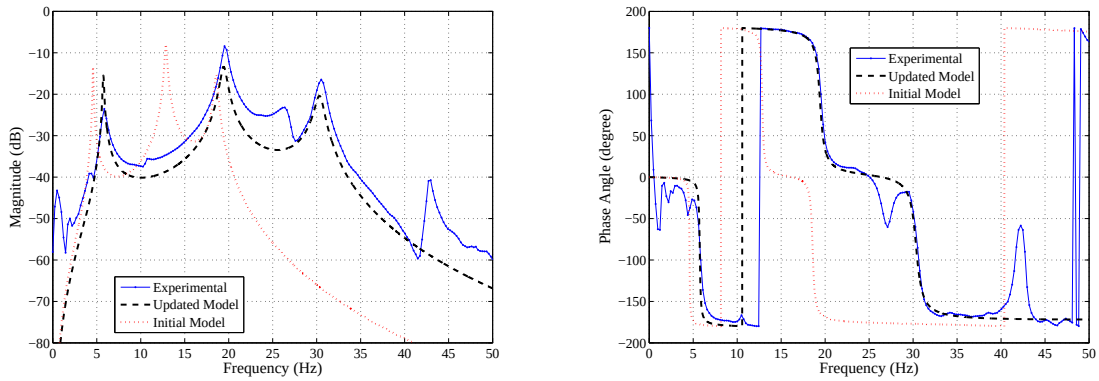

(a) Amplitude (b) Phase

Figure 5.7: FRF measured at first floor

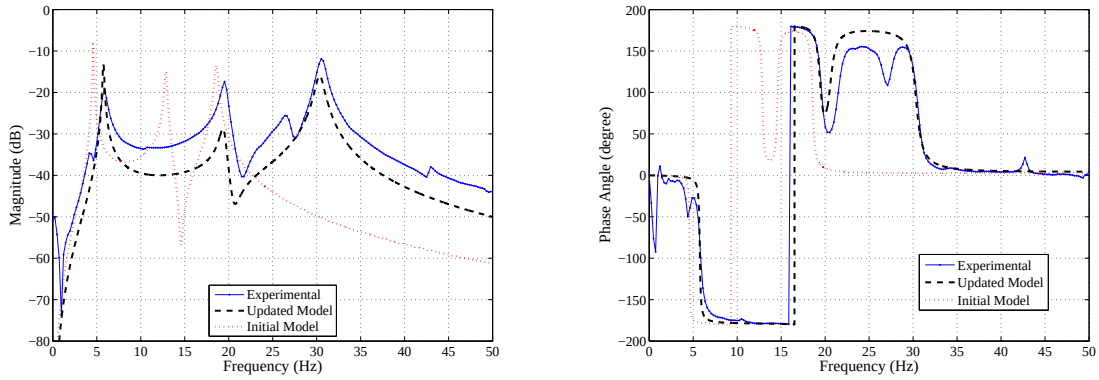

(a) Amplitude (b) Phase

Figure 5.8: FRF measured at second floor

in the model. This is not further analyzed. For simulations studies, the analytical model based on the update damping coefficients and mode shapes corresponding to natural frequencies 5.7302, 19.2600 and 30.0966Hz are considered. Although the amplitude and phase curves obtained in updated model match well with the experimental curve measured at all the floors, there remains a scope for fine-tunning the obtained model using various system identification algorithms.

Further model refinement in this direction is not carried out as the updated model predicts the experimental results obtained under the earthquake excitement quite well (as shown

in later section in this chapter). Moreover, a multi-storey building behaves as a single degree of freedom system under base isolation (Naeim and Kelly (1999) [243]) and therefore higher frequencies contribute less to the total displacement. Moreover as the main thrust of the present study is to validate the efficiency of the proposed GA optimized FLC through experimental study and system identification is a separate study in itself and therefore is not pursued further. Thus further numerical analysis is undertaken with the model given in Eq. 5.6.

The convergence of the PSO algorithm for the multi-objective cost function (Ψ), see Eq. 5.3 and cost functions related to natural frequencies (J_ω), damping coefficients (J_ζ) and mode shapes (J_ϕ) are shown in Fig. 5.10(a). It can be seen from Fig. 5.10 that the optimization converges in very few generations. Figure 5.10(b) shows the convergence of each of the cost functions J_ω, J_ζ and J_ϕ.

To compare the analytically obtained modal shapes with that extracted from the experiments, various mode shape factors are reported in the literature from which two of them are selected and attempted in this study. They are modal scale factor (MSF), and modal assurance criterion (MAC) (Friswell and Mottershead, (1995) [121]; Ewins (2000) [108] and Kwon and Lin (2005a, b) [199, 200]).

The modal scale factor (MSF), given in Eq. 5.7, determines the scaling of the mode shapes. The MSF also resolves the problem that the measured and analytical mode shapes could be

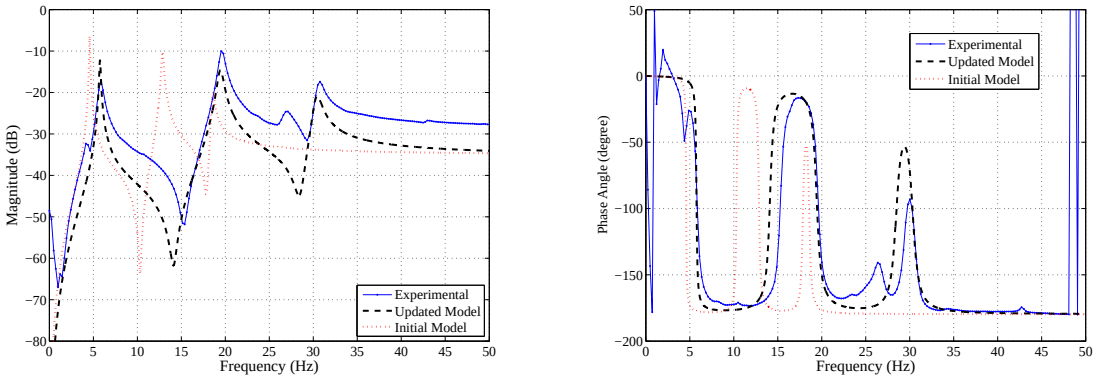

(a) Amplitude (b) Phase

Figure 5.9: FRF measured at third floor

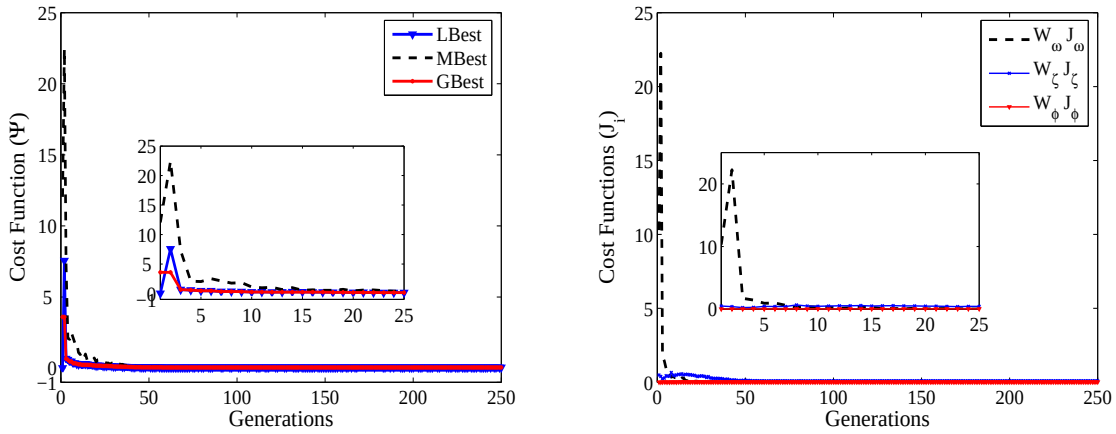

(a) PSO convergence: Multi-objective cost function

(b) PSO convergence: J_ω, J_ζ and J_ϕ

Figure 5.10: PSO convergence for all cost functions

$180°$ out of phase. The MSF obtained for the updated model is $MSF = [0.783;\ 0.728,\ 0.726]^T$. This shows that the updated model has mode shapes in-phase with the experimental mode shapes but in scaled form.

$$MSF_k = \frac{[\phi_k^a]^T [\phi_k^m]}{[\phi_k^m]^T [\phi_k^m]} \tag{5.7}$$

Modal assurance criterion (MAC) should be used in order to compare analytical and experimental data properly. The MAC criterion is defined by the following expression

$$MAC_{j,k} = \frac{\left([\phi_j^m]^T [\phi_k^a]\right)^2}{\left([\phi_j^m]^T [\phi_j^m]\right)\left([\phi_k^a]^T [\phi_k^a]\right)} \tag{5.8}$$

The MAC has values between zero and one according to the closeness between eigenvectors of analytical and experimental modes. If the modal pair are in order, then the MAC matrix will have values close to one on the diagonal and close to zero elsewhere. Figure 5.11 shows the MAC values of experimental and predicted model. The diagonal values obtained are 0.9848, 0.9809 and 0.9934, which show a very good relation between experimental and analytical

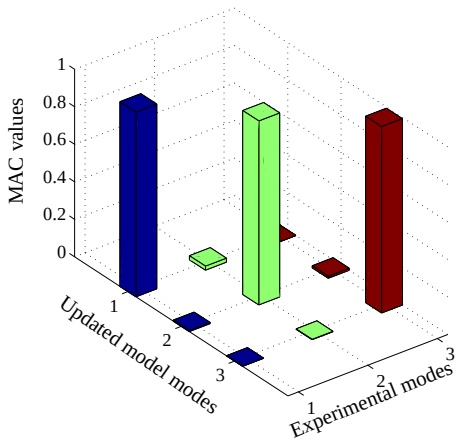

Figure 5.11: MAC values for experiment and updated mode shapes

mode shapes. The MAC matrix obtained using the updated model is given in Eq. 5.9.

$$MAC = \begin{bmatrix} 0.9848 & 0.0216 & 0.0002 \\ 0.0058 & 0.9809 & 0.0111 \\ 0.0012 & 0.0018 & 0.9934 \end{bmatrix} \tag{5.9}$$

5.3.2 Base isolator characterization

The equation of motion of a base isolated structure subjected to seismic excitation is given by Eq. 2.15 of Chapter 2. For the three storey base hybrid base isolated building considered for the experimental investigation in the present study is given below (see Fig. 5.12),

$$M_a\,\ddot{U}_{3\times1} + C_a\,\dot{U}_{3\times1} + K_a\,U_{3\times1} = -M_a\,R_{3\times1}\,(\,\ddot{x}_g + \ddot{x}_b) \tag{5.10}$$

$$R^T_{1\times3}\,M_a\,\left[\ddot{U} + \,R\,(\,\ddot{x}_g + \ddot{x}_b)\right]_{3\times1} + \,m_b\,\,(\,\ddot{x}_g + \ddot{x}_b) + c_b\,\dot{x}_b + k_b\,x_b + f_b + f_c = 0 \tag{5.11}$$

Equation 5.10 represents the superstructure dynamics with M_a, C_a and K_a representing the superstructure updated mass, damping and stiffness matrices, respectively (given by Eq. 5.6). The floor displacements relative to the base isolator are given by U, *i.e.*, $U = [x_1,\, x_2,\, x_3]^T$.

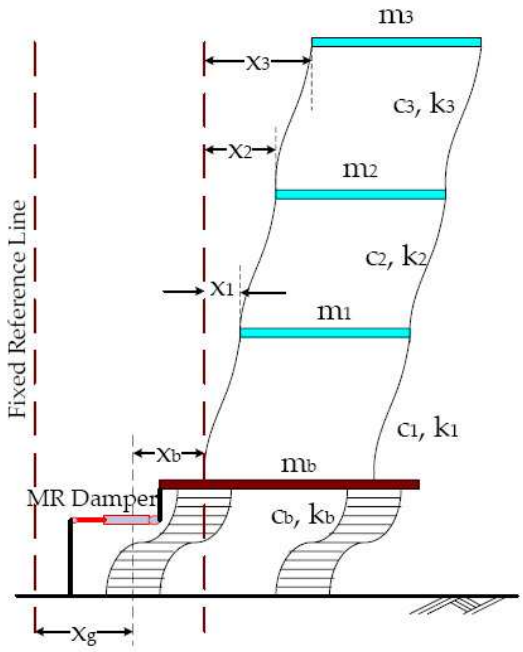

Figure 5.12: Schematic diagram of hybrid base isolated building

x_i represents relative displacement of i^{th} floor of the superstructure. $R = [1,\ 1,\ 1]^T$ is the earthquake influence co-efficient vector. x_b denotes displacement of the base isolator relative to the ground (shake table).

The dynamic of the base isolator is given by Eq. 5.11. The mass, damping and stiffness of the base isolator is represented by m_b, c_b and k_b, respectively. $\ddot{x}_g$ is the seismic ground acceleration input to the system. The nonlinear damping force that can arise due the friction in the sliding bearing is represented by f_b and the MR damper restoring force is represented as f_c. The details about the measurement of f_c is given in Chapter 3. The identification of base mass (m_b), base damping (c_b), base stiffness (k_b) and the nonlinear force generated due to the sliding friction (f_b) is referred to as base isolator characterization in this study.

The mass of the base is measured to be equal to 38kg. The stiffness of the linear springs attached coaxially with the sliding isolator is measured using servo-hydraulic testing machine. The measured stiffness of each of the springs is obtained as 2.162kN/m. The experimental force-displacement relation and the linear fit to the experimental relation are shown in Fig. 5.13.

No classical damping is assumed for the sliding isolator (*i.e.*, c_b is assumed to be zero)

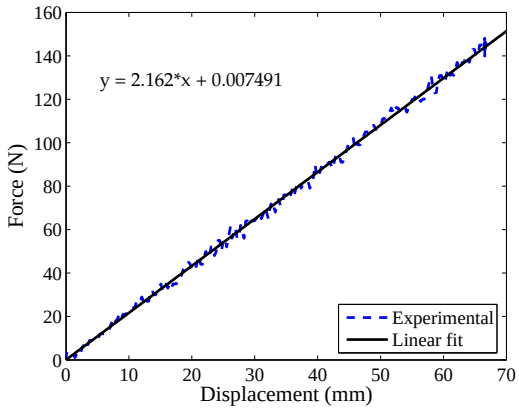

Figure 5.13: Schematic diagram of hybrid base isolated building

but nonlinear friction (f_b) is considered. The total force in sliding bearings is considered as ($f_b = \mu w z_w$), where μ is the coefficient of friction at the bearing and w is the normal load at the bearing. z_w is the Wen's hysteretic parameter (Wen (1976) [371]) used to model friction (Sahasrabudhe and Nagarajaiah (2005) [301]; Madden et al. (2002) [216]).

The coefficient of friction at the bearing (Sahasrabudhe and Nagarajaiah (2005) [301]; Madden et al. (2002) [216]) is given by,

$$\mu = \mu_{max} - (\mu_{max} - \mu_{min})e^{-\lambda|\dot{x}_b|} \tag{5.12}$$

where μ ranges from μ_{max} at large velocities of sliding to μ_{min} at very low velocities. λ is a constant having units of time per unit length and $\dot{x}_b$ is the velocity across the isolator. The value to μ_{max} and μ_{min} is determined through experiments.

The Wen's hysteretic variable (z_w) is given by (Sahasrabudhe and Nagarajaiah (2005) [301]),

$$Y\dot{z}_w + \gamma_w |\dot{x}_b| z_w + \beta_w \dot{x}_b z_w^2 - A_w \dot{x}_b = 0 \tag{5.13}$$

where the constants Y, A_w, γ_w, and β_w are the shape parameters of the hysteresis loop which are calibrated using the experimental data.

Tests with sinusoid input excitation at the base is carried out with varied frequencies ranging from 1Hz to 3Hz and amplitudes ranging from 2mm to 10mm, to determine frictional damping at the sliding isolator. Particle swarm optimization algorithm is used to optimize

the variables, μ_{max}, μ_{min}, Y and λ. The value for A_w, γ_w and β_w have been considered as 1, 0.9 and 0.1, respectively (Sahasrabudhe and Nagarajaiah (2005) [301]; Madden et al. (2002) [216]).

Particle swarm optimization algorithm is employed to minimize the cost function given by,

$$J_{bi} = W_1 \sum((x_b - \hat{x}_b)^2/(\hat{x}_b^2)) + W_2 \sum((\dot{x}_b - \dot{\hat{x}}_b)^2/(\dot{\hat{x}}_b^2)) + W_3 \sum((\ddot{x}_b - \ddot{\hat{x}}_b)^2/(\ddot{\hat{x}}_b^2)) \quad (5.14)$$

where, W_i denotes weights and ($\hat{.}$) denotes the variables obtained from the experiments. The optimal values for the variables obtained are $\mu_{max} = 1.1303$, $\mu_{min} = 0.2853$, $Y = 0.2526$ and $\lambda = 0.6191$. Figures 5.14-5.15 show the experimental and analytical responses for sinusoidal excitations of amplitude 2mm and frequency 1Hz.

5.4 Seismic Input Excitations

Actual earthquake records are used to evaluate the performance of the hybrid control strategy developed in this study. The seismic time-history data are downloaded from the PEER strong motion database (2007) [274]. Both the X and Y direction seismic records are considered separately in the experimental study. Details of the excitation data used in the study are presented in the ensuing section.

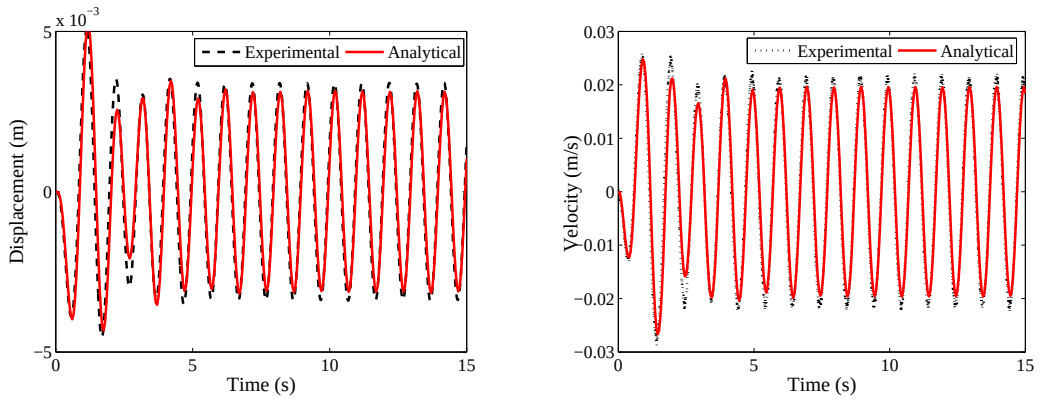

(a) Displacement time history

(b) Velocity time history

Figure 5.14: Displacement and velocity time history at 2mm amplitude and 1Hz of sinusoidal excitations (experimental and analytical responses)

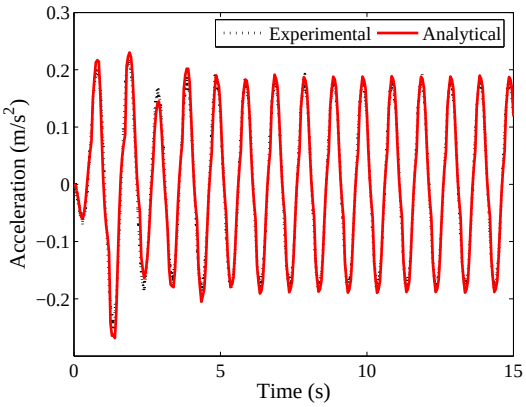

Figure 5.15: Acceleration time history at 2mm amplitude and 1Hz of sinusoidal excitations (experimental and analytical responses)

The amplitude of the input seismic excitation data is scaled down such that the base isolated building has a maximum isolator displacement within a range of $0.1\ m$-$0.15\ m$ as the experimentally designed isolator has a maximum displacement capacity of $0.17\ m$. Peak ground acceleration (PGA), peak ground velocity (PGV) and peak ground displacement (PGD) values of the earthquake time history data are tabulated in the Table 5.2. Table 5.2 also shows the scaling factor used for the experimental study.

Seismic data and source stations

The seismic data and their measurement station considered are given next. The time histories of the full scale earthquake data along with its frequency content for Bigbear (1992) and N. Palm Springs (1986) earthquakes are shown in Figs. 5.16 - 5.19. Time histories of other earthquakes records are given in Appendix C.

- Big Bear, 28^{th} June 1992: Magnitude 6.4 M at station: 23542 San Bernardino Hospital
- Cape Mendocino, 25^{th} April 1992: Magnitude: 7.1 M at station: 89509 Eureka - Myrtle & West, distance from the fault rupture is 44.6 km
- Chi-Chi-Taiwan, 20^{th} September 1999: Magnitude: 7.6 M at station: ALS, distance from fault rupture is 15.29 km

Table 5.2: Seismic Records Considered for the Experimental Study

Earthquake Name	**Direction**	**Scaling**	**PGA** ($\times 10\ m/s^2$)	**PGV** ($\times 10^{-2}\ m/s$)	**PGD** ($\times 10^{-2}\ m$)
Big Bear	X (180)	1	0.101	11.9	3.35
Big Bear	Y (90)	1	0.092	13.8	3.53
Capemend	X (00)	1	0.154	20.2	5.89
Capemend	Y (90)	0.5	0.178	28.3	11.41
Chi Chi	X (east)	0.5	0.183	39.3	10.37
Chi Chi	Y (north)	0.5	0.163	21.9	8.64
Coalinga	X (360)	1	0.281	25.8	3.71
Coalinga	Y (270)	1	0.227	23.6	5.83
Elcentro	X (180)	0.5	0.313	29.8	13.32
Elcentro	Y (270)	0.3	0.215	30.2	23.91
Loma Prieta	X (180)	0.25	0.215	45.0	26.10
Loma Prieta	Y (90)	0.25	0.247	38.5	17.83
Npalm Spring	X (45)	0.5	0.218	31.4	8.51
Npalm Spring	Y (135)	0.4	0.205	40.9	14.96
Kobe	X (00)	0.5	0.079	18.3	9.26
Kobe	Y (90)	0.5	0.064	17.0	8.03

- Coalinga, 2^{nd} May 1983: Magnitude: 6.4 at station: 46314 Cantua Creek School, distance from the fault rupture is 25.5 km
- Imperial Valley, 19^{th} May 1940: Magnitude: 7.0 M at station: 117 El-Centro Array-#9, distance from fault rupture is 8.3 km
- Kobe, 16^{th} January 1995: Magnitude: 6.9 M at station: 0 OSAJ, at a distance of 8.5 to the fault rupture
- Loma Prieta, 18^{th} October 1989: Magnitude: 6.9 M at station: 1028 Hollister City Hall at

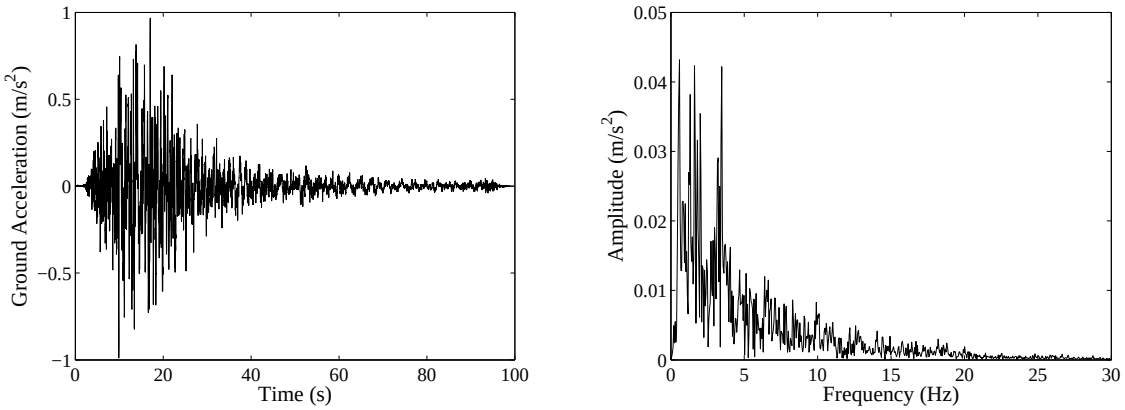

(a) Time history: Big-bear (X) (b) Frequency: Big-bear (X)

Figure 5.16: Seismic input excitation: Big-bear, X-direction (Frequency content upto 30 Hz)

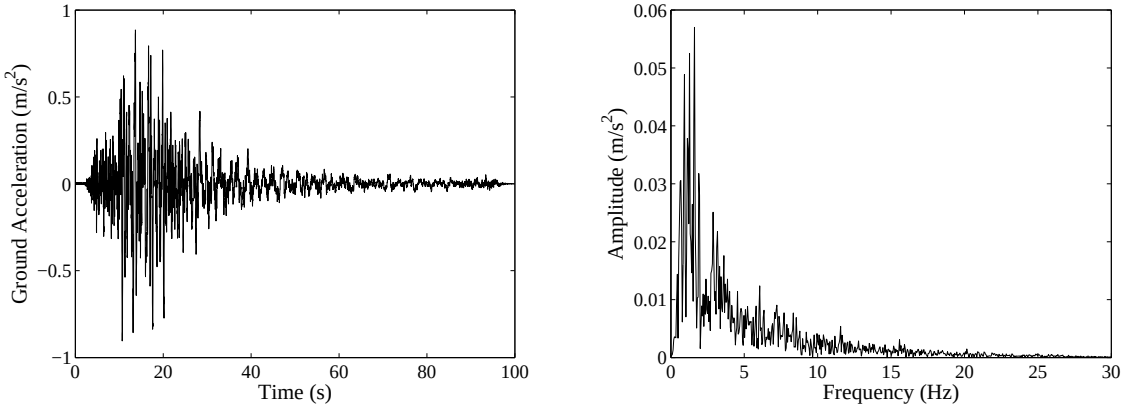

(a) Time history: Big-bear (Y) (b) Frequency: Big-bear (Y)

Figure 5.17: Seismic input excitation: Big-bear, Y-direction (Frequency content up to 30 Hz)

a distance of 28.2 km to the fault rupture

- N. Palm Springs, 8^{th} July 1986: Magnitude: 6.0 M recorded at station 5071 Morongo Valley, at a distance 10.1 km closest to the fault rupture.

5.4.1 Shake table dynamics

The shake table employed for the purpose of the experimental study has 6-DOF movements, *i.e.*, 3-axes (translation and rotation) shake table (more details in Appendix A). The shake

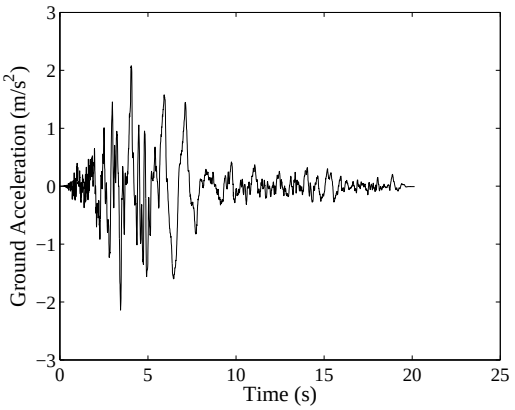

(a) Time history: N. palm springs (X)

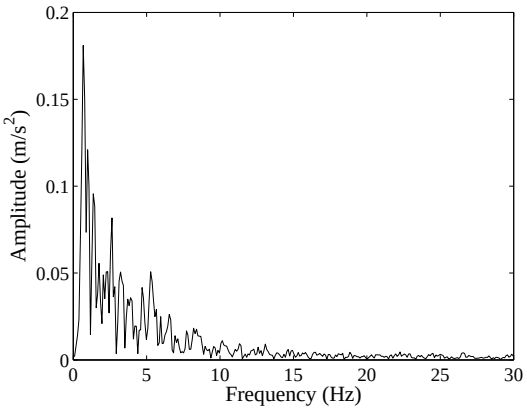

(b) Frequency: N. palm springs (X)

Figure 5.18: Seismic input excitation: N. palm springs, X-direction (Frequency content upto 30 Hz)

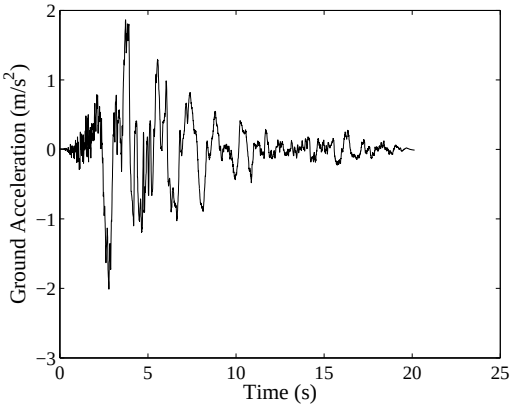

(a) Time history: N. palm springs (Y)

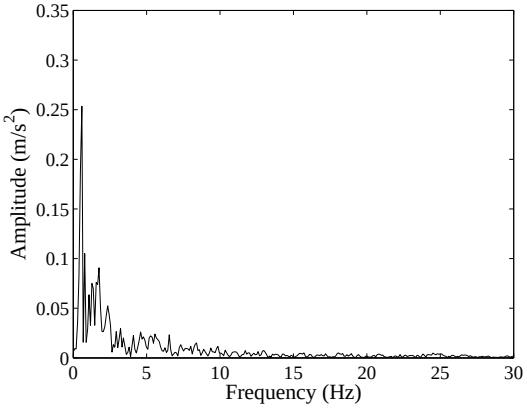

(b) Frequency: N. palm springs (Y)

Figure 5.19: Seismic input excitation: N. palm springs, Y-direction (Frequency content up to 30 Hz)

table is set-up to operate in a displacement controlled mode. Displacement data of seismic events are fed into the actuators, that control the motion of the shake table, such that the same displacement can be provided by the shake table to the structures mounted on it. Since, the shake table motion is controlled by actuators, there remains a difference between the input seismic displacement and the the displacement obtained from the shake table as an output. This difference is referred to as shake table dynamics.

Figure 5.20 shows the recorded seismic displacement (referred to as analytical) and displacement measured from the shake table (referred to as experimental) for two different earthquake records. As seen from the Fig. 5.20 the amplitudes of the excitation remain same but there remains a phase difference between the input and output displacement of the shake table. For the present analysis this phase difference is not accounted for in the analytical verification of the experimental study.

5.5 Experimental and Analytical Study

The main objective of the present study is to validate the efficiency of the GA optimized FLC using experiments. To have a through understanding of the base isolation mechanism (both simple isolation and hybrid), the experiments are carried out for six cases, namely, fixed base, simple base isolation (with out MR damper) and four MR damper supplemented hybrid control cases. They are referred to in the subsequent discussions as,

- FB: fixed base condition (building without isolator and damper),
- BI: building with simple base isolation (no MR damper),
- building with hybrid base isolation (a combination of MR damper and isolators). The hybrid control scheme has been tested for control cases of MR damper. They are,

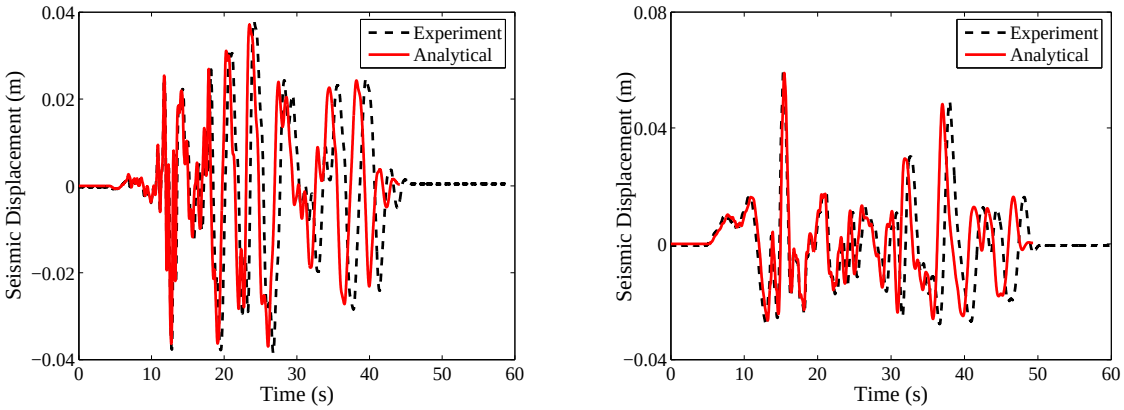

(a) Seismic Displacement: Coalinga (X)

(b) Seismic Displacement: Capemend (X)

Figure 5.20: Shake table dynamics showing phase lag between input and output data

- 'passive off' control case (0A): MR damper at zero ampere current/ (0 volts) voltage, (constant voltage supply)
- 'passive on' control case (1A): MR damper with one ampere input current supply (*i.e.*, 2.5 volts), (constant voltage supply)
- SFLC control case (SFLC): MR damper with simple FLC monitored input voltage supply, (variable voltage supply details in Chapter 4)
- GAFLC control case (GAFLC): MR damper with GA optimized FLC monitored input voltage supply (variable voltage supply details in Chapter 4)

The responses measured in the experimental study are all the floor inter-storey drifts, relative base displacement, absolute displacement at shake table and acceleration at all floors, base and shake table. Data is acquired using DEWETRON acquisition system (DEWETRON (2007) [88]) (details in Appendix A) at a sampling rate of 1 kHz (see Fig. 5.1 for details). The acquisition system has a low pass filter of 30 Hz. No further data filtering is done off-line. Control actions are computed using a DSP-based, real-time controller manufactured by dSPACE® (2005) [94]. The FLC is encoded in MATLAB® Simulink® using real time workshop (RTW) interface and dSPACE® hardware and software (dSPACE® (2005) [94]). The base plate acceleration at the damper location and pseudo velocity (obtained by integrating acceleration data in real time) are used as a feedback to the RTW to decide on the voltage required by the MR damper based on encoded FLC algorithm.

Some of the experimental results obtained for the near-fault and far-fault earthquakes are discussed in the next section. The complete set of results obtained in the experimental program are compiled as an appendix (Appendix C). Analytical simulations using the updated building model under the set of earthquakes are also presented and compared with experimental results.

5.5.1 Experimental and analytical study of the test structure

Fixed base building

For the analytical simulation of the experimental results, N. Palm Spring (X-dir) seismic ground motion (having near field behaviour) is considered. The results obtained from the analytical study and the experimental investigation are shown together in Fig. 5.21.

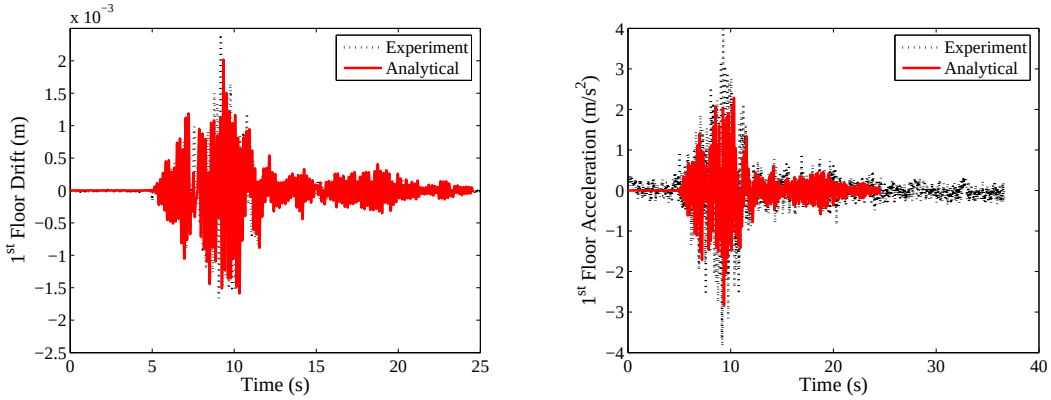

(a) First floor inter-storey drift

(b) First floor acceleration

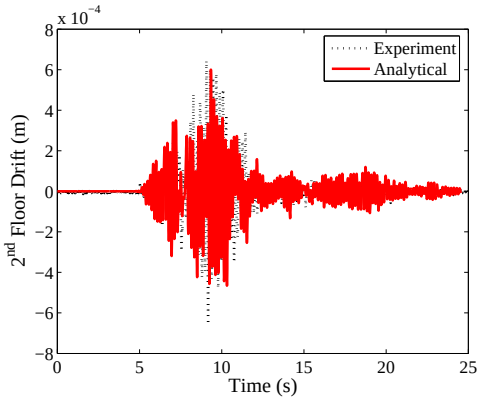

(c) Second floor inter-storey drift

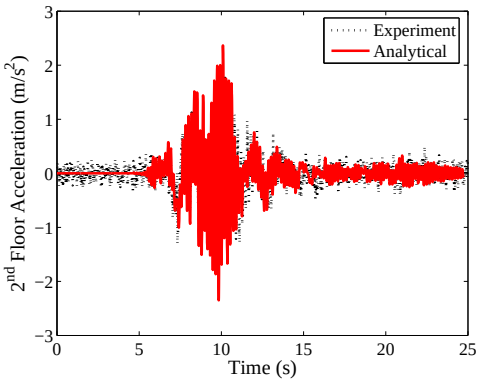

(d) Second floor acceleration

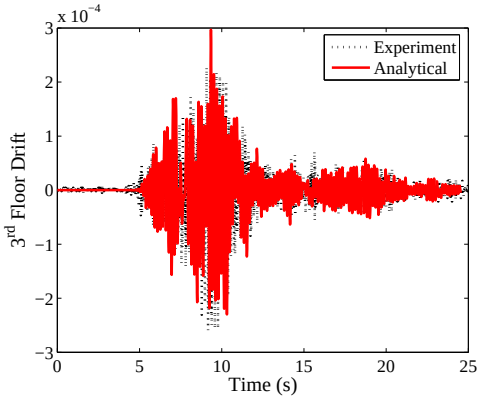

(e) Third floor inter-storey drift

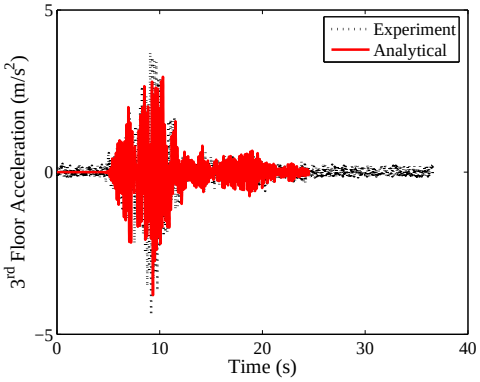

(f) Third floor acceleration

Figure 5.21: Floor responses of fixed base building (N. palm springs (X))

Figures 5.21(a), (b) show the first floor displacement and acceleration responses of the

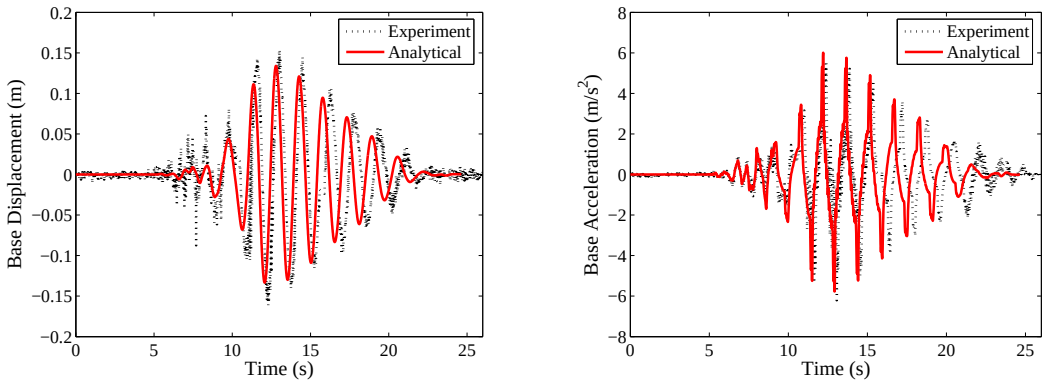

(a) Isolator drift

(b) Isolator acceleration

Figure 5.22: Isolator responses of simple base isolated building (N. palm springs (X))

experimental building, respectively. Second and third floor relative displacement and acceleration are shown in Figs. 5.21(c) and (d), respectively, whereas the third floor responses are shown in Figs. 5.21(e) and (f). Both experimental and analytical results are plotted together for better comparison. The match between the analytical and experimental results are quite evident from the figures. The peak inter storey drift and acceleration are observed to be 0.0024m and 4.41m/s^2 at 50% scaling of the input excitation. This could cause considerable distress to the building and may results in considerable occupant discomfort in full scale seismic excitation and full scale building.

Base isolated building

Figure 5.22 shows the isolator displacement and acceleration for both experimentally measured and simulated results. The peak isolator relative displacement is found to be 0.1615m, where as the analytically obtained maximum isolator drift is 0.1339m. This shows a good match between the analytical and experimentally obtained results. A phase shift is observed between the experimental and the analytical results. This is due to the shake table dynamics, which has introduced a phase lag between the original seismic displacement data and the data obtained as an output from the shake table.

Figure 5.23 shows the floor inter-storey drift and acceleration response of the base isolated building. From Figs. 5.23(a)-(f) one can see a good correlation between the experimental and analytical responses. The floor inter-storey response plots in Figs. 5.23(a), (c) and (e) show a

noisy output from the capacitance type LVDT, which makes the floor maximum floor drift to be more than that of fixed base condition.

5.5.2 Hybrid base isolated building experimental study

Hybrid base isolated building experimental study is conducted using an MR damper in conjunction with the sliding isolators. Four different cases are explored to study the relative benefits of each of them. Results from the 'passive-off' case, where MR damper acts as a passive damper with damping similar to MR damper driven at 0 A current are reported first. Then successively 'passive-on' (MR damper driven at 1A current) case and variable input current cases are discussed. In variable input current set-up, the MR damper is first driven by a simple fuzzy logic controller and then by a genetically optimized fuzzy logic controller. Requirement of a separate hardware to encode real time GA to optimize FLC at sampling rate constrains the experimental study to off-line trained GA-FLC. Nevertheless this remains as a scope for further experimental study. The control algorithms to drive MR damper are encoded in a DSP based hardware chip provided with dSPACE® (dSPACE (2005) [94]) and MATLAB® Simulink® with RTW. Figure 5.24 shows the simulink flow diagram for the dSPACE real time control application used in the experimental study of the base isolated building.

Passive off condition

The responses of 'passive-off' condition are shown in Fig. 5.25. Figures 5.25(a) and (b) show the comparison of analytical and experimental results of the relative displacement and acceleration response at the base isolator level. A good match is seen between experimental and analytical results. The base isolator displacement is reduced with the usage of MR damper passive damping. The floor drifts and accelerations are also observed to be less than that of FB and BI cases. Therefore, hybrid base isolation mechanism is more effective than base isolation acting alone in reducing structural vibration under seismic excitations.

Passive on condition

In 'passive-on' condition MR damper provides maximum damping force to the structure. The numerical and experimental responses of 'passive-on' condition are shown in Fig. 5.26. A

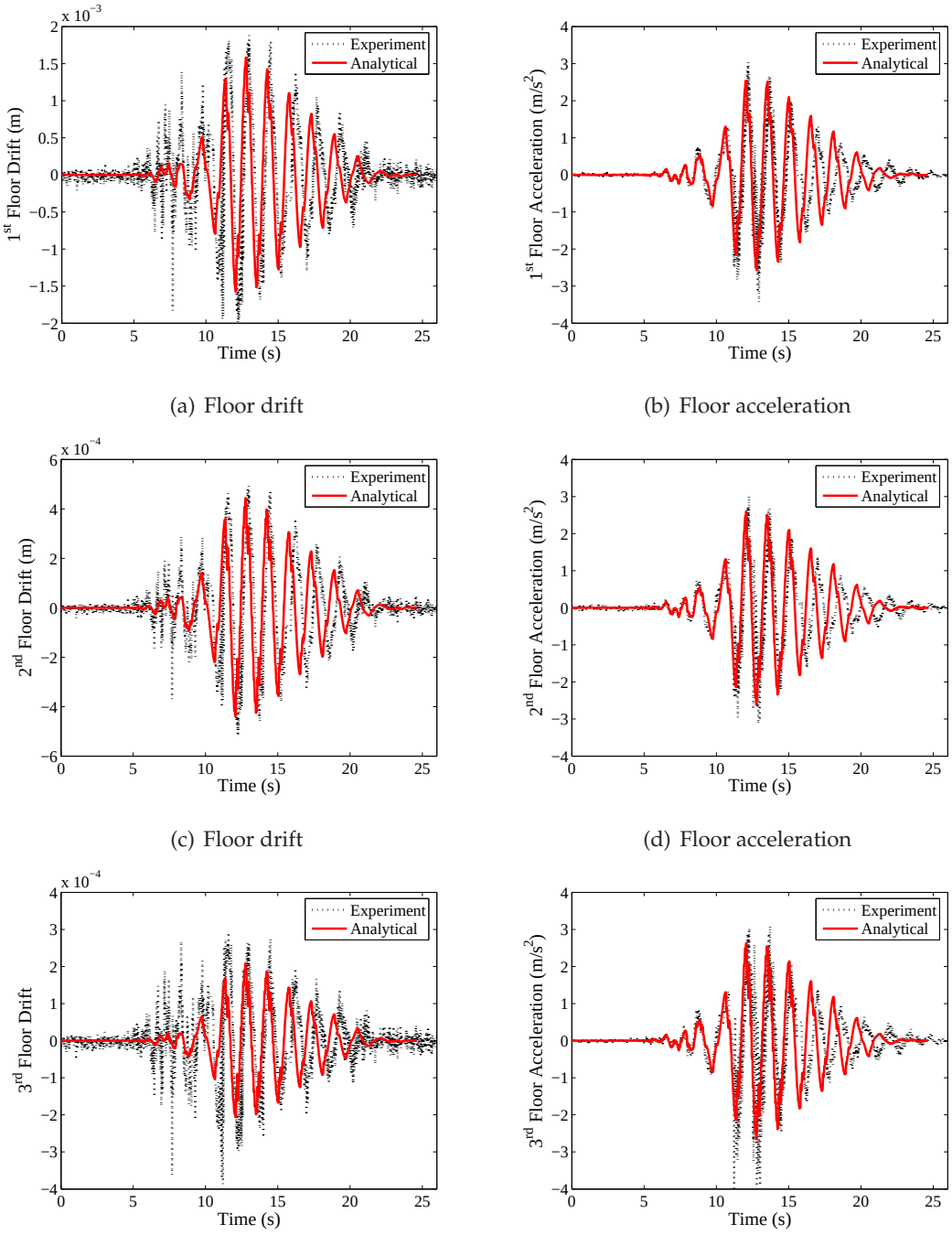

(a) Floor drift

(b) Floor acceleration

(c) Floor drift

(d) Floor acceleration

(e) Floor drift

(f) Floor acceleration

Figure 5.23: Floor responses of simple base isolated building (N. palm springs (X))

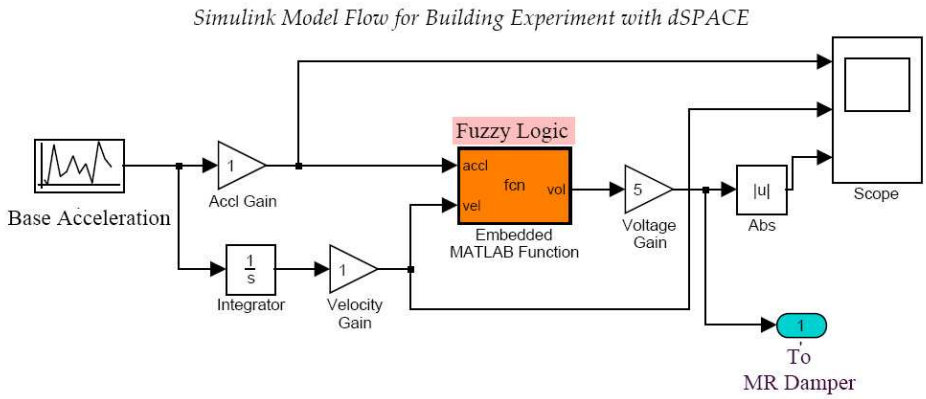

Figure 5.24: Simulink model for hybrid isolated building experiment with dSPACE

good match is observed between experimental and analytical results. The base isolator displacement is the least in this case compared to other hybrid isolation cases, whereas the floor responses have gone higher than 'passive-off' case (see Table 5.3).

SFLC monitored MR damper control

Fuzzy logic based intelligent controller (FLC) (detailed discussion in Chapter 4) to monitor MR damper input voltage provides a slow and smooth change in voltage input to the damper. Therefore, FLC driven variable current/voltage monitoring of MR damper provides an improved performance of MR damper having goodness of both 'passive-off' and 'passive-on' cases, *i.e.*, it helps in reducing isolator displacement as well as prevents the rise in the acceleration too much (as seen in 'passive-on' case). Simple FLC (SFLC) is a FLC whose parameters are chosen manually based on human experience. One can see Chapter 4 for details on the parameters of SFLC.

The numerical and experimental responses of the three storey building with SFLC driven hybrid isolation are shown in Fig. 5.27. A good agreement is seen between experimental and analytical results. The initial starting position of the base isolator is not zero as observed from the Fig. 5.27(a). This is because in most of the experiments the base of the building does not reach its initial zero position as the seismic excitation ends. An effort is carried out to manually position the structure to its zero reference condition but still some difference remains.

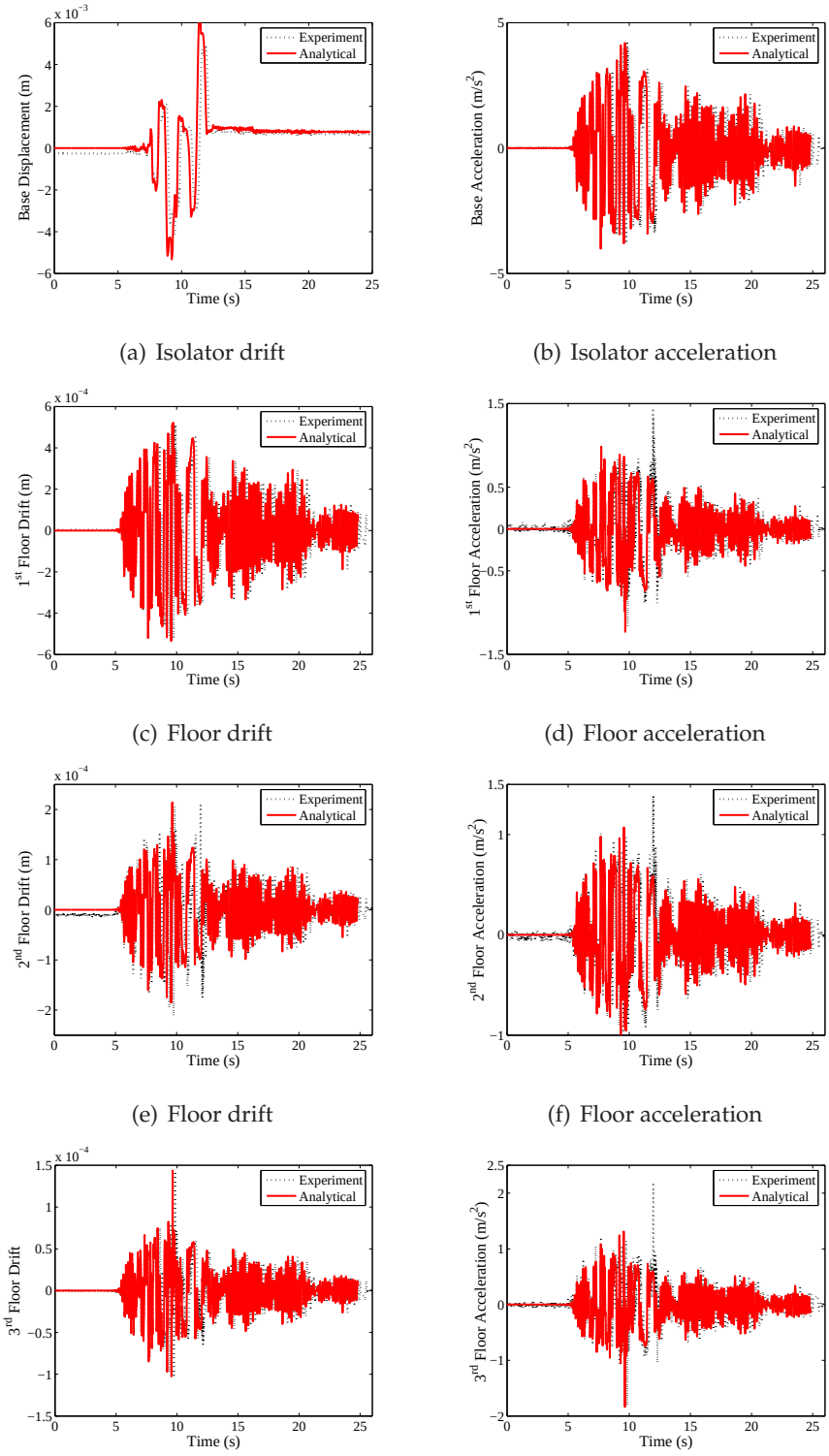

(a) Isolator drift

(b) Isolator acceleration

(c) Floor drift

(d) Floor acceleration

(e) Floor drift

(f) Floor acceleration

(g) Floor drift

(h) Floor acceleration

Figure 5.25: Hybrid isolated building responses under N. palm springs (X) (MR damper 'passive-off' condition)

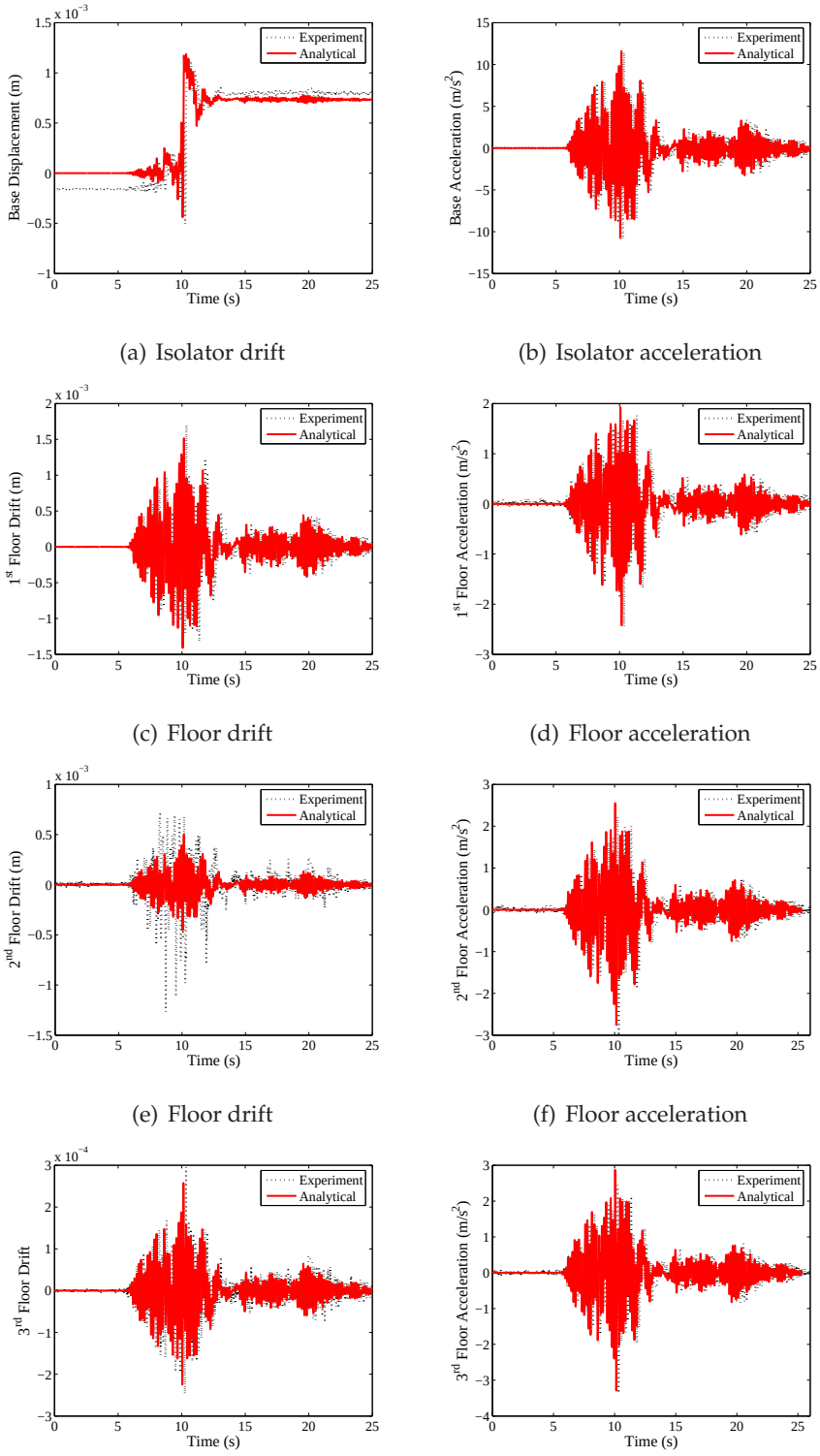

(a) Isolator drift (b) Isolator acceleration

(c) Floor drift (d) Floor acceleration

(e) Floor drift (f) Floor acceleration

(g) Floor drift (h) Floor acceleration

Figure 5.26: Hybrid isolated building responses under N. palm springs (X) (MR damper 'passive-on' condition)

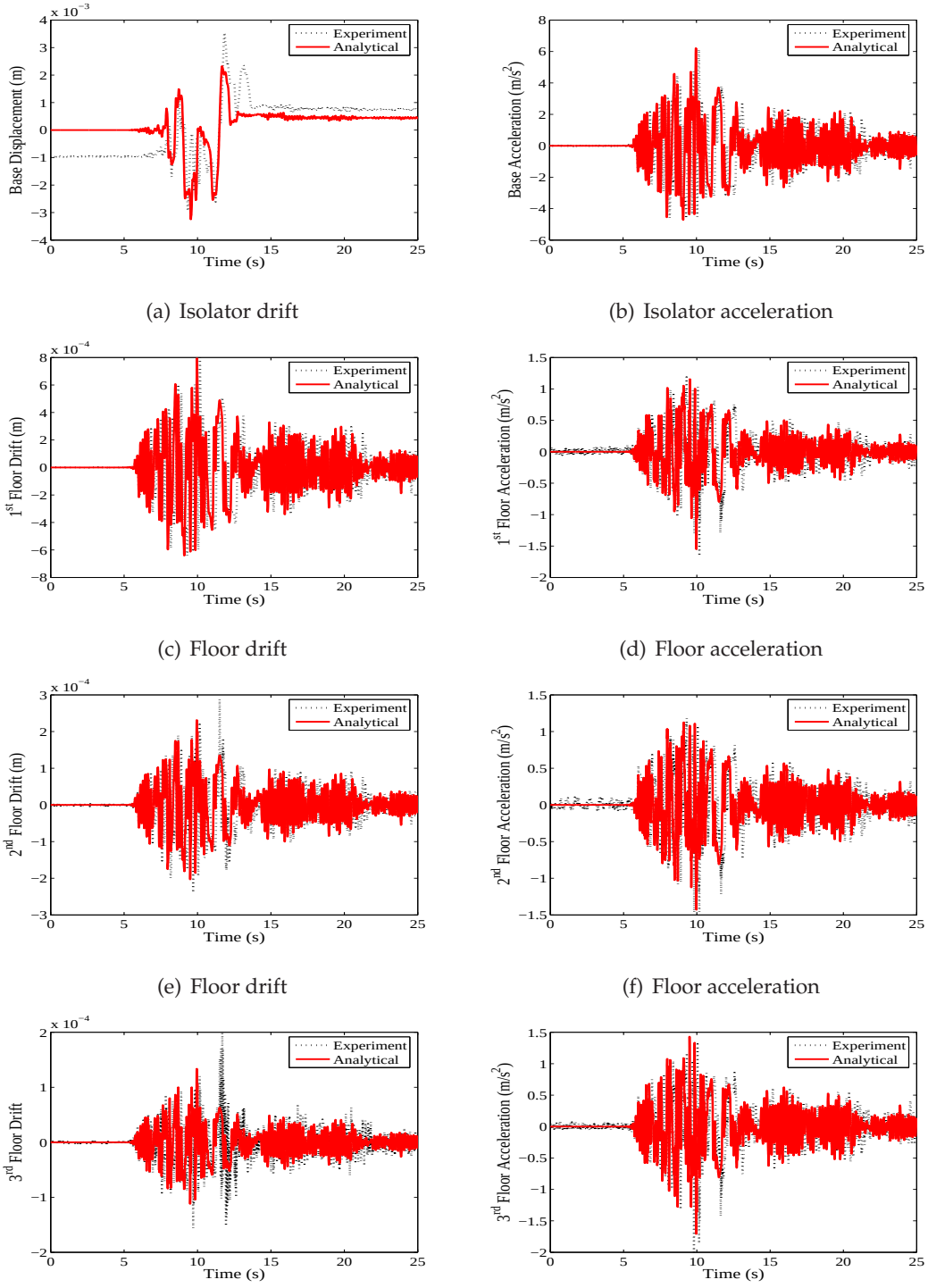

(a) Isolator drift

(b) Isolator acceleration

(c) Floor drift

(d) Floor acceleration

(e) Floor drift

(f) Floor acceleration

(g) Floor drift

(h) Floor acceleration

Figure 5.27: Hybrid isolated building responses under N. palm springs (X) (SFLC monitored MR damper)

GA-FLC monitored MR damper control

Since, in SFLC, the parameters are chosen based on experience of the control designer, it is never optimal. To obtain an optimal FLC, an optimization is carried out using micro-GA. The optimization algorithm and the optimization schemes are discussed in details in Chapter 4. For the experimental study an off-line trained FLC is adopted. The hybrid base isolated building is given an initial displacement of 0.025m (maximum stroke of MR damper) and then allowed to come to rest. The FLC is optimized such that it minimizes the following cost function.

$$J_{ga} = \left\| \frac{x_b}{x_{b_{unc}}} \right\| + \left\| \frac{\ddot{x}_b}{\ddot{x}_{b_{unc}}} \right\| \tag{5.15}$$

The above cost function considers minimization of L_2 norm of the ratio of base displacement (x_b) with controller and base displacement ($x_{b_{unc}}$) with-out controller and at the same time minimizing the corresponding ratio of acceleration norm.

Figure 5.28 shows the rule base surface obtained from the optimization process. The input MFs partitioning for acceleration and velocity input variables are shown in Fig. 5.29. Figure 5.30 shows the output MF partitioning obtained as a result of the optimization process.

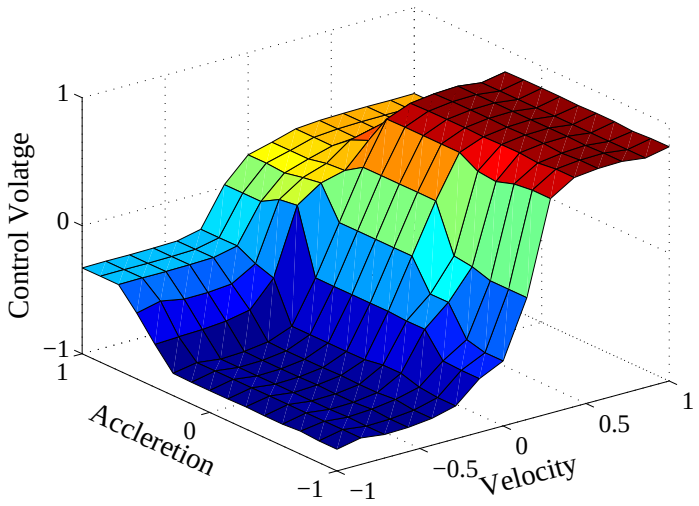

Figure 5.28: Optimal fuzzy rule base for GAFLC based MR damper monitoring

The responses of GAFLC condition are shown in Fig. 5.31. A good agreement is seen between experimental and analytical results except in the case of isolator drift (Fig. 5.31(a)).

The experimental peak displacement in the GA-FLC case is found to be 0.0028m which is less than SFLC case and higher than 'passive-on' case. This reduction in isolator displacement has resulted in the increase in the isolator acceleration. But the increase is not much in respect to the 'passive-on' case. A comparison of the different control cases are given in next section.

5.5.3 Comparison of experimental test results

The main thrust of the experimental study is to evaluate the performance of the GA optimized FLC for hybrid structural control. To assess the performance a comparative analysis of the experimental results are carried out. Comparative results of all test cases for some typical seismic motion cases considering near fault and far fault earthquakes are reported. The important consideration in the analysis of hybrid base isolation is the isolator displacement, the acceleration at the isolation level and the acceleration in the super structure. Displacement and acceleration at the isolation are discussed separately next and the maximum values for the super structure response are tabulated.

Base isolator displacement

It is discussed in an earlier section that the seismic base isolator undergoes large base displacement under near fault seismic motions. To restrict this large base displacement supplemental dampers are used. In this study a single MR damper is implemented for the hybrid base isolation mechanism. Figure 5.32 shows the plot for different test control case under N. Palm

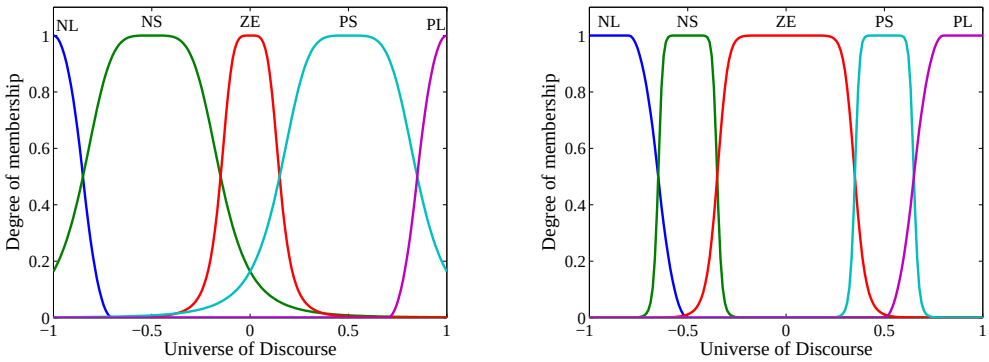

(a) MFs for acceleration input

(b) MFs for velocity input

Figure 5.29: MF partitioning for input variables used in 'GAFLC' based hybrid control

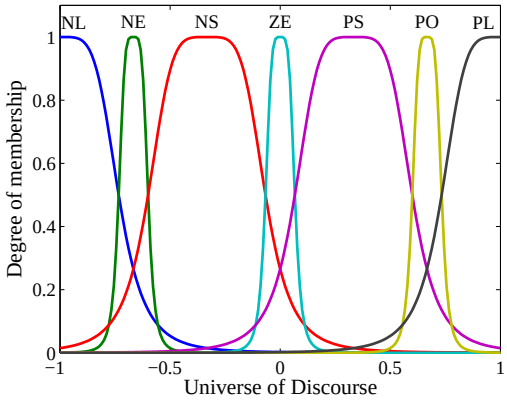

Figure 5.30: MF partitioning for output voltage used in 'GAFLC' based hybrid control

Spring (X) earthquake (near fault behavior is seen from the pulse nature of the seismic displacement (Fig. 5.32(a))). Figure 5.32(a) shows the input seismic displacement as measured from the LVDT connected to the shake table, whereas Figs. 5.32(b) to 5.32(f) show the isolator displacement under various test conditions.

The legends in the figures have the following meaning; 'BI' represents isolator displacement when only base isolation is acting; 'passive-off' represents MR damper driven with 0A current supply, *i.e.*, when no voltage is supplied to the MR damper; similarly, 'passive-on' represents hybrid isolation condition, when 2.5V voltage (or one ampere current) is supplied to the MR damper; 'SFLC' represents the condition when the MR damper is monitored by a manually designed FLC and 'GAFLC' represents the condition when the MR damper is monitored by a GA optimized FLC.

As shown in Figs. 5.32(a) and 5.32(b), for a maximum of $0.05\ m$ displacement at the support, the isolator level displacement at no MR damper condition is $0.16\ m$ (see Table 5.3). In 'passive-off' condition this isolator displacement is brought down to $0.005\ m$. The hybrid base isolation mechanism reduces the drift demand on the isolators in near field earthquakes. Similarly, the isolator displacement is found to be a minimum in all test cases of the MR damper. 'Passive on' case provides the least isolator displacement of $0.001\ m$. The variable voltage input to MR damper, provided by SFLC and GAFLC, provides a performance in between the 'passive off' and 'passive on' cases. In the case of SFLC and GAFLC the isolator displacement are found to be $0.0035\ m$ and $0.0028\ m$ respectively.

Figure 5.33 shows displacement responses for the test structure under El-Centro (X-direction)

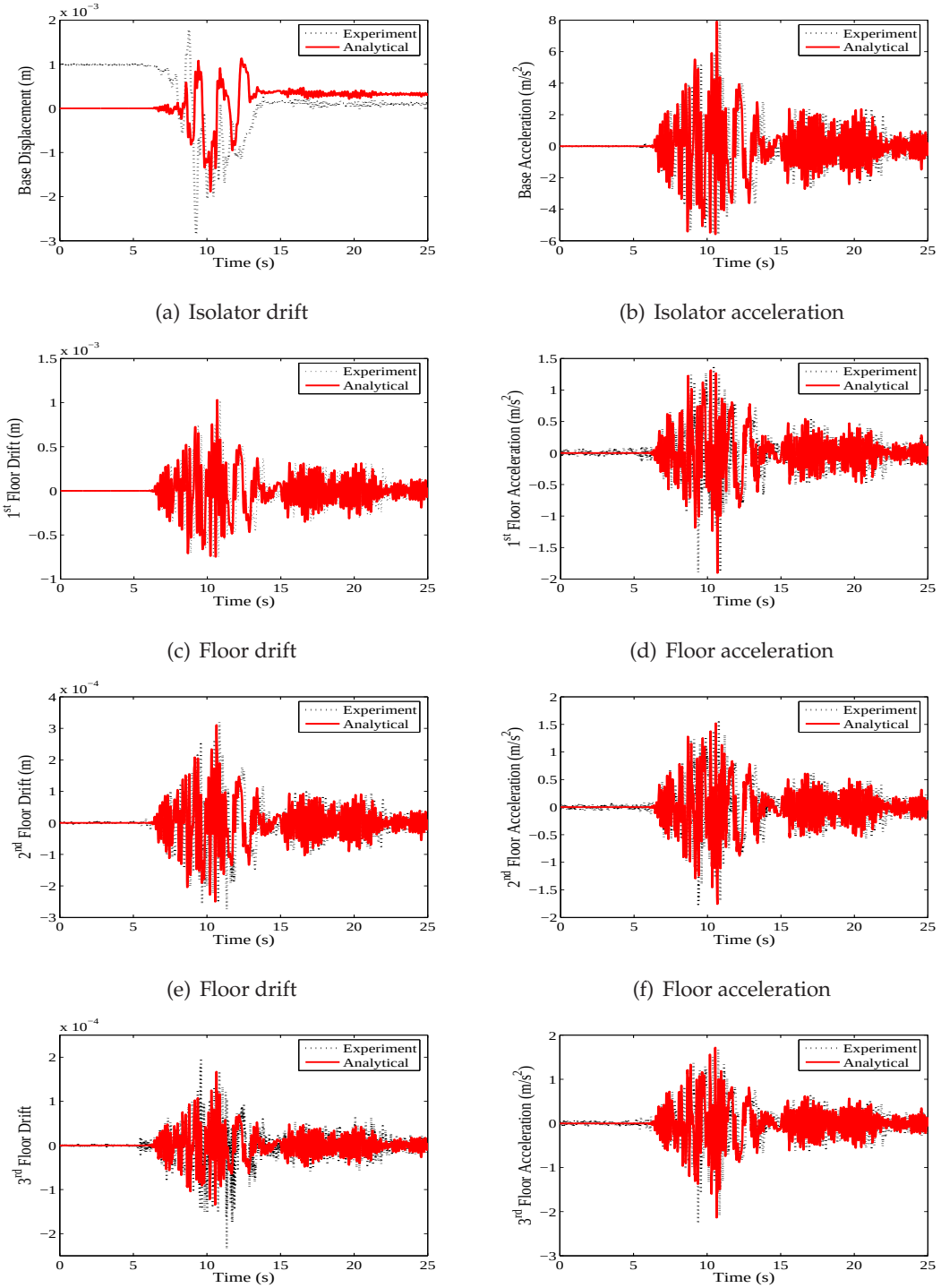

(a) Isolator drift

(b) Isolator acceleration

(c) Floor drift

(d) Floor acceleration

(e) Floor drift

(f) Floor acceleration

(g) Floor drift

(h) Floor acceleration

Figure 5.31: Hybrid isolated building responses under N. palm springs (X) (GAFLC monitored MR damper)

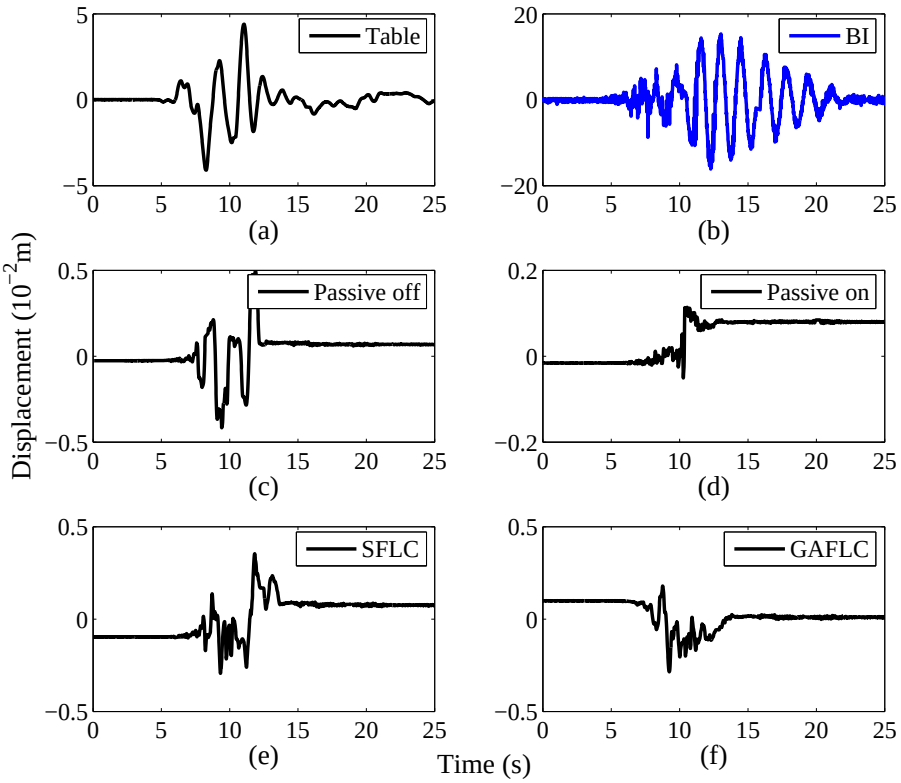

Figure 5.32: Displacement under N. Palm Spring (X) earthquake: (a) excitation input at shake table, (b)-(f) isolator displacement for different control strategies

earthquake (has far-fault nature). It is to be noted that the isolator displacement is not as much as seen in N. Palm Spring case (compare Figs. 5.32(a) and 5.33(a)). Although the maximum displacements of the seismic input excitation are same, the isolator displacement in El-Centro earthquake (under no MR damper case) is $0.05\ m$ only, which is three times lesser than obtained in N. Palm Spring earthquake motion. The isolator displacement in 'passive off' condition is found to be $0.01\ m$, whereas in 'passive on' case it is $0.0030\ m$. The corresponding isolator displacement in SFLC and GAFLC cases are found to be $0.0035\ m$ and $0.0027\ m$. The least displacement is found in GAFLC case.

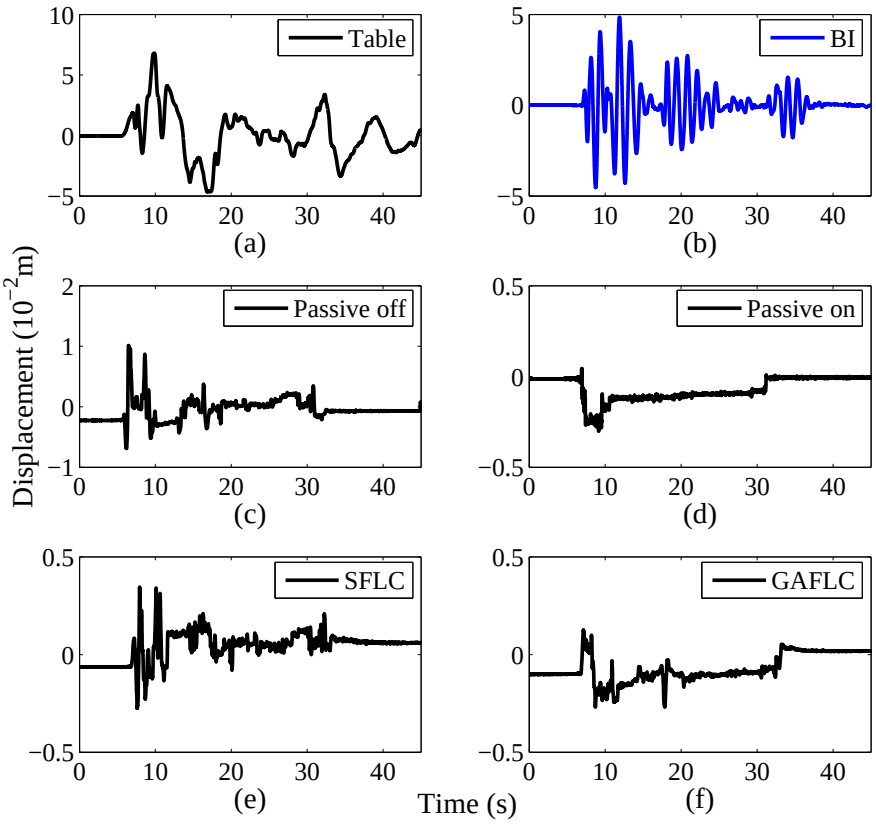

Figure 5.33: Displacement under El-Centro (X) earthquake: (a) excitation input at shake table, (b)-(f) isolator displacement for different control strategies

Acceleration at the isolation

Seismic isolators reduce super structure drift and acceleration at the cost of increase displacement at the base. Therefore, minimizing isolator displacement increases the super structure drift and acceleration, as well as, the acceleration at the isolation level. Therefore, addition of damping devices increases the acceleration level as they decrease the isolator displacement. Therefore, a trade-off should be considered between the isolator displacement and the acceleration at the isolation level. The displacement response of the test structure at isolation level for a near-fault and a far-fault seismic excitation are discussed earlier. Discussion on the acceleration at isolation level are presented here.

Figure 5.34 shows the acceleration measured at shake table and at base isolator under N.

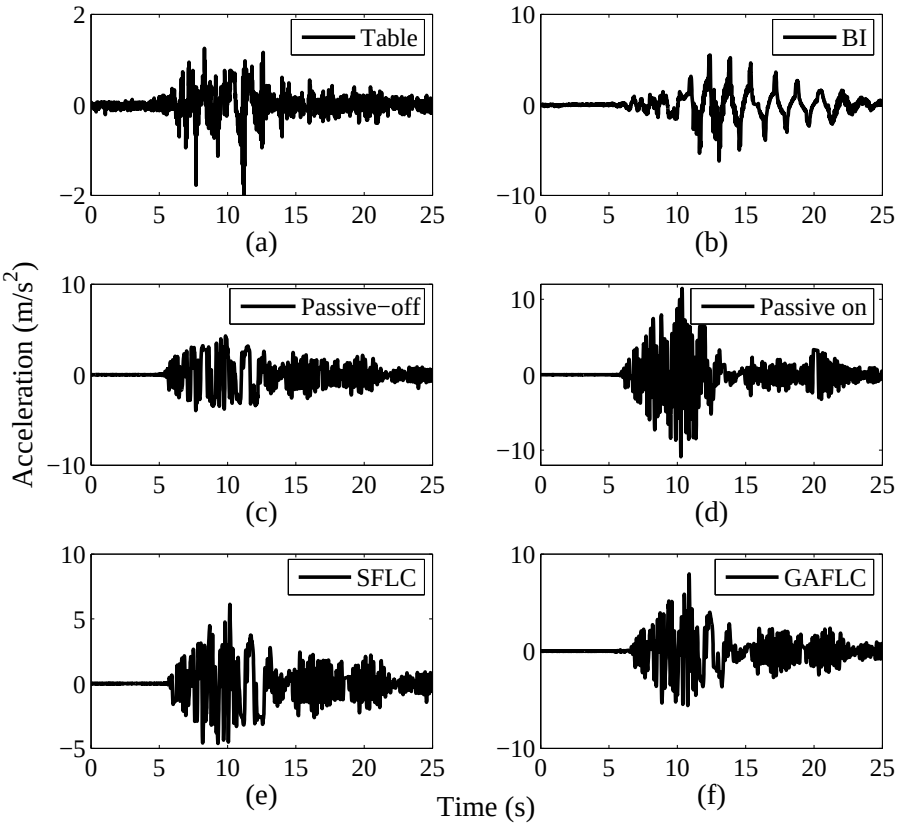

Figure 5.34: Acceleration under N. Palm Spring (X-dir) earthquake: (a) Excitation input, (b)-(f) Isolator acceleration at different cases

Palm Spring seismic ground motion. Figure 5.34(a) shows the acceleration time-history of the input seismic excitation as measured from the shake table. The acceleration at the isolation level is found to be $6.2067\ m/s^2$ for the base isolation without MR damper case (Fig. 5.34(b)). In the 'passive off' case the acceleration is reduced to $4.2783\ m/s^2$ (Fig. 5.34(c)), whereas in the 'passive-on' case the acceleration increased to $11.4227\ m/s^2$ (see Fig. 5.34(d) Table 5.3). This is because the base displacement is reduced to the least in the 'passive-on' case. The acceleration response for the SFLC case and for the GAFLC case are shown in Figs. 5.34(e) and 5.34(f) and are found to be $6.1148\ m/s^2$ and $7.9447\ m/s^2$, respectively.

Similarly the acceleration response measured at the shake table and at the base isolator are shown in Fig. 5.35. Figure 5.35(a) shows the seismic acceleration input to the structural

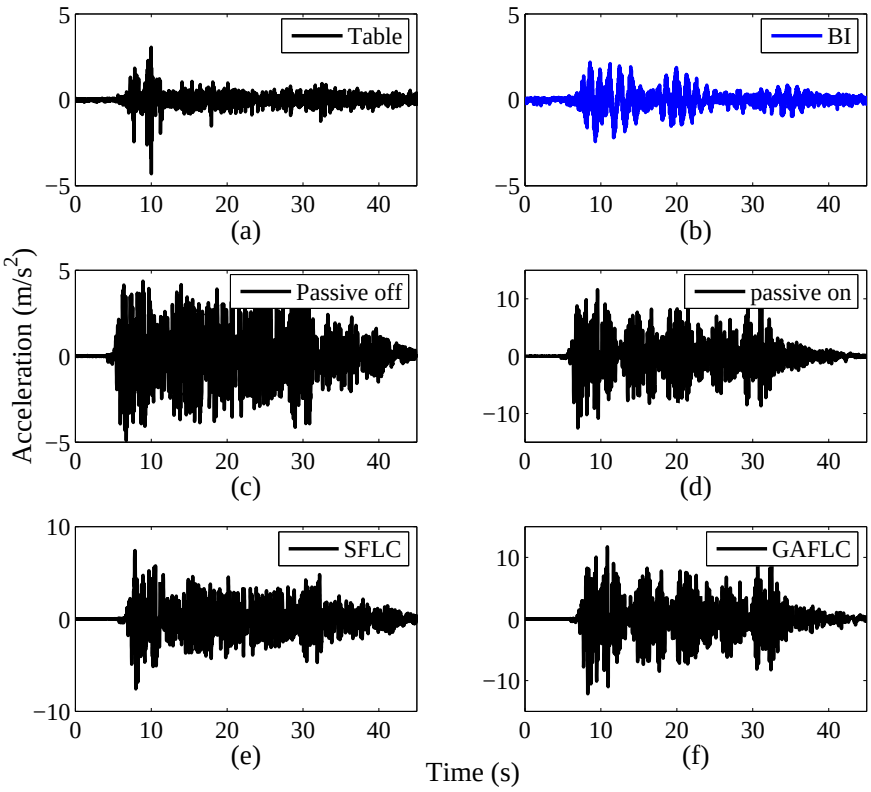

Figure 5.35: Acceleration under El-Centro (X-dir) earthquake: (a) Excitation input, (b)-(f) Base acceleration at different cases

system. Figures 5.35(b)-5.35(f) show the acceleration response for the simple base isolation and hybrid with 'passive-off', passive-on', SFLC and GAFLC conditions respectively. It is observed that the acceleration is increased from $2.4341\ m/s^2$ in simple isolation to $4.9030\ m/s^2$ in 'passive-off' condition. The acceleration response obtained for 'passive-on', SFLC and GAFLC cases are $12.5279\ m/s^2$ $7.5768 m/s^2$ and $12.1523\ m/s^2$ respectively. In this case also the maximum acceleration is observed in 'passive-on' case.

Voltage input to MR damper

One important motivation behind the adoption of FLC based MR damper monitoring is to provide smooth voltage (variable voltage) update across the MR damper, *i.e.*, there is no sudden jump in the voltage time history. Figure 5.36 shows the voltage input to the MR damper

under N. Palm Spring seismic motion for SFLC and GAFLC. The variable voltage input to the MR damper is evident from the Fig. 5.36. Figure 5.36(a) shows the experimental and analytical input voltage in SFLC based hybrid control and Fig. 5.36(b) shows the experimental and analytical input voltage in the GAFLC based hybrid control. It is seen that the voltage input is more in case of GAFLC than SFLC and in both the cases maximum 5 volts is not supplied to the MR damper.

Comparison of results

The maximum displacement and the acceleration responses of the test building under various test conditions are tabulated in Table 5.3 for N. Palm Spring seismic motion and in Table 5.4 for El-Centro seismic motion. While carrying out the tests the measurements are started a few seconds before the application of the earthquake records and stopped a few seconds beyond the earthquake record. This makes the meaning of normed responses unrealistic for the present analysis and therefore the normed responses are not reported. Structural responses obtained in fixed base condition building (building without isolation and dampers) is also provided in the Tables 5.3-5.4. Since, in the fixed base condition set-up the base plate is not provided the entries in Tables 5.3-5.4 corresponding to the response at isolator level for fixed base condition is kept zero.

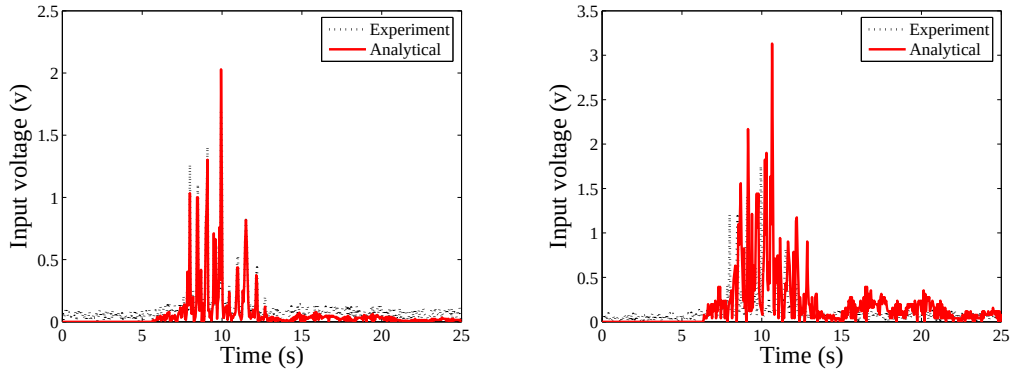

(a) MR damper voltage (SFLC) (b) MR damper voltage (GAFLC)

Figure 5.36: Variable voltage input for SFLC and GAFLC based hybrid control (N. Palm spring (X))

The maximum base displacement is found in the case where the isolation is not supplemented with a damper. At the same time, the introduction of the base isolator reduces the super structure inter-storey drift (except at third floor) and acceleration at all the floors. Similarly, both super structure inter-storey drift and acceleration at all floors are reduced by the hybrid isolation in 'passive-off' condition (0A). 'Passive-off' hybrid condition also decreases the response at the isolator level (both relative displacement and floor acceleration). In 'passive-on' condition (1A) a decrease in isolator displacement is observed but at the cost of an increase in isolator acceleration. The super structure inter-storey drift is observed to be higher than that observed for the fixed base condition in second and third floor, but the super structure acceleration response remained lower than the corresponding fixed base values. A better performance is observed for the variable voltage control using FLC. SFLC results in a decrease in the super structure inter-storey drift and the acceleration in comparison to that of the fixed base condition and the simple base isolated system. The super structure responses when SFLC is applied offered responses that are comparable to the 'passive-off' case, but resulted in a decreased base displacement more than that of seen in the 'passive off' case. Similar, performance is improvement in the GAFLC case. In this case also the super structure acceleration responses are far better than that seen in the fixed base and simple base isolated case.

Table 5.3: Experimental Results: Peak Responses under N. Palm Spring (X) earthquake

Test Case	**Relative Displacements ($\times 10^{-2}$ m)**				**Floor Acceleraions (m/s^2)**			
	BI	*FF*	*SF*	*TF*	*BI*	*FF*	*SF*	*TF*
Fixed Base	0.0000	0.2363	0.0656	0.0259	0.0000	4.1331	3.1831	4.4149
Base Isolated	16.1450	0.1993	0.0520	0.0387	6.2067	3.4458	3.1298	4.0787
0A	0.4944	0.0527	0.0213	0.0143	4.2783	1.4427	1.3976	2.1875
1A	0.1139	0.1708	0.1268	0.0296	11.4227	2.4429	2.9560	3.2977
SFLC	0.3543	0.0800	0.0288	0.0205	6.1148	1.6576	1.4659	2.0359
GAFLC	0.2859	0.1026	0.0320	0.0235	7.9447	1.8944	1.7624	2.2667
BI: *Base Isolator* *FF*: 1^{st} *floor* *SF*: 2^{nd} *floor* *TF*: 3^{rd} *floor*								

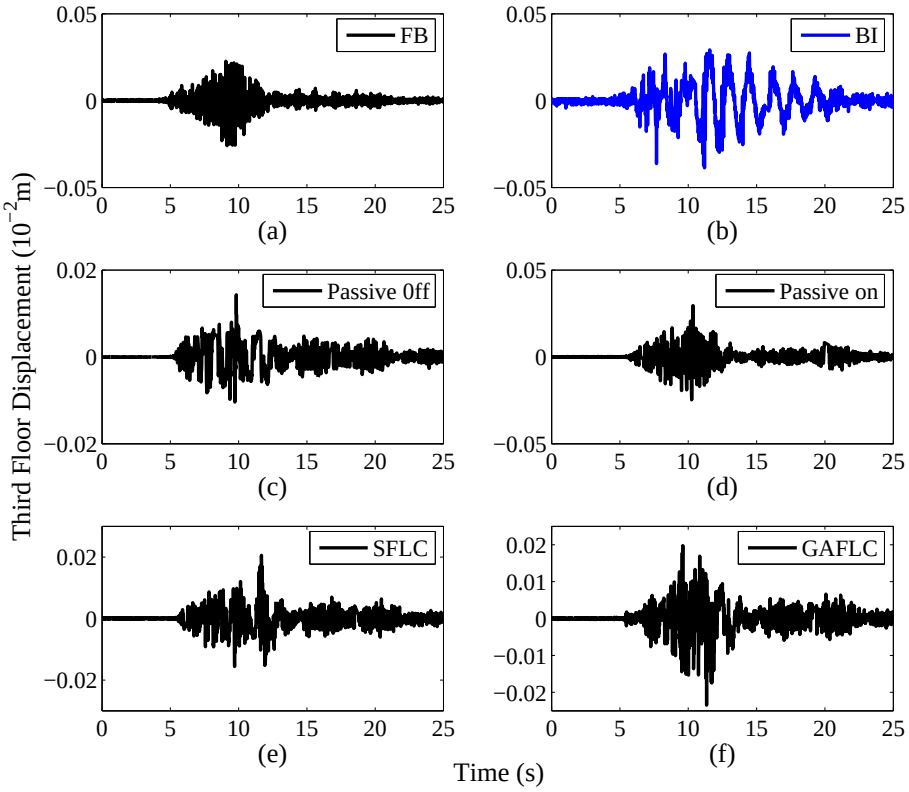

Figure 5.37: Inter-storey drift at 3^{rd} floor under N. Palm Spring (X) earthquake

GAFLC decrease the isolator displacement more than that observed in other case (except for 'passive-on' case) with a marginal increase in base acceleration.

The third floor inter-storey drift responses for various control cases under N. Palm Spring (X-dir) seismic ground motion are shown in Fig. 5.37. Figure 5.37(a) shows the 3^{rd} floor inter-storey drift for fixed base condition. It is observed that the inter-storey drift is reduced by the hybrid isolation system in relation to the fixed base condition. The reduction in third floor drift is maximum in 'passive-off' case of the hybrid control scheme. This can be attributed to the fact that at no voltage condition, the damper develops less hysteresis (see Chapter 3 for details) and therefore does not provide much resistance to the base motion besides a moderate energy dissipation. This results in higher base displacement and lower super structure response. The simple isolation case could not provide similar performance in decreasing the third floor response as it does not have any energy dissipating device connected to it.

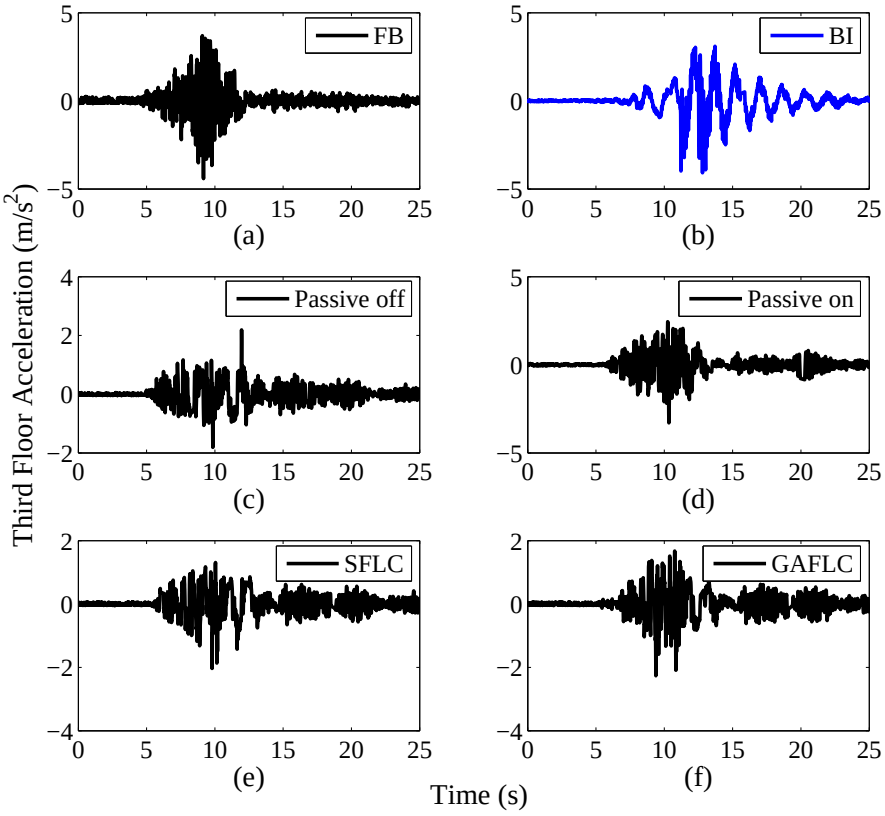

Figure 5.38: Acceleration time history at 3^{rd} floor under N. Palm Spring (X) earthquake

Similar to the third floor inter-storey drift, the third floor acceleration is shown in Fig. 5.38. The floor acceleration is observed to decrease using isolation system and it is further decreased on use of hybrid isolation. Among the hybrid mechanisms, the acceleration response is lowest in 'passive-off' case, where as it is the maximum in 'passive-on' case because of increased transmissivity with the damper activation. Both the FLCs provide a displacement and acceleration response that is a trade-off between the 'passive-off' and 'passive-on' cases, which is evident from the variable voltage input nature of FLC algorithms.

Figure 5.39 shows the force provided by the MR damper to reduce the base displacement for the four control cases. From Fig. 5.39(a), it appears that the force provided for 'passive-off' condition is the highest, but that may be due to some sudden jerks, but overall the force provided by the damper at 'passive-on' condition is maximum. It may also be observed that the force provided by the MR damper operated by GAFLC requires less force than 'passive-on'

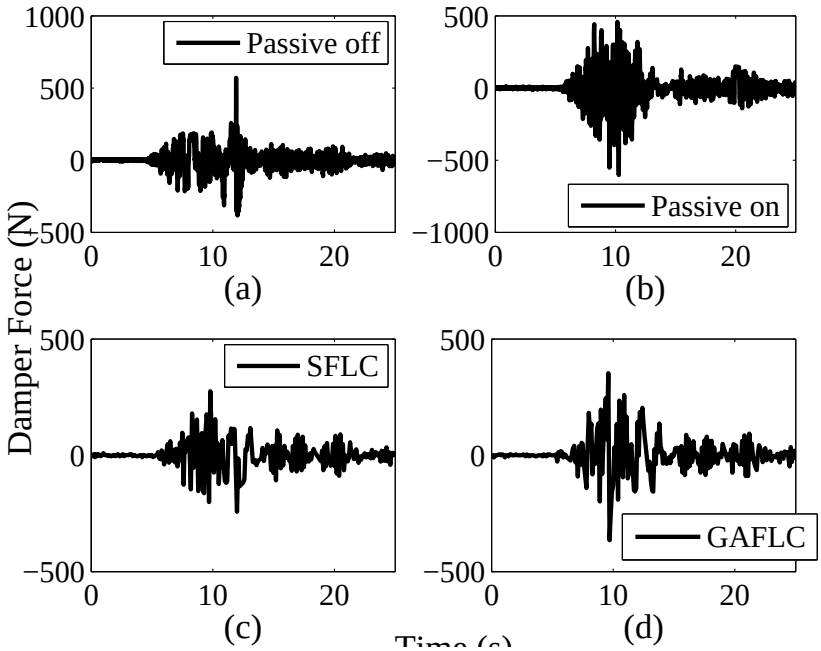

Figure 5.39: MR damper force time history under N. Palm Spring (X) earthquake

case and marginally higher force than 'passive-off' case to provide a better trade-off between the base displacement and base acceleration (see objective function in Eq. 5.15).

Peak values of responses under El-Centro (X-dir) earthquake are given in Table 5.4. The displacement response at the base isolator is measured relative to the ground and the floor displacement are inter-storey drifts.

Similar to the N. Palm Spring seismic motion, the peak base displacement is found to be when the isolation is not supplemented with a damper (0.0485m). Unlike N. Palm Spring earthquake the floor inter-storey drifts are reduced to $10\% - 20\%$ of their respective values in fixed base condition. Similarly, the floor accelerations are also reduced to $20\% - 25\%$ of their respective values in fixed base condition. This shows the efficiency of the base isolators under far-fault seismic motion. If one compares the performances of simple base isolation mechanism given in Table 5.4 (far fault ground motion) with Table 5.3 (where responses under a near-fault seismic motion are tabulated), it can be observed that simple base isolation is efficient in reducing structural responses in far-fault motion and similar effectiveness is not realized in near-fault motions.

Table 5.4: Experimental Results: Peak Responses under El-Centro (X) earthquake

Test Case	**Relative Displacements** ($\times 10^{-2}\ m$)				**Floor Acceleraions** (m/s^2)			
	BI	*FF*	*SF*	*TF*	*BI*	*FF*	*SF*	*TF*
Fixed Base	0.0000	0.3150	0.0783	0.0802	0.0000	6.6422	4.7754	5.9761
Base Isolated	4.8553	0.0596	0.0175	0.0091	2.4341	1.4091	1.2225	1.6091
0A	1.0122	0.0649	0.0247	0.0169	4.9030	1.5124	1.3334	2.1764
1A	0.3018	0.1963	0.2102	0.0465	12.5279	2.5878	3.3258	3.7917
SFLC	0.3455	0.0957	0.0355	0.0384	7.5768	1.8549	1.7715	2.1276
GAFLC	0.2694	0.1597	0.0528	0.0456	12.1523	2.7093	2.8704	3.3359
BI: *Base Isolator* *FF*: 1^{st} *floor* *SF*: 2^{nd} *floor* *TF*: 3^{rd} *floor*								

Addition of MR damper as supplemental damping device has not only reduced the base drift but increased all floor inter-storey drift as well as acceleration at all floors and base in comparison to the values obtained for the simple base isolated system. The hybrid control mechanism has shown a similar trend as seen in N. Palm Spring seismic motion. The 'passive-off' control case provided poor performance in decreasing isolator displacement, whereas the 'passive-on' case provided effective control. The FLCs respond in between the 'passive-off' and 'passive-on' control cases. Similarly, the acceleration responses are lower in 'passive-off' case but highest in 'passive-on' case.

The third floor inter-storey drift responses for various control cases under El-Centro (X-dir) seismic ground motion are shown in Fig. 5.40. Figure 5.40(a) shows the 3^{rd} floor inter-storey drift at fixed base condition. The reduction in the inter-storey drift on installation of base isolation is evident from Fig. 5.40(b). Figure 5.40 also shows the increase in third floor inter-storey drift in hybrid isolation cases than that obtained with simple isolation.

Similarly, the third floor acceleration is shown in Fig. 5.41. The floor acceleration is observed to decrease using simple and hybrid isolation systems. There is a rise in floor acceleration in hybrid isolation case in comparison to that obtained with simple isolation.

Figure 5.42 shows the force provided by the MR damper to reduce the base displacement

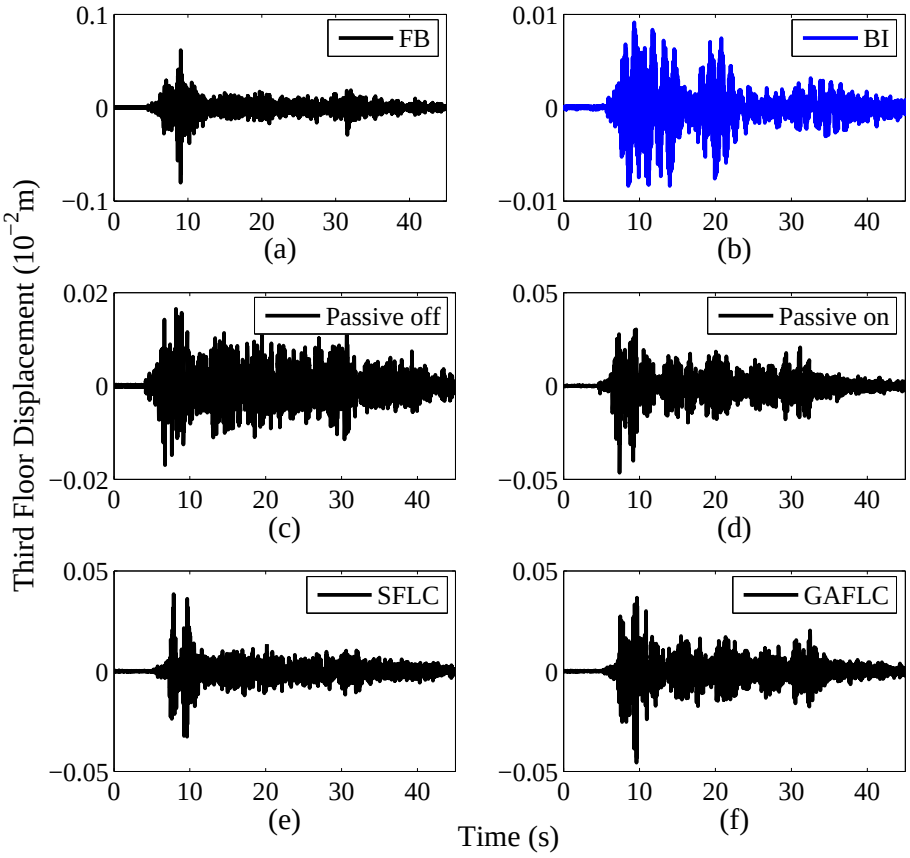

Figure 5.40: Inter-storey drift at 3^{rd} floor under El-Centro (X) earthquake

for the four hybrid control cases. It is observed that from Fig. 5.39(c) that the force provided at 'passive-on' condition is the highest. Similar to N. Palm Spring seismic motion, it is observed that the force provided by the MR damper operated by GAFLC requires less force than 'passive-on' case to provide a better trade-off between the minimization of base displacement and base acceleration (see objective function in Eq. 5.15).

Power spectral density (psd) of third floor inter storey drift for fixed base building and simple base isolation system are shown in Fig. 5.43. A peak near 5Hz is observed in the psd of fixed base building which is absent in the base isolated system, which shows a peak at about 1Hz. Therefore the fundamental frequency of the structure is shifted to 1Hz on introduction of base isolation. Figure 5.44 shows the psd of relative displacement at the isolator for simple base isolation and for the four cases of hybrid isolation system. An enlarged view upto 5Hz is

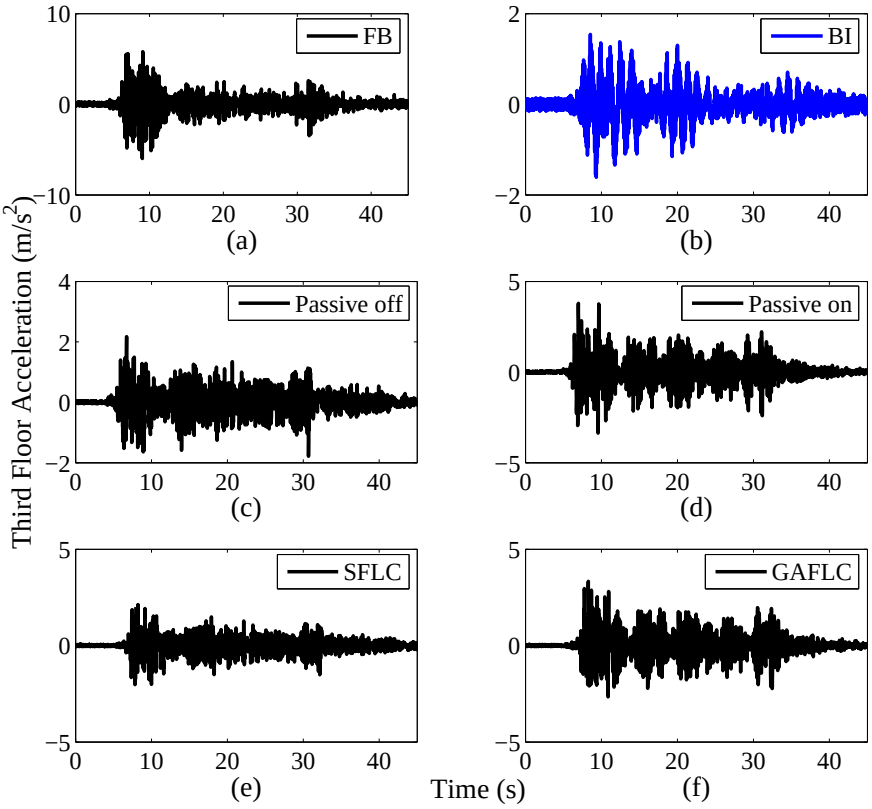

Figure 5.41: Acceleration at 3^{rd} floor under El-Centro (X) earthquake

shown in Fig. 5.44(b). Figure 5.44(b) shows that the peaks in the simple base isolation system are eliminated by all four hybrid control strategies.

Tables 5.5 and 5.6 show the peak responses of the experimental results obtained under the eight seismic records with X and Y components of seismic motions, respectively. Tables 5.3 and 5.6 provide the peak responses (relative displacement and acceleration) obtained at the base and peak responses across all the floors of the superstructure. The peak control force provided by the MR damper is also given in the Tables. The maximum inter-storey drift ($max(d_i)$) and acceleration ($max(\ddot{x}_i)$) across all floors in the fixed base condition of the building are also provided.

In Tables 5.5 and 5.6 maximum inter storey floor drift in the superstructure is represented as $max(d_i)$. The higher value of peak inter storey drift is observed in fixed base building.

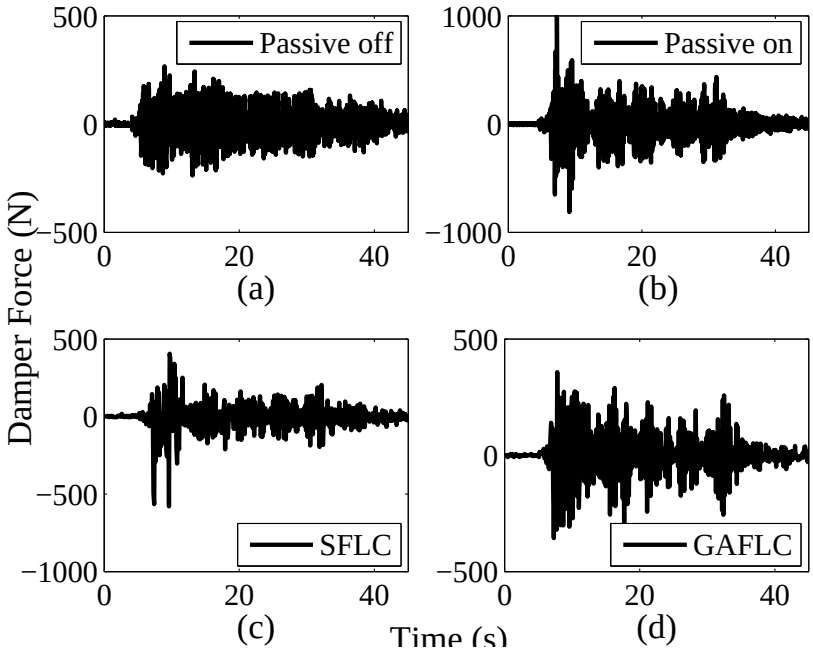

Figure 5.42: MR damper force time history under El-Centro (X) earthquake

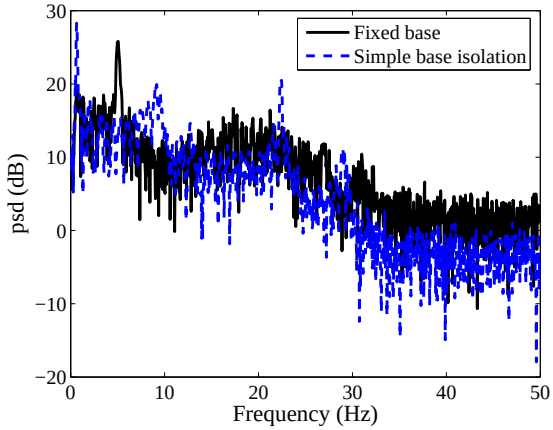

Figure 5.43: PSD of third floor drift for fixed base and simple base isolation under N. Palm spring (X) earthquake

This peak value of inter storey drift has come down with the simple base isolation mechanism except for Big-Bear (X), Chichi (X) and N. Palm Spring (Y) seismic motions. The peak floor displacements in simple base isolated structure are found to be of same values as that of fixed

base building. The four hybrid control conditions show a mixed performance when the peak inter storey drift is considered. For some seismic motions (like, Big Bear (X)) $\max d_i$ has increased for all four conditions and for Coalinga (X) seismic motion building with the hybrid control has shown better performance than fixed base building.

It is evident from the Table 5.5, that among the four hybrid control conditions ('passive-off', 'passive-on', SLFC and GAFLC) the larger base displacement (x_b) is seen in 'passive-off' case except in Big-Bear (X) seismic motion. SFLC based MR damper monitoring provides highest base displacement among the hybrid control conditions in Big-Bear (X) earthquake. Similarly, in Y-direction components of seismic excitations for Loma-prieta and Kobe excitations hybrid isolated building monitored by SFLC has shown highest base displacement. In all other seismic record 'passive-off' condition of MR damper provides larger base displacement.

Base isolator acceleration is found to be minimum when the building is tested with 'passive-off' MR damper condition. Experiments of the hybrid isolation system when MR damper is at 'passive-on' condition, *i.e.*, 1 ampere current is supplied to the MR damper, has shown larger base accelerations levels than other hybrid control conditions. This is not the case with Coalinga (X) seismic motion, where the hybrid base isolated building with GAFLC monitored MR damper has shown a little higher accelerations levels than 'passive-on' case.

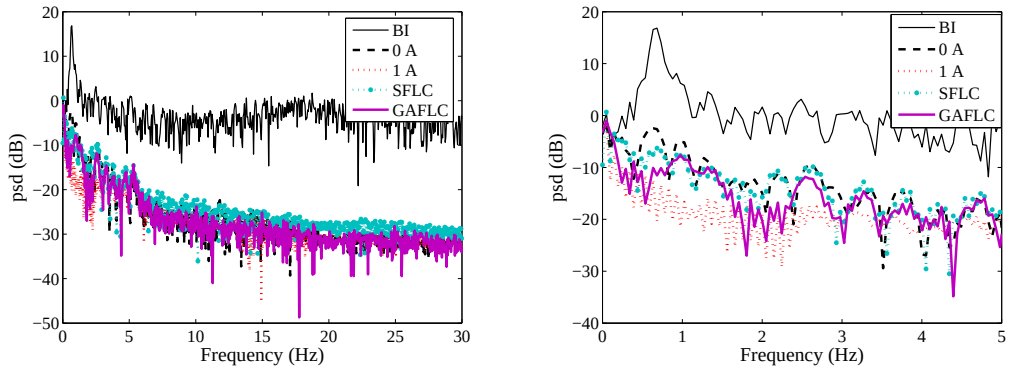

(a) PSD of base isolator displacement

(b) PSD of base isolator displacement (enlarged view)

Figure 5.44: PSD of isolator relative displacement for different control strategies under N. Palm spring (X) earthquake

Table 5.5: Peak Responses of Experimental Results under X-direction seismic motion

State	Control	Earthquake records							
		Big-Bear	Cape-mend	Chichi	Coal-inga	El-Centro	Loma-prieta	N.Palm Spring	Kobe
x_b (10^{-2}m)	Base Isolated	5.985	7.838	8.549	5.416	4.855	6.982	16.145	2.790
	Passive-off	0.013	1.166	0.434	2.425	1.012	0.081	0.494	0.055
	Passive-on	0.148	0.126	0.026	0.950	0.302	0.010	0.114	0.010
	SFLC	0.243	0.538	0.314	0.861	0.346	0.082	0.354	0.056
	GAFLC	0.224	0.144	0.140	0.519	0.269	0.068	0.286	0.047
$max(d_i)$ (10^{-2}m)	Fixed Base	0.064	0.438	0.108	0.719	0.315	0.073	0.236	0.074
	Base Isolated	0.066	0.096	0.108	0.061	0.060	0.077	0.199	0.031
	Passive-off	0.151	0.071	0.292	0.101	0.065	0.039	0.053	0.045
	Passive-on	0.135	0.170	0.050	0.201	0.210	0.076	0.171	0.079
	SFLC	0.080	0.113	0.101	0.217	0.096	0.067	0.080	0.050
	GAFLC	0.087	0.168	0.057	0.227	0.160	0.048	0.103	0.061
$\ddot{x}_b$ (m/s)	Base Isolated	2.329	5.079	9.949	2.782	2.434	3.054	6.207	1.642
	Passive-off	11.409	4.397	3.908	10.267	4.903	3.192	4.278	3.157
	Passive-on	10.168	11.962	7.569	15.619	12.528	5.712	11.423	5.950
	SFLC	6.320	7.116	4.176	16.952	7.577	3.249	6.115	3.453
	GAFLC	6.541	11.338	4.980	17.363	12.152	3.533	7.945	4.140
$max(\ddot{x}_i)$ (m/s)	Fixed Base	1.727	6.211	1.806	9.406	6.642	2.005	4.415	1.278
	Base Isolated	1.363	2.335	1.410	1.562	1.609	1.974	4.079	0.504
	Passive-off	2.902	1.902	1.272	4.861	2.176	0.979	2.188	0.686
	Passive-on	2.829	3.047	1.896	5.001	3.792	1.363	3.298	1.441
	SFLC	1.601	1.956	1.294	4.308	2.128	0.780	2.036	0.754
	GAFLC	1.683	3.476	1.970	4.356	3.336	0.898	2.267	0.956
f_c	Passive-off	451	153	133	268	219	220	249	128
	Passive-on	405	622	382	1102	673	244	474	237
	SFLC	329	327	347	1235	580	250	275	145
	GAFLC	408	398	277	1138	358	153	366	116

d_i: Inter storey drift at i^{th} floor *x_b: Base displacement* *$\ddot{x}_i$: Absolute acceleration at i^{th} floor*

In the above discussions it is pointed out that simple base isolation systems provide efficient vibration control of the structure in far-fault seismic excitations, but undergo large displacement under near-fault excitations. This prohibits the use of simple isolation system for

Table 5.6: Peak Responses of Experimental Results under Y-direction seismic motion

State	**Control**	**Earthquake records**							
		Big-Bear	Cape-mend	Chichi	Coal-inga	El-Centro	Loma-prieta	N.Palm Spring	Kobe
x_b (10^{-2}m)	Base Isolated	7.241	6.019	5.182	11.881	2.250	2.6907	11.017	4.101
	Passive-off	0.534	0.446	0.318	2.006	0.163	0.0387	0.327	0.027
	Passive-on	0.045	0.054	0.131	0.388	0.027	0.0089	0.022	0.008
	SFLC	0.387	0.188	0.205	0.752	0.110	0.0408	0.266	0.035
	GAFLC	0.157	0.058	0.165	0.608	0.050	0.0537	0.098	0.024
$max(d_i)$ (10^{-2}m)	Fixed Base	0.177	0.134	0.195	0.320	0.132	0.073	0.092	0.054
	Base Isolated	0.077	0.066	0.061	0.166	0.029	0.039	0.094	0.033
	Passive-off	0.058	0.054	0.053	0.082	0.049	0.037	0.045	0.039
	Passive-on	0.113	0.117	0.135	0.168	0.114	0.076	0.102	0.060
	SFLC	0.222	0.058	0.067	0.144	0.055	0.039	0.050	0.046
	GAFLC	0.069	0.116	0.085	0.169	0.106	0.043	0.062	0.039
$\ddot{x}_b$ (m/s)	Base Isolated	3.936	4.203	2.020	4.444	0.971	1.886	4.482	1.190
	Passive-off	4.190	3.636	4.250	6.254	3.805	2.844	3.919	2.592
	Passive-on	8.507	9.265	10.450	12.815	8.348	5.741	8.067	4.656
	SFLC	4.999	4.022	5.134	10.539	4.171	2.965	4.148	2.840
	GAFLC	5.225	8.722	6.322	12.664	8.024	3.249	4.657	2.814
$max(\ddot{x}_i)$ (m/s)	Fixed Base	2.713	6.798	3.486	6.035	2.122	1.158	2.843	1.440
	Base Isolated	1.691	1.746	1.717	2.431	0.404	1.045	3.007	0.805
	Passive-off	1.625	0.908	1.460	2.331	1.343	0.837	1.288	0.622
	Passive-on	2.104	2.525	2.678	3.281	2.093	1.525	1.983	1.067
	SFLC	1.750	0.987	1.320	2.587	1.418	0.815	1.887	0.636
	GAFLC	1.587	2.040	1.699	3.173	1.976	0.849	2.124	0.724
f_c	Passive-off	137	141	136	204	341	169	263	116
	Passive-on	362	270	443	515	335	295	340	184
	SFLC	520	189	278	442	207	138	547	142
	GAFLC	253	281	322	499	259	153	590	86

d_i: *Inter storey drift at* i^{th} *floor* x_b: *Base displacement* $\ddot{x}_i$: *Absolute acceleration at* i^{th} *floor*

protection of structures and the instruments housed within in near-fault seismic regions. MR

dampers can be used as supplemental damping devices along with the isolators in such situations. As seen from the experimental study, MR damper with a suitable control strategy can reduce the base isolator displacement demand as well as the floor drifts and accelerations. MR damper can be operated in 'passive-off' and 'passive-on' cases, which result in totally different control scenarios. In 'passive-off' case base displacement is not reduced efficiently but the base and the structural floor accelerations remain near the levels realized with simple base isolation. On the contrary, the 'passive-on' case provides a control situation where the displacement at the base is reduced efficiently at the cost of increase in base and floor accelerations.

It is to be noted that both of these conditions ('passive-off' and 'passive-on') are not desirable. The intension of providing isolation to a structure is to reduce floor drifts and acceleration levels which are obtained at the cost of larger displacement at the base. Therefore, with the restriction in base displacement using supplemental damper floor responses (drifts and accelerations) increase, which are not desirable. Again larger base displacement as in case of 'passive-off' case may not be desirable based on the structural design limits. Therefore a performance that has goodness of both 'passive-off' and 'passive-on' conditions of MR damper is preferred.

A trade-off between 'passive-off' and 'passive-on cases is observed in FLC (both SFLC and GAFLC) driven MR control cases except for Big Bear (X) seismic motion (see Table 5.5). In Big Bear (X) seismic motion the hybrid isolated building responses is found to be minimum in constant voltage supply ('passive-off' and 'passive-on) than that of variable voltage supply (SFLC and GAFLC). For the same seismic motion the isolator acceleration is found to be higher in constant voltage supply than that of variable voltage supply. In some of seismic motions GAFLC has shown lower bearing displacement with lower acceleration values than 'passive-on' MR damper condition (for *e.g.*, El-Centro (X) seismic motion). SFLC does not increase the base acceleration but also does not provide sufficient reduction of base displacement, whereas the GAFLC provides a displacement reduction similar to the 'passive-on' case with little increase in the base acceleration obtained in the 'passive-off' case (see Table 5.6).

It is to be noted that the FLC in GAFLC case is trained off-line to minimize the L_2 norm of base displacement and acceleration, when the structure is subjected to an initial displacement of 0.025m and not for any seismic record. Therefore a better performance may be observed

when the FLC is optimized on-line. The on-line FLC optimization study has been carried out for a benchmark base isolated building and has been reported in Chapter 7.

5.6 Summary

In this chapter the experimental investigation of a three storey building is reported. The building vibration (inter-storey drift and floor acceleration) is reduced using a hybrid control scheme containing four sliding base isolator and an MR damper. Experiments are conducted for fixed-base, base-isolated, and base-isolation with MR damper. After idealizing the building as a shear building model from the physical dimensions of the building, necessary system identification to determine update modal parameters is performed using a PSO based optimization scheme. The updated model is verified through various parameter based procedures reported in the literature and through comparison of simulated and experimental results obtained. The updated model is found to match well with the experimental building and finally the model has been adopted to carry out further experimental investigation.

The main objective of the chapter is to validate the performance of intelligent controller developed in Chapter 4 through experimental investigation. All the cases of MR damper based hybrid control is reported along with base isolation and fixed base building results. It is pointed out that the simple base isolation systems provide efficient vibration control of the structure in far-fault seismic excitations, but undergoes large displacement under near-fault excitations. As seen from the experimental study, MR damper reduced the base isolator displacement demand as well as the floor drifts and accelerations as compared to the fixed base condition in all four control cases. MR damper, operated in 'passive-off' and 'passive-on' cases shows totally different control scenarios. In 'passive-off' case base displacement has not been reduced efficiently but the base and the structural floor acceleration remained near to simple isolation case. On the contrary, the 'passive-on' case provided a control situation where the displacement at the base has been reduced efficiently at the cost of increase in base and floor acceleration.

A trade-off between 'passive-off' and 'passive-on case is observed in the FLC (both SFLC and GAFLC) driven MR control cases. SFLC does not increase the base acceleration but also does not provide sufficient minimization to base displacement, whereas the GAFLC provides

a displacement minimization similar to the 'passive-on' case with little increase in base acceleration from that of 'passive-off' case. A good agreement of the numerical and experimental results are observed.

Application of the controllers used for experimental study to a full scale benchmark building will be presented in Chapter 7. In the next chapter (Chapter 6) a few more MR damper monitoring semi-active control algorithms are developed based on the mathematical model of the structure. Their performances on the laboratory scale building are presented through numerical simulations.

Chapter 6

Nonlinear Control: Backstepping and Dynamic Inversion

6.1 Overview

As has been discussed in the literature survey presented in Chapter 2, MR damper input current/voltage monitoring algorithms have been developed in the frame work of intelligent based control schemes and model based control schemes. Intelligent controllers are efficient in controlling the structural displacements responses with slight increase in the structural acceleration response (see Chapter 4 and Chapter 5). This makes the applications of intelligent method based control algorithms interesting. Chapter 4 developed a fuzzy logic based intelligent controller to monitor MR damper current, where the velocity and acceleration at the damper location are used to decide the required MR damper monitoring current. The fuzzy controller has been optimized using genetic algorithm and particle swarm optimization. In Chapter 5, the performance of the optimal fuzzy logic controller has been evaluated through a series of experiments with scaled near-fault and far-fault seismic excitations.

Intelligent controllers need training for its optimal performance and consequently are model specific. Moreover, stability criteria are not well developed in these algorithms. This drawback of intelligent controllers limits their applications in structural vibration control. In this chapter two model based stable controllers to monitor MR damper input current/voltage using feedback from structural responses are developed. Nonlinear control algorithms like dynamic inversion (Isidori (1995) [155]) and integral backstepping (Krstic et al. (1995) [193])

are used to design semi-active control algorithms. The dynamics of supplied and commanded current input to MR damper is considered while developing these nonlinear algorithms.

In the next section, a detailed discussion on dynamic inversion (DI) based MR damper current controller is presented. Thereafter, the proposed DI based controller is extended for multiple MR dampers, which finds more application in practical structural control problems. A classical optimization technique is employed to design the optimal controller. Integral backstepping (IB) based MR damper current monitoring algorithm is then developed. Numerical simulation results of the algorithms applied to the building model considered for the experimental study in Chapter 5 are been reported. Finally, the chapter concludes with a summary, that highlights the suitability of these algorithms in larger problems that are presented in Chapter 7 through benchmark applications.

6.2 Introduction

Model based semi-active control algorithms, whether it is clipped optimal or Lyapunov based strategy, need the measurement of the force the damper provides. Thereafter, the mathematical information regarding the structure is used for the calculation of control forces to compare with damper force, obtained experimentally. An 'on-off' control strategy is adopted (switches the damper current/voltage between zero and its maximum value) by comparing the measured force from MR damper and force prescribed by an optimal control algorithm, (*e.g.*, LQG, Lyapunov, *etc.*, that are classified as primary controllers in this chapter). Therefore, there is a need for control algorithms that can change the MR damper current (and thus voltage) slowly and smoothly, such that all current values between zero and maximum current can be covered, based on the feedback from the structure.

Furthermore, the current/voltage supplied to the MR damper is different from the current/voltage (commanded current) that drives the magnetic flux in the MR damper. The dynamics of which is represented by Eq. 3.12 and Eq. 3.20 given in Chapter 3. This dynamics has little effect when a constant current/voltage is supplied across the damper as commanded current lags the supplied current in milliseconds. This phenomenon is shown in Fig. 6.1. Figure 6.1(a) shows the suppled current to commanded current dynamics for a variable input current and Fig. 6.1(b) shows the dynamics for a on-off control strategy.

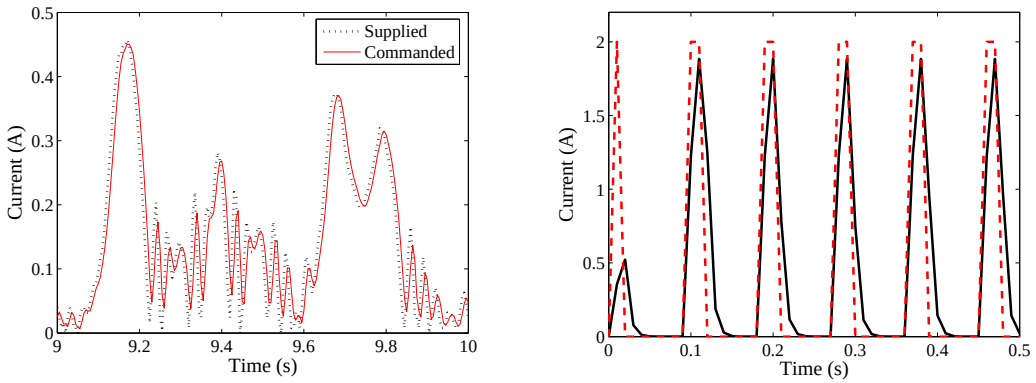

(a) Variable input current

(b) On-off control strategy

Figure 6.1: Supplied and commanded input current dynamics

However, this is not true during seismic vibration mitigation as the supplied current/voltage level changes frequently. Therefore while providing a variable current/voltage input to the MR damper the supplied and commanded current dynamics should be incorporated within the control algorithm. Semi-active control algorithms widely used in the literature fail to consider the above current dynamics. This makes the dynamics of current/voltage supply and the driver current/voltage an important factor to be considered while selecting semi-active control algorithms to monitor MR damper current/voltage.

In this chapter two model based control algorithms are developed to monitor MR damper supply current to MR damper such that the goals of smooth change in input current incorporating the dynamics of input current into the algorithm are realized.

6.3 Dynamic Inversion Based MR Damper Monitoring

Dynamic inversion (DI) control methodology has gained popularity among control engineers in recent years and has been applied to different types of aircraft applications, such as F-16, F-18 HARV2, F-1173, Su-274, X-38 and VSTOL aircraft (Adams and Banda (1993) [4]; Reiner et al. (1995) [289]; Ito et al. (2001) [156]). DI is a control synthesis technique by which existing deficient or undesirable dynamics are nullified and replaced by designer-specified desirable dynamics. This tunning of system dynamics is accomplished by a careful algebraic selection of a feedback function. It is for this reason that the DI methodology is also called feedback

linearization technique. Details of feedback linearization and DI are available in Slotine and Li (1991) [320]; Isidori (1995) [155]; Marquez (2003) [227].

Like all other model based systems, a fundamental assumption in this approach is that the plant dynamics is perfectly modeled, and therefore can be canceled exactly by the feedback functions. In this chapter DI is used for a two stage controller formulation. The first stage contains a primary controller which provides the force required to obtain a desired closed loop response of the system. Thereafter, DI is used to predict the required MR damper current/voltage such that it can track the force prescribed by the primary controller. Figure 6.2 shows the schematic diagram of the proposed two stage controller incorporating dynamic inversion as the second stage controller. Therefore the overall control scheme forms a new two stage stabilizing state feedback control design approach. For multiple control actuators dynamic inversion technique is integrated with classical optimization technique to provide optimal values of input current/voltage to the MR dampers. This approach is coined as '*optimal dynamic inversion*' control strategy.

Next, the formulation of the two stage controller is detailed for multi-input single output (MISO) systems and extended to multi-input multi-output (MIMO) systems, which contains multiple MR dampers.

6.3.1 Multi-Input Single Output Systems

To formulate the proposed two-stage controller let us consider a MISO system in state space form as given in Eq. 6.1.

$$\dot{X} = A\,X + B\,u + E\,\ddot{x}_g \tag{6.1}$$

Where $X \in \mathbb{R}^n$ is the state of the system, $u \in \mathbb{R}^1$ is the damper force, $\ddot{x}_g$ is the input excitation to the system. $A \in \mathbb{R}^{n\times n}$, $B \in \mathbb{R}^{n\times 1}$ and $E \in \mathbb{R}^{n\times 1}$ are system state matrix, controller location vector and influence vector for support excitation, respectively. The damper force ($u(t)$) is given by Eq. 3.9 in Chapter 3 and is repeated here for completeness.

$$f_c(t) = c_0\dot{x}_{mr} + k_0 x_{mr} + \alpha z_{mr} \tag{6.2}$$

Where f_c is the MR damper force represented as $u(t)$ in Eq. 6.1. The damper parameters for seismic application are tabulated in Table 3.3 of Chapter 3.

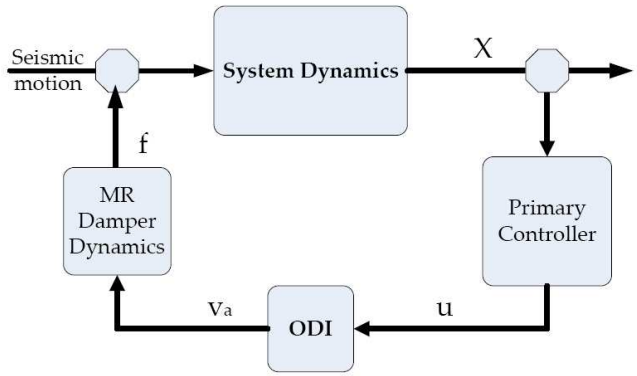

Figure 6.2: Schematic diagram of two stage dynamic inversion controller

For simplification, it is assumed that the system is perfectly observable, controllable and the all states are measurable. For practical application with reduced states and measurement noise, a benchmark highway bridge structure is considered. The complete set of equations for the application are also reported and discussed in Chapter 7.

Primary controller design: LQR

A LQR (linear quadratic regulator) control algorithm is considered as the first stage or primary controller. The LQR is designed to obtain optimal control force required to minimize the cost function defined in Eq. 6.3.

$$J_1 = \lim_{\tau \to \infty} \frac{1}{\tau} \left[\int_0^{\tau} \{(X)^T Q(X) + u^T R u\} dt \right] \tag{6.3}$$

Where Q and R are weighting matrices used to appropriately weight the states and calculate the controller force required. Minimization of performance index in Eq. 6.3 with system dynamics (Eq. 6.1) as constraint gives a state feedback form of the control force required (Bryson and Ho (1975) [45]).

$$f(t) = -K_g X \tag{6.4}$$

where K_g is feedback gain matrix and X is the measured states (states are assumed to be perfectly measured). The feedback gain (K_g) is obtained using *'lqr'* function available with Control Toolbox® in MATLAB ((2004) [230]). *'lqr'* function in MATLAB designs a linear quadratic

state-feedback regulator for continuous plant with system dynamics in the form of Eq. 6.1. *'lqr'* function calculates the optimal gain matrix K_g such that the state-feedback law given by Eq. 6.4 minimizes the quadratic cost function given in Eq. 6.3. It also solves the associated algebraic Riccati equation.

Once the state feedback form of the optimal control force is obtained, it is necessary to compute the current/voltage to be supplied to the MR damper such that MR damper provides similar control force. A dynamic inversion based approach is adopted to obtain a closed form solution of input current to be supplied to the MR damper to obtain the desired optimal force.

Secondary controller design: Dynamic Inversion

The secondary controller is designed with a goal to minimize the error between the primary controller and the control force supplied by the MR damper in a L_2 normed sense. To meet the aforementioned goal, an error term is defined as given in Eq. 6.5.

$$e = \frac{1}{2}\{u(t) - f(t)\}^2 \tag{6.5}$$

The error dynamics is formulated to minimize the error (e) between the primary controller force and damper force.

$$\begin{gathered} \dot{e} + k_e e = 0 \\ \{\dot{u}(t) - \dot{f}(t)\}\{u(t) - f(t)\} + \tfrac{k_e}{2}\{u(t) - f(t)\}^2 = 0 \end{gathered} \tag{6.6}$$

In Eq. 6.6, $k_e > 0$ serves as a gain. For a better physical interpretation, one may choose it as $k_e = \frac{1}{\tau_c}$, where $\tau_c > 0$ serves as a *'time constant'* for the error $e(t)$ to decay. The stability of the controller and its tracking efficiency is defined by the gain k_e. It should be noted that Eq. 6.6 contains dynamics of primary control force ($\dot{f}$) and the force provided by the MR damper ($\dot{u}$). Equation 6.4 provides $\dot{f}(t)$ and Eq. 6.2 provides $\dot{u}(t)$, which are given in Eqs. 6.7 and 6.8, respectively.

$$\dot{f}(t) = -K_g \dot{X} \tag{6.7}$$

$$\begin{aligned} \dot{u}(t) \;=\; & \left(C_{0a}\ddot{x}_{mr} + K_{0a}\dot{x}_{mr} + \alpha_a \dot{z}_{mr}\right) - \left(C_{0b}\dot{x}_{mr} + K_{0b}x_{mr} + \alpha_b z_{mr}\right)\eta\hat{i}_c \\ & + \left(C_{0b}\ddot{x}_{mr} + K_{0b}\dot{x}_{mr} + \alpha_b \dot{z}_{mr}\right)\hat{i}_c + \left(C_{0b}\dot{x}_{mr} + K_{0b}x_{mr} + \alpha_b z_{mr}\right) i_a \end{aligned} \tag{6.8}$$

Definitions of respective terms in Eq. 6.8 are given in Chapter 3. Current supplied to the MR damper is represented by i_a, whereas the current driving the magnetic flux, *i.e.*, at the damper magnetic coils (also known as commanded current) is represented by i_c. $\hat{i}_c$ represents the measured value of commanded current obtained from on-line integration of Eq. 3.20 (Chapter 3) using Simulink® (Mathworks (2004) [230]). Substituting $\dot{u}(t)$ from Eq. 6.8 into Eq. 6.6, following simplified form of the supply current is obtained.

$$i_a = \frac{\dot{f} + \frac{k_e}{2}(u - f) - \begin{bmatrix} (C_{0a}\ddot{x}_{mr} + K_{0a}\dot{x}_{mr} + \alpha_a \dot{z}_{mr}) \\ -(C_{0b}\dot{x}_{mr} + K_{0b}x_{mr} + \alpha_b z_{mr})\,\eta\hat{i}_c \\ +(C_{0b}\ddot{x}_{mr} + K_{0b}\dot{x}_{mr} + \alpha_b \dot{z}_{mr})\,\hat{i}_c \end{bmatrix}}{(C_{0b}\dot{x}_{mr} + K_{0b}x_{mr} + \alpha_b z_{mr})} \tag{6.9}$$

It is to be noted that when the system dynamics at the damper location goes to zero (particularly in steady state condition) or in any situation where x_{mr}, and $\dot{x}_{mr}$ ($z_{mr} \to 0$ as $x, \dot{x}_{mr} \to 0$) simultaneously go to zero, an unstable situation may arise in the computed applied current. However, this is unlikely as in that case prescribed force by the primary controller should be zero and the algorithm ends up in a $\frac{0}{0}$ position. To avoid such a numerically unstable situation, the supply current near the zero state condition is redefined as shown in Eq. 6.10.

$$i_{a,redefined} = \begin{bmatrix} 0 & x_{mr} < \text{tol}_1 \;\&\; \dot{x}_{mr} < \text{tol}_2 \\ i_a & \text{otherwise} \end{bmatrix} \tag{6.10}$$

Where value for tolerance (tol_1 and tol_2) are to be set by the designer. Physically when a vibration at damper location stops the MR damper stops providing any force as it is a semi-active system. Therefore i_a is redefined to match the physical behaviour of the damper.

6.3.2 Multi-Input Multi-Output Systems

Most of the real world structures need multiple controller for their vibration mitigation due to their huge masses. Therefore it becomes necessary to extend control algorithms for systems with multiple inputs and multiple outputs (MIMO). Moreover, huge structures are modeled using hundreds of degrees of freedom. For controller implementation a reduced order model is constructed considering few important natural frequencies (Soong (1990) [322]). In this section DI is designed for a reduced order MIMO system.

The controller developed here is used for a benchmark highway bridge control (Agrawal et al. (2005) [7]; Tan and Agrawal (2005) [353]), detailed in Chapter 7. The derivation presented here is consistent with the application of the benchmark bridge structure. Unlike MISO system the controller development is carried out using voltage as the input to the MR damper. This is done because MR dampers used in Chapter 7 to study the benchmark highway bridge require voltages as primary inputs. Nevertheless, as discussed in Chapter 3, voltage and current input to the MR damper can be used synonymously as they are linearly related.

Consider a reduced order system model (concept of reduced order system has been discussed in Chapter 2) for controller design as given in Eqs. 6.11 - 6.13.

$$\dot{\mathbf{X}}^r = \mathbf{A}\mathbf{X}^r + \mathbf{B}^r\mathbf{u} + \mathbf{E}^r\ddot{\mathbf{x}}_g \tag{6.11}$$

$$\dot{\mathbf{y}}_z = \mathbf{C}_r^z\mathbf{X}^r + \mathbf{D}_r^z\mathbf{u} + \mathbf{F}_r^z\ddot{\mathbf{x}}_g \tag{6.12}$$

$$\dot{\mathbf{y}}_m = \mathbf{C}_r^m\mathbf{X}^r + \mathbf{D}_r^m\mathbf{u} + \mathbf{F}_r^m\ddot{\mathbf{x}}_g + \nu \tag{6.13}$$

Where, the subscript r in Eqs. 6.11 - 6.13 refers to the reduced order model. In the above equations, X refers to the states of the system, A, B and E are the system state matrices, $\ddot{x}_g$ is the ground acceleration vector in two directions. The regulated output y_z and the measurement output y_m are given in Eqs. 6.12 and 6.13, respectively. The matrices C, D and F are mapping matrices of appropriate dimensions and ν denotes the measurement noise.

Primary Controller Design: LQG

In the first stage, the LQG (Linear Quadratic Guassian) control algorithm is used to obtain optimal force required to minimize an infinite horizon performance index defined in Eq. 6.14. The reduced-order system model shown in Eqs. 6.11 - 6.13 is employed for the controller design.

$$J_1 = \lim_{\tau\to\infty}\frac{1}{\tau}E\left[\int_0^\tau\{(C_r^zX^r + D_r^zu)^T\mathbf{Q}(C_r^zX^r + D_r^zu) + u^T\mathbf{R}u\}dt\right] \tag{6.14}$$

Where $\mathbf{Q}$ and $\mathbf{R}$ are weighting matrices used to appropriately weight the regulated outputs and the controller force required respectively. Minimization of performance index in Eq. 6.14

with system dynamics (Eq. 6.11) as constraint gives a state feedback form of the control force (Eq. 6.15).

$$f(t) = -K_g \hat{X}^r \tag{6.15}$$

where K_g (obtained using function *'lqry'* in Control Toolbox® of MATLAB (2004) [230]) is feedback gain matrix and $\hat{X}^r$ is the Kalman estimate of the system states. *'lqry'* function in MATLAB designs a linear quadratic state-feedback regulator for continuous plant with output weighting. *'lqry'* function calculates the optimal gain matrix K_g such that the state-feedback law given by Eq. 6.15 minimizes the quadratic cost function given in Eq. 6.14. The difference between the cost functions in Eqs. 6.3 and 6.14 is that Eq. 6.14 contains quadratic form of system output variables and the control variables, whereas Eq. 6.3 contains quadratic form of system state variables and the control variables.

The separation principle allows the control and estimation problems to be considered separately. The Kalman filter optimal estimator is given by,

$$\dot{\hat{X}}^r = A_r \hat{X}^r + B_r u + L(y_m - C_r^m X^r - D_r^m u) \tag{6.16}$$

where L is the observer gain matrix of the stationary Kalman filter.

Once the state feedback form of the optimal control force is obtained, it is necessary to calculate the amount of voltage to be supplied to each MR damper, given the local values of the states. The dynamic inversion based approach discussed previously is used in conjunction with optimization theory to obtain a closed form solution of input voltage to be supplied to each MR dampers. The combined algorithm is coined as 'Optimal Dynamic Inversion' strategy.

Secondary controller design: Optimal Dynamic Inversion

Optimal dynamic inversion (ODI) is formulated by combining classical optimization technique with dynamic inversion, such that an optimized voltage supply is provided to each damper in a set. The advantage of using optimal dynamic inversion technique is that it leads to a closed form stable state feedback solution of the voltage supplies to MR dampers.

The formulation of optimal dynamic inversion is in many ways similar to the one developed for MISO system. But the formulation is shown again to maintain the flow with voltage

as the input to the MR damper. Similar to MISO systems the second stage controller is designed with a goal to minimize the error between the primary controller and the control force to be supplied by the MR damper in a L_2 normed sense. To meet the aforementioned goal, an error term is defined as given in Eq. 6.17.

$$e = \frac{1}{2}\{u(t) - f(t)\}^T P\{u(t) - f(t)\} \tag{6.17}$$

Where $P > 0$ is an user defined positive definite weighing matrix. A diagonal P matrix is considered in present case, so that the overall controller tracking error reduces to sum of the square of errors in each damper (as shown in Eq. 6.18).

$$e = \sum_{i=1}^{N} \left[P_{ii}\{u_i(t) - f_i(t)\}^2\right]; \quad i = 1, \ldots, N; \tag{6.18}$$

Where P_{ii} denotes i^{th} diagonal element of matrix P. Therefore, $e(t) \rightarrow 0$ signifies $u_i(t) \rightarrow f_i(t) \forall i \in [1, N]$. Using the principle of dynamic inversion (Ali and Padhi (2006, 2007) [26, 27]; Padhi and Balakrishnan (2007) [269]), the controller is designed such that the following stable error dynamics is satisfied.

$$\begin{gathered} \dot{e} + k_e e = 0 \\ \{\dot{u}(t) - \dot{f}(t)\}^T P\{u(t) - f(t)\} + \tfrac{k_e}{2}\{u(t) - f(t)\}^T P\{u(t) - f(t)\} = 0 \end{gathered} \tag{6.19}$$

Where, $k_e > 0$ serves as a gain and can be defined as in MISO system. Since, P is a diagonal matrix, Eq. 6.19 on simplification reduces to,

$$\sum_{i=1}^{N} [P_{ii}(u_i - f_i)\dot{u}_i] = \sum_{i=1}^{N} \left[P_{ii}\{\frac{k_e}{2}(u_i - f_i)^2 + (u_i - f_i)\dot{f}_i)\}\right] \tag{6.20}$$

It should be noted that Eq. 6.20 contains dynamics of primary controller and the force provided by the MR damper. One can notice that the dynamics of MR damper hysteretic force ($\dot{u}_i$), at a particular damper location, will contain the dynamics of its voltage update, *i.e.*, the dynamics between voltage supplied and commanded voltage. As in MISO controller design, the substitutions of Eqs. 6.7 and 6.8 for every i^{th} damper in Eq. 6.20 and simplification lead to the following form,

$$I_1 v_{a1} + I_2 v_{a2} + \cdots + I_N v_{aN} = \Gamma \tag{6.21}$$

where

$$I_i = \eta P_{ii} \left(\sum_{j=1}^{R} K_{g(ij)} \hat{X}_j^r - u_i \right) \left(C_{0b} \dot{x}_{mr(i)} + \alpha_b z_{mr(i)} \right) \quad i = 1, \ldots, N \tag{6.22}$$

and

$$\Gamma = \sum_{i=1}^{N} P_{ii} \begin{bmatrix} \frac{k_e}{2} \left(\sum_{j=1}^{R} K_{g(ij)} \hat{X}_j^r - u_i \right)^2 + \\ \left(\sum_{j=1}^{R} K_{g(ij)} \hat{X}_j^r - u_i \right) \left(\sum_{j=1}^{R} K_{g(ij)} \dot{\hat{X}}_j^r \right) - \\ \left(\sum_{j=1}^{R} K_{g(ij)} \hat{X}_j^r - u_i \right) \begin{pmatrix} C_{0a} \ddot{x}_{mr(i)} + \alpha_a \dot{z}_{mr(i)} + \\ C_{0b} \left(\ddot{x}_{mr(i)} - \eta \dot{x}_{mr(i)} \right) \hat{v}_{c(i)} + \\ \alpha_b \left(\dot{z}_{mr(i)} - \eta z_{mr(i)} \right) \hat{v}_{c(i)} \end{pmatrix} \end{bmatrix} \tag{6.23}$$

In Eq. 6.23, R denotes the total number of reduced order states, $K_{g(ij)}$ denotes i^{th} row and j^{th} column element of the feedback gain matrix K_g obtained in first stage controller design. $\hat{X}_j^r$ is the j^{th} element of the estimated state vector. The responses at the location of i^{th} damper is represented by $(.)_{mr(i)}$. It is to be noted that Eq. 6.23 contain time-derivative of the state variable $\hat{X}^r$. Therefore, apart from the assumption that the governing system dynamics should be in control affine form, the primary controller should provide a state feedback form of the controller. As discussed in MISO controller design the measured value of commanded voltage $\hat{v}_{c(i)}$ has to be evaluated on-line using Simulink® (Mathworks (2004) [230]).

However, note that Eq. 6.21 is a single equation with N variables $v_{a(i)}, i = 1, \ldots, N$ and hence have an infinite set of solutions. To obtain a unique solution, we minimize the cost function formulated in Eq. 6.24

$$J_2 = \frac{1}{2} \left(\omega_1 v_{a(1)}^2 + \cdots + \omega_N v_{a(N)}^2 \right) \tag{6.24}$$

subject to the constraint given by Eq. 6.21. An implication in choosing this cost function is that we wish to obtain the solution that will lead to a minimum voltage supply to obtain the prescribed primary controller force ($f_i(t)$). Note that, choosing appropriate values for $\omega_1, \ldots, \omega_N > 0$ in Eq. 6.24 give a control designer the flexibility of putting relative importance of the control magnitude at different spatial locations over the structure.

To use techniques of constrained optimization, we first formulate the following augmented

cost function

$$\bar{J}_2 = \frac{1}{2}\left(\omega_1 v_{a(1)}^2 + \cdots + \omega_N v_{a(N)}^2\right) + \lambda\left[I_1 v_{a(1)} + \cdots + I_N v_{a(N)}\right] \tag{6.25}$$

where λ is the Lagrange multiplier, which is a free variable needed to convert the constrained optimization problem to a free optimization problem. In Eq. 6.25, λ and $v_{a(i)}, i = 1, \ldots, N$ are free variables, with respect to which the minimization has to be carried out. The necessary condition of optimality for i^{th} damper location is given by

$$\begin{aligned} \frac{\partial \bar{J}_2}{\partial v_{a(i)}} &= 0; \\ \frac{\partial \bar{J}_2}{\partial \lambda} &= 0; \end{aligned} \tag{6.26}$$

Solution of Eq. 6.26 leads to,

$$\omega_n v_{a(i)} + I_i \lambda = 0, \tag{6.27}$$

$$I_1 v_{a(1)} + \cdots + I_N v_{a(N)} = \Gamma \tag{6.28}$$

Solution of Eq. 6.27 and Eq. 6.28, leads to,

$$\lambda = \frac{-\Gamma}{\sum_{i=1}^{N} I_i^2/\omega_i} \tag{6.29}$$

$$v_{a(i)} = \frac{I_i \Gamma}{\omega_i \sum_{i=1}^{N} I_i^2/\omega_i} \tag{6.30}$$

As a special case, if we consider $\omega_1 = \ldots = \omega_N$ (*i.e.*, equal importance is given to all controllers), we have,

$$v_{a(i)} = \frac{I_i \Gamma}{\|I\|_2^2} \tag{6.31}$$

From Eqs. 6.30 and 6.31, it is clear that when $\|I\|_2^2 \to 0$ (which happens when all of $I_1, \ldots, I_N \to 0$) and $\Gamma \not\to 0$, we have the problem of control singularity in the sense that $v_{a(i)} \to \infty$. This can take place when $x_{mr(i)} \to 0$, $\dot{x}_{mr(i)} \to 0$ and $z_{mr(i)} \to 0$ simultaneously.

Note that if the number of controllers N is large, probably the occurrence of such a singularity is a rare possibility, since all of $I_1, \ldots, I_N \to 0$ simultaneously is a strong condition.

Nonetheless such a case may arise in steady state condition. More important, this issue of control singularity will always arise when $x_{mr(i)} \to 0$ and $\dot{x}_{mr(i)} \to 0$ for all controller location (which is the primary goal of the control design). Hence, whenever such a case arises, to avoid the issue of control singularity, similar to MISO controller design, the supply voltage $v_{a(i)}$ is set to 0, *i.e.*, the MR dampers are shifted to their passive-off condition beyond $x_i \leq \text{tol}_1$ and $\dot{x}_i \leq \text{tol}_2$ to be defined by the user.

6.4 Integral Backstepping Based MR Damper Monitoring

In the preceding section design of a model based controller to monitor MR damper current/voltage is detailed. It has certain new features. Unlike other model based controllers it provides a gradual switch of damper current and so the actual current input required is provided (not switching between maximum and zero current). Furthermore, the DI based technique considers the input current dynamics of MR damper in its algorithm development. Nevertheless it has a drawback in that one needs to design an intermediate controller like H_2/LQG and then employing dynamic inversion to determine the current required to be supplied to the MR damper such that the control force prescribed by the intermediate controller is supplied. Another short fall of the above controller is that it needs an estimate of commanded current for its design. The main scope of this section is to design a stable semi-active controller maintaining the good features of the DI algorithm but eliminating the intermediate primary controller. For this the integral backstepping controller proposed by Krstic et al. (1995) [193] is adopted in this study.

In recent adaptive and robust control literature, the backstepping design provides a systematic framework for the design of tracking and regulation strategies (see Krstic et al. (1995) [193]; Krstic and Smyshlyaev (2007) [194]), suitable for a large class of state feedback linearizable nonlinear systems. Integrator backstepping is used to systematically design controllers for systems with known nonlinearities. The approach can be extended to handle systems with unknown parameters, via, adaptive backstepping. However, adaptive backstepping design for nonlinear control may dramatically increase the complexity of the controller. In the present chapter integrator backstepping is applied to deduce the current required by the MR damper to reduce structural responses.

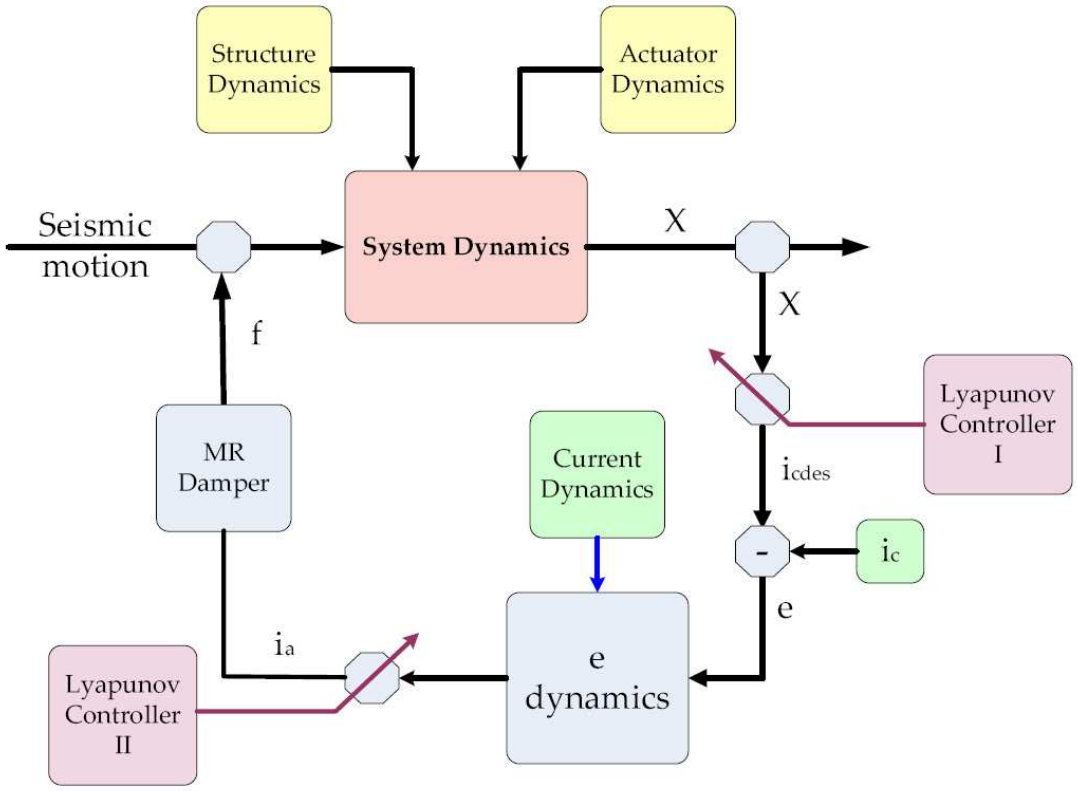

Figure 6.3: Schematic diagram of integral backstepping based MR damper monitoring

The development of the algorithm is shown in the schematic diagram, Fig. 6.3. It is also a two-stage controller, where in the first stage a Lyapunov controller is deviced to stabilize the dynamics of the structural system. Thereafter, considering the MR damper input current dynamics a second Lyapunov based controller is developed to stabilize the full system considering structural system and the MR damper. The developmentis shown with mathematical details in the next section.

The integral backstepping based semi-active MR damper current monitoring is developed for a SDOF system. Extension to MDOF system can be developed similar to that in dynamic inversion controller. This exercise is not carried out further in this study. The hybrid base isolated building considered for the experimental study is in effective a SDOF system due to base isolation. A study of the performance of the hybrid isolation system with backstepping based MR damper monitoring is reported.

6.4.1 System Model

A SDOF model is considered with MR damper connected to it. The linear dynamics of SDOF system with MR damper is given by,

$$m\ddot{x} + c\dot{x} + kx + u(t) = f(t) \tag{6.32}$$

where m, c and k are mass, damping and stiffness parameters of the SDOF system and $(\cdot)$ denotes derivative *w.r.t.* time (t). $u(t)$ is the MR damper control force and $f(t)$ is the external excitation force. $u(t)$ is added as the system restoring force since MR damper act as a passive device in the absence of driver current.

The maximum stroke of the MR damper RD-1005-3 (MR Dampers (2006) [240]) is $\pm$25mm and it is advisable to keep a safe passage of 6mm. Therefore, we restrict the maximum displacement of the MR damper during operation to $\pm$20mm of displacement. The MR damper parameters (c_{0a}, c_{0b}, k_{0a}, k_{0b}, α_a,α_b) are determined taking $x_a = 20\ mm$ as discussed in Chapter 3. The MR damper constant and the other parameter are defined in Table 3.3 of Chapter 3.

Substituting $u(t) = c_0\dot{x}_{mr} + k_0 x_{mr} + \alpha z_{mr}$ from Eq. 3.9 in Eq. 6.32 and then re-writing the closed loop system dynamics considering the MR damper dynamics (and neglecting the external forcing term) in state space form one gets,

$$\begin{aligned}
\dot{x}_1 &= x_2\ ; \\
\dot{x}_2 &= -\tfrac{1}{m}\{(k+k_{0a})x_1 + (c+c_{0a})x_2 + \alpha_a\, x_3\} - \tfrac{1}{m}\{k_{0b}x_1 + c_{0b}x_2 + \alpha_b x_3\}\, i_c\ ; \\
\dot{x}_3 &= -\gamma\ |\dot{x_2}|\, x_3\, |x_3|^{n-1} - \beta\dot{x_2}\, |x_3|^n + \ A\, \dot{x_2}\ ; \\
\dot{i}_c &= -\eta(i_c - i_a)\ ;
\end{aligned} \tag{6.33}$$

In Eq. 6.33 the evolutionary variable z_{mr} (see Eq. 3.9) is replaced with x_3. Since a SDOF system is considered $x_{mr} = x = x_1$ and $\dot{x}_{mr} = \dot{x} = x_2$. The variable z_{mr} is responsible for the hysteretic behavior of the MR damper and it evolves with time. Therefore it is a hidden variable and is considered as an additional state variable.

Equation 6.33 can be rewritten in the following standard form

$$\begin{aligned} \dot{X} &= F_1(t, X) + G_1(t, X)\, i_c \\ \dot{i}_c &= F_2(t, X, i_c) + G_2(t, X, i_c)\, i_a \end{aligned} \tag{6.34}$$

where X, F_1, G_1, F_2 and G_2 are given in Eq. 6.35.

$$\begin{aligned} X &= [x_1, x_2, x_3]^T; \\ F_1 &= \begin{bmatrix} x_2 \\ -\frac{1}{m}\{(k + k_{0a})x_1 + (c + c_{0a})x_2 + \alpha_a\, x_3\} \\ -\gamma\ |\dot{x_2}|\, x_3\, |x_3|^{n-1} - \beta \dot{x_2}\, |x_3|^n + A\, \dot{x_2} \end{bmatrix}; \\ G_1 &= \begin{bmatrix} 0, -\frac{1}{m}\{k_{0b}x_1 + c_{0b}x_2 + \alpha_b x_3\}, 0 \end{bmatrix}^T; \\ F_2 &= -\eta i_c\,; \quad G_2 = \eta\,; \end{aligned} \tag{6.35}$$

$()^T$ represents transpose operation.

6.4.2 Backstepping Controller Design

Equation 6.34 is a second order strict feedback form of the system given by Eq. (6.33). We define a dummy variable i_{dum} such that it satisfies the following relation.

$$i_a = \frac{1}{G_2(t, X, i_c)}(i_{dum} - F_2(t, X, i_c)) \tag{6.36}$$

The dummy variable (i_{dum}) is defined to convert the second order strict feedback system to a simplified form amenable for integrator backstepping application. Combining Eq. 6.34 and Eq. 6.36 we reduce the strict feedback system to an integrator backstepping form (Eq. 6.37).

$$\begin{aligned} \dot{X} &= F_1(t, X) + G_1(t, X)\, i_c \\ \dot{i}_c &= i_{dum} \end{aligned} \tag{6.37}$$

The design objective is $X(t) \to 0$ as $t \to \infty$. The control law can be synthesized in two steps. We regard commanded current, i_c to the damper as the real current driver, first. By choosing the Lyapunov candidate function of the system as, $V_1 = 1/2(kx_1^2 + mx_2^2 + qx_3^2)$, we

get,

$$\dot{V}_1 = \begin{bmatrix} -\{(c+c_{0a})x_2^2 + \gamma q\,|x_2x_3|\,x_3^2\} - \dots \\ \{k_{0a}x_1x_2 + (\alpha_a - Aq)x_2x_3 + q\beta x_2x_3^3 + (k_{0b}x_1x_2 + c_{0b}x_2^2 + \alpha_b x_2x_3)\,i_c\} \end{bmatrix} \tag{6.38}$$

The Lyapunov-time-derivative $\dot{V}_1$ should be made negative-definite to get a stable closed loop system. The first term in $\dot{V}_1$ *i.e.*, $\{(c+c_{0a})x_2^2 + \gamma q\,|x_2x_3|\,x_3^2\}$ is free of current variable i_c and is negative-definite ($\forall x_1,\ x_2,\ x_3$). q is positive constant given by $\frac{\alpha_a}{A}$. Out of many solutions, we select designed commanded current $i_{c_{des}}$ to be (as this simple form makes $\dot{V}_1 < 0\,\forall\, x_1,\ x_2,\ x_3 \neq 0$),

$$i_{c_{des}} = \frac{k_d x_1^2 - K_{0a}x_1x_2 - q\beta x_2x_3^3}{k_{0b}x_1x_2 + c_{0b}x_2^2 + \alpha_b x_2x_3} \tag{6.39}$$

where $k_d \geq 0$ is a positive constant to be decided by the designer. In the present analysis $k_d = 1$ is considered, which makes $\dot{V}_1 = -\{(c+c_{0a})x_2^2 + \gamma q\,|x_2x_3|\,x_3^2 + k_d x_1^2\} \leq 0\ \forall X \neq 0$ in Eq. 6.38. There can be a numerical stability problem when all $x_1 \to 0$, $x_2 \to 0$ and $x_3 \to 0$ simultaneously. Therefore, a tolerance is set for all the state variables below which the damper input current is kept at zero.

Nevertheless, i_c is a state variable and perfect tracking to $i_{c_{des}}$ is desired and hardly achieved in reality. Therefore, an error variable e (given in Eq. 6.40) as the target error of the designed variable is defined.

$$e = i_c - i_{c_{des}} \tag{6.40}$$

The error dynamics is given by

$$\begin{aligned} \dot{e} &= \dot{i}_c - \dot{i}_{c_{des}} \\ &= i_{dum} - i_{c_{des,X}}\,\dot{X} \end{aligned} \tag{6.41}$$

where $i_{c_{des,X}}$ is the derivative of $i_{c_{des}}$ *w.r.t.* state X. Choosing a second Lyapunov function as $V_2 = V_1 + \frac{1}{2}e^2$ and the current variable i_{dum} as given in Eq. 6.42, it can be shown that the system defined in (Eq. 6.37) becomes asymptotically stable (see Krstic et al. (1995) [193]; Marquez (2003) [227]).

$$i_{dum} = i_{c_{des,X}}\,[F_1(t,X) + G_1(t,X)i_c] - V_{1,X}.G_1(t,X) - K(i_c - i_{c_{des}}) \tag{6.42}$$

with F_1 and G_1 defined in Eq. 6.35 and $K > 0$ is any constant to be decided by the designer. For our analysis $K = 1$ is considered. The applied current to the MR damper can be obtained by substituting Eq. 6.42 into Eq. 6.36.

6.5 Results and Discussion

Simulations are carried out for the three storey hybrid base isolated building model (shown in Fig. 6.4) that has been considered for the experimental study in Chapter 5. Details about the hybrid isolated building and its parameters are discussed in Chapter 5. The base damping is considered to be 2% of the critical damping in the numerical simulation carried out in this chapter. Simulations are carried out for dynamic inversion and integrator backtepping controller. First the simulation is run for the control of impulsive force on the system. The impulsive force response is simulated by setting the system with an initial velocity (Chopra (2005) [67]) at the base. Second the performance of the proposed MR damper current monitoring techniques is shown under a set of seismic motion considered for the experimental study. Details of the seismic ground motion data and their scaling factors are detailed in Table 5.2 of Chapter 5. For the seismic analysis a comparison is reported with GA-FLC controller developed in Chapter 4 and LQR-clipped optimal control algorithms (clipped optimal control algorithm is discussed in Chapter 2). In the analysis reported in the next section the uncontrolled state of the structure is assumed to be the building with only the base isolator (without MR damper, *i.e.*, simple base isolation), and the controlled state is considered to be the building with base isolator and a single MR damper connected at the base. This is to show the benefits of supplemental damping device attached to isolator in comparison to the simple isolation system.

The MR damper parameters taken for the present analysis are given in Table 3.3 of Chapter 3. The maximum input current allowed for the damper is $2\ A$. The maximum force the damper can provide is $\pm 2250\ N$.

6.5.1 Results: Dynamic Inversion

The three storey base isolated building is simulated with a single MR damper connected at the base of the building as shown in Fig. 6.4. Therefore, dynamic inversion based controller

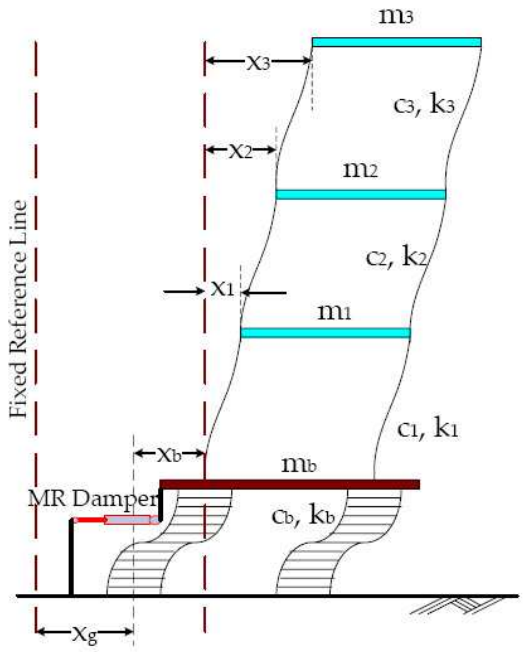

Figure 6.4: Schematic diagram of hybrid base isolated building

developed for the MISO system is employed for the analysis. The primary controller force is obtained using LQR algorithm ('lqr' function available with Control Toolbox® (MATLAB (2004) [230])). The matrix $Q = 5 \times 10^3\ I_{8\times 8}$ and $R = 1 \times 10^{-4}$ are considered for the study. $I_{8\times 8}$ is an identity matrix of dimension (8×8). The gain, k_e is taken as 10. All the simulations are performed with the above mentioned parameters. In Eq. 6.10, $\text{tol}_1 = 1 \times 10^{-5}\ m$ and $\text{tol}_2 = 1 \times 10^{-5}\ m/s$ are considered for the simulation studies.

Impulsive force analysis

The building is set into vibration with an initial velocity and from rest to simulate the impulsive force analysis. The initial velocity of $\dot{u}_b = \frac{1}{m_b}\ m/s$ is given at the base isolator. Figure 6.5 shows the time history of the uncontrolled (simple base isolation) and controlled system responses (base isolation with MR dampers. The uncontrolled and controlled displacement time histories and acceleration time histories at the base isolator and at the third floor of the building are shown. The responses have been shown for $5\ s$ as the controlled system response die down within $5\ s$. As seen from the Fig. 6.5 the base displacement is reduced but at the cost of

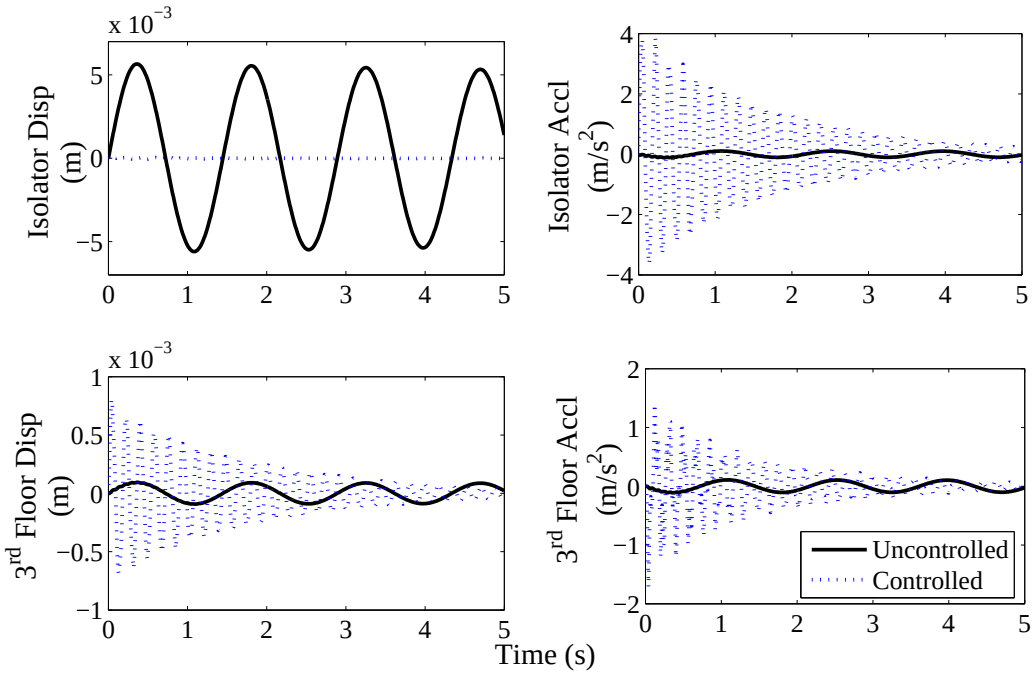

Figure 6.5: Base isolator and 3^{rd} floor displacement and acceleration responses under impulsive force (Uncontrolled and DI based control)

an increase in the superstructure responses.

Figure 6.6 shows the input current supplied to the MR damper and the corresponding control force provided by the MR damper. As can be seen from the Fig. 6.6 the input current does not switch between the zero and maximum ampere current and in fact captures current values in between the zero and maximum current. This is one of the objectives behind use of the dynamic inversion based MR damper current monitoring. Therefore the DI based algorithm satisfactorily performs the design objectives.

The tracking performance of the DI based algorithm is shown in Fig. 6.7. It is observed that the DI based MR damper current monitoring can successfully track the control signal prescribed by LQR algorithm.

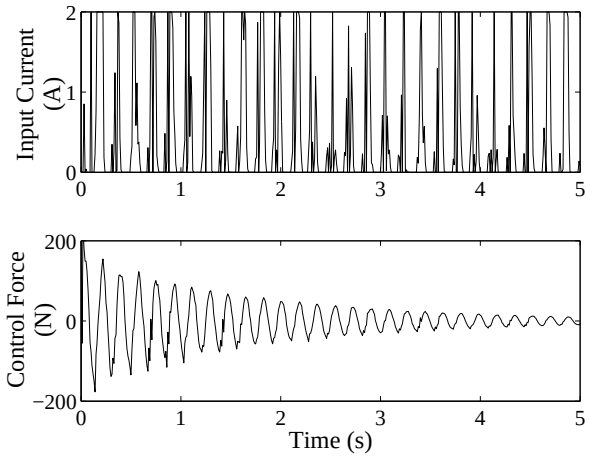

Figure 6.6: Input current and damper force under impulsive force (DI based control)

Seismic analysis

Figure 6.8 shows the time history of the uncontrolled and controlled system responses (displacement and acceleration) of base isolator and at the third floor under El-Centro ground motion. The uncontrolled (simple base isolation) and controlled (hybrid isolation) displacement and acceleration responses are shown together for better comparison. The peak displacement

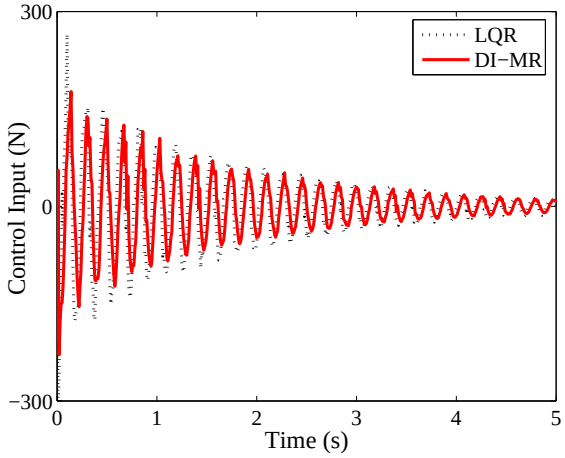

Figure 6.7: LQR prescribed control force tracking by MR damper using DI

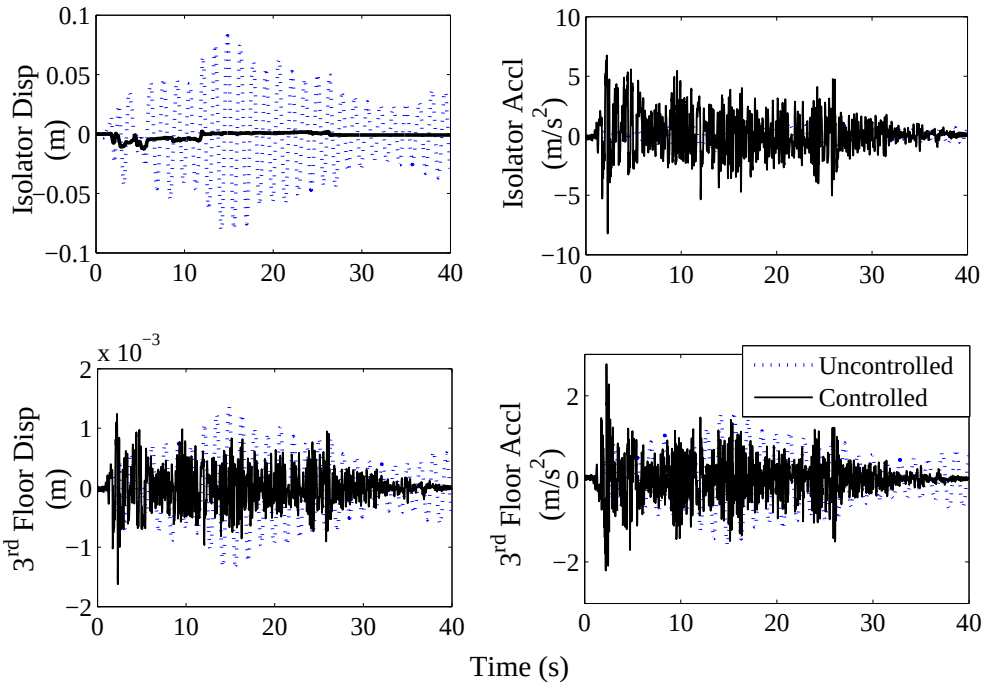

Figure 6.8: Base isolator and 3^{rd} floor displacement and acceleration responses under El-Centro (X) (Uncontrolled and DI based control)

response of the isolator in simple isolation condition is found to be $0.0827\ m$, which is reduced to $0.0123\ m$ by the DI monitored MR damper. The third floor shows a slight increase in the displacement response from $0.0014\ m$ in uncontrolled condition to $0.0016\ m$ in MR damper controlled case. The acceleration responses at the isolator and at the superstructure are increased due to the implementation of MR damper, which is very usual for hybrid base isolated structures. Since the MR damper decreases the isolator displacement, the superstructure responses increase. The base acceleration of $1.5631\ m/s^2$ in uncontrolled case is increased to $8.2246\ m/s^2$ in the MR controlled case. A drop in the isolator velocity from $0.3847\ m/s$ in uncontrolled case to $0.0690\ m/s$ in controlled case is also observed. The control force provided by the MR damper and the corresponding input current to the MR damper are shown in Fig. 6.9. It is clear from the input current time history that the supplied current reaches the maximum but also considers current values in between zero and maximum current ($2\ A$).

Similar to Fig. 6.8, the responses due to N. Palm Spring seismic ground motion is shown

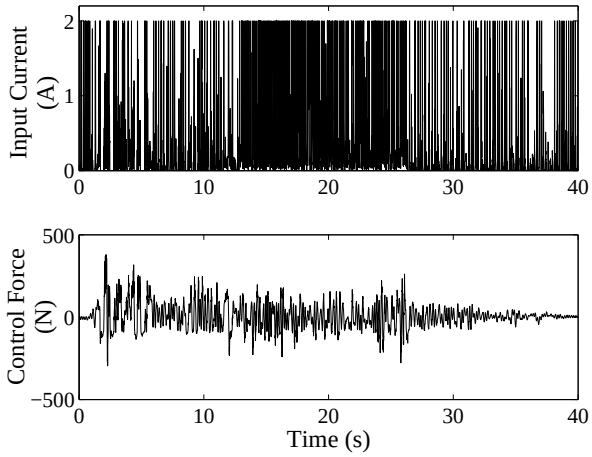

Figure 6.9: Input current and damper force under El-Centro (DI based control)

in Fig. 6.10. A maximum isolator displacement of $0.2077\ m$ is reduced to $0.0113\ m$. Unlike the case of Elcentro seismic ground motion a better performance of MR damper is observed in N. Palm Spring earthquake. The isolator acceleration and the superstructure displacement responses are reduced using MR damper. Only the superstructure acceleration response is increased over that of the uncontrolled case. The control force provided by the MR damper and the corresponding input current to the MR damper in the N. Palm Spring seismic motion are shown in Fig. 6.11. Similar to the Elcentro case, DI based algorithm provides current values in between the zero and maximum current range.

The tracking performance of the DI algorithm for the Elcentro earthquake case is shown in Fig. 6.12. Figure 6.12 contains both the force prescribed by the LQR algorithm and the force provided by the MR damper using input from the DI based tracking algorithm.

6.5.2 Results: Integrator backstepping

Base isolated structures behave as rigid masses over the base under seismic ground motion (Chopra (2005) [67]). Therefore SDOF models provide good approximation to these systems for quick calculation under ground motion (Chopra (2005) [67]). The integrator backstepping based algorithm is developed assuming a SDOF system with mass equal to the total mass of the three storey base isolated building and stiffness equal to that of the base stiffness. The system damping is assumed to be 2% of critical damping. The tolerance for the simulation

studies with backstepping is set to $\text{tol}_1 = 1 \times 10^{-5}\ m$ for isolator displacement and $\text{tol}_2 = 1 \times 10^{-5}\ m/s$ for isolator velocity.

Impulsive force analysis

Similar to the simulation studies with DI based control, the building is set to vibration with an initial velocity of $\dot{u}_b = \frac{1}{m_b}\ m/s$ at the base isolator to simulate impulsive force on the structure. Figure 6.13 shows the time history of the uncontrolled and controlled system responses. The uncontrolled and controlled displacement time histories and acceleration time histories at the base isolator and at the third floor of the building are shown. The responses are shown for $5\ s$ as the controlled system responses die down within $5\ s$. As seen from the Fig. 6.13 the base displacement is reduced but at the cost of an increase in the superstructure responses.

Figure 6.14 shows the input current supplied to the MR damper and the corresponding control force provided by the MR damper. An exponential drop in current supplied to damper

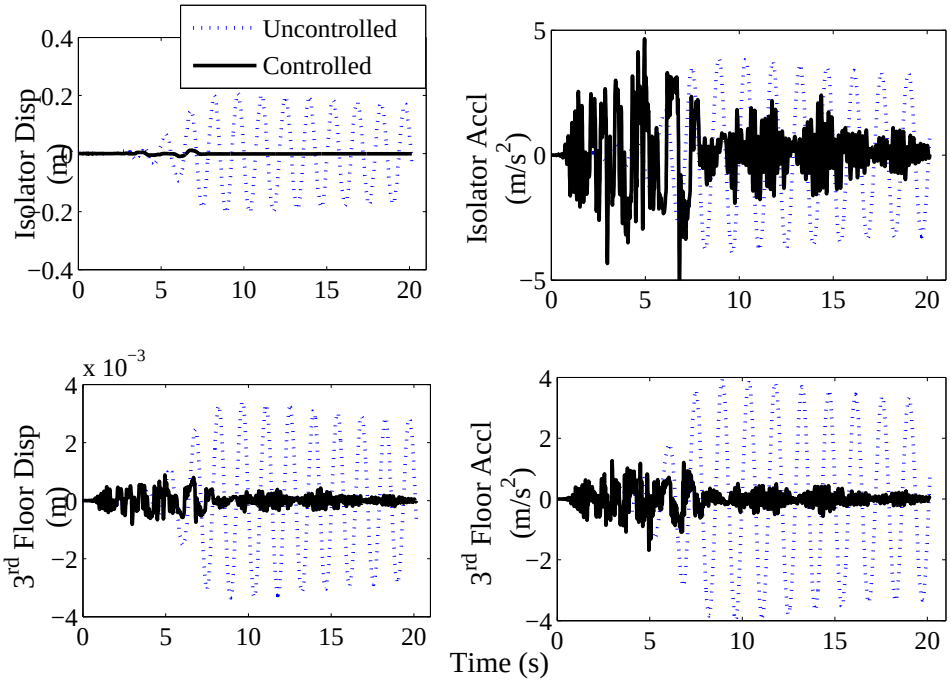

Figure 6.10: Base isolator and 3^{rd} floor displacement and acceleration responses under N. Palm Spring (X) (Uncontrolled and DI based control)

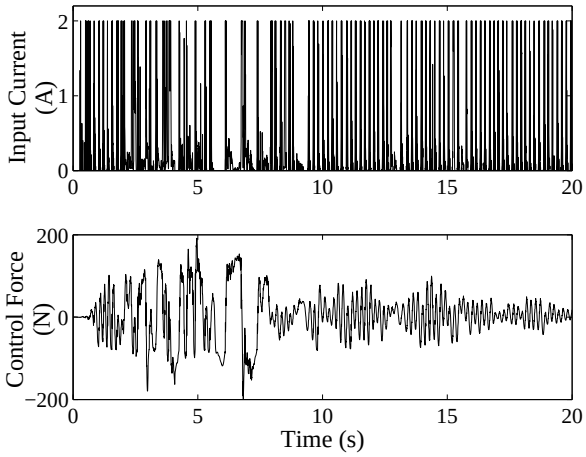

Figure 6.11: Input current and damper force under N. Palm Spring (DI based control)

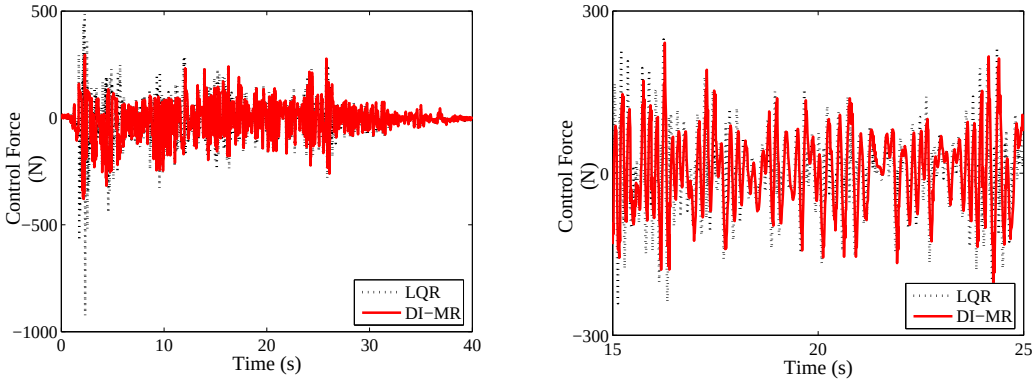

(a) Tracking performance of MR damper with DI

(b) Tracking performance of MR damper with DI (enlarged)

Figure 6.12: Tracking performance of MR damper with DI (El-Centro (X))

can be seen in the Fig. 6.14, which is due to first order error dynamics considered while developing the backstepping based control algorithm. The input current decreases with the decrease in the system responses (compare Figs. 6.13 and 6.14). Therefore, Lyapunov controller satisfactorily mitigates the structural vibration and also does not show jumps in the input current (from maximum and zero ampere current). It also captures current values in between the zero and maximum current. This is one of the objectives behind the development of the controller in the present chapter.

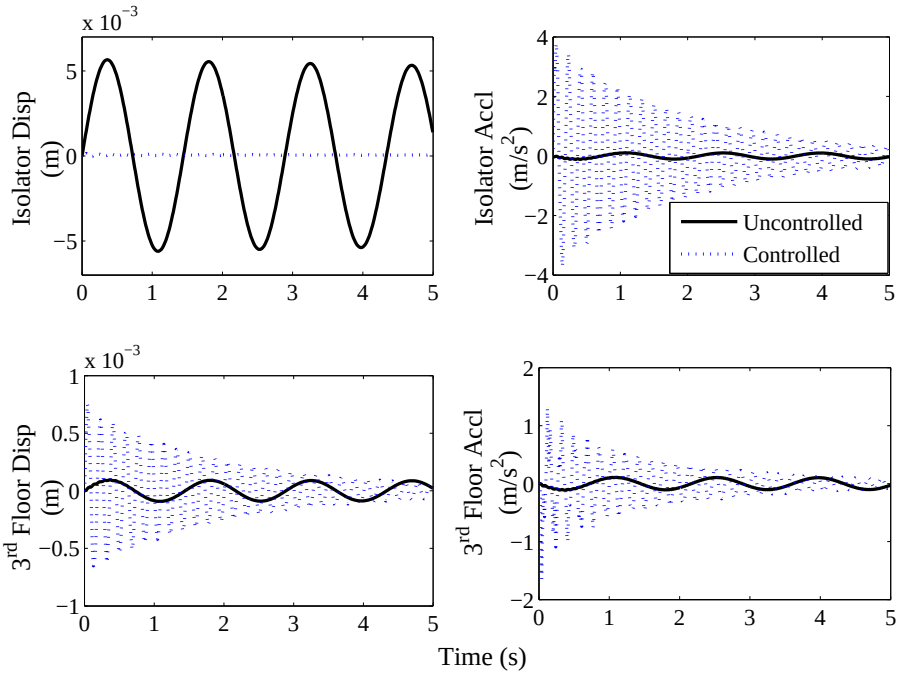

Figure 6.13: Base isolator and 3^{rd} floor displacement and acceleration responses under impulsive force (Uncontrolled and backstepping control)

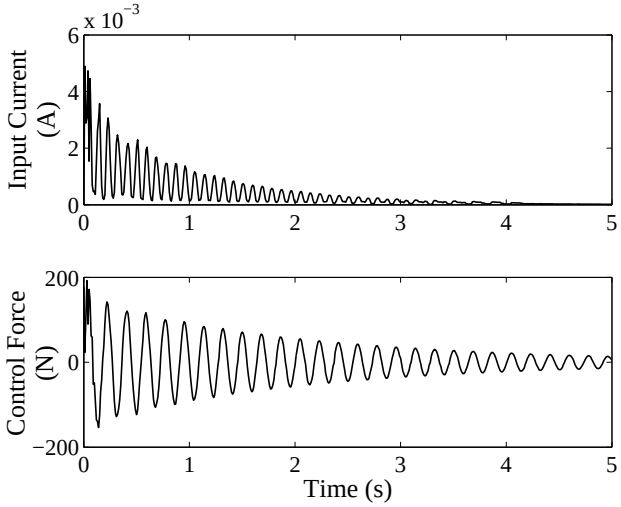

Figure 6.14: Input current and damper force under impulsive force (backstepping control)

Seismic analysis

Figure 6.15 shows the time histories of the uncontrolled (simple isolation) and controlled system (hybrid isolation) responses of base isolator and at the third floor under El-Centro ground

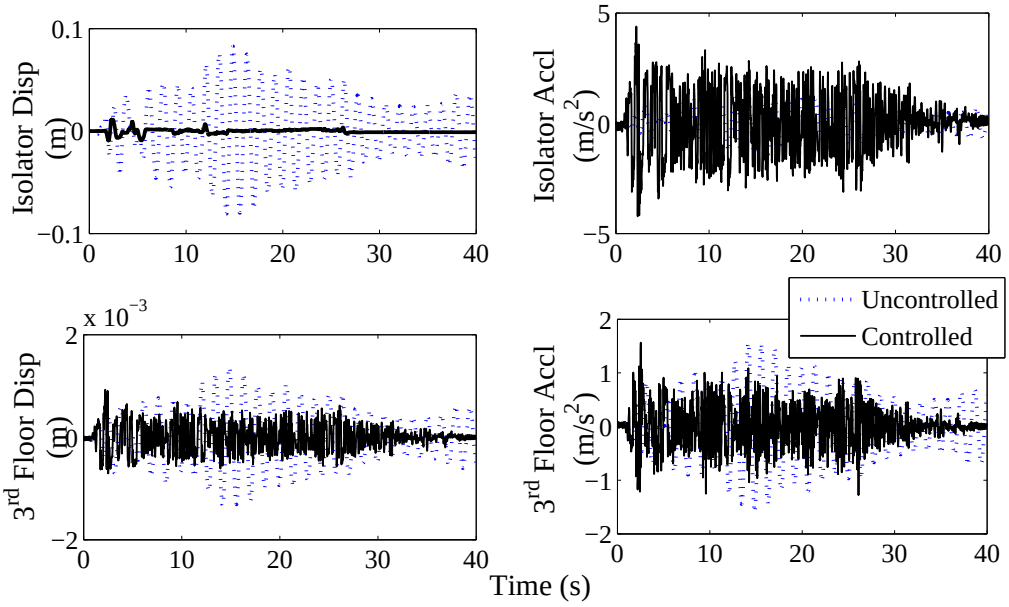

Figure 6.15: Base isolator and 3^{rd} floor displacement and acceleration responses under El-Centro (X) (Uncontrolled and backstepping control)

motion. The uncontrolled and controlled displacement and acceleration responses are shown together for better comparison. The peak displacement response of the isolator is found to be $0.0827\ m$, which is reduced to $0.0112\ m$ by the integral backstepping monitored MR damper. The isolator acceleration is observed to increase from $1.5631\ m/s^2$ to $4.3883\ m/s^2$ with backstepping based control, which is a smaller increase in comparison to that obtained through DI based control.

The third floor displacement is also reduced from $0.0014\ m$ in uncontrolled (simple isolation) condition to $0.0009\ m$ in MR damper controlled (hybrid isolation) case but at the same time the acceleration has gone up. The control force provided by the MR damper and the corresponding input current to the MR damper are shown in Fig. 6.16. It is clear from the input current time history shown in Fig. 6.16 that only a small amount current input is needed to mitigate the vibration caused by the Elcentro ground motion. Therefore, switching the input current from zero to maximum based on system responses decreases the system performance under seismic motions.

Similar to Fig. 6.15, the responses under N. Palm Spring seismic ground motion are shown

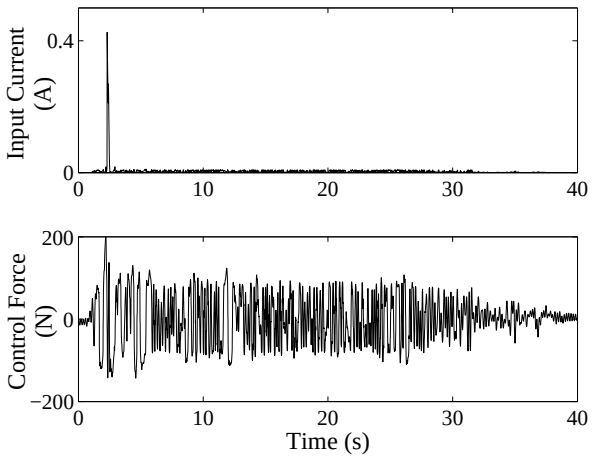

Figure 6.16: Input current and damper force under El-Centro (X) (backstepping control)

in Fig. 6.17. The performance of the backstepping based controller is quite evident from the Fig. 6.17 itself. A maximum isolator displacement of $0.2077\ m$ is reduced to $0.0157\ m$. The isolator acceleration and the superstructure displacement responses are also reduced using backstepping based MR damper control. Only the superstructure acceleration responses increased over that of the uncontrolled case.

The current input to the MR damper for the above performance is shown in Fig. 6.18. Figure 6.18 also shows the force provided by the MR damper to the system. It is seen that the MR damper maximum current input is not required.

6.6 Comparative Analysis of Control Strategies

This section reports a comparative analysis of four control strategies. The four control strategies selected are the following,

- DI: Dynamic inversion based MR damper current monitoring. The method is developed in this Chapter and reported in an earlier section. This is a two-stage control scheme, where the primary controller is selected as the LQR control method

- IB: Integrator backstepping based MR damper current monitoring. This method is also developed in this chapter and discussed in an earlier section

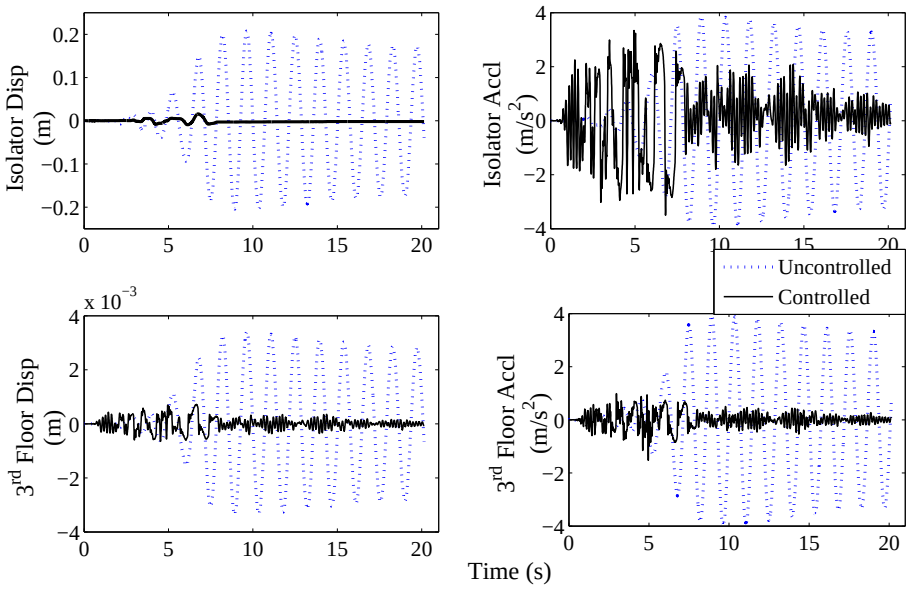

Figure 6.17: Base isolator and 3^{rd} floor displacement and acceleration responses under N. Palm Spring (X) (Uncontrolled and backstepping control)

- CO: LQR clipped optimal strategy is adopted for the comparative analysis as this is the widely used model based control scheme in the literature. Details of the clipped optimal strategy has been discussed in the Chapter 2 and can also be found in Dyke

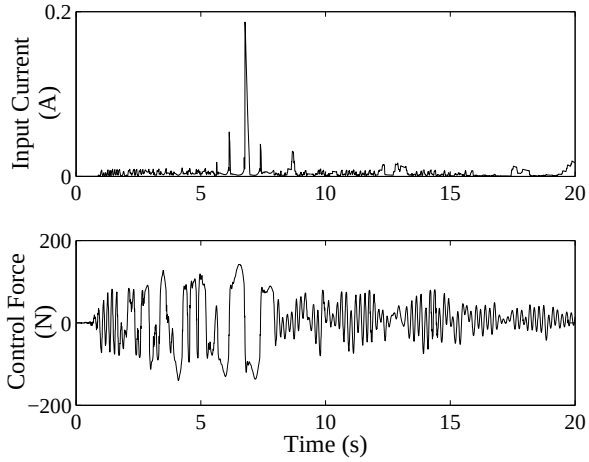

Figure 6.18: Input current and damper force under N. Palm Spring (X) (backstepping control)

et al. (1995,1996a, b) [98, 99, 100]. The parameter considered for the LQR control is the same as in the DI based two stage controller. The parameters are provided in the preceding section

- GA-FLC: Intelligent technique based optimal fuzzy logic controller developed in Chapter 4 ia adopted as the fourth control scheme for comparative analysis.

The three storey hybrid base isolated building considered for the experimental study in Chapter 5 and also for the numerical simulations in the preceding section in this chapter is considered for the comparative study. All the sixteen seismic ground motion data are considered (see Table 5.2 of Chapter 5). For the comparison of different control schemes a set of performance indices are considered and are given in Table 6.1. In Table 6.1, $|.|$ denotes

Table 6.1: Performance Indices for Comparative Study of Control Strategies

Peak Base Displacement $J_1 = \frac{t_{max}\lvert x_{b\ c}(t)\rvert}{t_{max}\lvert x_{b\ unc}(t)\rvert}$	**Peak Floor Displacement** $J_2 = \frac{t_{max}\lvert x_{n\ c}(t)\rvert}{t_{max}\lvert x_{n\ unc}(t)\rvert}$	**Peak Base Velocity** $J_3 = \frac{t_{max}\lvert \dot{x}_{b\ c}(t)\rvert}{t_{max}\lvert \dot{x}_{b\ unc}(t)\rvert}$
Peak Floor velocity $J_4 = \frac{t_{max}\lvert \dot{x}_{n\ c}(t)\rvert}{t_{max}\lvert \dot{x}_{n\ unc}(t)\rvert}$	**Peak Base Acceleration** $J_5 = \frac{t_{max}\lvert \ddot{x}_{b\ c}(t)\rvert}{t_{max}\lvert \ddot{x}_{b\ unc}(t)\rvert}$	**Peak Floor Acceleration** $J_6 = \frac{t_{max}\lvert \ddot{x}_{n\ c}(t)\rvert}{t_{max}\lvert \ddot{x}_{n\ unc}(t)\rvert}$
Peak Control Force $J_7 = t_{max}\lvert u(t)\rvert$	**Peak Current Input** $J_8 = t_{max}\lvert i_a(t)\rvert$	– –
RMS Base Displacement $J_9 = \frac{t_{max}\lVert x_{b\ c}(t)\rVert}{t_{max}\lVert x_{b\ unc}(t)\rVert}$	**RMS Floor Displacement** $J_{10} = \frac{t_{max}\lVert x_{n\ c}(t)\rVert}{t_{max}\lVert x_{n\ unc}(t)\rVert}$	**RMS Base Velocity** $J_{11} = \frac{t_{max}\lVert \dot{x}_{b\ c}(t)\rVert}{t_{max}\lVert \dot{x}_{b\ unc}(t)\rVert}$
RMS Floor Velocity $J_{12} = \frac{t_{max}\lVert \dot{x}_{n\ c}(t)\rVert}{t_{max}\lVert \dot{x}_{n\ unc}(t)\rVert}$	**RMS Base Acceleration** $J_{13} = \frac{t_{max}\lVert \ddot{x}_{b\ c}(t)\rVert}{t_{max}\lVert \ddot{x}_{b\ unc}(t)\rVert}$	**RMS Floor Acceleration** $J_{14} = \frac{t_{max}\lVert \ddot{x}_{n\ c}(t)\rVert}{t_{max}\lVert \ddot{x}_{n\ unc}(t)\rVert}$

the absolute value and $\|.\|$ denotes the L_2 norm. The subscripts (x_c) and (x_{unc}) denotes the controlled and uncontrolled responses, respectively. The peak of the responses is considered over time (t_{max}). The floor responses are computed as the maximum over the floor, where n denotes the n^{th} floor ($n = 1,\ 2,\ 3$).

The results obtained from numerical study of various control strategies are tabulated in Tables 6.2 and 6.3 for X direction component of seismic motions and in Tables 6.4 and 6.5 for Y direction component of seismic motion. The normalized maximum responses are shown in Tables 6.2 and 6.4, while the response norms are shown in Tables 6.3 and 6.5 respectively.

Tables 6.2 - 6.5 contain all the controller performances together for better comparison. All four controllers reduce the base isolator displacement response (J_1) in both X direction and Y direction components of seismic motions. The base displacement reduces to a range of 1% to 5% of its value at no damper case (simple isolation system). This shows the performance of the hybrid isolation technique in reducing isolator displacement. LQR-CO is observed to reduce the base displacement more than any other controller for X-direction component of seismic motion, whereas GA-FLC is observed to perform better in reducing base displacement in Y-direction component of seismic motion.

Superstructure displacement (J_2) is increased in most of the simulations with seismic excitations (in both X and Y components) for the LQR-CO and GA-FLC cases. Integrator backstepping based MR damper monitoring provides reduction in the floor displacement responses for all seismic motions except for Coalinga (X direction) seismic data, where it provides less increase than other controllers. Therefore, superstructure performance is seen to better in backstepping based control scheme.

The isolator velocity (J_3) is reduced with an increase in superstructure velocity (J_4) response in all four control schemes. In this case also backstepping based control scheme shows better performance.

It is to be noted that the decrease in base isolator displacement response, increases the isolator acceleration response. From the performance index (J_5), it is observed that the isolator acceleration is increased by all control schemes under all seismic motions, except under Chichi earthquake with backstepping control scheme, where a decrease of about 23% is seen from that of simple base isolation strategy. The maximum increase in acceleration is seen for clipped optimal strategy for all X-direction components of seismic motions and GA-FLC for all Y-direction components of seismic motions. The minimum increase is observed in integral backstepping based MR damper control.

The superstructure peak acceleration response is seen to decrease with all control schemes under almost all seismic motions except under Coalinga (X) and El-Centro (X) seismic motions, where an increase in storey acceleration is seen. Among all controllers the increase in the acceleration response is least in backstepping based controller. DI performs better than other two controllers. LQR-CO performs worst in most of the seismic excitation cases.

It should be noted that the isolator displacement is reduced by the clipped optimal algorithm better than other controller. This large decrease in the isolator displacement has increased the isolator accelerations. This is one of the drawback of the clipped optimal strategy. As there is no variable current input between zero and maximum to the MR damper, the damper provides a force to the system which is not optimal.

As shown by the performance index, J_7, the maximum control force (in newton) is provided by the clipped optimal case in most of the seismic excitations. Performance index, J_8 shows the corresponding maximum current supplied to the MR damper in amperes.

Similar performances as discussed above for all four control schemes can be observed in the L_2 norm responses tabulated in Tables 6.3 and 6.5.

From the above discussions, it can be concluded that the performance of the controllers are a trade-off between the isolator displacement and the superstructure acceleration. This is also observed in the experimental study carried out and reported in Chapter 5. A control designer has to select a control scheme based on the priority of the project. As an example base isolators are provided with an intension to reduce the superstructure displacement and acceleration responses, such that instruments housed inside remain safe during seismic motions. Therefore reducing base displacement to the full range of the MR damper disrupts the primary intention with which base isolation is provided. A trade-off has to be made between the acceptable base displacement and acceptable isolator accelerations. In such a scenario, a designer can allow a certain free movement to the isolator without damper and after a certain limit the damper should act such that the total displacement should not go beyond the acceptable limit of base displacement. The free movement of the isolator will keep the superstructure and isolator responses at lower value and the damper action beyond a certain limit, on the other hand, will reduce the base displacement slightly.

Table 6.2: Peak Responses of Hybrid Base Isolated Building for X-direction Seismic Motion

PI	Control	Earthquake Records							
		Big Bear	Capemend	Chichi	Coalinga	El Centro	Loma prieta	N.Palm Spring	Kobe
J_1	DI	0.057	0.027	0.043	0.150	0.148	0.036	0.055	0.022
	IB	0.050	0.062	0.044	0.299	0.136	0.033	0.076	0.023
	CO	0.008	0.032	0.006	0.236	0.027	0.002	0.007	0.003
	GA-FLC	0.012	0.016	0.006	0.089	0.035	0.004	0.007	0.005
J_2	DI	0.552	0.428	0.257	1.861	1.197	0.361	0.260	0.855
	IB	0.340	0.251	0.173	1.449	0.682	0.310	0.210	0.657
	CO	0.795	0.664	0.348	2.691	1.517	0.654	0.505	1.300
	GA-FLC	0.735	0.545	0.360	1.956	1.375	0.734	0.509	1.480
J_3	DI	0.103	0.082	0.054	0.375	0.179	0.048	0.075	0.075
	IB	0.114	0.137	0.065	0.559	0.341	0.051	0.079	0.092
	CO	0.057	0.059	0.017	0.506	0.162	0.015	0.053	0.028
	GA-FLC	0.042	0.039	0.013	0.226	0.107	0.010	0.040	0.019
J_4	DI	4.542	3.400	2.099	15.063	11.038	2.145	2.059	5.072
	IB	3.253	2.527	1.725	8.230	6.735	2.777	1.981	4.492
	CO	5.598	5.272	2.506	24.124	12.197	3.575	4.073	7.651
	GA-FLC	5.421	4.579	2.444	12.703	11.132	4.260	3.998	9.270
J_5	DI	2.802	1.950	1.277	8.671	5.262	1.677	1.332	3.992
	IB	1.436	1.116	0.770	6.608	2.807	1.523	0.892	3.034
	CO	3.567	2.895	1.530	12.376	6.814	3.063	2.123	6.139
	GA-FLC	3.336	2.461	1.614	9.712	6.095	3.400	2.280	6.869
J_6	DI	0.687	0.871	0.336	2.761	1.915	0.471	0.422	1.035
	IB	0.581	0.466	0.241	1.587	0.983	0.362	0.381	0.779
	CO	1.080	0.888	0.444	4.401	2.263	0.678	0.784	1.435
	GA-FLC	0.862	0.670	0.407	2.676	1.810	0.780	0.664	1.610
J_7	DI	327	336	214	912	379	115	199	118
	IB	129	166	127	512	204	92	142	91
	CO	320	427	255	823	362	220	314	219
	GA-FLC	321	361	284	742	393	241	383	238
J_8	DI	2	2	2	2	2	2	2	2
	IB	0.02	0.03	0.041	0.27	0.43	0.01	0.19	0.01
	CO	2	2	2	2	2	2	2	2
	GA-FLC	0.13	0.18	0.07	0.49	0.21	0.021	0.19	0.02

Table 6.3: Response Norms of Hybrid Base Isolated Building for X-direction Seismic Motion

PI	Control	Earthquake Records							
		Big Bear	Capemend	Chichi	Coalinga	El Centro	Loma prieta	N.Palm Spring	Kobe
J_9	DI	0.037	0.014	0.015	0.086	0.093	0.060	0.023	0.046
	IB	0.016	0.024	0.015	0.122	0.067	0.019	0.033	0.032
	CO	0.006	0.046	0.008	0.075	0.029	0.003	0.010	0.002
	GA-FLC	0.004	0.016	0.007	0.054	0.023	0.006	0.009	0.003
J_{10}	DI	0.167	0.163	0.092	0.768	0.552	0.242	0.128	0.349
	IB	0.156	0.137	0.090	0.658	0.457	0.243	0.123	0.346
	CO	0.255	0.206	0.113	1.000	0.810	0.303	0.193	0.451
	GA-FLC	0.292	0.220	0.127	1.122	0.874	0.376	0.212	0.515
J_{11}	DI	0.015	0.016	0.010	0.145	0.060	0.014	0.024	0.009
	IB	0.020	0.029	0.013	0.230	0.092	0.016	0.032	0.010
	CO	0.006	0.009	0.002	0.147	0.029	0.004	0.006	0.007
	GA-FLC	0.005	0.007	0.002	0.077	0.023	0.004	0.006	0.006
J_{12}	DI	1.123	1.030	0.478	4.506	3.783	1.238	0.754	2.031
	IB	1.015	0.781	0.444	3.106	2.915	1.229	0.669	1.944
	CO	1.876	1.355	0.664	7.788	6.019	1.869	1.324	2.956
	GA-FLC	2.120	1.392	0.799	6.139	6.103	2.556	1.445	3.587
J_{13}	DI	0.794	0.761	0.435	3.630	2.583	1.176	0.609	1.643
	IB	0.713	0.625	0.417	2.989	2.089	1.131	0.576	1.618
	CO	1.172	0.989	0.526	4.581	3.732	1.406	0.891	2.085
	GA-FLC	1.345	1.021	0.589	5.216	4.024	1.737	0.980	2.374
J_{14}	DI	0.189	0.218	0.099	0.914	0.648	0.258	0.143	0.383
	IB	0.174	0.152	0.095	0.717	0.519	0.256	0.134	0.370
	CO	0.292	0.240	0.122	1.288	0.946	0.328	0.217	0.496
	GA-FLC	0.322	0.237	0.136	1.206	0.961	0.407	0.232	0.560

Table 6.4: Peak Responses of Hybrid Base Isolated Building for Y-direction Seismic Motion

PI	Control	Earthquake Records							
		Big Bear	Capemend	Chichi	Coalinga	El Centro	Loma prieta	N.Palm Spring	Kobe
J_1	DI	0.042	0.036	0.041	0.122	0.066	0.114	0.083	0.017
	IB	0.051	0.045	0.037	0.181	0.078	0.112	0.107	0.011
	CO	0.004	0.003	0.007	0.091	0.010	0.003	0.003	0.002
	GA-FLC	0.003	0.004	0.006	0.050	0.014	0.003	0.003	0.002
J_2	DI	0.230	0.421	0.309	0.732	0.948	0.738	0.440	0.499
	IB	0.196	0.223	0.272	0.648	0.663	0.611	0.382	0.470
	CO	0.384	0.599	0.642	1.265	1.456	1.198	0.674	0.843
	GA-FLC	0.364	0.516	0.639	0.941	1.498	1.324	0.678	1.003
J_3	DI	0.059	0.079	0.053	0.181	0.100	0.130	0.131	0.042
	IB	0.076	0.085	0.070	0.243	0.106	0.136	0.133	0.038
	CO	0.023	0.026	0.054	0.169	0.051	0.027	0.022	0.019
	GA-FLC	0.018	0.024	0.041	0.082	0.053	0.016	0.018	0.013
J_4	DI	1.943	3.872	2.687	4.850	6.451	6.799	3.669	4.456
	IB	1.900	2.102	2.505	3.785	5.337	6.311	3.347	4.269
	CO	2.962	4.146	5.288	9.026	11.192	8.451	5.938	7.021
	GA-FLC	2.780	3.828	4.722	5.940	10.022	8.235	5.112	7.225
J_5	DI	1.218	1.761	1.626	3.760	4.234	4.003	2.223	2.266
	IB	0.811	1.023	1.156	3.351	2.774	3.166	1.525	2.109
	CO	1.692	2.626	2.921	5.664	6.603	5.559	3.053	3.930
	GA-FLC	1.661	2.391	2.905	4.415	6.846	6.145	3.104	4.614
J_6	DI	0.291	0.656	0.445	1.023	1.266	0.843	0.641	0.648
	IB	0.294	0.275	0.407	0.780	0.947	0.745	0.432	0.577
	CO	0.502	0.754	0.737	1.783	1.776	1.358	0.779	0.978
	GA-FLC	0.412	0.577	0.731	1.116	1.658	1.395	0.753	1.095
J_7	DI	262	209	182	479	237	135	163	98
	IB	142	123	115	366	100	101	131	83
	CO	264	275	353	485	260	216	245	158
	GA-FLC	299	289	338	476	288	237	262	181
J_8	DI	2	2	2	2	2	2	2	2
	IB	0.03	0.05	0.02	0.67	0.01	0.02	0.01	0.01
	CO	2	2	2	2	2	2	2	2
	GA-FLC	0.09	0.08	0.14	0.28	0.07	0.02	0.04	0.01

Table 6.5: Normed Responses of Hybrid Base Isolated Building for Y-direction Seismic Motion

PI	Control	Earthquake Records							
		Big Bear	Capemend	Chichi	Coalinga	El Centro	Loma prieta	N.Palm Spring	Kobe
J_9	DI	0.015	0.030	0.022	0.072	0.057	0.198	0.079	0.028
	IB	0.014	0.022	0.014	0.068	0.023	0.129	0.067	0.015
	CO	0.007	0.001	0.007	0.034	0.012	0.001	0.001	0.001
	GA-FLC	0.003	0.001	0.005	0.033	0.018	0.002	0.002	0.001
J_{10}	DI	0.096	0.109	0.175	0.304	0.516	0.529	0.329	0.160
	IB	0.092	0.103	0.170	0.274	0.474	0.532	0.319	0.160
	CO	0.140	0.151	0.251	0.419	0.795	0.631	0.492	0.184
	GA-FLC	0.155	0.168	0.293	0.461	0.945	0.681	0.559	0.237
J_{11}	DI	0.010	0.008	0.015	0.060	0.027	0.033	0.049	0.003
	IB	0.016	0.013	0.018	0.085	0.032	0.037	0.063	0.003
	CO	0.003	0.003	0.005	0.038	0.014	0.008	0.008	0.003
	GA-FLC	0.002	0.003	0.005	0.023	0.014	0.007	0.008	0.003
J_{12}	DI	0.599	0.679	1.086	1.654	3.592	3.092	1.805	0.970
	IB	0.578	0.599	1.031	1.417	3.225	3.088	1.603	0.967
	CO	0.990	1.001	1.729	2.892	5.970	4.062	3.417	1.192
	GA-FLC	1.091	1.160	2.064	2.723	6.972	4.499	4.013	1.703
J_{13}	DI	0.452	0.531	0.818	1.465	2.400	2.697	1.601	0.758
	IB	0.425	0.491	0.785	1.269	2.182	2.561	1.487	0.745
	CO	0.644	0.697	1.157	1.937	3.657	2.918	2.270	0.851
	GA-FLC	0.715	0.774	1.350	2.145	4.345	3.148	2.574	1.093
J_{14}	DI	0.107	0.127	0.194	0.341	0.587	0.573	0.360	0.173
	IB	0.102	0.112	0.186	0.298	0.534	0.569	0.338	0.171
	CO	0.156	0.168	0.277	0.486	0.896	0.688	0.537	0.201
	GA-FLC	0.169	0.183	0.319	0.492	1.041	0.734	0.608	0.259

6.7 Summary

The nonlinear force-input current/voltage relation of MR damper introduces challenges in modeling the damper characteristic as well as in developing proper control strategy to effectively use the damper capacity. Existing model based algorithms switch the MR damper input current/voltage between zero and maximum, based on force feedback from the damper and the desired control force. Another drawback of existing algorithms is that none of them consider the dynamics of the input current/voltage in the algorithms. These two drawbacks in existing control schemes formed two objectives of the present chapter.

In this chapter, two model based semi-active control algorithms are developed using modern nonlinear control techniques. The developed algorithms not only update the current/voltage supply to the damper smoothly, but also take care of the MR damper supplied to commanded current/voltage dynamics in the algorithms.

Firstly, dynamic inversion based semi-active control scheme is developed for a MISO system. Later the method is extended to a MIMO system, where DI is clubbed with classical optimization technique to provide an optimal damper current/voltage. These algorithms are two stage controller and DI is used to track the force prescribed by the primary controller. Therefore, its performance is dependent on the performance of the primary controller and it also requires the measurement of MR damper force in real time. To avoid this drawback of DI based approach another model based stable controller is designed. Displacement and velocity at the damper location are needed for feedback to the algorithm. The technique is stable in Lyapunov sense. The performances of DI and integral backstepping are shown taking the hybrid base isolated building considered in Chapter 5. The simulation studies have shown that the controllers are effective in reducing the structural responses under impulsive force as well as due to earthquake ground motions. Finally the performances of the controllers are compared with the widely used clipped optimal algorithm and optimal FLC developed in Chapter 4.

The MIMO ODI is applied on a benchmark highway bridge. Details of the benchmark highway bridge and the performance of MIMO ODI are given in Chapter 7.

Chapter 7

Benchmark Applications

7.1 Overview

In the preceding chapters details of various semi-active control algorithms to monitor the current/voltage supply to the MR damper have been presented. '*Optimal FLC*' based on micro GA (μ GA) and PSO optimization schemes have been discussed in Chapter 4. Later in Chapter 5, performance of the proposed '*optimal FLC*' has been established through an experimental study on a laboratory scaled three storey benchmark building. In Chapter 6, a couple of model based semi-active control algorithms namely, '*optimal dynamic inversion*' and '*integral backstepping*' have been proposed to monitor MR damper input current and their effectiveness have been shown through a numerical simulation of the same three storey base isolated building considered for the experimental study in Chapter 5. In this chapter the performance of the proposed semi-active control algorithms has been evaluated through numerical simulations on full scale benchmark structures. A benchmark base isolated building structure and a benchmark highway bridge are considered as two examples and later vibration mitigation of a stay cable with sag is presented. Therefore the chapter has been organized into three sections: the first provides the details of the study on the benchmark building example, while the second section details of the studies on semi-active control of the benchmark highway bridge and the example of the stay cable with sag has been outlined in third section of the chapter. Finally, a summary of the findings from the benchmark studies is presented.

7.2 Background to Benchmark

There have been several benchmark structural control exercises defined for investigating the effectiveness of various control strategies for a series of Civil Engineering structures (Caughey (1998) [55]; Spencer et al. (1998a, b) [328, 327]; Ohtori et al. (2004) [268]; Yang et al. (2004) [394]; Dyke et al. (2003) [96]). The objective of these benchmark studies has been to provide well defined structural models with a broad set of carefully chosen parameters, performance measures and guidelines to the participants, so that researchers can evaluate their control algorithms on a common platform. The evaluation ranges from competing control strategies, including devices, algorithms, sensors, *etc*, to optimization of location of control devices and sensor locations. Carefully defined analytical benchmark problems are an excellent alternative to expensive experimental benchmark test structures (Caughey (1998) [55]; Ohtori et al. (2004) [268]).

The last decade has shown the development of well-defined analytical benchmark problems for studying response control strategies for building and bridge structures subjected to seismic and wind excitations, by broad consensus effort of the ASCE structural control committee (Caughey (1998) [55]; Spencer et al. (1998a, b) [328, 327]; Ohtori et al. (2004) [268]; Yang et al. (2004) [394]; Dyke et al. (2003) [96]). These studies included three generations of earthquake excited and a wind excited benchmark building models (Caughey (1998) [55]; Spencer et al. (1998a, b) [328, 327]; Ohtori et al. (2004) [268]; Yang et al. (2004) [394]) and a benchmark cable-stayed bridge problem (Dyke et al. (2003) [96]; Caicedo et al. (2003) [49]).

Recently, the ASCE structural control committee has developed a smart base isolated benchmark building problem and a smart benchmark highway bridge problem. The benchmark building model selected is a base plus eight storey building defined and studied by various investigators (Nagarajaiah et al. (2006) [252]; Nagarajaiah and Narasimhan (2006) [248]; Nagarajaiah et al. (2008) [251]; Narasimhan and Nagarajaiah (2006) [259]; Narasimhan et al. (2006, 2008) [261, 260]; Erkus and Johnson (2006) [107]). The smart base isolated benchmark exercise has been developed with a capability to model three different kinds of base isolation systems, namely, linear elastomeric systems with low damping or supplemental high damping, frictional systems, bilinear or nonlinear elastomeric systems or any combination thereof. The objective of the study is to develop supplemental damping mechanisms to reduce the isolator displacement at near fault and far fault seismic excitations, while preserving the primary

objectives of securing the safety of the structure and occupant comfort.

Highway bridges should perform in working condition in the aftermath of hazardous seismic motions to carry on with the rescue operations. Therefore, performance evaluation of highway bridges under several near and far fault seismic motion is an important objective for structural control engineers. To meet this objective, the problem definition for a benchmark highway bridge model, based on the newly constructed $91/5$ highway bridge in southern California bridge to provide systematic and standardized means by which competing control strategies, including devices, control algorithms and sensors, have been provided by Agrawal et al. (2005) [7]; Tan and Agrawal (2005) [353]; Nagarajaiah et al. (2006) [250].

In this chapter, the recently developed hybrid base isolated benchmark building, the benchmark highway bridge and a stay cable with sag are considered for the performance evaluation of the control strategies proposed in preceding chapters.

7.3 Base Isolated Benchmark Building

Building structures are isolated from the harmful effects of seismic ground excitations using base isolation systems, such as sliding and elastomeric bearing systems, with an intension to reduce the super-structure response and to protect sensitive instruments housed inside. Seismic excitations caused by fault-normal component of near-fault ground motions increase base displacement beyond specified limits. This causes the bearing to fail, defeating the purpose of base isolation. Current practice is to provide nonlinear passive dampers to limit the bearing displacements. However, this increases the forces in the superstructure and also at the isolation level. Active and semi-active devices present attractive alternatives to passive nonlinear devices. Active and Semi-active control of linear and nonlinear structures using novel devices such as MR dampers, electro-rheological (ER) dampers and variable stiffness systems have gained significant attention in the recent years (Spencer and Nagarajaiah (2003) [326]).

The efficacy of an optimal FLC to monitor semi-active MR damper has been established with an experimental study in the Chapter 5. Here exploration of the suitability of the optimal FLC algorithm applied to a full scale benchmark base isolated building is presented through numerical simulations. In this chapter, a study is conducted on the phase-II of the base isolated benchmark building.

The phase-I of the smart base-isolated building benchmark has been reported in Narasimhan et al. (2006) [261]; Nagarajaiah and Narasimhan (2006) [248]. In phase-II of the benchmark study, same benchmark superstructure is considered but with nonlinear isolation system. The nonlinear isolation system consists of a combination of linear and hysteretic (friction and lead-rubber) bearings along with nonlinear control devices. The superstructure is assumed linear with lateral-torsional behaviour and the nonlinearities arising from the nonlinear bearing and device characteristics are limited to the isolation level only. In phase-II, the participants need to compare the results of their controllers with the sample Lyapunov controller and other controllers presented by Nagarajaiah and Narasimhan (2006) [248] for nonlinear friction isolation system.

7.3.1 Benchmark Building Definition

The benchmark structure is a L-shaped nonlinear base isolated eight-storey, steel-braced framed building, 82.4 m long and 54.3 m wide, similar to an existing building in Los Angeles, California (Narasimhan et al. (2006) [261]). The floor plan is shown in Fig. 7.1(a). The isolators are connected between the superstructure and the footings below at the column locations. Isolator and MR damper connection detailing is shown in Fig. 7.1(b). The steel superstructure is supported on a reinforced concrete base slab, which is integrated with concrete columns, and drop panels have been provided below each column location. The isolators are located between these drop panels and the footings (Fig. 7.1(b)).

Narasimhan et al. (2006) [261] modeled the superstructure as a three dimensional linear elastic system. The superstructure members, such as beam, column, bracing, and floor slab are all incorporated in the model. Floor slabs and the base slab have been idealized to be rigid in plane and consisted of three master degrees of freedom (DOF) per floor at the center of mass. The combined model of the superstructure (24 DOF) and isolation system (3 DOF) consisted of 27 degrees of freedom. All twenty four modes in the fixed base building case are used by Narasimhan et al. (2006) [261] in modeling the superstructure. The superstructure damping ratio is assumed to be 5% in all fixed base modes. The computed natural periods for the first nine fixed base modes are reported to be 0.78, 0.27 and 0.15 seconds in the North-South direction, 0.89, 0.28 and 0.15 seconds in the East-West direction and 0.66, 0.21 and 0.12 seconds in torsion. The study considered a nominal isolation system consisting of 61 friction

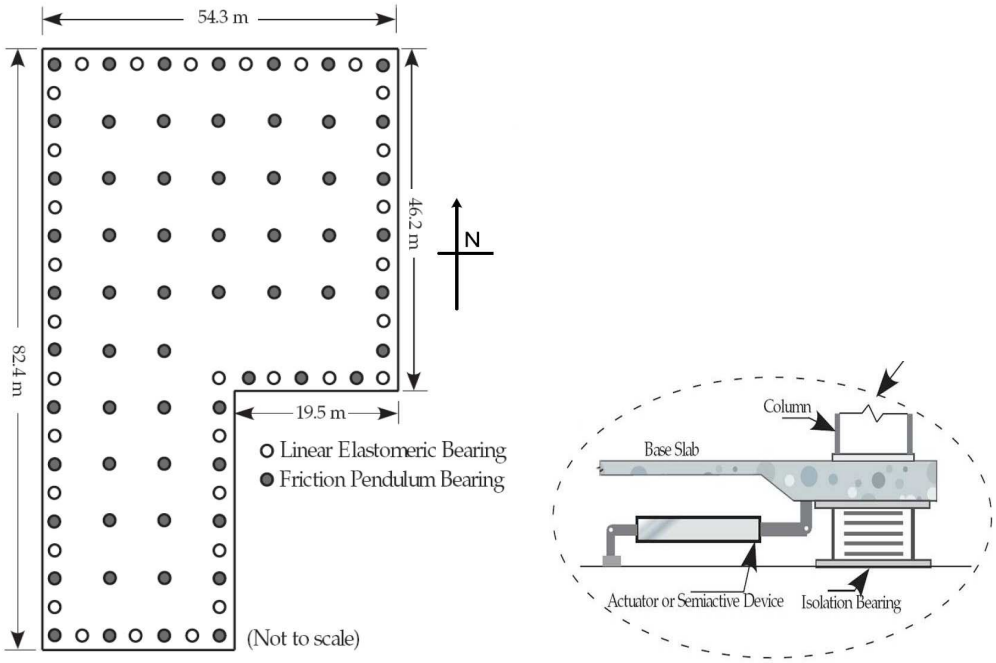

(a) Building plan showing bearing locations (b) MR damper and isolator connection

Figure 7.1: Base isolated benchmark building details (Narasimhan et al. (2006) [261])

pendulum bearings and 31 linear elastomeric bearings as shown in Fig. 7.1(a). Further details of the problem definition can be found in Nagarajaiah et al. (2006) [252]; Nagarajaiah and Narasimhan (2006) [248]; Narasimhan et al. (2006) [261] and Erkus and Johnson (2006) [107]; Nagarajaiah et al. (2008) [251].

Isolator design

In the benchmark exercise, several isolation elements are included so that any combination of these can be used to model the isolation system completely. The isolation elements consisted of elastic, viscous, hysteretic elements for bilinear elastomeric bearings and hysteretic elements for sliding bearings. The hysteretic elements can be uni-axial or biaxial. The linear elastic and viscous elements that are generally used to model linear elastomeric bearings and fluid dampers are used for modeling bilinear elastomeric isolation systems with corresponding equivalent linear properties. In the benchmark study, the biaxial hysteretic behaviour of

bilinear elastomeric bearings and/or frictional bearings are modeled using the biaxial interaction equations of Bouc-Wen hysteretic model proposed by Park et al. (1986) [271]. This is given in Eq. 7.1.

$$\{U^y\} \left\{ \begin{array}{c} \dot{z}_x \\ \dot{z}_y \end{array} \right\} = \alpha \left\{ \begin{array}{c} \dot{U}_x \\ \dot{U}_y \end{array} \right\} - [\mathbb{Z}_w] \left\{ \begin{array}{c} \dot{U}_x \\ \dot{U}_y \end{array} \right\} \tag{7.1}$$

where $[\mathbb{Z}_w]$ is given by,

$$[\mathbb{Z}_w] = \left[\begin{array}{cc} z_x^2 \left(\gamma sgn(\dot{U}_x z_x) + \beta\right) & z_x z_y \left(\gamma sgn(\dot{U}_y z_y) + \beta\right) \\ z_x z_y \left(\gamma sgn(\dot{U}_x z_x) + \beta\right) & z_y^2 \left(\gamma sgn(\dot{U}_y z_y) + \beta\right) \end{array} \right]$$

z_x and z_y are dimensionless hysteretic variables that are bounded by values ± 1. α, β, γ are dimensionless scalar quantities to be obtained through experimental studies of the bearings. U_x, U_y and $\dot{U}_x$, $\dot{U}_y$, represent the displacements and velocities in the x and y directions, respectively, at the isolation bearing or device and U^y is the displacement at yielding of the bearing. Equation 7.1 accounts for biaxial interaction of both sliding and bilinear hysteretic bearings. When yielding commences Eq. 7.1 leads to $z_x = cos(\theta)$ and $z_y = sin(\theta)$ provided $\frac{\alpha}{\beta+\gamma} = 1$ with $\theta = tan^{-1}(\frac{\dot{U}_x}{\dot{U}_y})$ and the resultant velocity $\dot{U} = \sqrt{\dot{U}_x^2 + \dot{U}_y^2}$. The biaxial interaction can be neglected when the off-diagonal terms of the matrix in $\mathbb{Z}_w$ are replaced by zeros. This results in an uniaxial model with two independent elements in two orthogonal directions.

The forces, f, mobilized in the elastomeric isolation bearings are modeled by a elastic-visco-plastic model with strain hardening characteristics given in Eq. 7.2.

$$f_x = k_p U_x + c_v \dot{U}_x + (k_e - k_p)\, U^y z_x \tag{7.2}$$

$$f_y = k_p U_y + c_v \dot{U}_y + (k_e - k_p)\, U^y z_y \tag{7.3}$$

Where k_e pre-yield stiffness, k_p is the post-yield stiffness, c_v is the viscous damping coefficient of the elastomeric bearing and U^y is the yield displacement. The viscous damping for the bearings is considered to be zero (*i.e.*, $c_v = 0$). The weight or average normal force (N) of the structure is related to the stiffness coefficients as $(k_e - k_p)\, U^y = \mu N$, with μ being the coefficient of friction for sliding bearings.

The benchmark study reported 61 friction pendulum bearings and 31 linear elastomeric

bearings in the nominal isolation system (Nagarajaiah et al. (2006) [252]). However, the participants have been permitted to replace them with other types of bearings. Three types of base isolation systems are considered for control design purposes

1. linear elastomeric isolation system with low damping

2. nonlinear friction isolation system representing friction pendulum system

3. bilinear elastomeric isolation system representing lead-rubber system.

The isolation systems and the corresponding sample control designs are described in detail in Erkus and Johnson (2006) [107]. In the present analysis the bearing properties of the benchmark exercise are kept unchanged.

Three dimensional benchmark building model

Base isolated buildings are designed such that the superstructure remains elastic. Hence, the superstructure in the benchmark study ismodeled as a three dimensional linear elastic shear building. In addition, the equations of motion of the isolated structure reported contain the fixed base properties of the building used for modeling the linear superstructure. Each nonlinear isolation bearing or device is modeled explicitly using the discrete biaxial BoucWen model (as discussed in previous section), and the forces in the bearings or devices reported to be transformed to the center of mass of the base using a rigid base slab assumption. The equations of motion for the elastic superstructure are reported in the following form

$$\mathbf{M}_{n\times n}\,\ddot{\mathbf{U}}_{n\times 1}+\mathbf{C}_{n\times n}\,\dot{\mathbf{U}}_{n\times 1}+\mathbf{K}_{n\times n}\,\mathbf{U}_{n\times 1}=-\mathbf{M}_{n\times n}\,\mathbf{R}_{n\times 3}\left(\ddot{\mathbf{U}}_{g}+\ddot{\mathbf{U}}_{b}\right)_{3\times 1} \tag{7.4}$$

in which, n is three times the number of floors (excluding base slab), $\mathbf{M}$ is the superstructure mass matrix, $\mathbf{C}$ (modal damping ratio=5%), and $\mathbf{K}$ are the superstructure damping and stiffness matrices, respectively in the fixed-base case and $\mathbf{R}$ is the matrix of earthquake influence coefficients. Furthermore, $\ddot{\mathbf{U}}$, $\dot{\mathbf{U}}$, and $\mathbf{U}$ represented the floor acceleration, velocity and displacement vectors relative to the base, $\ddot{\mathbf{U}}_b$ is the vector of base accelerations relative to the ground and $\ddot{\mathbf{U}}_g$ is the vector of ground accelerations. The equations of motion for the base has

been reported as follows,

$$\mathbf{R}_{3\times n}^{T}\,\mathbf{M}_{n\times n}\,\left[\ddot{\mathbf{U}}_{n\times 1}+\,\mathbf{R}_{n\times 3}\left(\ddot{\mathbf{U}}_{g}+\ddot{\mathbf{U}}_{b}\right)_{3\times 1}\right]_{n\times 1}+\,\mathbf{M}_{b_{3\times 3}}\,\left(\ddot{\mathbf{U}}_{g}+\ddot{\mathbf{U}}_{b}\right)_{3\times 1} \\ +\mathbf{C}_{b_{3\times 3}}\,\dot{\mathbf{U}}_{b_{3\times 1}}+\mathbf{K}_{b_{3\times 3}}\,\mathbf{U}_{b_{3\times 1}}+\mathbf{f}_{3\times 1}=0 \tag{7.5}$$

in which $\mathbf{M}_b$ is the diagonal mass matrix of the rigid base, $\mathbf{C}_b$ is the resultant damping matrix of viscous isolation elements, $\mathbf{K}_b$ is the resultant stiffness matrix of elastic isolation elements, $\mathbf{f}$ is the vector containing the nonlinear bearing forces, device forces and control forces. The state space form of the above Eqs. 7.4-7.5 are reported in Narasimhan et al. (2006) [261].

7.3.2 Performance Evaluation Criteria

The benchmark problem (Narasimhan et al. (2006) [261]) defines a set of nine evaluation criteria to evaluate the capabilities of each proposed control strategy. The performances indices are shown in Table 7.1 and more details can be found in Nagarajaiah et al. (2006) [252]; Narasimhan et al. (2006) [261].

The indices J_1 through J_5 measure the peak values of base shear (V_0), structural shear (V_1), base displacement (x_b), inter-storey drift (d_f) and floor accelerations (a_f), respectively. These values are normalized by their respective uncontrolled values (represented by $(\hat{})$); uncontrolled refers to the case when there is no force feedback to the structure and the control devices are disconnected from the structural system (*i.e.*, the building with only the isolation bearing). The performance index J_6 measures the maximum control force (f_d) developed in the device normalized by the peak base shear. The indices, J_7 and J_8 measure the RMS values of the base displacement (σ_d) and base acceleration (σ_a), respectively normalized by their uncontrolled values. The index J_9 measures the energy dissipated by the semi active device as a percentage of the input excitation energy. In the Table 7.1, (f) represents the floor number ($1 \cdots 8$), $\langle . \rangle$ denotes inner product, $|.|$ denotes absolute value and $\|.\|$ means vector norm. The performance indices are to be simulated for a set of near-fault and far-fault seismic excitations ($\ddot{U}_g$). The earthquake records considered in the benchmark study are the fault-parallel and fault-normal components of Newhall, Sylmar, El Centro, Rinaldi, Kobe, Jiji and Erzinkan.

Table 7.1: Performance Indices for the Benchmark Study

Peak Base Shear $J_1 = \frac{t_{max}\lvert V_0(t)\rvert}{t_{max}\lvert \hat{V}_0(t)\rvert}$	**Peak Structure Shear** $J_2 = \frac{t_{max}\lvert V_1(t)\rvert}{t_{max}\lvert \hat{V}_1(t)\rvert}$	**Peak Base Displacement** $J_3 = \frac{t_{max}\lvert x_b(t)\rvert}{t_{max}\lvert \hat{x}_b(t)\rvert}$
Peak Inter storey Drift $J_4 = \frac{t,\ f_{max}\lvert d_f(t)\rvert}{t,\ f_{max}\lvert \hat{d}_f(t)\rvert}$	**Peak Floor Acceleration** $J_5 = \frac{t,\ f_{max}\lvert a_f(t)\rvert}{t,\ f_{max}\lvert \hat{a}_f(t)\rvert}$	**Peak Control Force** $J_6 = \frac{t_{max}\lvert f_d(t)\rvert}{t_{max}\lvert V_0(t)\rvert}$
RMS Base Displacement $J_7 = \frac{i_{max}\lVert \sigma_d(t)\rVert}{i_{max}\lVert \sigma_{\hat{d}}(t)\rVert}$	**RMS Floor Acceleration** $J_8 = \frac{f_{max}\lVert \sigma_a(t)\rVert}{f_{max}\lVert \sigma_{\hat{a}}(t)\rVert}$	**Energy Dissipated by Devices** $J_9 = \frac{\left[\int_0^T f_d(t)\ \dot{x}_b(t)\ dt\right]}{\int_0^T \left\langle V_0(t)\ \dot{U}_g(t)\right\rangle\ dt}$

7.3.3 Optimal Fuzzy Logic Controller Design

An optimized fuzzy logic control algorithm developed and detailed in Chapter 4, is applied to mitigate the vibration of the phase-II smart base isolated benchmark building with nonlinear isolation systems. The fuzzy system is optimized using micro-genetic algorithm (μ-GA). Acceleration and relative velocity responses at the damper locations are taken as inputs to the FLC system. Voltage required by the magneto-rheological damper is obtained as an output from the FLC. The use of magneto-rheological dampers in the benchmark study as a control device along with isolation bearings in the building renders the overall system nonlinear. The advantage of using a fuzzy rule base is its inherent ability to handle nonlinearities and uncertainties in structural behaviour, input excitation, sensor and actuator dynamics. Therefore, FLC driven MR damper provides added robustness to the control mechanism. Moreover, as described in the preceding chapters FLC driven MR damper voltage monitoring provides a gradual and smooth change of voltage. In this study, number of sensors and actuators and their locations are kept same as in the sample provided in the benchmark study.

For the genetic algorithm (GA) employed in this study, each chromosome represented a complete fuzzy logic controller as defined by MATLAB® [230] fuzzy inference files (FIS). In this study 44 strings of binary GA-chromosome (instead of 40 string considered in Chapter 4), are used to encode each FLC. First set of 9 binary strings are set to modify the rule base, next 7×3 strings code the input-output MF type and parameter. The remaining 14 strings are used

to code the input scaling gains. The output scaling gain is kept as 1 since, the input to the MR damper block (see Fig. 7.2) is unity (as defined by the benchmark study).

Two different GA optimized FLCs are compared, (i) optimization scheme where only the membership function type, parameters and pre-scaling gains are modified at every simulation time step (*i.e.*, real time) keeping the rule base fixed (henceforth, called as FRB-FLC), and (ii) optimization scheme where the membership function type, parameters, pre-scaling gains along with the rule base are optimized (henceforth, called ARB-FLC) at every simulation time step. ARB-FLC uses all 44 strings for its optimization and for FRB-FLC, 35 $(44-$ first $9)$ binary strings are used. ARB-FLC needs an initial rule base, which it modifies to minimize the objective functions given by Eqs. 7.6 and 7.7. FLC input-output relation in the first mode of vibration of the structure (Ahlawat and Ramaswamy (2003) [16]) is exploited to design the initial adaptive rule base keeping the symmetry in the rule base intact. To achieve the symmetry in rule base, a geometric approach is taken which reduces the required chromosome length and thereby the search space is reduced. This reduces the computational overhead of the optimization scheme. Further details about the optimization scheme, optimization variable and their encoding for GA application are presented in Chapter 4.

7.3.4 Numerical Simulation and Results

Figure 7.2 shows the simulink block diagram for the benchmark building control. The nonlinear analysis block contains mathematical details of the building with nonlinear isolator. The control block is the FLC controller and in the control device block, MR damper mathematical formulation are encoded. In this study the FLC parameters are optimized in real-time. This is a limitation in the experimental study in Chapter 5 due to non-availability of GA encoded hardware (Chen et al. (2006) [64]), which can do GA optimization in real time. Simple GA requires intensive computation for on-line FLC optimization on a PC. A hardware implementation of GA using FPGA (re-programmable field-programmable gate arrays) decreases the computational time by $2-3$ order of its time in simple PC (Scott et al. (1995) [311]). These issues are problem and model specific. A flexible GA chip, which can perform dynamically various fitness function computation, four different cross over operations, and over a thousand different types of mutation operation has been developed by Chen et al. (2006) [64]. Real time applications of GA-FLC using FPGA and fuzzy chips have been reported widely, from

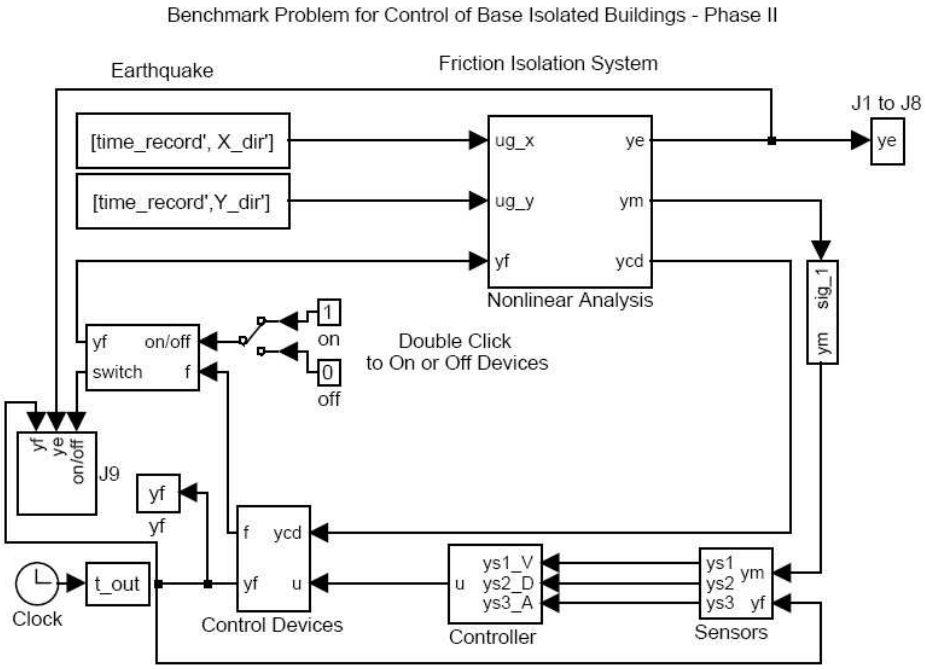

Figure 7.2: Simulink diagram of GA-FLC based benchmark building study

laboratory scaled power system and automotive active suspension system to structural control (Rahman and Uddin (2001) [283]; Osaimi et al. (2005) [24]; Shook et al. (2007) [316]; Wang and Kazmierski (2005) [365]).

Hailin and Dongmin (2001) [135] reported a adaptive fuzzy controller optimized by hardware based GA (FPGA) and applied it to feedback control of an inverted pendulum with a chromosome length of 32 bits and population of 32 members. It has been reported that the proposed hardware GA processor is effective and efficient to solve optimal control problems. The reported processor can complete optimization within 26.5ms. The optimization method proposed in the present paper using restart GA is computationally more efficient than simple GA and therefore suitable for real time FLC optimization. Hardware GA in combination with a fuzzy control chip should have a wide application in the field of real time control systems and can be implemented in the benchmark building realistically.

Base isolations are provided to isolate the superstructure from catastrophic earthquake excitations. But, the excessive displacement that the isolators undergo in near-fault ground motion is a cause for concern for the structural engineers. Nonlinear passive dampers are

provided to limit the bearing displacement in such situations. This however, increases the forces in the superstructure and at the isolation level.

In the present study MR dampers are installed to reduce bearing displacement without increase in the superstructure and isolation level shear forces. The FLC is optimized at every simulation time step using GA to meet this demand, *i.e.*, reduce bearing displacement (normalized *w.r.t.* uncontrolled bearing displacement). The constraints are kept on the increase in base shear and superstructure acceleration level. Therefore the normalized values of base shear and superstructure acceleration are kept near to unity. Absolute values (|.|)are taken to minimize the maximum values irrespective of the direction of the motion. Therefore, the weighted multi-objective function to be optimized by GA is taken to be,

$$\phi_1 = w_1 \left(\frac{|V_0(t)|}{\left|\hat{V}_0(t)\right|} - 1 \right) + w_2 \left(\frac{|x_b(t)|}{|\hat{x}_b(t)|} \right) + w_3 \left(\frac{f_{max}\,|a_f(t)|}{f_{max}\,|\hat{a}_f(t)|} - 1 \right) \tag{7.6}$$

where, $V_0(t)$, $x_b(t)$, $a_f(t)$ and their corresponding ($\hat{.}$) variables are described in Table 7.1. w_i's are the weights for each objective. By suitably adjusting the weights a set of non-dominated pareto optimal solution can be obtained. For on-line application one has to chose one such non-dominated solution. In present analysis, results for $w_1 = w_3 = 1.0$ and $w_2 = 4.0$ (user choice) *i.e.*, higher importance to bearing displacement is reported.

Simulations with on-line automatic selection of optimal FLC parameters are run for all given earthquake time histories in both fault-parallel and fault-normal directions with FRB-FLC and ARB-FLC to minimize the optimization cost function (Eq. 7.6). The convergence of GA with generation is shown in Fig. 7.3 obtained in El-centro and Rinaldi earthquakes after 1s of simulation run.

Results are tabulated for both FRB-FLC and ARB-FLC along with the results from the sample Lyapunov controller as shown in Tables 7.2 and 7.3. The performance function results for both the proposed cases, fixed and adaptive FLC, are seen to be comparable to the corresponding values reported for the sample controller.

In this example the objective is to reduce base displacement and from the Tables 7.2 and 7.3 it can be noticed that the row containing J_3 is minimum for the ARB-FLC simulations. Almost all performance indices for ARB-FLC are observed to be better than sample controller provided with the benchmark exercise. In some cases [for *e.g.*, Jiji (FP-X FN-Y) and El-Centro

Table 7.2: Performance Indices of benchmark building (Eq. 7.6), [FP-X & FN-Y]

PI	Control	Newhall	Sylmar	El-Centro	Rinaldi	Kobe	Jiji	Erzinkan
	Lyapunov	1.0200	0.9900	1.2800	0.9500	1.1200	0.8500	0.9800
J_1	**FRB–FLC**	1.0916	1.0080	1.0852	1.1225	1.0936	0.9082	1.0729
	ARB–FLC	1.0122	0.9208	1.2490	0.9290	1.0708	0.8391	1.0034
	Lyapunov	0.9300	1.0200	1.2100	0.9200	1.2600	0.8600	0.9900
J_2	**FRB–FLC**	1.0830	1.0089	1.1281	1.2067	1.1556	0.9194	1.0987
	ARB–FLC	0.9520	0.9100	1.2231	0.9412	1.3998	0.8306	1.0082
	Lyapunov	0.7000	0.7500	0.4800	0.8000	0.6100	0.7200	0.7000
J_3	**FRB–FLC**	0.8410	0.7727	0.7328	0.8301	0.7394	0.6993	0.7242
	ARB–FLC	0.6877	0.8021	0.4422	0.7906	0.5898	0.4596	0.6420
	Lyapunov	1.2000	1.1300	1.2400	1.0200	1.3700	0.9500	1.0300
J_4	**FRB–FLC**	1.0790	0.9228	1.0412	1.1879	1.1440	0.8563	1.0053
	ARB–FLC	1.2034	0.9412	1.2446	1.0003	1.4212	0.8404	1.0545
	Lyapunov	1.1600	1.5600	1.2600	1.7300	1.5600	1.3000	1.4000
J_5	**FRB–FLC**	1.2564	1.2176	1.1603	1.5366	1.2487	0.9406	1.2506
	ARB–FLC	1.1565	1.0710	1.1004	1.4821	1.5817	1.0507	1.3549
	Lyapunov	0.2900	0.2400	0.4300	0.2700	0.3200	0.1700	0.2600
J_6	**FRB–FLC**	0.2678	0.2805	0.3686	0.2953	0.3267	0.4310	0.2976
	ARB–FLC	0.2419	0.2103	0.4074	0.2639	0.3358	0.3864	0.2528
	Lyapunov	0.5600	0.5800	1.0500	0.7500	0.6500	0.7100	0.6100
J_7	**FRB–FLC**	0.9132	0.8037	0.9549	0.8731	0.8664	0.7536	0.8047
	ARB–FLC	0.5805	0.6490	0.9268	0.6979	0.5857	0.4218	0.5161
	Lyapunov	1.3600	1.3300	1.3700	1.5300	1.3800	1.6100	1.1200
J_8	**FRB–FLC**	1.3709	1.2370	1.3530	1.4359	1.4000	1.3275	1.1340
	ARB–FLC	1.3523	1.0241	1.3401	1.4366	1.4082	1.7953	1.0694
	Lyapunov	0.4400	0.4700	0.4300	0.4400	0.4300	0.3300	0.4800
J_9	**FRB–FLC**	0.4996	0.3495	0.3344	0.4382	0.4896	0.4478	0.4040
	ARB–FLC	0.4093	0.2580	0.2406	0.4171	0.3781	0.4687	0.4402

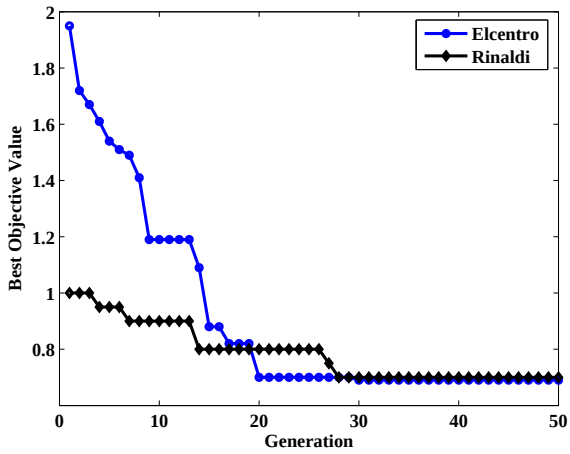

Figure 7.3: Convergence of GA: objective function best values (Eq. 7.6)

(FN-X FP-Y) earthquakes] the decrease in base displacement is found to be $0.6 - 0.7$ times more efficient than the corresponding values obtained in Lyapunov case (sample controller). Simulation results for Jiji earthquake show an increase in RMS acceleration in both direction for ARB-FLC case. For better comparison the performance values are plotted against performance indices for Jiji earthquake and shown in Fig. 7.4.

It is observed from Fig. 7.4 that the performance of FRB-FLC is comparable to ARB-FLC and in many aspects better than Lyapunov controller. Comparable performance of the FRB-FLC is possible as the base isolated building acts as a single degree-of-freedom system and the fixed rule base taken is optimal for single degree-of-freedom as its input-output relation is based on the first mode of vibration of a structure.

The base displacements at the center of mass of the base for Lyapunov, FRB-FLC, ARB-FLC controller under Kobe earthquake are shown in Fig. 7.5 for both X and Y directions of motion. ARB-FLC shows the lowest displacement at the mass center of the base, whereas FRB-FLC shows highest in X-direction and Lyapunov in Y-direction. The total MR damper force required to control the base isolated building is shown in Fig. 7.6. The controller force in Lyapunov case has considerable fluctuation from the beginning of the excitation and continues till the end of the excitation. Both FRB-FLC and ARB-FLC show no such fluctuation. The reason for this is that the Lyapunov controller switches the MR damper voltage between its minimum and maximum voltage values, therefore the controller force also fluctuates a lot. In case of the FLC (both FRB & ARB) the voltage change in MR damper is gradual and therefore

Table 7.3: Performance Indices of benchmark building (Eq. 7.6), [FN-X & FP-Y]

PI	Control	Newhall	Sylmar	El–Centro	Rinaldi	Kobe	Jiji	Erzinkan
	Lyapunov	1.0200	1.0000	1.4400	0.9200	1.1800	0.8600	1.0100
J_1	**FRB–FLC**	1.0985	1.0167	1.5281	1.1154	0.9878	0.9008	1.0882
	ARB–FLC	1.0219	0.9905	1.4278	1.0453	1.1964	0.8004	1.0441
	Lyapunov	0.8900	1.0400	1.2400	0.8800	1.1400	0.8700	0.9900
J_2	**FRB–FLC**	1.0439	0.9472	1.3065	1.1011	0.9902	0.8153	0.9604
	ARB–FLC	0.9487	1.0037	1.4646	1.0220	1.3711	0.8122	0.9945
	Lyapunov	0.7200	0.7900	0.7700	0.7600	0.5500	0.7100	0.5900
J_3	**FRB–FLC**	0.8672	0.7835	0.8213	0.8330	0.7738	0.7500	0.6719
	ARB–FLC	0.6817	0.8109	0.5429	0.7510	0.5910	0.6373	0.6002
	Lyapunov	1.1100	0.9200	1.2000	0.9300	1.3900	0.9000	1.0400
J_4	**FRB–FLC**	1.1451	0.8963	1.1559	1.1868	1.0890	0.7998	0.9996
	ARB–FLC	1.3086	0.8767	1.4868	1.0523	1.4934	0.8501	1.0559
	Lyapunov	1.2800	1.6200	1.2900	1.3400	1.5300	0.9500	1.5600
J_5	**FRB–FLC**	1.2523	1.2320	1.2413	1.4502	1.4963	0.9016	1.0306
	ARB–FLC	1.5201	1.3236	1.3865	1.3959	1.4416	0.9369	1.0708
	Lyapunov	0.2900	0.2300	0.4000	0.3000	0.3100	0.1700	0.2500
J_6	**FRB–FLC**	0.2210	0.2238	0.3985	0.2292	0.4225	0.1745	0.2237
	ARB–FLC	0.2504	0.1553	0.3813	0.2498	0.3759	0.1814	0.2370
	Lyapunov	0.5600	0.5900	0.8900	0.7900	0.6200	0.6800	0.5100
J_7	**FRB–FLC**	0.6277	0.6999	0.8765	0.8495	0.7020	0.7244	0.7113
	ARB–FLC	0.5906	0.5875	0.8930	0.7770	0.5662	0.5562	0.5055
	Lyapunov	1.3100	1.1900	1.2900	1.8500	1.3600	1.1300	1.0600
J_8	**FRB–FLC**	1.2459	1.0983	1.4204	1.7094	1.3704	1.2413	1.1198
	ARB–FLC	1.3896	1.0343	1.3798	1.5365	1.3774	1.4659	0.9906
	Lyapunov	0.4400	0.4700	0.4200	0.4400	0.4200	0.3400	0.4800
J_9	**FRB–FLC**	0.4246	0.4356	0.4819	0.4161	0.4203	0.3729	0.5111
	ARB–FLC	0.4010	0.3286	0.5033	0.4298	0.3565	0.3450	0.4196

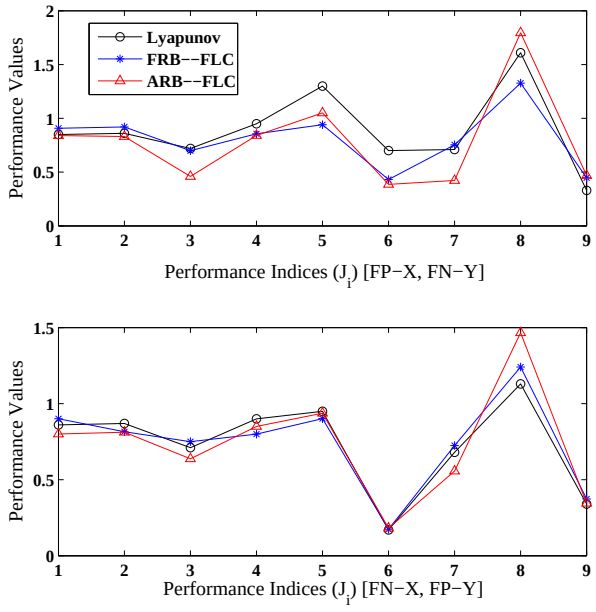

Figure 7.4: Comparison of performance values under Jiji earthquake (Eq. 7.6)

such fluctuations do not arise.

FRB-FLC employs less controller force and therefore bearing displacement is more (see Fig. 7.5) as compared to that of ARB-FLC. But both the FLCs use less controller force than the Lyapunov controller. Figure 7.7 shows the hysteretic force-displacement loops for the isolator and the MR damper located near the center of the mass of the building at base.

To see the effect of different optimization cost functions on the performance of the controller, another objective function taking into account the controller force in the previous objective function (Eq. 7.6) is defined. Therefore the new objective function can be stated as,

$$\phi_2 = w_1 \left(\frac{|V_0(t)|}{\left|\hat{V}_0(t)\right|} - 1 \right) + w_2 \left(\frac{|x_b(t)|}{|\hat{x}_b(t)|} \right) + w_3 \left(\frac{f_{max}\,|a_f(t)|}{f_{max}\,|\hat{a}_f(t)|} - 1 \right) + w_4 \frac{|f_d(t)|}{|V_0(t)|} \tag{7.7}$$

where w_i $(i = 1, 2, 3)$ has same value as in Eq. 7.6, and $w_4 = 1$. The control force is normalized *w.r.t.* to the base shear at the isolation level. Results are shown (Fig. 7.8) comparing the performance of adaptive rule base (ARB-FLC) with objective functions given in Eqs. 7.6 and 7.7. In Fig. 7.8, ϕ_1 and ϕ_2 are referred to the objective functions in Eqs. 7.6 and 7.7 respectively. No significant change is observed in the second objective case except for the decrease in peak

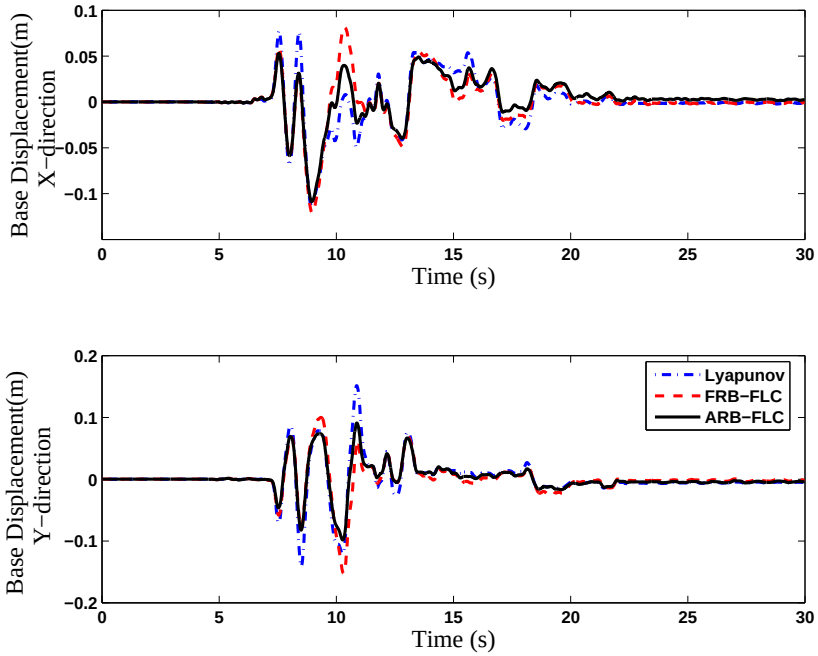

Figure 7.5: Displacement at the center of mass of the base under Kobe earthquake (FP-X, FN-Y) (Eq. 7.6)

control force required (J_6) and slight increase in the bearing displacement.

Stability of ARB-FLC

Only few methods are available that guarantee or check stability of fuzzy controllers (Battaini et al. (1998) [40]). Validation of stability is performed with simulations and tests to check whether the closed loop system returns to rest from disturbance that is caused by the external excitation. In practice one simulates the closed loop system with the state variables that seems to show the worst response. The test consists of checking the ability of the controller to reduce the transient response and to drive the system quickly to the stable position after the external excitation stops. In this study stability tests are performed considering scaled up (1.5 times) input earthquake excitations. To assess stability of the system, free vibration of the system for an additional 10 seconds after the earthquake excitation is carried out. The stability check is performed for all earthquake records and for Lyapunov controller and ARB-FLC. Figures 7.9 to 7.11 show the response plots Kobe earthquake corresponding to the stability analysis.

Figure 7.9 shows the displacement time history at the center of mass of the building at base isolation level. It is evident from Fig. 7.9 that both the controllers are effective in bringing down the base displacement to rest within the time (10 seconds). But, it is observed from the acceleration time histories (Fig. 7.10) that the acceleration in case ARB-FLC dies down fast, Lyapunov controller, on the contrary, does not show a slow down of acceleration rather it shows an increase in acceleration. The same nature of time history is observed in case of total control force (Fig. 7.11). The reason can be attributed to the switch of MR damper voltage from minimum to maximum values in the Lyapunov control.

To observe the behaviour of ARB-FLC under parameter variation simulations are carried out with 20% increase in total mass at the base and all other parameters unchanged. The acceleration response at the base center of the building for Rinaldi earthquake is shown in Fig. 7.13. Figure 7.13 shows displacement and acceleration at the mass center of the base for both X and Y direction motions. Similar to scaled up earthquake, the acceleration response in the Lyapunov control case continues vibrating 10s after the seismic excitation is over, but

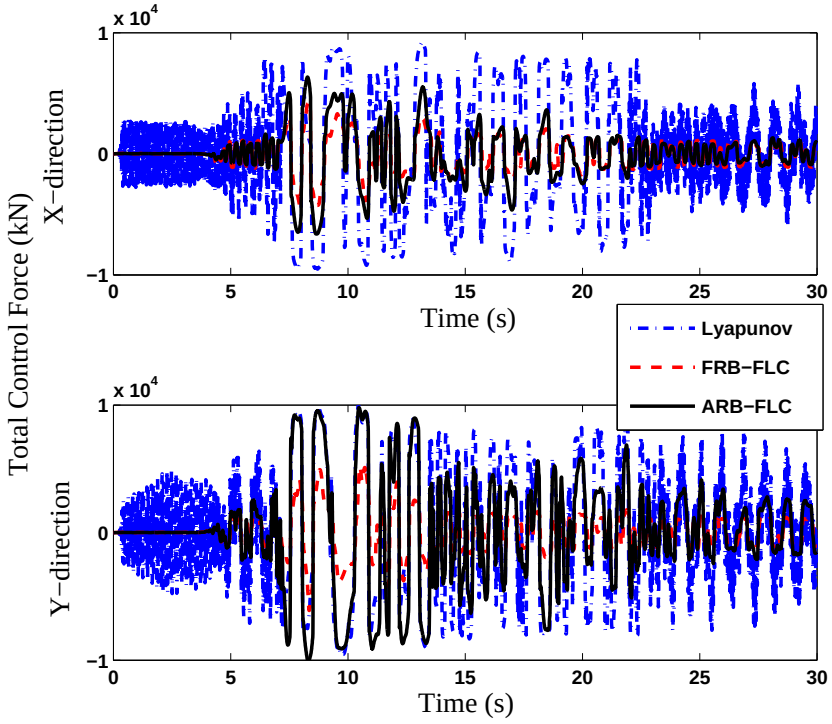

Figure 7.6: Total control force under Kobe earthquake (FP-X, FN-Y) (Eq. 7.6)

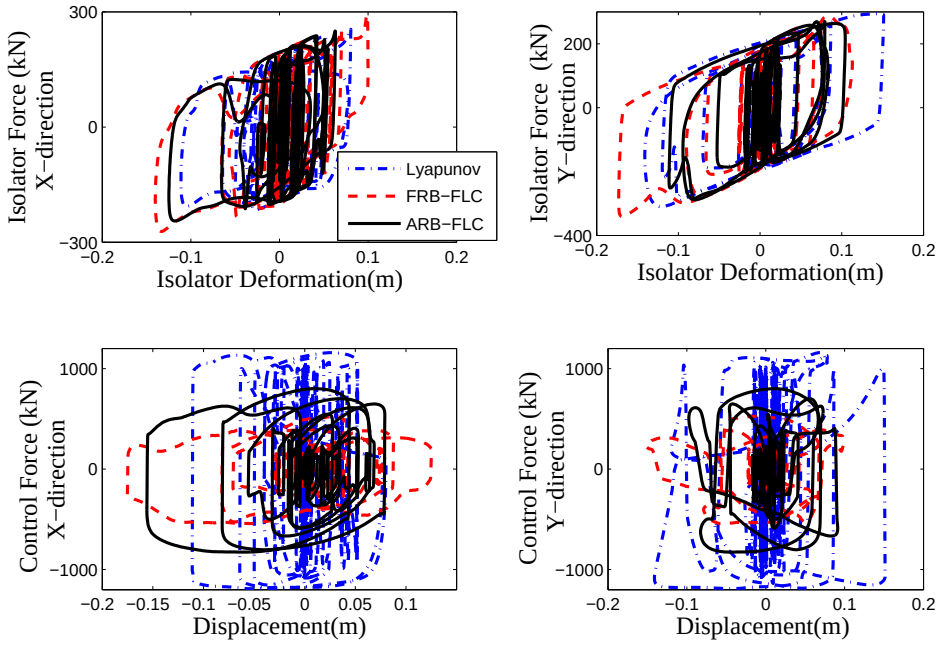

Figure 7.7: Force displacement loops under Kobe earthquake (FP-X, FN-Y)] (Eq. 7.6)

the ARB-FLC bring downs the vibration levels to zero.

It is evident from Figs. 7.9 to 7.13 that the performance of the ARB-FLC controller is superior to the Lyapunov controller in reducing the building responses and bringing down the responses to rest within minimal time for parameter uncertainty (scaled up earthquake time history and structure mass).

7.4 Benchmark Highway Bridge

A highway over-crossing or bridge, connecting major transportation routes, is a key node in transportation network. It must remain operational following severe earthquakes. Therefore, a higher level of performance with less structural damage is mandatory for such bridges. Recent earthquakes, such as Northridge and Kobe, have demonstrated the importance of maintaining the operation of bridge structures. Seismic base isolation is the most widely used earthquake protective scheme for bridges. The seismic isolation bearings, which usually replace conventional bridge bearings, decouple the superstructure from the piers and abutments during earthquakes, thereby significantly reducing the seismic forces induced in

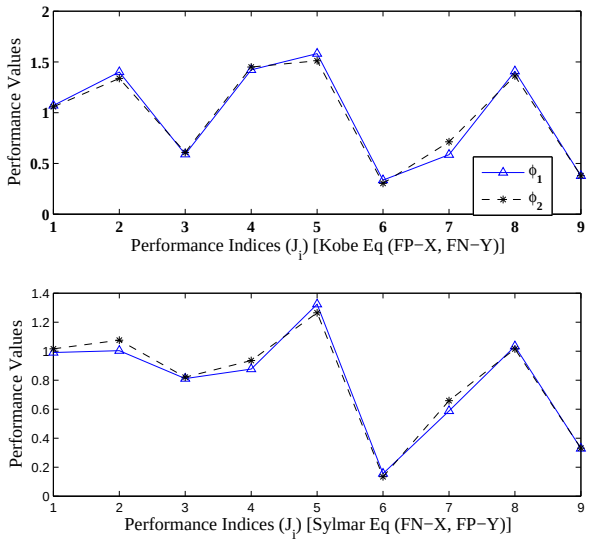

Figure 7.8: Performance of ARB-FLC with different objective functions (ϕ_1 = Eq. 7.6, ϕ_2 = Eq. 7.7)

the bridge super-structure leading to reduced strength and ductility demands on the bridge

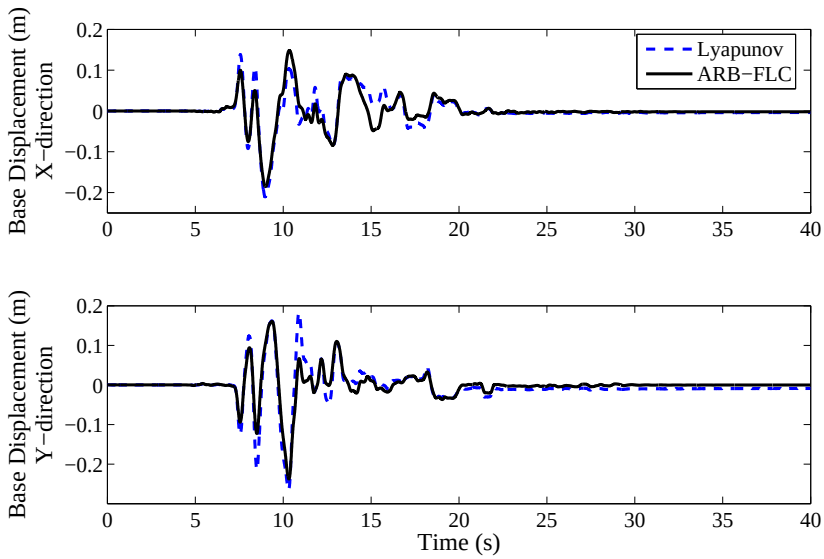

Figure 7.9: Stability test for scaled-up EQ: Displacement at the mass center of the base under Kobe earthquake (FP-X, FN-Y)

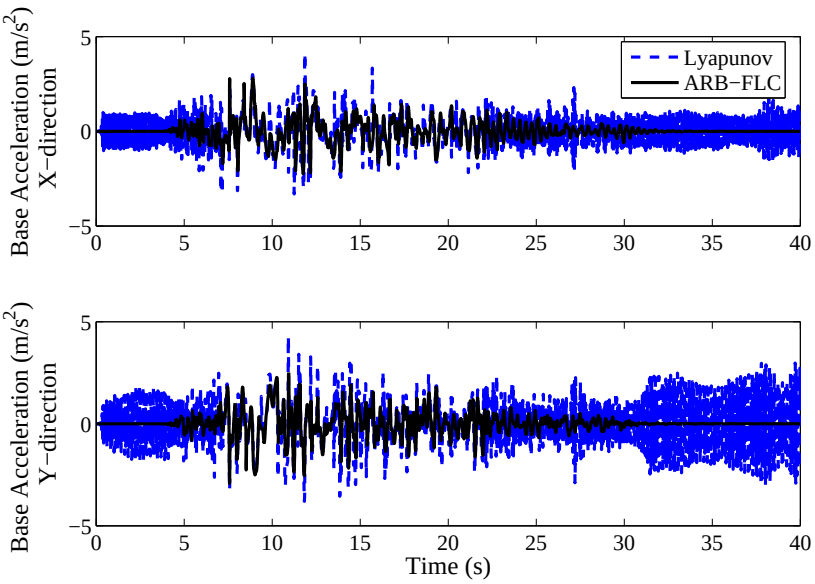

Figure 7.10: Stability test for scaled-up EQ: Acceleration at the mass center of the base under Kobe earthquake (FP-X, FN-Y)

(Kawashima and Unjoh (1994) [179]; Yang et al. (1995) [402]; Saiidi et al. (1999) [304]). However, serious damages can occur to the bridge with isolation bearings in cases of near source excitations due to large displacement of the isolation devices and nonlinear behaviour of the bridge columns. In order to reduce their vulnerability to severe earthquakes, "hybrid" base isolated bridges, where the performance of the base isolation system is improved by adding passive, active and semi-active devices, have been proposed and studied extensively by various researchers (Yang et al. (1995) [402]; Nagarajaiah et al. (1993) [253]; Sahasrabudhe and Nagarajaiah (2005a) [302]). It has also been demonstrated by several researchers that "hybrid" base isolation systems are capable of reducing excessive displacement of bearings or significant damage to bridge piers (Kawashima and Unjoh (1994) [179]; Nagarajaiah et al. (1993) [253]; Feng and Shinozuka (1990) [111]).

The discussions above demonstrate the necessity of studying highway bridge with various control techniques and control devices. Benchmark highway bridge structural control has been developed by Agrawal et al. (2005) [7]; Tan and Agrawal (2005) [353]; Nagarajaiah et al. (2006) [250] with the objective to assess the performance of various control schemes and devices.

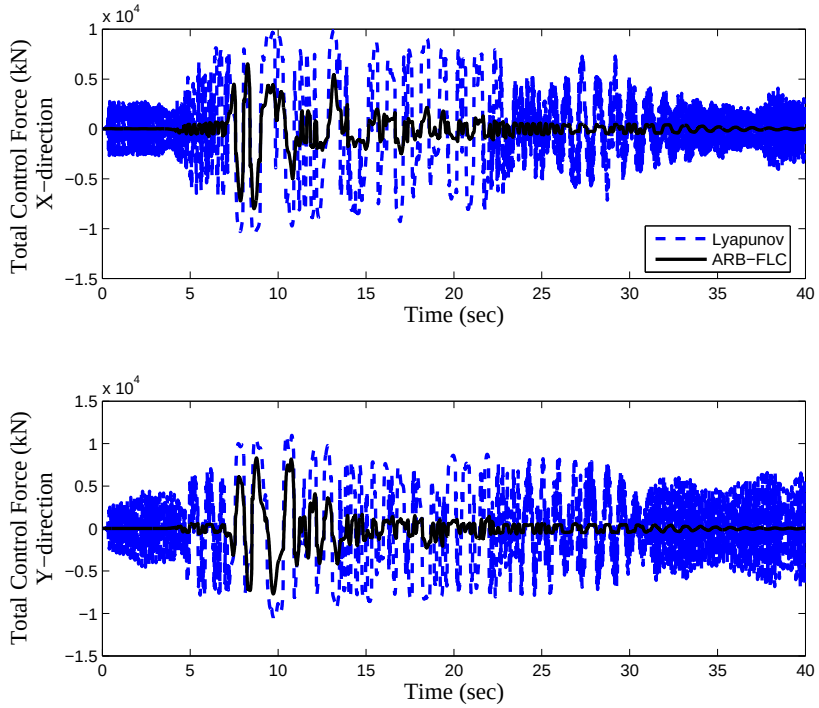

Figure 7.11: Stability test for scaled-up EQ: Total control force under Kobe earthquake (FP-X, FN-Y)

7.4.1 Benchmark highway bridge definition

The highway bridge selected for benchmark studies is a two-span, cast-in-place pre-stressed concrete box-girder bridge on $91/5$ over crossing located in Orange County of southern California, USA. The Whittier-Ellsinore fault is 11.6km to the north-east, and the Newport-Inglewood fault zone is 20km to the southwest of the bridge site. As the bridge must remain operational following severe earthquakes, it has been selected for the benchmark study (Agrawal et al. (2005) [7]).

In the benchmark study, the bridge is isolated using nonlinear lead-rubber seismic bearings at the abutment ends and at the central pier. Phase-I and phase-II of the study are developed based on the positions of the bearings. The phase-I of the benchmark study includes four isolators on each abutment and phase-II includes one bearing on each center bent column in addition to isolators on abutments. Additional details of the bridge are reported in the bridge definition paper (Agrawal et al. (2005) [7]; Tan and Agrawal (2005) [353]; Nagarajaiah et al.

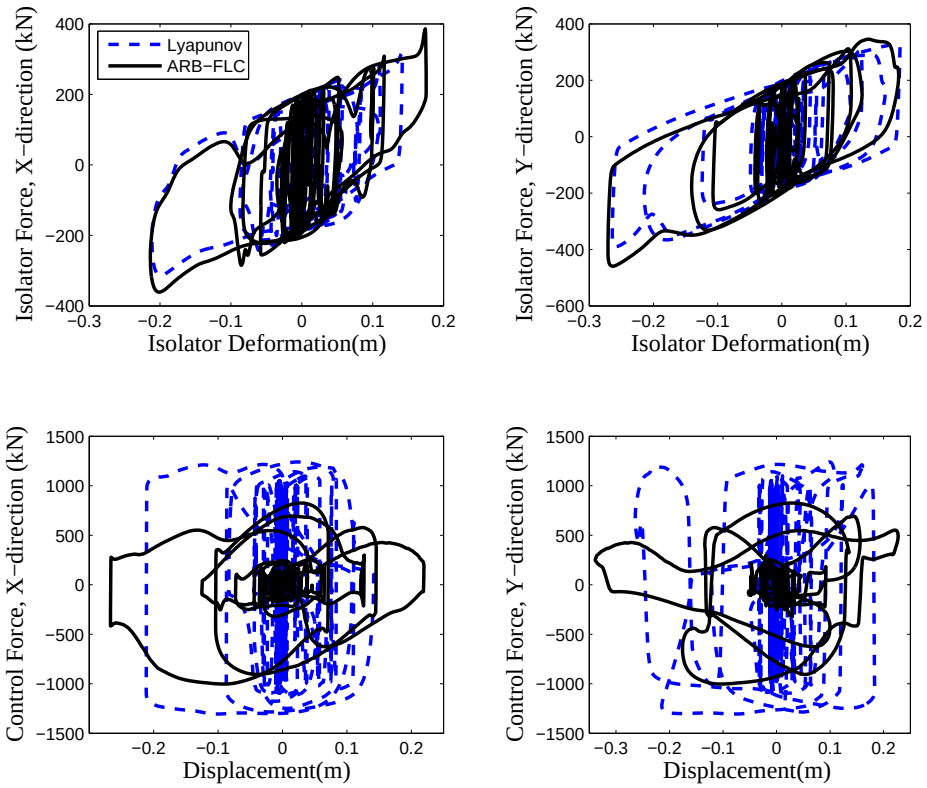

Figure 7.12: Stability test: Force displacement loops under Kobe earthquake (FP-X, FN-Y)

(2006) [250]).

Bridge model

A detailed three-dimensional finite element model has been reported in the benchmark definition paper (Tan and Agrawal (2005) [353]) in order to compute the structural properties of the system. The deck structure elements are assumed to be linear and the element stiffness and mass matrices are reported to be derived from the finite-element model and assembled at the nodes using lumped mass and stiffness approximations.

The nonlinear elements are added to the linear elastic deck elements and the augmented model is considered for evaluating structural responses. The nonlinear equations of motion are solved using Newmark's integration scheme. For the controller design, a linearized reduced order model has been provided from the full-order evaluation model based on model

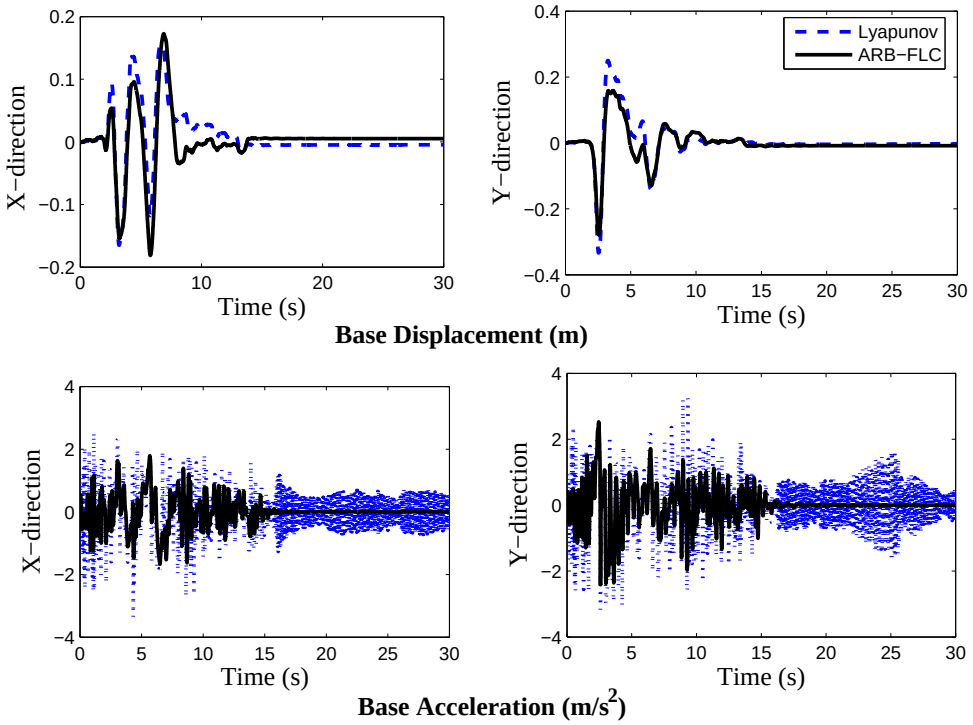

Figure 7.13: Stability test for scaled-up mass: Base displacement and acceleration under Rinaldi earthquake (FP-X, FN-Y)

reduction techniques (Tan and Agrawal (2005) [353]). A general discussion of the model reduction technique is presented in Chapter 2 and details of the model reduction technique carried out for the benchmark highway bridge have been reported in Tan and Agrawal (2005) [353]. The resulting reduced order model is observed to capture the dynamics of the full-order model accurately in the modes of interest. The reduced order system model for controller design is given as,

$$\dot{\mathbf{X}}^r = \mathbf{A}\mathbf{X}^r + \mathbf{B}^r\mathbf{u} + \mathbf{E}^r\ddot{\mathbf{u}}_g \tag{7.8}$$

$$\dot{\mathbf{y}}_z = \mathbf{C}_r^z\mathbf{X}^r + \mathbf{D}_r^z\mathbf{u} + \mathbf{F}_r^z\ddot{\mathbf{u}}_g \tag{7.9}$$

$$\dot{\mathbf{y}}_m = \mathbf{C}_r^m\mathbf{X}^r + \mathbf{D}_r^m\mathbf{u} + \mathbf{F}_r^m\ddot{\mathbf{u}}_g + \nu \tag{7.10}$$

where, the subscript r in Eqs. 7.8-7.10 refers to the reduced order model. In the above equations, X refers to the states of the system, A, B and E are the system state matrices, $\ddot{u}_g$ is the ground acceleration vector in two directions. The regulated output (y_z) and the measurement output (y_m) equations are given in Eqs. 7.9 and 7.10 respectively. The matrices C, D and F are mapping matrices of appropriate dimensions and ν denotes the measurement noise. Detailed discussions are given in the benchmark definition paper (Agrawal et al. (2005) [7]).

Ground motions are considered to be applied to the bridge simultaneously in two directions at all support points ignoring spatial variability. The bridge is analyzed for 6 earthquakes records considering both near source and far source seismic excitations. Four orthogonal MR dampers, located between each abutment-end and deck of the bridge are assumed for phase-I of the benchmark study and two additional orthogonal MR dampers are considered in phase-II of the study. Figure 7.14 shows the locations of sensors, actuators and isolation bearings for phase-II of the benchmark study. A set of 21 evaluation criteria is defined to consider the effectiveness of control design.

7.4.2 Performance criteria

A set of 21 evaluation criteria are proposed by the benchmark problem definition to evaluate the effectiveness of different control devices and algorithms. These evaluation criteria are classified into three categories, namely, peak responses, normed responses and control requirements. The first eight evaluation criteria measure the reduction in peak response quantities of the benchmark bridge *e.g.*, peak base shear (J_1), peak overturning moment (J_2), peak midspan displacement (J_3), peak midspan acceleration (J_4), peak deformation at the bearings (J_5), peak curvature at bent column (J_6), peak dissipated energy (J_7), number of plastic connections (J_8). All the responses are normalized *w.r.t.* their corresponding uncontrolled responses. The second set of six criteria are based on normed values over the entire time duration of an earthquake. They are respectively normed base shear, normed base moment, normed midspan displacement, normed midspan acceleration, normed bearing deformation and normed ductility. The next four evaluation criteria are for quantifying a measure of control resource required by the controller itself, namely, peak force, peak device stroke, peak power, total power. Last three evaluation criteria are number of devices, number of sensors and total computational resources used. Details on how these performance indices have been

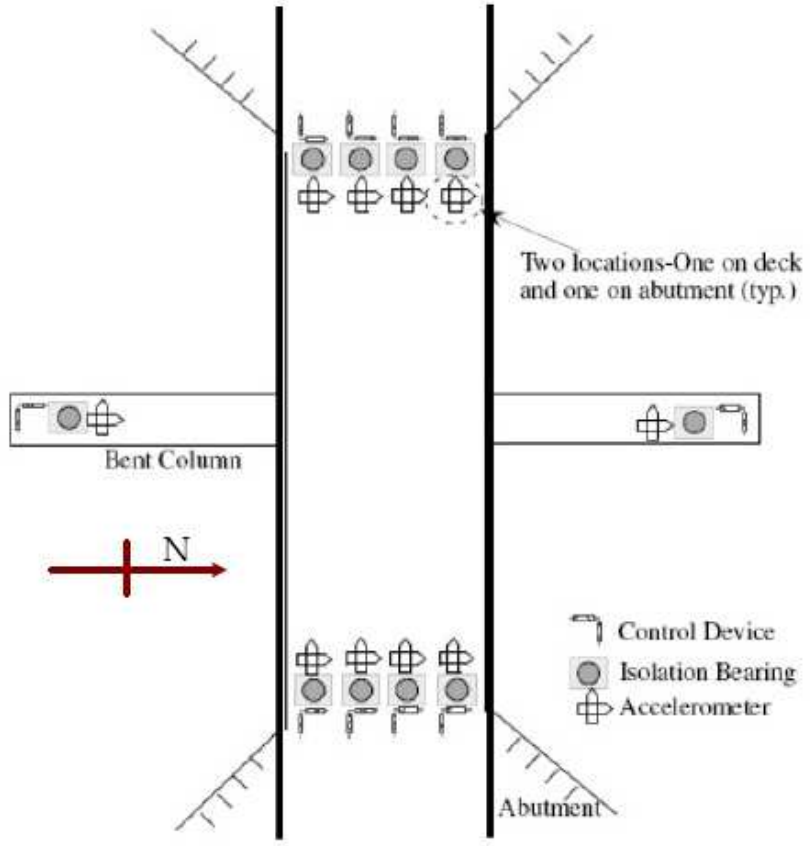

Figure 7.14: Benchmark highway bridge (phase-II): actuators, isolators and accelerometer locations (Agrawal et al. (2005) [7])

formulated are provided in benchmark definition paper (Agrawal et al. (2005) [7]).

The performance indices are simulated for a set of earthquake excitations. The earthquake excitations considered in this benchmark study are 'Npalmspr', 'Chichi', 'Elcentro', 'Northridge', 'Turk-Bolu' and 'Kobe-NIS'. Earthquake records are considered in both X and Y directions simultaneously.

7.4.3 Controller design

For the benchmark highway bridge control design problem, the two stage optimal dynamic inversion based control algorithm proposed in Chapter 6 and an ANFIS (Adaptive Network based Fuzzy Inference System) driven active controller are studied.

ANFIS

Fuzzy systems are powerful in representing linguistic and structured knowledge by means of fuzzy set theory, but it is up to the experts to establish the knowledge base to be used in these systems. Therefore, formation of appropriate fuzzy inference rules and membership functions remains a thorny issue. Furthermore, static fuzzy rules and membership functions are vulnerable to changes in system parameters. One way to get rid of sensitivity to parameter changes is to optimize the fuzzy system parameters using optimization technique or to combine a fuzzy system with an artificial neural network (ANN) referred to as hybrid neuro-fuzzy control (Jang (1993,1996) [160, 161]; Faravelli and Yao (1997) [110]; Jang et al. (2005) [162]). ANN is capable of establishing a nonlinear map between the input and the output through a set of training data. ANN learns the changes in the given input and accommodate these changes in the output and therefore acts as an function approximation tool. Therefore, ANN can be employed to create or modify the fuzzy rules to adopt with the changes in parameters. An example of hybrid fuzzy-neural network based model is an Adaptive Neuro Fuzzy Inference System (ANFIS) developed by Jang (1993,1996) [160, 161]. ANFIS has been applied in a number of applications successfully, *e.g.*, nonlinear system identification, nonlinear control, function approximation, rule-based process controls, time-series prediction problems, and so on.

The schematic diagram of a typical ANFIS is shown in Fig. 7.15. It is a network structure consisting of nodes and relational links where rectangular nodes are adaptive and represent the input and the output fuzzy subsets (membership function). Each output depends on nodal parameters that are adjusted by the learning rule to minimize the overall error between the desired and obtained output. The architecture of ANFIS can be fitted to different inference schemes but the Takagi and Sugeno type are computationally more efficient (MATLAB (2004) [230]; Jang et al. (2005) [162]) and has been adopted in the present study. Details of ANFIS and underlying mathematics can be found in Jang (1993,1996) [160, 161]; Jang et al. (2005) [162].

As shown in Fig. 7.15, each node of the first layer is connected to exactly one of the 'n' input variables (here only two input variables, velocity and acceleration data are considered) and stores the parameters of the input membership functions (fuzzification). The nodes of the second layer are antecedents of the fuzzy rules. Third layer nodes compute the degree of fulfillment for each rule. The nodes in layer four compute the output values of the rules

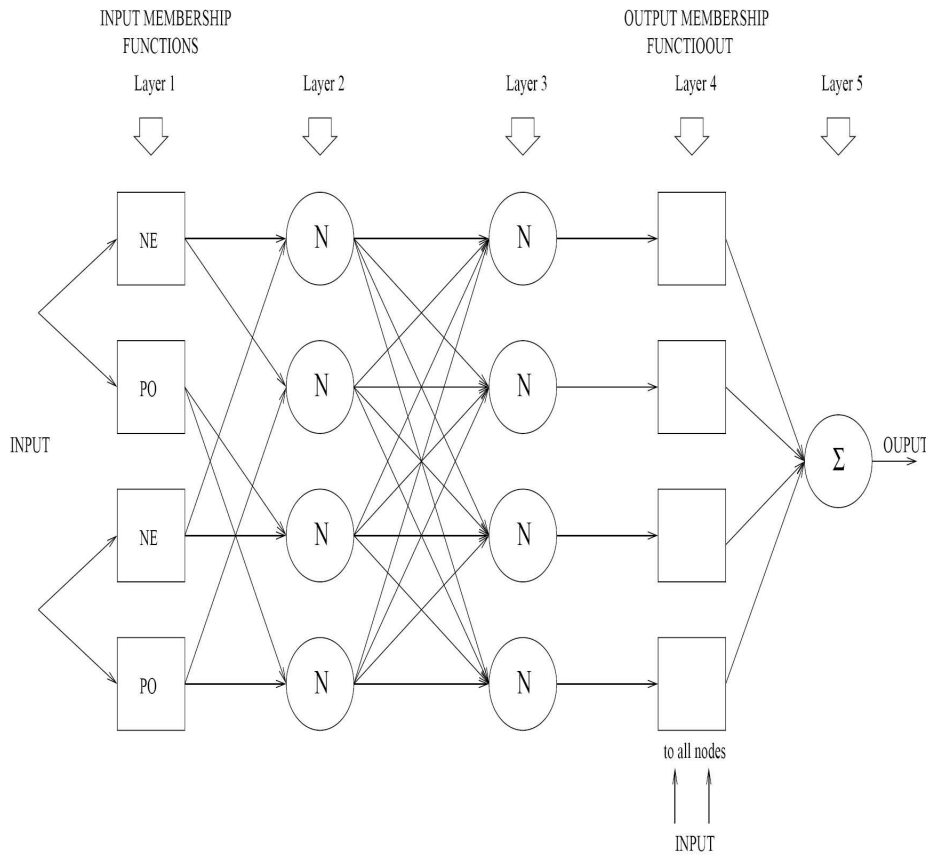

Figure 7.15: Schematic diagram of ANFIS

(fuzzy inference). The node in the fifth layer node is the output nodes and computes the crisp output value (defuzzification). ANFIS requires a predefined structure of the fuzzy system that it trains modifies for the given input-output data set.

In the present study, the predefined structure of the fuzzy systems consisted of three membership functions in both the inputs and five membership functions for the output. The membership function considered is the '*gbellmf*' available with MATLAB fuzzy logic toolbox (MATLAB (2004) [230]). The simulation of benchmark bridge with the sample LQG driven actuator is used as the training and validation data for the ANFIS, *i.e.*, control force provided by the LQG algorithm is used as the desired output for the ANFIS. ANFIS networks are trained separately only for the longitudinally directed actuators and transversely directed actuators are monitored using SFLC (see Chapter 4 for details on SFLC). The longitudinal direction actuators are trained separately for near source and far source earthquake excitations. Therefore

two different ANFIS networks have been trained and two SFLC blocks are used for the benchmark bridge analysis (see Fig. 7.16).

Of the eight actuators deployed for longitudinal, four peripheral actuators (two on each end) are trained using ANFIS with near source seismic excitation and the remaining four are trained with far fault seismic excitation. 50% of excitation data of each of the eartquakes forms the training and testing data set. This data set is then applied to the benchmark bridge simulink model and the control force output from the LQG sample controller formed the desired output of the training program. ANFIS GUI in fuzzy logic tool box of MATLAB (2004 [230]) is employed for the training and testing of the network. Backpropagation algorithm optimizes the neural weights associated with ANFIS.

Two accelerometers located at the abutments ends are used for the training of the network. The velocity input for the ANFIS network is obtained by integrating the accelerometer data. Acceleration and velocity feedback from the central bent columns are given as inputs to SFLC. Therefore, instead of 8 accelerometer data the hybrid approach needs only four accelerometer data. ANFIS based active control is applied to the phase-I of the benchmark bridge study.

Optimal dynamic inversion

The two stage control algorithm developed in Chapter 6 provides a closed form feedback solution to monitor MR damper voltage (the benchmark problem has been designed to provide voltage as an input to the MR damper) based on system responses. The primary controller is designed first (first stage) depending on the reduced order benchmark bridge model (Eq. 7.8) based on LQG algorithm. The primary controller provides a state dependent feedback controller to minimize a predefined cost function. The goal then is to supply the required voltage to the MR damper so that it produces the same force. In this chapter the dynamic inversion based controller developed in Chapter 6 is employed to track the force prescribed by the primary controller. The tracking error is minimized in a L_2 norm sense for a set of controllers and the voltage supply to each damper, required to minimize the tracking error is optimized. The complete derivation of the proposed optimal dynamic inversion algorithm in the context of benchmark highway bridge is given in Chapter 6.

The proposed technique is successfully applied to phase-I and phase-II of the benchmark highway bridge exercise and presented in a later section. The semi-active control devices are

assumed to be located at the isolation level between the deck and the isolators on bridge piers for phase-I and in addition at center column for phase-II of the study (see Fig. 7.14). Each location consists of a single orthogonal pair to control the responses in both directions. Therefore, for phase-I, a total of 16 sample MR dampers (there are no dampers at center bent columns) have been used and a total of 20 MR dampers are used in phase-II case. The performance of the controller is analyzed in terms of the performance indices defined in the benchmark problem definition. The results of the present controller are compared with the results of the sample controller presented in the benchmark study. The main advantage of the controller developed lies in its closed form state feedback solution of MR damper voltage requirement, which allows a smooth and gradual change in MR damper input voltage. Furthermore as shown in Chapter 6 the proposed approach considers the MR damper input voltage to commanded voltage dynamics.

Numerical simulations are done for both the phase-I and phase-II of the benchmark exercise with optimal dynamic inversion technique. In the first stage, the LQG (linear quadratic Guassian) control algorithm is used to obtain optimal force required to minimize an infinite horizon performance index defined in Eq. 6.14 of Chapter 6. For the sake of completeness, infinite horizon performance index is given here,

$$J_1 = \lim_{\tau \to \infty} \frac{1}{\tau} E\left[\int_0^\tau \{(C_r^z X^r + D_r^z u)^T \mathbf{Q}(C_r^z X^r + D_r^z u) + u^T \mathbf{R} u\} dt\right] \tag{7.11}$$

The primary controllers for both phase-I and phase-II of the study are designed with weight matrix $R = 10^{-5} I_{N\times N}$, where N denotes the total number of controllers considered and

$$Q = \begin{bmatrix} q_d I & 0 \\ 0 & q_a I \end{bmatrix}$$

in which $q_d = 5 \times 10^7$ is the weight for the displacements and deformation of the bridge bearings, and $q_a = 0.1 q_d$ is the weight for the midspan accelerations. These weight matrices are taken from the benchmark control design paper (Tan and Agrawal (2005) [353]). A reduced order model of the benchmark bridge with 28 states is used for the controller design but performances of the controller has been evaluated from the full order system model with 430 states. To design optimal dynamic inversion controller the parameters taken are tabulated in

Table 7.4: MR Damper Parameter Values for Benchmark Bridge Study (Tan and Agrawal (2005) [353])

Parameter	Value	Unit	Parameter	Value	Unit
α_a	4.961×10^5	N cm^{-1}	α_b	1.087×10^5	N cm^{-1} V^{-1}
C_{0a}	4.40	N sec cm^{-1}	C_{0b}	44	N sec m^{-1} V^{-1}
γ	3	cm^{-1}	β	3	cm^{-1}
η	50	s^{-1}	A	1.2	–
n	1	–	k_e	10	–
tol_1	10^{-4}	–	tol_2	10^{-5}	–
P_{ii}	1	–	–	–	–

Table 7.4. The MR damper parameter values are also taken from the benchmark study (Tan and Agrawal (2005) [353]), such that it can provide a maximum of 1000 kN force.

7.4.4 Numerical simulation and results: phase-I study

Numerical Simulations for the phase-I benchmark bridge exercise are carried out with ANFIS driven actuator and optimal dynamic inversion based MR damper.

ANFIS driven controller results

Figure 7.16 shows the hybrid ANFIS and FLC control approach employed for the control of the benchmark highway bridge.

Comparison of response obtained at west end (see Fig. 7.14) for LQG control and ANFIS under Northridge earthquake (transverse direction) are shown in Figs. 7.17-7.19 respectively. Figure 7.17(a) shows the bearing deformation and Fig. 7.17(b) shows the mid span acceleration time history at bearing at west end of the bridge. The displacement performance of the structure remains same as the LQG controller but the acceleration peak decreases in the ANFIS control case. Base shear time history is shown in Fig. 7.18. The bent column curvature is shown in Fig. 7.19 for both the right and the left column. The column curvature is observed to decrease in the ANFIS case than that of the LQG case.

Performance indices obtained through the simulation with ANFIS are tabulated in Table 7.5. Comparison of LQG and ANFIS based control design for twenty one performance indices are tabulated in Table 7.6. It is evident from Table 7.5 that the hybrid system reduces most of the peak responses by about 30% in comparison to corresponding LQG controller based response and nearly 12% and 20% respectively for abutment displacement and mid span acceleration at the cost of increase in peak control force by 20% without reaching the actuator maximum limit. Moreover, the present method needs less number of sensors than the LQG based control system. Therefore, probability of failure of control scheme due to sensor failure is less than that of LQG control case.

Dynamic inversion driven MR damper controller results

A total of sixteen MR dampers are deployed for the Phase-I study. Four pairs of orthogonal dampers are located at each end of the bridge and no dampers are considered to be placed in the central column. The number and locations of accelerometers and displacement sensors employed to estimate the reduced order states of the system are kept same as in the benchmark

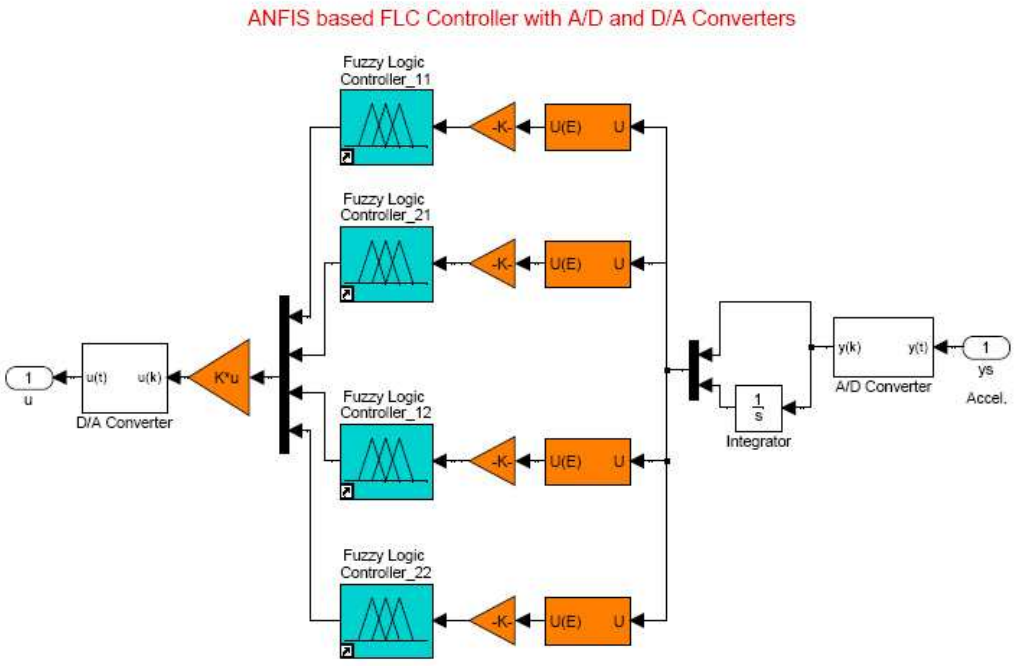

Figure 7.16: Simulink block diagram of ANFIS driven active control

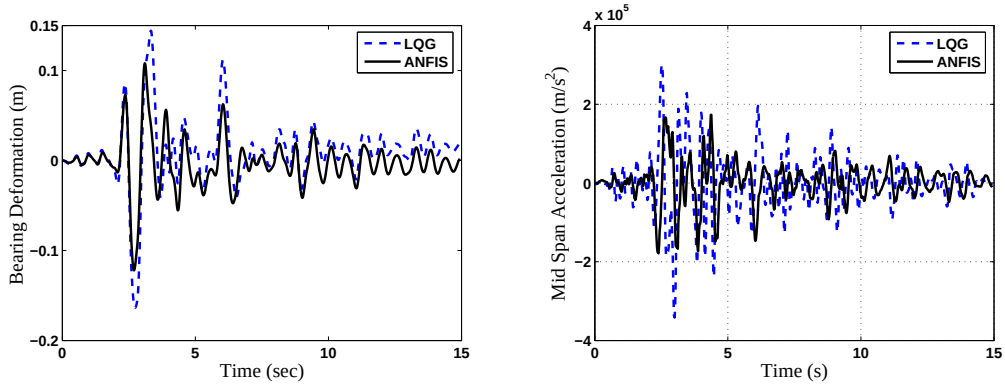

(a) Bearing deformation time history (b) Mid span acceleration time history

Figure 7.17: Displacement and acceleration time history under Northridge earthquake with ANFIS control, phase-I highway bridge

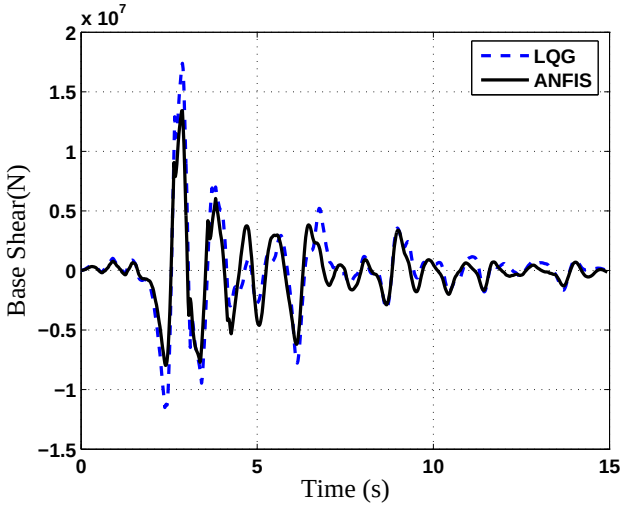

Figure 7.18: Base shear under Northridge earthquake with ANFIS control, phase-I highway bridge

study. It is to be noted that force transducers are not needed in the present control scheme, rather accelerations at the damper locations are needed for feedback. Therefore, a total of $12 + 16 = 28$ sensors are required at most for the present study. However, it is to be noted that this number of sensors could be reduced by suitably choosing the measured states for estimation of the reduced states. The velocities are obtained by means of a second order filter that approximates an integrator (Nagarajaiah et al. (2005) [250]). Present analysis is carried

out assuming equal importance of all the dampers, *i.e.*, $\omega_1 = \cdots = \omega_N = 1$ (Eq. 6.30 of Chapter 6). Equation 6.31 is used for updating voltage supply to MR dampers. It is to be noted that a designer has the flexibility of choosing any appropriate function for $\omega_i,\ i = 1, \ldots, N$ to give more importance to a particular damper (*i.e.*, one may give double importance to the dampers at central column location, so that displacement at central column gets reduced).

Figure 7.20 shows the simulink block diagram of the dynamic inversion based MR damper control of benchmark highway bridge. The dynamic inversion block is coded as an embedded code in MATLAB Simulink (MATLAB (2004) [230]).

The dynamic inversion controller design are optimized separately for a set of dampers acting at a particular direction, *i.e.*, $N = 8$ is considered in Eq. 6.30. This is done, such that the dampers input voltages in a particular direction are optimized to provide forces that are required in that particular direction. It is to be noted that one can use the full set of controllers (*i.e.*, $N = 16$) with proper choice of weights (*i.e.*, ω_i) to mitigate responses due to torsional vibration of the bridge structure. This is not done in the present study due the constraint in the program files provided with the benchmark study.

The simulation results for the given seismic data are tabulated in Table 7.7. It is seen from the Table 7.7 that base shear (J_1) is decreased in all earthquake records and more than

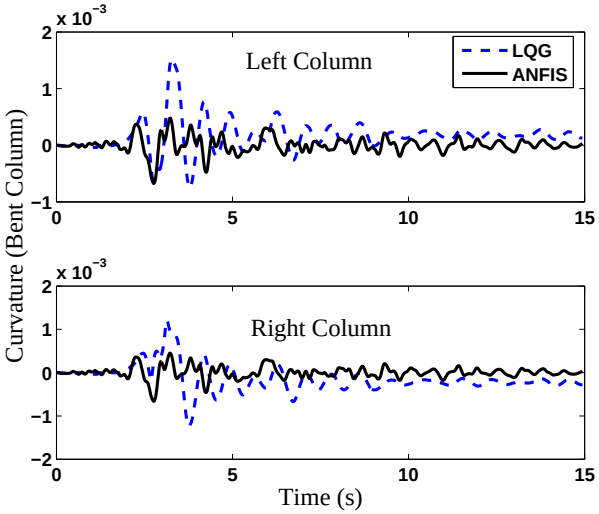

Figure 7.19: Curvature at bent column under Northridge earthquake with ANFIS control, phase-I highway bridge

Table 7.5: Performance Indices Obtained with ANFIS based Active Control for Benchmark Highway Bridge, Phase-I

Performance Index	**N. Palm Spring**	**Chichi**	**El-Centro**	**Northridge**	**Turkey Bolu**	**Kobe NIS**
J_1 **(Base Shear)**	0.834336	0.787776	0.810144	0.78624	0.861888	0.801984
J_2 **(Base Moment)**	0.755616	0.929568	0.739392	0.928416	0.9432	0.720768
J_3 **(Midspan Disp)**	0.811392	0.75408	0.822144	0.774624	0.72432	0.704256
J_4 **(Midspan Accl)**	0.938304	0.863904	0.847296	0.86688	0.812832	0.904032
J_5 **(Bearing Deform)**	0.849888	0.742272	0.682848	0.775584	0.89616	0.585984
J_6 **(Ductility)**	0.755616	0.663264	0.739392	0.67296	0.420384	0.720768
J_7 **(Dissip Energy)**	0	0.5303	0	0.575	0.3425	0
J_8 **(Plastic Connec)**	0	0.6667	0	1	0.3333	0
J_9 **(Norm Base Shear)**	0.747365	0.808808	0.656747	0.763399	0.874601	0.712257
J_{10} **(Norm Base Moment)**	0.677313	0.752388	0.630084	0.781235	0.540631	0.680771
J_{11} **(Norm Midspan Disp)**	0.701792	0.708071	0.645463	0.740467	0.558194	0.697788
J_{12} **(Norm Midspan Accl)**	0.840658	0.755391	0.674583	0.745836	0.794612	0.756847
J_{13} **(Norm Bearing Deform)**	0.762125	0.746837	0.509145	0.766948	0.978399	0.542815
J_{14} **(Norm Ductility)**	0.677313	0.478205	0.630084	0.71435	0.185822	0.680771
J_{15} **(Peak Force)**	0.00759	0.02189	0.00484	0.02211	0.01353	0.00693
J_{16} **(Peak Dev. Stroke)**	0.93742	0.81444	0.71962	0.80949	0.916146	0.66198
J_{17} **(Peak Power)**	0.02904	0.10582	0.02255	0.1265	0.0572	0.02442
J_{18} **(Total Power)**	0.00671	0.01452	0.00341	0.01727	0.01177	0.0044
J_{19} **(No. of Devices)**	16	16	16	16	16	16
J_{20} **(No. of Sensors)**	6	6	6	6	6	6
J_{21} **(Comp Resource)**	22	22	22	22	22	22

35% decrease is observed for Chichi, El-Centro and Northridge earthquake data. A similar performance is observed in case of base moment (J_2) also. Noticeable increase in performance is seen in midspan displacement where more than 50% decrease in displacement compared to the uncontrolled case is achieved for Chichi and Northridge earthquake records.

The decrease in midspan displacement increased the acceleration in many records, *e.g.*, in El-Centro, a 28% increase in accleration are observed. In the same earthquake record a decrease in 62% in bearing deformation is observed. It is interesting to note that the application

Table 7.6: Performance Indices Obtained for Comparative Analysis of ANFIS and LQG (Sample Controller) for Benchmark Highway Bridge, Phase-I

Performance Index	**Average Values**		**Maximum Values**	
	ANFIS	LQG	ANFIS	LQG
J_1 **(Base Shear)**	0.813728	0.8693	0.861888	0.9502
J_2 **(Base Moment)**	0.83616	0.8565	0.9432	0.9782
J_3 **(Midspan Disp)**	0.765136	0.7865	0.822144	0.8669
J_4 **(Midspan Accl)**	0.872208	0.8488	0.938304	0.8986
J_5 **(Bearing Deform)**	0.755456	0.7611	0.89616	0.937
J_6 **(Ductility)**	0.662064	0.7123	0.755616	0.8516
J_7 **(Dissip Energy)**	0.2413	0.2447	0.575	0.6244
J_8 **(Plastic Connec)**	0.333333333	0.3333	1	1
J_9 **(Norm Base Shear)**	0.7605295	0.8006	0.874601	0.8937
J_{10} **(Norm Base Moment)**	0.677070333	0.716	0.781235	0.878
J_{11} **(Norm Midspan Disp)**	0.675295833	0.7142	0.740467	0.8047
J_{12} **(Norm Midspan Accl)**	0.761321167	0.7645	0.840658	0.7976
J_{13} **(Norm Bearing Deform)**	0.7177115	0.5942	0.978399	0.8211
J_{14} **(Norm Ductility)**	0.561090833	0.6277	0.71435	0.8274
J_{15} **(Peak Force)**	0.012815	0.0142	0.02211	0.023
J_{16} **(Peak Dev. Stroke)**	0.809849333	0.7254	0.93742	0.9019
J_{17} **(Peak Power)**	0.060921667	0.0657	0.1265	0.1105
J_{18} **(Total Power)**	0.00968	0.0109	0.01727	0.015
J_{19} **(No. of Devices)**	16	16	16	16
J_{20} **(No. of Sensors)**	6	12	6	12
J_{21} **(Comp Resource)**	22	28	22	28

of the proposed control scheme resulted in the reduction of the ductility factor (*i.e.*, peak (J_6) or normed (J_{14})) significantly. Further, in all of the cases dissipated energy (J_7) of the curvatures at the end of bent columns and the number of plastic connections (J_8) are greatly reduced with the proposed control scheme. Thus, damage in the bridge is significantly reduced. Peak power (J_{17}) and total power (J_{18}) are not of concern for semi-active control based on MR dampers as they operate on battery power. To compare with the sample semiactive control

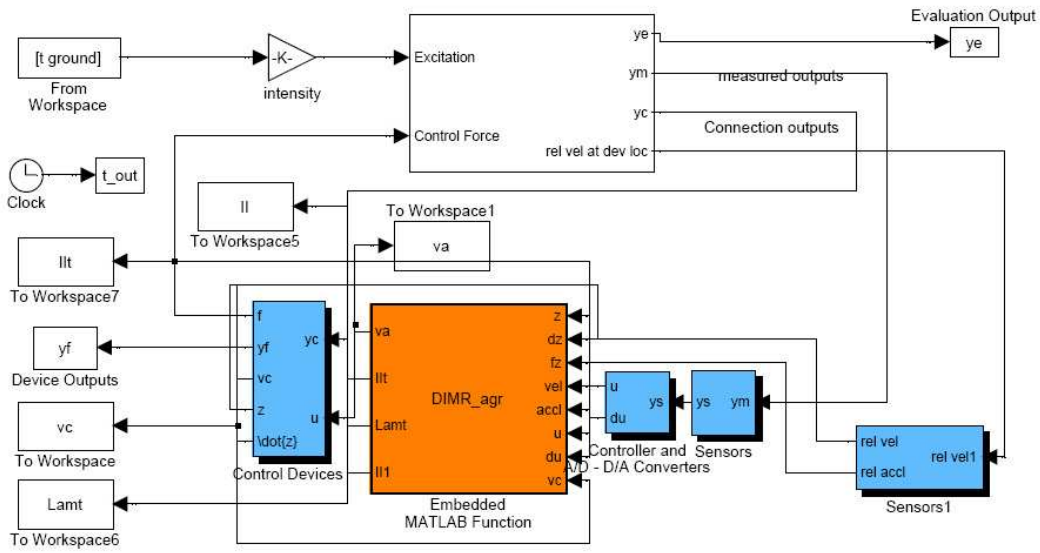

Figure 7.20: Simulink diagram of ODI based MR damper voltage monitoring for the benchmark highway bridge

provided with benchmark bridge control exercise (Tan and Agrawal (2005) [353]), the average, minimum and maximum values of performance indices over all earthquake records have been shown in Fig. 7.21.

Figure 7.21 shows the comparison of the first 16 performance indices as remaining are same for the proposed control scheme and the sample provided with benchmark study. It is evident from Fig. 7.21 that the average performance is improved with the proposed controller. It is interesting to see a potential reduction in the dissipated energy at the bent columns (J_7) and the number of plastic connection formed (J_8) in the present case. Average peak midspan acceleration and its normed value is higher than that of the proposed sample controller. Minimum and maximum values of performance indices over all earthquake records has also been shown in Fig. 7.21 for better comparison.

Figures 7.22 and 7.23 show simulated response-time histories obtained under N. Palm Spring-1986 earthquake record. For better comparison, benchmark bridge with isolators but without controller (uncontrolled, shown with $(\cdots)$ dashed line), benchmark bridge with sample semi-active controller (SA-Sample, shown with solid line) and with proposed controller (SA-ODI, shown with wider solid line) are shown together in Figs. 7.22 and 7.23.

Table 7.7: Performance Indices obtained with DI control for benchmark highway bridge, Phase-I

Performance Index	N. Palm Spring	Chichi	El-Centro	Northridge	Turkey Bolu	Kobe NIS
J_1 **(Base Shear)**	0.9451	0.6206	0.6398	0.6537	0.9766	0.9523
J_2 **(Base Moment)**	0.8043	0.9308	0.5157	0.9162	0.9256	0.9528
J_3 **(Midspan Disp)**	0.8371	0.4628	0.5903	0.4527	0.6395	0.9544
J_4 **(Midspan Accl)**	0.9682	0.7458	1.2841	1.0342	1.0212	0.9277
J_5 **(Bearing Deform)**	1.0153	0.4365	0.3804	0.4598	0.6370	0.8807
J_6 **(Ductility)**	0.9043	0.1854	0.5157	0.2196	0.2038	0.9528
J_7 **(Dissip Energy)**	0	0.0050	0	0.0936	0	0
J_8 **(Plastic Connec)**	0	0.1667	0	0.2500	0	0
J_9 **(Norm Base Shear)**	0.8924	0.5985	0.6639	0.8974	0.9132	0.9030
J_{10} **(Norm Base Moment)**	0.8511	0.4585	0.6075	0.7583	0.4676	0.8867
J_{11} **(Norm Midspan Disp)**	0.8658	0.4738	0.6817	0.7703	0.6266	0.9061
J_{12} **(Norm Midspan Accl)**	0.9906	0.6169	0.9257	0.8929	1.1623	0.9526
J_{13} **(Norm Bearing Deform)**	0.5076	0.5579	0.7037	0.8764	0.9048	0.6555
J_{14} **(Norm Ductility)**	0.8511	0.3352	0.6075	0.7889	0.0450	0.8867
J_{15} **(Peak Force)**	0.0054	0.0630	0.0567	0.0630	0.0617	0.0023
J_{16} **(Peak Dev. Stroke)**	0.9773	0.4180	0.3498	0.4188	0.6314	0.8683
J_{17} **(Peak Power)**	–	–	–	–	–	–
J_{18} **(Total Power)**	–	–	–	–	–	–
J_{19} **(No. of Devices)**	16	16	16	16	16	16
J_{20} **(No. of Sensors)**	26	26	26	26	26	26
J_{21} **(Comp Resource)**	28	28	28	28	28	28

Time-histories for both X and Y directions are shown. It is evident form the Figs. 7.22 and 7.23 that the responses are improved with proposed controller. Figure 7.22 shows the time-history of midspan displacement (Figs. 7.22(a) & 7.22(b)), bearing deformation (Figs. 7.22(c) & 7.22(d)) and curvature at bent column (Figs. 7.22(e) & 7.22(f)). Bearing deformation (Fig. 7.22(c)) and curvature at the bent column (Fig. 7.22(e)) are seen to improve more with ODI based MR damper controller. Figure 7.23 shows the time-history of midspan acceleration (Figs. 7.23(a) & 7.23(b)), base shear (Figs. 7.23(c) & 7.23(d)) and control force provided

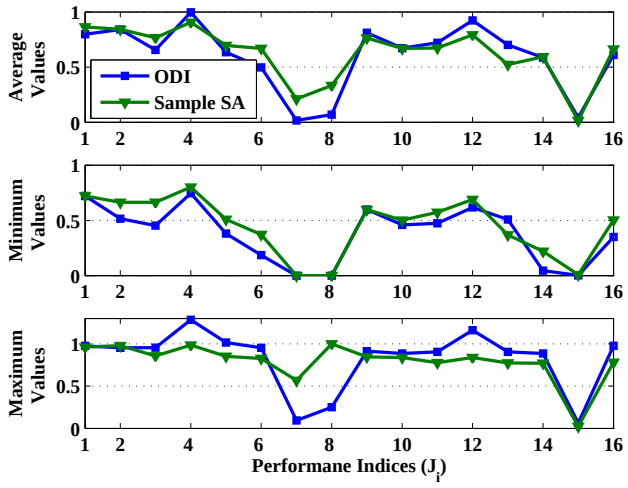

Figure 7.21: Performance values obtained with ODI base semi-active control of phase-I benchmark highway bridge

(Figs. 7.23(e) & 7.23(f)).

A comparison of ANFIS driven active control and DI based semi-active control can be made from Tables 7.5 and 7.7. The base shear in the ANFIS driven active control has shown a better performance in N. Palm Spring, Turkey Bolu and Kobe NIS seismic motions, whereas the DI based semi-active control has shown better performance in other earthquakes. The overall performance is seen to be better in DI based control for Chichi, El-Centro and Northridge earthquake, except for increase in acceleration responses. For other three earthquake namely, N. Palm Spring, Turkey Bolu and Kobe NIS, performance of ANFIS based control is seen to be better.

7.4.5 Numerical simulation and results: phase-II study

The phase-II of the benchmark highway bridge considered a total of twenty MR dampers installed on the bridge. Four pairs of orthogonal dampers are located at each of the bridge end and one pair of dampers have been considered to be placed at each of the central columns. The number and locations of accelerometers and displacement sensors employed for state observation are kept same as in the benchmark study. This includes two accelerometers located at the center bent columns. Therefore, a total of $12 + 20 - 2 = 30$ sensors are required for the study of phase-II benchmark problem. For the phase-II study, only dynamic inversion based

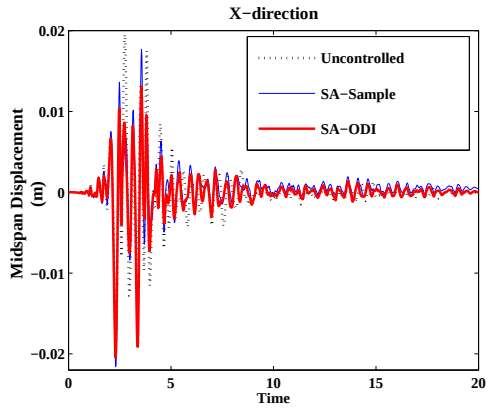

(a) Midspan Displacement: X-direction

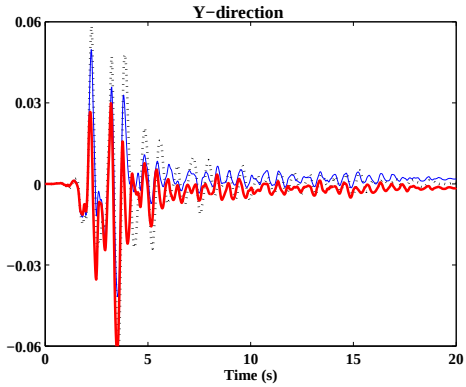

(b) Midspan Displacement: Y-direction

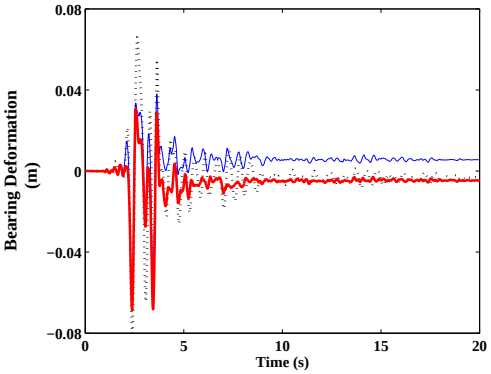

(c) Bearing Deformaion: X-direction

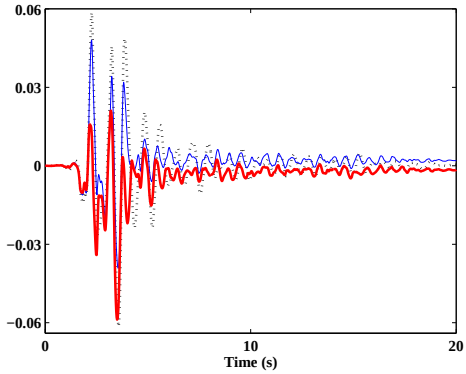

(d) Bearing Deformaion: Y-direction

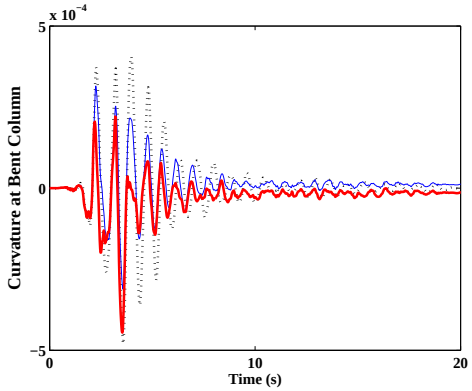

(e) Curvature at Bent Column: X-direction

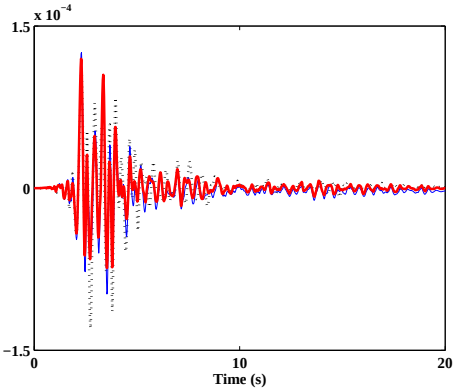

(f) Curvature at Bent Column: Y-direction

Figure 7.22: Simulation plots for phase-I benchmark bridge with ODI based semi-active control (N. Palm Spring)

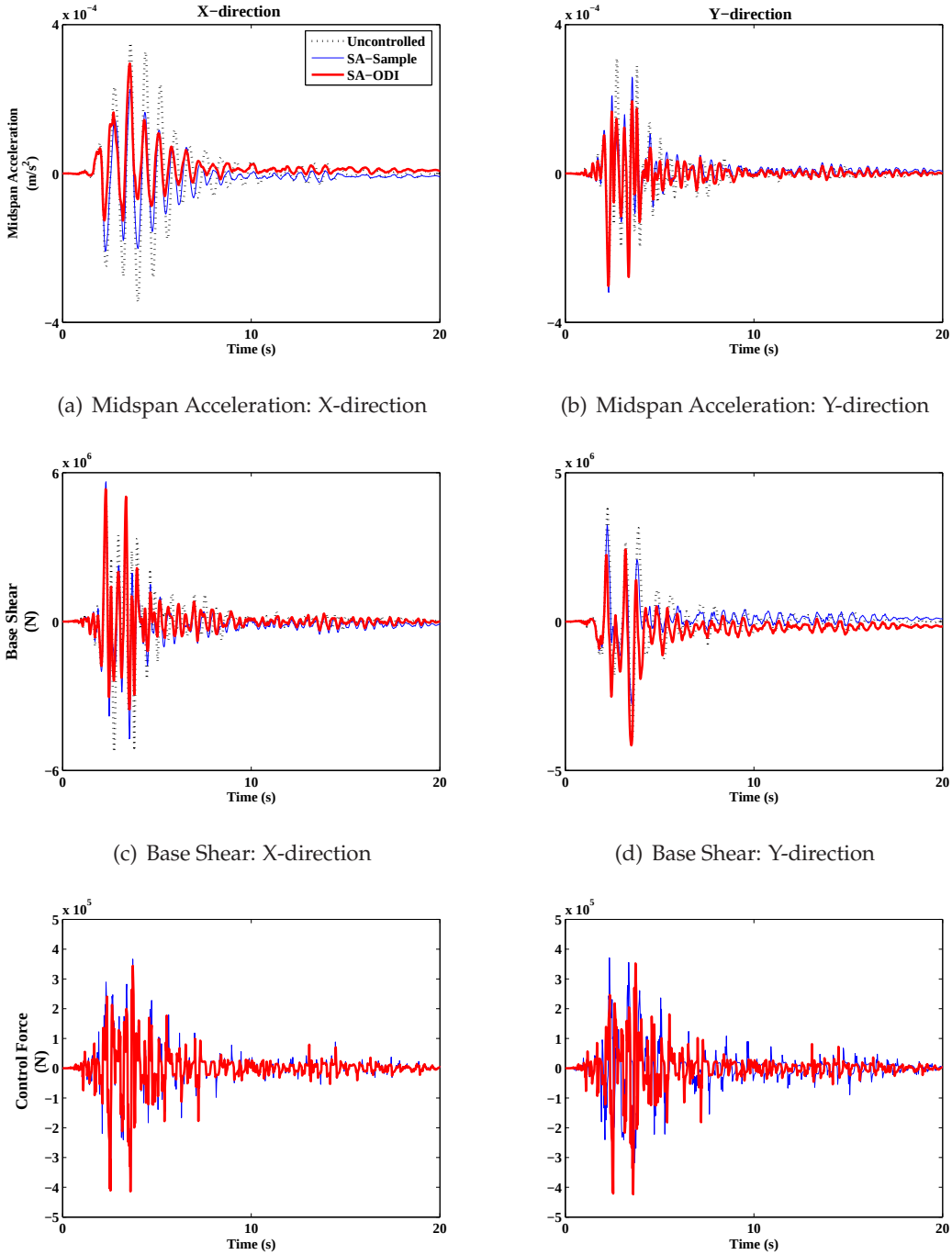

(a) Midspan Acceleration: X-direction

(b) Midspan Acceleration: Y-direction

(c) Base Shear: X-direction

(d) Base Shear: Y-direction

(e) Control Force: X-direction

(f) Control Force: Y-direction

Figure 7.23: Simulation plots for phase-I benchmark bridge with ODI based semi-active control (N. Palm Spring)

MR damper voltage monitoring control are studied. The parameters (Q, R) for the LQG based primary controller for the phase-II study is kept same as in the Phase-I study.

Dynamic inversion driven MR damper controller results for phase-II study

Similar to Phase-I study, Phase-II analysis is carried out assuming equal importance to all the dampers, *i.e.*, $\omega_1 = \cdots = \omega_N = 1$ has been taken in Eq. 6.30. The optimal dynamic inversion controller design is optimized separately for each directions, *i.e.*, $N = 10$ is taken in Eq. 6.31.

Table 7.8 shows the performance indices obtained with the ODI based MR damper controller across all the earthquake records. Performance in phase-II has not shown similar improvement as in the phase-I case. Addition of MR dampers at the central columns has shown no development of plastic connection and therefore damage decreases. The midspan displacement has decreased across all the earthquake records. An improved performance of 43% has been observed in midspan displacement with El-Centro earthquake data. This decrease in midspan displacement has shown an increase in corressponding acceleration across all earthquake records.

Comparison of proposed control scheme with that of sample semi-active controller provided with benchmark study (Tan and Agrawal (2005) [353]) is shown in Fig. 7.24. Similar to Fig. 7.21, Fig 7.24 contains average, minimum and maximum performance values over all earthquake records. It is evident from Fig 7.24 that a consistent performance is seen across all performance indices (J_i), whereas in case of sample controller provided with benchmark study, peak acceleration (J_4) is seen to reach a value of 1.9.

Time-histories of midspan displacement (Figs. 7.25(a) and 7.25(b)), bearing deformation (Figs. 7.25(c) and 7.25(d)) and curvature at bent column (Figs. 7.25(e) and 7.25(f)) obtained in simulation with Chichi earthquake record are shown in Fig. 7.25. Figure 7.26 shows the time-history of midspan acceleration (Figs. 7.26(a) and 7.26(b)), base shear (Figs. 7.26(c) - 7.26(d)) and control force provided (Figs. 7.26(e) - 7.26(f)). Similar to the phase-I case Figs. 7.25 and 7.26 show the time-history for uncontrolled, semi-active sample controller and semi-active ODI controller for both X and Y directions.

It is evident from Figs. 7.25(a) and 7.25(b) that the midspan displacements along both the directions are reduced using semi-active controller. Proposed controller performs better in this case in comparison to sample controller. Similar conclusion can be drawn for the case of

Table 7.8: Performance Indices Obtained with DI based Semi-active Control of Phase-II Benchmark Bridge

Performance Index	**N. Palm Spring**	**Chichi**	**El-Centro**	**Northridge**	**Turkey Bolu**	**Kobe NIS**
J_1 **(Base Shear)**	0.8997	0.9591	0.7214	0.8838	0.8385	0.8871
J_2 **(Base Moment)**	0.8894	1.0737	0.6981	0.8987	0.8567	0.8816
J_3 **(Midspan Disp)**	0.8376	0.8091	0.5699	0.9514	0.6449	0.6370
J_4 **(Midspan Accl)**	1.4998	1.0599	1.3194	0.9408	0.9444	1.5033
J_5 **(Bearing Deform)**	0.7862	0.8046	0.6127	0.9502	0.6459	0.6370
J_6 **(Ductility)**	0.8894	1.0737	0.6981	0.8987	0.8567	0.8816
J_7 **(Dissip Energy)**	0	0	0	0	0	0
J_8 **(Plastic Connec)**	0	0	0	0	0	0
J_9 **(Norm Base Shear)**	0.9971	1.1751	1.0607	0.8413	0.9123	0.6091
J_{10} **(Norm Base Moment)**	1.0057	1.1747	1.0583	0.8310	0.9122	0.5939
J_{11} **(Norm Midspan Disp)**	0.9811	1.0281	0.7885	0.8751	0.5952	0.7238
J_{12} **(Norm Midspan Accl)**	1.2944	1.2031	1.0885	1.0046	0.9403	1.0812
J_{13} **(Norm Bearing Deform)**	0.9948	1.0329	0.8373	0.9043	0.6023	0.7517
J_{14} **(Norm Ductility)**	1.0057	1.1747	1.0583	0.8310	0.9122	0.5939
J_{15} **(Peak Force)**	0.0036	0.0051	0.0042	0.0049	0.0045	0.0035
J_{16} **(Peak Dev. Stroke)**	0.7862	0.8046	0.6127	0.9502	0.6459	0.6370
J_{17} **(Peak Power)**	–	–	–	–	–	–
J_{18} **(Total Power)**	–	–	–	–	–	–
J_{19} **(No. of Devices)**	20	20	20	20	20	20
J_{20} **(No. of Sensors)**	30	30	30	30	30	30
J_{21} **(Comp Resource)**	28	28	28	28	28	28

bearing deformation (Figs. 7.25(a) - 7.25(b)). The increase in acceleration response is evident from Figs. 7.26(a) and 7.26(b) but they also show that the proposed controller is effective in comparison to sample controller. Figs. 7.26(e) and 7.26(f) show the control force time-history, it is evident that the control force provided by the proposed controller is less than that of sample controller and this makes the midspan acceleration less than that in sample controller case. Reduced control force is attributed to the fact that the ODI based controller does not

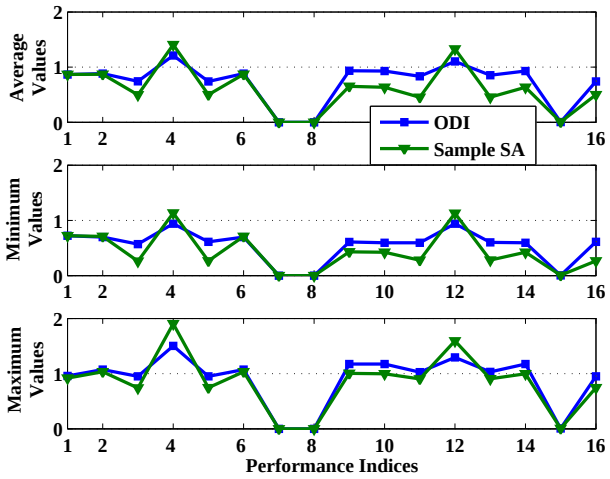

Figure 7.24: Performance values obtained with ODI base semi-active control of phase-II benchmark highway bridge

swap the voltage between maximum and zero, rather, provides an optimal voltage supply to each of the dampers.

It is observed from Tables 7.7 and 7.8 that the number of plastic connections formed in the seismic analysis of the benchmark bridge is decreased in phase-II than that of in phase-I of the study. Therefore, MR dampers present at the center bent columns do not allow plastic hinges to form at the column. This increases the operational performance of the bridge after a seismic hazard and therefore phase-II is desirable for practical implementation.

7.5 Stay Cable with Sag

In the third example, a stay cable vibration mitigation is considered. Stay cables are important structural element for many Civil Engineering structures and are extensively used in the field in applications ranging from long span bridges to marine cables, transmission tower to temporary structures. Their importance in Civil structures is increasing due to their immense tensile strength. They are the main load carrying members in long-span bridges and temporary structures. Long-span bridge cables are susceptible to vibration under wind, and earthquake due to their high flexibility, relatively small mass and very low inherent damping. Unexpectedly large oscillation occurring in stays of cable stayed bridges and vertical hangers of suspension

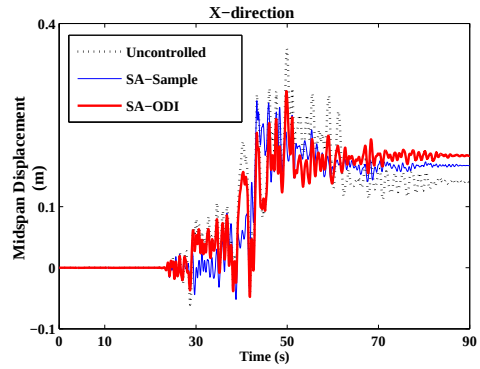

(a) Midspan Displacement: X-direction

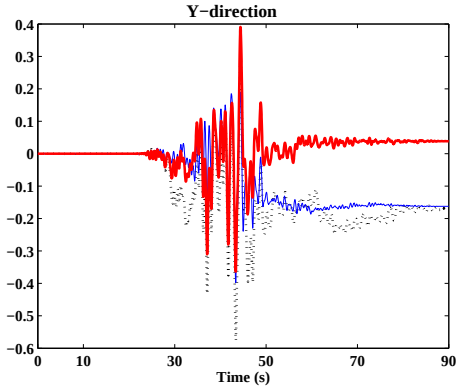

(b) Midspan Displacement: Y-direction

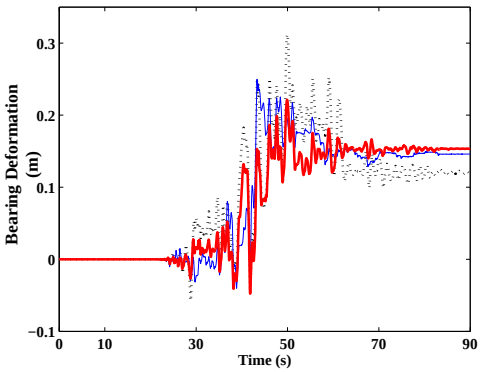

(c) Bearing Deformaion: X-direction

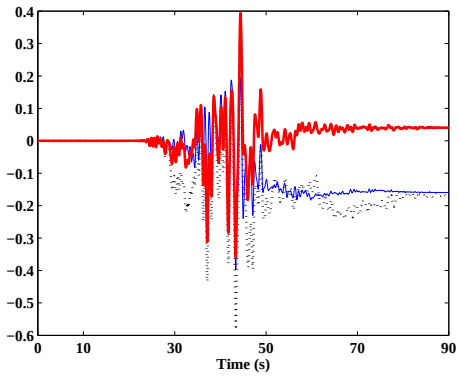

(d) Bearing Deformaion: Y-direction

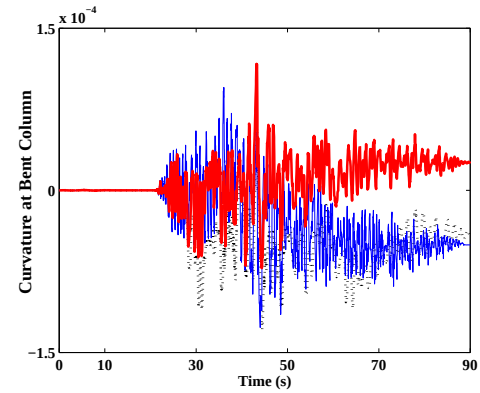

(e) Curvature at Bent Column: X-direction

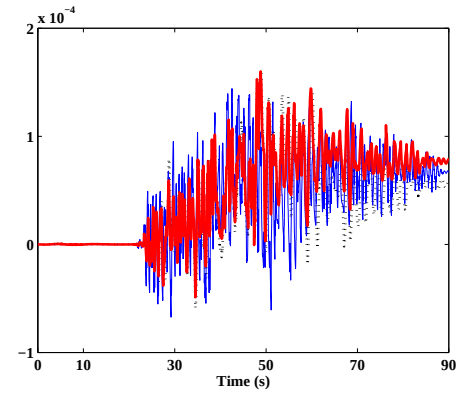

(f) Curvature at Bent Column: Y-direction

Figure 7.25: Simulation plots for phase-I benchmark bridge with ODI based semi-active control (Chichi)

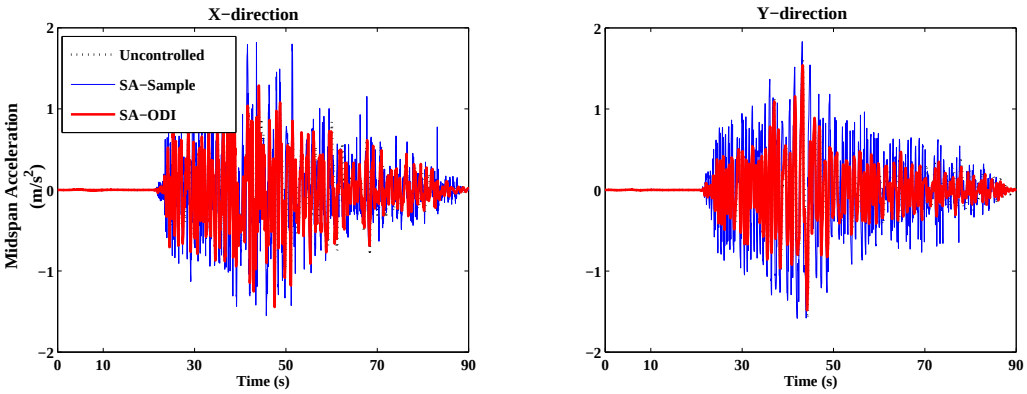

(a) Midspan Acceleration: X-direction

(b) Midspan Acceleration: Y-direction

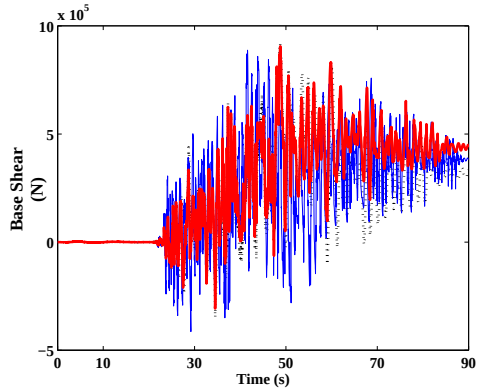

(c) Base Shear: X-direction

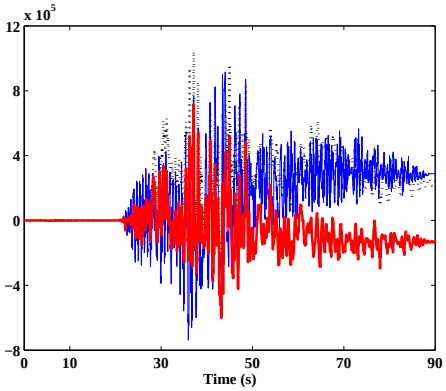

(d) Base Shear: Y-direction

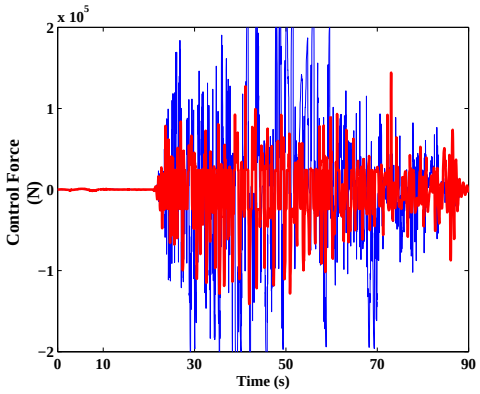

(e) Control Force: X-direction

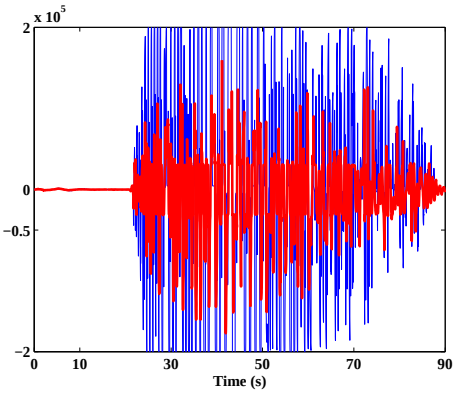

(f) Control Force: Y-direction

Figure 7.26: Simulation plots for phase-I benchmark bridge with ODI based semi-active control (Chichi)

and arch bridges are due to movement in their support point, *i.e.*, tower top and deck connection in case of stay cables. In particular, Hikami and Shiraishi (1987) [144] reported that light to moderate wind combined with light to moderate rain can induce galloping motion in cables. Low inherent damping of cables need to be supported by control measures to mitigate such excessive vibration levels.

In the past decade, cable vibration control techniques by means of various passive measures including aerodynamic, mechanical and structural means have been extensively investigated (Fujino and Susumpow (1994) [124]; Warnitchai et al. (1995) [368]) and installed in a number of bridges such as Brotonne Bridge in France, Dongting Lake Bridge in Honk Kong and the Aratsu Bridge in Japan. Performance of passive dampers increases with increase in distance between point of installation and support. Present day cable stayed bridges are several thousands meters long making each cable length nearly 500m, therefore installation of passive dampers becomes difficult. Numerous researchers have studied active vibration control of cables through the application of transverse force and/or by changing the axial stiffness by provision of tensile force (Susumpow and Fujino (1995) [347];Warnitchai et al. (1995) [368]; Zhou et al. (2006) [422]).

Stay cables are distributed parameter systems and are governed by partial differential equations (PDE) of motion. Control theory is not well developed for PDE systems and much of the research is underway (Christofides (2001) [73]). Design-then-approximate (DTA) and approximate-then design (ATD) approaches are mainly followed for control of PDE systems (Ito and Ravindran (2000)[157]). In DTA approach the control objective is set on the PDE and an algorithm is developed to act on the PDE itself. Then the PDE with control solution is approximated together. Whereas in ATD approach the PDE is first approximated to a set of ODE and the control objective as well as the algorithm is developed on the system of ODEs. Most of the cable control problem uses ATD approach and the same is followed in the present analysis.

In the present study a nonlinear response characteristics of a stay cable are developed. The control objective is met with an MR damper driven by fuzzy rule base. FLC driven MR damper provides inherent robustness to the system. In the next section details of the stay cable vibration model under support motion is outlined and then the control techniques are given. Finally a comparison of the proposed control method with other classical control strategies

are provided.

Stay cable model

Cables remain attached to structural system like the bridge deck or supports at tower top, and experience support motion during either the movement of the deck or tower or both. Therefore, cable problems need to be analysed as a support motion problem. In this section motion of a single cable is investigated where the effects of global vibration is taken into account as motions at cable supports, *i.e.*, anchorages.

Consider an uniform cable (as shown in Fig. 7.27) of chord length L, area of cross-section A, modulus of elasticity E and mass per unit length m. The stay cables in a cable-stayed bridge have small depth to span ratio. Thus, the static configuration of the cable can be assumed to be parabolic in the gravity plane. The differential equation for the static configuration of a parabolic cable is given by (Irvine (1981) [154]).

$$H\frac{d^2w^s}{dx^2} = -mg \tag{7.12}$$

Where H is the static horizontal tension of the cable, x is the longitudinal coordinate of the cable system (see Fig. 7.27). Figure 7.27 shows a stay cable with supports at different heights making an angle θ with the horizontal axis. u, v, and w are the displacements along x, y, and z axes respectively. Static and dynamic profile of the cable is shown in Fig. 7.27 with support motions at supports a and b. Superscript s denotes the quantities referred to in the static equilibrium state.

The equations of motion for the cable under dynamic equilibrium are found using Lagrange formulation. Lagrange's equations of motion are given as (Warnitchai et al. (1995) [368]),

$$\begin{aligned}
\frac{\partial}{\partial t}\left(\frac{\partial T_c}{\partial \dot{x}_n}\right) + \frac{\partial U_c}{\partial \dot{x}_n} &= \int_0^L X\frac{\partial u}{\partial \dot{x}_n} \\
\frac{\partial}{\partial t}\left(\frac{\partial T_c}{\partial \dot{y}_n}\right) + \frac{\partial U_c}{\partial \dot{y}_n} &= \int_0^L Y\frac{\partial v}{\partial \dot{y}_n} \\
\frac{\partial}{\partial t}\left(\frac{\partial T_c}{\partial \dot{z}_n}\right) + \frac{\partial U_c}{\partial \dot{z}_n} &= \int_0^L Z\frac{\partial w}{\partial \dot{z}_n}
\end{aligned} \tag{7.13}$$

where, X, Y, Z are external forces along x, y, z axes. The kinetic energy, T_c, and potential

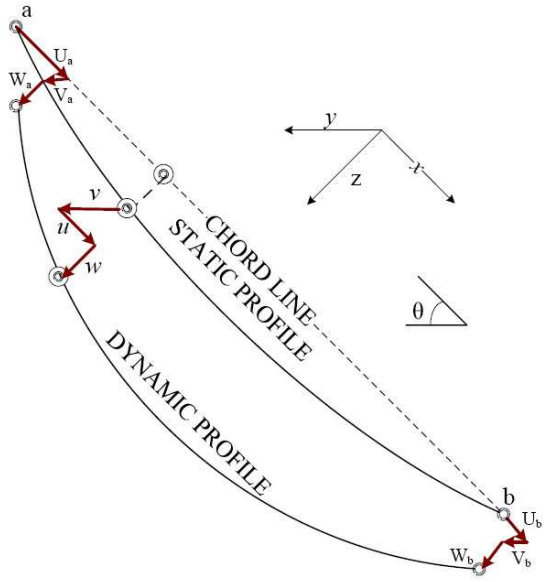

Figure 7.27: Schematic diagram of Stay cable

energy, U_c are given by,

$$T_c = \int_0^L \frac{1}{2} m \left[\left(\frac{\partial u}{\partial t} \right)^2 + \left(\frac{\partial v}{\partial t} \right)^2 + \left(\frac{\partial w}{\partial t} \right)^2 \right] dx \tag{7.14}$$

$$U_c = \frac{1}{2} EAL\epsilon^2 + \frac{1}{2} H \int_0^L \frac{1}{2} m \left[\left(\frac{\partial u}{\partial t} \right)^2 + \left(\frac{\partial v}{\partial t} \right)^2 + \left(\frac{\partial w}{\partial t} \right)^2 \right] dx \tag{7.15}$$

where ϵ is the Green-Lagrange strain-displacement relationship given as (Nayfeh and Pai (2004) [262]),

$$\epsilon(x,t) = \frac{\partial u}{\partial x} + \frac{\partial w^s}{\partial t} \frac{\partial w}{\partial t} + \frac{1}{2} \left[\left(\frac{\partial u}{\partial t} \right)^2 + \left(\frac{\partial v}{\partial t} \right)^2 + \left(\frac{\partial w}{\partial t} \right)^2 \right] \tag{7.16}$$

An uniform time varying strain ($\epsilon(t)$) is assumed and therefore integration of Eq. 7.16 over the domain $[0,\ L]$ gives the time varying strain, as shown in Eq. 7.17.

$$\epsilon(t) = \frac{u_b - u_a}{L} + \frac{1}{L} \int_0^L \left\{ \frac{\partial w^s}{\partial t} \frac{\partial w}{\partial t} + \frac{1}{2} \left[\left(\frac{\partial u}{\partial t} \right)^2 + \left(\frac{\partial v}{\partial t} \right)^2 + \left(\frac{\partial w}{\partial t} \right)^2 \right] \right\} dx \tag{7.17}$$

The non-homogeneous boundary conditions arising due to support motion are

$$\begin{aligned} u(0,t) = u_a(t), \quad v(0,t) = v_a(t), \quad w(0,t) = w_a(t) \\ u(L,t) = u_b(t), \quad v(L,t) = v_b(t), \quad w(L,t) = w_b(t) \end{aligned} \tag{7.18}$$

Cable analysis with support motion

To analyze the cable under support motion the total time dependent displacements are separated into two parts, quasi-static motions denoted by superscript q and modal motions denoted by superscript m.

$$\begin{aligned} u(x,t) = u^q(x,t) + u^m(x,t), \quad v(x,t) = v^q(x,t) + v^m(x,t), \\ w(x,t) = w^q(x,t) + w^m(x,t) \end{aligned} \tag{7.19}$$

The quasi-static motions are the displacements of a cable, which moves as an elastic tendon due to support movements while the modal motions are expressed as a combination of modes of a cable with fixed ends. By definition, quasi-static motions satisfy the time dependent boundaries statically.

To determine the analytical form of the quasi-static displacements, nonlinear PDE model (nonlinearity due to the presence of τ given by Eq. 7.21) of the stay cable vibration is considered (Irvine, (1981) [154]).

$$\begin{aligned} \frac{\partial}{\partial s}\left[(T+\tau)\frac{\partial}{\partial s}(u^s+u)\right] + X = m\frac{\partial^2 u}{\partial t^2} \\ \frac{\partial}{\partial s}\left[(T+\tau)\frac{\partial}{\partial s}(v^s+v)\right] + Y = m\frac{\partial^2 v}{\partial t^2} \\ \frac{\partial}{\partial s}\left[(T+\tau)\frac{\partial}{\partial s}(w^s+w)\right] + Z = m\frac{\partial^2 w}{\partial t^2} \end{aligned} \tag{7.20}$$

Assuming that the cable deforms in the elastic range, the dynamic tension τ can be separated from static tension T (Irvine, (1981) [154]) and can be given as,

$$\tau(x,t) = EA\epsilon(x,t) \tag{7.21}$$

where $\epsilon(x,t)$ is given in Eq. 7.16. The nonlinear strain displacement relation makes a cable system nonlinear in nature.

Further approximations are made to obtain a reasonably simple model for quasi-static analysis. It is known that the dynamic behaviour of a tightly stressed cable is characterized by its transverse in plane and out of plane motions and its longitudinal motions are less effective. Therefore, the axial inertia force in equation is very small and can be omitted. The axial distributed force X is assumed to be zero. The assumptions result in a constant quasi-static dynamic stress over the span and consequently the dynamic strain is constant. They are small and hence the linearized simple homogeneous forms of Eq. 7.20 are employed and the second order terms from strain displacement relation are neglected. The explicit solutions for quasi-static motions are analytically obtained and are given in Eq. 7.22 (Warnitchai et al. (1995) [368]).

$$\begin{aligned} u^q = \quad & u_a + \tfrac{E_q}{E}\left(u_b - u_a\right)\tfrac{x}{L} + \tfrac{\lambda^2 E_q}{4E}\left(u_b - u_a\right)\left[\tfrac{x}{L} - \tfrac{2x^2}{L^2} + \tfrac{4}{3}\tfrac{x^3}{L^3}\right] \\ & -\tfrac{1}{2}\left(w_b - w_a\right)\tfrac{\lambda AL}{H}\left[\tfrac{x}{L} - \tfrac{x^2}{L^2}\right] \\ v^q = \quad & v_a + \left(v_b - v_a\right)\tfrac{x}{L} \\ w^q = \quad & w_a + \left(w_b - w_a\right)\tfrac{x}{L} - \tfrac{1}{2}\left(u_b - u_a\right)\tfrac{\lambda LA^3 E_q}{H^2}\left[\tfrac{x}{L} - \tfrac{x^2}{L^2}\right] \end{aligned} \tag{7.22}$$

The modal equations with homogeneous boundary condition are solved using standard Galerkin approach as shown in Eq. 7.23, neglecting the longitudinal motion of the cable.

$$v^m(x,t) = \textstyle\sum_{n=1}^{N} \phi_n(x) y_n(t), \quad w^m(x,t) = \sum_{n=1}^{N} \psi_n(x) z_n(t) \tag{7.23}$$

where $\phi(x)$ and $\psi(x)$ are shape functions that are considered to be sine functions, *i.e.*, $\phi_n(x) = \psi_n(x) = sin\left(\frac{n\pi x}{L}\right)$. Substituting Eq. 7.23 in Eq. 7.13, and satisfying the orthogonality condition of the sine terms, the governing nonlinear differential equations of motion of stay cable are obtained as

$$\begin{aligned} m_{y_n}\left(\ddot{y}_n + 2\xi_{y_n}\dot{y}_n + \omega_{y_n}^2 y_n\right) + \sum_k v_{nk}\left(y_k^2 + z_k^2\right) y_n + \sum_k 2\beta_{nk} z_k y_n + \\ 2\eta_n\left(u_b - u_a\right) y_n + \zeta_n\left(\ddot{v}_a + (-1)^{n+1}\ddot{v}_b\right) = \quad F_{y_n} \end{aligned} \tag{7.24}$$

$$\begin{aligned} m_{z_n}\left(\ddot{z}_n + 2\xi_{z_n}\dot{z}_n + \omega_{z_n}^2 z_n\right) + \sum_k v_{nk}\left(y_k^2 + z_k^2\right) z_n + \sum_k 2\beta_{nk} z_k z_n + \\ \sum_k 2\beta_{kn}\left(y_k^2 + z_k^2\right) + 2\eta_n\left(u_b - u_a\right) z_n + \zeta_n\left(\ddot{w}_a + (-1)^{n+1}\ddot{w}_b\right) - \alpha_n\left(\ddot{u}_b - \ddot{u}_a\right) = \quad F_{zn} \end{aligned} \tag{7.25}$$

where

$$
\begin{array}{lll}
m_{y_n} = m_{z_n} = \frac{1}{2}mL, & \omega_{y_n} = \frac{n\pi}{L}\sqrt{\frac{H}{m}}, & \omega_{z_n} = \frac{n\pi}{L}\sqrt{\frac{H}{m}\left(1+k_n\right)} \\
k_n = \left(\frac{2\lambda^2}{\pi^4 n^4}\right)\left(1+(-1)^{n+1}\right)^2, & v_{nk} = \frac{EA\pi^4 n^2 k^2}{8L^3} & \beta_{nk}\frac{EA^2\pi\gamma n^2}{4HL}\frac{\left(1+(-1)^{n+1}\right)}{k} \\
\eta_n = \frac{E_q A\pi^2 n^2}{4L^2} & \zeta_n = \frac{mL}{n\pi} & \alpha_n = \frac{mL^2A^2E_q\gamma}{n^3\pi^3H^2}\left(1+(-1)^{n+1}\right) \\
E_q = \frac{E}{1+\lambda^2/12} & \lambda^2 = \frac{EA}{H}\left(\frac{\gamma AL}{H}\right)^2, & \gamma = mgcos\left(\theta\right)
\end{array}
\tag{7.26}
$$

where, subscript n denotes parameters corresponding to the n^{th} mode shape of the motion, *i.e.*, $n = 1, 2, 3, \cdots, N$

7.5.1 Controller Design

The nonlinear vibration in cables under earthquake or wind induced excitations results in severe damage or even catastrophic failure of long-span bridges. Control of large cable vibration amplitude has become an important issue in recent years. The choice of lighter materials offering high strength have magnified this problem further. Various passive systems have been proposed for control of cable vibration and the viscous damper has been widely employed. The damper in stay cable should be located within 5% of its span length from a support for aesthetic reasons. Therefore, placement of damper at an optimal location so as to reduce the amplitudes of vibration remains a debatable issue. The present study compares various control strategies that can be adopted for cable vibration control.

Passive viscous fluid damper

The most widely used passive system for cable vibration control is the viscous fluid damper, where, the movement of a piston in a cylinder containing viscoelastic fluid causes the system to dissipate energy (Agrawal et. al. (2003) [12]). The force from the passive viscous damper installed between the deck and cable is given by,

$$f_d(t) = C_d\left|\dot{x}_d\right|^{\alpha_d} sign(\dot{x}_d) \tag{7.27}$$

Where, $\dot{x}_d$ is the velocity across the damper location in the cable, and C_d is an experimentally determined damping coefficient with the units of force per velocity raised to the power, α_d, a real positive exponent with typical values in the range of $0.35 - 1$ for seismic applications (Agrawal et al. (2003) [12]). Equation 7.27 represents a linear viscous damper at $\alpha_d = 1$. Linear viscous dampers are very effective in reducing the seismic demands on the structure. However, they may develop excessive forces when large structural velocities occur for long period structures subject to near-fault ground motions (Agrawal et al. (2003) [12]). Nonlinear viscous dampers have become popular recently because of their nonlinear force-velocity relationships and their ability to limit the peak damper forces at large structural velocities while providing sufficient supplemental damping. Both linear and nonlinear viscous dampers are used in this study for cable vibration control.

Magneto-rheological dampers

The MR damper parameters and model are selected as reported in Agrawal et al. (2005) [7] and given in Table 7.4. Agrawal et al. (2005) [7] considers a simple Bouc-Wen model the MR damper modeling. A SFLC and GAFLC based MR damper voltage monitoring are considered for the present study.

7.5.2 Numerical Simulation and Results

A test cable for analysis and control is taken from Susumpow and Fujino (1995) [347]. The parameters of the cable are: cable length, $L = 205$m; area $A = 7.2e - 3\text{m}^2$; elastic modulus $E = 1.962e11\text{N/m}^2$; horizontal cable tension $H = 2932560$N; $\theta = 38.7\pi/180$; $m = 60.1992$kg. The cable differential equations given in Eq. 7.24 is converted to state space form taking 10 sine terms for the Galerkin projection. Vibration analysis is carried out for motion at left support only with time history taken from El-Centro earthquake data, with the other support assumed to be fixed. The relative motion of the support is of interest in the present study and issues related to the spatial variability of vibration under multi-support excitation are not carried out in the present study.

The damper is considered to be located at $0.02L$, which is found to be the optimal location for passive dampers (Johnson et al. (2000) [167]). The maximum displacement and acceleration over time at every point in the span of the stay cable are shown in Fig. 7.28. It can be seen

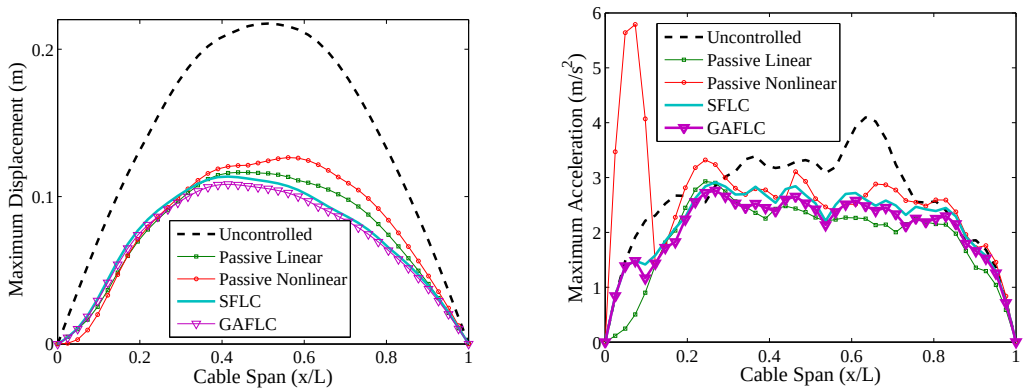

(a) Maximum Displacement (b) Maximum Acceleration

Figure 7.28: Peak displacement and acceleration along span of cable

from the Fig. 7.28(a) that the performance of the passive and semi-active control technique are almost similar, except for a region far away from the damper location. The performance of GA-FLC is found to be better at those far away positions. This is because the semi-active damper is trained to minimize the magnitude of the displacement over the span of the cable. It is interesting to note that the nonlinear passive fluid damper could not perform as well as other dampers and increases the acceleration at the damper location. The midspan displacement and acceleration for uncontrolled and GA-FLC controlled responses are shown in Fig. 7.29. As shown in Fig. 7.29(a) the performance of the GA-FLC based MR damper control is better for displacement control of cables but not for acceleration response (see Fig. 7.29(b)).

The performance values for the different types of control schemes are tabulated in Table 7.9 and Table 7.10 for transverse vibration and lateral vibration respectively. The values are normalized with respect to their corresponding values for the uncontrolled state. Only the modal responses are compared as the pseudo-static responses are same for all the control and uncontrolled states.

From Table 7.9 it is evident that performance of the semi-active controller is better in minimizing the maximum and L_2 norm responses of the cable (displacement and velocity) but the performance of the passive dampers are found to be better in controlling the acceleration response of the cable. The maximum displacement response in the transverse direction of the cable is reduced by more than 40% of its uncontrolled values (see first column of Table 7.9). Similarly the velocity and acceleration responses are observed to reduce by $29 - 38\%$ and

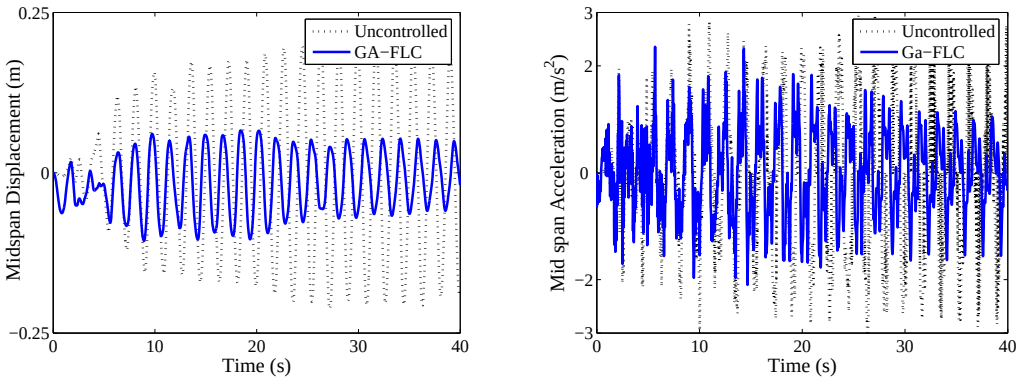

(a) Midspan displacement (b) Midspan acceleration

Figure 7.29: Midspan displacement and acceleration time history of the cable

Table 7.9: Performance of control techniques in transverse direction (z)

Control	Max($\|w^m\|$)	Max($\|\dot{w}^m\|$)	Max($\|\ddot{w}^m\|$)	$\|w^m\|$	$\|\dot{w}^m\|$	$\|\ddot{w}^m\|$
Passive Linear	0.5107	0.6367	0.8639	0.3560	0.3698	0.4350
Passive Nonlinear	0.5719	0.7188	1.7188	0.5229	0.5483	0.5996
SFLC	0.5465	0.6641	0.8595	0.5355	0.5586	0.6009
GA-FLC	0.5162	0.6201	0.8151	0.5110	0.5306	0.5726
	$\|.\|$ =Absolute values			$\|.\|$= L_2 Norm values		

$14 - 19\%$ respectively. In case on nonlinear model of passive fluid damper the acceleration response has seen to increase at the damper location to upto 70% of uncontrolled acceleration.

The normalized responses of the lateral direction vibration of the stay cable are tabulated in Table 7.10. The uncontrolled responses are not reduced as no controller is connected to reduce the lateral vibration. Although no damper is connected in lateral direction the transverse direction damper minimized the responses by $10 - 20\%$ for all control cases. The possibility of having multiple dampers in a skew plane is not considered in the present study. It is likely that this would improve the lateral direction control.

Table 7.10: Performance of control techniques in lateral direction(y)

Control	Max($\|v^m\|$)	Max($\|\dot{v}^m\|$)	Max($\|\ddot{v}^m\|$)	$\|v^m\|$	$\|\dot{v}^m\|$	$\|\ddot{v}^m\|$
Passive Linear	0.9943	1.0112	1.0150	0.9970	0.9970	1.0298
Passive Nonlinear	0.9041	0.9109	0.8569	0.9002	0.9002	0.8880
SFLCr	0.8160	0.8512	0.9140	0.8765	0.8672	0.8727
GA-FLC	0.7980	0.808	0.8051	0.7998	0.7998	0.8207
	$\|.\|$ =Absolute values			$\|.\|$= L_2 Norm values		

7.6 Summary

In this chapter, applications of the control strategies developed in this dissertations for semi-active MR damper control are reported for two benchmark exercises and a stay cable problem. The benchmark exercises considered are nonlinear base isolated benchmark building and benchmark highway bridge. The performance of fuzzy logic based intelligent control algorithm for MR damper monitoring developed in Chapter 4 has been investigated for the nonlinear base isolated benchmark building. Both optimal rule base FLC and fixed rule base FLC are implemented on the benchmark exercise and compared with the performance of Lyapunov based sample control, provided with the benchmark exercise. In optimal rule base FLC, optimization is carried out at every simulation steps using micro-GA optimization technique. Micro-GA is selected for on-line optimization as it uses few chromosomes and restarts its search after the convergence of a set of chromosomes and continues till maximum number of generations is covered. Since micro-GA uses less function evaluation it is faster than simple GA and therefore suitable for on-line applications. A better performance of the building vibration control with both the FLC (FRB-FLC and ARB-FLC) is observed when compared to the sample Lyapunov controller. Furthermore, it is shown that the proposed FLC schemes have better stability than Lyapunov based clipped optimal scheme.

A two stage optimal dynamic inversion approach to monitor the MR damper voltage is implemented to mitigate the vibration of the benchmark highway bridge under various near and far field seismic inputs. Linear Quadratic Gaussian controller is used as the primary controller to derive the amount of control force required to control the highway bridge. Then an

optimal dynamic inversion based approach is adopted to predict the amount of voltage to be supplied to the MR damper such that it produces the force prescribed by the LQG controller. The main advantage of the optimal dynamic inversion based approach is that it provides a closed form stable solution to the supply voltage to MR damper and therefore suitable for real time applications. Furthermore, the optimal dynamic inversion based approach considers the input voltage and commanded voltage dynamics into consideration. The proposed semi-active control technique is applied to both phase-I and phase-II of the study. The performance of the proposed controller is observed to better than the sample controller provided. ANFIS driven FLC controller is also tried on the phase-I study of the exercise. ANFIS has shown better performance in the vibration control of the benchmark study than the sample controller provided.

Finally a stay cable with sag example is considered to investigate the performance of the optimal FLC controller. In cable stayed bridges the cables are connected between deck and tower and therefore any movement in the deck and/or in tower transfer to cables as a support motion. Therefore, the stay cable is assumed to be excited at the supports by the deck and tower movements. Three dimensional nonlinear analysis of the stay is carried out to derive the transverse and lateral direction equations of motion for the stay cable under support excitations. A single MR damper is considered to act in the transverse direction. Passive dampers modeled as linear and nonlinear controller, and semi-active control using MR device monitored by SFLC and GA-FLC are considered for cable vibration mitigation. Nearly 50% mitigation of displacement with respect to the uncontrolled excitation is observed in each of the devices. It is observed that GA-FLC monitored MR damper control outperforms other controllers except in acceleration response where passive damper model considering nonlinearity shows much better result. It is found that the damper connected in the transverse direction can provide a control efficiency of $10 - 20\%$ in the out of plane motion of the cable.

Chapter 8

Conclusions

8.1 Summary

In this study the state-of-the-art in vibration control of structures has been assessed and special focus is given towards the hybrid control strategy for base isolated structures. Based on the limitations identified in the state-of-the-art, the objective of this dissertation has been to investigate the effect of base isolated structures under a broad spectrum of earthquakes (near-field and far field ground motions) and then to develop means for mitigating the seismic induced vibrations in base isolated structures. The focus of the study is on semi-active vibration control using MR damper as a control device. It has also been found that the development of the analytical model and semi-active control algorithm to monitor MR damper current/voltage is a challenging task and presents many interesting open problems. The development of analytical model that can accommodate the effect of amplitude of excitation in the Bouc-wen model required to describe the MR damper hysteretic character is one of the outcomes of this study. A fuzzy based intelligent controller and two model based semi-active control algorithms are developed. Experimental verification of the intelligent optimal control on a three storey base isolated structure with supplemental MR dampers is investigated. Finally simulations of benchmark base isolated building, benchmark highway bridge and a stay cable with proposed controllers are performed.

Conclusions for the various studies undertaken in this dissertation are highlighted in the next section.

8.2 Conclusion

The contribution of this dissertation study can be summarized as

- A fundamental understanding of the behavior of the magnetorheological (MR) dampers has been developed through the modeling, design and experimental verification of a RD-1005-3 MR damper developed by LORD corporation (2008) [214] for small scale applications. Analytical and experimental results have shown that the MR damper is one of the most promising new semi-active devices for structural control vibration reduction, having an inherent ability to provide a simple and robust interface between electronic controls and mechanical components, thereby enabling reliable, fast-acting semi-active vibration control of structural systems. Experiments on the MR damper in various conditions have been conducted. These experiments comprised current/voltage dependent tests, amplitude dependent tests, frequency-dependent tests and constant peak velocity tests. Effect of temperature on the MR damper performance has not been studied due to practical limitations. The overall performance of the MR damper is very promising, and the experimental results have shown that the damper behavior under various configurations is quite consistent. An amplitude and frequency dependence of the Bouc-Wen hysteretic parameters has been observed in the experimental study. Based on these results an amplitude dependent modified Bouc-Wen model has been proposed that provides an improved nonlinear force-supply current/voltage mapping.

- A fuzzy logic based intelligent controller (FLC) has been developed to monitor the MR damper current/voltage supply such that the algorithm can make use of full current/voltage range available in the damper for control applications. Optimization of FLC parameters for structural applications is a computationally intensive task. A new geometric procedure has been developed to determine optimal rule base of FLC with fewer variables. Micro genetic algorithm, which is suitable for parallel processing and on-line application, has been used to optimize the FLC parameters. A comparative analysis of the convergence of the micro GA has been carried out with particle swarm optimization (PSO) based optimization technique. Examples considered in the chapter show better performance of the proposed optimal FLC than fixed rule base FLC or manually configured FLC.

- An experimental investigation has been carried out to study the performance of the proposed optimal FLC on a three storey base isolated building model. The experiments have been conducted for fixed base model, simple base isolated model and hybrid base isolation with supplemental MR damper cases with a combination of near and far field seismic motions. A total of sixteen earthquake records has been considered for the experimental investigation. The hybrid base isolation study comprises of the building responses with MR damper at 0 ampere, 1 ampere current and MR damper monitored by manually configured FLC (SFLC) and optimal FLC (GA-FLC). The base isolated building increased the base displacement with a decrease in inter-storey drifts and acceleration levels. A larger displacement at base of the building has been observed for the near field seismic motions. With supplemental MR damper these large displacements are found to reduce with a slight increase in inter-storey drifts and accelerations. Among the various MR damper current supply conditions, 'passive-on' condition is seen to reduce displacement better than others but at the cost of an increase in floor accelerations. FLC driven variable current monitoring of MR damper has seen to offer a trade-off between displacement response and acceleration responses of the structure. In this aspect optimal FLC has been found to perform better.

- Dynamics of the MR damper supply current/voltage and commanded current/voltage should be considered during variable current/voltage control of MR damper under seismic excitations. Two model based control algorithms have been developed to consider this aspect in the semi-active control algorithm. Numerical simulations of the proposed model based algorithms on the analytical model of the three storey base isolated building considered for the experimental study has been reported. The proposed control algorithms have been found to perform better than existing semi-active control algorithms. The main advantage of these algorithms is that it provides a closed form solution for the current/voltage requirement of the MR damper and therefore are applicable for real time control applications. Stability of the proposed control techniques have been shown using impulsive force analysis of the structure and also analytically through the Lyapunov stability criteria.

- The performance of the proposed FLC and the model based controllers has been evaluated through a set of performance criteria developed for the benchmark studies. The performance of the proposed controllers has been found to be satisfactory and in most of the cases out performs the controller provided with the benchmark studies.

- Stay cable vibration under deck and tower movement due to wind/earthquake induced excitation has been modeled as a support motion phenomenon and detailed derivation of the equation of motion of the cable has been provided with various control mechanism. A comparison of passive, active and semi-active control mechanism has been presented. FLC driven MR damper is seen to provide better control over any other control mechanism reported in the literature.

8.3 Recommendations from the Thesis

Few recommendations that can be made from the thesis work are enumerated below,

1. Simple base isolations can not provide sufficient safety to structures under near fault seismic motions. Base isolated structures should be supplemented with damping devices to protect them from damages due to near-fault seismic motions

2. It has been observed from the simulations and experiments that the performance of the controllers are a trade-off between the isolator displacement and the superstructure accelerations. A control designer should select a control scheme based on the priority of the project. As an example base isolators are provided with an intension to reduce the superstructure displacement and acceleration responses, such that instruments housed inside remain safe during seismic motions. Therefore reducing base displacement to the full range of the MR damper disrupts the primary intention with which base isolation is provided. A trade-off has to be made between the acceptable base displacement and acceptable isolator accelerations in such a situations through simulations and small scale experimental studies

3. A designer can also allow a limited free movement to the isolator without damper and after that limit the damper should act such that the total displacement should not go beyond the acceptable limit of the base displacement. The free movement of the isolator

will keep the superstructure and isolator responses at lower value and the damper action beyond a certain limit, on the other hand, will reduce the base displacement slightly

4. It is recommended to use variable voltage supply to MR dampers as it helps to avoid large base displacements and also higher storey accelerations.

5. It is also recommended to consider MR damper supplied-commanded voltage dynamics in MR damper voltage monitoring algorithms.

8.4 Future Research Directions

There are still many issues that need to be addressed and further explored in the area of response control of structures, such as the development of highly efficient and reliable control systems, large scale testing of various control devices, applications of control in the design and retrofit of structures, code adoption of seismic protective systems in future design guidelines, etc. In terms of the application of seismic protective systems in earthquake engineering, ground motion characteristics needs to be better addressed in the future design and application of various control systems.

Based on the present study following recommendation for future studies can be suggested

1. Due to hardware constraints and the computational efforts required in real time optimization using genetic algorithm, the experimental study has been performed using off-line optimization. The experimental study can be conducted using various hardware that are specifically made for GA optimization. Further investigation can be carried out with 3D building considering bi-directional seismic excitation supplied simultaneously and considering the torsional response of building in the analysis.

   Experimental validation of integral backstepping and dynamic inversion based control actions on the three storey base isolated building remains to be explored.

   Extensions of the experimental investigations to laboratory scaled bridge structures and stay cables may be undertaken and could possibly consider the issues of the spatial variability under multi-support excitations.

2. Parallel processing of GA code to decrease the demand on computation remains an alternative to the use of simple GA code for on-line optimization of FLC parameters.

3. Experimental investigation may be carried out to explore the dependency of the Bouc-Wen parameter on frequency of excitation. Judgment on the suitability of the Bouc-Wen model in predicting the MR damper hysteretic phenomenon has to be supported with various experiments.

4. Model based semi-active control algorithms are very sensitive to the accuracy of the mathematical model of the structure. The proposed model based algorithms should be supported with procedures to identify structural parameters. This remains to be further investigated using adaptive backstepping, fuzzy backstepping *etc*. Robust backstepping technique may be further explored to reduce the sensitivity of the model based algorithms to noise.

   Along with the mathematical models for the structures, neuro based training algorithms should be supplemented to consider the uncertainty in modeling arising out of the flexibility at connections, effect of nonlinearity (material and geometric), *etc*. Thereafter the controller should be designed on these hybrid models.

5. Development of graphic user interface for the proposed semi-active control algorithms which can be easily implemented as a macro to various commercially available FEM softwares for analysis and design of structures will be very interesting.

6. At present many base isolated structures have been constructed in various cities in India, which shows the growing interest in the developments of base isolated structures in the country. But the present Indian building codes do not provide any design specification for base isolated building structures nor for hybrid base isolated structures. Laboratory experiments like the one carried out in the present study can throw much light in developing such codes for practicing engineers. In such a case, scale up issues in control, material response to forces, *etc.*, are additional issues that need to be addressed.

Bibliography

[1] Abdel-Rohman, M. (1987). "Feasibility of active control of tall buildings against wind." *J. Structural Engineering, ASCE*, 113, 349–362.

[2] Abdel-Rohman, M. and Leipholz, H. H. E. (1983). "Control of tall buildings." *J. Structural Engineering, ASCE*, 109, 628–645.

[3] Abe, M. and Fujino, Y. (1994). "Dynamic characterization of multiple tuned mass dampers and some design formulas." *Earthquake Engineering & Structural Dynamics*, 23, 813–835.

[4] Adams, R. J. and Banda, S. S. (1993). "Robust flight control design using dynamic inversion and structured singular value synthesis." *IEEE Transactions on Control Systems Technology*, 1(2), 80–92.

[5] Adhikari, R., Yamaguchi, H., and Yamazaki, T. (1998). "Modal space sliding-mode control of structures." *Earthquake Engineering & Structural Dynamics*, 27, 1303–1314.

[6] Agrawal, A. K. (2006). "A personal communication." *Visiting professor, Department of Civil Engineering, IISc*, (in 2006).

[7] Agrawal, A. K., Tan, P., Nagarajaiah, S., and Zhang, J. (2005). "Benchmark structural control problem for a seismically excited highway bridge, part I: Problem definition." *http://www-ce.engr.ccny.cuny.edu/People/Agrawal/index.htm*, (downloaded: July 2005).

[8] Agrawal, A. K., Xu, Z., and He, W. L. (2006). "Ground motion pulse-based active control of a linear base-isolated benchmark building." *Structural Control & Health Monitoring*, 13(2-3), 792–808.

[9] Agrawal, A. K. and Yang, J. N. (1996). "Optimal polynomial control of seismic excited linear structures." *J. Engineering Mechanics, ASCE*, 122, 753–761.

[10] Agrawal, A. K. and Yang, J. N. (1997). "Static output polynomial control for linear structures." *J. Engineering Mechanics, ASCE*, 123, 639–643.

[11] Agrawal, A. K. and Yang, J. N. (2000). "A semi-active hybrid isolation system for buildings subjected to near-field earthquakes." *Proceedings of* 14^{th} *Conference on Analysis and Computation held in Conjunction with ASCE Structures Congress, Philadelphia*. In CD.

[12] Agrawal, A. K., Yang, J. N., and He, W. L. (2003). "Application of semi-active control systems to benchmark cable-stayed bridge." *J. Structural Engineering, ASCE*, 129(7), 884–894.

[13] Agrawal, A. K., Yang, J. N., and Wu, J. C. (1998). "Application of optimal polynomial controller to a benchmark problem." *Earthquake Engineering & Structural Dynamics*, 27(11), 1291–1302.

[14] Ahlawat, A. S. (2002). *Intelligent Optimal Control of Earthquake or Wind Induced Flexural and Torsionally Coupled Vibrations in Buildings*. Ph.D Thesis, Indian Institute of Science, Bangalore, India.

[15] Ahlawat, A. S. and Ramaswamy, A. (2001). "Multiobjective optimal structural vibration control using fuzzy logic control system." *J. Structural Engineering, ASCE*, 127(1), 1330–1337.

[16] Ahlawat, A. S. and Ramaswamy, A. (2003). "Multiobjective optimal absorber system for torsionally coupled seismically excited structures." *Engineering Structures*, 25, 941–950.

[17] Ahlawat, A. S. and Ramaswamy, A. (2004). "Multiobjective optimal fuzzy logic controller driven active and hybrid control systems for seismically excited nonlinear buildings." *J. Engineering Mechanics, ASCE*, 130(4), 416–423.

[18] Ahmadi, G. and Fan, F. G. (1990). "Nonstationary Kanai-Tajimi models for El-Centro 1940 and Mexico City 1985 earthquake." *Probabilistic Engineering Mechanics*, 5, 171–181.

[19] Aiken, I. D. and Kelly, J. M. (1990). *Earthquake simulator testing and analytical studies of two energy-absorbing systems for multistory structures*. Report No. UCB/EERC-90/03, University of California, Berkeley, CA.

[20] Aiken, I. D. and Kelly, J. M. (1992). "Comparative study of four passive energy dissipation systems." *Bulletins NZ National Society of Earthquake Engineering*, 25(3), 175–192.

[21] Akbay, Z. and Aktan, H. M. (1990). "Intelligent energy dissipation devices." *Proceedings of 4^{th} U.S. National Conference on Earthquake Engineering, Palm Springs, USA*. 427–435.

[22] Akbay, Z. and Aktan, H. M. (1991). "Actively regulated friction slip devices." *Proceedings 6^{th} Canadian Conference on Earthquake Engineering, Toronto, Canada*, S. Pantazopoulo, ed. 367–374.

[23] Akbay, Z. and Aktan, H. M. (1995). "Abating earthquake effects on buildings by active slip brace devices." *Shock & Vibration*, 2, 133–142.

[24] Al-Osaimi, S. A., Abdennour, A., and Al-Sulaiman, A. A. (2005). "Hardware implementation of a fuzzy logic stabilizer on a laboratory scale power system." *Electric Power Systems Research*, 74, 9–15.

[25] Alavi, B. and Krawinkler, H. (2004). "Behavior of moment-resisting frame structures subjected to near-fault ground motions." *Earthquake Engineering & Structural Dynamics*, 33, 687–706.

[26] Ali, S. F. and Padhi, R. (2006). "Active vibration suppression of beams with discrete actuators using optimal dynamic inversion." *9^{th} International Conference on Control, Automation, Robotics and Vision, IEEE, Singapore*.

[27] Ali, S. F. and Padhi, R. (2007). "Active vibration suppression of one-dimensional nonlinear structures using optimal dynamic inversion." *Proceedings of IEEE Multi-conference on Systems and Control, Singapore*.

[28] Ali, Z. and Mo, J. (2001). *Intelligent Control Systems Using Soft Computing Methodologies*. CRC Press.

[29] Ang, A. H. S. and Tang, W. H. (1984). *Probability Concepts in Engineering Planning and Design, Vol-II*. John Wiley & Sons Inc, New York.

[30] Aprile, A., Inaudi, J. A., and Kelly, J. (1997). "Evolutionary model of viscoelastic dampers for structural applications." *J. Engineering Structures, ASCE*, 123, 551–560.

[31] Arima, F., Miyazaki, M., Tanaka, H., and Yamazaki, Y. (1988). "A study on building with large damping using viscous damping walls." *Proceedings of 9^{th} World Conference on Earthquake Engineering, Tokyo, Japan*. 821–826.

[32] Arslan, A. and Kaya, M. (2001). "Determination of fuzzy logic membership functions using genetic algorithms." *Fuzzy Sets and Systems*, 118, 297–306.

[33] Asher, J., Young, R., and Ewing, R. (1994). "Seismic isolation design of the San Bernardino County Medical Center replacement project." *Proceedings of* 1^{st} *World Conference on Structural Control, Los Angeles, Univ. of Southern California, USA*, G. Housner, S. Masri, and A. Chassiakos, eds. FA3:58–97.

[34] Asher, J. W. and Others (1990). "Seismic isolation of the USC university hospital." *Proceedings* 4^{th} *U.S. National Conference on Earthquake Engineering, Palm Springs, USA*. 529–538.

[35] Asher, J. W., Young, R. P., and Ewing, R. D. (1996). "Seismic isolation design of the San Bernardino county medical center replacement project." *Structural Design of Tall Buildings*, 5, 265–279.

[36] Baker, J. (1987). "Reducing bias and inefficiency in the selection algorithm." *Proceedings of the* 2^{nd} *International Conference on Genetic Algorithms and their Application, Massachusetts Institute of Technology*, J. J. Grefenstette, ed. 14–21.

[37] Balendra, T., Wang, C. M., and Cheong, H. F. (1995). "Effectiveness of tuned liquid column dampers for vibration control of towers." *Engineering Structures*, 17, 668–675.

[38] Banerji, P., Murudi, M., Shah, A. H., and Popplewell, N. (2000). "Tuned liquid dampers for controlling earthquake response of structures." *Earthquake Engineering & Structural Dynamics*, 29, 587–602.

[39] Bani-Hani, K. and Ghaboussi, J. (1998). "Neural networks for structural control of a benchmark problem: active tendon system." *Earthquake Engineering & Structural Dynamics*, 27, 1225–1245.

[40] Battaini, M., Casciati, F., and Faravelli, L. (1998). "Fuzzy control of structural vibration: An active mass system driven by fuzzy controller." *Earthquake Engineering & Structural Dynamics*, 27(11), 1267–1276.

[41] Bertero, V. V., Mahin, S. A., and Herrara, R. A. (1978). "Aseismic design implications of near-fault san fernando earthquake records." *Earthquake Engineering & Structural Dynamics*, 6(1), 31–42.

[42] Bouc, R. (1967). "Forced vibration of mechanical systems with hysteresis." *Proceedings of the 4^{th} World Conference on Nonlinear Oscillations, Prague, Czechoslovakia*.

[43] Braae, M. and Rutherford, D. A. (1979). "Selection of parameters for a fuzzy logic controller." *Fuzzy Sets and Systems*, 2, 185–199.

[44] Breneman, S. E. and Smith, H. A. (1998). "Design of h_∞ output feedback controllers for the AMD benchmark problem." *Earthquake Engineering & Structural dynamics*, 27(11), 1277–1289.

[45] Bryson, A. E. and Ho, Y. C. (1975). *Applied Optimal Control*. London: Taylor and Francis.

[46] Buckle, I. G. and Mayes, R. L. (1990). "Seismic isolation history, application, and performance a world view." *Earthquake Spectra*, 6, 161–201.

[47] Bullen, K. E. and Bolt, B. A. (1985). *An Introduction to the Theory of Seismology*. Cambridge University Press, New York, N.Y.

[48] Burton, S. A., Makris, N., Konstantopoulos, I., and Antsaklis, P. J. (1996). "Modeling the response of ER damper: phenomenology and emulation." *Earthquake Spectra*, 122, 897–906.

[49] Caicedo, J. M., Dyke, S. J., Moon, S. J., Bergman, L. A., Turan, G., and Hague, S. (2003). "Phase II benchmark control problem for seismic response of cable-stayed bridges." *J. Structural Control & Health Monitoring*, 10(3–4), 137–168.

[50] Carlson, J. and Spencer, B. J. (1996a). "Magneto-rheological fluid dampers: scalability and design issues for application to dynamic hazard mitigation." *Proceedings of 2^{nd} Workshop on Structural Control: Next Generation of Intelligent Structures, Hong Kong, China*. 99–109.

[51] Carlson, J. D. and Spencer, B. F. J. (1996b). "Magneto-rheological fluid dampers for semi-active seismic control." *Proceedings of 3^{rd} International Conference on Motion and Vibration Control, Chiba, Japan*. 3:35–40.

[52] Casciati, F. (1997). "Checking the stability of a fuzzy controller for nonlinear structures." *Micro Computers in Civil Engineering*, 12, 205–215.

[53] Casciati, F., Faravelli, L., and Yao, T. (1995). "The tuning of fuzzy controllers for active structural control." *Applications of Statistics and Probability*, 2, 741–746.

[54] Casciati, F., Faravelli, L., and Yao, T. (1996). "Control of nonlinear structures using the fuzzy control approach." *Nonlinear Dynamics*, 11, 171–187.

[55] Caughey, T. K. (1998). "The benchmark problem." *Earthquake Engineering & Structural Dynamics*, 27(11), 1125.

[56] Celebi, M. (1996). "Successful performance of base isolated hospital building during the 17 january 1994 Northridge earthquake." *Structural Design of Tall Buildings*, 5(2), 95–109.

[57] Chang, C. C. and Roschke, P. (1998). "Neural network modeling of a magnetorheological damper." *J. Intelligent Material Systems and Structures*, 9, 755–764.

[58] Chang, C. C. and Zhou, L. (2002). "Neural network emulation of inverse dynamics for a magnetorheological damper." *J. Structural Engineering, ASCE*, 128(2), 231–239.

[59] Chang, K. C., Chen, S., Hsu, C., Chou, F., and Lai, M. (1994). "Inelastic seismic behavior of three storey steel frame with added viscoelastic damper." *Proceedings* 1^{st} *World Conference on Structural Control, LA, Univ. Southern California, USA*, G. Housner, S. Masri, and A. Chassiakos, eds. 1: WP3–03–WP3–12.

[60] Chang, K. C., Soong, T. T., Oh, S. T., and Lai, M. L. (1992). "Effect of ambient temperature on viscoelastically damped structure." *J. Structural Engineering, ASCE*, 118(7), 1955–1973.

[61] Chang, K. C., Soong, T. T., Oh, S. T., and Lai, M. L. (1995). "Seismic behaviour of steel frame with added viscoelastic dampers." *J. Structural Engineering, ASCE*, 121(10), 1418–1426.

[62] Chang, S. P., Makris, N., Whittaker, A. S., and Thompson, A. C. T. (2002). "Experimental and analytical studies on the performance of hybrid isolation systems." *Earthquake Engineering & Structural Dynamics*, 31, 421–443. DOI: 10.1002/eqe.117.

[63] Chao, C. T. and Teng, C. C. (1997). "A PD-like self-tuning fuzzy controller without steady-state error." *Fuzzy Sets and Systems*, 87, 141–154.

[64] Chen, S. D., Chen, P. Y., and Wang, Y. M. (2006). "A flexible genetic algorithm chip.

[65] Chipperfield, A., Fleming, P., Pohlheim, H., and Fonseca, C. (2006). "Genetic Algorithm Tool-Box: For use with MATLAB, Ver-1.2." *Automatic Control Systems Engineering, University of Sheffield*, downloaded 2006.

[66] Choi, S. B., Lee, S. K., and Park, Y. P. (2001). "A hysteresis model for the field-dependent damping force of a magnetorheological damper." *J. Sound and Vibration*, 245(2), 375–383.

[67] Chopra, A. K. (2005). *Dynamics of Structures: Theory and Application to Earthquake Engineering*. Pearson Education.

[68] Christenson, R. E. and Spencer, B. F. J. (1999). "Coupled building control using "Smart" dampers." *Proceedings of* 13^{th} *ASCE Engineering Mechanics Conference, Baltimore, Maryland, USA*.

[69] Christenson, R. E., Spencer, B. F. J., and Johnson, E. A. (1999). "Coupled building control using active and smart damping strategies." Vol. 31. 187–195.

[70] Christenson, R. E., Spencer, B. F. J., and Johnson, E. A. (2001). "Experimental verification of semi-active damping of stay cables." *Proceedings of American Control Conference, Arlington, VA*. 5058–5063.

[71] Christenson, R. E., Spencer, B. F. J., and Johnson, E. A. (2002). "Studies on the smart damping of stay cables." *ASCE Structures Congress, Denver, Colorado*.

[72] Christenson, R. E., Spencer, B. F. J., Johnson, E. A., and Seto, K. (2000). "Coupled building control using "Smart" damping strategies." *Smart Systems for Bridges, Structures, and Highways, the* 7^{th} *SPIE Annual International Smart Structures and NDE Symposium, Newport Beach, CA*.

[73] Christofides, P. (2001). *Nonlinear and Robust Control of PDE Systems - Methods and Applications to Transport-Reaction Processes*. Birkhauser, Boston.

[74] Clark, A. J. (1999). "Multiple passive tuned mass damper for reducing earthquake induced building motion." *Proceedings of* 9^{th} *World Conference on Earthquake Engineering, Tokyo, Japan*. 5:779–784.

[75] Clark, P., Aiken, I., Tajirian, F., Kasai, K., Ko, E., and Kimura, I. (1999). "Design procedures for buildings incorporating hysteretic damping devices." *Proceedings of International Post-SmiRT Conference Seminar on Seismic Isolation, Passive Energy Dissipation and Active Control of Vibrations of Structures, Cheju, South Korea*. 1:317–337.

[76] Clough, R. W. and Penzien., J. (1993). *Dynamics of Structures*. Mc Graw-Hill.

[77] Colajanni, P. and Papia, M. (1997). "Hysteretic characterization of friction-damped braced frames." *J. Structural Engineering, ASCE*, 123, 1020–1028.

[78] Constantinou, M., Symans, M., Tsopelas, P., and Taylor, D. (1993). "Fluid viscous dampers in applications of seismic energy dissipation and seismic isolation." *Proceedings of ATC:*17 − 1 *Seminar on Seismic Isolation, Passive Energy Dissipation, and Active Control, San Francisco, California*. 2:581–591.

[79] Constantinou, M. C., Soong, T. T., and Dargush, G. F. (1998). *Passive energy dissipation systems for structural design and retrofit*. Monograph No. 1, Multidisciplinary Center for Earthquake Engineering Research, State Univ. of New York, Buffalo, NY.

[80] Constantinou, M. C. and Symans, M. D. (1992). *Experimental and analytical investigation of seismic response of structures with supplemental fluid viscous dampers*. Report No. NCEER-92-0032, National Center for Earthquake Engineering Research, Buffalo, NY.

[81] Constantinou, M. C. and Symans, M. D. (1993). "Experimental study of seismic response of buildings with supplemental fluid dampers." *Earthquake Engineering & Structural Dynamics*, 2, 93–132.

[82] Crosby, P., Kelly, J. M., and Singh, J. (1994). "Utilizing viscoelastic dampers in the seismic retrofit of a thirteen story steel frame building." *Structures Congress XII, Atlanta, GA*. 1286–1291.

[83] Dai, S. H. and Wang, M. O. (1982). *Reliability Analysis in Engineering Application*. Van Nostrand Reinhold, New York.

[84] Dargush, G. F. and Soong, T. (1995). "Behavior of metallic plate dampers in seismic passive energy dissipation system." *Earthquake Spectra*.

[85] Den-Hartog, J. P. (1947). *Mechanical Vibrations*. New York:McGraw-Hill, Inc.

[86] DeStefano, A., Sabia, D., and Sabia, L. (1999). "Probabilistic neural networks for seismic damage mechanism prediction." *Earthquake Engineering & Structural Dynamics*, 28, 807–821.

[87] DEWEsoft (2007). *Software to measure, process, analyze and store data, Release* 6. DEWETRON Ges.m.b.H., Austria, URL: http://www.dewesoft.org/index.php.

[88] DEWETRON (2007). *DEWE* 4011 *with DEWE* $30-16$ *module*. DEWETRON Ges.m.b.H., Austria, URL: http://www.dewetron.com/en/.

[89] Dodwell, D. and Cherry, S. (1994). "Structural control using semi-active friction damper." *Proceedings of* 1^{st} *World Conference on Structuctural Control, LA, Univ. Southern California, USA*. FA1:59–68.

[90] Dominguez, A., Sedaghati, R., and Stiharu, I. (2004). "Modelling the hysteresis phenomenon of magnetorheological dampers." *Smart Materials & Structures*, 13, 1351–1361.

[91] Dominguez, A., Sedaghati, R., and Stiharu, I. (2006). "A new dynamic hysteresis model for magnetorheological dampers." *Smart Materials & Structures*, 15, 1179–1189.

[92] Dounis, A., Tiropanisy, P., Syrcos, G., and Tseles, D. (2007). "Evolutionary fuzzy logic control of base-isolated structures in response to earthquake activity." *J. Structural Control & Health monitoring*, 14, 62–82.

[93] Driankov, D., Hellendoorn, H., and Reinfrank, M. (1992). *An Introduction to Fuzzy Control*. Narosa Publishing House, Kolkata.

[94] dSPACE (2005). *Release* 5, *Hardware Card No.*-11229. dSPACE GmbH, Germany, URL: http://www.dspace.com.

[95] Dyke, S. J. (1998). "Seismic protection of a benchmark building using magnetorheological dampers." *Proceedings of* 2^{nd} *World Conference on Structural Control, Kyoto, Japan*.

[96] Dyke, S. J., Caicedo, J. M., Turan, G., Bergman, L. A., and Hague, S. (2003). "Phase I: Benchmark control problem for seismic response of cable-stayed bridges." *J. Structural Engineering, ASCE*, 129(7), 857–872.

[97] Dyke, S. J. and Spencer, B. F. J. (1997). "A comparison of semi–active control strategies for the MR damper." *Proceedings of the IASTED International Conference, Intelligent Information Systems, The Bahamas*.

[98] Dyke, S. J., Spencer, B. F. J., Quast, P., Sain, M. K., Kaspari, D. C. J., and Soong, T. T. (1995). "Acceleration feedback control of mdof structures." *J. Engineering Mechanics, ASCE.*, 122(9), 907–918.

[99] Dyke, S. J., Spencer, B. F. J., Sain, M. K., and Carlson, J. D. (1996a). "Modeling and control of magnetorheological dampers for seismic response reduction." *Smart Materials & Structures*, 5, 565–575.

[100] Dyke, S. J., Spencer, B. F. J., Sain, M. K., and Carlson, J. D. (1996b). "Seismic response reduction using magnetorheological dampers." *Proceedings* 13^{th} *IFAC World Congress, San Francisco*. L:145–150.

[101] Dyke, S. J., Spencer, B. F. J., Sain, M. K., and Carlson, J. D. (1998). "An experimental study of MR dampers for seismic protection." *Smart Materials & Structures*, 7, 693–703.

[102] Eberhart, R. C. and Shi, Y. (2000). "Comparing inertia weights and constriction factors in particle swarm optimization." *Proceedings of the Congress on Evolutionary Computing, CA, USA*. 84–88.

[103] EERI (1999). *Lessons Learnt Over Time Learning from Earthquakes Series: Volume II Innovative Recovery in India*. Earthquake Engineering Research Institute, Oakland (CA), USA (available at www.nicee.org/readings/EERI-Report.htm).

[104] Ehrgott, R. and Masri, S. (1992). "Modeling the oscillatory dynamic behavior of electrorheological materials in shear." *Smart Materials & Structures*, 1, 275–285.

[105] Encyclopedia, W. H. (2008). *An Encyclopedia of Housing Construction in Seismically Active Areas of the World*. URL: http://www.world-housing.net/whereport1view.php?id=100037, downloaded: 22^{th} July.

[106] Erdik, M. and Durukal, E. (2001). "A hybrid procedure for the assessment of design basis earthquake ground motions for near-fault conditions." *Soil Dynamics & Earthquake Engineering*, 21(5), 431–443.

[107] Erkus, B. and Johnson, E. A. (2006). "Smart base isolated benchmark building part III: A sample controllers for bilinear isolation." *J. Structural Control and Health monitoring*, 13(2–3), 605–625.

[108] Ewins, D. J. (2000). *Modal Testing: Theory, Practice and Application, Second Edition*. Research Studies Press LTD., Baldock, Hertfordshire, England.

[109] Faravelli, L. and Yao, T. (1996). "Use of adaptive networks in fuzzy control of Civil structures." *Microcomputers in Civil Engineering*, 11, 67–76.

[110] Faravelli, L. and Yao, T. (1997). "Elements of fuzzy structural control." *Uncertainty Modeling in Vibration and Fuzzy Analysis of Structural Systems*, B. M. Ayyub, A. Guran, and A. Haldar, eds., World Scientific, Singapore, Singapore, 147–165.

[111] Feng, Q. and Shinozuka, M. (1990). "Use of a variable damper for hybrid control of bridge response under earthquake." *Proceedings of U.S. National Workshop on Structural Control Research, Univ. of Southern California, Los Angelos*. 107–112.

[112] Feng, Q., Shinozuka, M., and Fujii, S. (1993). "Friction-controllable sliding isolated systems." *J. Engineering Mechanics, ASCE*, 119(9), 1845–1864.

[113] Ferry, J. D. (1980). *Viscoelastic properties of polymers*. New York:John Wiley.

[114] Field, R. V. J., Bergman, L. A., and Hall, W. B. (1995). "Computational of probabilistic stability measures for a controlled distributed parameter system." *Probabilistic Engineering Mechanics*, 10, 181–189.

[115] Field, R. V. J., Voulgaris, P. G., and Bergman, L. A. (1996). "Probabilistic stability robustness of structural system." *J. Engineering Mechanics, ASCE*, 122(10), 1012–1021.

[116] Filiatrault, A. and Cherry, S. (1990). "Seismic design spectra for friction-damped structures." *J. Structural Engineering, ASCE*, 116, 1334–1355.

[117] Filiatrault, A., Tremblay, R., and Kar, R. (2000). "Performance evaluation of friction spring seismic damper." *J. Structural Engineering, ASCE*, 126, 491–499.

[118] FitzGerald, T. F., Anagnos, T., Goodson, M., and Zsutty, T. (1989). "Slotted bolted connection in aseismic design for concentrically braced connections." *Earthquake Spectra*, 5, 383–391.

[119] Friswell, M. I., Garvey, S. D., and Penny, J. E. T. (1995). "Model reduction using dynamic and iterated IRS techniques." *J. Sound and Vibration*, 186(2), 311–323.

[120] Friswell, M. I., Garvey, S. D., and Penny, J. E. T. (1998). "The convergence of the iterated IRS method." *J. Sound and Vibration*, 211(1), 3123–132.

[121] Friswell, M. I. and Mottershead, J. E. (1995). *Finite element model updating in structural dynamics*. Kluwer Academic, The Netherlands.

[122] Friswell, M. I., Penny, J. E. T., and Garvey, S. D. (1998). "A combined genetic and eigen sensitivity algorithm for the location of damage in structures." *Computers and Structures*, 69, 547–556.

[123] Fujino, Y., Sun, L. M., Pacheco, B. M., and Chaiseri, P. (1992). "Tuned liquid damper (TLD) for suppressing horizontal motions of structures." *J. Engineering Mechanics, ASCE*, 118, 2017–2030.

[124] Fujino, Y. and Susumpow, T. (1994). "An experimental study on active control of in plane cable vibration by axial support motion." *Earthquake Engineering & Structural Dynamics*, 23, 1283–1297.

[125] Fujita, T. (1980). *Seismic isolation and response control for nuclear and non-nuclear structures*. Special Issue for the Exhibition of 11^{th} International Conference on SMiRT, Tokyo, Japan.

[126] Fujita, T., Shimazaki, M., Hayamizu, Y., Aizawa, S., Higashino, M., and Haniuda, N. (1994). "Semi-active seismic isolation system using controllable friction damper." *Bulletins ERS*, 27, 21–31.

[127] Gamoto, D. and Filisko, F. (1991). "Dynamic mechanical studies of electrorheological materials: moderate frequencies." *J. Rheology*, 35(3), 399–425.

[128] Gavin, H., Hanson, R. D., and Filisko, F. (1996a). "Electrorheological dampers, part 1: Analysis and design." *J. Applied Mechanics, ASME*, 63, 669–675.

[129] Gavin, H., Hanson, R. D., and Filisko, F. (1996b). "Electrorheological dampers, part 2: Testing and modeling." *J. Applied Mechanics, ASME*, 63, 676–682.

[130] Ghaboussi, J. and Joghataie, A. (1995). "Active control of structures using neural networks." *J. Engineering Mechanics, ASCE*, 121(4), 555–567.

[131] Goh, J. C. and Caughey, T. K. (1985). "On the stability problem caused by finite actuator dynamics in the colocated control of large space structures." *International J. Control*, 41(3), 803–811.

[132] Grigorian, C. E., Yang, T. S., and Popov, E. P. (1993). "Slotted bolted connection energy dissipator." *Earthquake Spectra*, 9(3), 491–504.

[133] Guyan, R. J. (1965). "Reduction of stiffness and mass matrices." *AIAA Journal*, 3, 380.

[134] Guzelkaya, M., Eksin, I., and Yesil, E. (2003). "Self-tuning of PID-type fuzzy logic controller coefficients via relative rate observer." *Engineering Applications of Artificial Intelligence*, 16, 227–236.

[135] Hailin, J. and Dongming, J. (2001). "Self-adaptation of fuzzy controller optimized by hardware-based GA." *Proceedings of* 6^{th} *IEEE International Conference on Solid-State and Integrated-Circuit Technology, Shanghai*, Vol. 2. 1147–1150.

[136] Hall, J. F., Heaton, T. H., Halling, M. W., and Wald, D. J. (1995). "Near source ground motion and its effects on flexible buildings." *Earthquake Spectra*, 11(4), 569–605.

[137] Haroun, M., Pires, J., and Won, A. (1994). "Active orifice control in hybrid liquid column dampers." *Proceedings of* 1^{st} *World Conference on Structural Control, LA, Univ. Southern California, USA*. FA1:69–78.

[138] Haupt, R. L. and Haupt, S. E. (2004). *Practical Genetic Algorithm* 2^{nd} *Edition*. Wiley Interscience.

[139] He, W. L. and Agrawal, A. K. (2005). "An analytical model for ground motion pulses during near-field earthquakes for the design of smart protective systems." *J. Structural Engineering, ASCE*, 13(2-3), 792–808.

[140] He, W. L. and Agrawal, A. K. (2007). "Passive and hybrid control systems for seismic protection of a benchmark cable-stayed bridge." *Structural Control & Health Monitoring*, 14(13), 1–14.

[141] Heaton, T., Hall, J. F., Halling, M., and Wald, D. (1995). "Response of high-rise and base-isolated buildings in a hypothetical Mw 7.0 blind thrust earthquake." *Science*, 267, 206–211.

[142] Helton, J. W. and Merino, O. (1998). *Classical Control using H_∞ Methods: Theory, Optimization and Design*. SIAM, Philadelphia.

[143] Higgins, C. and Kasai, K. (1998). "Experimental and analytical simulation of wind response for a full-scale VE-damped steel frame." *J. Wind Engineering and Industrial Aerodynamics*, 77, 297–313.

[144] Hikami, Y. and Shiraishi, N. (1987). "Rain induced vibration of cables in cable-stayed bridges." *J. Wind Engineering and Industrial Aerodynamics*, 29, 471–478.

[145] Housner, G., Soong, T., and Masri, S. (1994). "Second generation of active structural control in Civil Engineering." *Proceedings of the 1^{st} World Conference on Structural Control, LA, Univ. of Southern California*, G. Housner, S. Masri, and A. Chassiakos, eds. TP3–117–TP3–126.

[146] Housner, G. W., Bergman, L. A., Caughey, T. K., Chassiakos, A. G., Masri, S. F., Skelton, R. E., Soong, T. T., Spencer, B. F. J., and Yao, J. T. P. (1997). "Structural control: Past, present and future." *J. Engineering Mechanics, ASCE*, 123(9), 897–970.

[147] Housner, G. W. and Jennings, P. C. (1964). "Generation of artificial earthquakes." *J. Engineering Mechanics Division, ASCE*, 97, 113–150.

[148] Hung, S., Kao, C., and Lee, J. (2000). "Active pulse structural control using artificial neural networks." *J. Engineering Mechanics, ASCE*, 126, 839–849.

[149] Hung, S. L. and Lai, C. M. (2001). "Unsupervised fuzzy neural network structural active pulse controller." *Earthquake Engineering & Structural Dynamics*, 30, 465–484.

[150] Hussain, S. and Satari, M. A. (2007). "Design of a seismic isolation system with supplemental viscous damping for a near-fault essential services facility." *Structural Engineers World Congress, Bangalore, India*. CD ROM.

[151] Inaudi, J. A. (1997). "Modulated homogeneous friction: a semi-active damping strategy." *Earthquake Engineering & Structural Dynamics*, 26, 361–376.

[152] Inaudi, J. A. and Kelly, J. M. (1993). "Hybrid isolation systems for equipment protection." *Earthquake Engineering & Structural Dynamics*, 22, 297–313.

[153] IOtech (2006). *Portable data acquisition solution*. IOtech Cleveland, Ohio, URL: http://www.iotech.com/index.html.

[154] Irvine, H. M. (1981). *Cable Structures*. Cambridge, Massachusetts MIT Press.

[155] Isidori, A. (1995). *Nonlinear Control Systems (Communications and Control Engineering)*. Springer Verlag, Berlin.

[156] Ito, D., Ward, D., and Valasek, J. (2001). "Robust dynamic inversion controller design and analysis for the X-38." *AIAA Guidance, Navigation, and Control Conference & Exhibition, Montreal, Canada*.

[157] Ito, K. and Ravindran, S. S. (2000). "A reduced basis method for control problems governed by partial differential equations." *International Series of Numerical Mathematics*, F. Kappel and K. Kunssch, eds., Vol. 126, Birkhauser, Basel, 153–168.

[158] Iyenger, R. N. and Iyenger, K. T. S. (1969). "Non-stationary random process model for earthquake accelerograms." *Bulletins Seismological Society of America*, 59, 1163–1188.

[159] Jabbari, F., Schmitendorf, W., and Yang, J. (1995). "Control for seismic excited buildings with acceleration feedback." *J. Engineering Mechanics, ASCE*, 21, 994–1002.

[160] Jang, J. S. R. (1993). "ANFIS: Adaptive Network Based Fuzzy Inference System." *IEEE Transactions on System, Man and Cybernetics*, 23(3), 665–685.

[161] Jang, J. S. R. (1996). "Input selection for ANFIS learning." *Proceedings of* 5^{th} *IEEE International Conference on Fuzzy Systems, New Orleans*. 2:1493–1499.

[162] Jang, J. S. R., Sun, C. T., and Mizutani, E. (2005). *Neuro Fuzzy and Soft Computing*. Pearson Education: India.

[163] Jangid, R. and Dutta, T. (1997). "Performance of multiple tuned mass dampers for torsionally coupled systems." *Earthquake Engineering & Structural Dynamics*, 26, 307–317.

[164] Jangid, R. S. (1999). "Optimum multiple tuned mass dampers for base-excited undamped system." *Earthquake Engineering & Structural Dynamics*, 28, 1041–1048.

[165] Jansen, L. M. and Dyke, S. J. (1999). "Investigation of nonlinear control strategies for the implementation of multiple magnetorheological dampers." 1999 *ASCE Engineering Mechanics Conference, Baltimore, Maryland*.

[166] Jansen, L. M. and Dyke, S. J. (2000). "Semiactive control strategies for MR dampers: comparative study." *J. Engineering Mechanics, ASCE*, 126(8), 795–803.

[167] Johnson, E. A., Baker, G. A., Spencer, B. F., and Fujino, Y. (2000). "Mitigating stay cable oscillation using semi-active damping." *Smart Structures and Materials* 2000*: Smart Systems for Bridges, Structures, and Highways, SPIE Vol.* 3988, S. C. Liu, ed. 207–216.

[168] Johnson, E. A., Baker, G. A., Spencer, B. F. J., and Fujino, Y. (2007). "Semi-active damping of stay cables." *J. Engineering Mechanics, ASCE*, 133(1), 1–11.

[169] Johnson, E. A., Christenson, R. E., and Spencer, B. F. J. (2003). "Semi-active damping of cables with sag." *Computer Aided Civil and Infrastructure Engineering*, 18(2), 132–146.

[170] Johnson, E. A., Ramallo, J. C., Spencer, B. F., and Sain, M. K. (1998). "Intelligent base isolation systems." *Proceedings of* 2^{nd} *World Conference Structural Control, Kyoto, Japan*. 367–376.

[171] Johnson, E. A., Voulgaris, P. G., and Bergman, L. A. (1998). "Multiobjective optimal structural control of the Notre Dame building model benchmark." *Earthquake Engineering & Structural Dynamics*, 27(11), 1165–1187.

[172] Juang, J. N., Sae-Ung, S., and Yang, J. N. (1980). "Active control of large building structures." *Structural Control*, H. H. E. Leipholz, ed., North Holland, Amsterdam, 663–676.

[173] Jung, H. J., Choi, K. M., Spencer, B. F. J., and Lee, I. W. (2005). "Application of some semi-active control algorithms to a smart base-isolated building employing MR dampers." *Structural Control & Health Monitoring*, 13, 693–704.

[174] Jung, H. J., Spencer, B. F. J., Ni, Y. Q., and Lee, I. W. (2004). "State-of-the-art of semi-active control systems using MR fluid dampers in Civil engineering applications." *Structural Engineering and Mechanics*, 17(3–4), 493–526.

[175] Kamath, G. M., Hurt, H. K., and Wereley, N. M. (1996). "Analysis and testing of bingham plastic behavior in semi-active electrorheological fluid dampers." *Smart Material & Structures*, 5, 576–590.

[176] Kamath, G. M. and Wereley, N. M. (1996). "A nonlinear viscoelastic-plastic model for electrorheological fluids." *Smart Material & Structures*, 6, 351–359.

[177] Kamath, G. M. and Wereley, N. M. (1997). "Nonlinear viscoelastic-plastic mechanisms based model of an electrorheological damper." *J. Guidance, Control, and Dynamics*, 20(6), 1125–1132.

[178] Karnopp, D., Crosby, M., and Harwood, R. (1974). "Vibration control using semi-active force generators." *J. Engineering for Industry*, 96(2), 619–626.

[179] Kawashima, K. and Unjoh, S. (1994). "Seismic response control of bridges by variable dampers." *J. Structural Engineering*, 120(9), 2583–2601.

[180] Kawashima, K., Unjoh, S., and Shimizu, K. (1992). "Experiments on dynamics characteristics of variable damper." *Proceedings of Japan National Symposium on Structural Response Control, Tokyo, Japan*.

[181] Kelly, J. M. (1986). "Aseismic base isolation: review and bibliography." *Soil Dynamics & Earthquake Engineering*, 5(3), 202–216.

[182] Kelly, J. M. (1999). "The role of damping in seismic isolation." *Earthquake Engineering & Structural Dynamics*, 28, 3–20.

[183] Kelly, J. M., Lietmann, G., and Soldatos, A. G. (1987). "Robust control of base isolated structures under earthquake excitation." *J. Optimization Theory and Applications*, 53, 159–180.

[184] Kennedy, J. and Eberhart, R. (1995). "Particle swarm optimization." *Proceedings of IEEE International Conference on Neural Networks, Perth, Australia*. 1942–1948.

[185] Kim, H. S. and Roschke, P. N. (2006a). "Design of fuzzy logic controller for smart base isolation system using genetic algorithm." *Engineering Structures*, 28, 84–96.

[186] Kim, H. S. and Roschke, P. N. (2006b). "Fuzzy control of base-isolation system using multi-objective genetic algorithm." *Computer Aided Civil and Infrastructure Engineering*, 21, 436–449.

[187] Kim, H. S., Roschke, P. N., Lin, P. Y., and Loh, C. H. (2006). "Neuro-fuzzy model of hybrid semi-active base isolation system with FPS bearings and an MR damper." *Engineering Structures*, 28, 947–958.

[188] King, R. E. (1999). *Computational Intelligence in Control Engineering*. Marcel Dekker Inc.

[189] Kobori, T., Takahashi, M., Nasu, T., Niwa, N., and Ogasawara, K. (1993). "Seismic response controlled structure with active variable stiffness system." *Earthquake Engineering & Structural Dynamics*, 22, 925–941.

[190] Koike, Y., Murata, T., Tanida, K., Ishii, T. K. K., and Takenaka, Y. (1994). "Development of V-shaped hybrid mass damper and its application to high-rise buildings." *Proceedings of* 1^{st} *World Conference Structural Control, LA, Univ. of Southern California*. FA2:3–12.

[191] Koshimura, K., Tatsumi, M., and Hata, K. (1994). "Vibration control of the main towers of the Akashi Kaikyo bridge." *Proceedings of* 1^{st} *World Conference Structural Control, LA, Univ. of Southern California*. TP3:98–106.

[192] Krishnakumar, K. (1989). "Microgenetic algorithms for stationary and non-stationary function optimization." *Proceedings of SPIE Intelligent Control and Adaptive Systems*, G. Rodriguez, ed., Vol. 1196. 289–296.

[193] Krstic, M., Kanellakopoulos, I., and Kokotovic, P. (1995). *Nonlinear and Adaptive Control Design*. John Willey & Sons, New York, NY.

[194] Krstic, M. and Smyshlyaev, A. (2007). "Backstepping boundary control-a tutorial." *Proceedings of the American Control Conference, New York City, NY*. 870–875.

[195] Kuo, B. C. (1995). *Automatic Control system,* 7^{th} *edition*. Prentice Hall, Englewood Cliffs, New Jersey.

[196] Kurata, N., Kobori, T., Takahashi, M., Ishibashi, T., Niwa, N., Tagami, J., and Midorikawa, H. (2000). "Forced vibration test of a building with semi-active damper system." *Earthquake Engineering & Structural Dynamics*, 29, 629–645.

[197] Kurata, N., Kobori, T., Takahashi, M., Niwa, N., and Midorikawa, H. (1999). "Actual seismic response controlled building with semi-active damper system." *Earthquake Engineering & Structural Dynamics*, 28, 1427–1447.

[198] Kwok, K. C. S. and Denoon, R. O. (2000). "Vibration control of wind-excited buildings and structures." *Proceedings of Advances in Structural Dynamics, Southampton, England*. 1:151–158.

[199] Kwon, K. S. and Lin, R. M. (2005a). "Robust damage location in structures using Taguchi method." *J. Structural Engineering*, 131(4), 629–642.

[200] Kwon, K. S. and Lin, R. M. (2005b). "Robust finite element model updating using Taguchi method." *J. Sound and Vibration*, 280(1–2), 63–76.

[201] Lasiecka, I. (1995). "Control of systems governed by partial differential equations: A historical perspective." *Proceedings of IEEE Conference on Decision and control, New Orleans, LA*. 2792–2796.

[202] Lee, H. J., Yang, G., Jung, H. J., Spencer, B. F. J., and Lee, I. W. (2005). "Semi-active neuro control of a base-isolated benchmark structure." *Structural Control & Health Monitoring*, 13, 682–692.

[203] Leipholz, H. H. E. and Abdel-Rohman, M. (1986). *Control of Structures*. Martinus Nijhoff Publishers, Dordrecht, The Netherlands.

[204] Leitmann, G. (1994). "Semi-active control for vibration attenuation." *J. Intelligent Material Systems and Structures*, 5, 841–846.

[205] Leva, A. and Piroddi, L. (2002). "NARX-based technique for the modelling of magneto-rheological damping devices." *Smart Materials & Structures*, 11, 79–88.

[206] Levy, R., Marianchik, E., Rutenberg, A., and Segal, F. (2000). "Seismic design methodology for friction damped braced frames." *Earthquake Engineering & Structural Dynamics*, 29, 1569–1585.

[207] Li, C. and Fadali, M. (2000). "Performance of multiple tuned mass dampers for attenuating undesirable oscillations of structures under the ground acceleration." *Earthquake Engineering & Structural Dynamics*, 29, 1405–1421.

[208] Li, C. and Reinhorn, A. M. (1995). *Experimental and analytical investigation of seismic retrofit of structures with supplemental damping: part 2-friction devices*. NCEER Report No. 95-0009, State University of New York at Buffalo, Buffalo, NY.

[209] Li, H. X. and Gatland, H. B. (1996). "Conventional fuzzy control and its enhancement." *IEEE Transactions on Systems, Man, and Cybernetics - Part B: Cybernetics*, 26(5), 791–797.

[210] Li, W. H., Yao, G. Z., Chen, G., Yeo, S. H., and Yap, F. F. (2000). "Testing and steady state modeling of a linear MR damper under sinusoidal loading." *Smart Materials & Structures*, 9, 95–102.

[211] Lin, C. C., Ueng, J. M., and Huang, T. C. (2000). "Seismic response reduction of irregular buildings using passive tuned mass dampers." *Engineering Structures*, 22(5), 513–524.

[212] Liu, D. A., Matheu, E. E., Singh, M. P., and Mook, D. T. (1999). "Neural-network control of building structures by a force-matching training scheme." *Earthquake Engineering & Structural Dynamics*, 28, 1601–1620.

[213] Liu, S. C. and Jhaveri, D. P. (1969). "Spectral simulation and earthquake site propoerties." *J. Engineering Mechanics Division, ASCE*, 95(EM5), 1145–1168.

[214] LORD Corporation (July, 2008). *MR Solutions: The Commercial Leader in MR Technology*. http://www.lord.com/Home/MagnetoRheologicalMRFluid/tabid/3317/Default.aspx.

[215] Lou, J. Y. K., Lutes, L. D., and Li, J. J. (1994). "Active tuned liquid damper for structural control." *Proceedings of* 1^{st} *World Conference Structural Control, LA, Univ. of Southern California*, G. W. Housner, S. F. Masri, and A. G. Chassiakos, eds. TP1:70–79.

[216] Madden, G. J., Symans, M. D., and Wongprasert, N. (2002). "Experimental verification of seismic response of building frame with adaptive sliding base-isolation system." *J. Structural Engineering, ASCE*, 128(4), 1037–1045.

[217] Madden, G. J., Wongprasert, N., and Symans, M. D. (2003). "Analytical and numerical study of a smart sliding isolation system for seismic protection of buildings." *Computer Aided Civil and Infrastructure Engineering*, 18, 19–30.

[218] Madsen, H. O., Krenk, S., and Lind, N. C. (1986). *Methods of Structural Safety*. Prentice Hall Inc., Englewood Cliff, NJ.

[219] Magana, M. E. and Rodellar, J. (1998). "Active nonlinear robust control of cable stayed bridges in the presence of strong vertical ground motion due to earthquakes." *Proceedings of* 2^{nd} *World Conference on Structural Control, Kyoto, Japan*. 3:1947–1956.

[220] Mahmoodi, P., Robertson, L. E., Yontar, M., Moy, C., and Feld, I. (1987). "Performance of viscoelastic dampers in World Trade Center towers." *Dynamic of Structures, Structures Congress, Orlando, FL*.

[221] Makris, N. (1991). "Fractional derivative model for viscous damper." *J. Structural Engineering, ASCE*, 117, 2708–2724.

[222] Makris, N. (1997). "Rigidity-plasticity-viscosity: can electrorheological dampers protect base-isolated structures from near-source ground motions?." *Earthquake Engineering & Structural Dynamics*, 26, 571–591.

[223] Makris, N., Burton, S. A., Hill, D., and Jordan, M. (1996). "Analysis and design of ER damper for seismic protection of structures." *J. Engineering Mechanics, ASCE*, 122, 1003–1011.

[224] Makris, N. and Chang, S. P. (2000). "Effect of viscous, viscoplastic, and friction damping in the response of seismically isolated structures." *Earthquake Engineering & Structural Dynamics*, 29, 85–107.

[225] Makris, N. and Dargush, G. (1994). "Generalized boundary element formulation for dynamic analysis of viscoelastic system." *Proceedings of* 1^{st} *World Conference on Structural Control, LA, Univ. of Southern California*, G. W. Housner, S. F. Masri, and A. G. Chassiakos, eds. FP1:73–81.

[226] Mamadani, E. H. (1974). "Application of fuzzy logic algorithms for control of simple dynamic plant." *Proceedings of the Institute of Electrical Engineers*, 29, 1585–1588.

[227] Marquez, H. J. (2003.). *Nonlinear Control Systems Analysis and Design*. Wiley Interscience.

[228] Martinez-Romero, E. (1993). "Experiences on the use of supplemental energy dissipators on building structures." *Earthquake Spectra*, 9, 581–625.

[229] Masri, S. F., Bekey, G. A., and Caughey, T. K. (1982). "On-line control of nonlinear flexible structures." *J. Applied Mechanics, ASME*, 49, 877–884.

[230] MATLAB (2004). *The software for Numerical Computing, Version* 7.0.1 *(R*14*)*. The MathWorks, URL: http://www.mathworks.com/index.html?ref=pt.

[231] Mavroeidis, G. P. and Papageorgiou, A. S. (2003). "A mathematical representation of near-fault ground motions." *Bulletin of the Seismological Society of America*, 93(3), 1099–1131.

[232] Mayes, R. L., Sveinsson, B. I., and Buckle, I. G. (1988). "Analysis, design and testing of the isolation system for the Salt Lake City and County Building." *Proceedings of International Seismic Isolation / Historic Preservation Symposium, Salt Lake City, UT*.

[233] McClamroch, N. H. and Gavin, H. P. (1995). "Closed loop structural control using electrorheological dampers." *Proceedings of American Control Conference, Seattle, Washington*. 4173–4177.

[234] Medeot, R. (2007). "Seismic isolation in europe." *Structural Engineers World Congress, Bangalore, India*. CD ROM.

[235] Meirovitch, L. (1990). *Dynamics and Control of Structure*. New York: Wiley.

[236] MEscope (2003). *ME'scope Visual SDM Pro, Version 4.0.0.6*. Vibrant Technologies, Scotts Valley, CA, URL: http://www.vibetech.com.

[237] Milne, J. (1886). "On construction in earthquake countries." *Minutes of proceedings of the institute of Civil Engineers, London*, 83, 278–291.

[238] Miyazaki, M. and Mitsusaka, Y. (1992). "Design of a building with 20% or greater damping." *Proceedings of* 10^{th} *World Conference on Earthquake Engineering, Madrid*. 4143–4148.

[239] Mottershead, J. E. and Friswell, M. I. (1993). "Model updating in structural dynamics: a survey." *J. Sound and Vibration*, 167(2), 347–375.

[240] MR Dampers (downloaded: July, 2006). *LORD Technical Data: RD*-1005 *Damper*. http://www.lordfulfillment.com/upload/DS7017.pdf.

[241] Mualla, I. H. and Belev, B. (2002). "Performance of steel frames with a new friction damper device under earthquake excitation." *Engineering Structures*, 24(3), 365–371.

[242] Nadathur, V. and Nagarajaiah, S. (2004). "Wind response control of building with variable stiffness tuned mass damper using empirical mode decomposition and Hilbert transform." *J. Engineering Mechanics, ASCE*, 130(4), 451–458.

[243] Naeim, F. and Kelly, J. M. (1999). *Design of Seismic Isolated Structures: From theory to practice*. John Wiley & Sons.

[244] Nagarajaiah, S. (1994). "Fuzzy controller for structures with hybrid isolation systems." *Proceedings of 1^{st} World Conference on Structural Control, Los Angeles, Univ. of Southern California*, G. W. Housner, S. F. Masri, and A. G. Chassiakos, eds. TA2–67–TA2–76.

[245] Nagarajaiah, S., Mao, Y. Q., and Sahasrabudhe, S. (2006). "Nonlinear seismic response spectra of smart sliding isolated structures with independently variable MR dampers and variables stiffness SAIVS system." *J. Structural Engineering and Mechanics*, 24(3), 375–393.

[246] Nagarajaiah, S. and Mate, D. (1998). "Semi-active control of continuously variable stiffness system." *Proceedings of 2^{nd} World Conference on Structural Control, Kyoto, Japan*. 1:397–405.

[247] Nagarajaiah, S. and Nadathur, V. (2005). "Semi-active control of wind excited building with variable stiffness TMD using short time fourier transform." *Engineering Structures*, 27, 431–441.

[248] Nagarajaiah, S. and Narasimhan, S. (2006). "Smart base isolated benchmark building part II: Phase I sample controllers for linear isolation system." *J. Structural Control & Health monitoring*, 13(2–3), 589–604.

[249] Nagarajaiah, S. and Narasimhan, S. (2007). "Seismic control of smart base isolated buildings with new semi-active variable damper." *Earthquake Engineering & Structural Dynamics*, 36(6), 729–749.

[250] Nagarajaiah, S., Narasimhan, S., Agrawal, A., and Tan, P. (2006). "Semiactive Lyapunov controller for phase II seismic isolated highway bridge benchmark." *http://www-ce.engr.ccny.cuny.edu/People/Agrawal/Highway%20Benchmark%20Problem.htm*, (downloaded: Jan 2006).

[251] Nagarajaiah, S., Narasimhan, S., and Johnson, E. (2008). "Structural control benchmark problem: Phase II nonlinear smart base isolated building subjected to near fault ground motions, Editorial." *J. Structural Control & Health Monitoring*, 15(5), 653–656.

[252] Nagarajaiah, S., Narasimhan, S., and Johnson, E. A. (2006). "Phase II smart base isolated benchmark building with nonlinear isolation systems." *Proceedings of* 4^{th} *World Conference on Structural Control and Monitoring, San Diego, California*.

[253] Nagarajaiah, S., Riley, M. A., and Reinhorn, A. (1993). "Control of sliding isolated bridges with absolute acceleration feedback." *J. Engineering Mechanics, ASCE*, 119(11), 2317–2332.

[254] Nagarajaiah, S. and Sahasrabudhe, S. (2006). "Seismic response control of smart sliding isolated buildings using variable stiffness systems: Experimental and numerical study." *Earthquake Engineering & Structural Dynamics*, 35(2), 177–197.

[255] Nagarajaiah, S., Sahasrabudhe, S., and Iyer, R. (2000). "Seismic response of sliding isolated bridges with smart dampers subjected to near source ground motions." *Proceedings of* 14^{th} *Conference on Analysis and Computation held in Conjunction with ASCE Structures Congress, ASCE, Philadelphia*. CD ROM.

[256] Nagarajaiah, S. and Sonmez, E. (2007). "Structures with semi-active variable stiffness single/multiple tuned mass dampers." *J. Structural Engineering, ASCE*, 133(1), 67–77.

[257] Nagarajaiah, S. and Varadarajan, N. (1999). "Novel semi-active variable stiffness tuned mass damper with real time tuning capability." *Proceedings of* 13^{th} *Engineering Mechanics Conference, ASCE, Baltimore, Maryland, USA*. CD ROM.

[258] Narasimhan, S. and Nagarajaiah, S. (2005). "STFT algorithm for semi-active control of base isolated buildings with variable stiffness isolation systems subjected to near fault earthquakes." *Engineering Structures*, 27, 514–523.

[259] Narasimhan, S. and Nagarajaiah, S. (2006). "Smart base isolated buildings with variable friction systems: H_∞ controller and novel SAIVF device." *Earthquake Engineering & Structural Dynamics*, 35(8), 920–942.

[260] Narasimhan, S., Nagarajaiah, S., and Johnson, E. A. (2008). "Smart base isolated benchmark building Part IV: Phase II problem definition and sample controllers for nonlinear isolation systems." *J. Structural Control & Health monitoring*, 13(2–3), 589–604.

[261] Narasimhan, S., Nagarajaiah, S., Johnson, E. A., and Gavin, H. P. (2006). "Smart base isolated benchmark building Part I: Problem definition." *J. Structural Control & Health monitoring*, 13(2–3), 573–588.

[262] Nayfeh, A. H. and Pai, P. F. (2004). *Linear and Nonlinear Structural Mechanics*. Wiley Series in Nonlinear Science, Wiley-Interscience.

[263] Neilsen, E., Lai, M., Soong, T., and Kelly, J. (1994). "Viscoelastic damper overview for seismic and wind applications." *Proceedings of* 1^{st} *World Conference on Structural Control, LA, Univ. Southern California*, G. W. Housner, S. F. Masri, and A. G. Chassiakos, eds. 3:FP3–42–FP3–51.

[264] Ni, Y. Q., Chen, Y., Ko, J. M., and Cao, D. Q. (2002). "Neuro-control of cable vibration using semi-active magneo-rheological dampers." *Engineering Structures*, 24, 295–307.

[265] Nims, D. K., Richter, P. J., and Bachman, R. E. (1993). "The use of the energy dissipating restraint for seismic hazard mitigation." *Earthquake Spectra*, 9, 467–489.

[266] O'Callahan, J. C. (1989). "A procedure for an improved reduced system (IRS) model." *Proceedings of* 6^{th} *International Modal Analysis Conference, Las Vegas*.

[267] Ohrui, S., Kabori, T., Sakomoto, M., Koshika, K., Nishimura, I., Sasaki, K., Kondo, A., and Fukushima (1994). "Development of active-passive composite tuned mass damper and an application to a high rise building." *Proceedings of* 1^{st} *World Conference on Structural Control, LA, Univ. of Southern California*, G. W. Housner, S. F. Masri, and A. G. Chassiakos, eds. 100–109.

[268] Ohtori, Y., Christenson, R. E., Spencer, B. F., and Dyke, S. J. (2004). "Benchmark problems in seismically excited nonlinear buildings." *J. Engineering Mechanics, ASCE*, 130(4), 366–385.

[269] Padhi, R. and Balakrishnan, S. N. (2007). "Optimal dynamic inversion control design for a class of nonlinear distributed parameter systems with continuous and discrete actuators." *IET Control Theory and Application*, 1(6), 1662–1671.

[270] Pall, A. and Marsh, C. (1982). "Response of friction damped braced frames." *J. Structural Division, ASCE*, 108, 1313–1323.

[271] Park, Y. J., Wen, Y. K., and Ang, A. H. S. (1986). "Random vibration of hysteretic systems under bi-directional ground motions." *Earthquake Engineering & Structural Dynamics*, 14(4), 543–557.

[272] Patten, W. N. (1998). "The I-35 walnut creek bridge: an intelligent highway bridge via semi-active structural control." *Proceedings of* 2^{nd} *World Conference on Structural Control, Kyoto, Japan*. 427–436.

[273] Patten, W. N. (1999). "Field test of an intelligent stiffener for bridges at the I-35 Walnut Creek bridge." *Earthquake Engineering & Structural Dynamics*, 28, 109–126.

[274] PEER (2007). *PEER Strong Motion Database*. University of California, Berkeley, URL: http://peer.berkeley.edu/smcat/search.html.

[275] Perry, C., Fierro, E., Sedarat, H., and Scholl, R. (1993). "Seismic upgrade in san francisco using energy dissipation devices." *Earthquake Spectra*, 9, 559–579.

[276] Philips, R. W. (1969). *Engineering applications of fluids with a variable yield stress*. Ph.D. Dissertation, University of California, Berkeley.

[277] Politopoulos, I. (2008). "A review of adverse effects of damping in seismic isolation." *Earthquake Engineering & Structural Dynamics*, 37, 447–465. DOI: 10.1002/eqe.763.

[278] Pong, W. S., Tsai, C. S., and Lee, G. C. (1994a). *Seismic study of building frames with added energy absorbing devices*. Report No. NCEER $94-0016$, State Univ. of New York at Buffalo, Buffalo, NY.

[279] Pong, W. S., Tsai, C. S., and Lee, G. C. (1994b). "Seismic study of viscoelastic dampers and TPEA devices for high-rise buildings." *Proceedings of* 1^{st} *World Conference on Structural Control, LA, Univ. of Southern California*, G. W. Housner, S. F. Masri, and A. G. Chassiakos, eds. 1:WP3–23–WP3–32.

[280] Pulido, G. T. and Coello, C. A. C. (2003). "The micro genetic algorithm 2: Towards online adaptation in evolutionary multiobjective optimization." *Evolutionary Multi-criterion*

Optimization, C. Fonseca, P. J. Fleming, E. Zitzler, K. Deb, and L. Thiele, eds., Springer, Berlin, 252–266.

[281] Qu, Z. Q., Jung, Y., and Selvam, R. P. (2003a). "Model condensation for non-classically damper systems–part I: Static condensation." *Mechanical Systems & Signal Processing*, 17(5), 1003–1016.

[282] Qu, Z. Q., Jung, Y., and Selvam, R. P. (2003b). "Model condensation for non-classically damper systems–part II: Iterative schemes for dynamic condensation." *Mechanical Systems & Signal Processing*, 17(5), 1017–1032.

[283] Rahman, M. A. and Uddin, M. N. (2003). "A novel genetic algorithm based fuzzy logic controller for IPM synchronous motor drive." *IEEE International Symposium on Industrial Electronics, ISIE-03, Rio de Janeiro, Brazil*. 2:1007–1010.

[284] Rai, D. C., Jain, S. K., Sahoo, D. R., Sharma, R., Kumar, H., Jain, A. K., and Patel, A. C. (2007). "Base-isolation system of a hospital building in Shimla, India." *Structural Engineers World Congress, Bangalore, India*. CD ROM.

[285] Ramallo, J. C., Johnson, E. A., Spencer, B. F., and Sain, M. K. (2000). "'Smart' base isolation systems." *Proceedings of* 14^{th} *Conference on Analysis and Computation held in Conjunction with ASCE Structures Congress, ASCE, Philadelphia*. CD ROM.

[286] Ramallo, J. C., Johnson, E. A., and Spencer, B. F. J. (2002). "Smart base isolation systems." *J. Engineering Mechanics, ASCE*, 128(10), 1088–1099.

[287] Reed, D., Yu, J., Yeh, H., and Gardarsson, S. (1998). "Investigation of tuned liquid dampers under large amplitude excitation." *J. Engineering Mechanics, ASCE*, 28, 671–686.

[288] Reigles, D. G. and Symans, M. D. (2006). "Supervisory fuzzy control of a base-isolated benchmark building utilizing a neuro-fuzzy model of controllable fluid viscous dampers." *Structural Control & Health Monitoring*, 13, 724–747.

[289] Reiner, J., Balas, G. J., and Garrard, W. L. (1995). "Robust dynamic inversion for control of highly maneuverable aircraft." *J. Guidance, Control, and Dynamics*, 18(1), 18–24.

[290] Reinhorn, A. M. and Li, C. (1995). *Experimental and analytical investigation of seismic retrofit of structures with supplement damping, part III: viscous damping wall*. Technical Report NCEER-95-0013, NCEER, Buffalo, NY.

[291] Reinhorn, A. M., Li, C., and Constantinou, M. C. (1995). *Experimental and analytical investigation of seismic retrofit of structures with supplement damping, part I: fluid viscous damping devices*. Technical Report NCEER-95-0001, NCEER, Buffalo, NY.

[292] Reinhorn, A. M. and Riley, M. A. (1994). "Control of bridge vibrations with hybrid devices." *Proceedings of* 1^{st} *World Conference on Structural Control, LA, Univ. of Southern California*, G. W. Housner, S. F. Masri, and A. G. Chassiakos, eds. 50–59.

[293] Rivera, M. A., Singh, M. P., and Suarez, L. E. (1999). "Dynamic condensation approach for non-classically damped structures." *AIAA Journal*, 37, 564–571.

[294] Rodellar, J., Barbat, A. H., and Molinares, N. (1994). "Response analysis of building with new nonlinear base isolation system." *Proceedings of* 1^{st} *World Conference on Structural Control, LA, Univ. Southern California*, G. W. Housner, S. F. Masri, and A. G. Chassiakos, eds. 2: TP1–31–TP1–40.

[295] Rofooei, F. R., Mobarake, A., and Ahmadi, G. (2001). "Generation of artificial earthquake records with a non-stationary Kanai-Tajimi model." *Engineering Structures*, 23, 827–837.

[296] Roorda, J. (1975). "Tendon control in tall structures." *J. Structural Engineering, ASCE*, 101(ST3), 505–521.

[297] Sadek, F. and Mohraz, B. (1998). "Semi-active control algorithms for structures with variable dampers." *J. Structural Engineering, ASCE*, 124(9), 981–990.

[298] Sadek, F., Mohraz, B., and Lew, H. (1998). "Single and multiple tuned liquid column dampers for seismic applications." *Earthquake Engineering & Structural Dynamics*, 27, 439–463.

[299] Sadek, F., Mohraz, B., Taylor, A., and Chung, R. (1997). "A method of estimating the parameters of tuned mass dampers for seismic applications." *Earthquake Engineering & Structural Dynamics*, 26, 617–635.

[300] Sahasrabudhe, S. and Nagarajaiah, S. (2005a). "Effectiveness of variable stiffness systems in base isolated bridges subjected to near fault earthquakes: Experimental study." *International J. Intelligent Material Systems and Structures*, 16(9), 743–756.

[301] Sahasrabudhe, S. and Nagarajaiah, S. (2005b). "Experimental study of sliding base-isolated building with magnetorheological dampers in near fault earthquakes." *J. Structural Engineering, ASCE*, 131(7), 1025–1034.

[302] Sahasrabudhe, S. and Nagarajaiah, S. (2005c). "Semi-active control of sliding isolated bridges using MR dampers: An experimental and numerical study." *Earthquake Engineering & Structural Dynamics*, 34(8), 965–983.

[303] Sahasrabudhe, S., Nagarajaiah, S., and Hard, C. (2000). "Experimental study of sliding isolated buildings with smart dampers subjected to near-source ground motions." *Proceedings of* 14^{th} *ASCE Engineering Mechanics Conference, Austin, Texas*. CD ROM.

[304] Saiidi, M., Maragakis, E., and Griffin, G. (1999). "Effect of base isolation on seismic response of multi-column bridges." *Structural Engineering & Mechanics*, 8, 411–419.

[305] Samali, B., Yang, J. N., and Liu, S. C. (1985). "Control of lateral torsional motion of buildings under seismic load." *J. Structural Engineering, ASCE*, 111(10), 2165–2180.

[306] Sastry, S. and Bodson, M. (1989). *Adaptive Control: Stability, Convergence and Robustness*. Prentice Hall, Englewood Cliffs, New Jersey.

[307] Scholl, R. E. (1993). "Design criteria for yielding and friction energy dissipators." *Proceedings of ATC* $17-1$ *on Seismic Isolation, Energy Dissipation and Active Control, San Francisco, California*. 485–495.

[308] Schurter, K. C. and Roschke, P. N. (2000). "Fuzzy modeling of a magnetorheological damper using ANFIS." *IEEE Fuzzy Conference, San Antonio, TX*.

[309] Schurter, K. C. and Roschke, P. N. (2001a). "Neuro-fuzzy control of structures using acceleration feedback." *Smart Materials & Structures*, 10(4), 770–779.

[310] Schurter, K. C. and Roschke, P. N. (2001b). "Neuro-fuzzy control of structures using magnetorheological dampers." *Proceedings of American Control Conference, Arlington, VA*. 1097–1102.

[311] Scott, S. D., Samal, A., and Seth, S. (1995). "HGA: a hardware-based genetic algorithm." *Proceedings of* 1995 *ACM third International Symposium on Field-programmable gate arrays, San Francisco, CA*. 53–59.

[312] Setareh, M. (1994). "Use of doubly tuned mass dampers for passive vibration control." *Proceedings of* 1^{st} *World Conference on Structural Control, LA, Univ. Southern California*, G. W. Housner, S. F. Masri, and A. G. Chassiakos, eds. 1: WP4–12–WP4–21.

[313] Shen, K. and Soong, T. (1995). "Modeling of viscoelastic dampers for structural applications." *J. Engineering Mechanics, ASCE*, 121, 694–701.

[314] Shinozuka, M. and Sato, Y. (1967). "Simulation of non-stationary random processes." *J. Engineering Mechanics Division, ASCE*, 93, 11–40.

[315] Shiraishi, T., Nakaya, N., and Morishita, S. (2002). "Structural control by a variable damper using MR fluid." 24–29.

[316] Shook, D., Lin, P. Y., Lin, T. K., and Roschke, P. N. (2007). "A comparative study in the semi-active control of isolated structures." *Smart Materials & Structures*, 16, 1433–1446.

[317] Singh, J. P. (1985). "Earthquake ground motions: Implications for designing structures and reconciling structural damage." *Earthquake Spectra*, 1(2), 239–270.

[318] Skelton, R., Iwasaki, T., and Grigoriadis, K. (1996). *An unified approach to control design*. Taylor and Francis, London.

[319] Skinner, R. I., Robinson, W., and McVerry, G. (1993). *An Introduction to Seismic Isolation*. Wiley, England.

[320] Slotine, J. E. and Li, W. (1991). *Applied Nonlinear Control*. Prentice Hall.

[321] Soda, S., Kusumoto, H., Chatani, R., Iwata, N., Fujitani, H., Shiozaki, Y., and Hiwatashi, T. (2003). "Semi-active seismic response control of base-isolated building with MR damper." *Smart Structures & Materials* 2003*: Damping and Isolation; Proceedings SPIE, San Diego, CA, USA*. 5052:460–467.

[322] Soong, T. T. (1990). *Active Structural Control: Theory and Practice*. Longman Scientific & Technical, John Wiley & Sons, NY.

[323] Soong, T. T. and Constantinou, M. C. (1994). *Passive and Active Structural Vibration Control in Civil Engineering*. Springer-Verlag, New York.

[324] Soong, T. T. and Dargush, G. F. (1997). *Passive Energy Dissipation Systems in Structural Engineering*. John Wiley & Sons, England.

[325] Soong, T. T. and Spencer, B. F. (2002). "Supplemental energy dissipation: State of the art and state of the practice." *Engineering Structures*, 24, 243–259.

[326] Spencer, B. F. and Nagarajaiah, S. (2003). "State of the art of structural control." *J. Structural Engineering, ASCE*, 129(7), 845–856.

[327] Spencer, B. F. J., Dyke, S. J., and Deoskar, H. S. (1998a). "Benchmark problems in structural control: Part II-active tendon system." *Earthquake Engineering & Structural Dynamics*, 27(11), 1140–1147.

[328] Spencer, B. F. J., Dyke, S. J., and Deoskar, H. S. (1998b). "Benchmark problems in structural control: Part I-active mass driver system." *Earthquake Engineering & Structural Dynamics*, 27(11), 1127–1139.

[329] Spencer, B. F. J., Dyke, S. J., Sain, M. K., and Carlson, J. D. (1997). "Phenomenological model for magnetorheological dampers." *J. Engineering Mechanics, ASCE*, 123(3), 230–238.

[330] Spencer, B. F. J., Johnson, E. A., and Ramallo, J. C. (2000). "'smart' isolation for seismic control." *JSME International Journal: Special Issue on Frontiers of Motion and Vibration Control (Series C)*, 43(3), 704–711.

[331] Spencer, B. F. J. and Sain, M. K. (1997). "Controlling buildings: A new frontier in feedback." *IEEE Control Systems*, 7(6), 19–35.

[332] Spencer, B. F. J., Sain, M. K., Kantor, J. C., and Montemagno, C. (1992). "Probabilistic stability measures for controlled structures subject to real parameter uncertainties." *Smart Materials & Structures*, 1(4), 294–305.

[333] Spencer, B. F. J., Suhardjo, J., and Sain, M. K. (1994). "Frequency domain optimal control strategies for aseismic protection." *J. Engineering Mechanics, ASCE*, 120, 135–159.

[334] Spencer, B. F. J., Timlin, T. L., Sain, M. K., and Dyke, S. J. (1996). "Series solution of a class of nonlinear optimal regulators." *J. Optimization Theory and Applications*, 91, 321–345.

[335] Spencer, J. B. F., Kaspari, D. C., and Sain, M. K. (1996). "Structural control design: A reliability based approach." *Proceedings of IEEE Conference on Decision and Control, Kobe, Japan*. 1062–1066.

[336] Spencer, J. B. F. and Soong, T. T. (1999). "New application and development of active, semi-active and hybrid control techniques for seismic and non-seismic vibration in the USAs." *Proceedings of International Post-SMiRT Conference Seminar on Seismic Isolation, Passive Energy Dissipation and Active Control of Vibration of Structures, Cheju, South Korea*. 467–488.

[337] Spencer, J. B. F., Yang, G., Carlson, J. D., and Sain, M. K. (1998). "'Smart dampers for seismic protection of structures: a full-scale study." *Proceedings of* 2^{nd} *World Conference on Structural Control, Kyoto, Japan*. 417–426.

[338] Stanway, R., Sproston, J., and Stevens, N. (1987). "Non-linear modeling of an electrorheological vibration damper." *J. Electrostatics*, 20, 167–184.

[339] Stanway, R., Sproston, J. L., and Stevens, N. G. (1985). "Non-linear identification of an electro-rheological vibration damper." *IFAC/IFORS Symposium on Identification and System Parameter Estimation, UK*. 195–200.

[340] Suarez, L. E. and Singh, M. P. (1992). "Dynamic condensation method for structural eigenvalue analysis." *AIAA Journal*, 30, 1046–1054.

[341] Subramaniam, R. S., Reinhorn, A. M., Riley, M. A., and Nagarajaiah, S. (1996). "Hybrid control of structures using fuzzy logic." *Microcomputer and Civil Engineering*, 11, 1–17.

[342] Suhardjo, J. (1990). *Frequency domain techniques for control of Civil engineering structures with some robustness considerations*. Ph.D. dissertation, Univ. of Notre Dame, Indiana.

[343] Suhardjo, J., Spencer, B. F., and Kareem, A. (1992a). "Active control of wind excited buildings: a frequency domain approach." *J. Wind Engineering and industrial Aerodynamics*, 41, 1985–1996.

[344] Suhardjo, J., Spencer, B. F., and Kareem, A. (1992b). "Frequency domain optimal control of wind excited buildings." *J. Engineering Mechanics, ASCE*, 118(12), 2463–2481.

[345] Sun, L. and Goto, Y. (1994). "Application of fuzzy theory to variable dampers for bridge vibration control." *Proceedings of* 1^{st} *World Conference on Structural Control, LA, Univ. of Southern California*, G. W. Housner, S. F. Masri, and A. G. Chassiakos, eds. WP1:31–40.

[346] Sun, L. M., Fujino, Y., and Koga, K. (1995). "A model of tuned liquid damper for suppressing pitching motions of structures." *Earthquake Engineering & Structural Dynamics*, 24, 625–636.

[347] Susumpow, T. and Fujino, Y. (1995). "Active control of multimode cable vibration by axial support motion." *J. Engineering Mechanics, ASCE*, 121(9), 964–972.

[348] Symans, M. D. and Constantinou, M. C. (1997). "Seismic testing of a building structure with semi-active fluid damper control system." *Earthquake Engineering & Structural Dynamics*, 26, 757–777.

[349] Symans, M. D. and Constantinou, M. C. (1999). "Semi-active control systems for seismic protection of structures: A state-of-the-art review." *Engineering Structures*, 21, 469–4877.

[350] Symans, M. D., Constantinou, M. C., Taylor, D. P., and Garnjost, K. D. (1994). "Semi-active fluid viscous dampers for seismic response control." *Proceedings of* 1^{st} *World Conference on Structural Control, LA, Univ. of Southern California*. 3–12.

[351] Symans, M. D. and Kelly, S. W. (1999). "Fuzzy logic control of bridge structures using intelligent semi-active seismic isolation systems." *Earthquake Engineering & Structural Dynamics*, 28, 37–60.

[352] Symans, M. D., Madden, G. J., and Wongprasert, N. (2000). "Experimental study of an intelligent base isolation system for buildings." *Proceedings* 12^{th} *World Conference on Earthquake Engineering, Aucland, New Zealand*. CD ROM.

[353] Tan, P. and Agrawal, A. K. "Benchmark structural control problem for a seismically excited highway bridge part-II: Sample control designs." *http://www-ce.engr.ccny.cuny.edu/People/Agrawal/index.htm*, (downloaded: July 2005).

[354] Tao, G. (2003). *Adaptive Control Design and Analysis*. Wiley Interscience, USA.

[355] Taylor, D. P. and Constantinou, M. P. (1996). "Fluid dampers for applications of seismic energy dissipation and seismic isolation." *Proceedings of* 11^{th} *World Conference on Earthquake Engineering, Acapulco, Mexico*. CD ROM.

[356] Tsai, C. S. and Lee, H. (1993). "Application to viscoelastic dampers to high rise buildings." *J. Structural Engineering, ASCE*, 119(4), 1222–1233.

[357] Tsai, H. and Lin, G. (1993). "Optimum tuned mass dampers for minimizing steady-state response of support excited and damped system." *Earthquake Engineering & Structural Dynamics*, 22, 957–973.

[358] Tsai, K., Chen, H., Hong, C., and Su, Y. (1993). "Design of steel triangular plate energy absorbers for seismic-resistant construction." *Earthquake Spectra*, 9, 505–528.

[359] Tsiatas, G. and Daly, K. (1994). "Controlling vibration with combination viscous/friction mechanisms." *Proceedings of* 1^{st} *World Conference on Structural Control, LA, Univ. of Southern California*, G. W. Housner, S. F. Masri, and A. G. Chassiakos, eds. 1:WP4–3–WP4–11.

[360] Uang, C. M. and V.Bertero, V. (1988). *Use of energy as a design criterion in earthquake resistant design*. Report No. UCB/EERC-88/18, University of California, Berkeley.

[361] Venini, P. and Wen, Y. K. (1994). "Hybrid vibration control of MDOF hysteretic structures with neural networks." *Proceedings of* 1^{st} *World Conference on Structural Control, LA, Univ. of Southern California*, G. W. Housner, S. F. Masri, and A. G. Chassiakos, eds. TA3:53–62.

[362] Wada, A., Huang, Y., and Iwata, M. (1999). "Passive damping technology for buildings in japan." *Progress in Structural Engineering and Materials*, 2, 1–15.

[363] Walters, M., Elsesser, E., and Allen, E. W. (1986). *Base isolation of the existing City and County Building in Salt Lake City*. Proc. Seminar on Base Isolation and Passive Energy Dissipation, Applied Technology Council, Report No. 17.

[364] Wang, D. H. and Liao, W. H. (2001). "Neural network modeling and controllers for magnetorheological fluid dampers." *IEEE International Fuzzy Systems Conference, Melbourne, Australia*. 1323–1326.

[365] Wang, L. and Kazmierski, T. J. (2005). "VHDL-AMS based genetic optimization of a fuzzy logic controller for automotive active suspension systems." *Proceedings of IEEE International Workshop on Behavioral Modeling and Simulation, Washington DC, USA*. 124–127.

[366] Wang, X. and Gordaninejad, F. (2000). "Study of field-controllable, electro- and magneto-rheological fluid dampers in flow mode using Herschel-Bulkley theory." *Proceedings of SPIE Smart Structure and Materials Conference, Newport Beach, California*. 3989:232–243.

[367] Wang, Y. P. and Liu, C. J. (1994). "Active control of sliding structures under earthquakes." *Proceedings of* 1^{st} *World Conference on Structural Control, LA, Univ. of Southern California*, G. W. Housner, S. F. Masri, and A. G. Chassiakos, eds. 3:FP1–23–FP1–32.

[368] Warnitchai, P., Fujino, Y., and Susumpow, T. (1995). "A non-linear dynamic model for cables and its application to a cable-structure system." *J. Sound and Vibration*, 187(4), 695–712.

[369] Weaver, J. W. and Johnston, P. R. (1987). *Structural Dynamics by Finite Elements*. Prentice Hall Inc., Englewood Cliffs, NJ, USA.

[370] Weiss, K. D., Carlson, J. D., and Nixon, D. A. (1994). "Viscoelastic properties of magneto- and electro-rheological fluids." *J. Intelligent Materials, Systems and Structures*, 5(11), 772–775.

[371] Wen, Y. K. (1976). "Method for random vibration of hysteretic systems." *J. Engineering Mechanics Division, ASCE*, 102(EM2), 249–263.

[372] Wereley, N., Pang, L., and Kamath, G. (1998). "Idealized hysteresis modeling of electrorheological and magnetorheological dampers." *J. Intelligent Materials, Systems and Structures*, 9, 642–649.

[373] Whittaker, A., Aiker, I., Bergman, D., Clark, P., Cohen, J., Kelly, J., and Scholl, R. (1993). "Code requirements for the design and implementation of passive energy dissipation systems." *Proceedings of ATC* $17-1$ *on Seismic Isolation, Energy Dissipation, and Active Control, San Francisco, California*. 497–508.

[374] Whorton, M. S., Calise, A. J., and Hsu, C. C. (1998). "A study of fixed order mixed norm design for a benchmark problem in structural control." *Earthquake Engineering & Structural Dynamics*, 27(11), 1315–1330.

[375] Wilson, C. M. D. (2005). *Fuzzy Control of Magnetorheological Dampers for Vibration Reduction of Seismically Excited Structures*. The Florida State University, FAMU-FSU College of Engineering.

[376] Wonder Box (downloaded: July 2008). *LORD Device Controller Kit*. http://www.lordfulfillment.com/upload/UI7000.pdf.

[377] Wongprasert, N. and Symans, M. D. (2005). "Experimental evaluation of adaptive elastomeric base-isolated structure using variable-orifice fluid dampers." *J. Structural Engineering, ASCE*, 131, 867–877.

[378] Woo, Z. W., Chung, H. Y., and Lin, J. J. (2000). "A PID type fuzzy controller with self-tuning scaling factors." *Fuzzy Sets and Systems*, 115, 321–326.

[379] Wu, J. C., Yang, J. N., and Agrawal, A. K. (1998). "Applications of sliding mode control to benchmark problems." *Earthquake Engineering & Structural Dynamics*, 27, 1247–1265.

[380] Xia, C. and Hanson, R. (1992). "Influence of adas element parameters on building seismic response." *J. Structural Engineering, ASCE*, 118, 1903–1918.

[381] Xia, Y. (2001). *Condition assessment of structures using dynamic data*. PhD thesis, Nanyang Technological University, Singapore.

[382] Xu, Y. L., Samali, B., and Kwok, K. C. S. (1992). "Control of along wind response of structures by mass and liquid dampers." *J. Engineering Mechanics, ASCE*, 118, 20–39.

[383] Xu, Z. (2006). *Design and assessment of seismic protective systems for near-field ground motions*. Ph.D. Dissertation, The City University of New York.

[384] Xu, Z. D., Shen, Y. P., and Guo, Y. Q. (2003). "Semi-active control of structures incorporated with magnetorheological dampers using neural-networks." *Smart Materials & Structures*, 12, 80–87.

[385] Yalla, S. and Kareem, A. (2003). "Semi-active tuned liquid column dampers: An experimental study." *J. Structural Engineering, ASCE*, 129(7), 960–971.

[386] Yamaguchi, H. and Harnpornchai, N. (1993). "Fundamental characteristics of multiple tuned mass dampers for suppressing harmonically forced oscillations." *Earthquake Engineering & Structural Dynamics*, 22, 51–62.

[387] Yang, G. (2001). *Large Scale Magneto-rheological Fluid Damper for Vibration Mitigation: Modeling, Testing and Control*. Ph.D dissertation, Univ. of Notre Dame, Indiana.

[388] Yang, G., Jung, H. J., and Spencer, B. F. J. (2001). "Dynamic model of full-scale MR dampers for Civil Engineering applications." *Proceedings of US-Japan Workshop on Smart Structures for Improved Seismic Performance in Urban Region, Seattle, WA*. 50–59.

[389] Yang, G., Spencer, B., Carlson, J. D. J., and Sain, M. (2002). "Large–scale MR fluid dampers: Modeling and dynamic performance considerations." *Engineering Structures*, 24, 309–323.

[390] Yang, G., Spencer, B. F., Jung, H. H., and Carlson, J. D. J. (2004). "Dynamic modeling of large-scale magnetorheological damper systems for Civil Engineering applications." *J. Engineering Mechanics, ASCE*, **130**, 1107–1114.

[391] Yang, G., Spencer, B. J., Carlson, J., and Sain, M. (2001). "Dynamic modeling and performance considerations on full-scale MR fluid dampers." *Proceedings of* 8^{th} *International Conference on Structural Safety and Reliability, Newport Beach, CA*.

[392] Yang, J. N. and Agrawal, A. K. (2002). "Semi-active hybrid control systems for nonlinear buildings against near-field earthquakes." *Engineering Structures*, 24(3), 271–280.

[393] Yang, J. N., Agrawal, A. K., and Chen, S. (1996). "Optimal polynomial control for seismically excited non-linear and hysteretic structures." *Earthquake Engineering & Structural Dynamics*, 25, 1211–1230.

[394] Yang, J. N., Agrawal, A. K., Samali, B., and Wu, J. C. (2004). "A benchmark problem for response control of wind excited tall buildings." *J. Engineering Mechanics, ASCE*, 130(4), 437–446.

[395] Yang, J. N., Bobrow, J., Jabbari, F., Leavitt, J., Cheng, C. P., and Lin, P. Y. (2007). "Full-scale experimental verification of resetable semi-active stiffness dampers." *Earthquake Engineering & Structural Dynamics*, 36(9), 1255–1273.

[396] Yang, J. N. and Giannopoulos, F. (1978). "Active tendon control of structures." *J. Engineering Mechanics, ASCE*, 104, 551–568.

[397] Yang, J. N. and Giannopoulos, F. (1979a). "Active control and stability of cable stayed bridge." *J. Engineering Mechanics Division, ASCE*, 105, 677–694.

[398] Yang, J. N. and Giannopoulos, F. (1979b). "Active control of two cable stayed bridge." *J. Engineering Mechanics Division, ASCE*, 105, 795–809.

[399] Yang, J. N., Kim, J. H., and Agrawal, A. K. (2000). "Resetting semi-active stiffness damper for seismic response control." *J. Structural Engineering, ASCE*, 126(12), 1427–1433.

[400] Yang, J. N. and Samali, B. (1983). "Control of buildings in along-wind motions." *J. Structural Engineering Division, ASCE*, 109, 50–68.

[401] Yang, J. N., Wu, J. C., Agrawal, A. K., and Hsu, S. (1997). "Sliding model control with compensator for wind and seismic response control." *Earthquake Engineering & Structural Dynamics*, 26, 1137–1156.

[402] Yang, J. N., Wu, J. C., Kawashima, K., and Unjoh, S. (1995). "Hybrid control of seismic-excited bridge structures." *Earthquake Engineering & Structural Dynamics*, 24, 1437–1451.

[403] Yang, J. N., Wu, J. C., and Li, Z. (1996). "Control of seismic excited buildings using active variable stiffness systems." *Earthquake Engineering & Structural Dynamics*, 18(8), 589–596.

[404] Yi, F. and Dyke, S. J. (2000). "Structural control systems: performance assessment." *Proceedings of the American Control Conference, Chicago, IL*.

[405] Yi, F., Dyke, S. J., Caicedo, J. M., and Carlson, J. D. (2001). "Experimental verification of multi-input seismic control strategies for smart dampers." *J. Engineering Mechanics, ASME*, 127(11), 1152–1164.

[406] Yi, F., Dyke, S. J., Frech, S., and Carlson, J. D. (1998). "Investigation of magnetorheological dampers for earthquake hazard mitigation." *Proceedings of* 2^{nd} *World Conference on Structural Control, Kyoto, Japan*.

[407] Yoshida, K., Kang, S., and Kim, T. (1994). "LQG control and H_∞ control of vibration isolation for multi degree of freedom systems." *Proceedings of* 1^{st} *World Conference on Structural*

Control, LA, Univ. of Southern California, G. W. Housner, S. F. Masri, and A. G. Chassiakos, eds. 2:TP4–43–TP4–52.

[408] Yoshida, M. and Matsumoto, S. (1998). "Control of axial temperature distribution in a packed-bed reactor." *J. Chemical Engineering of Japan*, 31(3), 381–390.

[409] Yoshida, O., Dyke, S. J., Giacosa, L. M., and Truman, K. Z. (2002). "Torsional response control of asymmetric buildings using smart dampers." 15^{th} *ASCE Engineering Mechanics Conference, New York, NY*.

[410] Yoshioka, H., Ramallo, J., and Spencer, B. F. J. (2002). "'Smart' base isolation strategies employing magnetorheological dampers." *J. Engineering Mechanics, ASCE*, 128(5), 540–441.

[411] Youssef, N. and Others (1995). "Passive control of the Los Angeles City Hall." *Proceedings Joint ASME/JSME Pressure Vessels and Piping Conference, Seismic Shock and Vibration Isolation, Honolulu, Hawaii*. 241–248.

[412] Yu, J. K., Wakahara, T., and Reed, D. A. (1999). "A non-linear numerical model of the tuned liquid damper." *Earthquake Engineering & Structural Dynamics*, 28, 671–686.

[413] Zadeh, L. A. (1965). "Fuzzy sets." *Information and Control*, 8, 338–353.

[414] Zhang, J. and Roschke, P. N. (1998). "Neural network simulation of magnetorheological damper behavior." *International Conference on Vibration Engineering, Dalian, China*. 25–30.

[415] Zhang, J. and Roschke, P. N. (1999). "Active control of a tall structure excited by wind." *J. Wind Engineering and Industrial Aerodynamics*, 83, 209–223.

[416] Zhang, R. H. and Soong, T. T. (1992). "Seismic design of viscoelastic dampers for structural application." *J. Structural Engineering, ASCE*, 118(5), 1375–1392.

[417] Zhang, R. H., Soong, T. T., and Mahmoodi, P. (1989). "Seismic response of steel frame structures with added viscoelastic dampers." *Earthquake Engineering & Structural Dynamics*, (5), 389–396.

[418] Zhao, Y. and Collins, E. G. J. (2003a). "Fuzzy PI control design for an industrial weigh belt feeder." *IEEE Transactions on Fuzzy Systems*, 11(3), 311–319.

[419] Zhao, Y. and Collins, E. G. J. (2003b). "Parallel parking of autonomous ground vehicles in tight spaces using fuzzy logic." *IEEE International Conference on Robotics and Automation, Taipei, Taiwan*.

[420] Zheng, L. (1992). "A practical guide to tune of proportional and integral PI like fuzzy controllers." *First IEEE International Conference on Fuzzy Systems, San Diego*. 633–640.

[421] Zhou, L., Chang, C. C., and Spencer, B. F. J. (2002). "Intelligent technology based control of motion and vibration using MR dampers." *Earthquake Engineering & Engineering Vibration*, 1(1), 100–110.

[422] Zhoua, Q., Nielsen, S. R. K., and Qu, W. L. (2006). "Semi-active control of three-dimensional vibrations of an inclined sag cable with magnetorheological dampers." *J. Sound and Vibration*, 296, 1–22.

[423] Zhu, G. G. and Skelton, R. (1994). "Output covariance constraint problem with disturbance feedback." *Proceedings* 1^{st} *World Conference on Structural Control, LA, Univ. of Southern California*, G. W. Housner, S. F. Masri, and A. G. Chassiakos, eds. 3:FP4–32–FP4–41.

[424] Zhu, W. Q. and Ying, Z. G. (2002). "Nonlinear stochastic optimal control of partially observable linear structures." *Engineering Structures*, 24(3), 333–342.

[425] Zuk, W. (1980). "The past and future of active control systems." *Proceedings of First International IUTAM Symposium On Structural Control, North-Holland*, H. H. E. Leipholtz, ed. 779–794.

Appendix A

Instruments and Sensor Details

This appendix details the equipment/devices used for experiments carried out and reported in chapter 3 and chapter 5.

Impact hammer

The Impact hammer has been employed for the impulse hammer test of the fixed base three storey building model. The impact hammer type 8202 with force transducer type 8200 has been used for the study. It has been manufactured by Brüel & Kjær with following characteristics,

- Weight of the hammer: 280 gm
- Sensitivity at the output of hammer: 1.01 pC/N
- Reference sensitivity: 4.02 pC/N

For the impact hammer test a charge amplifier (B & K type 2635) has been employed. The amplifier has a sensitivity range of 0.01mV to 10V/pC. For data acquisition in impulse hammer test, 8 channel IOtech, DaqBoard-2000 with a sampling speed of 200K samples per second has been used. The software used in connection with IOtech is DasyLab, version 6.00.01. Figure A.1 shows the assembly of an impulse hammer, the charge amplifier and the signal conditioner.

For modal analysis MEscope VES, Visual SDM Pro. software package VT-580 (version:4.0.0.6) has been used.

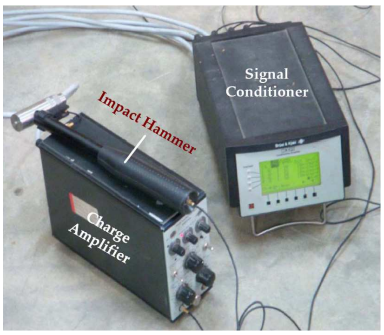

Figure A.1: Impulse hammer, Signal Conditioner and Charge amplifier

DEWETRON Data Acquisition System

DEWETRON data acquisition system ([88]) has been used to measure and store the acceleration and floor inter storey drift data for experiments with seismic excitations. The model used for the study is DEWETRON-DEWE 4011 supplemented with DEWE 30-16 module. The DEWETRON system has the following characteristics,

- DEWE 4011: A total 64 channels can be operated of which 16 channels are for voltage type transducers and 16 channels are for Strain gauge measurement.

- DEWE $30-16$ has 13 channels in total of which 3 ICP type inputs, 1 temperature input, 1 impact hammer, 8 strain gauge inputs.

- Types of filter: DEWETRON system has 6 types of filters for signal processing. In the experimental study a first order Butterworth filter with 30Hz low pass cut-off has been used.

DEWEsoft Software

DEWEsoft software ([87]) comes with DEWETREON system. DEWEsoft-6-PROF: 2007 has been used for the experimental data acquisition. Simultaneous data acquisition is a salient features of DEWEsoft software. The experimental data has been sampled at 1kHz frequency.

dSPACE

For the real time control of the hybrid base isolated building dSPACE hardware and software ([94]) has been employed. dSPACE software release-5 (2005) has been used with hardware card no. 11229 compatible with MATLAB, Release 14 (2004). A DSP connector box in conjunction with the dSPACE card has been used to interface the dSPACE application running on the PC with associated hardware. The DSP connector box of Model No. $DES1104$ manufactured by 'Spranktronics' has been used for the study.

LORD Wonder Box Device Controller

LORD Wonder Box® device controller kit (Wonder Box (2008) [376]) is a companion product for the magnetorheological(MR) fluid devices. The kit includes a device controller, 12 volt DC power supply and two banana plugs. The Wonder Box provides a closed-loop current control to compensate for changing electrical loads up to the limits of the power supply. A LORD Wonder Box is shown in Fig. A.2(a). The overall dimensions of the device is $63.5\ mm$ x $27.9\ mm$ x $88.9\ mm$ in (LxWxH). The signal input to the Wonder Box can be set at a maximum of $1\ kHz$ frequency with a maximum current output of 2 ampere. The Pulse Width Modulation (PWM) Frequency of the Wonder Box is $30\ kHz$ unfiltered.

The Wonder Box controller may be operated as an interface device for PLC or for computer control of MR fluid devices. If manual operation is desired, a potentiometer is provided to control the current supplied to an attached device. The device can be operated in a pulse mode, for *e.g.*, current to the device may be switched on and off by depressing a switch on the side of the controller.

The output current is linearly proportional to the input voltage as shown in Fig. A.2(b). The input voltage and output current test of Wonder Box used in the experimental study has been presented in Fig. A.2(b) has been obtained The output current will be $0.0\ A$ when the control input is approximately $0.4 - 0.6$ Volts at the BNC terminal.

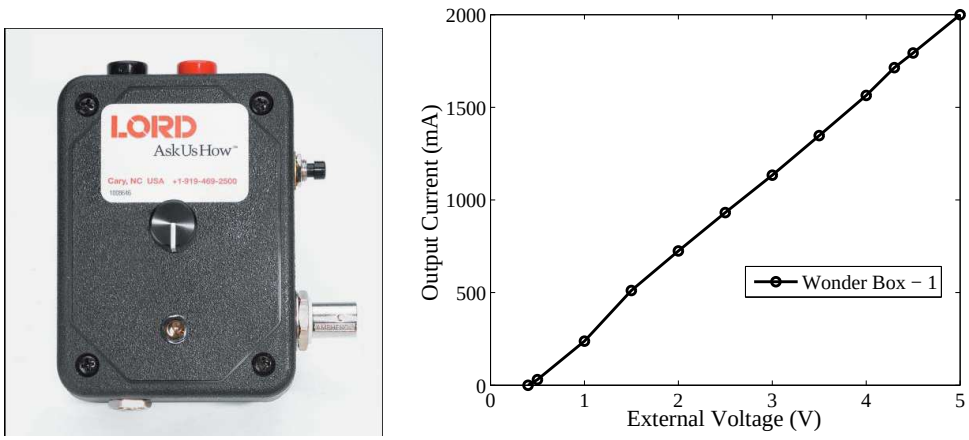

(a) LORD Wonder Box® [376] (b) Current-voltage relation

Figure A.2: Wonder Box: (a) Photograph of Wonder Box, (b) Calibration of Wonder Box

RD-1005-3 Magnetorheological Damper

Magnetorheological devices for commercial applications ranging from automobile engineering to medical technology are manufactured by LORD Corporation (2008) [214]. For the experimental study presented in chapter 3 and chapter 5, RD-1005-3 MR damper has been employed. RD-1005-3 MR damper is a product of RD-1005 series, which is a trademark of LORD Corporation (LORD Corporation (2008) [214]). It is a monotube MR fluid device with a single sided piston. As a magnetic field is applied to the MR fluid inside the monotube housing, the damping characteristics of the RD-1005-3 changes within under 10-milliseconds. A schematic diagram of RD-1005 series has been shown in Fig. 3.2 of chapter 3.

The specifications of RD-1005-3 MR damper has been given in Table A.1. The device has a capacity to provide a peak to peak force of 2224 N at a velocity of 51 mm/s at a continuous supply of 1 A current. The input current can be varied to a maximum (represented as Max. in Table A.1) of 1 ampere (continuous supply) and 2 ampere (intermittent supply). The response time to reach 90% of its maximum level during a 0 A to 1 A step at 51mm/s is 25-milliseconds. The technical details about RD-1005-3 MR damper are given in Table A.1 (MR Dampers (2006) [240]).

Table A.1: Properties of MR Damper RD-1005-3

Parameter	**Value**	**Parameter**	**Value**
Extended length	208 mm	Compressed length	155 mm
Body diameter	41.4 mm	Shaft diameter	10 mm
Max. tensile force	4448 N	Weight	800 g
Device stroke	$\pm$25 mm	Response time	$<$ 25 ms
Input Voltage	12 v DC	Max. current supply	2 A
Operating temp.	71° C (Max)	Storage temp.	$-40°$ C $-$ 100° C

APLAB Power Supplier

Aplab is a power conversion devices, including standard and custom AC/DC power supplies as well as DC/DC converters. This instrument has been used to provide a DC current supply to the Wonder Box for MR damper testing. APLAB-L3205 manufactured by APLAB Ltd., Thane, India has serial number 0204372.

Shake Table

A 3 axis shake table (Bi-00-300-D) having 6 degrees of freedom manufactured bu BISS (Bangalore Integrated System Solutions) (P) Ltd., in collaboration with Structures Laboratory, Department of Civil Engineering, IISc. The shakes table operates with displacement input. The pay load of the shake table is 500kg with $0 - 15$Hz of operating frequency range. It is a 1m $\times$ 1m square plate, whose motion is monitored by 8 servo-hydraulic actuators. The input displacement signal is tracked using a PID controller.

Force Sensor

A force transducer (Model Number-1050V4) has been attached to the MR damper to measure the force across the MR damper. The force sensor has been manufactured by Dytran Instruments. The maximum capacity of the sensor was 500 LbF with a range of 10 mV/LbF.

Appendix B

MR Damper Experimental Results

Overview

Extensive experimental results MR damper testing under sinusoidal displacement excitation have been provided in this appendix. Only the force-displacement and the force-velocity hysteretic curves have been shown. Details of the experimental test set-up, nature of loading *etc* have been documented in chapter 3. Tests have been conducted for a set of frequencies, amplitude of excitation at various input current to the MR damper. Therefore, a set of frequencies (0.1, 0.25, 0.50, 1.0, 1.5, 2.0, 2.5, 3.0 Hz), amplitude (2.5, 5.0, 10.0, 15.0, 20.0 mm) and current supply (0.0, 0.25, 0.50, 0.75, 1.0 A) formed the test program.

The results are reported in a way, such that it provides information about the change in the hysteretic behaviour of the MR damper over amplitude of excitation and input current. Each page of the appendix contains, all the test results for different amplitude and input current at a particular frequency of excitation. Therefore, each page provides 5 figures corresponding to 5 different amplitude of excitation. Each one of these 5 figures contains 5 different curves, each showing test results at a particular input current. This will help to have a glance at the change in hysteretic behaviour with amplitude over the 5 figures and with input current over different curves at a particular figure. For frequency of excitation $\omega = 2.5$ Hz and $\omega = 3.0$ Hz, the experiments could not be carried out at amplitudes higher than 15 mm and 10 mm respectively, therefore results upto these amplitudes have been provided.

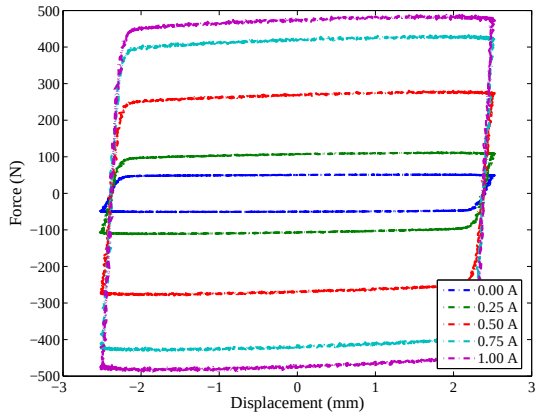

(a) 2.5 mm amplitude

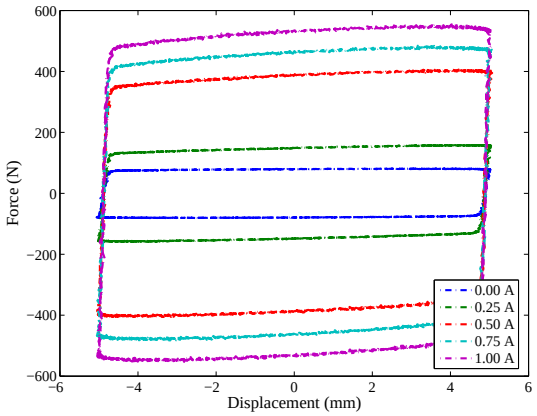

(b) 5.0 mm amplitude

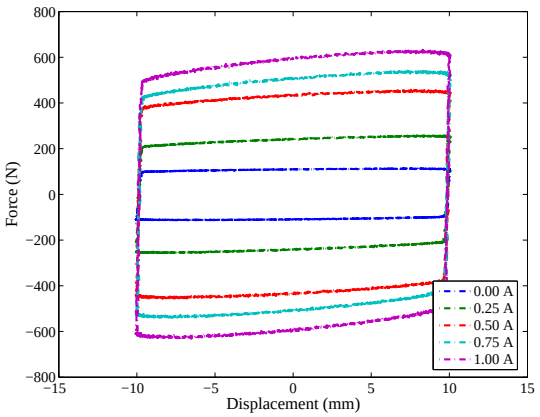

(c) 10 mm amplitude

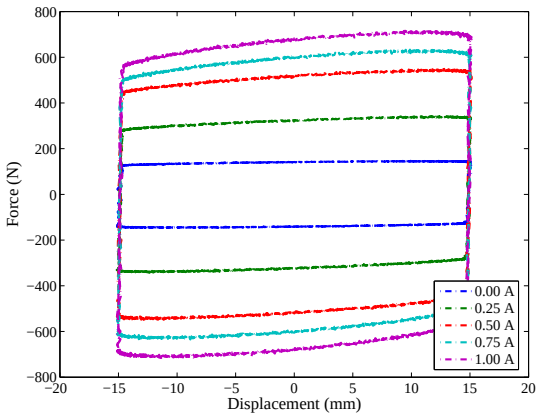

(d) 15 mm amplitude

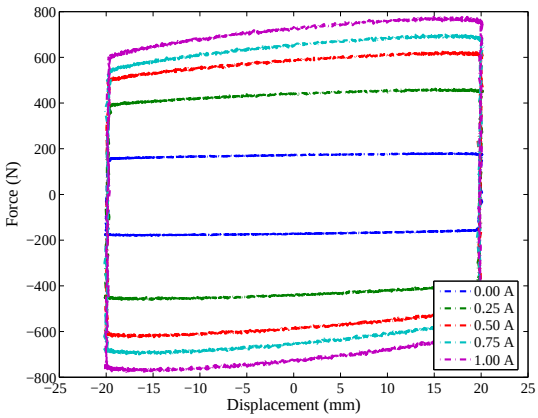

(e) 20 mm amplitude

Figure B.1: MR damper force-displacement hysteretic curves for ($\omega = 0.1$ Hz)

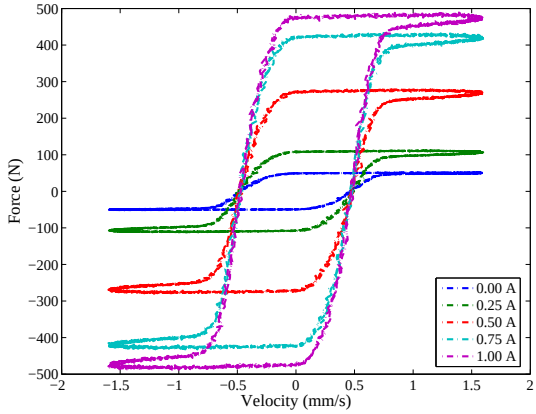

(a) 2.5 mm amplitude

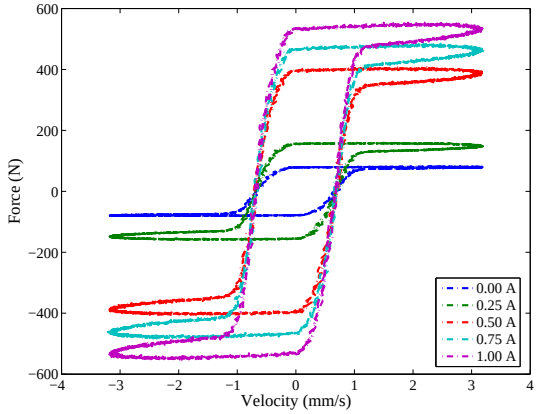

(b) 5.0 mm amplitude

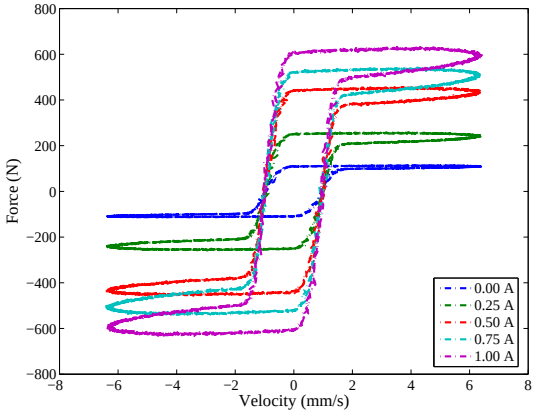

(c) 10 mm amplitude

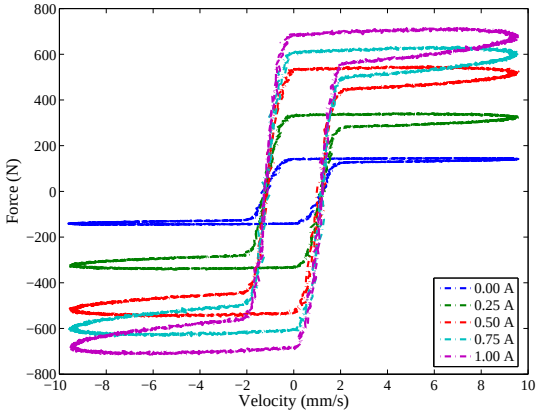

(d) 15 mm amplitude

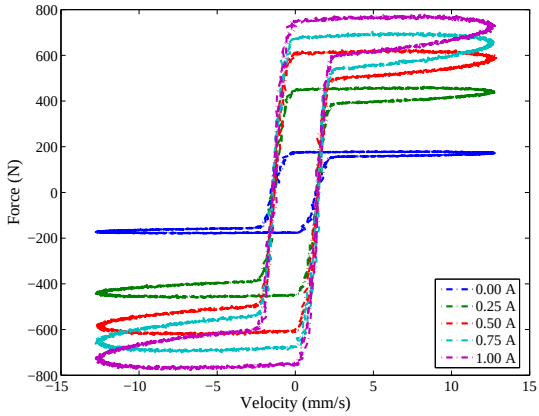

(e) 20 mm amplitude

Figure B.2: MR damper force-velocity hysteretic curves for ($\omega = 0.1$ Hz)

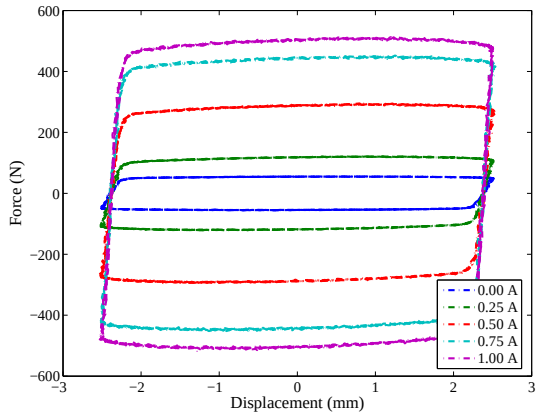

(a) 2.5 mm amplitude

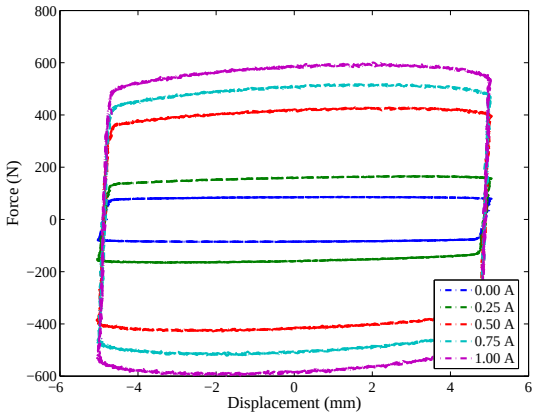

(b) 5.0 mm amplitude

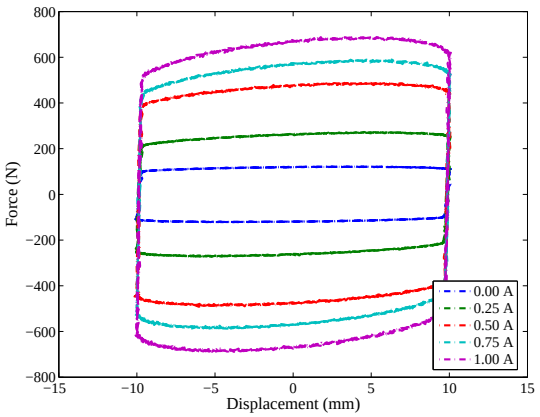

(c) 10 mm amplitude

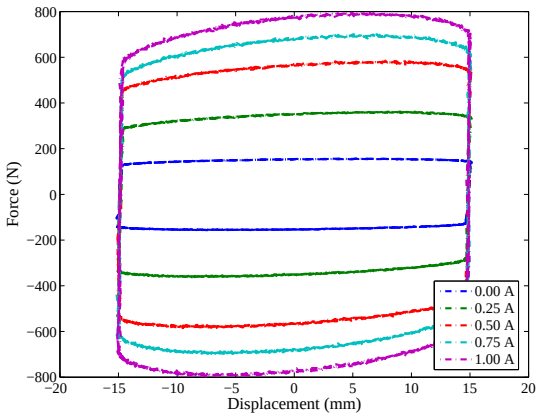

(d) 15 mm amplitude

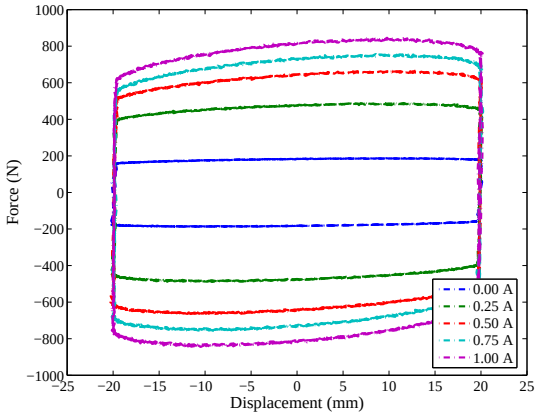

(e) 20 mm amplitude

Figure B.3: MR damper force-displacement hysteretic curves for ($\omega = 0.25$ Hz)

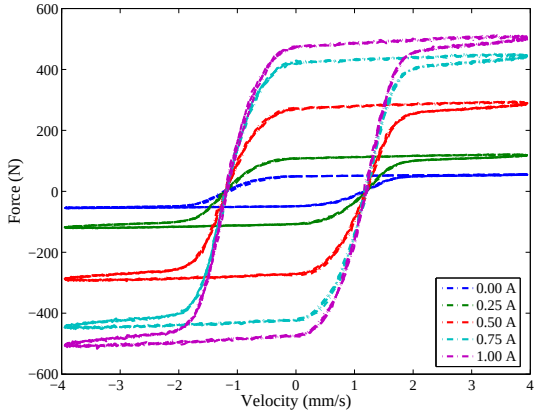

(a) 2.5 mm amplitude

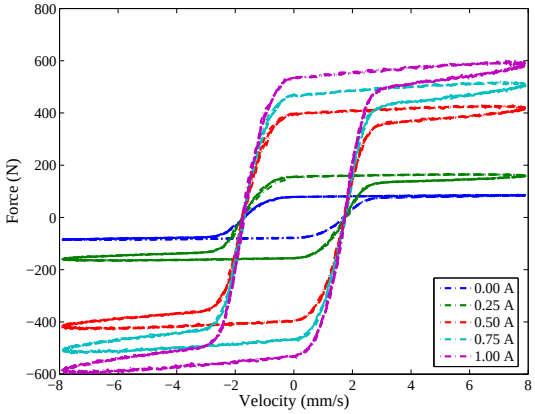

(b) 5.0 mm amplitude

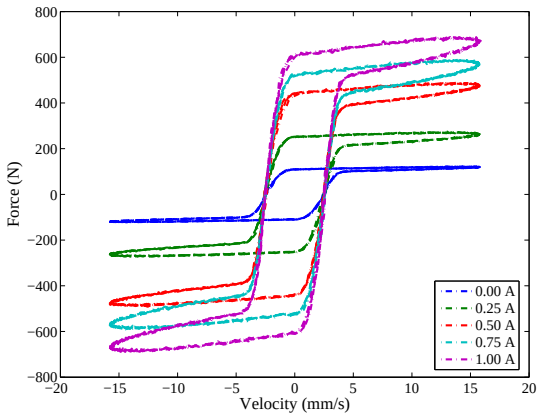

(c) 10 mm amplitude

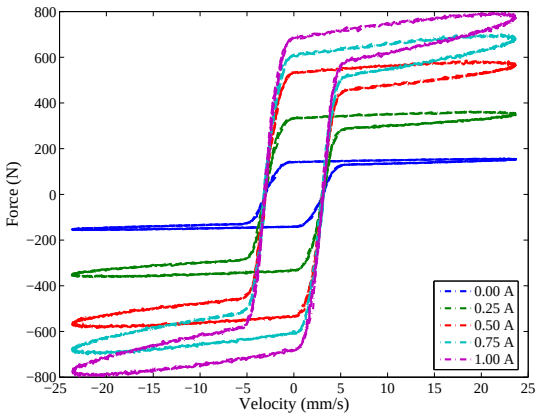

(d) 15 mm amplitude

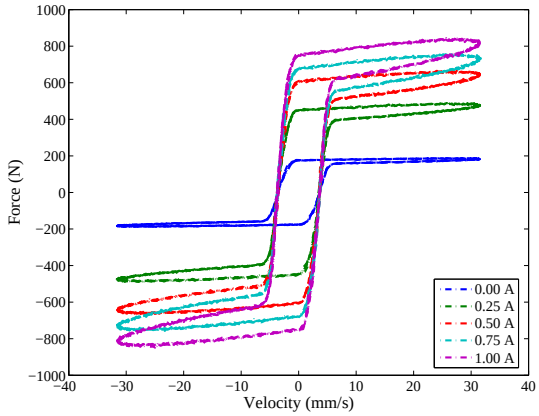

(e) 20 mm amplitude

Figure B.4: MR damper force-velocity hysteretic curves for ($\omega = 0.25$ Hz)

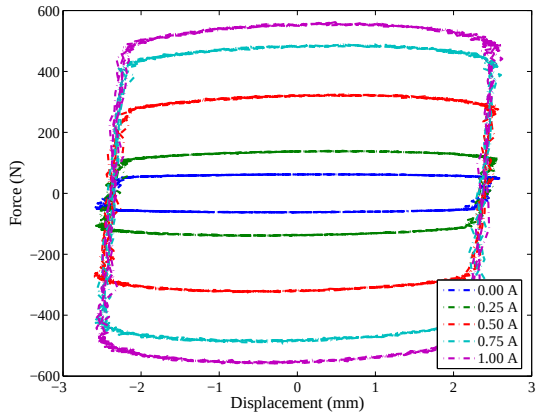

(a) 2.5 mm amplitude

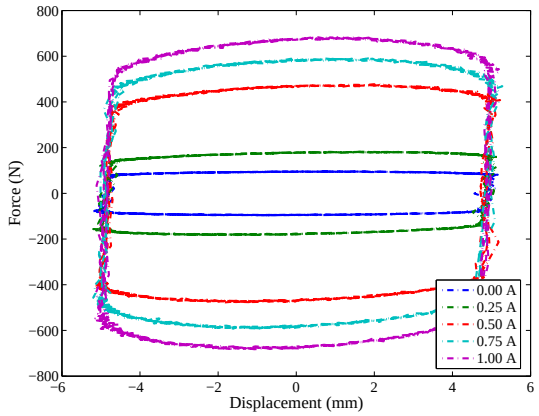

(b) 5.0 mm amplitude

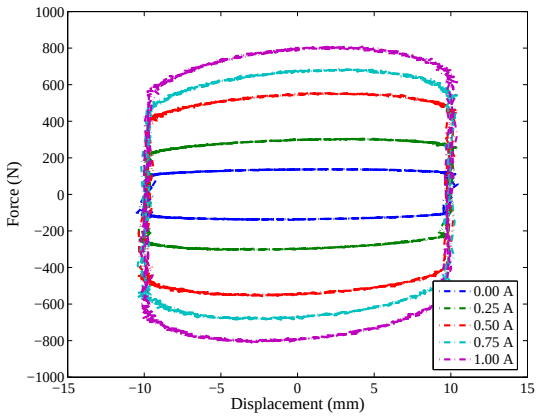

(c) 10 mm amplitude

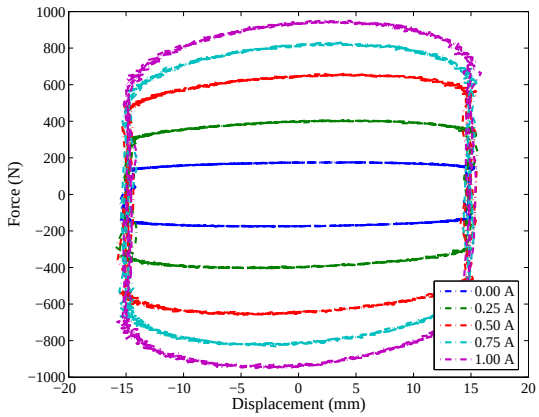

(d) 15 mm amplitude

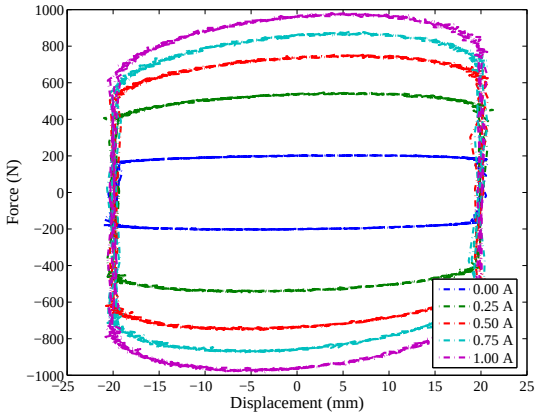

(e) 20 mm amplitude

Figure B.5: MR damper force-displacement hysteretic curves for ($\omega = 0.5$ Hz)

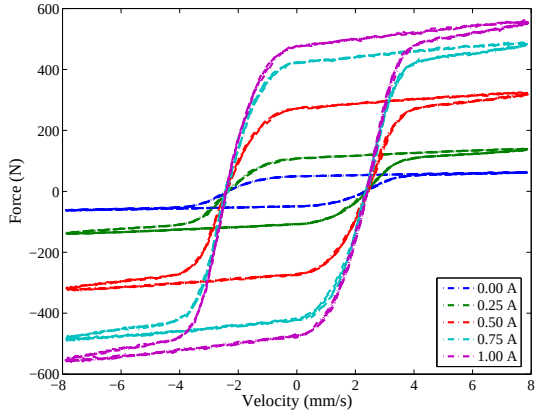

(a) 2.5 mm amplitude

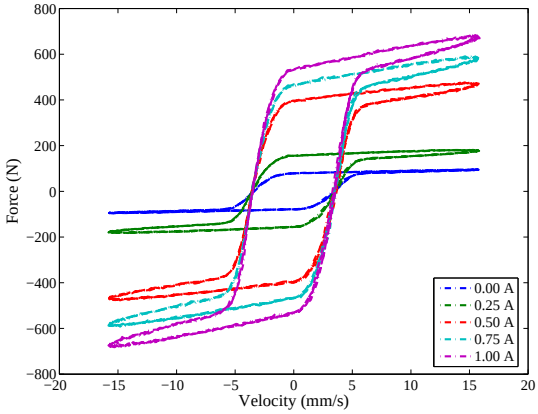

(b) 5.0 mm amplitude

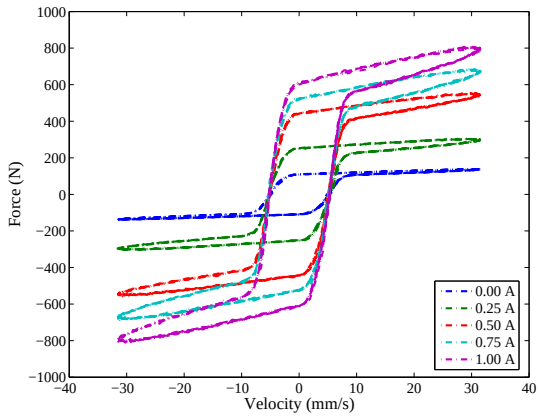

(c) 10 mm amplitude

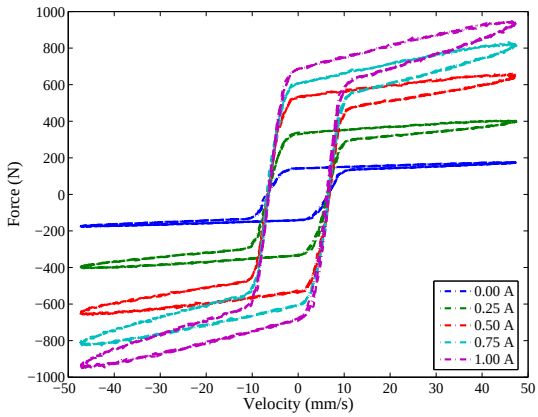

(d) 15 mm amplitude

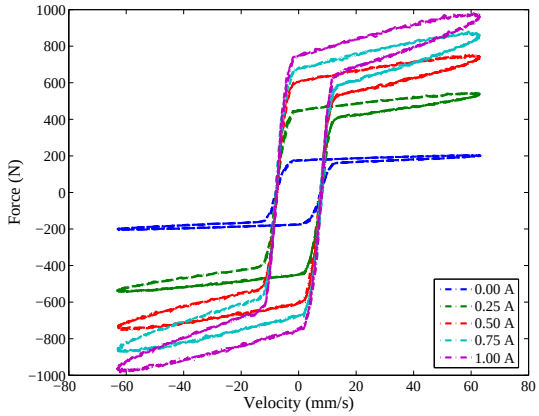

(e) 20 mm amplitude

Figure B.6: MR damper force-velocity hysteretic curves for ($\omega = 0.5$ Hz)

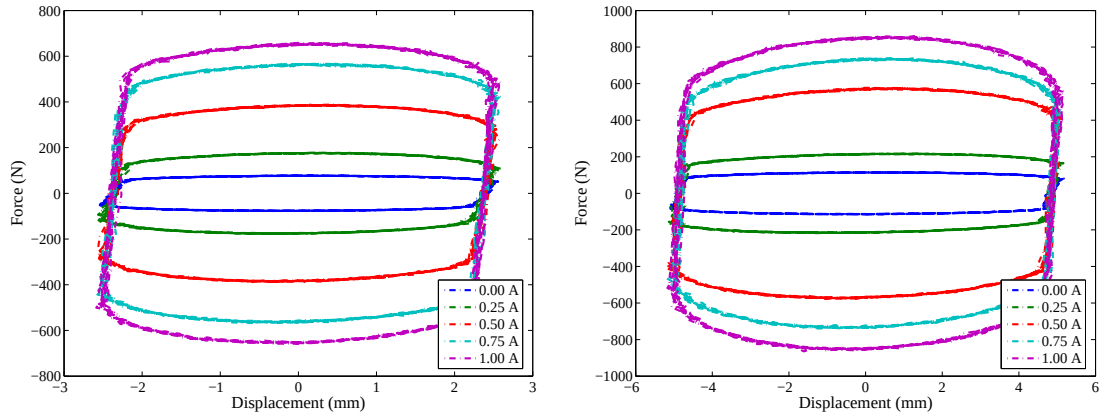

(a) 2.5 mm amplitude

(b) 5.0 mm amplitude

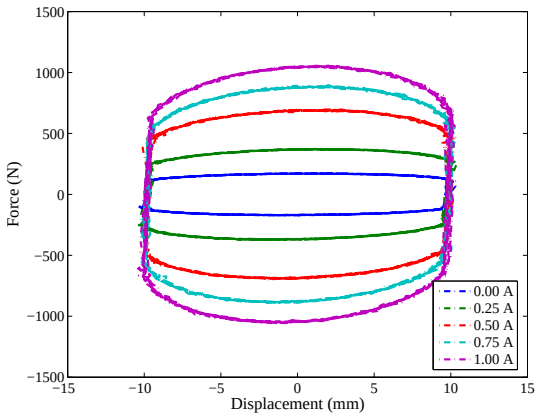

(c) 10 mm amplitude

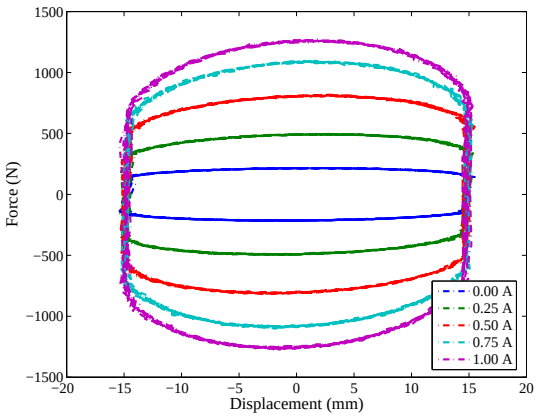

(d) 15 mm amplitude

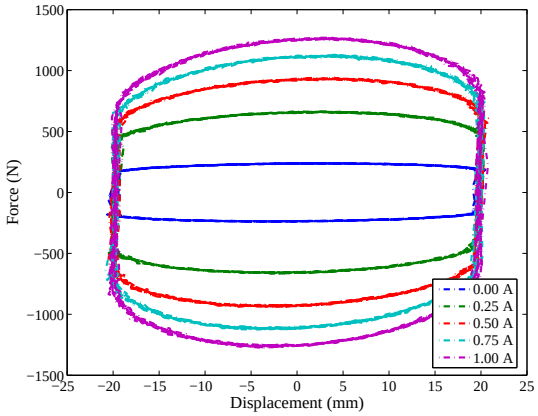

(e) 20 mm amplitude

Figure B.7: MR damper force-displacement hysteretic curves for ($\omega = 1.0$ Hz)

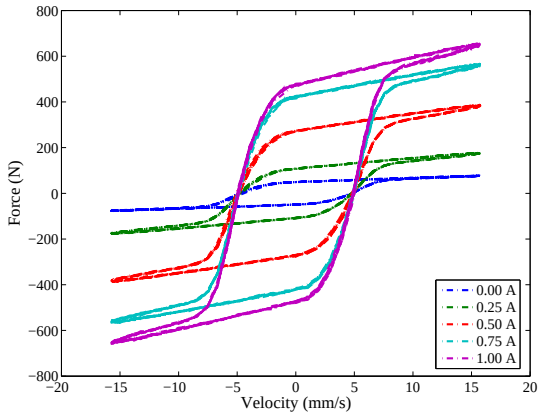

(a) 2.5 mm amplitude

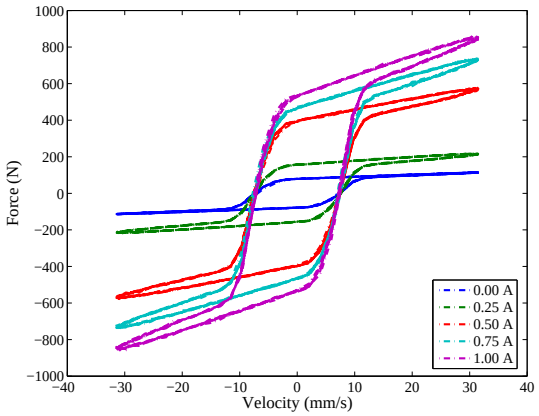

(b) 5.0 mm amplitude

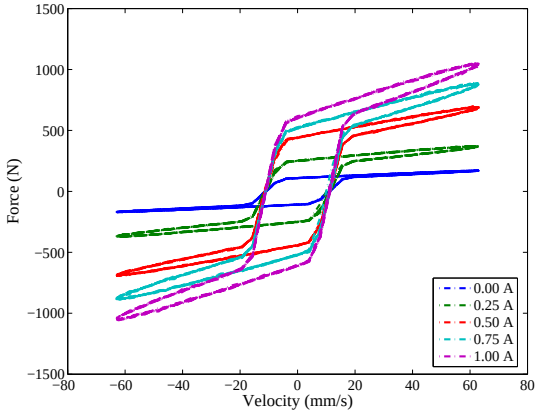

(c) 10 mm amplitude

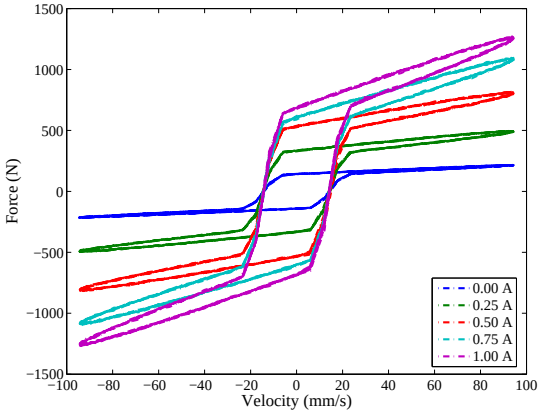

(d) 15 mm amplitude

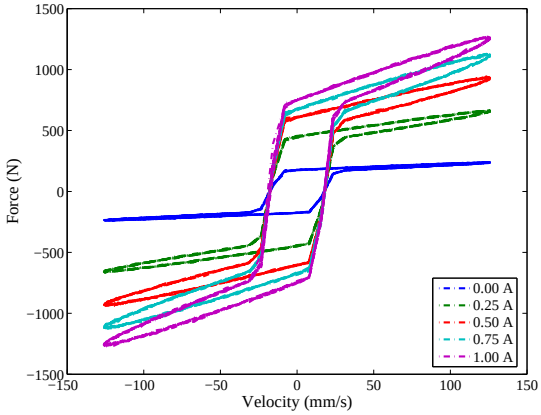

(e) 20 mm amplitude

Figure B.8: MR damper force-velocity hysteretic curves for ($\omega = 1.0$ Hz)

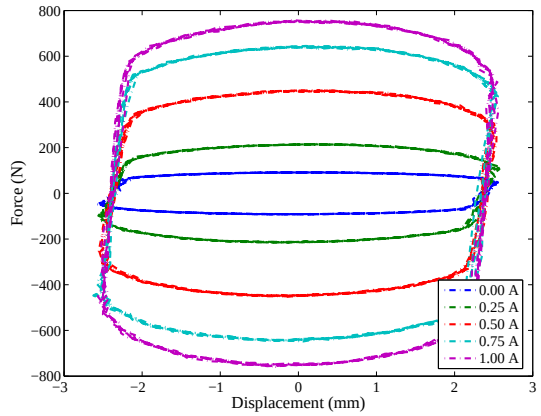

(a) 2.5 mm amplitude

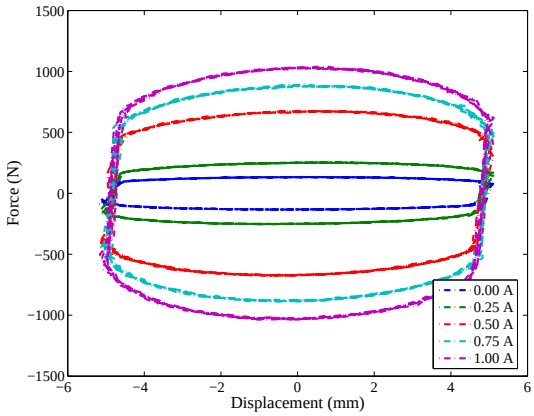

(b) 5.0 mm amplitude

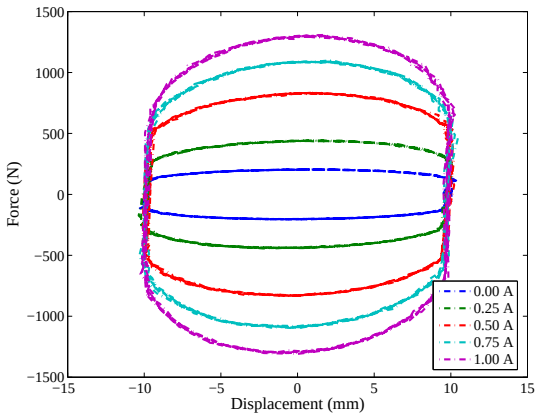

(c) 10 mm amplitude

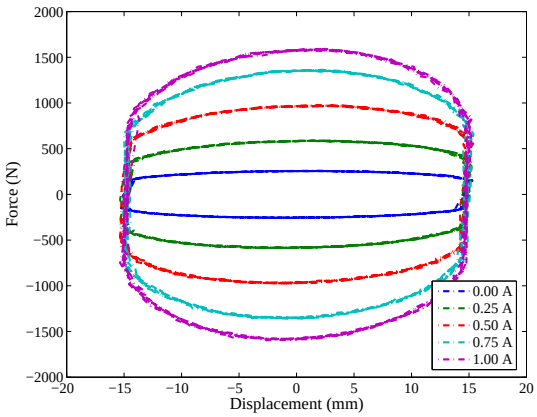

(d) 15 mm amplitude

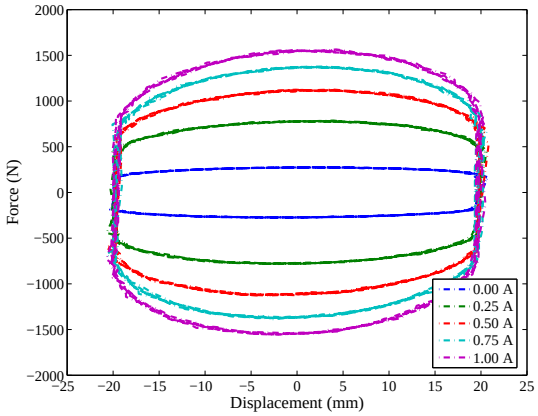

(e) 20 mm amplitude

Figure B.9: MR damper force-displacement hysteretic curves for ($\omega = 1.5$ Hz)

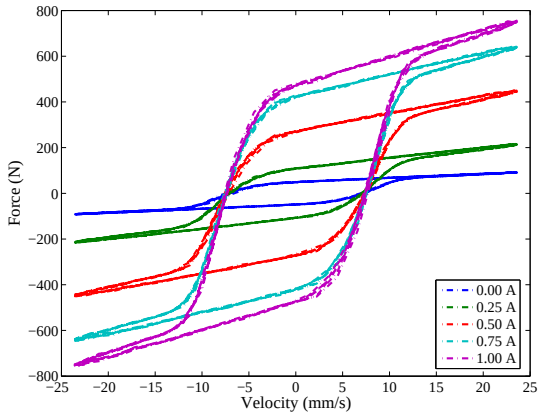

(a) 2.5 mm amplitude

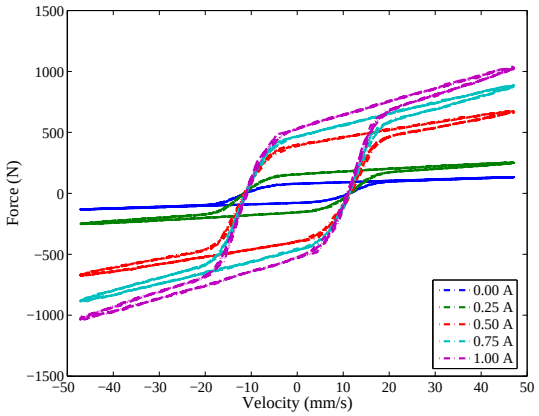

(b) 5.0 mm amplitude

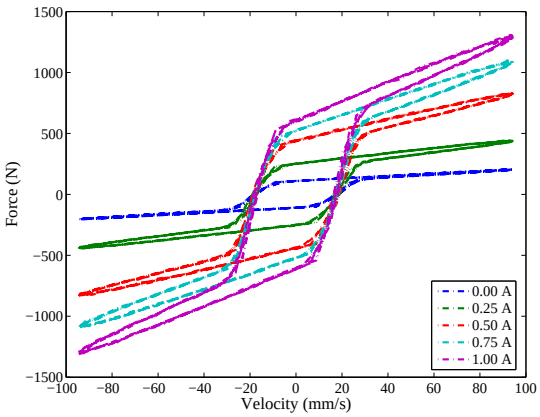

(c) 10 mm amplitude

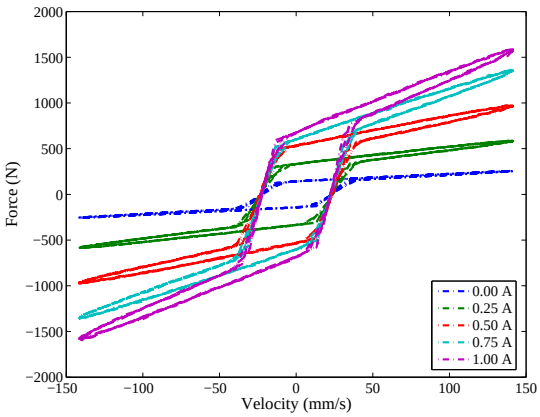

(d) 15 mm amplitude

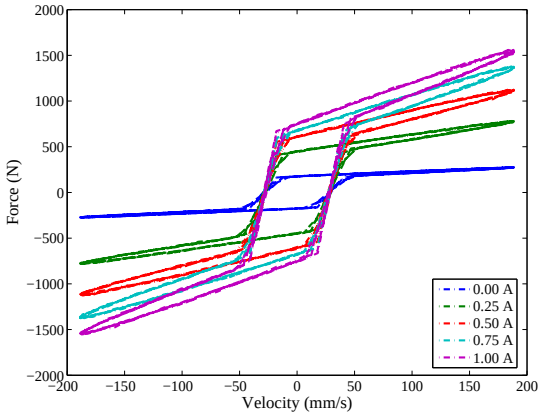

(e) 20 mm amplitude

Figure B.10: MR damper force-velocity hysteretic curves for ($\omega = 1.5$ Hz)

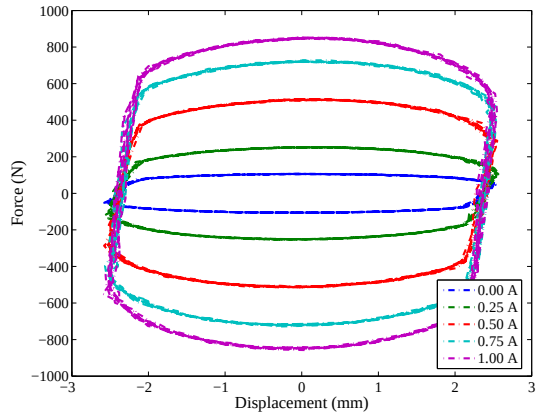

(a) 2.5 mm amplitude

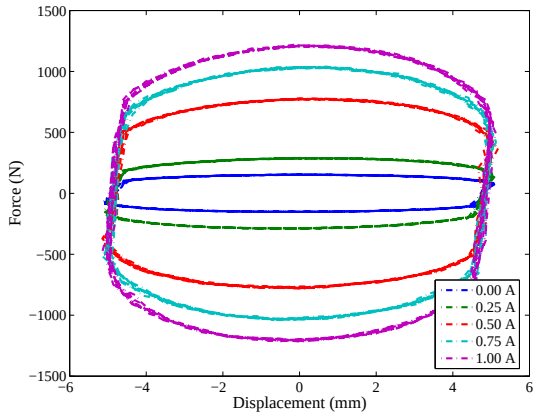

(b) 5.0 mm amplitude

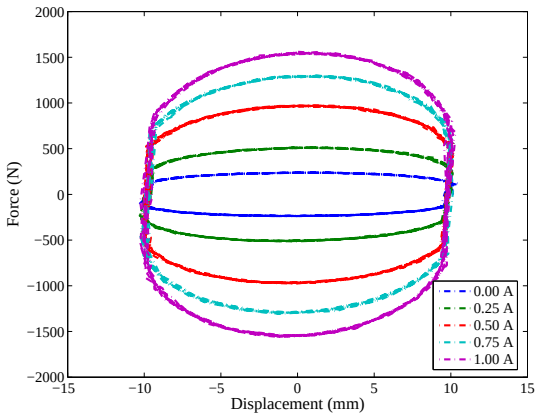

(c) 10 mm amplitude

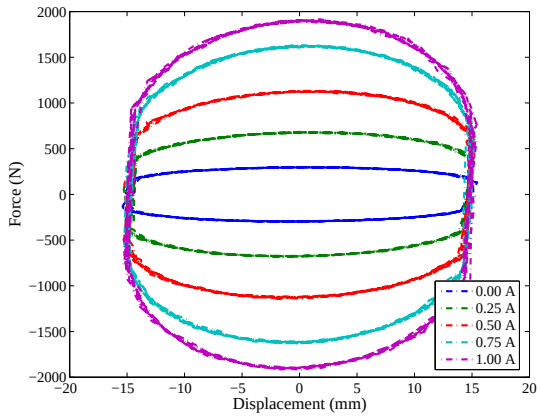

(d) 15 mm amplitude

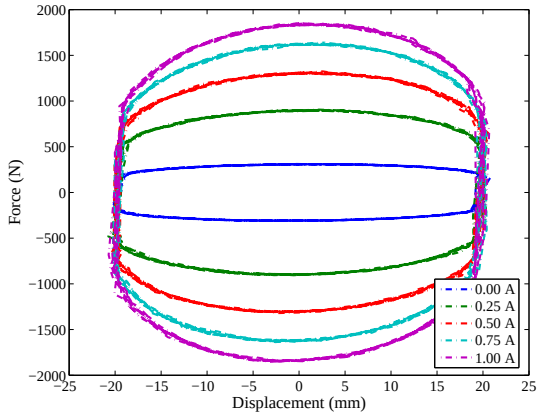

(e) 20 mm amplitude

Figure B.11: MR damper force-displacement hysteretic curves for ($\omega = 2.0$ Hz)

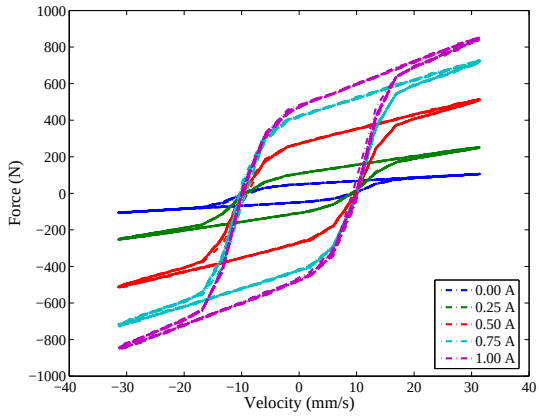

(a) 2.5 mm amplitude

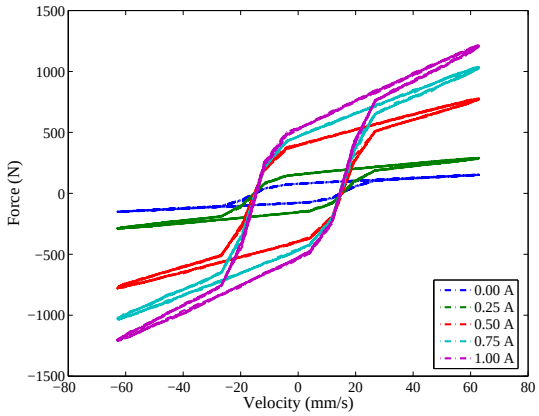

(b) 5.0 mm amplitude

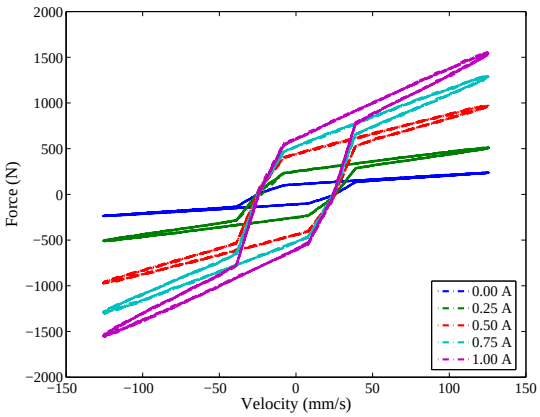

(c) 10 mm amplitude

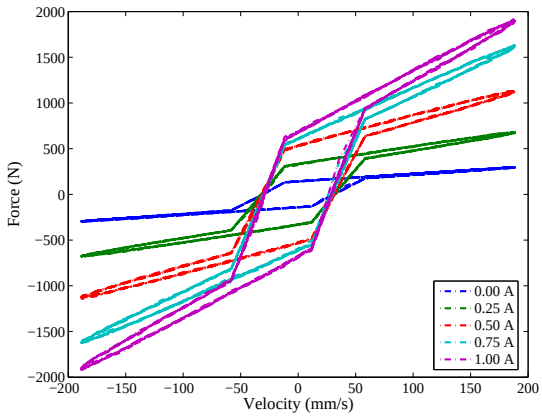

(d) 15 mm amplitude

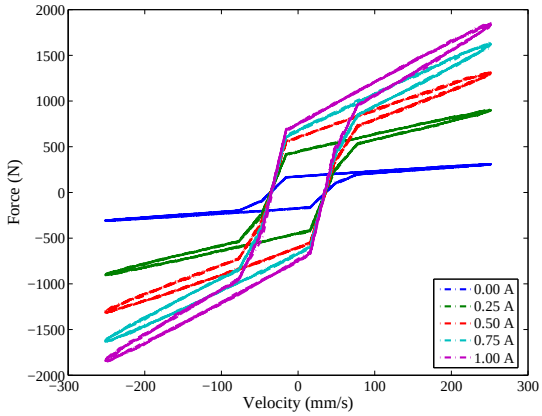

(e) 20 mm amplitude

Figure B.12: MR damper force-velocity hysteretic curves for ($\omega = 2.0$ Hz)

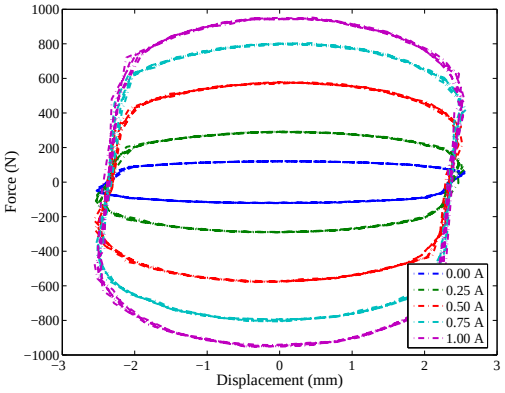

(a) 2.5 mm amplitude

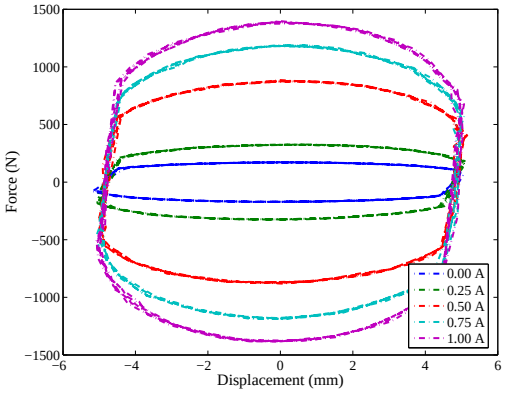

(b) 5.0 mm amplitude

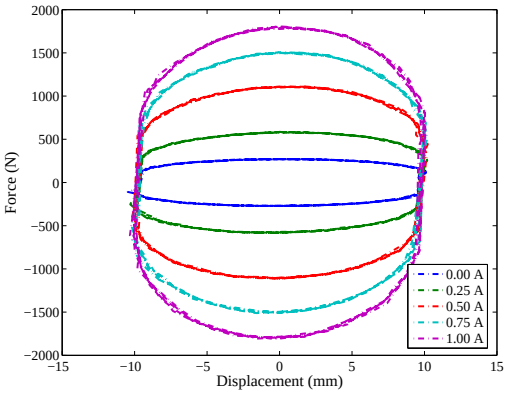

(c) 10 mm amplitude

Figure B.13: MR damper force-displacement hysteretic curves for ($\omega = 2.5$ Hz)

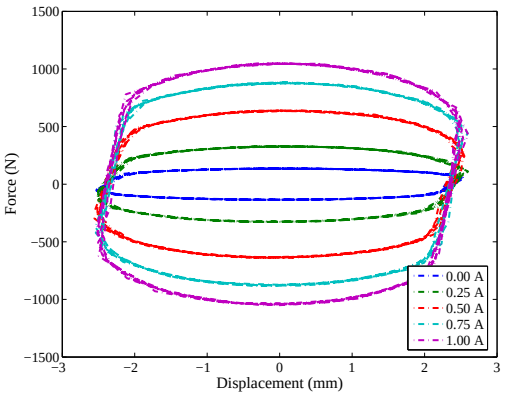

(a) 2.5 mm amplitude

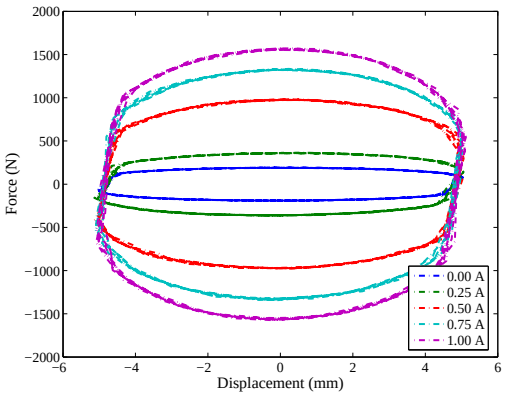

(b) 5.0 mm amplitude

Figure B.14: MR damper force-displacement hysteretic curves for ($\omega = 3.0$ Hz)

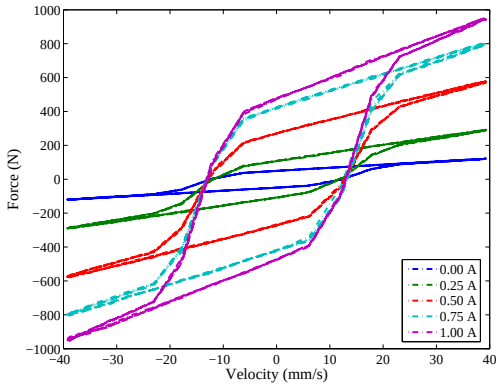

(a) 2.5 mm amplitude

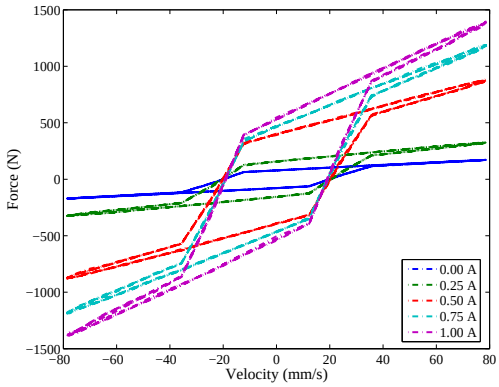

(b) 5.0 mm amplitude

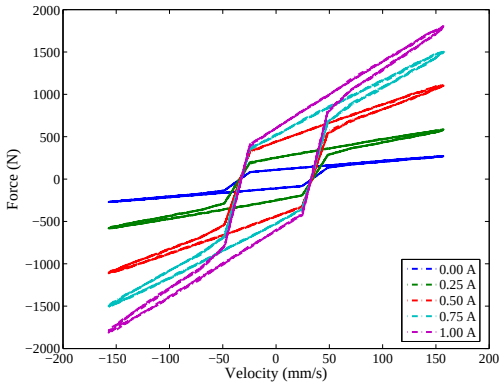

(c) 10 mm amplitude

Figure B.15: MR damper force-velocity hysteretic curves for ($\omega = 2.5$ Hz)

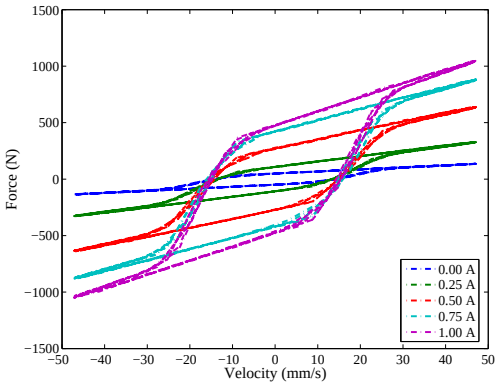

(a) 2.5 mm amplitude

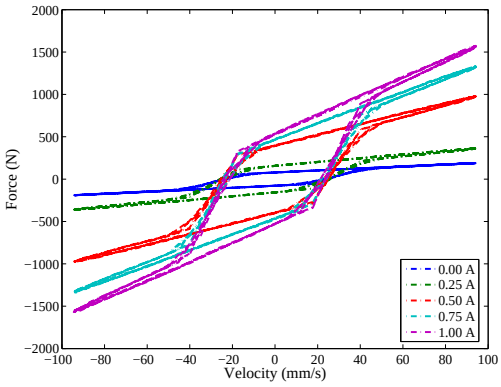

(b) 5.0 mm amplitude

Figure B.16: MR damper force-velocity hysteretic curves for ($\omega = 3.0$ Hz)

Appendix C

Building Control Experimental Results

Overview

Extensive experimental results of the hybrid base isolated three storey building have been presented here. The experimental investigation has been carried out for,

- Fixed base building
- Simple base isolated building
- Hybrid base isolated building: 'passive-off' case
- Hybrid base isolated building: 'passive-on' case
- Hybrid base isolated building: 'SFLC' case
- Hybrid base isolated building: 'GAFLC' case

Five accelerometers, three capacitance type LVDT and two spring LVDT have been connected to the building to measure the responses at various floor levels. One force transducer has been connected between the MR damper and the base isolator to measure the damper force. Eight seismic record considering X and Y components of motions have been considered to investigate the controller performance. Therefore at total of sixteen earthquake records have been employed for the study. Details of the experimental study with a few earthquake results have been provided in chapter 5. In the present appendix a complete set of time histories have been provided under all seismic records.

The results are reported in a way, such that information regarding a response can be observed for all control strategies together. Figures are provided for the displacement and acceleration time histories at the base isolator and at the third floor as a representation of the superstructure response. Control force provided by the MR damper at the four control cases has also been reported. Peak response have been tabulated to compare responses across all control test cases.

Big Bear X-direction seismic motion

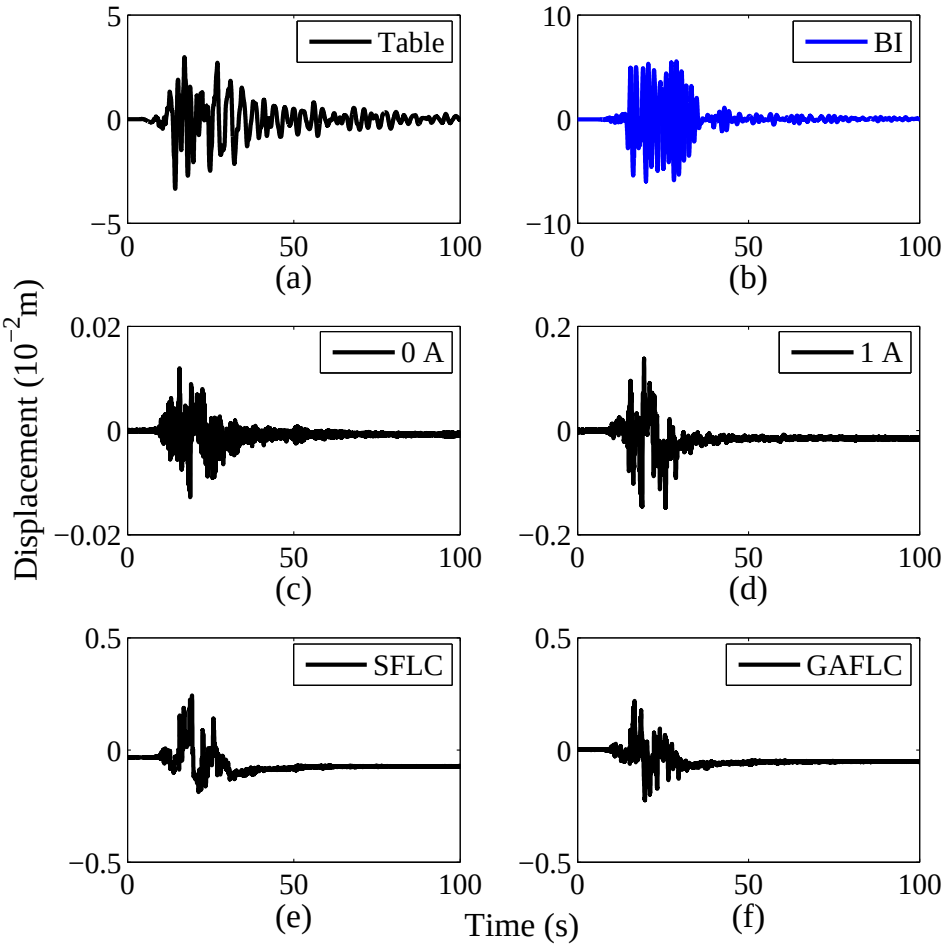

Figure C.1: Displacement time history at (a) Shake table, (b)-(f) Base isolator (Big Bear (X-dir))

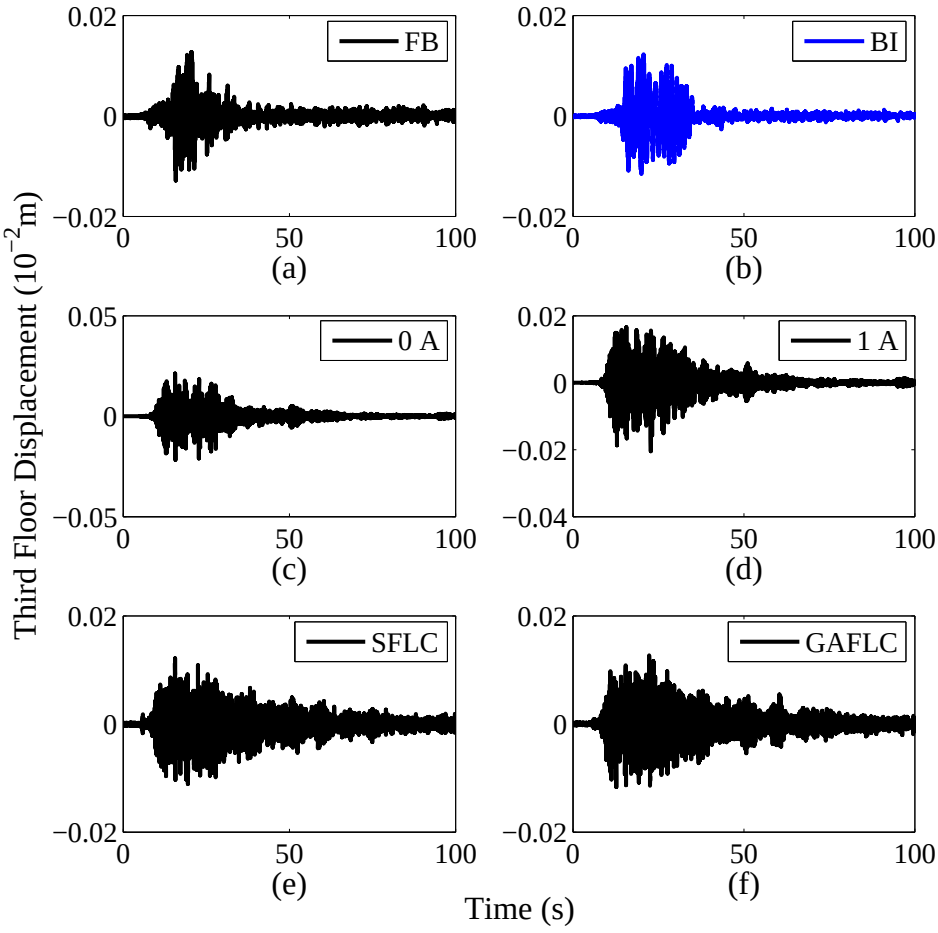

Figure C.2: 3^{rd} floor displacement time history (Big Bear (X-dir))

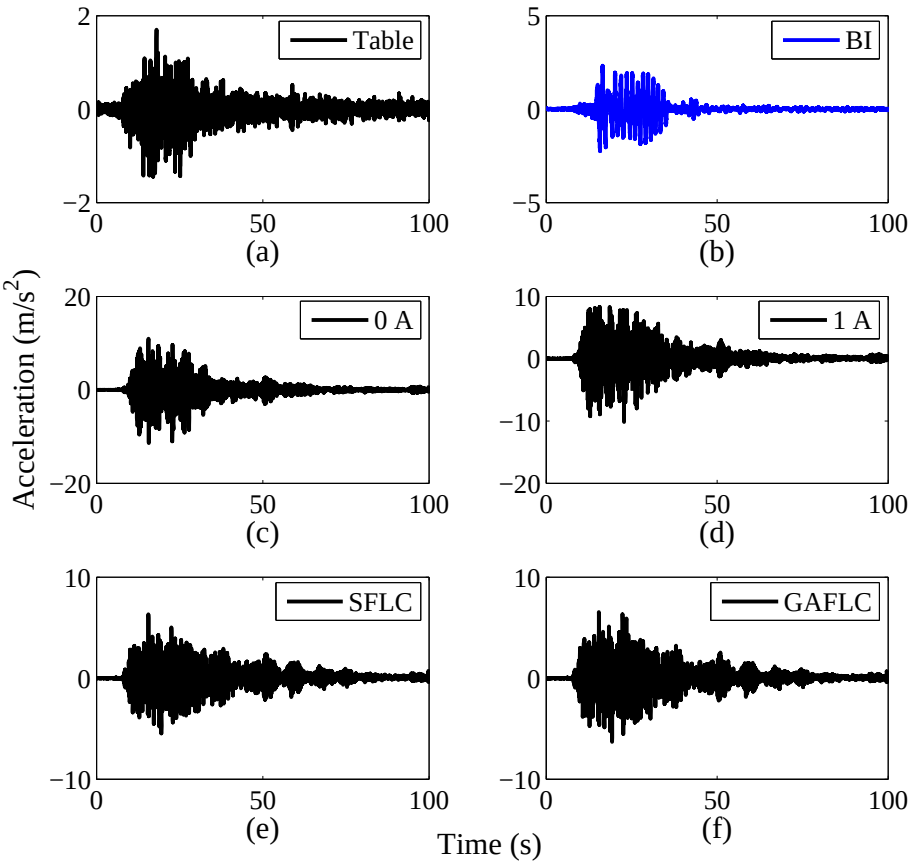

Figure C.3: Acceleration time history at (a) Shake table, (b)-(f) Base isolator (Big Bear (X-dir))

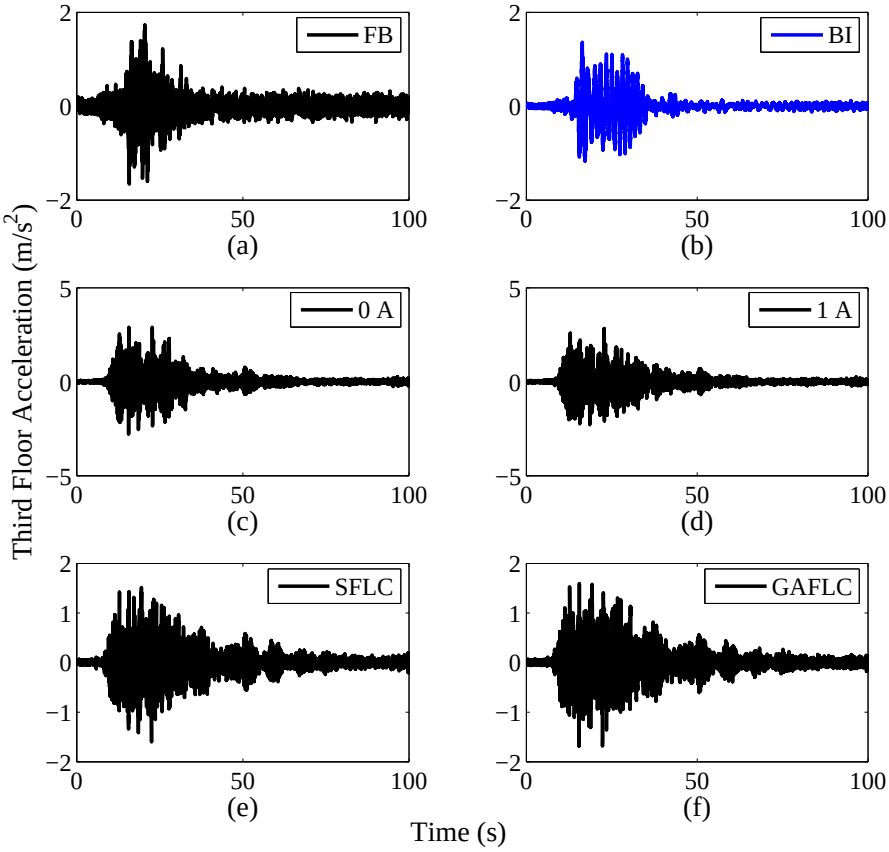

Figure C.4: 3^{rd} floor acceleration time history (Big Bear (X-dir))

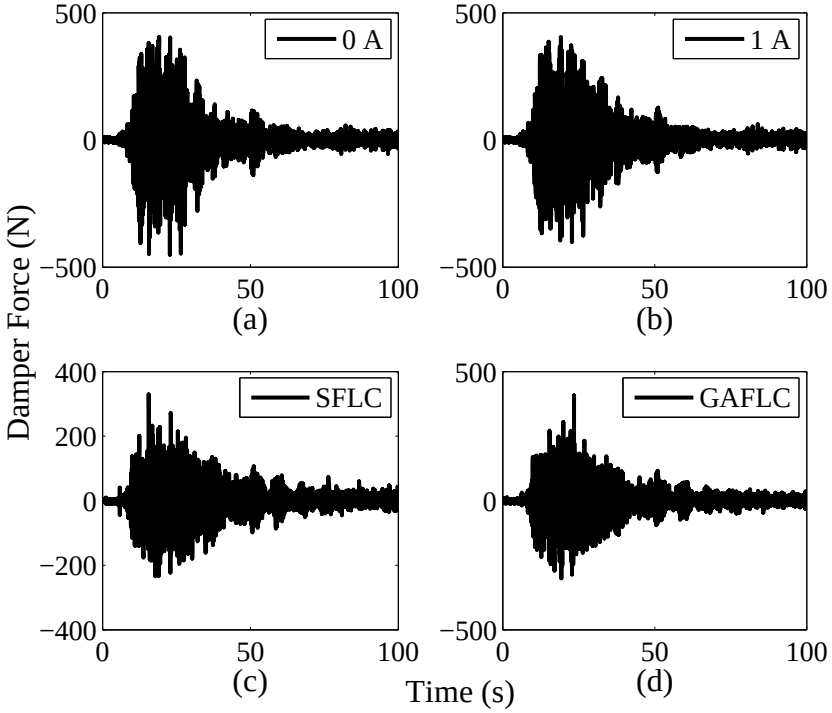

Figure C.5: MR damper force time history (Big Bear (X-dir))

Table C.1: Peak responses under Big Bear (X-direction) earthquake

Test Case	**Relative Displacements** ($\times 10^{-2}$ m)				**Floor Accelerations** (m/s^2)			
	BI	*FF*	*SF*	*TF*	*BI*	*FF*	*SF*	*TF*
Fixed Base	–	0.0641	0.0229	0.0129	–	1.5712	1.5071	1.7265
Base Isolated	5.9849	0.0662	0.0259	0.0123	2.3293	1.2735	1.2822	1.3627
Passive-off (0A)	0.0128	0.1506	0.0449	0.0217	11.4094	2.1940	2.7166	2.9024
Passive-on (1A)	0.1484	0.1354	0.0379	0.0204	10.1683	1.9244	2.4154	2.8289
SFLC	0.2429	0.0804	0.0647	0.0122	6.3197	1.5161	1.4067	1.6006
GAFLC	0.2240	0.0871	0.0250	0.0127	6.5412	1.4652	1.6480	1.6832
BI: *Base Isolator* *FF*: 1^{st} *floor* *SF*: 2^{nd} *floor* *TF*: 3^{rd} *floor*								

Big Bear Y-direction seismic motion

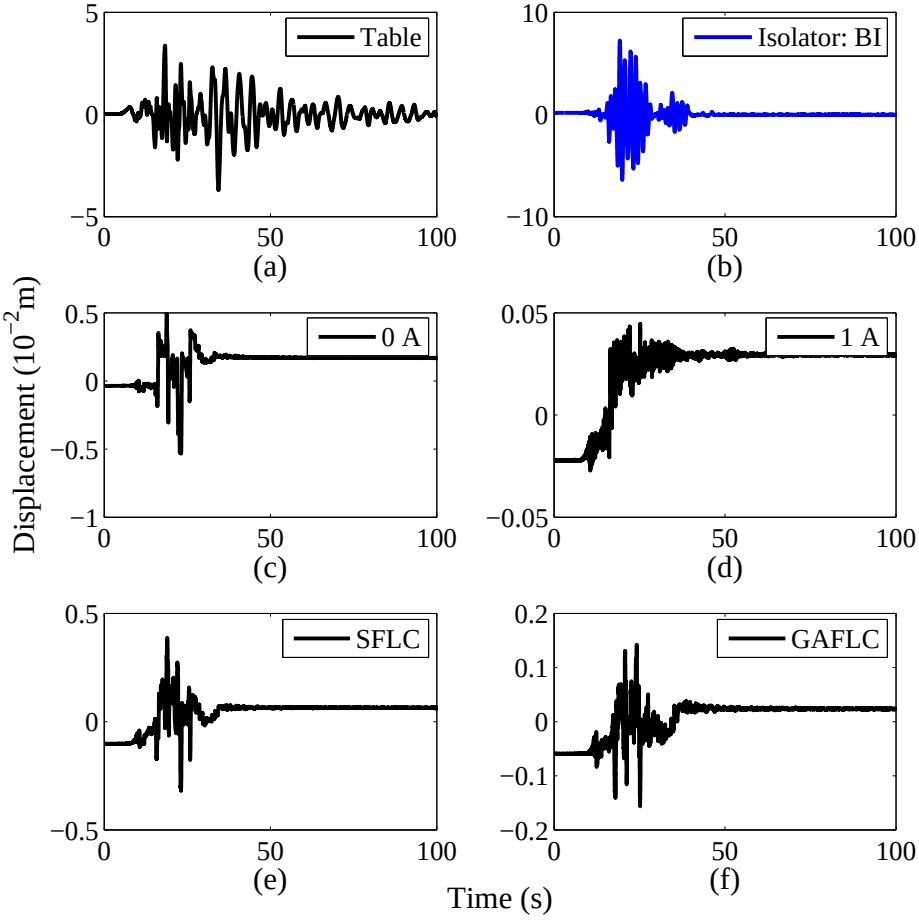

Figure C.6: Displacement time history at (a) Shake table, (b)-(f) Base isolator (Big Bear (Y-dir))

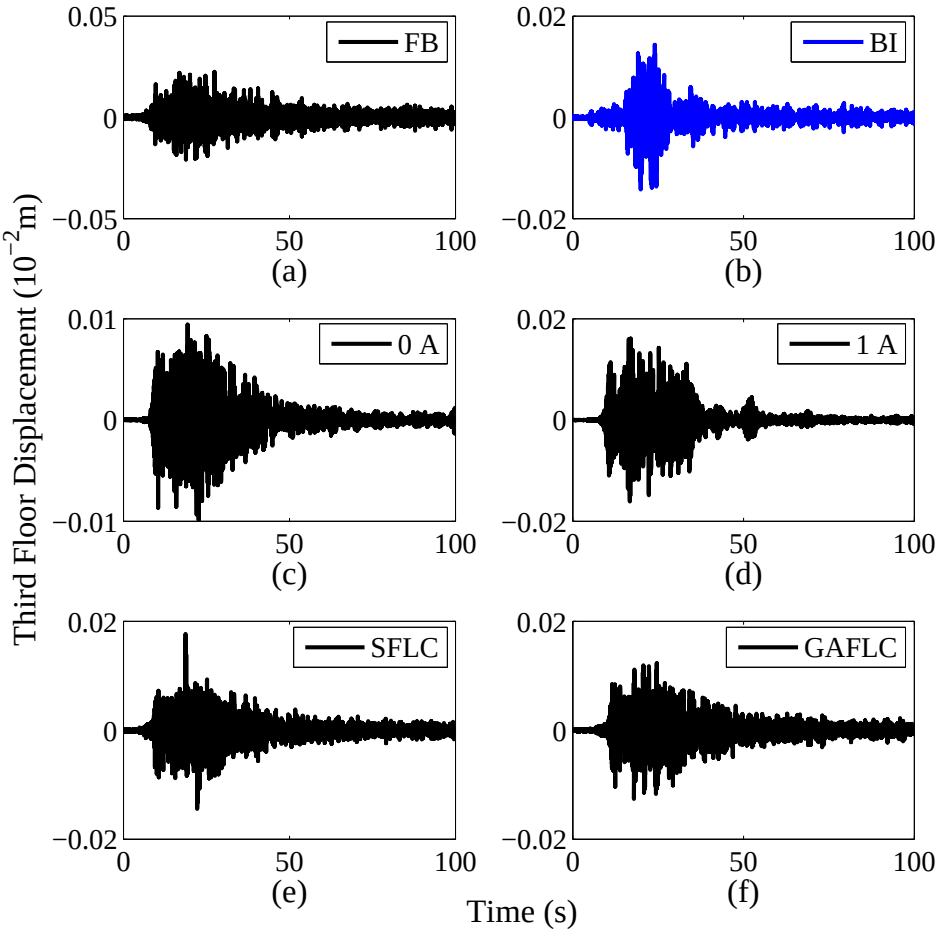

Figure C.7: 3^{rd} floor displacement time history (Big Bear (Y-dir))

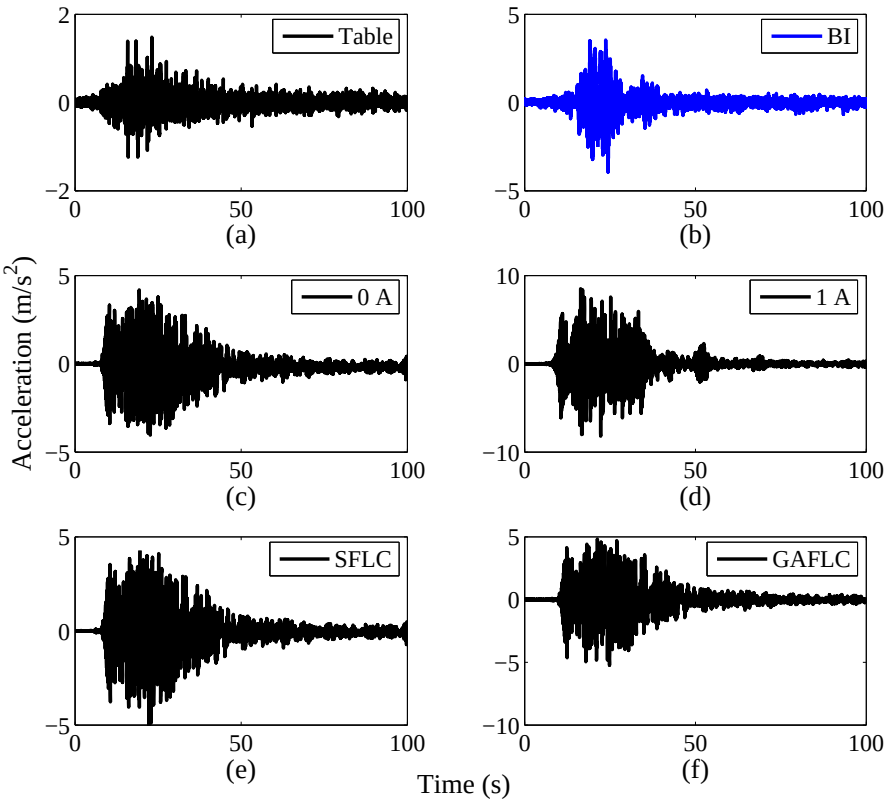

Figure C.8: Acceleration time history at (a) Shake table, (b)-(f) Base isolator (Big Bear (Y-dir))

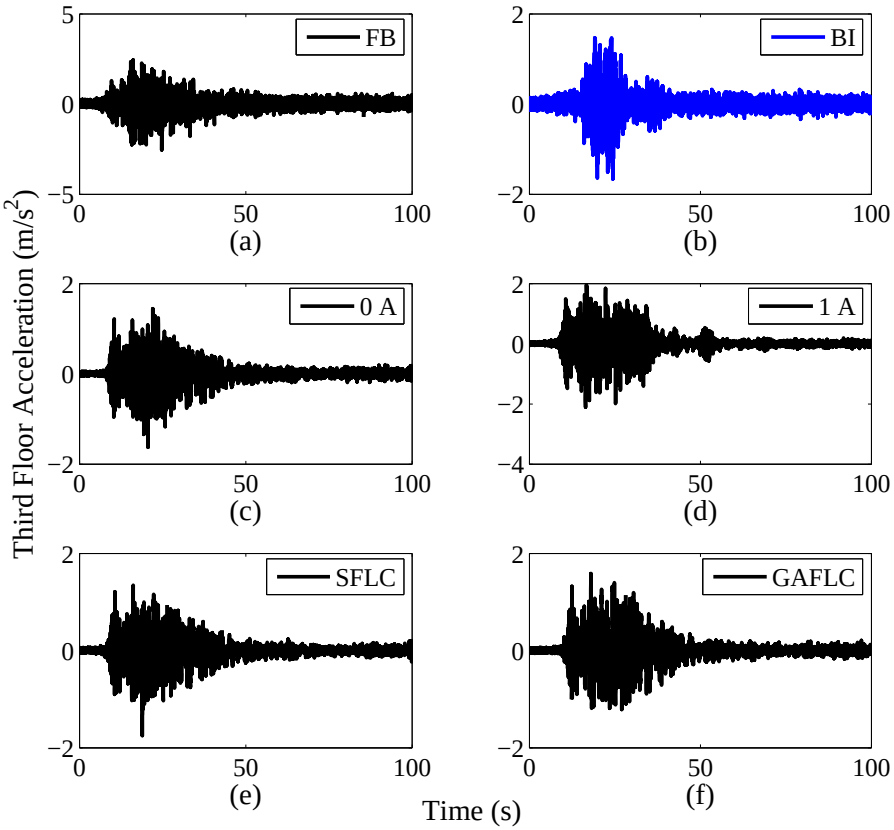

Figure C.9: 3^{rd} floor acceleration time history (Big Bear (Y-dir))

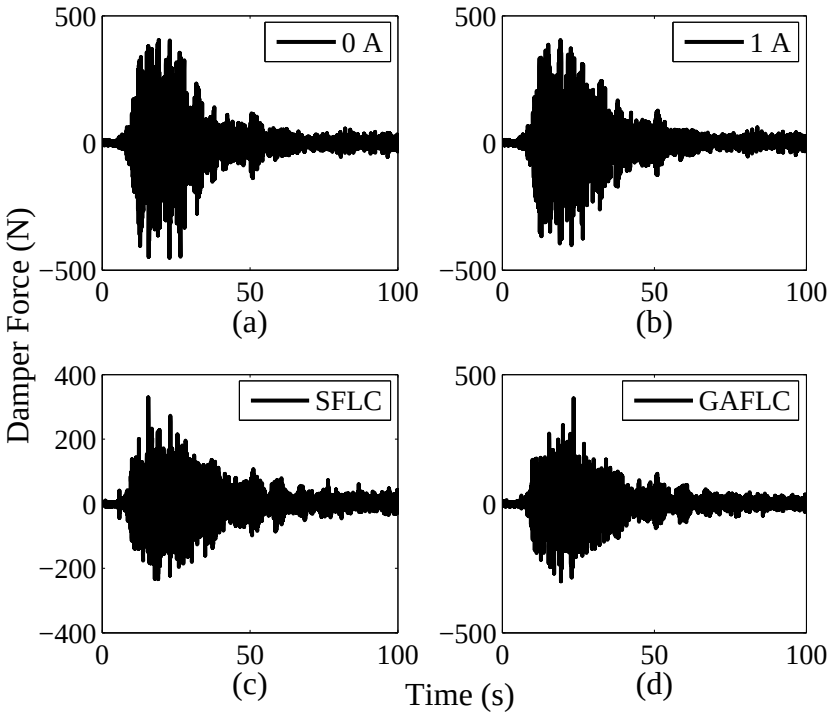

Figure C.10: MR damper force time history (Big Bear (Y-dir))

Table C.2: Peak responses under Big Bear (Y-direction) earthquake

Test Case	**Relative Displacements** ($\times 10^{-2}\ m$)				**Floor Accelerations** (m/s^2)			
	BI	*FF*	*SF*	*TF*	*BI*	*FF*	*SF*	*TF*
Fixed Base	–	0.1773	0.0452	0.0224	–	2.7127	2.3691	2.5442
Base Isolated	7.2412	0.0768	0.0258	0.0143	3.9361	1.6910	1.3422	1.6607
0A	0.5339	0.0584	0.0193	0.0099	4.1896	1.0908	1.1983	1.6247
1A	0.0446	0.1131	0.0343	0.0161	8.5066	1.7246	2.0392	2.1035
SFLC	0.3873	0.0874	0.2220	0.0177	4.9990	1.7171	1.4907	1.7496
GAFLC	0.1565	0.0691	0.0230	0.0126	5.2248	1.3061	1.3800	1.5866
BI: *Base Isolator*	*FF*: 1^{st} *floor*		*SF*: 2^{nd} *floor*		*TF*: 3^{rd} *floor*			

Capemend X-direction seismic motion

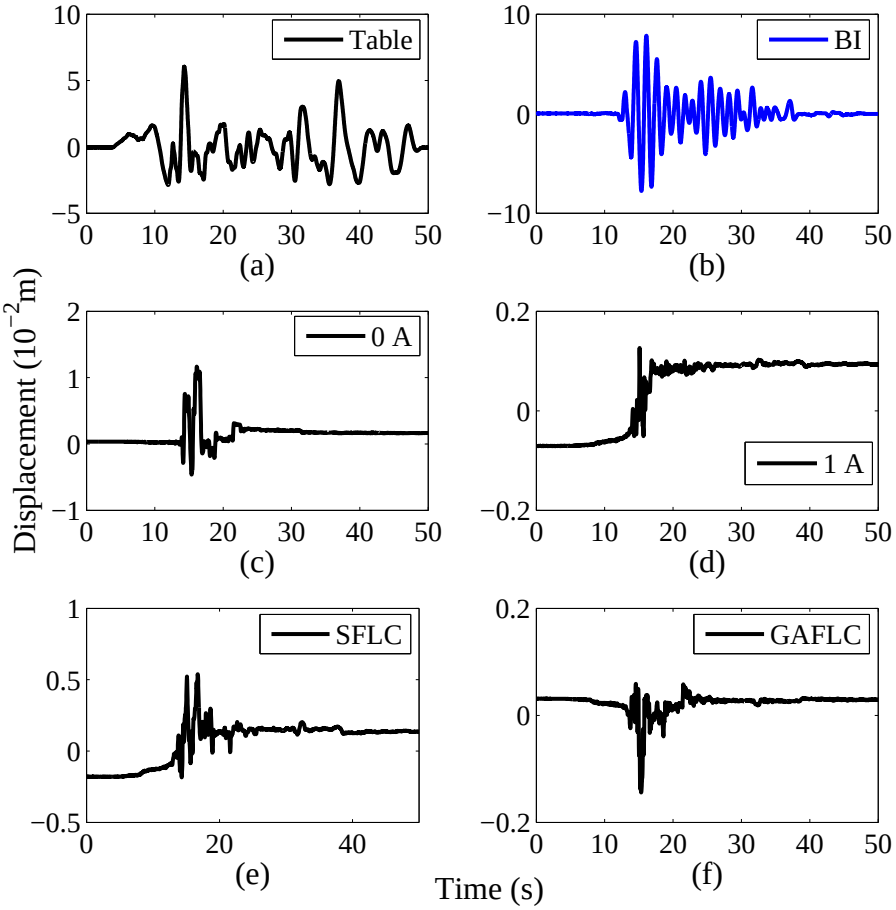

Figure C.11: Displacement time history at (a) shake Table, (b)-(f) Base isolator (Capemend (X-dir))

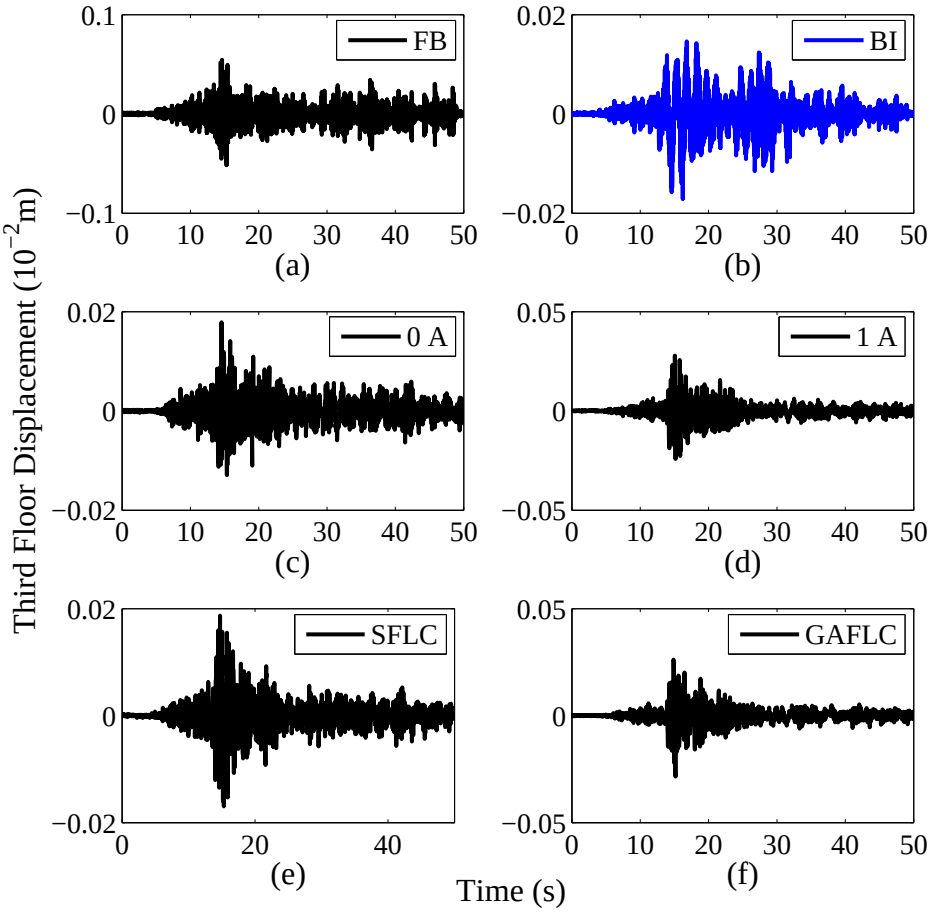

Figure C.12: 3^{rd} floor displacement time history (Capemend (X-dir))

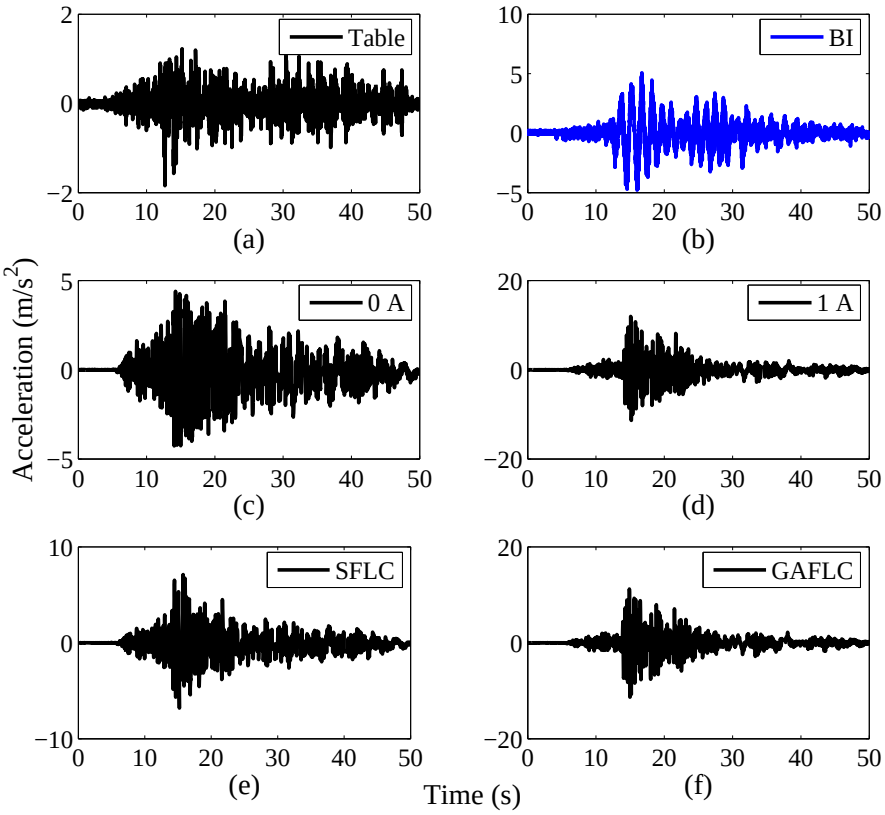

Figure C.13: Acceleration time history at (a) shake Table, (b)-(f) Base isolator (Capemend (X-dir))

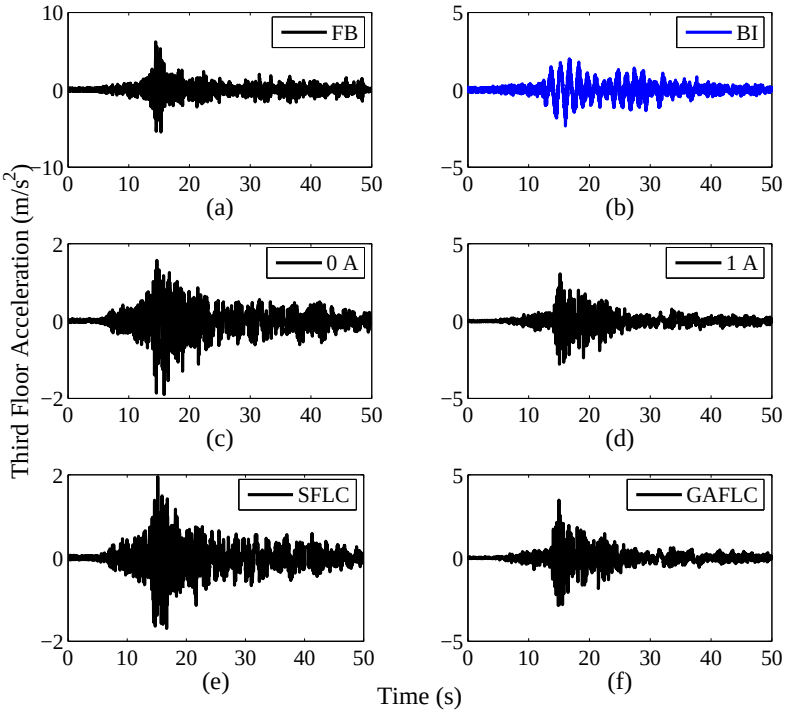

Figure C.14: 3^{rd} floor acceleration time history (Capemend (X-dir))

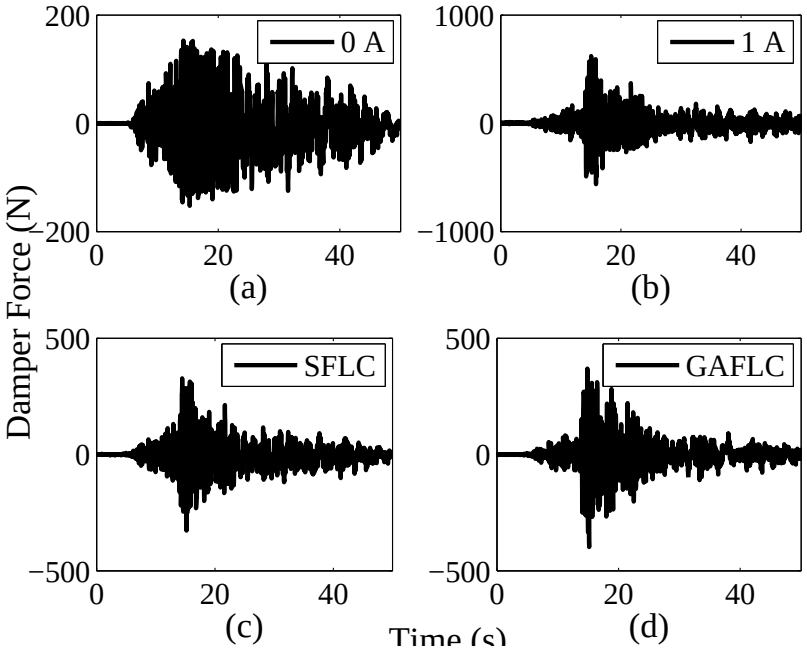

Figure C.15: MR damper force time history (Capemend (X-dir))

Table C.3: Peak responses under Capemend (X-direction) earthquake

Test Case	**Relative Displacements** ($\times 10^{-2}\ m$)				**Floor Accelerations** (m/s^2)			
	BI	*FF*	*SF*	*TF*	*BI*	*FF*	*SF*	*TF*
Fixed Base	–	0.4375	0.1188	0.0545	–	4.4919	5.8279	6.2105
Base Isolated	7.8382	0.0961	0.0351	0.0171	5.0788	1.9687	1.8653	2.3354
0A	1.1664	0.0709	0.0248	0.0179	4.3972	1.7055	1.3243	1.9015
1A	0.1262	0.1696	0.0524	0.0279	11.9615	2.4096	2.8457	3.0473
SFLC	0.5384	0.1130	0.0302	0.0187	7.1158	1.7588	1.5541	1.9560
GAFLC	0.1441	0.1682	0.0492	0.0284	11.3377	2.7468	3.2063	3.4758
BI: *Base Isolator*		*FF*: 1^{st} *floor*		*SF*: 2^{nd} *floor*		*TF*: 3^{rd} *floor*		

Capemend Y-direction seismic motion

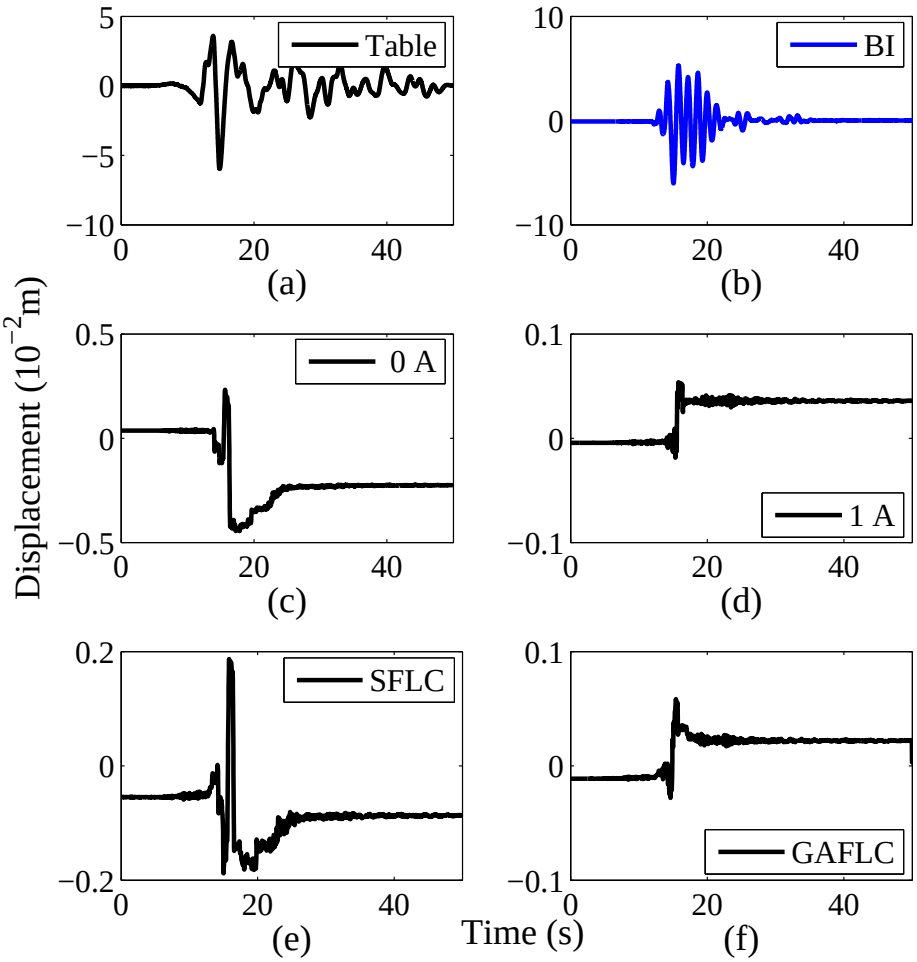

Figure C.16: Displacement time history at (a) Shake table, (b)-(f) Base isolator (Capemend (Y-dir))

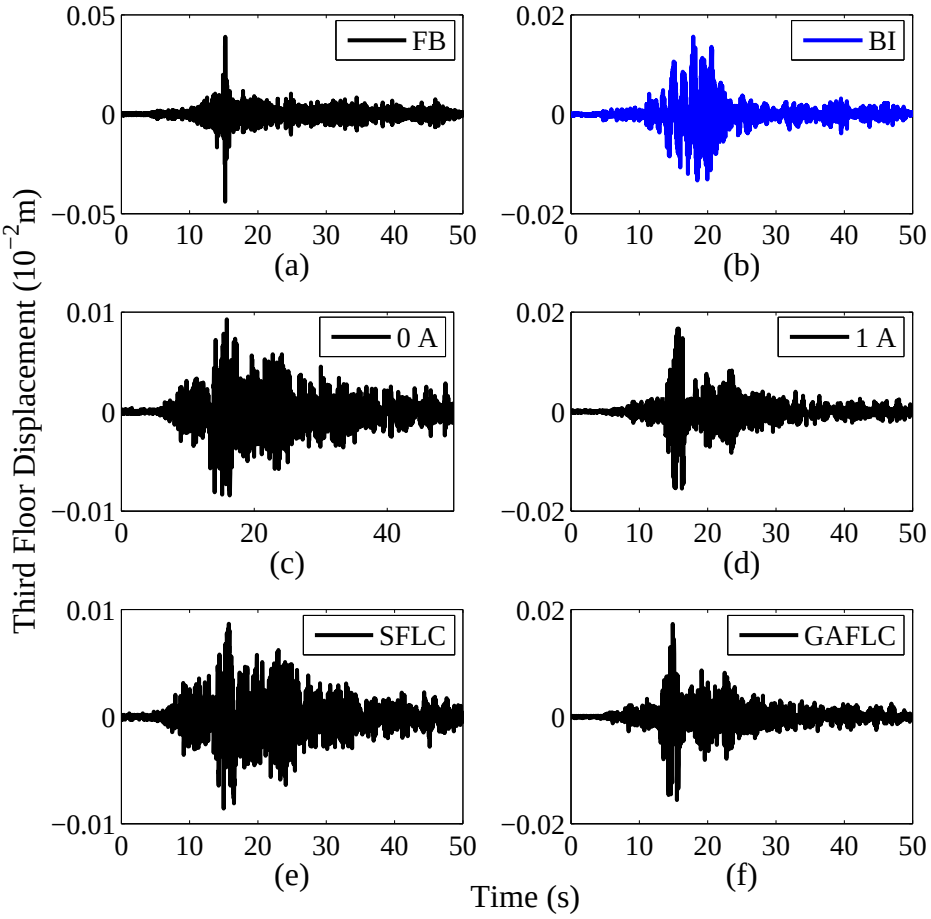

Figure C.17: 3^{rd} floor displacement time history (Capemend (Y-dir))

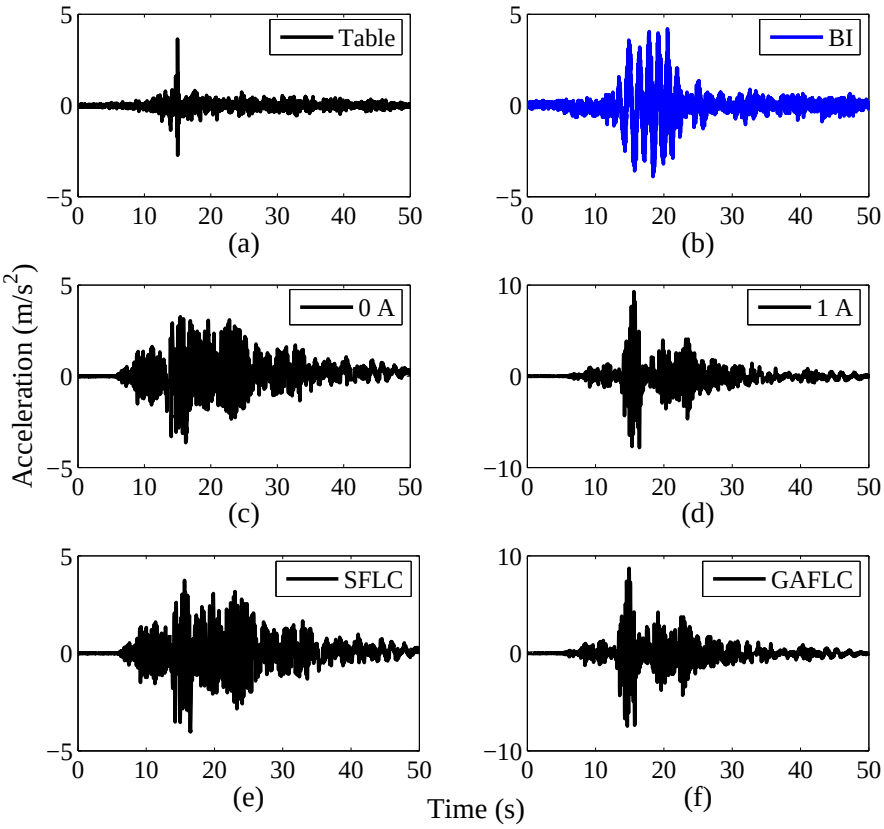

Figure C.18: Acceleration time history at (a) Shake table, (b)-(f) Base isolator Capemend (Y-dir)

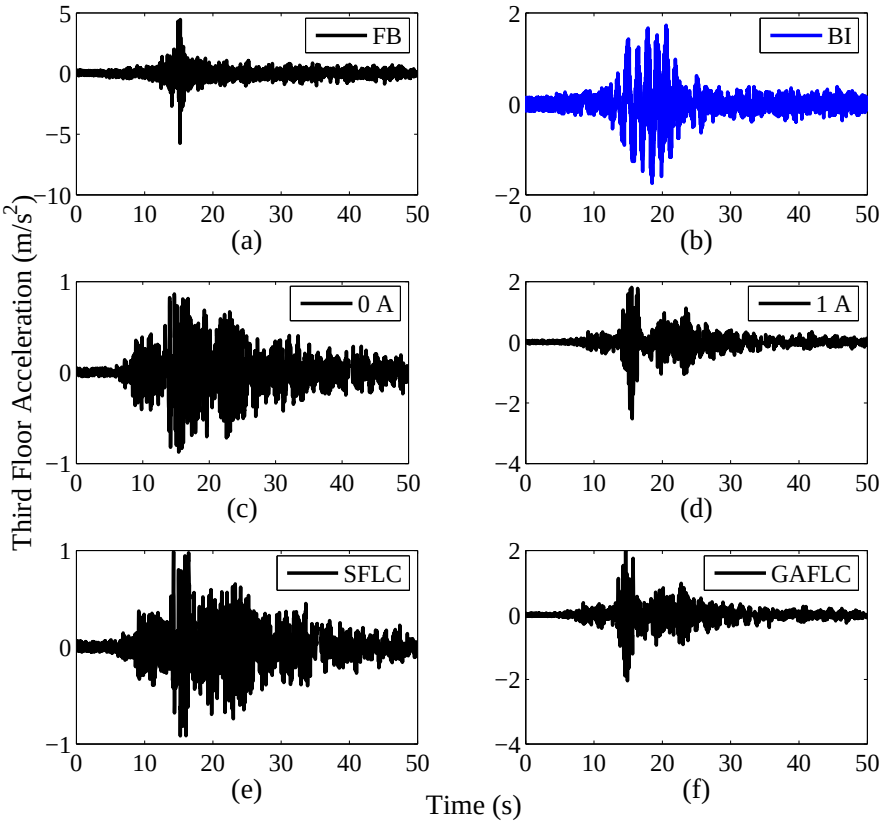

Figure C.19: 3^{rd} floor acceleration time history (Capemend (Y-dir))

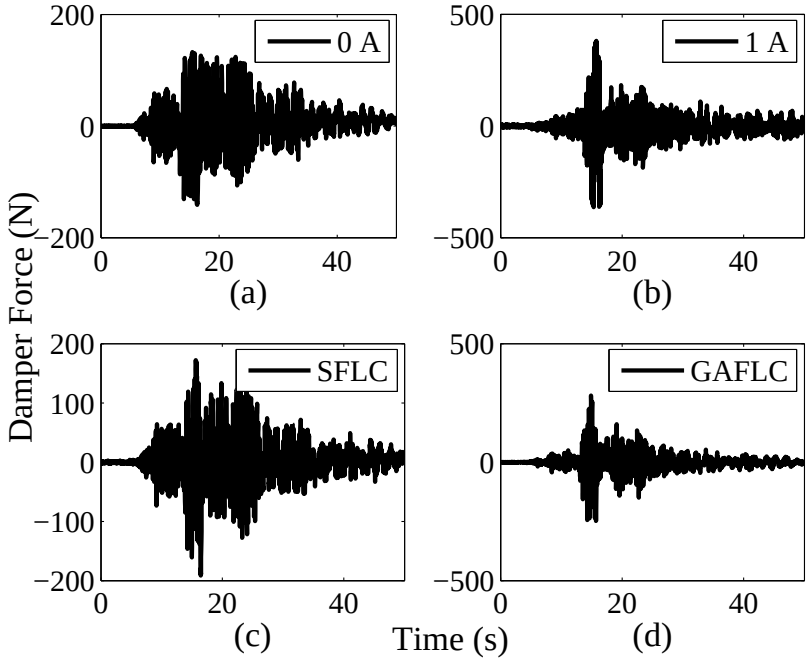

Figure C.20: MR damper force time history (Capemend (Y-dir))

Table C.4: Peak responses under Capemend (Y-direction) earthquake

Test Case	**Relative Displacements** ($\times 10^{-2}\ m$)				**Floor Accelerations** (m/s^2)			
	BI	*FF*	*SF*	*TF*	*BI*	*FF*	*SF*	*TF*
Fixed Base	–	0.1337	0.0445	0.0440	–	6.7977	3.3407	5.7520
Base Isolated	6.0187	0.0656	0.0245	0.0156	4.2025	1.5448	1.4659	1.7463
0A	0.4455	0.0542	0.0151	0.0093	3.6363	0.9083	0.8140	0.8731
1A	0.0537	0.1165	0.0355	0.0167	9.2650	1.7423	2.1465	2.5246
SFLC	0.1879	0.0583	0.0157	0.0087	4.0221	0.9187	0.9710	0.9867
GAFLC	0.0584	0.1160	0.0346	0.0173	8.7224	1.5504	1.7920	2.0397
BI: *Base Isolator*	*FF*: 1^{st} *floor*		*SF*: 2^{nd} *floor*		*TF*: 3^{rd} *floor*			

Chichi X-direction seismic motion

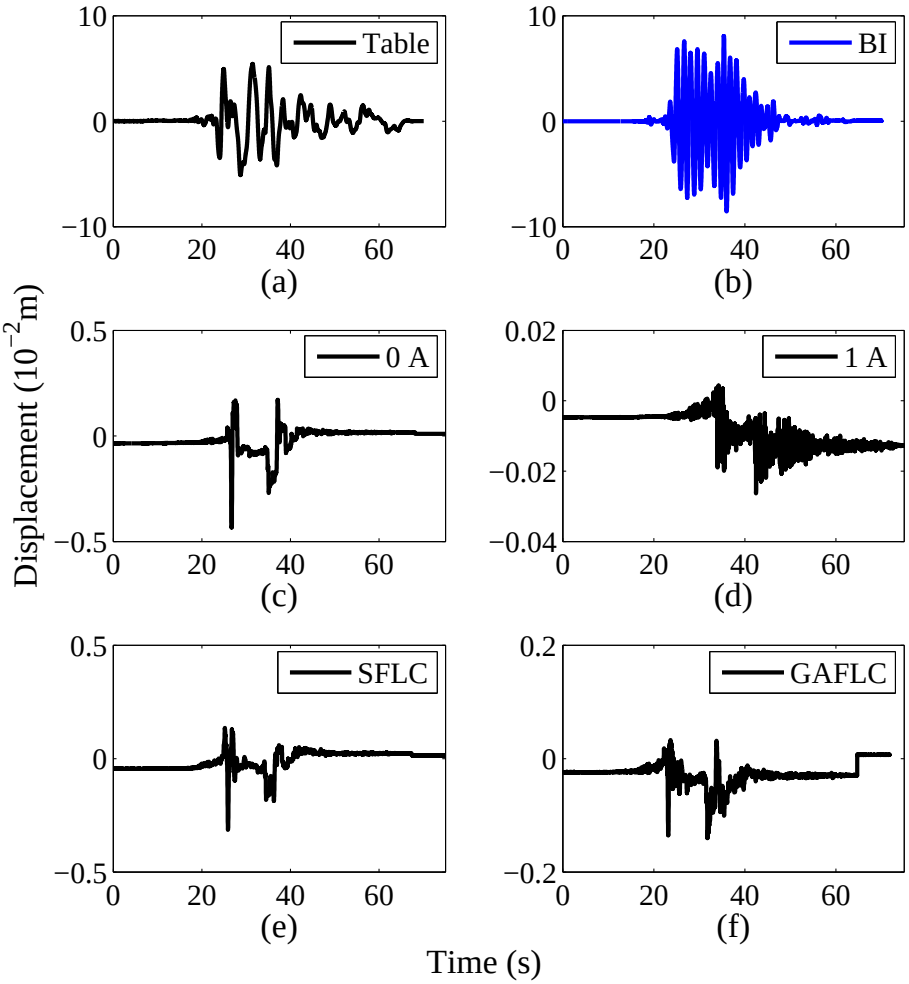

Figure C.21: Displacement time history at (a) Shake table, (b)-(f) Base isolator (Chi Chi (X-dir))

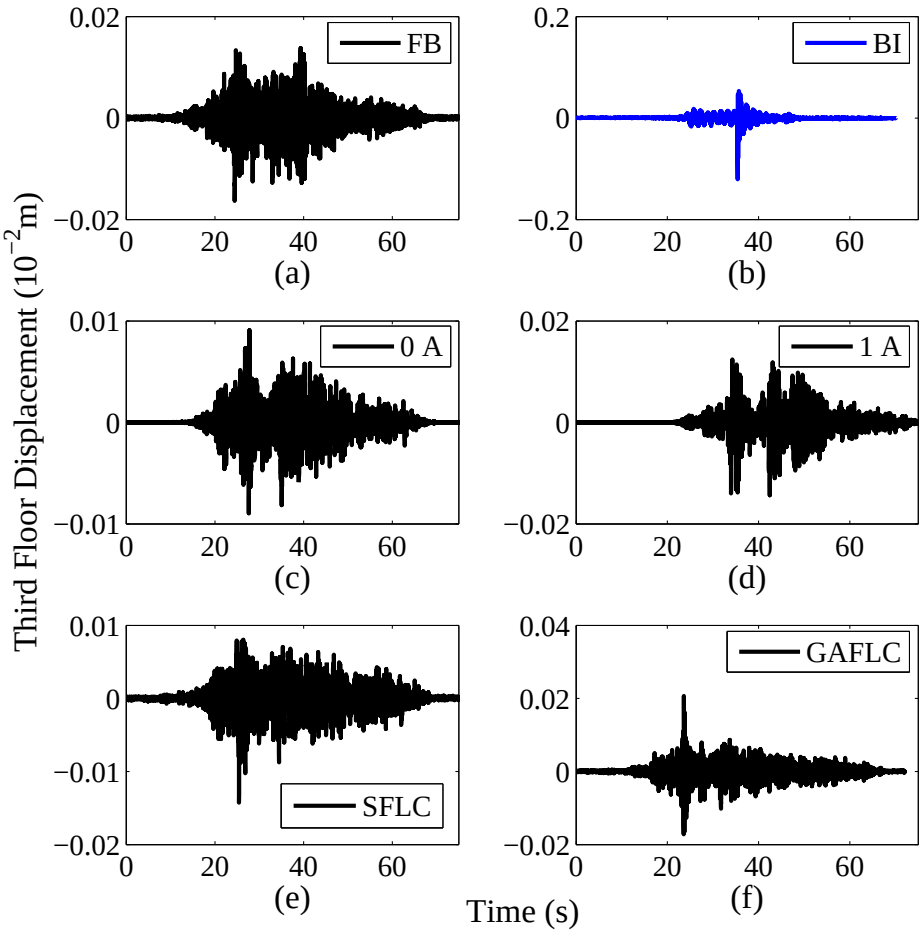

Figure C.22: 3^{rd} floor displacement time history (Chi Chi (X-dir))

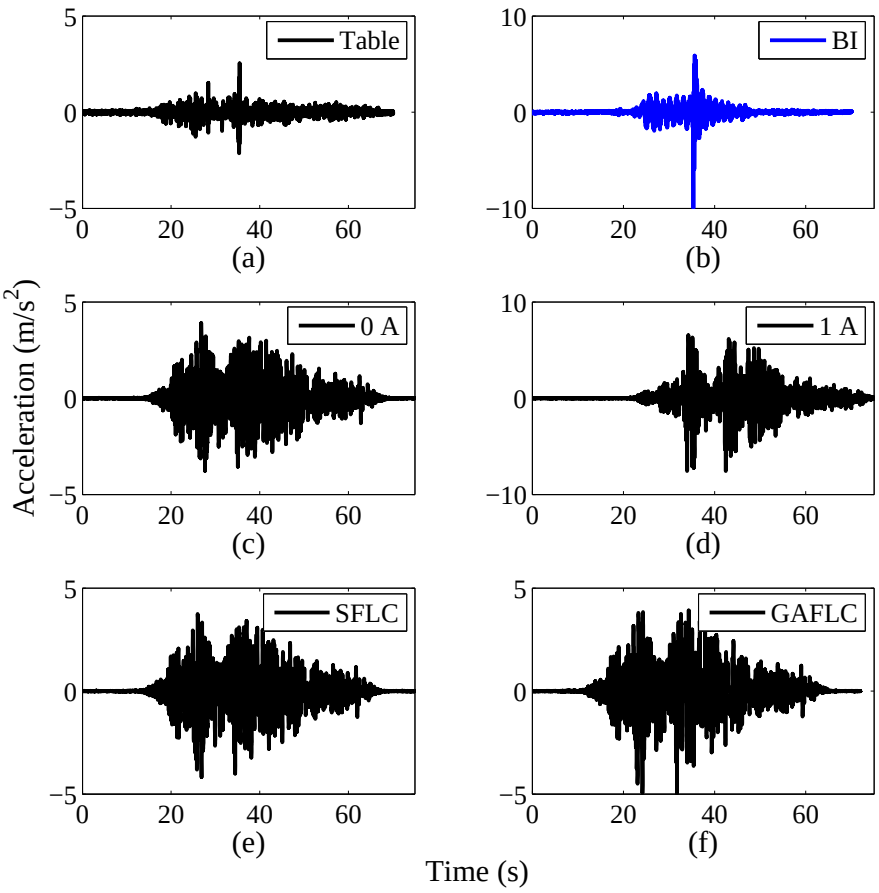

Figure C.23: Acceleration time history: (a) Excitation input, (b)-(f) Isolator acceleration at different cases (Chi Chi (X-dir))

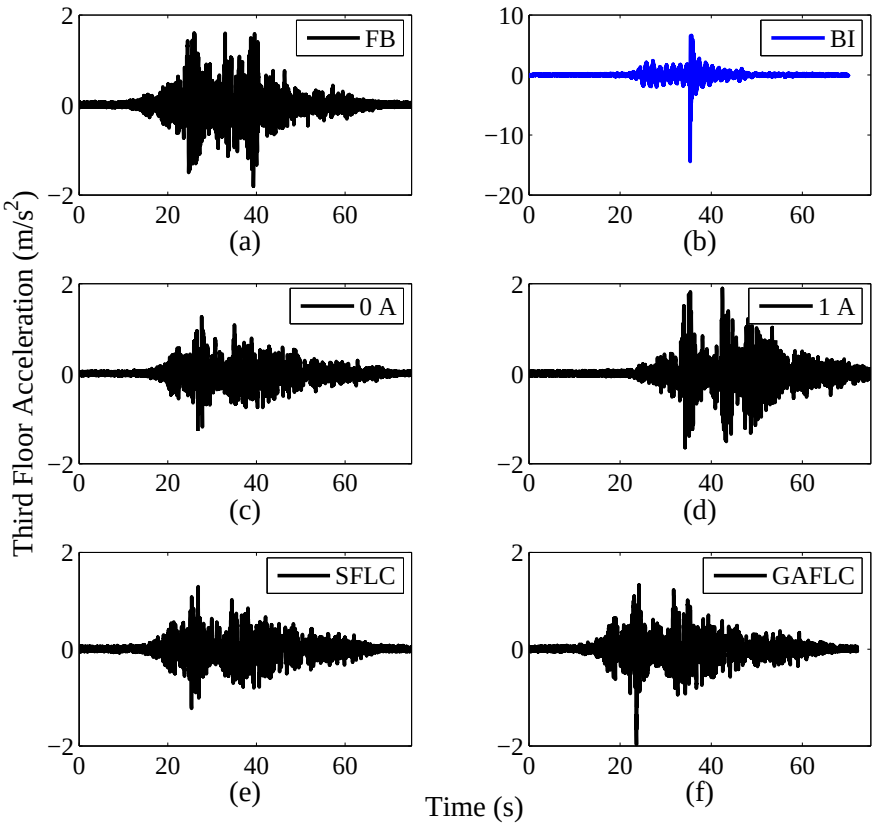

Figure C.24: 3^{rd} floor acceleration time history (Chi Chi (X-dir))

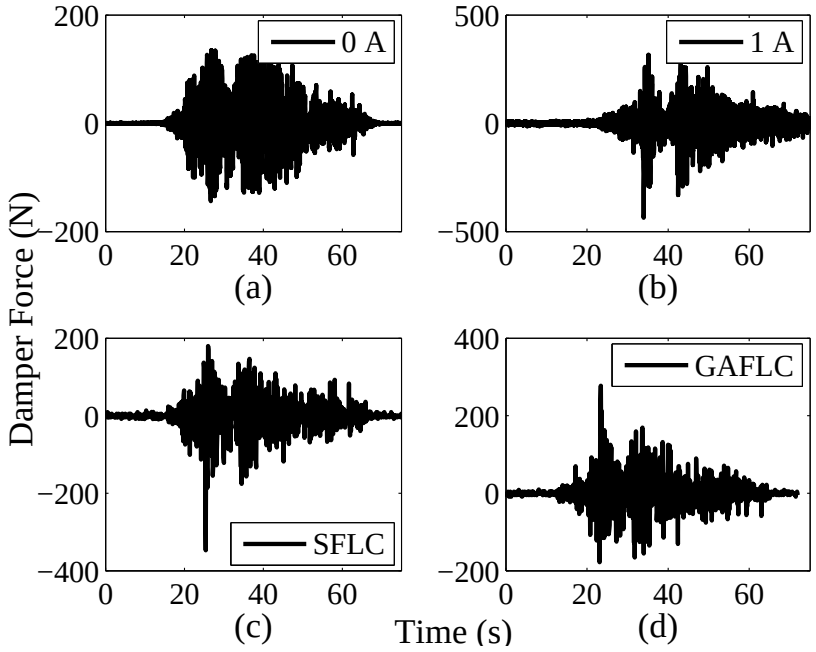

Figure C.25: MR damper force time history (Chi Chi (X-dir))

Table C.5: Peak responses under Chichi (X-direction) earthquake

Test Case	**Relative Displacements** ($\times 10^{-2}\ m$)				**Floor Acceleraions** (m/s^2)			
	BI	*FF*	*SF*	*TF*	*BI*	*FF*	*SF*	*TF*
Fixed Base	0.0000	0.0924	0.1083	0.0163	0.0000	1.3789	1.6057	1.8057
Base Isolated	8.5491	0.2918	0.1854	0.1207	9.9487	11.4929	7.7028	14.4098
0A	0.4337	0.0496	0.0167	0.0091	3.9075	0.9975	1.0671	1.2715
1A	0.0263	0.1007	0.0380	0.0143	7.5690	1.4811	1.7667	1.8955
SFLC	0.3144	0.0566	0.0183	0.0143	4.1762	0.9798	1.0612	1.2937
GAFLC	0.1401	0.0663	0.0214	0.0207	4.9797	1.8994	1.6848	1.9697
BI: *Base Isolator* *FF*: 1^{st} *floor* *SF*: 2^{nd} *floor* *TF*: 3^{rd} *floor*								

Chichi Y-direction seismic motion

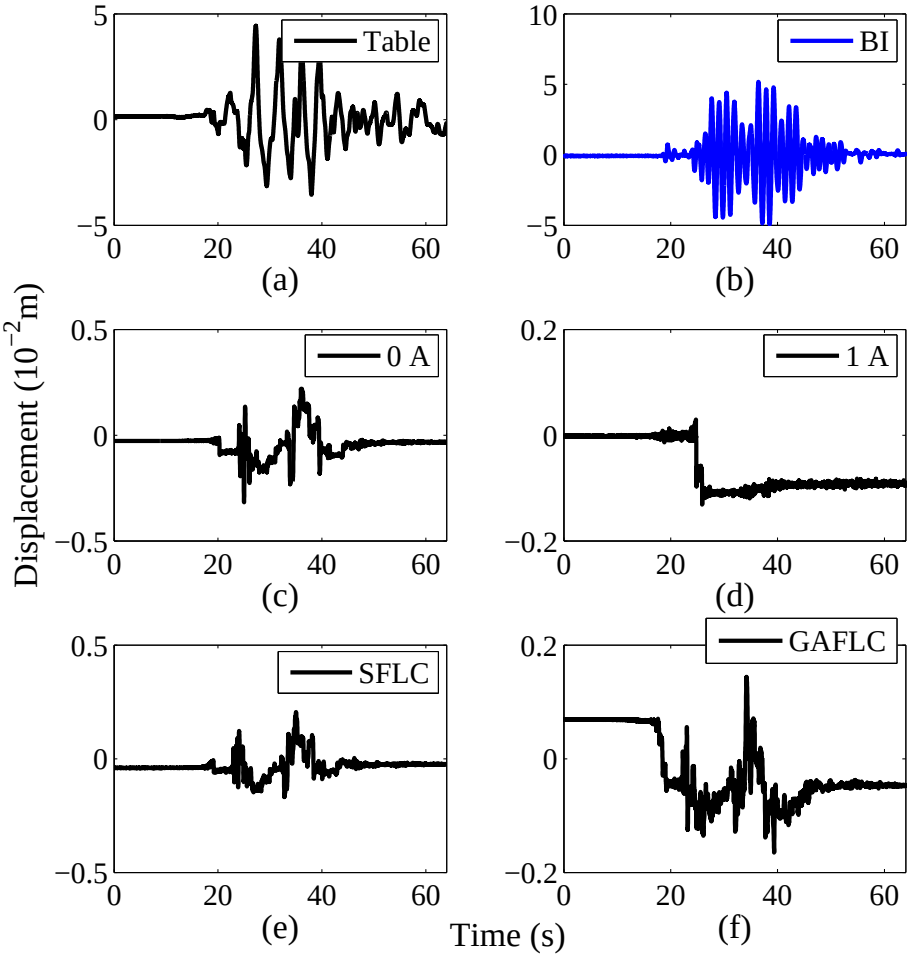

Figure C.26: Displacement time history: (a) Excitation input, (b)-(f) Isolator displacement at different cases (Chi Chi (Y-dir))

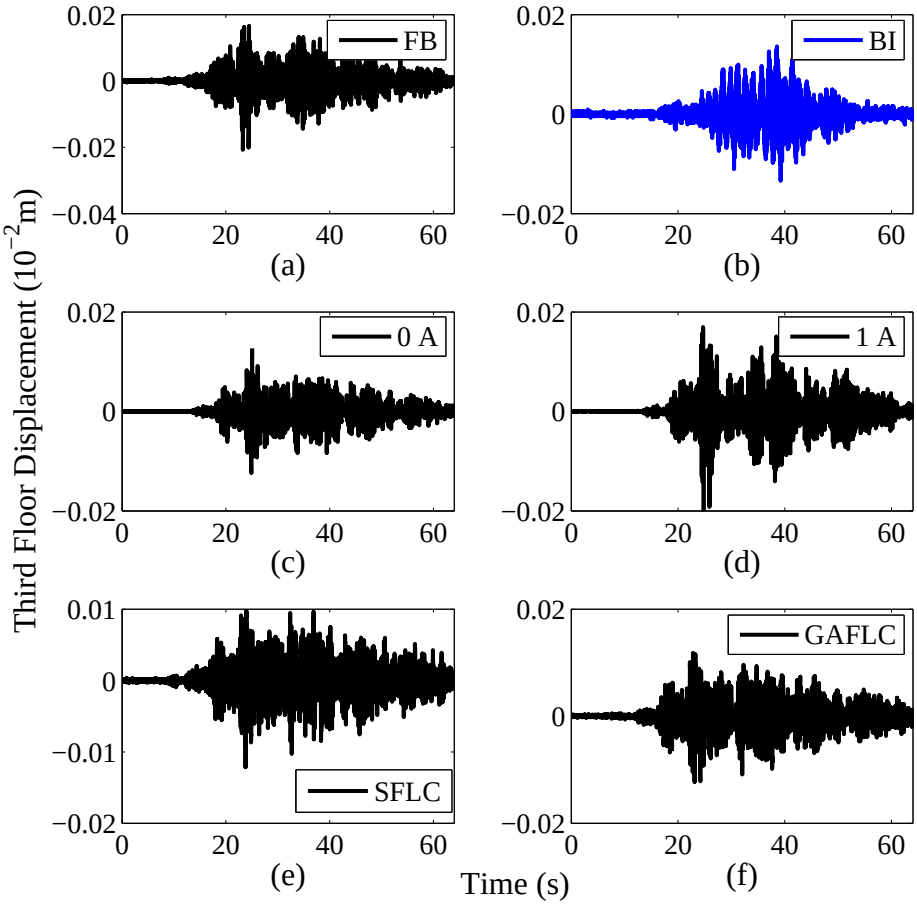

Figure C.27: 3^{rd} floor displacement time history (Chi Chi (Y-dir))

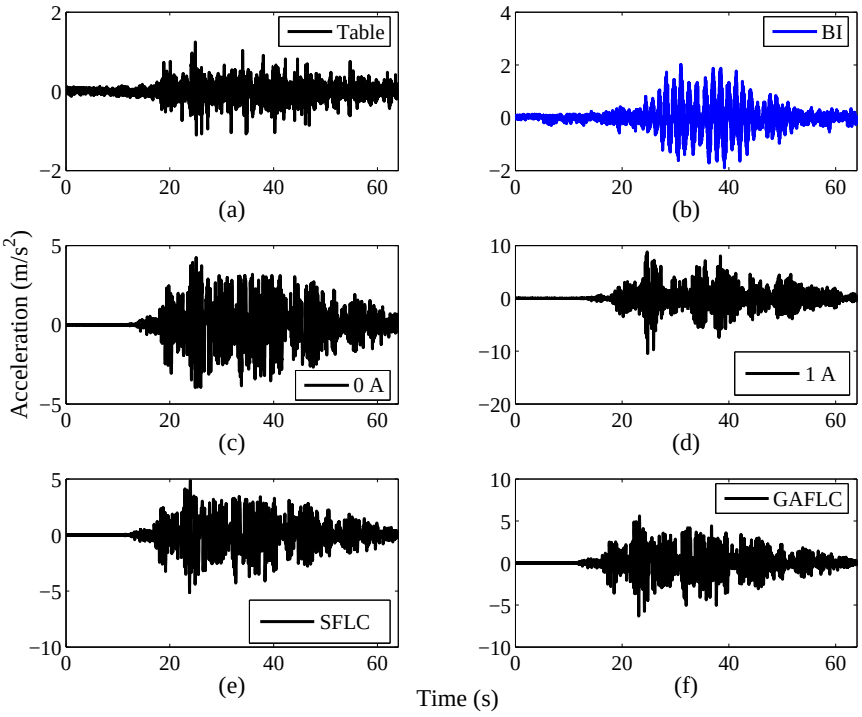

Figure C.28: Acceleration time history: (a) Excitation input, (b)-(f) Isolator acceleration at different cases (Chi Chi (Y-dir))

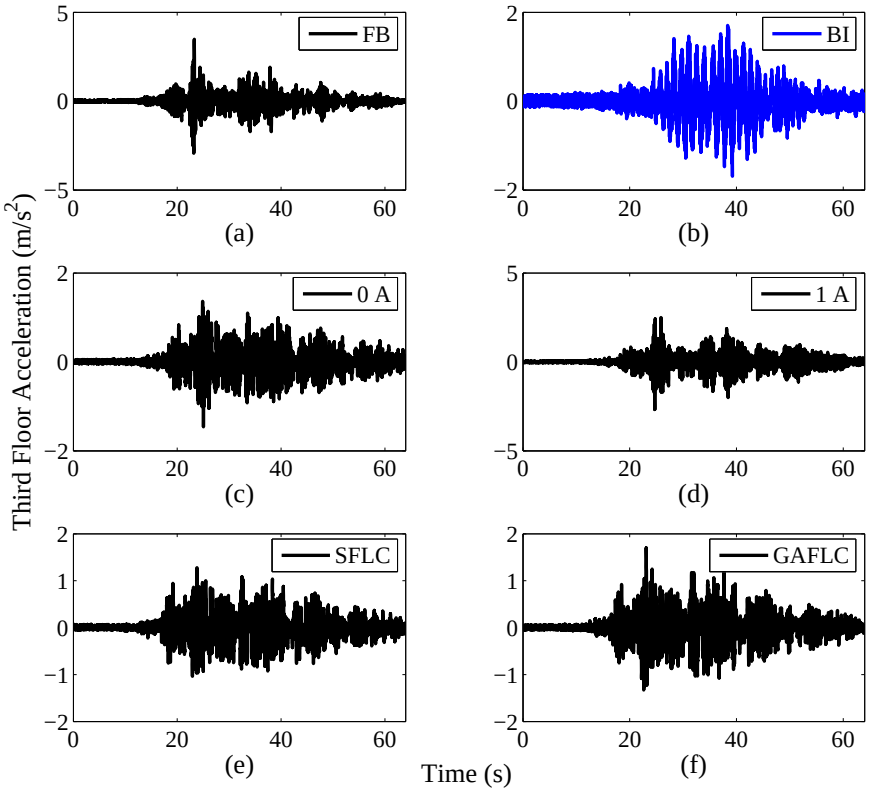

Figure C.29: 3^{rd} floor acceleration time history (Chi Chi (Y-dir))

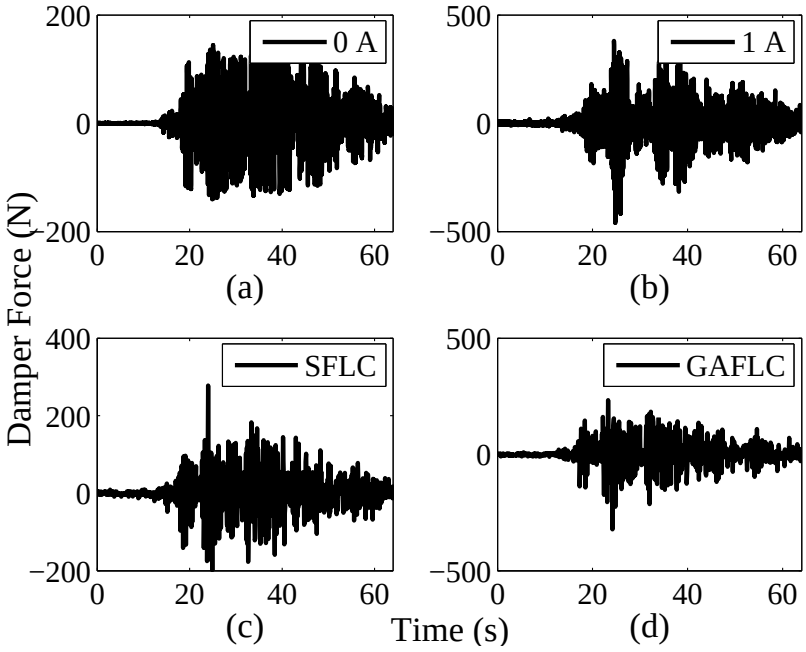

Figure C.30: MR damper force time history (Chi Chi (Y-dir))

Table C.6: Peak responses under Chichi (Y-direction) earthquake

Test Case	**Relative Displacements** ($\times 10^{-2}\ m$)				**Floor Accelerations** (m/s^2)			
	BI	*FF*	*SF*	*TF*	*BI*	*FF*	*SF*	*TF*
Fixed Base	0.0000	0.1951	0.1372	0.0208	0.0000	2.5929	3.2897	3.4862
Base Isolated	5.1824	0.0606	0.0245	0.0136	2.0196	1.7172	1.5229	1.7059
0A	0.3175	0.0526	0.0201	0.0126	4.2502	0.9282	0.9825	1.4601
1A	0.1312	0.1348	0.0486	0.0208	10.4497	2.0100	2.3804	2.6777
SFLC	0.2053	0.0674	0.0219	0.0121	5.1342	1.3204	1.0524	1.2780
GAFLC	0.1651	0.0847	0.0244	0.0123	6.3218	1.5336	1.5251	1.6994
BI: *Base Isolator* *FF*: 1^{st} *floor* *SF*: 2^{nd} *floor* *TF*: 3^{rd} *floor*								

Coalinga X-direction seismic motion

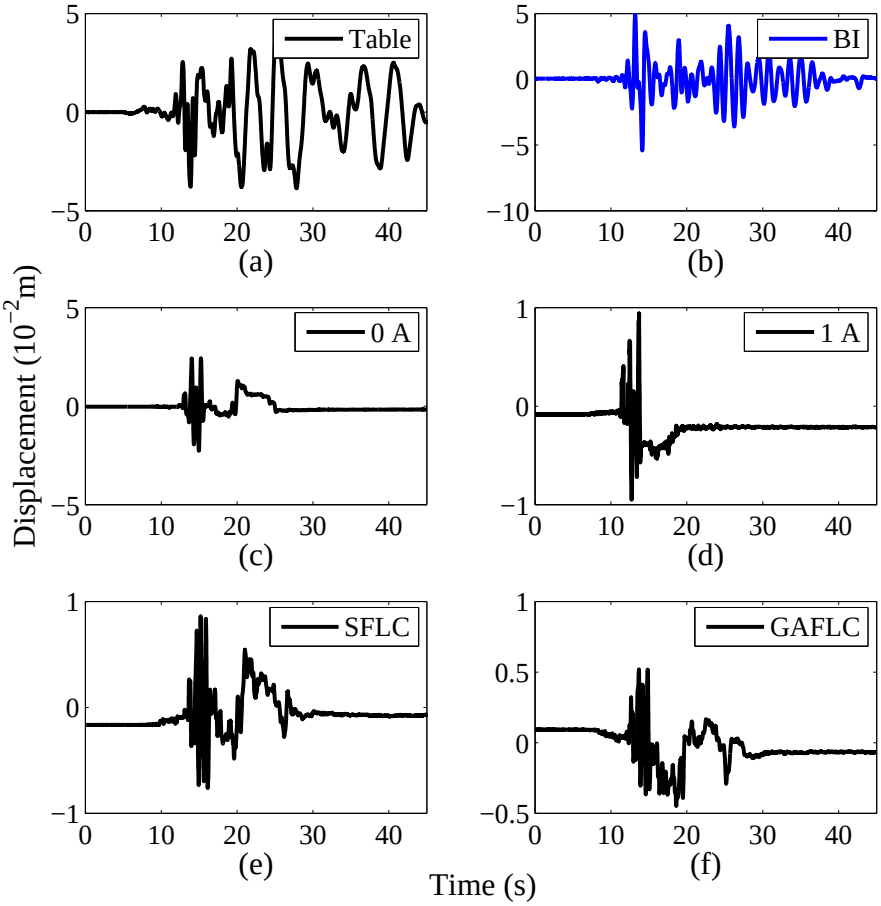

Figure C.31: Displacement time history: (a) Excitation input, (b)-(f) Isolator displacement at different cases (Coalinga (X-dir))

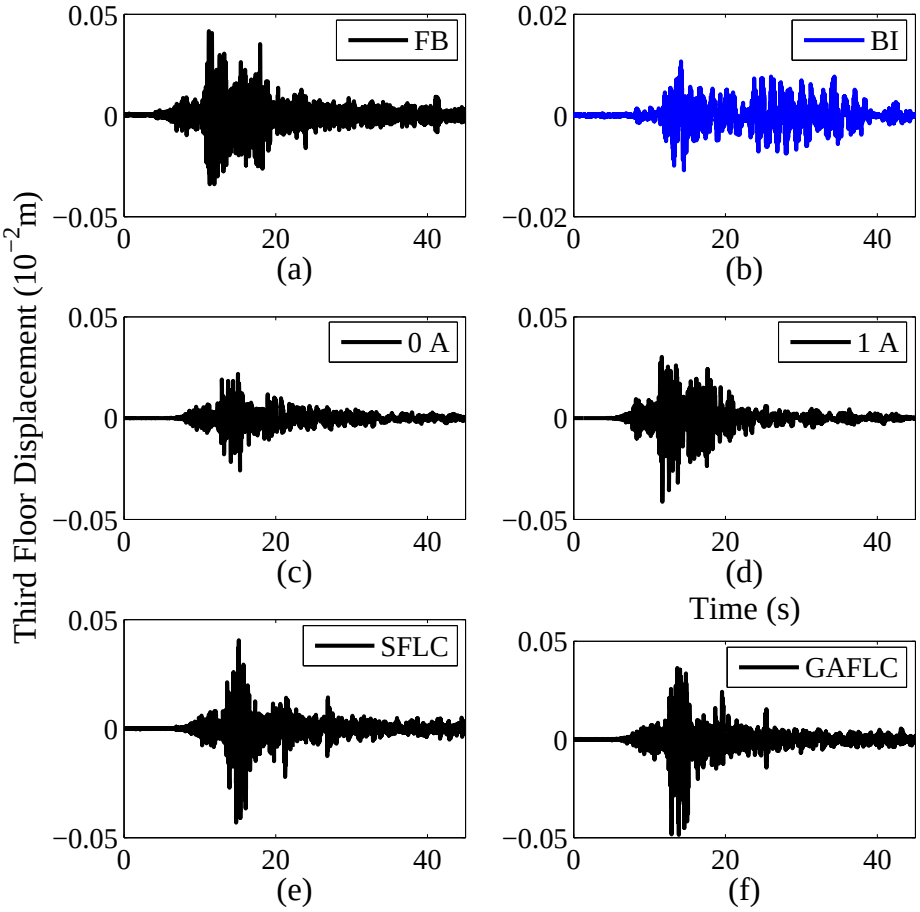

Figure C.32: 3^{rd} floor displacement time history (Coalinga (X-dir))

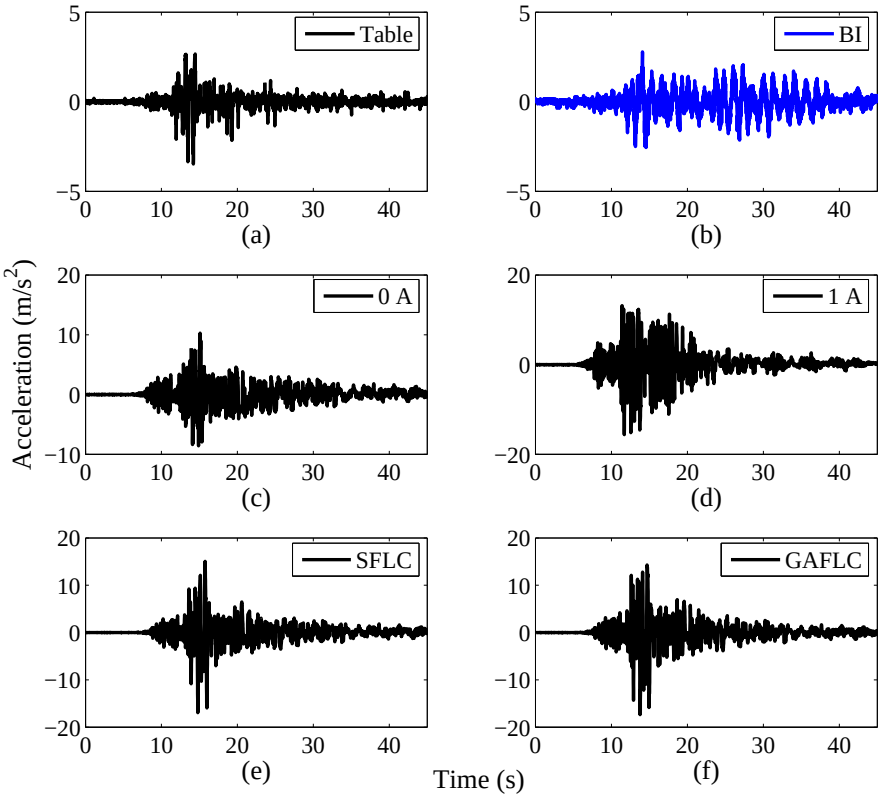

Figure C.33: Acceleration time history: (a) Excitation input, (b)-(f) Isolator acceleration at different cases (Coalinga (X-dir))

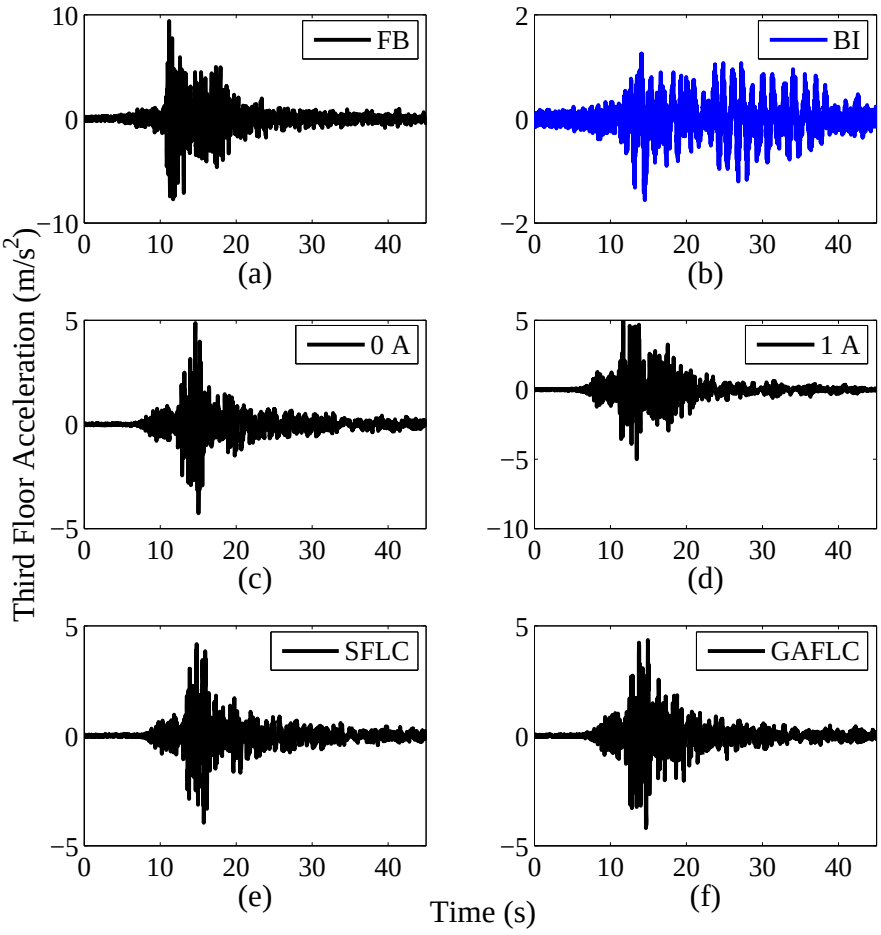

Figure C.34: 3^{rd} floor acceleration time history (Coalinga (X-dir))

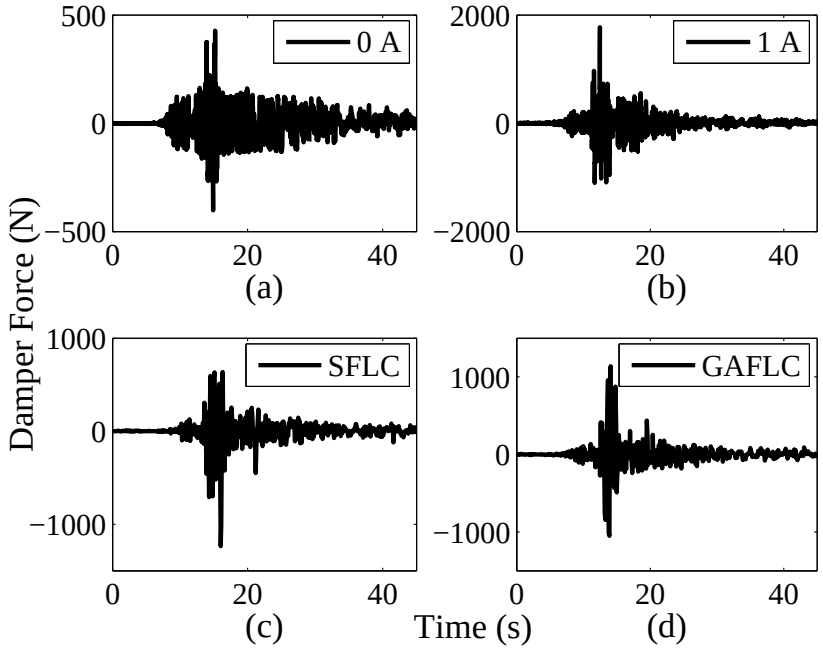

Figure C.35: MR damper force time history (Coalinga (X-dir))

Table C.7: Peak responses under Coalinga (X-direction) earthquake

Test Case	**Relative Displacements** ($\times 10^{-2}$ m)				**Floor Accelerations** (m/s^2)			
	BI	*FF*	*SF*	*TF*	*BI*	*FF*	*SF*	*TF*
Fixed Base	0.0000	0.7189	0.1091	0.0416	0.0000	5.8844	7.2832	9.4058
Base Isolated	5.4164	0.0610	0.0230	0.0108	2.7815	1.2246	1.3913	1.5617
0A	2.4251	0.1014	0.0344	0.0259	10.2671	4.1591	3.7037	4.8609
1A	0.9504	0.2006	0.0764	0.0413	15.6192	4.1525	4.8036	5.0006
SFLC	0.8608	0.2168	0.0756	0.0431	16.9518	4.3076	3.5022	4.1706
GAFLC	0.5191	0.2271	0.0767	0.0486	17.3626	4.2210	4.2770	4.3564
BI: *Base Isolator*	*FF*: 1^{st} *floor*		*SF*: 2^{nd} *floor*		*TF*: 3^{rd} *floor*			

Coalinga Y-direction seismic motion

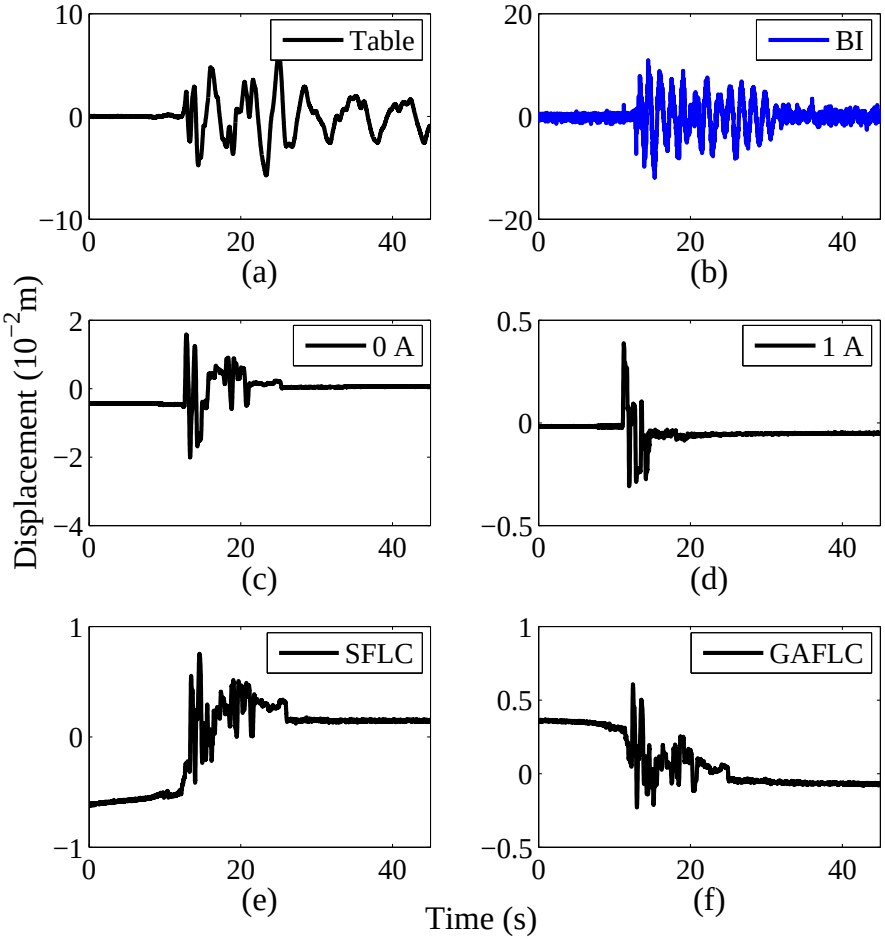

Figure C.36: Displacement time history: (a) Excitation input, (b)-(f) Isolator displacement at different cases (Coalinga (Y-dir))

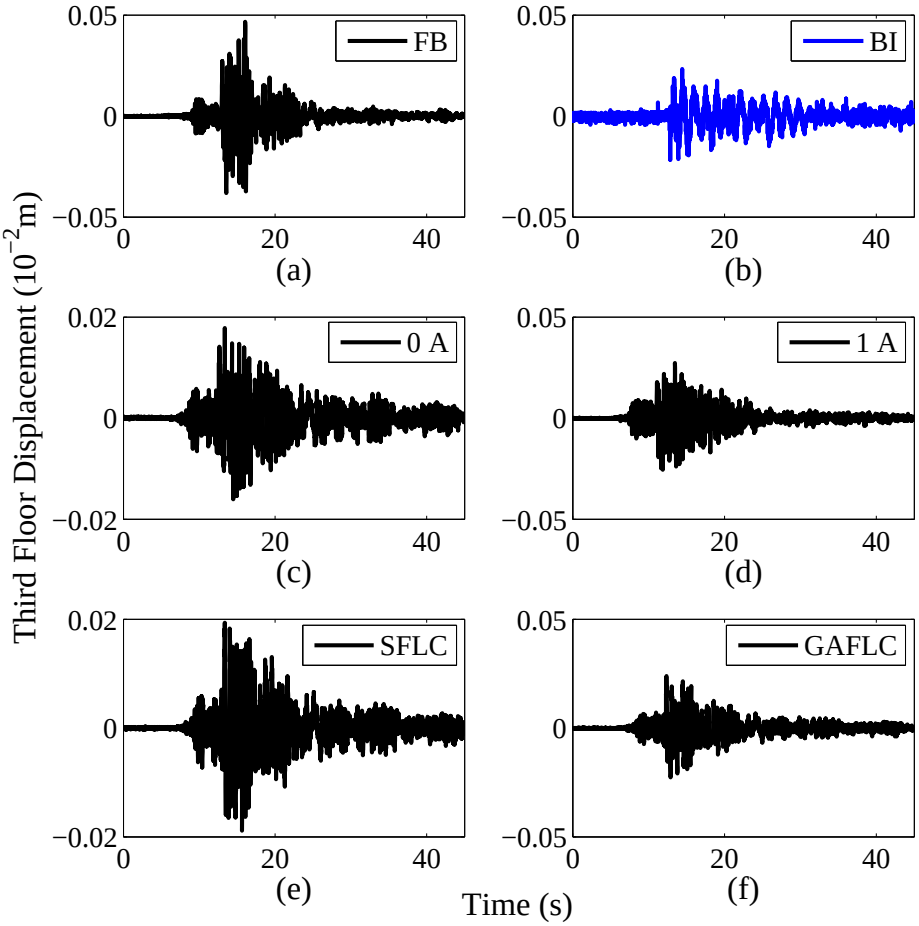

Figure C.37: 3^{rd} floor displacement time history (Coalinga (Y-dir))

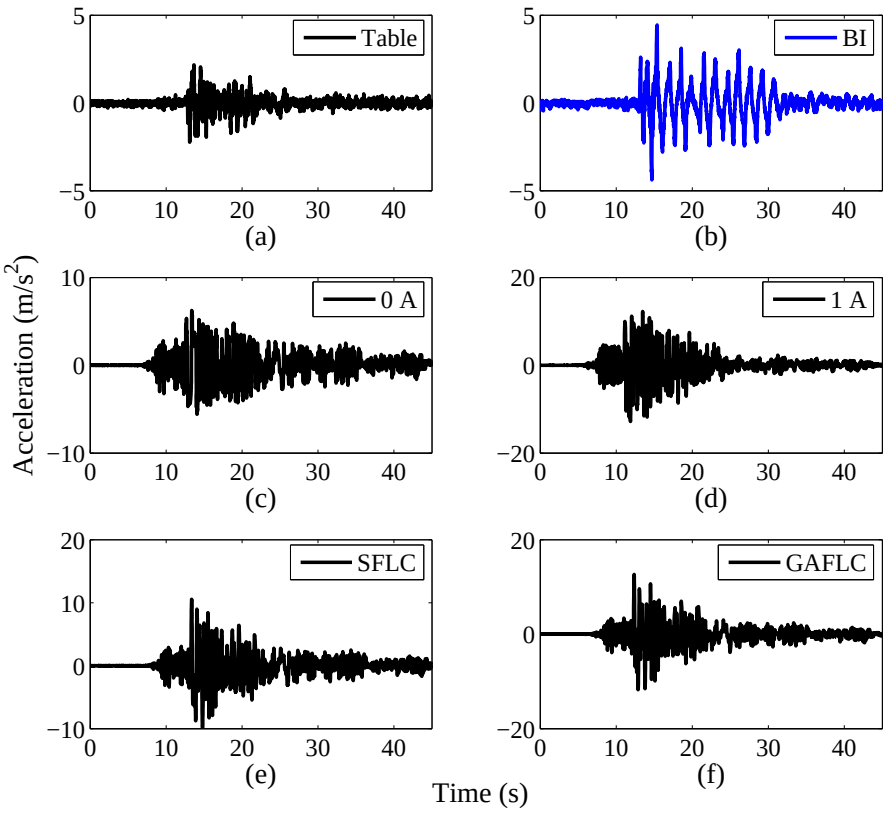

Figure C.38: Acceleration time history: (a) Excitation input, (b)-(f) Isolator acceleration at different cases (Coalinga (Y-dir))

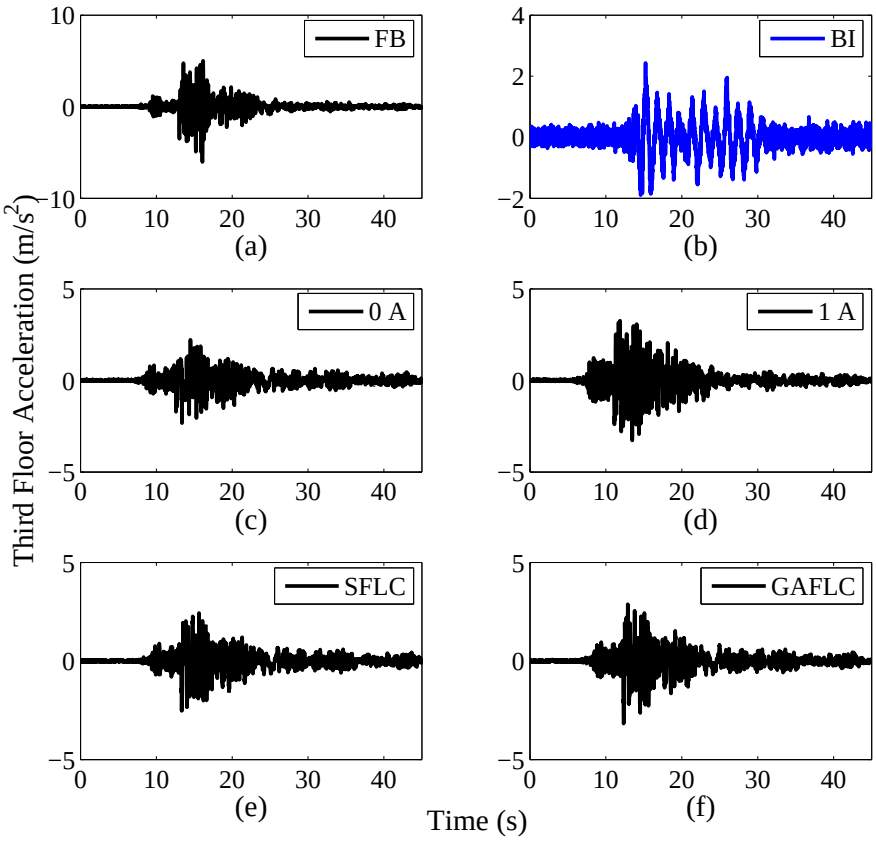

Figure C.39: 3^{rd} floor acceleration time history (Coalinga (Y-dir))

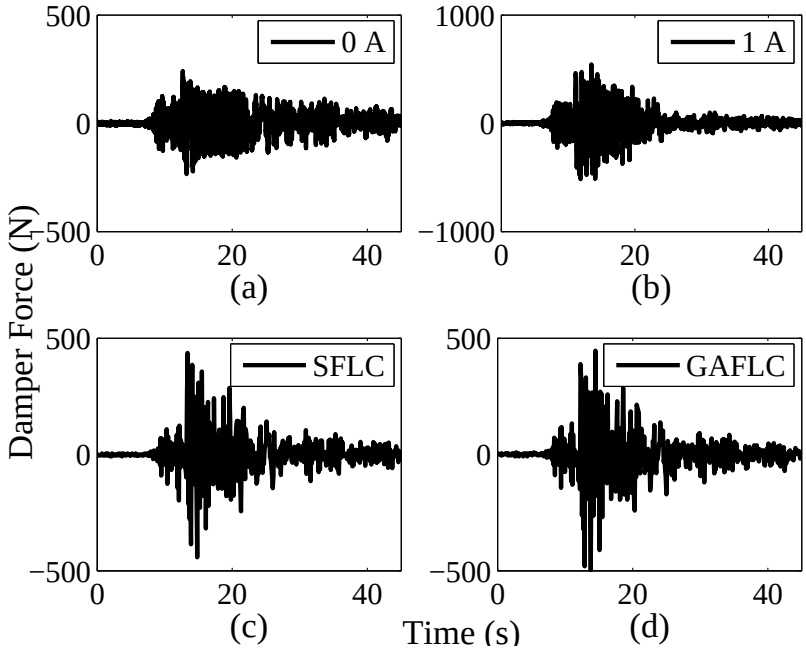

Figure C.40: MR damper force time history (Coalinga (Y-dir))

Table C.8: Peak responses under Coalinga (Y-direction) earthquake

Test Case	**Relative Displacements** ($\times 10^{-2}\ m$)				**Floor Accelerations** (m/s^2)			
	BI	*FF*	*SF*	*TF*	*BI*	*FF*	*SF*	*TF*
Fixed Base	0.0000	0.3196	0.0937	0.0467	0.0000	4.5222	5.3941	6.0353
Base Isolated	11.8814	0.1662	0.0435	0.0233	4.4438	1.9074	1.9771	2.4314
0A	2.0058	0.0818	0.0276	0.0178	6.2536	1.6427	1.4554	2.3312
1A	0.3883	0.1679	0.0532	0.0273	12.8152	2.6368	2.9919	3.2808
SFLC	0.7523	0.1438	0.0401	0.0193	10.5393	2.5869	2.3364	2.5255
GAFLC	0.6079	0.1692	0.0509	0.0239	12.6640	2.8509	2.8992	3.1729
BI: *Base Isolator* *FF*: 1^{st} *floor* *SF*: 2^{nd} *floor* *TF*: 3^{rd} *floor*								

El-Centro X-direction seismic motion

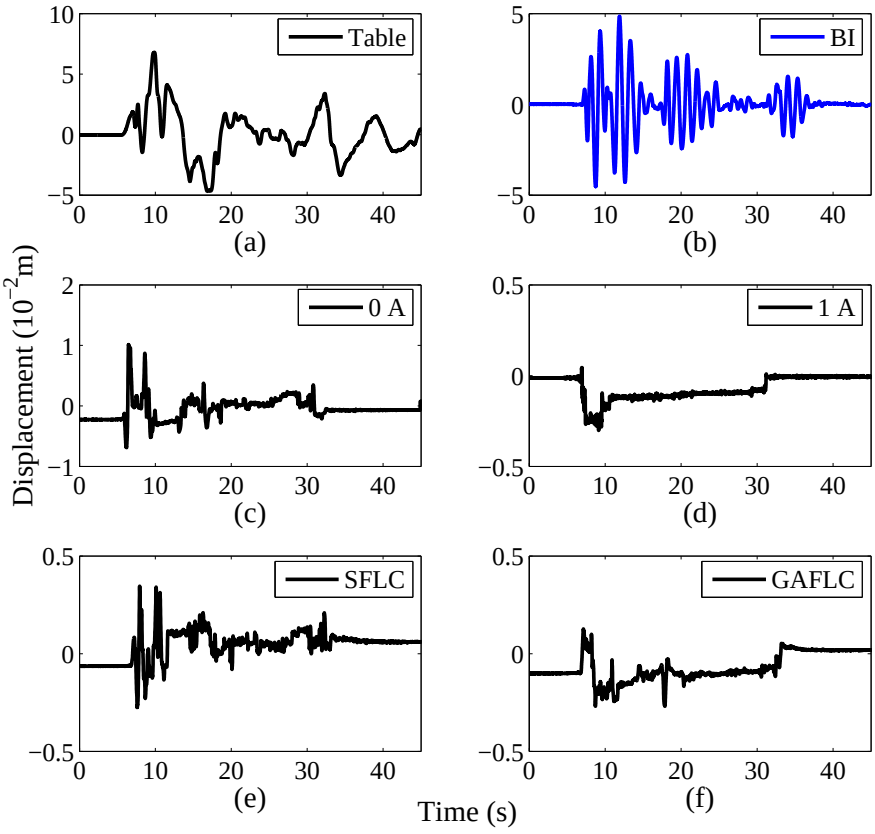

Figure C.41: Displacement time history: (a) Excitation input, (b)-(f) Isolator displacement at different cases (El-Centro (X-dir))

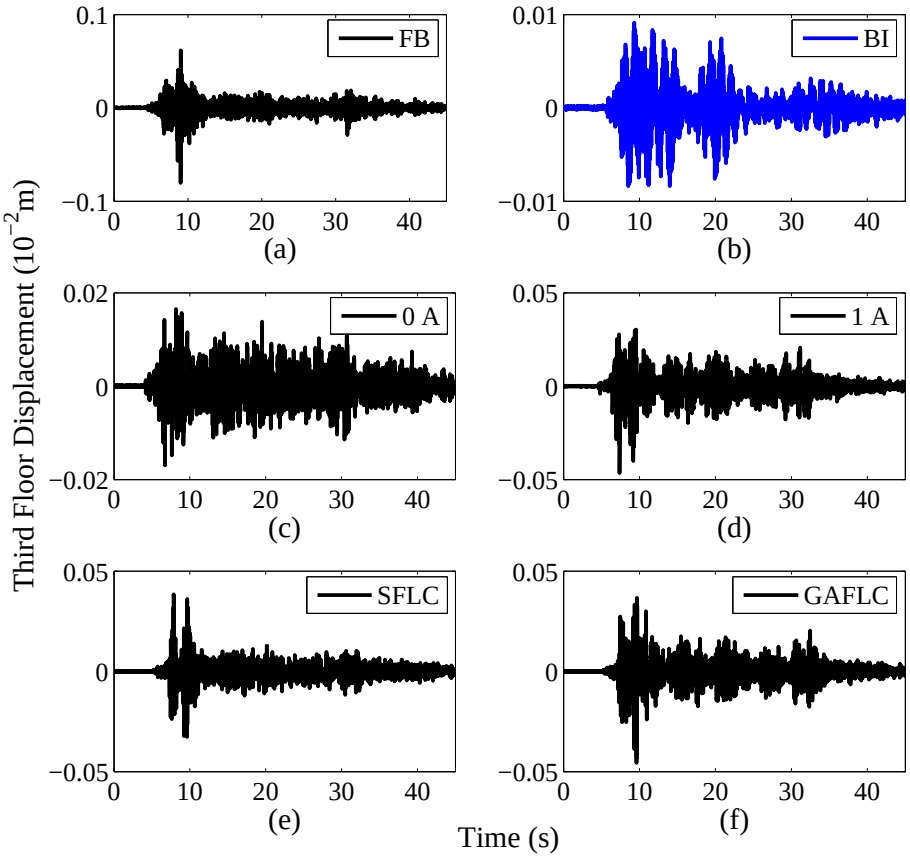

Figure C.42: 3^{rd} floor displacement time history (El-Centro (X-dir))

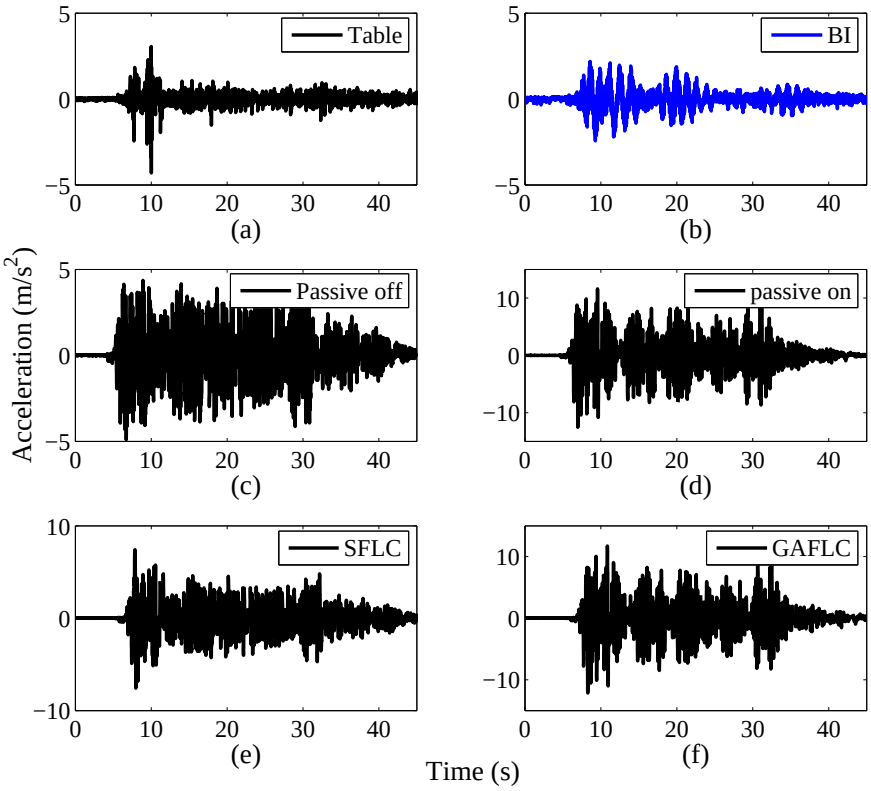

Figure C.43: Acceleration time history: (a) Excitation input, (b)-(f) Isolator acceleration at different cases (El-Centro (X-dir))

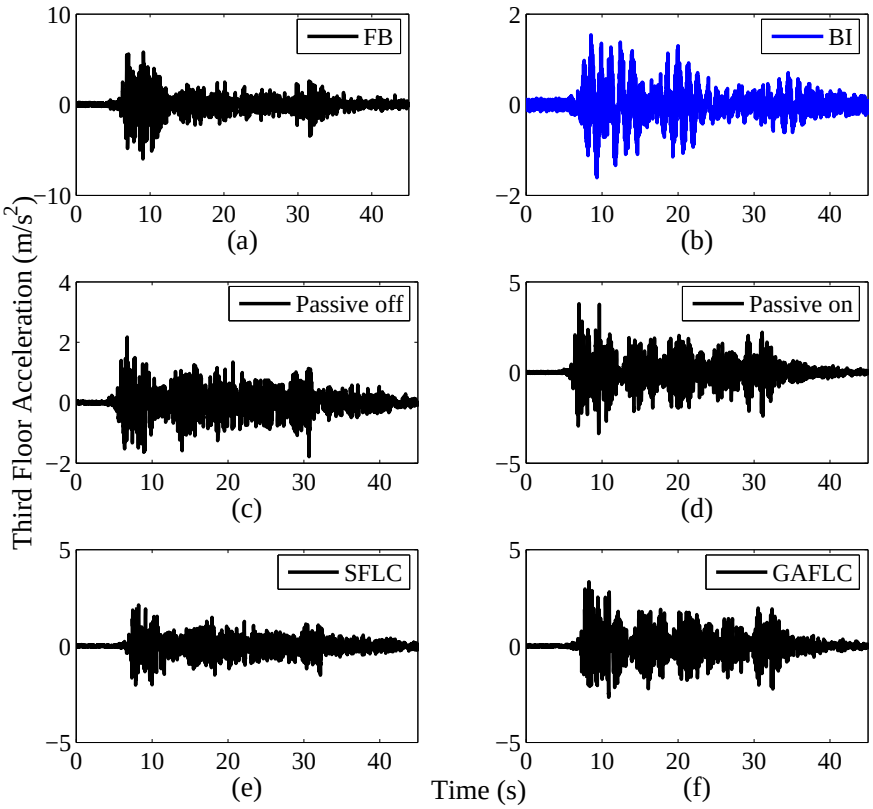

Figure C.44: 3^{rd} floor acceleration time history (El-Centro (X-dir))

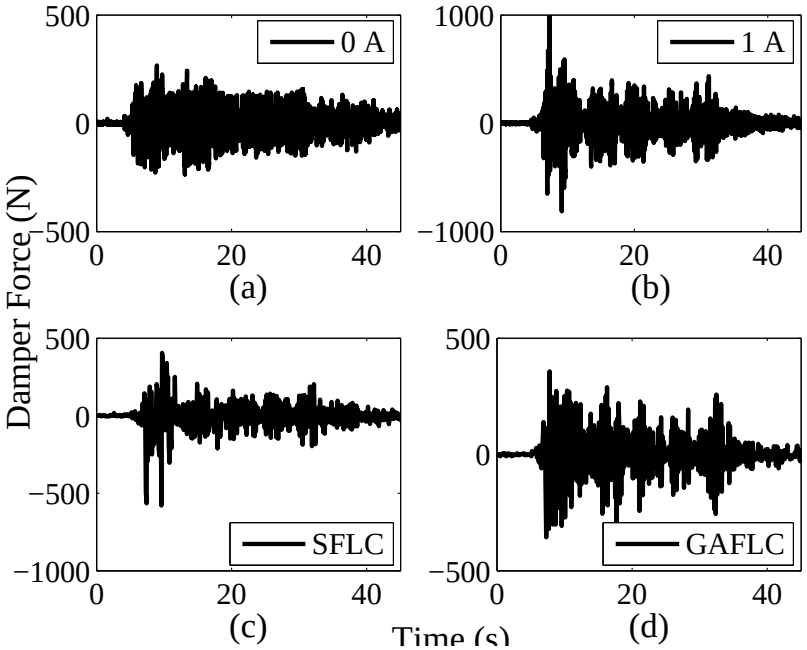

Figure C.45: MR damper force time history (El-Centro (X-dir))

Table C.9: Peak responses under El-Centro (X-direction) earthquake

Test Case	**Relative Displacements** ($\times 10^{-2}\ m$)				**Floor Accelerations** (m/s^2)			
	BI	*FF*	*SF*	*TF*	*BI*	*FF*	*SF*	*TF*
Fixed Base	0.0000	0.3150	0.0783	0.0802	0.0000	6.6422	4.7754	5.9761
Base Isolated	4.8553	0.0596	0.0175	0.0091	2.4341	1.4091	1.2225	1.6091
0A	1.0122	0.0649	0.0247	0.0169	4.9030	1.5124	1.3334	2.1764
1A	0.3018	0.1963	0.2102	0.0465	12.5279	2.5878	3.3258	3.7917
SFLC	0.3455	0.0957	0.0355	0.0384	7.5768	1.8549	1.7715	2.1276
GAFLC	0.2694	0.1597	0.0528	0.0456	12.1523	2.7093	2.8704	3.3359
BI: *Base Isolator* *FF*: 1^{st} *floor* *SF*: 2^{nd} *floor* *TF*: 3^{rd} *floor*								

El-Centro Y-direction seismic motion

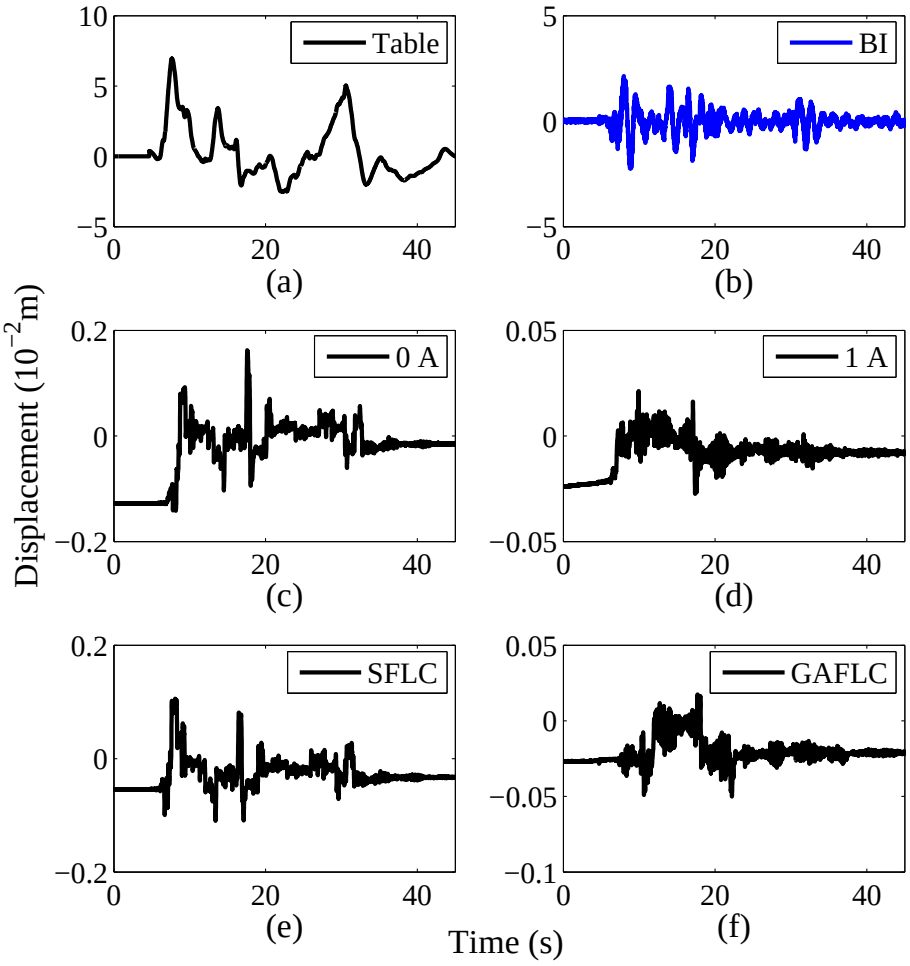

Figure C.46: Displacement time history: (a) Excitation input, (b)-(f) Isolator displacement at different cases (El-Centro (Y-dir))

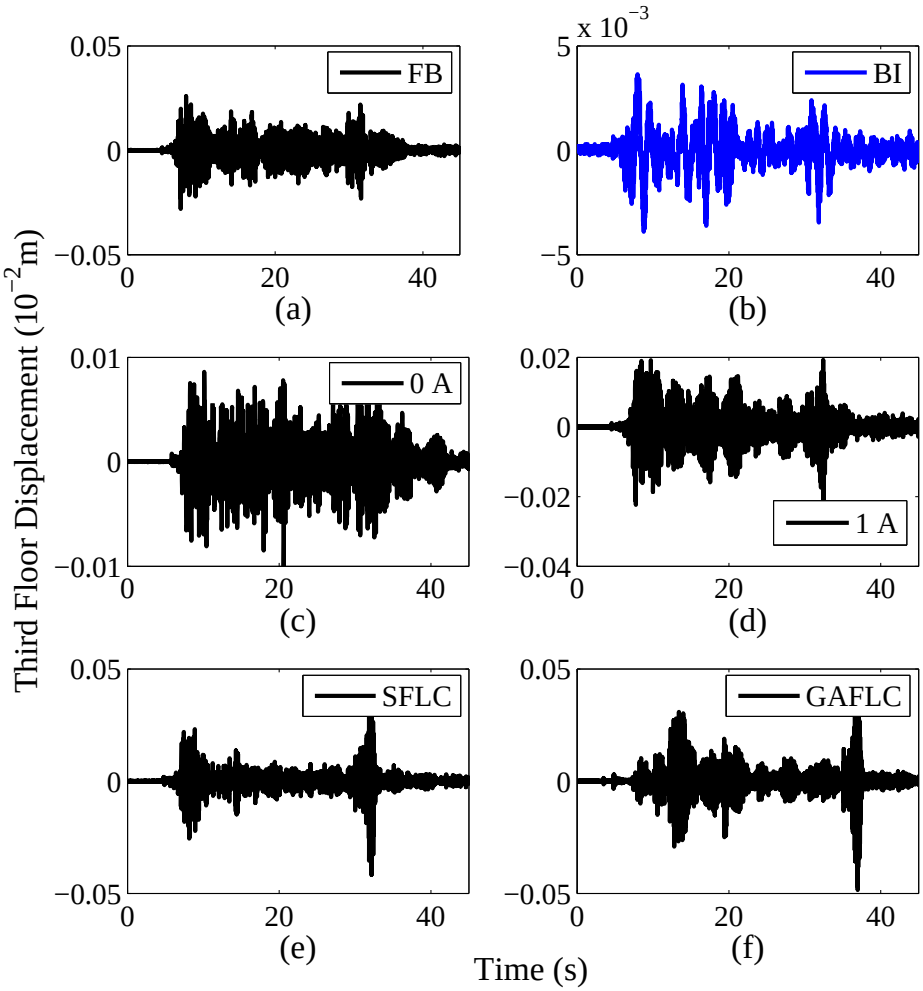

Figure C.47: 3^{rd} floor displacement time history (El-Centro (Y-dir))

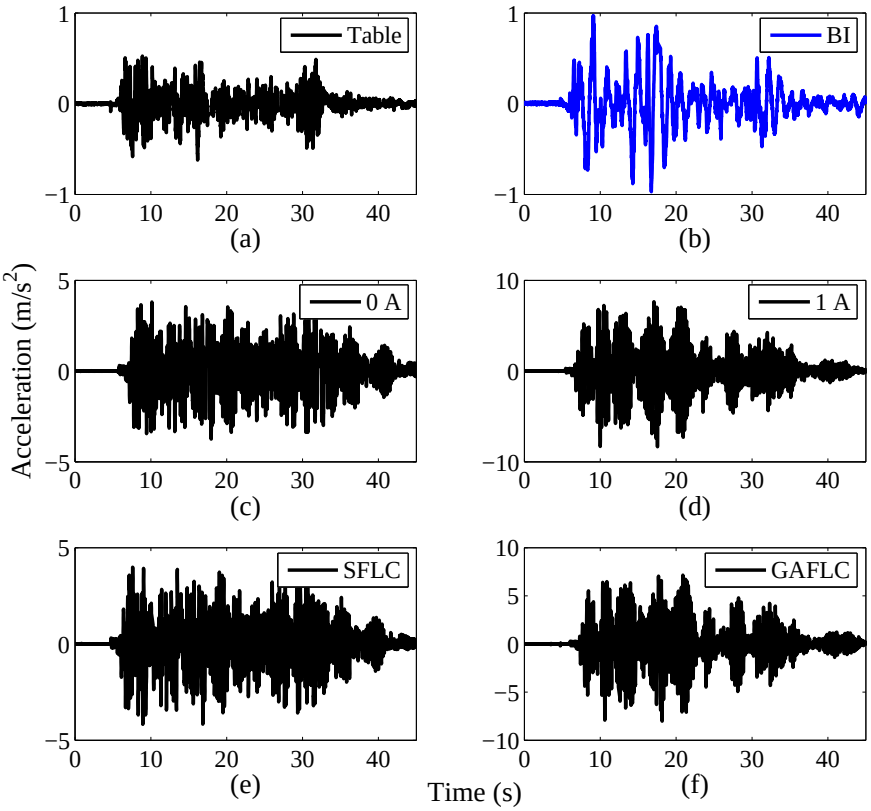

Figure C.48: Acceleration time history: (a) Excitation input, (b)-(f) Isolator acceleration at different cases (El-Centro (Y-dir))

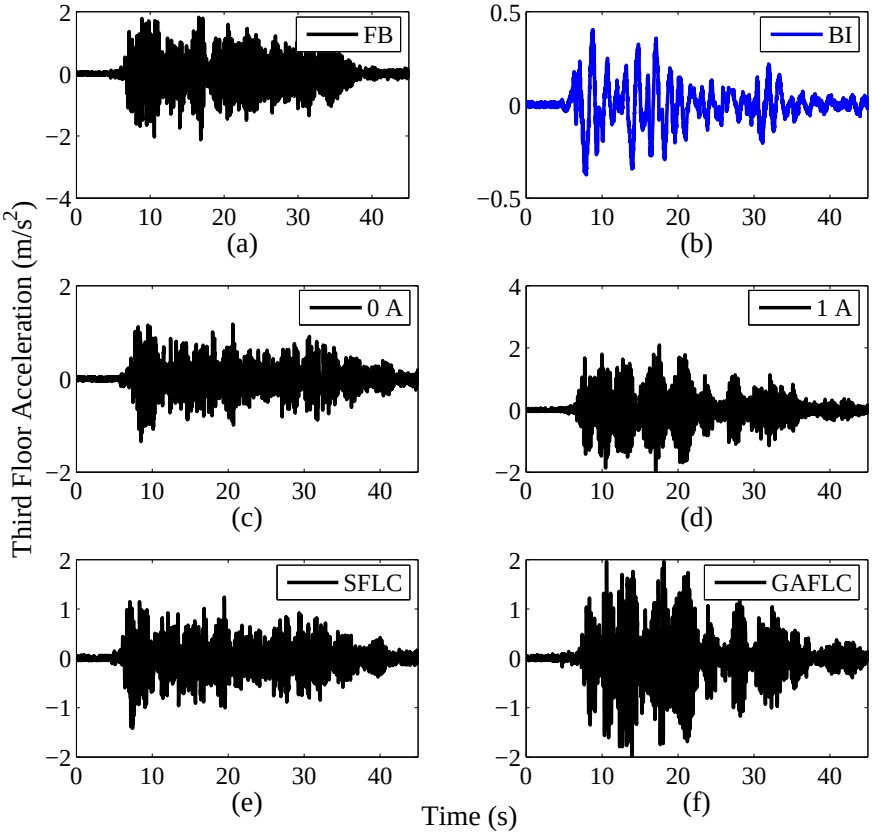

Figure C.49: 3^{rd} floor acceleration time history (El-Centro (Y-dir))

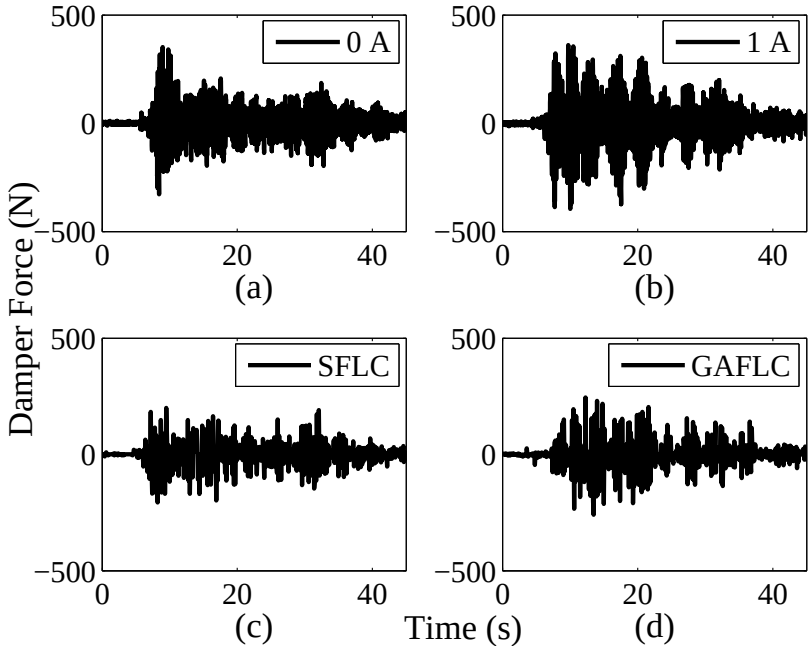

Figure C.50: MR damper force time history (El-Centro (Y-dir))

Table C.10: Peal responses under El-Centro (Y-direction) earthquake

Test Case	**Relative Displacements** ($\times 10^{-2}\ m$)				**Floor Accelerations** (m/s^2)			
	BI	*FF*	*SF*	*TF*	*BI*	*FF*	*SF*	*TF*
Fixed Base	0.0000	0.1170	0.1321	0.0281	0.0000	1.7160	1.9510	2.1215
Base Isolated	2.2501	0.0292	0.0079	0.0039	0.9709	0.3959	0.3998	0.4037
0A	0.1625	0.0494	0.0182	0.0100	3.8048	1.0293	1.2953	1.3429
1A	0.0274	0.1136	0.0827	0.0224	8.3478	1.5942	1.8917	2.0927
SFLC	0.1097	0.0551	0.0205	0.0417	4.1712	1.2843	1.2442	1.4183
GAFLC	0.0501	0.1060	0.0324	0.0484	8.0236	1.7225	1.8598	1.9762
BI: *Base Isolator* *FF*: 1^{st} *floor* *SF*: 2^{nd} *floor* *TF*: 3^{rd} *floor*								

N. Palm Spring X-direction seismic motion

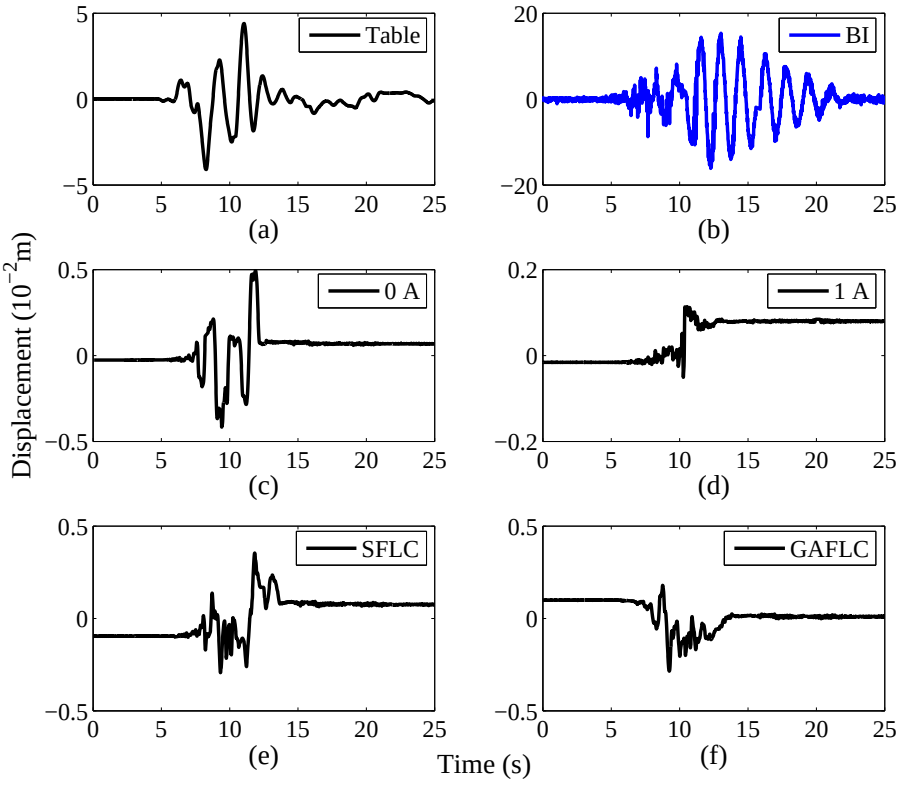

Figure C.51: Displacement time history: (a) Excitation input, (b)-(f) Isolator displacement at different cases (N. Palm Spring (X-dir))

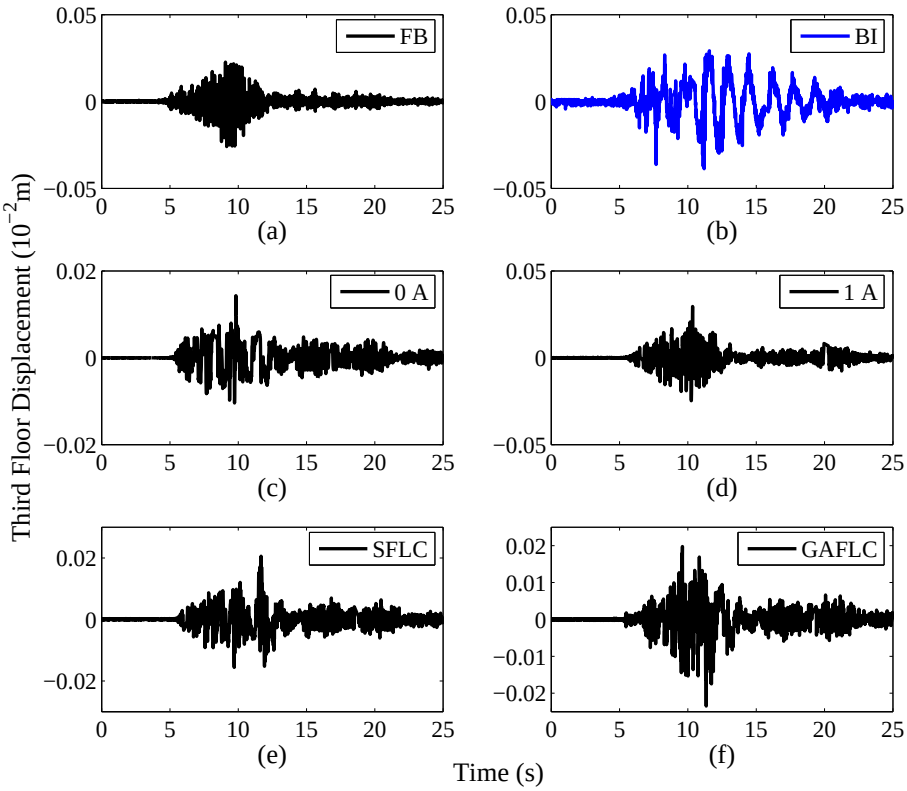

Figure C.52: 3^{rd} floor displacement time history (N. Palm Spring (X-dir))

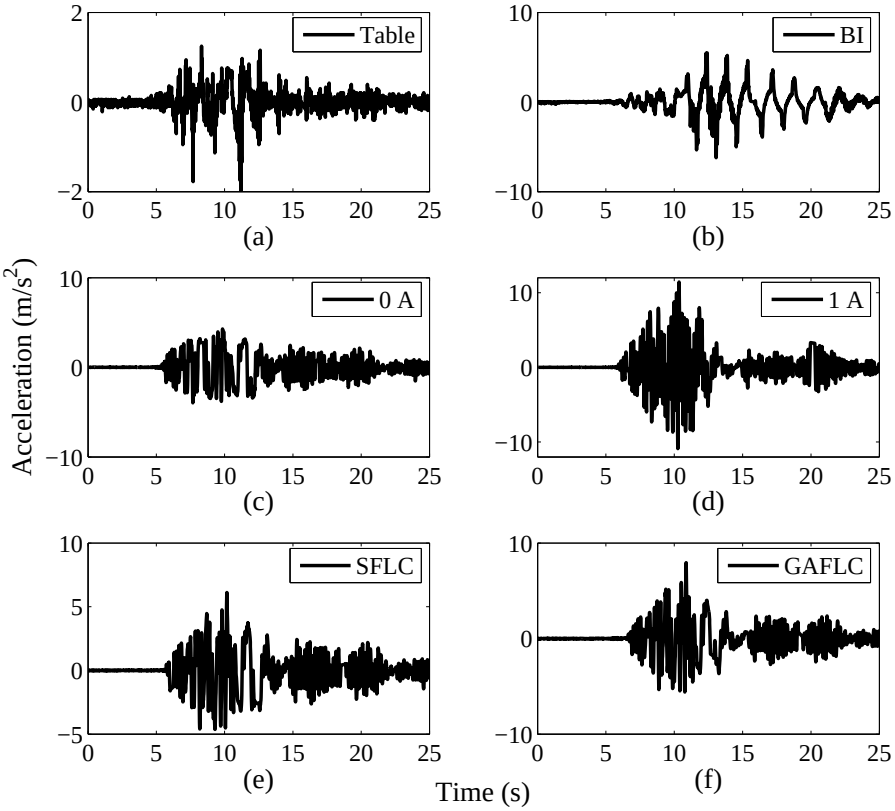

Figure C.53: Acceleration time history: (a) Excitation input, (b)-(f) Isolator acceleration at different cases (N. Palm Spring (X-dir))

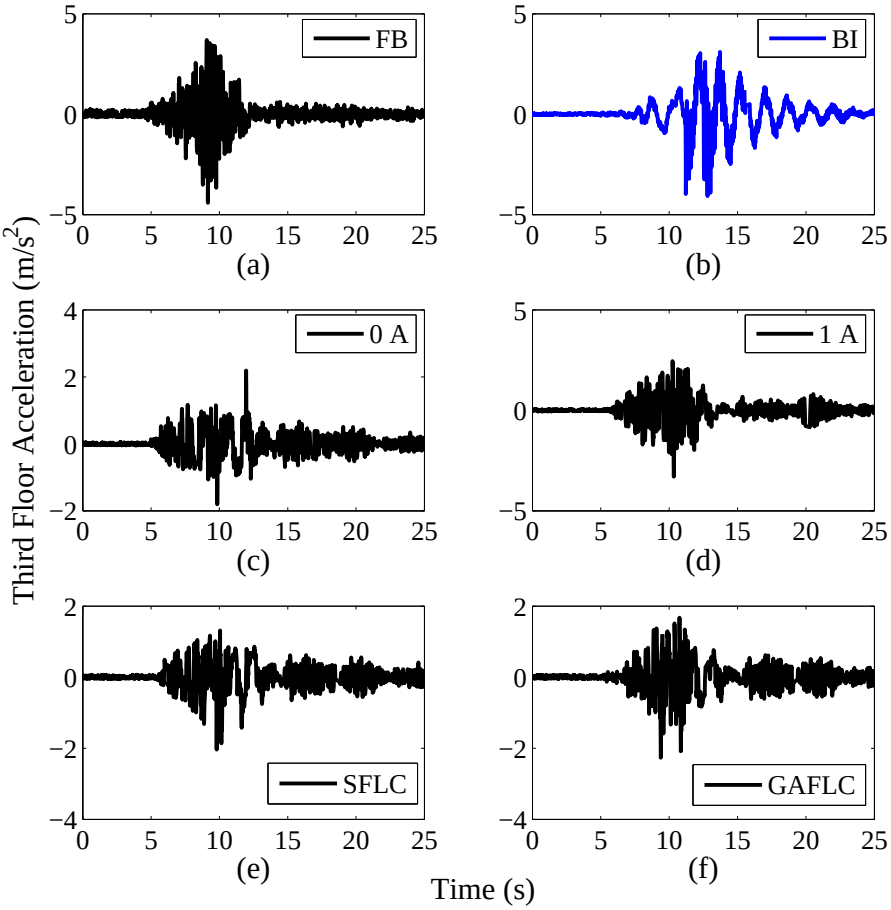

Figure C.54: 3^{rd} floor acceleration time history (N. Palm Spring (X-dir))

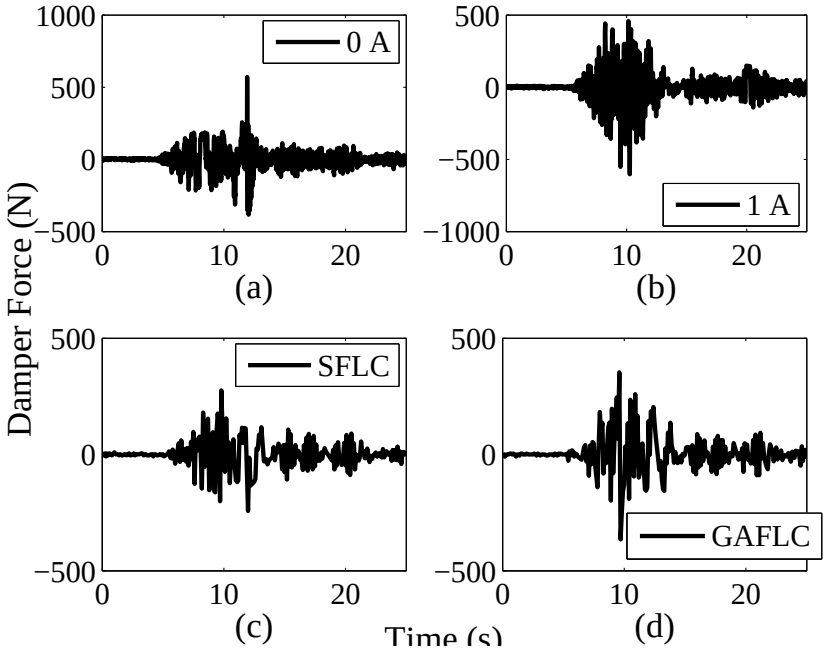

Figure C.55: MR damper force time history (N. Palm Spring (X-dir))

Table C.11: Peak responses under N. Palm Spring (X-direction) earthquake

Test Case	**Relative Displacements** ($\times 10^{-2}$ m)				**Floor Accelerations** (m/s^2)			
	BI	*FF*	*SF*	*TF*	*BI*	*FF*	*SF*	*TF*
Fixed Base	0.0000	0.2363	0.0656	0.0259	0.0000	4.1331	3.1831	4.4149
Base Isolated	16.1450	0.1993	0.0520	0.0387	6.2067	3.4458	3.1298	4.0787
0A	0.4944	0.0527	0.0213	0.0143	4.2783	1.4427	1.3976	2.1875
1A	0.1139	0.1708	0.1268	0.0296	11.4227	2.4429	2.9560	3.2977
SFLC	0.3543	0.0800	0.0288	0.0205	6.1148	1.6576	1.4659	2.0359
GAFLC	0.2859	0.1026	0.0320	0.0235	7.9447	1.8944	1.7624	2.2667
BI: *Base Isolator* *FF*: 1^{st} *floor* *SF*: 2^{nd} *floor* *TF*: 3^{rd} *floor*								

N. Palm Spring Y-direction seismic motion

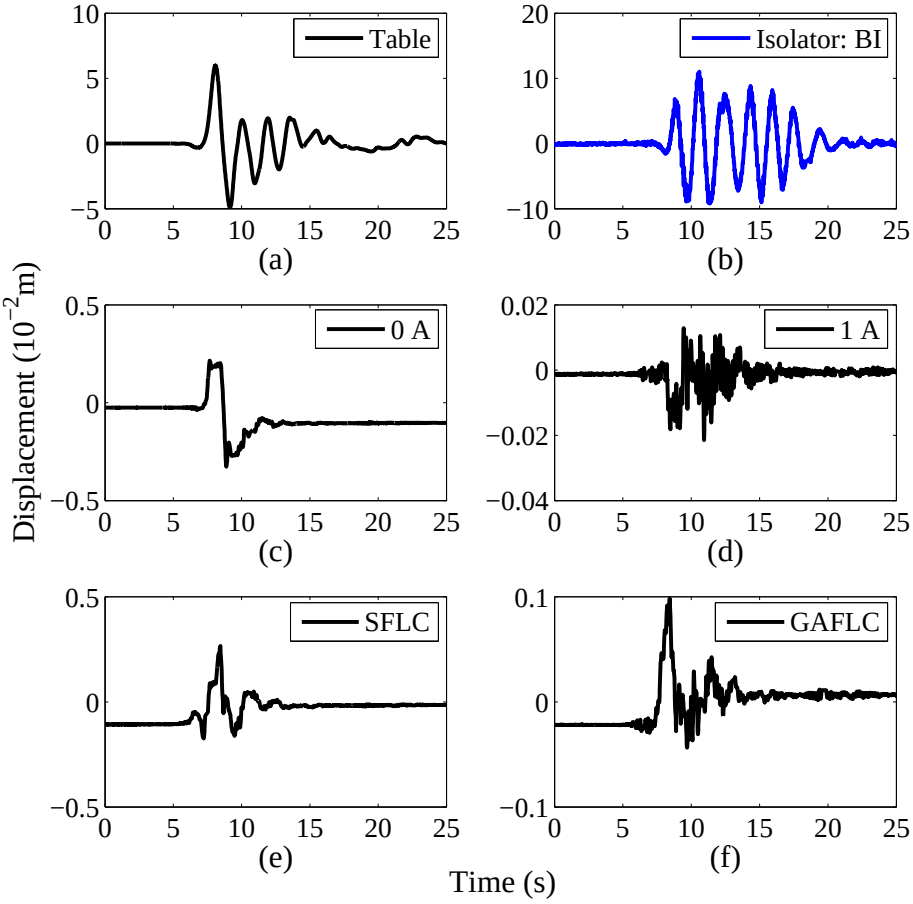

Figure C.56: Displacement time history: (a) Excitation input, (b)-(f) Isolator displacement at different cases (N. Palm Spring (Y-dir))

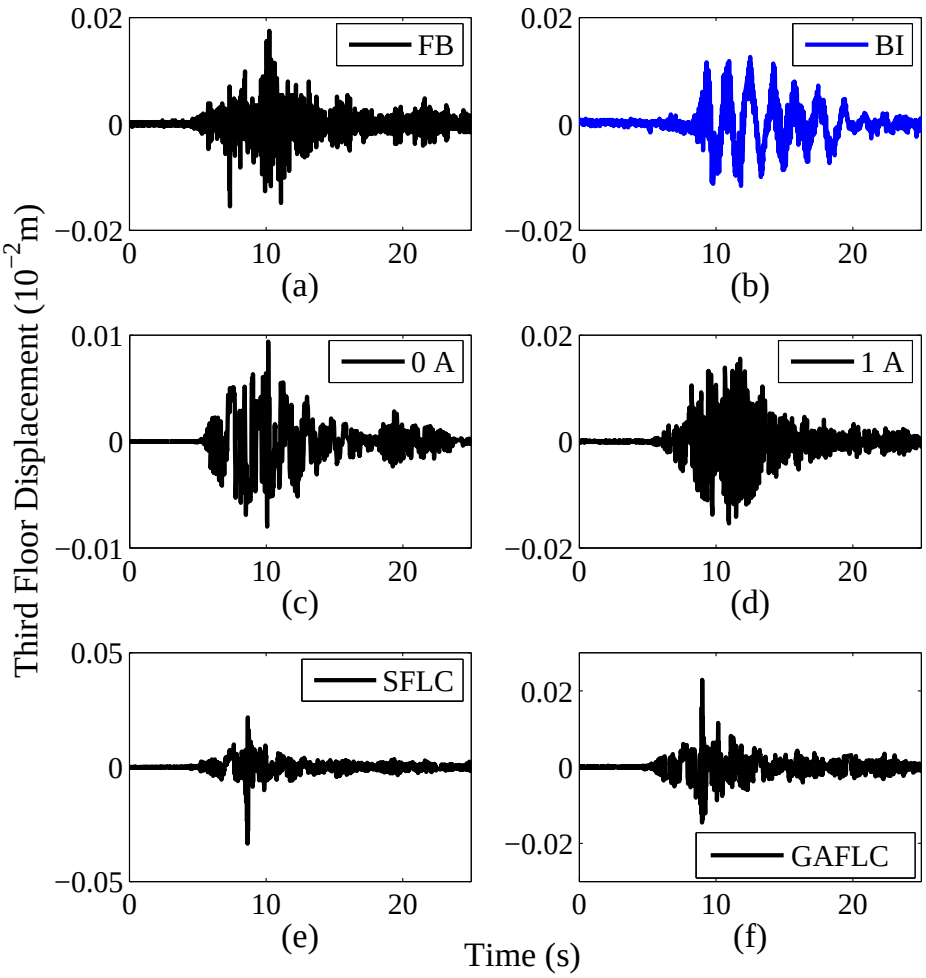

Figure C.57: 3^{rd} floor displacement time history (N. Palm Spring (Y-dir))

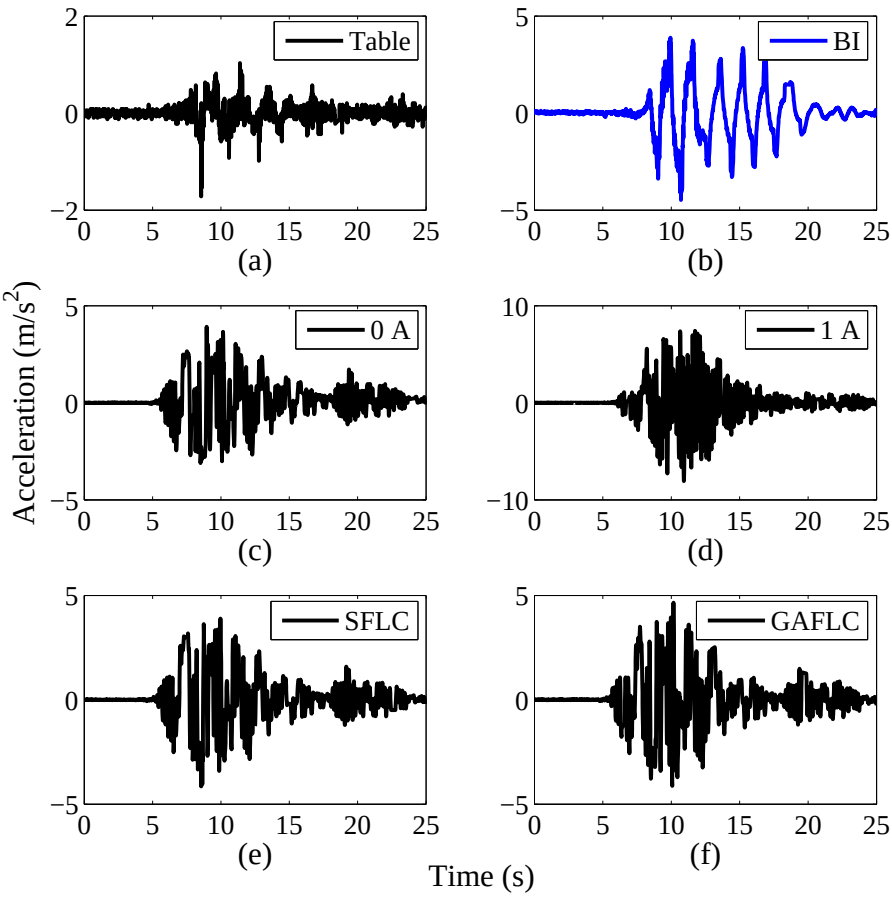

Figure C.58: Acceleration time history: (a) Excitation input, (b)-(f) Isolator acceleration at different cases (N. Palm Spring (Y-dir))

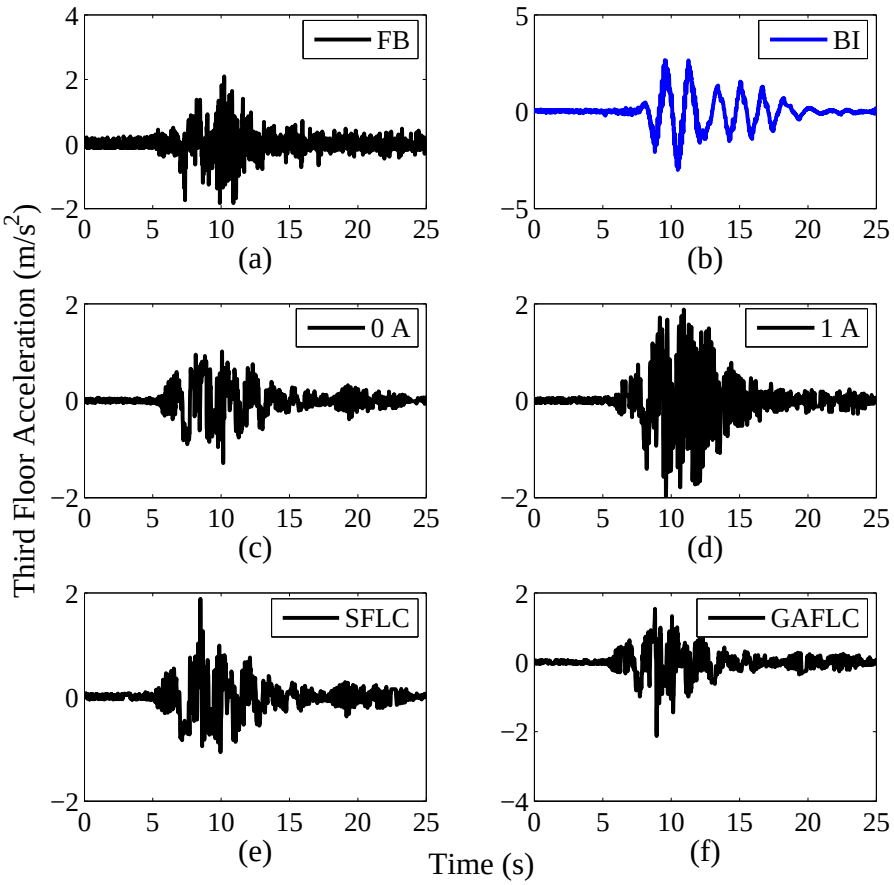

Figure C.59: 3^{rd} floor acceleration time history (N. Palm Spring (Y-dir))

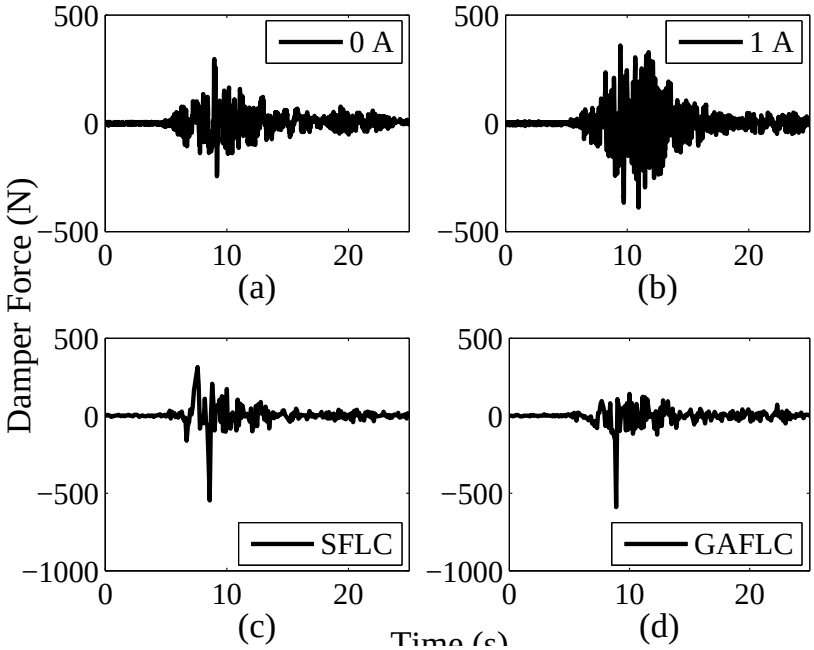

Figure C.60: MR damper force time history (N. Palm Spring (Y-dir))

Table C.12: Peak responses under N. Palm Spring (Y-direction) earthquake

Test Case	**Relative Displacements** ($\times 10^{-2}\ m$)				**Floor Accelerations** (m/s^2)			
	BI	*FF*	*SF*	*TF*	*BI*	*FF*	*SF*	*TF*
Fixed Base	0.0000	0.0921	0.0349	0.0175	0.0000	2.8427	1.8281	2.0923
Base Isolated	11.0172	0.0943	0.0246	0.0126	4.4816	2.9955	3.0073	3.0061
0A	0.3272	0.0449	0.0202	0.0094	3.9185	0.8442	0.9528	1.2879
1A	0.0215	0.1023	0.0693	0.0156	8.0670	1.4871	1.8144	1.9828
SFLC	0.2659	0.0499	0.0303	0.0335	4.1475	1.5297	1.4649	1.8872
GAFLC	0.0984	0.0621	0.0182	0.0229	4.6567	1.3756	1.8827	2.1236
BI: *Base Isolator* *FF*: 1^{st} *floor* *SF*: 2^{nd} *floor* *TF*: 3^{rd} *floor*								

Kobe X-direction seismic motion

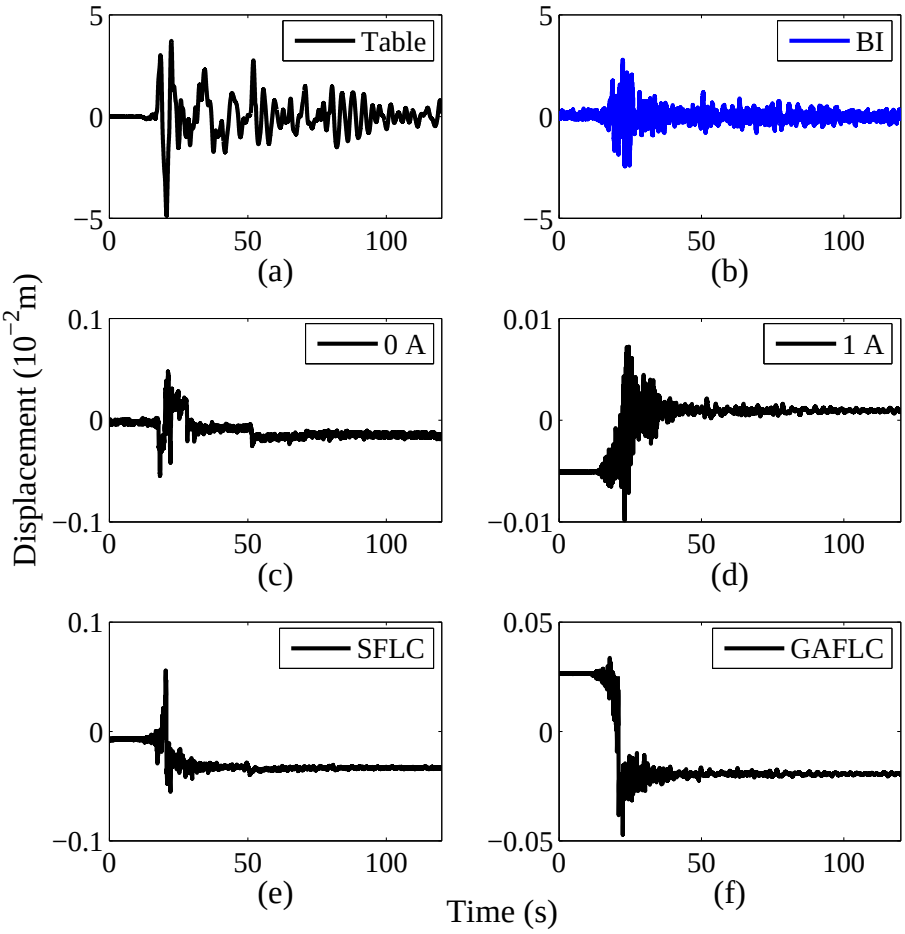

Figure C.61: Displacement time history: (a) Excitation input, (b)-(f) Isolator displacement at different cases (Kobe (X-dir))

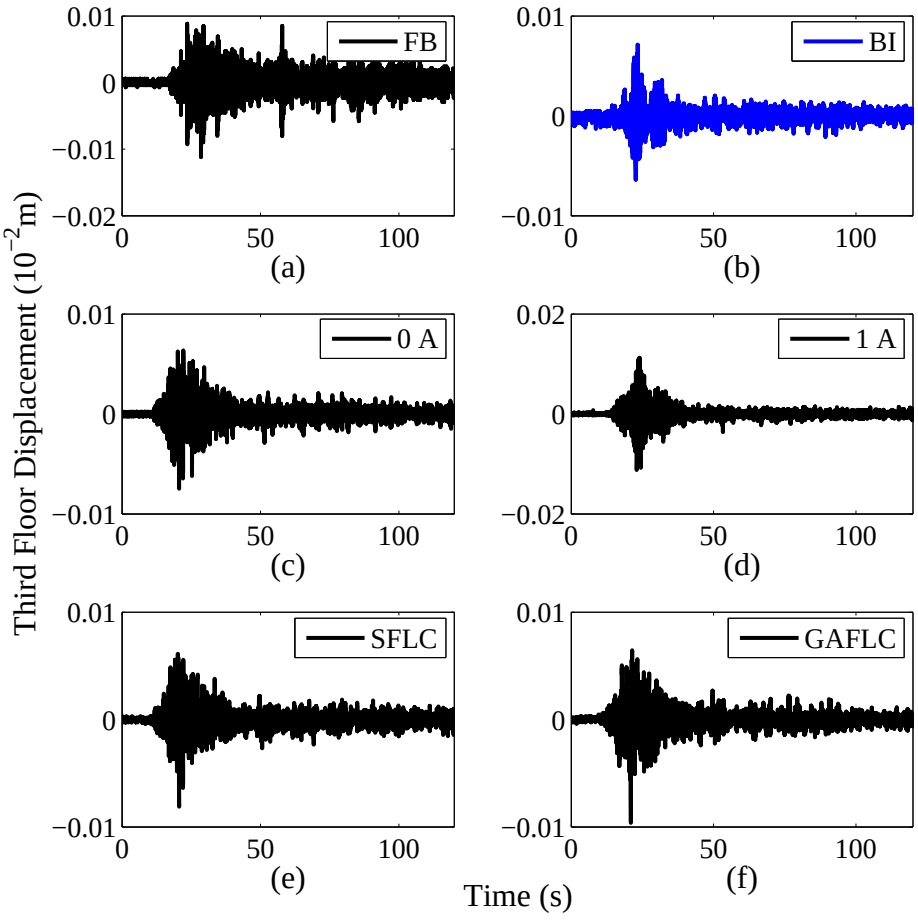

Figure C.62: 3^{rd} floor displacement time history (Kobe (X-dir))

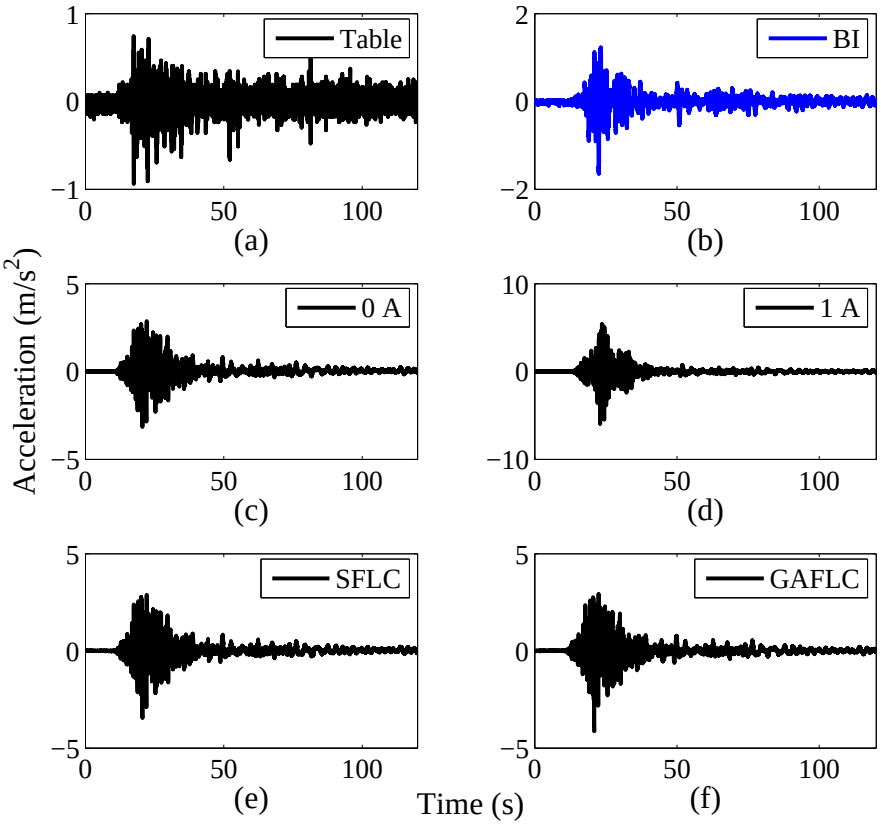

Figure C.63: Acceleration time history: (a) Excitation input, (b)-(f) Isolator acceleration at different cases (Kobe (X-dir))

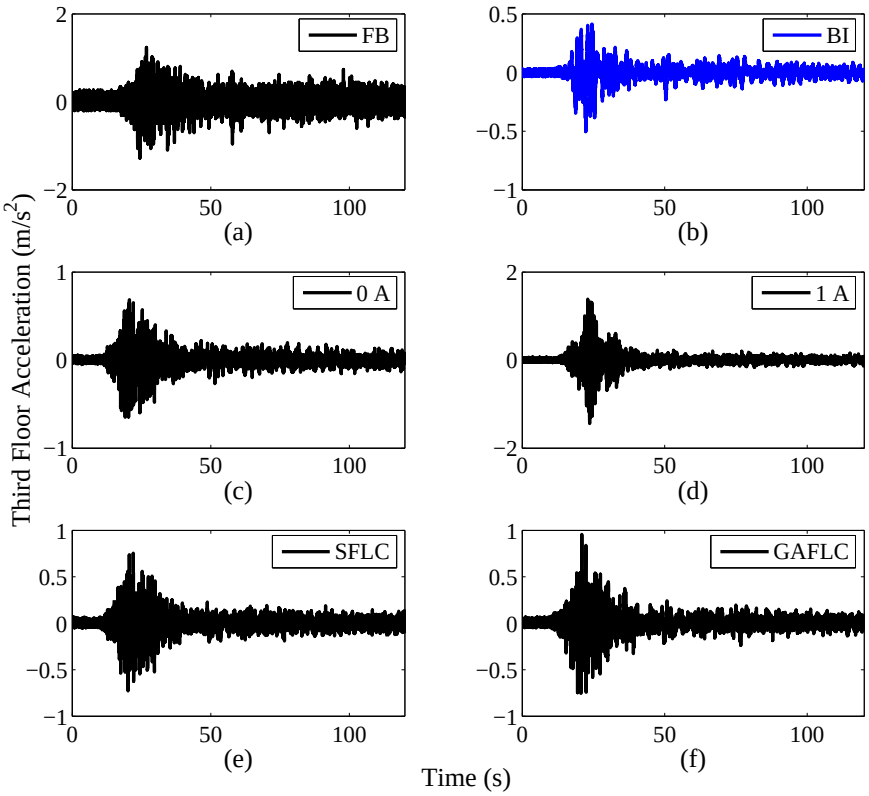

Figure C.64: 3^{rd} floor acceleration time history (Kobe (X-dir))

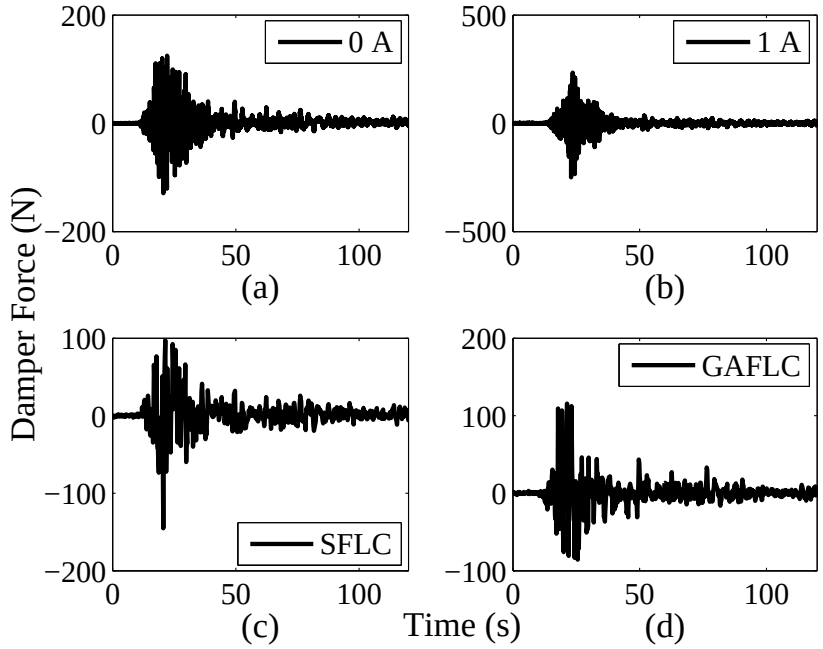

Figure C.65: MR damper force time history (Kobe (X-dir))

Table C.13: Peak responses under Kobe (X-direction) earthquake

Test Case	**Relative Displacements** ($\times 10^{-2}$ m)				**Floor Accelerations** (m/s^2)			
	BI	*FF*	*SF*	*TF*	*BI*	*FF*	*SF*	*TF*
Fixed Base	0.0000	0.0738	0.0115	0.0112	0.0000	1.1144	1.2258	1.2779
Base Isolated	2.7897	0.0308	0.0081	0.0071	1.6422	0.5015	0.4596	0.5035
0A	0.0550	0.0453	0.0137	0.0075	3.1571	0.5573	0.6287	0.6862
1A	0.0099	0.0791	0.0231	0.0112	5.9497	1.1374	1.3512	1.4414
SFLC	0.0555	0.0504	0.0146	0.0081	3.4534	0.6137	0.6971	0.7540
GAFLC	0.0472	0.0612	0.0172	0.0096	4.1395	0.7789	0.8161	0.9563
BI: *Base Isolator* *FF*: 1^{st} *floor* *SF*: 2^{nd} *floor* *TF*: 3^{rd} *floor*								

Kobe Y-direction seismic motion

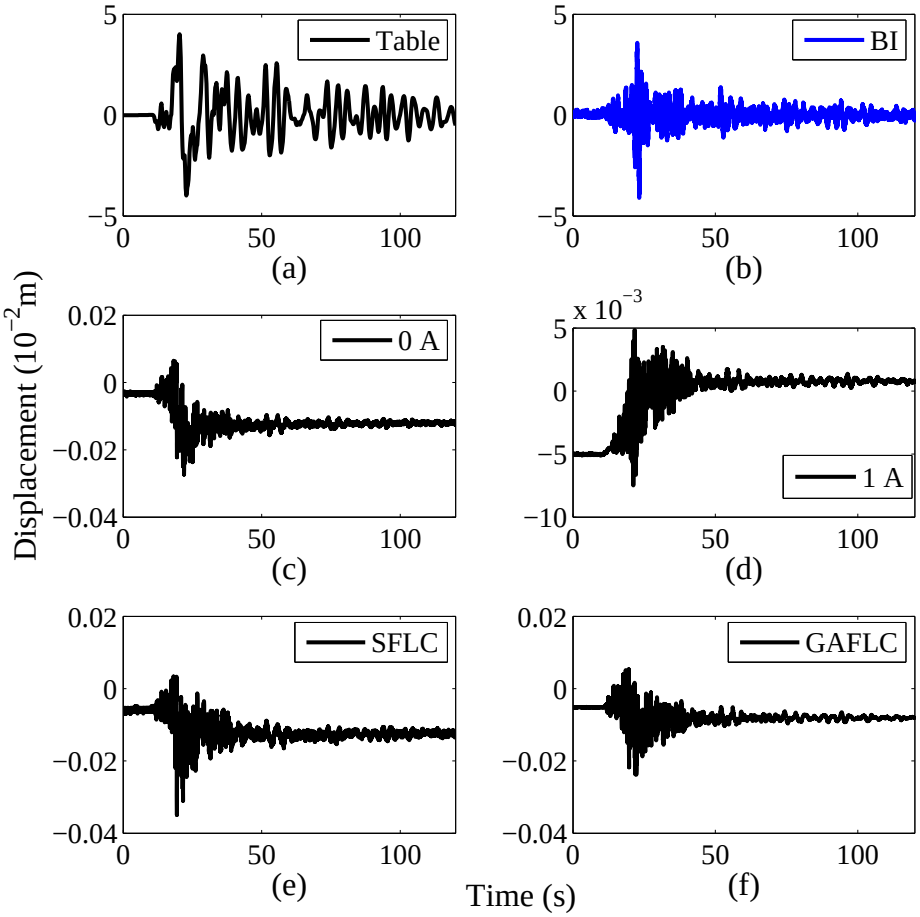

Figure C.66: Displacement time history: (a) Excitation input, (b)-(f) Isolator displacement at different cases (Kobe (Y-dir))

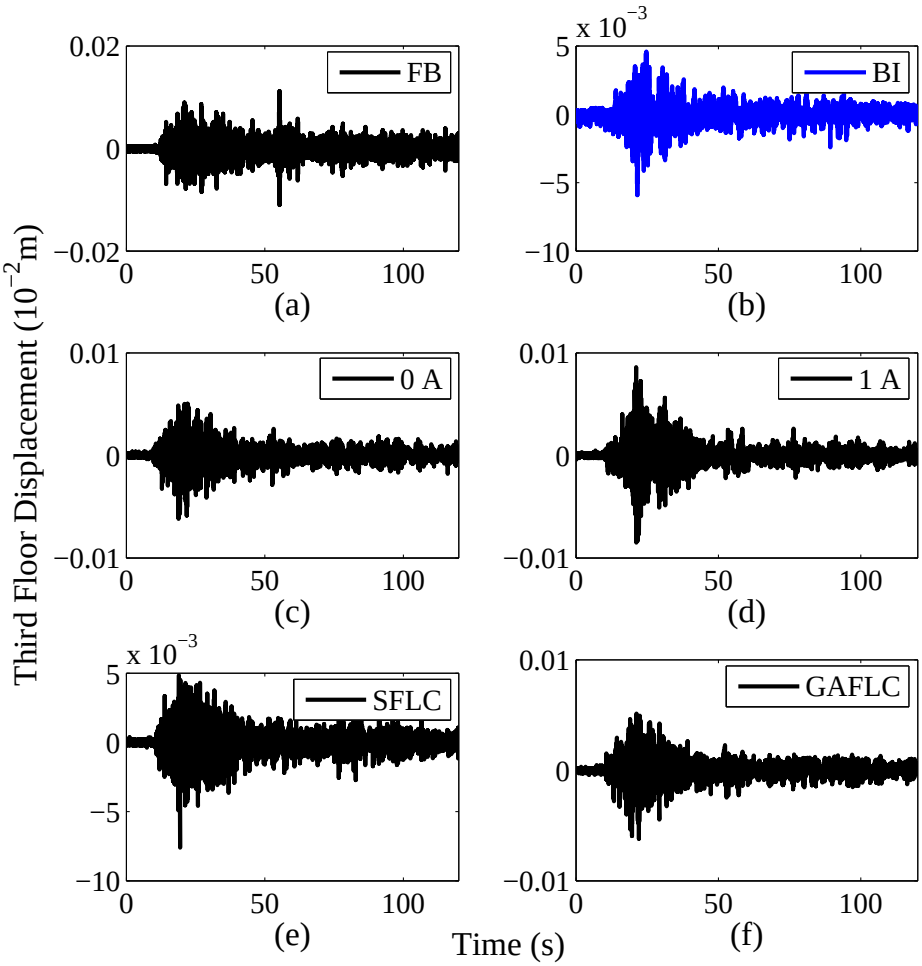

Figure C.67: 3^{rd} floor displacement time history (Kobe (Y-dir))

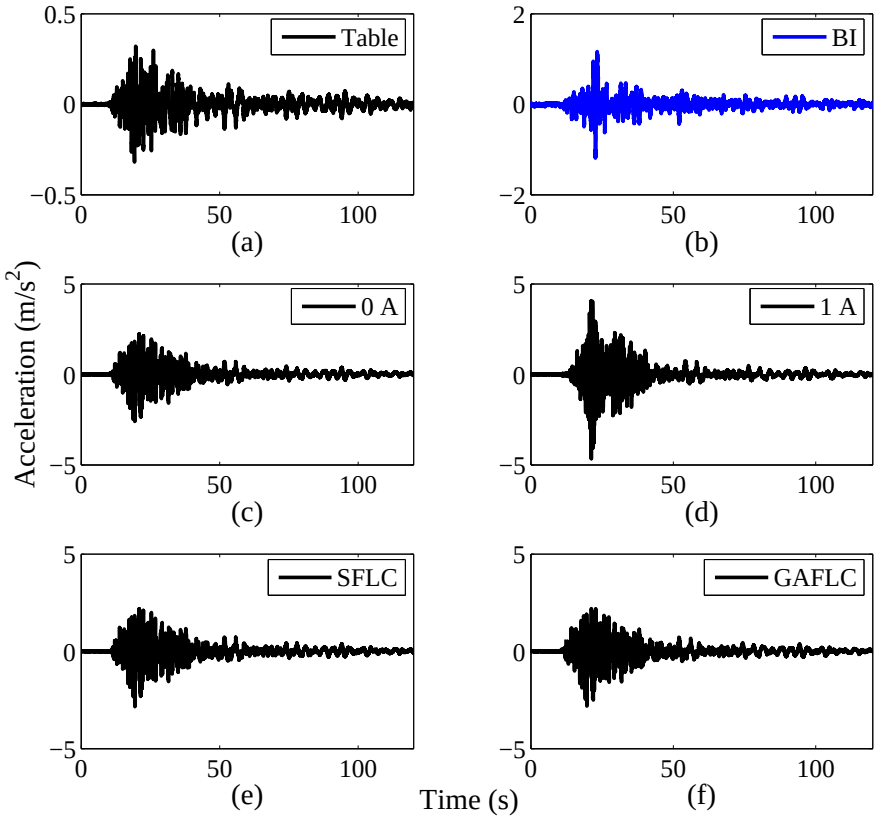

Figure C.68: Acceleration time history: (a) Excitation input, (b)-(f) Isolator acceleration at different cases (Kobe (Y-dir))

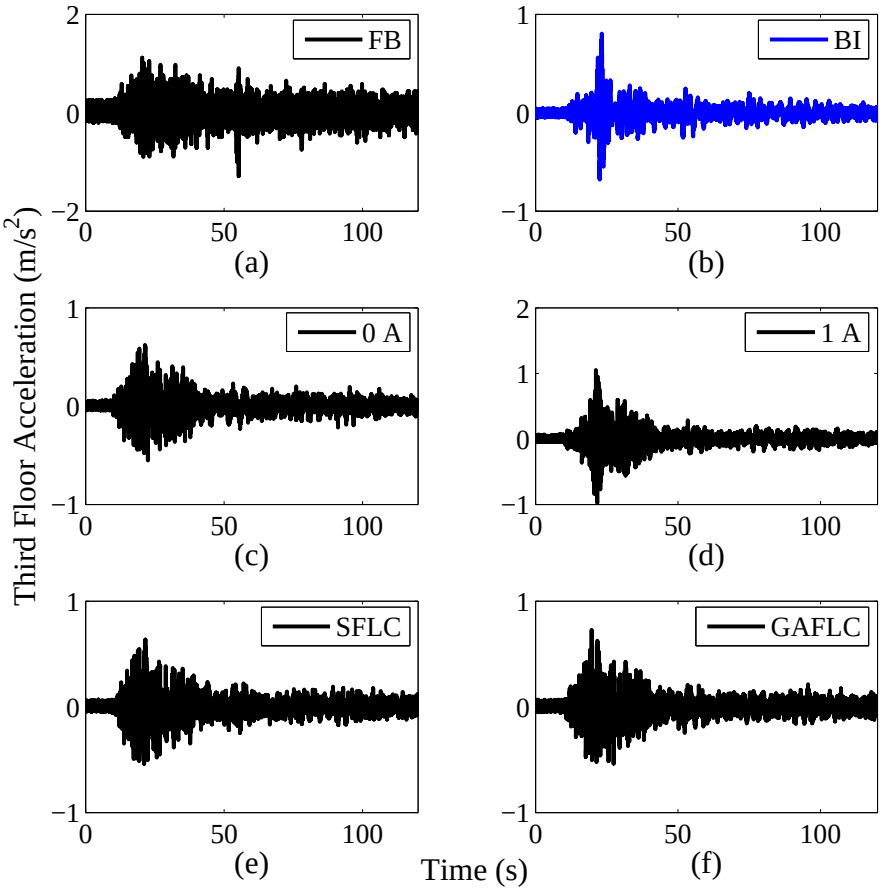

Figure C.69: 3^{rd} floor acceleration time history (Kobe (Y-dir))

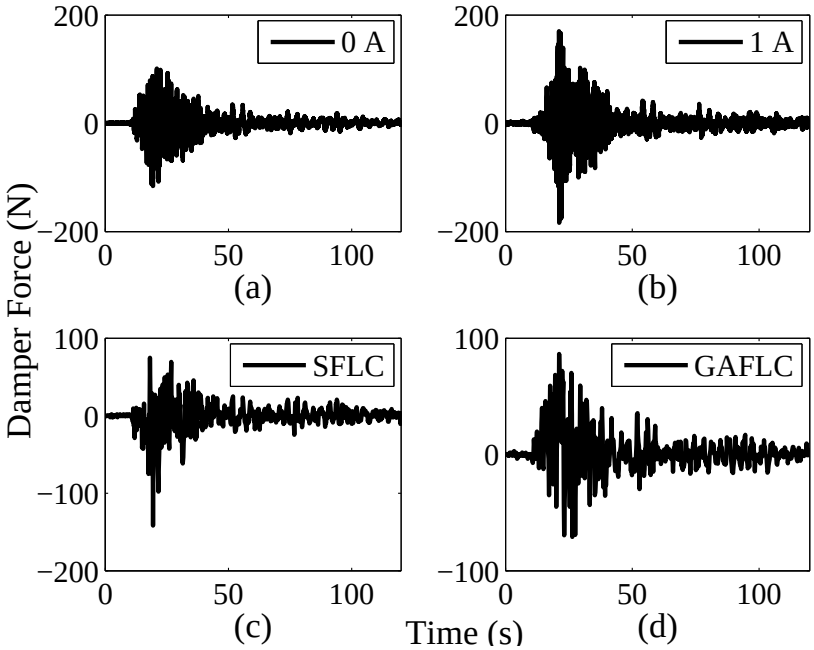

Figure C.70: MR damper force time history (Kobe (Y-dir))

Table C.14: Peak responses under Kobe (Y-direction) earthquake

Test Case	**Relative Displacements** ($\times 10^{-2}\ m$)				**Floor Accelerations** (m/s^2)			
	BI	*FF*	*SF*	*TF*	*BI*	*FF*	*SF*	*TF*
Fixed Base	0.0000	0.0536	0.0100	0.0112	0.0000	1.4402	1.0686	1.2874
Base Isolated	4.1009	0.0331	0.0088	0.0059	1.1899	0.7176	0.7390	0.8048
0A	0.0274	0.0392	0.0109	0.0062	2.5920	0.5595	0.5954	0.6217
1A	0.0075	0.0602	0.0179	0.0086	4.6559	0.9117	1.0673	1.0524
SFLC	0.0350	0.0460	0.0130	0.0076	2.8395	0.5667	0.6147	0.6358
GAFLC	0.0238	0.0394	0.0116	0.0062	2.8136	0.5275	0.6638	0.7243
BI: *Base Isolator*	*FF*: 1^{st} *floor*		*SF*: 2^{nd} *floor*		*TF*: 3^{rd} *floor*			

Loma Prieta X-direction seismic motion

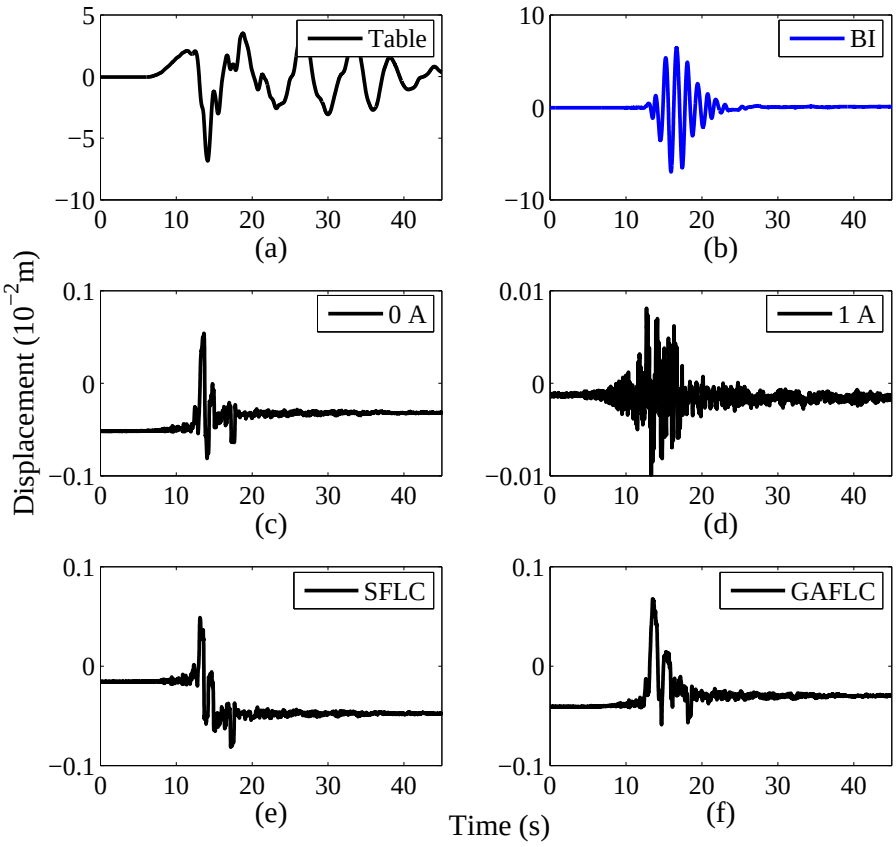

Figure C.71: Displacement time history: (a) Excitation input, (b)-(f) Isolator displacement at different cases (Loma Prieta (X-dir))

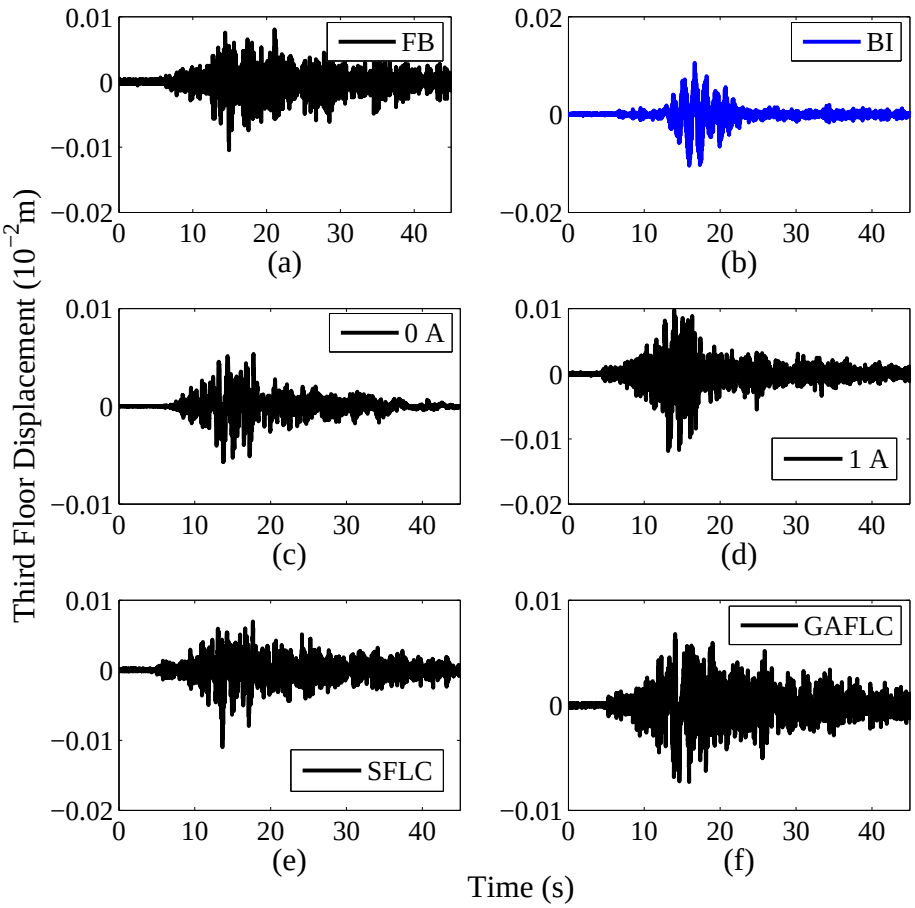

Figure C.72: 3^{rd} floor displacement time history (Loma Prieta (X-dir))

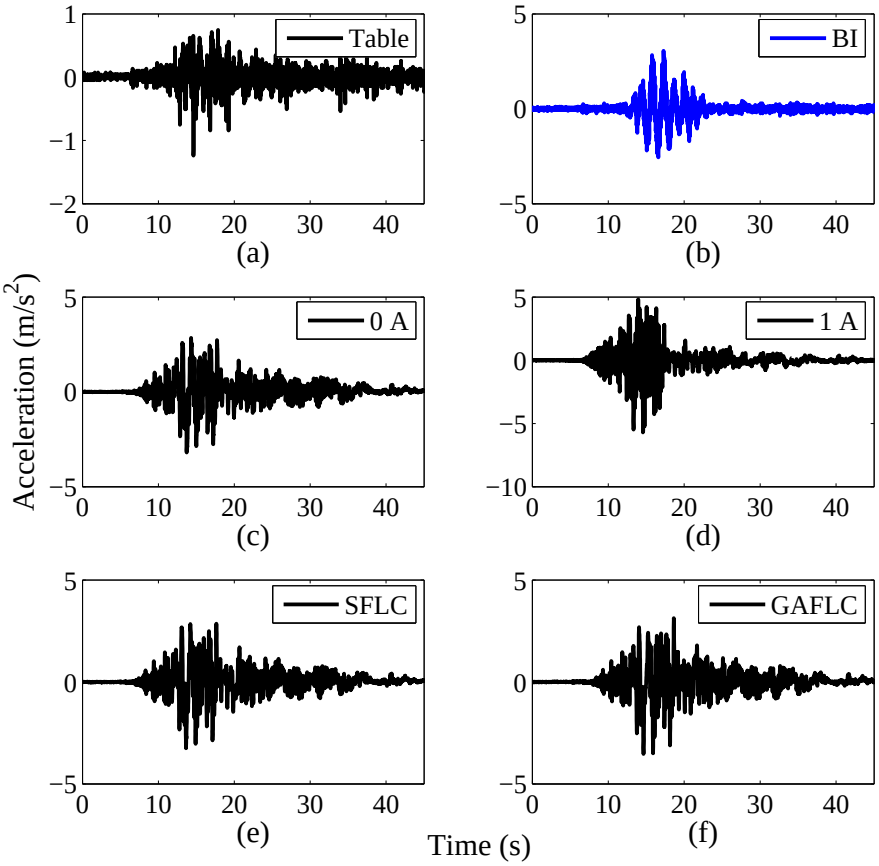

Figure C.73: Acceleration time history: (a) Excitation input, (b)-(f) Isolator acceleration at different cases (Loma Prieta (X-dir))

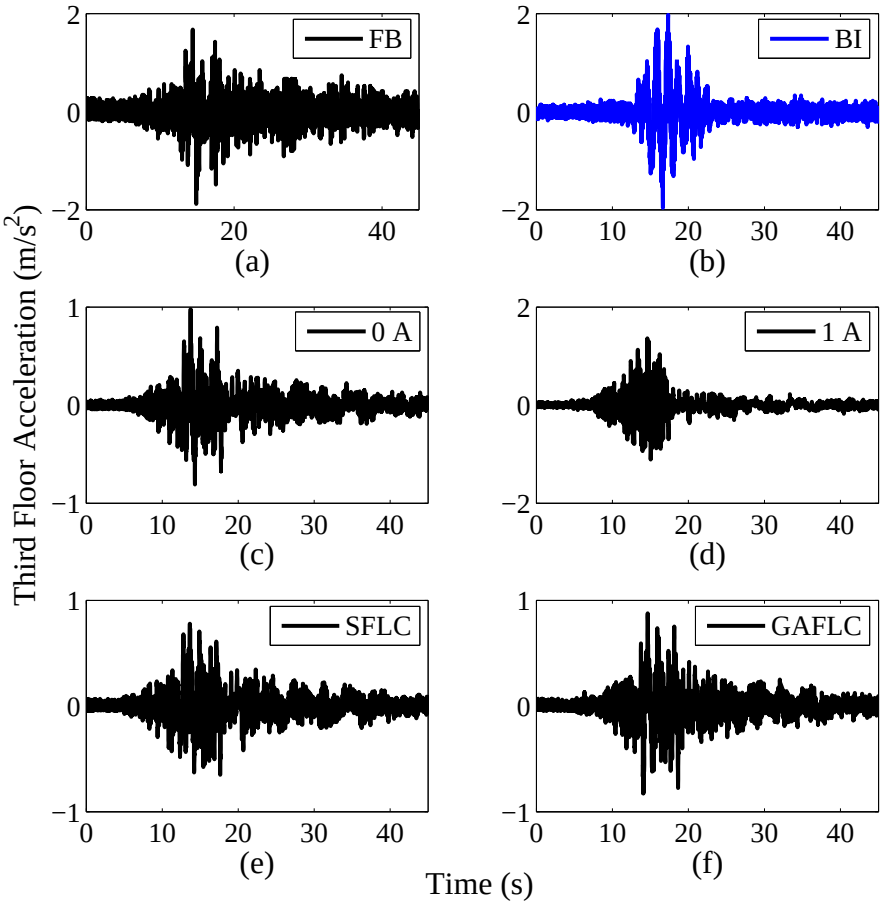

Figure C.74: 3^{rd} floor acceleration time history (Loma Prieta (X-dir))

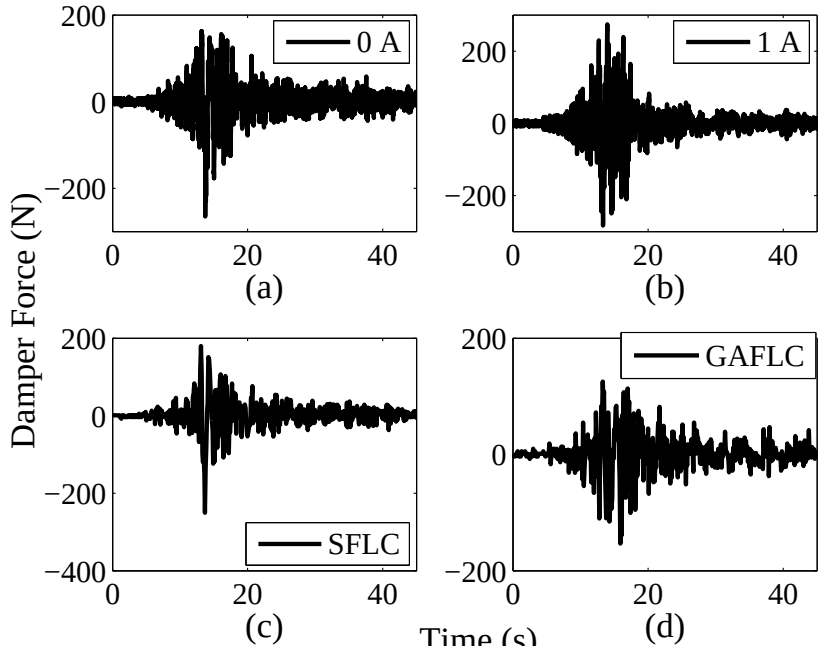

Figure C.75: MR damper force time history (Loma Prieta (X-dir))

Table C.15: Peak responses under Loma Prieta (X-direction) earthquake

Test Case	**Relative Displacements** ($\times 10^{-2}\ m$)				**Floor Accelerations** (m/s^2)			
	BI	*FF*	*SF*	*TF*	*BI*	*FF*	*SF*	*TF*
Fixed Base	0.0000	0.0732	0.0258	0.0105	0.0000	1.6228	2.0049	1.8812
Base Isolated	6.9819	0.0769	0.0253	0.0106	3.0539	1.5580	1.7181	1.9744
0A	0.0812	0.0393	0.0141	0.0057	3.1921	0.7080	0.6990	0.9791
1A	0.0099	0.0763	0.0552	0.0119	5.7117	1.1801	1.3414	1.3631
SFLC	0.0815	0.0393	0.0670	0.0110	3.2491	0.7534	0.6932	0.7797
GAFLC	0.0677	0.0477	0.0141	0.0073	3.5330	0.8257	0.8980	0.8768
BI: *Base Isolator* *FF*: 1^{st} *floor* *SF*: 2^{nd} *floor* *TF*: 3^{rd} *floor*								

Loma Prieta Y-direction seismic motion

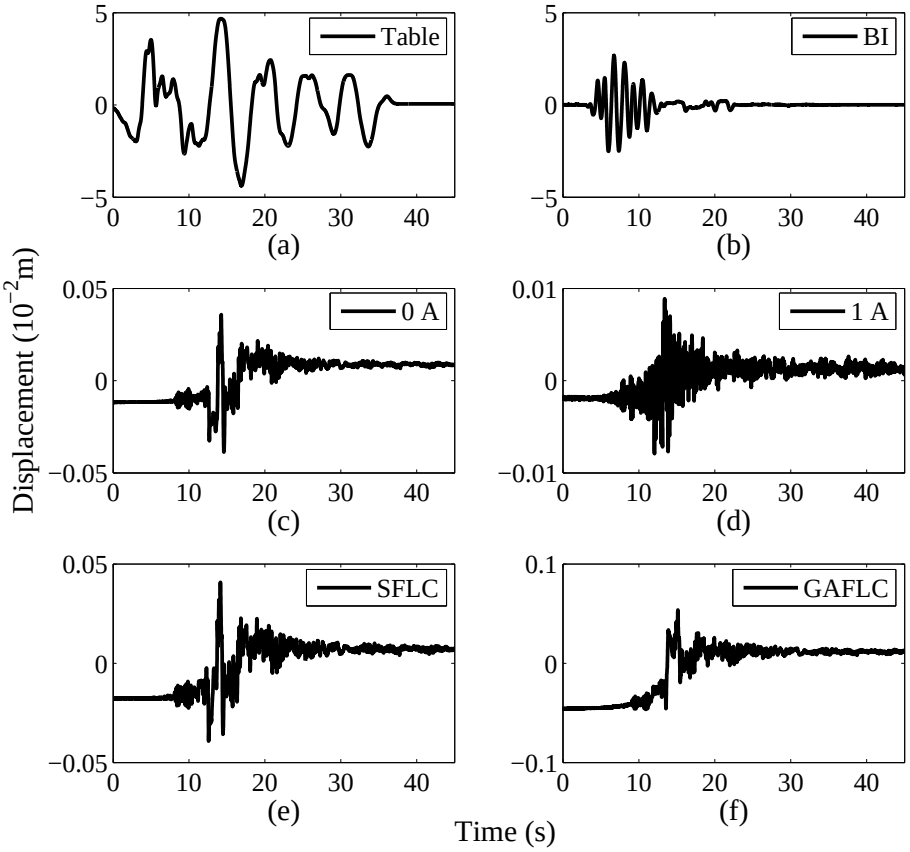

Figure C.76: Displacement time history: (a) Excitation input, (b)-(f) Isolator displacement at different cases (Loma Prieta (Y-dir))

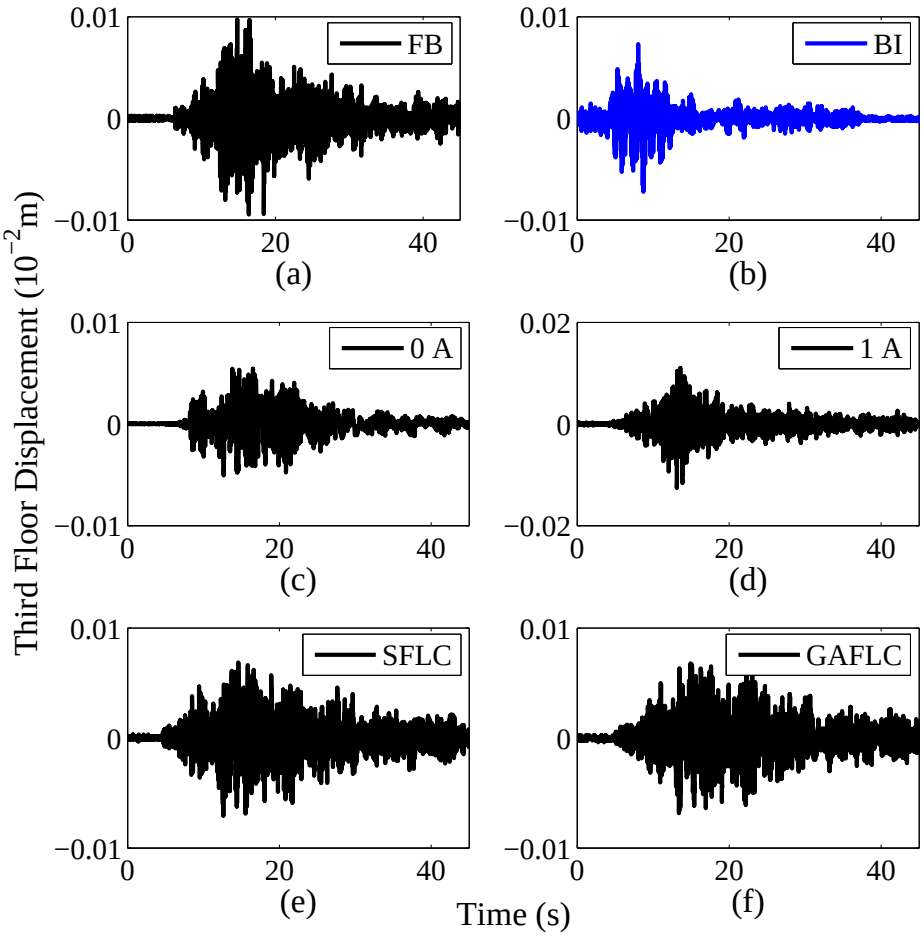

Figure C.77: 3^{rd} floor displacement time history (Loma Prieta (Y-dir))

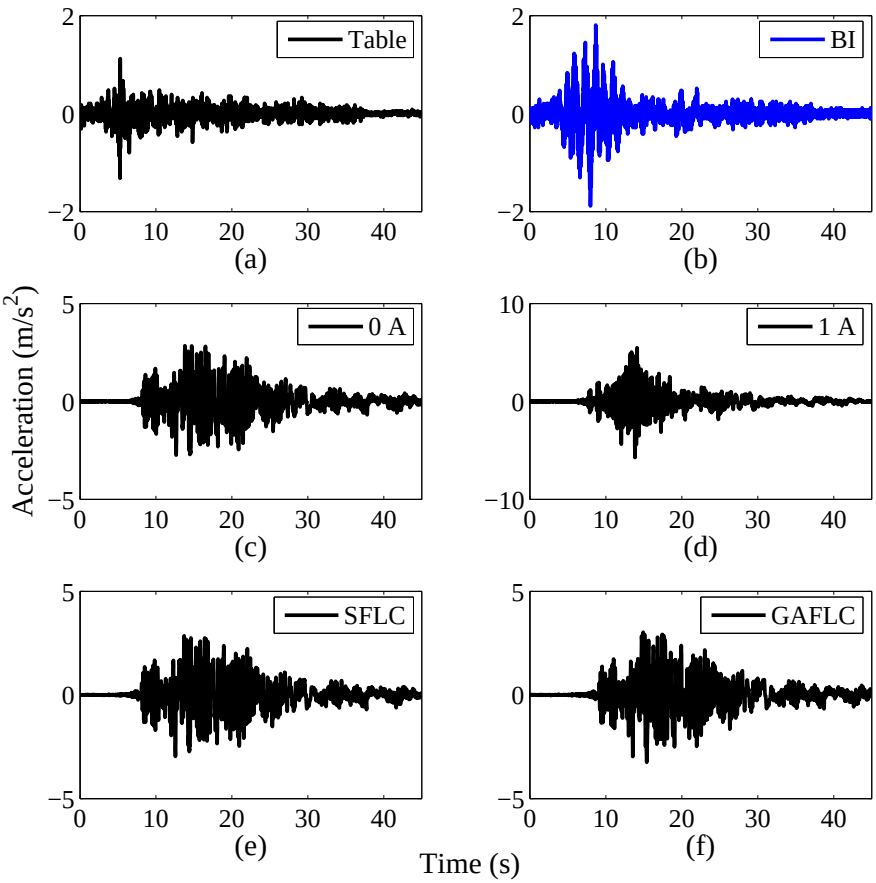

Figure C.78: Acceleration time history: (a) Excitation input, (b)-(f) Isolator acceleration at different cases (Loma Prieta (Y-dir))

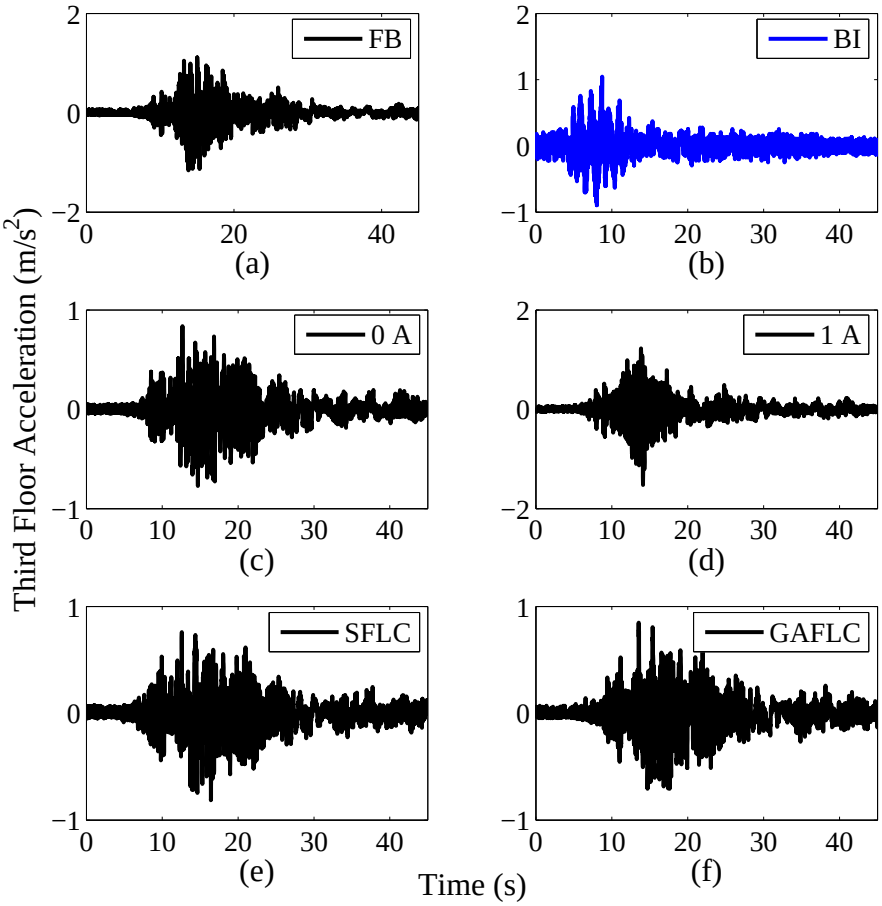

Figure C.79: 3^{rd} floor acceleration time history (Loma Prieta (Y-dir))

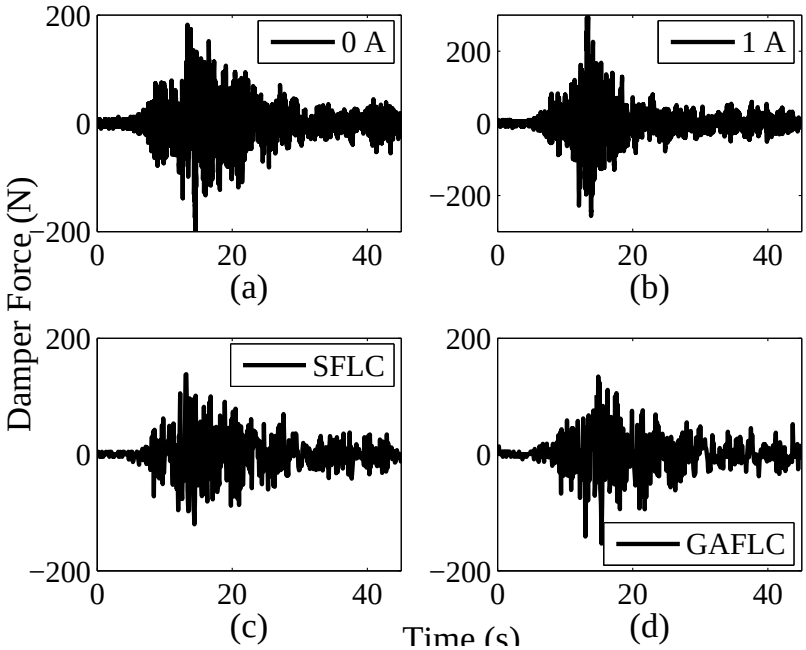

Figure C.80: MR damper force time history (Loma Prieta (Y-dir))

Table C.16: Peak responses under Loma Prieta (Y-direction) earthquake

Test Case	**Relative Displacements** ($\times 10^{-2}\ m$)				**Floor Accelerations** (m/s^2)			
	BI	*FF*	*SF*	*TF*	*BI*	*FF*	*SF*	*TF*
Fixed Base	0.0000	0.0626	0.0732	0.0098	0.0000	0.9574	1.0891	1.1582
Base Isolated	2.6907	0.0391	0.0129	0.0073	1.8861	0.8160	0.7676	1.0452
0A	0.0387	0.0366	0.0137	0.0054	2.8444	0.6944	0.7608	0.8366
1A	0.0089	0.0755	0.0539	0.0126	5.7410	1.0757	1.3675	1.5246
SFLC	0.0408	0.0394	0.0123	0.0071	2.9654	0.6963	0.7119	0.8146
GAFLC	0.0537	0.0425	0.0125	0.0068	3.2490	0.8347	0.7823	0.8491
BI: *Base Isolator* *FF*: 1^{st} *floor* *SF*: 2^{nd} *floor* *TF*: 3^{rd} *floor*								